

Spring 1-1-2016

# Optimization of Pressure Probe Placement and Data Analysis of Engine-Inlet Distortion

Sibylle F. Walter

University of Colorado at Boulder, sibylle.walter@gmail.com

Follow this and additional works at: [https://scholar.colorado.edu/asen\\_gradetds](https://scholar.colorado.edu/asen_gradetds)

 Part of the [Aerodynamics and Fluid Mechanics Commons](#)

## Recommended Citation

Walter, Sibylle F., "Optimization of Pressure Probe Placement and Data Analysis of Engine-Inlet Distortion" (2016). *Aerospace Engineering Sciences Graduate Theses & Dissertations*. 154.  
[https://scholar.colorado.edu/asen\\_gradetds/154](https://scholar.colorado.edu/asen_gradetds/154)

This Dissertation is brought to you for free and open access by Aerospace Engineering Sciences at CU Scholar. It has been accepted for inclusion in Aerospace Engineering Sciences Graduate Theses & Dissertations by an authorized administrator of CU Scholar. For more information, please contact [cuscholaradmin@colorado.edu](mailto:cuscholaradmin@colorado.edu).

**Optimization of pressure probe placement and data analysis  
of engine-inlet distortion**

by

**S. F. Walter**

B.S., University of Maryland, College Park, 2007

M.S., University of Colorado at Boulder, 2012

A thesis submitted to the  
Faculty of the Graduate School of the  
University of Colorado in partial fulfillment  
of the requirements for the degree of  
Doctor of Philosophy  
Department of Aerospace Engineering Sciences  
2016

This thesis entitled:  
Optimization of pressure probe placement and data analysis of engine-inlet distortion  
written by S. F. Walter  
has been approved for the Department of Aerospace Engineering Sciences

---

Prof. Ryan P. Starkey

---

Prof. Brian Argrow

---

Prof. John Daily

---

Prof. Alireza Doostan

---

Prof. Peter Hamlington

---

Prof. James Nabity

Date \_\_\_\_\_

The final copy of this thesis has been examined by the signatories, and we find that both the content and the form meet acceptable presentation standards of scholarly work in the above mentioned discipline.

Walter, S. F. (Ph.D., Aerospace Engineering Sciences)

Optimization of pressure probe placement and data analysis of engine-inlet distortion

Thesis directed by Prof. Ryan P. Starkey

Abstract:

The purpose of this research is to examine methods by which quantification of inlet flow distortion may be improved upon. Specifically, this research investigates how data interpolation effects results, optimizing sampling locations of the flow, and determining the sensitivity related to how many sample locations there are. The main parameters that are indicative of a "good" design are total pressure recovery, mass flow capture, and distortion. This work focuses on the total pressure distortion, which describes the amount of non-uniformity that exists in the flow as it enters the engine. All engines must tolerate some level of distortion, however too much distortion can cause the engine to stall or the inlet to unstart. Flow distortion is measured at the interface between the inlet and the engine.

To determine inlet flow distortion, a combination of computational and experimental pressure data is generated and then collapsed into an index that indicates the amount of distortion. Computational simulations generate continuous contour maps, but experimental data is discrete. Researchers require continuous contour maps to evaluate the overall distortion pattern. There is no guidance on how to best manipulate discrete points into a continuous pattern. Using one experimental, 320 probe data set and one, 320 point computational data set with three test runs each, this work compares the pressure results obtained using all 320 points of data from the original sets, both quantitatively and qualitatively, with results derived from selecting 40 grid point subsets and interpolating to 320 grid points. Each of the two, 40 point sets were interpolated to 320 grid points using four different interpolation methods in an attempt to establish the best method for interpolating small sets of data into an accurate, continuous contour map. Interpolation methods investigated are bilinear, spline, and Kriging in Cartesian space, as well as angular in polar space.

Spline interpolation methods should be used as they result in the most accurate, precise, and visually correct predictions when compared results achieved from the full data sets.

Researchers were interested if fewer than the recommended 40 probes could be used – especially when placed in areas of high interest - but still obtain equivalent or better results. For this investigation, the computational results from a two-dimensional inlet and experimental results of an axisymmetric inlet were used. To find the areas of interest, a uniform sampling of all possible locations was run through a Monte Carlo simulation with a varying number of probes. A probability density function of the resultant distortion index was plotted. Certain probes are required to come within the desired accuracy level of the distortion index based on the full data set. For the experimental results, all three test cases could be characterized with 20 probes. For the axisymmetric inlet, placing 40 probes in select locations could get the results for parameters of interest within less than 10% of the exact solution for almost all cases. For the two dimensional inlet, the results were not as clear. 80 probes were required to get within 10% of the exact solution for all run numbers, although this is largely due to the small value of the exact result.

The sensitivity of each probe added to the experiment was analyzed. Instead of looking at the overall pattern established by optimizing probe placements, the focus is on varying the number of sampled probes from 20 to 40. The number of points falling within a 1% tolerance band of the exact solution were counted as good points. The results were normalized for each data set and a general sensitivity function was found to determine the sensitivity of the results. A linear regression was used to generalize the results for all data sets used in this work. However, they can be used by directly comparing the number of good points obtained with various numbers of probes as well. The sensitivity in the results is higher when fewer probes are used and gradually tapers off near 40 probes. There is a bigger gain in good points when the number of probes is increased from 20 to 21 probes than from 39 to 40 probes.

## Dedication

I want to extend a warm thank you to everyone who has helped me through this experience - whether by helping me with my research, keeping me focused, or even getting my mind off my research for a while. I'm afraid that I could write a whole dissertation thanking each and every one of you. Getting through this PhD was a team effort and I thank you from the bottom of my heart for being on my team!

To my parents, Kim and Marianne, I want to say thank you for all you have done over the past three decades for me. I wouldn't have made it this far without your unwavering, unconditional, loving support and encouragement, even when I didn't want to listen. Your insistence that I keep up with my math was probably good advice after all.

To my siblings, Dirk, Katja, and Rasmus, for teaching me at an early age to roll with the punches and not to sweat the small stuff. Each one of you left me a blueprint on how to be successful. Being the youngest does have its advantages after all.

To my in-laws, Nancy and Marty, for accepting me into your family and being there to lend a helping hand when I needed it.

To my non-academic teachers - Diane, Jeff, Joe, Nalini - thank you for being incredibly generous with advice and encouragement.

And lastly, but certainly not least, I would like to thank my husband, Brad. To list all the ways you've been a lifesaver over the past few years is impossible. I'm sure there will be many more ups and downs, but I am so glad that you're on this ride next to me. I love you and can't wait for our next chapter together.

## Acknowledgements

This work was funded in large part by the NASA Aeronautics Research Mission Directorate via the NASA Aeronautics Scholarship Program, grant number NNX14AE13H.

Further funding was provided by the Graduate Assistantship in Areas of National Need fellowship and three teaching assistantships through the Department of Aerospace Engineering Sciences.

I wish to thank my committee members for their time and effort spent helping me with my research and dissertation. A special thank you to Dr. Ryan Starkey, my research adviser and committee chairman, for the years of support. Another special thank you to my co-adviser Dr. James Nabity for all of his guidance. Thank you to Dr. Brian Argrow, Dr. John Daily, Dr. Alireza Doostan, and Dr. Peter Hamlington for agreeing to serve on my committee and guide me through this process.

I would like to acknowledge NASA Glenn Research Center's Inlets and Nozzles branch for providing me with experience and assistance through my two internships. A very special thank you to David O. Davis and J. D. Saunders for taking me under their wing and opening up a whole new world of research to me. Another very special thank you to John Slater for providing me with computational data.

To everyone in the Busemann Advanced Concepts Laboratory, thank you for all the advice and support. Special thank you to Kevin Basore, Matt Cannella, Ben Dunham, Tim Jung, Naveen Penmetsa, Greg Rancourt, and Nate Woods.

## Contents

### Chapter

<b>1</b>	<b>Introduction</b>	<b>1</b>
1.1	Historical Context . . . . .	1
1.2	Problem Statement . . . . .	3
1.3	Assumptions . . . . .	4
1.4	Overview . . . . .	4
<b>2</b>	<b>Background</b>	<b>6</b>
2.1	Combined Cycle Engine Definition . . . . .	7
2.2	Air Breathing Reusable Launch Vehicle Engine Work to Date . . . . .	11
2.2.1	Sänger I and II . . . . .	12
2.2.2	Tsien Spaceplane . . . . .	15
2.2.3	X15 . . . . .	16
2.2.4	The Aerospaceplane and NASP . . . . .	16
2.2.5	SR-71 Blackbird Program . . . . .	21
2.2.6	Falcon Program . . . . .	22
2.3	Inlet Distortion . . . . .	24
2.3.1	What is Flow Distortion? . . . . .	25
2.3.2	Why is Characterizing Flow Distortion Important? . . . . .	26
2.3.3	How is Flow Distortion Defined? . . . . .	28



2.3.4	Work to Date on Flow Distortion . . . . .	29
2.3.5	Distortion Index Definition . . . . .	43
2.4	Summary of Findings . . . . .	46
<b>3</b>	<b>The IMX and YF12 Inlets</b>	<b>48</b>
3.1	Small-Scale Inlet Mode Transition Experiment (IMX) . . . . .	48
3.1.1	Experimental Set-up . . . . .	49
3.1.2	Data Analysis . . . . .	53
3.1.3	Computational Fluid Dynamics . . . . .	59
3.1.4	Findings and Limitations . . . . .	63
3.2	YF12 Scaled Inlet . . . . .	64
3.2.1	Experimental Set-up . . . . .	65
3.2.2	Data Analysis . . . . .	67
3.2.3	Findings and Limitations . . . . .	68
3.3	Summary of Findings . . . . .	69
<b>4</b>	<b>Interpolation of Pressure Data via Surrogate Modeling</b>	<b>71</b>
4.1	Background . . . . .	71
4.2	Methodology . . . . .	72
4.2.1	Surrogate Model . . . . .	73
4.2.2	Interpolation Methods . . . . .	74
4.2.3	Bilinear Interpolation . . . . .	76
4.2.4	Spline Interpolation . . . . .	78
4.2.5	Kriging Interpolation . . . . .	80
4.2.6	Measures of Success . . . . .	81
4.3	Results . . . . .	84
4.3.1	Accuracy and Precision . . . . .	84
4.3.2	Location Predictions . . . . .	88

4.3.3	Impact on Derived Quantities . . . . .	99
4.3.4	Visual Accuracy . . . . .	105
4.4	Conclusions . . . . .	110
<b>5</b>	<b>Interpolation of Experimental and Computational Pressure Data</b>	<b>112</b>
5.1	Background . . . . .	112
5.2	Methodology . . . . .	113
5.3	Results . . . . .	114
5.3.1	Interpolation Accuracy and Precision . . . . .	115
5.3.2	Location Predictions . . . . .	120
5.3.3	Visual Accuracy . . . . .	126
5.3.4	Derived Quantities Results . . . . .	128
5.3.5	Summary of Results . . . . .	143
5.4	A Note on The Tolerance Level . . . . .	144
5.5	Conclusions . . . . .	146
<b>6</b>	<b>Optimizing Probe Placement</b>	<b>148</b>
6.1	Background . . . . .	148
6.2	Methodology . . . . .	151
6.3	Results . . . . .	153
6.3.1	Computational Data – IMX . . . . .	153
6.3.2	Experimental Data – YF12 . . . . .	168
6.4	Conclusions . . . . .	180
<b>7</b>	<b>Probe Placement Sensitivity Analysis</b>	<b>182</b>
7.1	Background . . . . .	182
7.2	Methodology . . . . .	183
7.3	Results . . . . .	184

7.4	Conclusions	189
<b>8</b>	<b>Conclusions</b>	<b>191</b>
8.1	Summary of Contributions	191
8.2	Dissertation Overview	193
8.3	Research Limitations	194
8.4	Future Work	195
	<b>Bibliography</b>	<b>196</b>
	<b>Appendix</b>	
<b>A</b>	<b>Appendix I: YF12 Data Error</b>	<b>206</b>
A.1	Error on the Raw Data	206
A.2	Error on Picking Data Points	207
A.3	Overall Error	209
<b>B</b>	<b>Appendix II: NASA GUI</b>	<b>211</b>
<b>C</b>	<b>Appendix III: Full Interpolation Results</b>	<b>213</b>
C.1	YF12 Inlet	213
C.1.1	Test Case 1	223
C.1.2	Test Case 2	257
C.1.3	Test Case 3	291
C.2	IMX Inlet	324
C.2.1	Run Number R300	334
C.2.2	Run Number R310	368
C.2.3	Run Number R320	402
C.3	Tabulation of Results	436

C.3.1 Accuracy – Mean of the Error . . . . .	436
C.3.2 Precision – Standard Deviation of the Error . . . . .	438
C.3.3 Location Prediction – In Tolerance . . . . .	440
C.3.4 Location Prediction – Under-Shot . . . . .	442
C.3.5 Location Prediction – Over-Shot . . . . .	444

## List of Tables

### Table

3.1	IMX CFD run conditions . . . . .	60
3.2	Freestream conditions the CFD was run at . . . . .	61
3.3	Test conditions for the three YF12 test cases.[1] . . . . .	64
3.4	Distortion index results for the experiment . . . . .	67
4.1	Surrogate model conditions . . . . .	73
4.2	Interpolation accuracy and precision for the surrogate model . . . . .	88
4.3	Mean interpolation location prediction results falling within, above, and below the tolerance band for the 180 degree low pressure pattern. . . . .	89
4.4	Mean interpolation location prediction results falling within, above, and below the tolerance band for the 4x45 degree low pressure pattern. . . . .	89
4.5	Mean interpolation location prediction results falling within, above, and below the tolerance band for the hub low pressure pattern. . . . .	89
5.1	Range and mean results for the mean error for all test cases and all clockings for the YF12 inlet. . . . .	116
5.2	Range and mean results for the standard deviation of the error for all test cases and all clockings for the YF12 inlet. . . . .	117
5.3	Range and mean results for the mean error for all test cases and all clockings for the IMX inlet. . . . .	119

5.4	Range and mean results for the standard deviation error for all test cases and all clockings for the IMX inlet. . . . .	119
5.5	Range and mean results for the in-tolerance locations for all test cases and all clockings for the YF12 inlet. These numbers do not include the 40 probes used for interpolation.	122
5.6	Range and mean results for the under-shot locations for all test cases and all clockings for the YF12 inlet. . . . .	123
5.7	Range and mean results for the over-shot locations for all test cases and all clockings for the YF12 inlet. . . . .	123
5.8	Range and mean results for the in-tolerance locations for all test cases and all clockings for the IMX inlet. These numbers do not include the 40 probes used for interpolation.	125
5.9	Range and mean results for the under-shot locations for all test cases and all clockings for the IMX inlet. . . . .	125
5.10	Range and mean results for the over-shot locations for all test cases and all clockings for the IMX inlet. . . . .	126
5.11	Results for the YF12 exact distortion indices . . . . .	129
5.12	Interpolation effects on the derived quantities for the YF12 inlet test case 1, clocking C1. . . . .	131
5.13	Results for the IMX exact distortion indices . . . . .	136
5.14	Interpolation effects on the derived quantities for the IMX inlet run number R300, clocking C1. . . . .	138
5.15	Summary of best interpolation method results for distortion indices . . . . .	143
5.16	Summary of best interpolation method results for accuracy, precision, and location prediction . . . . .	144
6.1	Tabulation of the mean and standard deviation in the error for <i>IDT</i> from the IMX CFD for all run numbers with respect to the 320 probe result. . . . .	159

6.2	Tabulation of the mean error in <i>IDT</i> from the IMX CFD for all run numbers with respect to the ARP1420 suggested, 40 probe layout. . . . .	160
6.3	Results for the <i>IDT</i> distortion index for the three IMX run numbers based on the sampled probes. . . . .	167
6.4	Relative error in the <i>IDT</i> distortion index for the three IMX run numbers based on the sampled probes. . . . .	167
6.5	Tabulation of the mean and standard deviation in the error for <i>IDT</i> from the YF12 inlet for all test cases. . . . .	172
6.6	Tabulation of the mean error in <i>IDT</i> from the YF12 experimental data for all run numbers with respect to the ARP1420 suggested, 40 probe layout. . . . .	172
6.7	Results for the <i>IDT</i> distortion index for the three YF12 run numbers based on the sampled probes. . . . .	179
6.8	Relative error in the <i>IDT</i> distortion index for the three YF12 run numbers based on the sampled probes. . . . .	179
6.9	Relative error in the <i>IDT</i> distortion index with respect to the ARP1420 layout for the three YF12 run numbers. . . . .	180
7.1	Average change in $n\Delta S$ . . . . .	187
7.2	Individual results for $n\Delta S$ of the 25-to-22 probe reduction scenario . . . . .	189
A.1	YF12 Raw Data Pixel Sizes . . . . .	208
A.2	Coordinates of known point as picked by DataThief. . . . .	208
A.3	DataThief results for a single point being picked 10 times. . . . .	209
C.1	Distortion index results for the YF12 inlet . . . . .	213
C.2	Interpolation results for the YF12 inlet test case 1, clocking C1. . . . .	224
C.3	Interpolation effects on the derived quantities for the IMX inlet run number R300, clocking C1. . . . .	228

C.4	Interpolation results for the YF12 inlet test case 1, clocking C2. . . . .	229
C.5	Interpolation effects on the derived quantities for the IMX inlet run number R300, clocking C2. . . . .	232
C.6	Interpolation results for the YF12 inlet test case 1, clocking C3. . . . .	233
C.7	Interpolation effects on the derived quantities for the IMX inlet run number R300, clocking C3. . . . .	236
C.8	Interpolation results for the YF12 inlet test case 1, clocking C4. . . . .	237
C.9	Interpolation effects on the derived quantities for the IMX inlet run number R300, clocking C4. . . . .	240
C.10	Interpolation results for the YF12 inlet test case 1, clocking C5. . . . .	241
C.11	Interpolation effects on the derived quantities for the IMX inlet run number R300, clocking C5. . . . .	244
C.12	Interpolation results for the YF12 inlet test case 1, clocking C6. . . . .	245
C.13	Interpolation effects on the derived quantities for the IMX inlet run number R300, clocking C6. . . . .	248
C.14	Interpolation results for the YF12 inlet test case 1, clocking C7. . . . .	249
C.15	Interpolation effects on the derived quantities for the IMX inlet run number R300, clocking C7. . . . .	252
C.16	Interpolation results for the YF12 inlet test case 1, clocking C8. . . . .	253
C.17	Interpolation effects on the derived quantities for the IMX inlet run number R300, clocking C8. . . . .	256
C.18	Interpolation results for the YF12 inlet test case 2, clocking C1. . . . .	258
C.19	Interpolation effects on the derived quantities for the IMX inlet run number R310, clocking C1. . . . .	262
C.20	Interpolation results for the YF12 inlet test case 2, clocking C2. . . . .	263
C.21	Interpolation effects on the derived quantities for the IMX inlet run number R310, clocking C2. . . . .	266



C.22	Interpolation results for the YF12 inlet test case 2, clocking C3. . . . .	267
C.23	Interpolation effects on the derived quantities for the IMX inlet run number R310, clocking C3. . . . .	270
C.24	Interpolation results for the YF12 inlet test case 2, clocking C4. . . . .	271
C.25	Interpolation effects on the derived quantities for the IMX inlet run number R310, clocking C4. . . . .	274
C.26	Interpolation results for the YF12 inlet test case 2, clocking C5. . . . .	275
C.27	Interpolation effects on the derived quantities for the IMX inlet run number R310, clocking C5. . . . .	278
C.28	Interpolation results for the YF12 inlet test case 2, clocking C6. . . . .	279
C.29	Interpolation effects on the derived quantities for the IMX inlet run number R310, clocking C6. . . . .	282
C.30	Interpolation results for the YF12 inlet test case 2, clocking C7. . . . .	283
C.31	Interpolation effects on the derived quantities for the IMX inlet run number R310, clocking C7. . . . .	286
C.32	Interpolation results for the YF12 inlet test case 2, clocking C8. . . . .	287
C.33	Interpolation effects on the derived quantities for the IMX inlet run number R310, clocking C8. . . . .	290
C.34	Interpolation results for the YF12 inlet test case 3, clocking C1. . . . .	292
C.35	Interpolation effects on the derived quantities for the IMX inlet run number R320, clocking C1. . . . .	296
C.36	Interpolation results for the YF12 inlet test case 3, clocking C2. . . . .	297
C.37	Interpolation effects on the derived quantities for the IMX inlet run number R320, clocking C2. . . . .	300
C.38	Interpolation results for the YF12 inlet test case 3, clocking C3. . . . .	301
C.39	Interpolation effects on the derived quantities for the IMX inlet run number R320, clocking C3. . . . .	304

C.40	Interpolation results for the YF12 inlet test case 3, clocking C4. . . . .	305
C.41	Interpolation effects on the derived quantities for the IMX inlet run number R320, clocking C4. . . . .	308
C.42	Interpolation results for the YF12 inlet test case 3, clocking C5. . . . .	309
C.43	Interpolation effects on the derived quantities for the IMX inlet run number R320, clocking C5. . . . .	312
C.44	Interpolation results for the YF12 inlet test case 3, clocking C6. . . . .	313
C.45	Interpolation effects on the derived quantities for the IMX inlet run number R320, clocking C6. . . . .	316
C.46	Interpolation results for the YF12 inlet test case 3, clocking C7. . . . .	317
C.47	Interpolation effects on the derived quantities for the IMX inlet run number R320, clocking C7. . . . .	320
C.48	Interpolation results for the YF12 inlet test case 3, clocking C8. . . . .	321
C.49	Interpolation effects on the derived quantities for the IMX inlet run number R320, clocking C8. . . . .	324
C.50	Distortion index results for the IMX inlet . . . . .	324
C.51	Interpolation results for the IMX inlet run number R300, clocking C1. . . . .	335
C.52	Interpolation effects on the derived quantities for the IMX inlet run number R300, clocking C1. . . . .	339
C.53	Interpolation results for the IMX inlet run number R300, clocking C2. . . . .	340
C.54	Interpolation effects on the derived quantities for the IMX inlet run number R300, clocking C2. . . . .	343
C.55	Interpolation results for the IMX inlet run number R300, clocking C3. . . . .	344
C.56	Interpolation effects on the derived quantities for the IMX inlet run number R300, clocking C3. . . . .	347
C.57	Interpolation results for the IMX inlet run number R300, clocking C4. . . . .	348

C.58	Interpolation effects on the derived quantities for the IMX inlet run number R300, clocking C4. . . . .	351
C.59	Interpolation results for the IMX inlet run number R300, clocking C5. . . . .	352
C.60	Interpolation effects on the derived quantities for the IMX inlet run number R300, clocking C5. . . . .	355
C.61	Interpolation results for the IMX inlet run number R300, clocking C6. . . . .	356
C.62	Interpolation effects on the derived quantities for the IMX inlet run number R300, clocking C6. . . . .	359
C.63	Interpolation results for the IMX inlet run number R300, clocking C7. . . . .	360
C.64	Interpolation effects on the derived quantities for the IMX inlet run number R300, clocking C7. . . . .	363
C.65	Interpolation results for the IMX inlet run number R300, clocking C8. . . . .	364
C.66	Interpolation effects on the derived quantities for the IMX inlet run number R300, clocking C8. . . . .	367
C.67	Interpolation results for the IMX inlet run number R310, clocking C1. . . . .	369
C.68	Interpolation effects on the derived quantities for the IMX inlet run number R310, clocking C1. . . . .	373
C.69	Interpolation results for the IMX inlet run number R310, clocking C2. . . . .	374
C.70	Interpolation effects on the derived quantities for the IMX inlet run number R310, clocking C2. . . . .	377
C.71	Interpolation results for the IMX inlet run number R310, clocking C3. . . . .	378
C.72	Interpolation effects on the derived quantities for the IMX inlet run number R310, clocking C3. . . . .	381
C.73	Interpolation results for the IMX inlet run number R310, clocking C4. . . . .	382
C.74	Interpolation effects on the derived quantities for the IMX inlet run number R310, clocking C4. . . . .	385
C.75	Interpolation results for the IMX inlet run number R310, clocking C5. . . . .	386

C.76	Interpolation effects on the derived quantities for the IMX inlet run number R310, clocking C5. . . . .	389
C.77	Interpolation results for the IMX inlet run number R310, clocking C6. . . . .	390
C.78	Interpolation effects on the derived quantities for the IMX inlet run number R310, clocking C6. . . . .	393
C.79	Interpolation results for the IMX inlet run number R310, clocking C7. . . . .	394
C.80	Interpolation effects on the derived quantities for the IMX inlet run number R310, clocking C7. . . . .	397
C.81	Interpolation results for the IMX inlet run number R310, clocking C8. . . . .	398
C.82	Interpolation effects on the derived quantities for the IMX inlet run number R310, clocking C8. . . . .	401
C.83	Interpolation results for the IMX inlet run number R320, clocking C1. . . . .	403
C.84	Interpolation effects on the derived quantities for the IMX inlet run number R320, clocking C1. . . . .	407
C.85	Interpolation results for the IMX inlet run number R320, clocking C2. . . . .	408
C.86	Interpolation effects on the derived quantities for the IMX inlet run number R320, clocking C2. . . . .	411
C.87	Interpolation results for the IMX inlet run number R320, clocking C3. . . . .	412
C.88	Interpolation effects on the derived quantities for the IMX inlet run number R320, clocking C3. . . . .	415
C.89	Interpolation results for the IMX inlet run number R320, clocking C4. . . . .	416
C.90	Interpolation effects on the derived quantities for the IMX inlet run number R320, clocking C4. . . . .	419
C.91	Interpolation results for the IMX inlet run number R320, clocking C5. . . . .	420
C.92	Interpolation effects on the derived quantities for the IMX inlet run number R320, clocking C5. . . . .	423
C.93	Interpolation results for the IMX inlet run number R320, clocking C6. . . . .	424

C.94	Interpolation effects on the derived quantities for the IMX inlet run number R320, clocking C6. . . . .	427
C.95	Interpolation results for the IMX inlet run number R320, clocking C7. . . . .	428
C.96	Interpolation effects on the derived quantities for the IMX inlet run number R320, clocking C7. . . . .	431
C.97	Interpolation results for the IMX inlet run number R320, clocking C8. . . . .	432
C.98	Interpolation effects on the derived quantities for the IMX inlet run number R320, clocking C8. . . . .	435
C.99	Mean of the error results for the YF12 inlet . . . . .	436
C.100	Mean of the error results for the IMX inlet . . . . .	437
C.101	Standard deviation of the error results for the YF12 inlet . . . . .	438
C.102	Standard deviation of the error results for the IMX inlet . . . . .	439
C.103	Locations where the interpolation results are within tolerance for the YF12 inlet . . . . .	440
C.104	Locations where the interpolation results are within tolerance for the IMX inlet . . . . .	441
C.105	Locations where the interpolation results are under tolerance for the YF12 inlet . . . . .	442
C.106	Locations where the interpolation results are under tolerance for the IMX inlet . . . . .	443
C.107	Locations where the interpolation results are over tolerance for the YF12 inlet . . . . .	444
C.108	Locations where the interpolation results are over tolerance for the IMX inlet . . . . .	445

## List of Figures

### Figure

2.1	J58 engine configurations	9
2.2	Over-under TBCC vehicle	10
2.3	NASA GTX vehicle	10
2.4	SABRE engine	11
2.5	Engine type performance chart	12
2.6	Engine program timeline	13
2.7	Sänger II spaceplane	15
2.8	X15 vehicle	17
2.9	NASP vehicle	19
2.10	X-43 model in wind tunnel	21
2.11	SR71 airplane taking off	23
2.12	Blackswift vehicle	24
2.13	Example of velocity profiles	25
2.14	Comparison of steady state and dynamic pressure readings	27
2.15	Sample compressor stall margin	28
2.16	Distortion screens	33
2.17	Proposed distortion test mechanism	33
2.18	Dynamic distortion test mechanism	34
2.19	Jet injection test mechanism for distortion	34

2.20	Modern distortion screens . . . . .	35
2.21	Rake configurations used in the YF12 experiment . . . . .	36
2.22	ARP1420 suggested pressure rake configuration . . . . .	37
2.23	Surge margin impacts due to circumferential distortion . . . . .	43
2.24	Surge margin impacts due to radial distortion . . . . .	45
3.1	Computer rendering of the IMX model. Image courtesy of NASA. . . . .	49
3.2	Photo showing bleed regions of the IMX model. Image courtesy of NASA. . . . .	50
3.3	Drawing of the low speed flow path mass flow plug location in the IMX model. Image courtesy of NASA. . . . .	51
3.4	Location of the static pressure taps in the IMX model. Image courtesy of NASA. . . . .	52
3.5	Visualization of the total pressure rakes and static taps in the IMX model's AIP. Image courtesy of NASA. . . . .	52
3.6	Visualization of the total pressure rakes and static taps in the IMX model's subsonic diffuser. Image courtesy of NASA. . . . .	53
3.7	Locations of the total pressure taps (red) and static pressure taps (cyan) at the AIP. . . . .	54
3.8	IMX cane curve with CFD conditions indicated as red triangles. . . . .	56
3.9	Sample IMX data analysis result . . . . .	59
3.10	CFD mesh used for the IMX RANS CFD . . . . .	60
3.11	Pressure results for IMX CFD runs R300, R310, and R320, with individual colorbars and an overall colorbar. . . . .	62
3.12	YF12 inlet used for the 320-probe experiment. Image from NASA[1] . . . . .	65
3.13	Subsets of probes chosen for analysis by the original researchers. . . . .	66
3.14	Clocking example of the 40 probe subset, with the darker color representing the clocking. . . . .	66
3.15	Raw pressure contour plots; scatter plot indicates probe locations. . . . .	68
4.1	Surrogate Model Patterns . . . . .	73

4.2	Histogram of the 100 lowest pressure readings for the YF12 experiment's test case 1	74
4.3	Surrogate Model Samples	75
4.4	ARP1420 suggested probe layout. Blue probes indicate total pressure probes while green indicate surface static pressure taps.	76
4.5	Diagram depicting bilinear interpolation points	77
4.6	Relative error in the surrogate model	85
4.7	Relative error in the surrogate model	86
4.8	Relative error in the surrogate model	87
4.9	Interpolation results falling within the 1% tolerance band	91
4.10	Interpolation results falling within the 1% tolerance band	92
4.11	Interpolation results falling within the 1% tolerance band	93
4.12	Interpolation results falling above the 1% tolerance band	94
4.13	Interpolation results falling above the 1% tolerance band	95
4.14	Interpolation results falling above the 1% tolerance band	96
4.15	Interpolation results falling below the 1% tolerance band	97
4.16	Interpolation results falling below the 1% tolerance band	98
4.17	Interpolation results falling below the 1% tolerance band	99
4.18	Impact of interpolation method on $K_\theta$ index	100
4.19	Impact of interpolation method on $K_r$ index	102
4.20	Impact of interpolation method on $IDC$ index	103
4.21	Impact of interpolation method on $IDT$ index	104
4.22	Visual accuracy of interpolation methods for the 180 degree pattern	107
4.23	Visual accuracy of interpolation methods for the 45 degree pattern	108
4.24	Visual accuracy of interpolation methods for the hub to tip pattern	109
5.1	Clocking example of the 40 probe subset, with the darker color representing the clocking.	114



5.2	Relative error . . . . .	116
5.3	Relative error . . . . .	118
5.4	Interpolation error for the YF12 inlet - symbols show locations that are within tolerance (o), over-predicted (+), and under-predicted (-). . . . .	121
5.5	Interpolation error for the IMX inlet - symbols show locations that are within tolerance (o), over-predicted (+), and under-predicted (-). . . . .	124
5.6	Contour plots for the full 320 and interpolated values for the YF12 inlet. . . . .	127
5.7	Contour plots for the full 320 and interpolated values for the IMX inlet. . . . .	128
5.8	YF12 ring distortion . . . . .	130
5.9	Barplots of the distortion indices for the zeroth clocking for the YF12 inlet. . . . .	132
5.10	Impact of interpolation method on $K_\theta$ index . . . . .	133
5.11	Impact of interpolation method on $K_r$ index . . . . .	133
5.12	Impact of interpolation method on $IDC$ index . . . . .	135
5.13	Impact of interpolation method on $IDT$ index . . . . .	135
5.14	IMX ring distortion . . . . .	137
5.15	Barplots of the distortion indices for the zeroth clocking for the IMX inlet. . . . .	139
5.16	Impact of interpolation method on $K_\theta$ index . . . . .	140
5.17	Impact of interpolation method on $K_r$ index . . . . .	140
5.18	Impact of interpolation method on $IDC$ index . . . . .	142
5.19	Impact of interpolation method on $IDT$ index . . . . .	142
5.20	Interpolation error for various tolerance levels for the YF12 inlet using the Kriging method - symbols show locations that are within tolerance (o), over-predicted (+), and under-predicted (-). . . . .	145
5.21	Interpolation error for various tolerance levels for the IMX inlet using the Kriging method - symbols show locations that are within tolerance (o), over-predicted (+), and under-predicted (-). . . . .	146

6.1	ARP1420 suggested probe layout. Blue probes indicate total pressure probes while green indicate surface static pressure taps. . . . .	149
6.2	AIP instrumentation for the IMX. . . . .	150
6.3	Uniform distribution of $f(x)$ for $a < x < b$ . . . . .	152
6.4	Results of the Monte Carlo sampling of the IMX CFD data . . . . .	154
6.5	Probability density function for the error in $IDT$ for run number R300. . . . .	156
6.6	Probability density function for the error in $IDT$ for run number R310. . . . .	157
6.7	Probability density function for the error in $IDT$ for run number R320. . . . .	158
6.8	Number of occurrences for each probe over all the samples that fell within 1% error of $IdT$ for run number 300. . . . .	161
6.9	Number of occurrences for each probe over all the samples that fell within 1% error of $IdT$ for run number 300. . . . .	161
6.10	Number of occurrences for each probe over all the samples that fell within 1% error of $IdT$ for run number 300. . . . .	162
6.11	Probe locations that occur the majority of times to land within 1% of the exact $IDT$ value for IMX run number R300. . . . .	163
6.12	Probe locations that occur the majority of times to land within 1% of the exact $IDT$ value for IMX run number R310. . . . .	164
6.13	Probe locations that occur the majority of times to land within 1% of the exact $IDT$ value for IMX run number R320. . . . .	165
6.14	Final configuration of probes to optimize detecting $IDT$ for the IMX inlet. . . . .	166
6.15	Probability density function for the error in $IDT$ for test case 1. . . . .	169
6.16	Probability density function for the error in $IDT$ for test case 2. . . . .	170
6.17	Probability density function for the error in $IDT$ for test case 3. . . . .	171
6.18	Number of occurrences for each probe over all the samples that fell within 1% error of $IdT$ for test case 1. . . . .	173

6.19	Number of occurrences for each probe over all the samples that fell within 1% error of $IdT$ for test case 2. . . . .	174
6.20	Number of occurrences for each probe over all the samples that fell within 1% error of $IdT$ for test case 3. . . . .	174
6.21	Probe locations that occur the majority of times to land within 1% of the exact $IDT$ value for YF12 test case TC1. . . . .	175
6.22	Probe locations that occur the majority of times to land within 1% of the exact $IDT$ value for YF12 test case TC2. . . . .	176
6.23	Probe locations that occur the majority of times to land within 1% of the exact $IDT$ value for YF12 test case TC3. . . . .	177
6.24	Final configuration of probes to optimize detecting $IDT$ for the YF12 inlet. . . . .	178
7.1	Ratio of good results for $IDT$ with respect to the number of probes . . . . .	185
7.2	Change in ratio of good results for $IDT$ with respect to the number of probes . . . . .	186
7.3	Linear regression of the normalized sensitivity function . . . . .	188
A.1	YF12 raw data . . . . .	207
A.2	YF12 raw data . . . . .	207
A.3	DataThief error sample picture . . . . .	208
A.4	Sample picture loaded in DataThief . . . . .	210
A.5	Raw data overlaid with DataThief points . . . . .	210
B.1	WIDGI graphical user interface . . . . .	212
C.1	YF12 ring distortion . . . . .	214
C.2	Absolute and relative errors in the distortion indices for the YF12 inlet. . . . .	215
C.3	Barplots of the distortion indices for the zeroth clocking for the YF12 inlet. . . . .	215
C.4	Barplots of the distortion indices for the first clocking for the YF12 inlet. . . . .	216
C.5	Barplots of the distortion indices for the second clocking for the YF12 inlet. . . . .	217

C.6	Barplots of the distortion indices for the third clocking for the YF12 inlet. . . . .	218
C.7	Barplots of the distortion indices for the fourth clocking for the YF12 inlet. . . . .	219
C.8	Barplots of the distortion indices for the fifth clocking for the YF12 inlet. . . . .	220
C.9	Barplots of the distortion indices for the sixth clocking for the YF12 inlet. . . . .	221
C.10	Barplots of the distortion indices for the seventh clocking for the YF12 inlet. . . . .	222
C.11	Test case 1 raw pressure data . . . . .	223
C.12	Zeroth clocking probe position . . . . .	224
C.13	Contour plots for the raw and interpolated values for the YF12 inlet. . . . .	225
C.14	Relative error . . . . .	226
C.15	Interpolation error for the YF12 inlet - symbols show locations that are within tolerance (o), over-predicted (+), and under-predicted (-). . . . .	227
C.16	First clocking probe position . . . . .	228
C.17	Contour plots for the raw and interpolated values for the YF12 inlet. . . . .	229
C.18	Relative error . . . . .	230
C.19	Interpolation error for the YF12 inlet - symbols show locations that are within tolerance (o), over-predicted (+), and under-predicted (-). . . . .	231
C.20	Second clocking probe position . . . . .	232
C.21	Contour plots for the raw and interpolated values for the YF12 inlet. . . . .	233
C.22	Relative error . . . . .	234
C.23	Interpolation error for the YF12 inlet - symbols show locations that are within tolerance (o), over-predicted (+), and under-predicted (-). . . . .	235
C.24	Third clocking probe position . . . . .	236
C.25	Contour plots for the raw and interpolated values for the YF12 inlet. . . . .	237
C.26	Relative error . . . . .	238
C.27	Interpolation error for the YF12 inlet - symbols show locations that are within tolerance (o), over-predicted (+), and under-predicted (-). . . . .	239
C.28	Fourth clocking probe position . . . . .	240

C.29	Contour plots for the raw and interpolated values for the YF12 inlet. . . . .	241
C.30	Relative error . . . . .	242
C.31	Interpolation error for the YF12 inlet - symbols show locations that are within tolerance (o), over-predicted (+), and under-predicted (-). . . . .	243
C.32	Fifth clocking probe position . . . . .	244
C.33	Contour plots for the raw and interpolated values for the YF12 inlet. . . . .	245
C.34	Relative error . . . . .	246
C.35	Interpolation error for the YF12 inlet - symbols show locations that are within tolerance (o), over-predicted (+), and under-predicted (-). . . . .	247
C.36	Sixth clocking probe position . . . . .	248
C.37	Contour plots for the raw and interpolated values for the YF12 inlet. . . . .	249
C.38	Relative error . . . . .	250
C.39	Interpolation error for the YF12 inlet - symbols show locations that are within tolerance (o), over-predicted (+), and under-predicted (-). . . . .	251
C.40	Seventh clocking probe position . . . . .	252
C.41	Contour plots for the raw and interpolated values for the YF12 inlet. . . . .	253
C.42	Relative error . . . . .	254
C.43	Interpolation error for the YF12 inlet - symbols show locations that are within tolerance (o), over-predicted (+), and under-predicted (-). . . . .	255
C.44	Test case 1 raw pressure data . . . . .	257
C.45	Zeroth clocking probe position . . . . .	258
C.46	Contour plots for the raw and interpolated values for the YF12 inlet. . . . .	259
C.47	Relative error . . . . .	260
C.48	Interpolation error for the YF12 inlet - symbols show locations that are within tolerance (o), over-predicted (+), and under-predicted (-). . . . .	261
C.49	First clocking probe position . . . . .	262
C.50	Contour plots for the raw and interpolated values for the YF12 inlet. . . . .	263

C.51	Relative error . . . . .	264
C.52	Interpolation error for the YF12 inlet - symbols show locations that are within tolerance (o), over-predicted (+), and under-predicted (-). . . . .	265
C.53	Second clocking probe position . . . . .	266
C.54	Contour plots for the raw and interpolated values for the YF12 inlet. . . . .	267
C.55	Relative error . . . . .	268
C.56	Interpolation error for the YF12 inlet - symbols show locations that are within tolerance (o), over-predicted (+), and under-predicted (-). . . . .	269
C.57	Third clocking probe position . . . . .	270
C.58	Contour plots for the raw and interpolated values for the YF12 inlet. . . . .	271
C.59	Relative error . . . . .	272
C.60	Interpolation error for the YF12 inlet - symbols show locations that are within tolerance (o), over-predicted (+), and under-predicted (-). . . . .	273
C.61	Fourth clocking probe position . . . . .	274
C.62	Contour plots for the raw and interpolated values for the YF12 inlet. . . . .	275
C.63	Relative error . . . . .	276
C.64	Interpolation error for the YF12 inlet - symbols show locations that are within tolerance (o), over-predicted (+), and under-predicted (-). . . . .	277
C.65	Fifth clocking probe position . . . . .	278
C.66	Contour plots for the raw and interpolated values for the YF12 inlet. . . . .	279
C.67	Relative error . . . . .	280
C.68	Interpolation error for the YF12 inlet - symbols show locations that are within tolerance (o), over-predicted (+), and under-predicted (-). . . . .	281
C.69	Sixth clocking probe position . . . . .	282
C.70	Contour plots for the raw and interpolated values for the YF12 inlet. . . . .	283
C.71	Relative error . . . . .	284

C.72	Interpolation error for the YF12 inlet - symbols show locations that are within tolerance (o), over-predicted (+), and under-predicted (-). . . . .	285
C.73	Seventh clocking probe position . . . . .	286
C.74	Contour plots for the raw and interpolated values for the YF12 inlet. . . . .	287
C.75	Relative error . . . . .	288
C.76	Interpolation error for the YF12 inlet - symbols show locations that are within tolerance (o), over-predicted (+), and under-predicted (-). . . . .	289
C.77	Test case 1 raw pressure data . . . . .	291
C.78	Zereth clocking probe position . . . . .	292
C.79	Contour plots for the raw and interpolated values for the YF12 inlet. . . . .	293
C.80	Relative error . . . . .	294
C.81	Interpolation error for the YF12 inlet - symbols show locations that are within tolerance (o), over-predicted (+), and under-predicted (-). . . . .	295
C.82	First clocking probe position . . . . .	296
C.83	Contour plots for the raw and interpolated values for the YF12 inlet. . . . .	297
C.84	Relative error . . . . .	298
C.85	Interpolation error for the YF12 inlet - symbols show locations that are within tolerance (o), over-predicted (+), and under-predicted (-). . . . .	299
C.86	Second clocking probe position . . . . .	300
C.87	Contour plots for the raw and interpolated values for the YF12 inlet. . . . .	301
C.88	Relative error . . . . .	302
C.89	Interpolation error for the YF12 inlet - symbols show locations that are within tolerance (o), over-predicted (+), and under-predicted (-). . . . .	303
C.90	Third clocking probe position . . . . .	304
C.91	Contour plots for the raw and interpolated values for the YF12 inlet. . . . .	305
C.92	Relative error . . . . .	306

C.93	Interpolation error for the YF12 inlet - symbols show locations that are within tolerance (o), over-predicted (+), and under-predicted (-). . . . .	307
C.94	Fourth clocking probe position . . . . .	308
C.95	Contour plots for the raw and interpolated values for the YF12 inlet. . . . .	309
C.96	Relative error . . . . .	310
C.97	Interpolation error for the YF12 inlet - symbols show locations that are within tolerance (o), over-predicted (+), and under-predicted (-). . . . .	311
C.98	Fifth clocking probe position . . . . .	312
C.99	Contour plots for the raw and interpolated values for the YF12 inlet. . . . .	313
C.100	Relative error . . . . .	314
C.101	Interpolation error for the YF12 inlet - symbols show locations that are within tolerance (o), over-predicted (+), and under-predicted (-). . . . .	315
C.102	Sixth clocking probe position . . . . .	316
C.103	Contour plots for the raw and interpolated values for the YF12 inlet. . . . .	317
C.104	Relative error . . . . .	318
C.105	Interpolation error for the YF12 inlet - symbols show locations that are within tolerance (o), over-predicted (+), and under-predicted (-). . . . .	319
C.106	Seventh clocking probe position . . . . .	320
C.107	Contour plots for the raw and interpolated values for the YF12 inlet. . . . .	321
C.108	Relative error . . . . .	322
C.109	Interpolation error for the YF12 inlet - symbols show locations that are within tolerance (o), over-predicted (+), and under-predicted (-). . . . .	323
C.110	IMX ring distortion . . . . .	325
C.111	Absolute and relative errors in the distortion indices for the IMX inlet. . . . .	326
C.112	Barplots of the distortion indices for the zeroth clocking for the IMX inlet. . . . .	326
C.113	Barplots of the distortion indices for the first clocking for the IMX inlet. . . . .	327
C.114	Barplots of the distortion indices for the second clocking for the IMX inlet. . . . .	328



C.115 Barplots of the distortion indices for the third clocking for the IMX inlet. . . . .	329
C.116 Barplots of the distortion indices for the fourth clocking for the IMX inlet. . . . .	330
C.117 Barplots of the distortion indices for the fifth clocking for the IMX inlet. . . . .	331
C.118 Barplots of the distortion indices for the sixth clocking for the IMX inlet. . . . .	332
C.119 Barplots of the distortion indices for the seventh clocking for the IMX inlet. . . . .	333
C.120 Run number R300 raw pressure data . . . . .	334
C.121 Zeroth clocking probe position . . . . .	335
C.122 Contour plots for the raw and interpolated values for the IMX inlet. . . . .	336
C.123 Relative error . . . . .	337
C.124 Interpolation error for the IMX inlet - symbols show locations that are within tolerance (o), over-predicted (+), and under-predicted (-). . . . .	338
C.125 First clocking probe position . . . . .	339
C.126 Contour plots for the raw and interpolated values for the IMX inlet. . . . .	340
C.127 Relative error . . . . .	341
C.128 Interpolation error for the IMX inlet - symbols show locations that are within tolerance (o), over-predicted (+), and under-predicted (-). . . . .	342
C.129 Second clocking probe position . . . . .	343
C.130 Contour plots for the raw and interpolated values for the IMX inlet. . . . .	344
C.131 Relative error . . . . .	345
C.132 Interpolation error for the IMX inlet - symbols show locations that are within tolerance (o), over-predicted (+), and under-predicted (-). . . . .	346
C.133 Third clocking probe position . . . . .	347
C.134 Contour plots for the raw and interpolated values for the IMX inlet. . . . .	348
C.135 Relative error . . . . .	349
C.136 Interpolation error for the IMX inlet - symbols show locations that are within tolerance (o), over-predicted (+), and under-predicted (-). . . . .	350
C.137 Fourth clocking probe position . . . . .	351

C.138 Contour plots for the raw and interpolated values for the IMX inlet. . . . .	352
C.139 Relative error . . . . .	353
C.140 Interpolation error for the IMX inlet - symbols show locations that are within tolerance (o), over-predicted (+), and under-predicted (-). . . . .	354
C.141 Fifth clocking probe position . . . . .	355
C.142 Contour plots for the raw and interpolated values for the IMX inlet. . . . .	356
C.143 Relative error . . . . .	357
C.144 Interpolation error for the IMX inlet - symbols show locations that are within tolerance (o), over-predicted (+), and under-predicted (-). . . . .	358
C.145 Sixth clocking probe position . . . . .	359
C.146 Contour plots for the raw and interpolated values for the IMX inlet. . . . .	360
C.147 Relative error . . . . .	361
C.148 Interpolation error for the IMX inlet - symbols show locations that are within tolerance (o), over-predicted (+), and under-predicted (-). . . . .	362
C.149 Seventh clocking probe position . . . . .	363
C.150 Contour plots for the raw and interpolated values for the IMX inlet. . . . .	364
C.151 Relative error . . . . .	365
C.152 Interpolation error for the IMX inlet - symbols show locations that are within tolerance (o), over-predicted (+), and under-predicted (-). . . . .	366
C.153 Run number R300 raw pressure data . . . . .	368
C.154 Zeroth clocking probe position . . . . .	369
C.155 Contour plots for the raw and interpolated values for the IMX inlet. . . . .	370
C.156 Relative error . . . . .	371
C.157 Interpolation error for the IMX inlet - symbols show locations that are within tolerance (o), over-predicted (+), and under-predicted (-). . . . .	372
C.158 First clocking probe position . . . . .	373
C.159 Contour plots for the raw and interpolated values for the IMX inlet. . . . .	374

C.160	Relative error . . . . .	375
C.161	Interpolation error for the IMX inlet - symbols show locations that are within tolerance (o), over-predicted (+), and under-predicted (-). . . . .	376
C.162	Second clocking probe position . . . . .	377
C.163	Contour plots for the raw and interpolated values for the IMX inlet. . . . .	378
C.164	Relative error . . . . .	379
C.165	Interpolation error for the IMX inlet - symbols show locations that are within tolerance (o), over-predicted (+), and under-predicted (-). . . . .	380
C.166	Third clocking probe position . . . . .	381
C.167	Contour plots for the raw and interpolated values for the IMX inlet. . . . .	382
C.168	Relative error . . . . .	383
C.169	Interpolation error for the IMX inlet - symbols show locations that are within tolerance (o), over-predicted (+), and under-predicted (-). . . . .	384
C.170	Fourth clocking probe position . . . . .	385
C.171	Contour plots for the raw and interpolated values for the IMX inlet. . . . .	386
C.172	Relative error . . . . .	387
C.173	Interpolation error for the IMX inlet - symbols show locations that are within tolerance (o), over-predicted (+), and under-predicted (-). . . . .	388
C.174	Fifth clocking probe position . . . . .	389
C.175	Contour plots for the raw and interpolated values for the IMX inlet. . . . .	390
C.176	Relative error . . . . .	391
C.177	Interpolation error for the IMX inlet - symbols show locations that are within tolerance (o), over-predicted (+), and under-predicted (-). . . . .	392
C.178	Sixth clocking probe position . . . . .	393
C.179	Contour plots for the raw and interpolated values for the IMX inlet. . . . .	394
C.180	Relative error . . . . .	395

C.181 Interpolation error for the IMX inlet - symbols show locations that are within tolerance (o), over-predicted (+), and under-predicted (-). . . . .	396
C.182 Seventh clocking probe position . . . . .	397
C.183 Contour plots for the raw and interpolated values for the IMX inlet. . . . .	398
C.184 Relative error . . . . .	399
C.185 Interpolation error for the IMX inlet - symbols show locations that are within tolerance (o), over-predicted (+), and under-predicted (-). . . . .	400
C.186 Run number R300 raw pressure data . . . . .	402
C.187 Zeroth clocking probe position . . . . .	403
C.188 Contour plots for the raw and interpolated values for the IMX inlet. . . . .	404
C.189 Relative error . . . . .	405
C.190 Interpolation error for the IMX inlet - symbols show locations that are within tolerance (o), over-predicted (+), and under-predicted (-). . . . .	406
C.191 First clocking probe position . . . . .	407
C.192 Contour plots for the raw and interpolated values for the IMX inlet. . . . .	408
C.193 Relative error . . . . .	409
C.194 Interpolation error for the IMX inlet - symbols show locations that are within tolerance (o), over-predicted (+), and under-predicted (-). . . . .	410
C.195 Second clocking probe position . . . . .	411
C.196 Contour plots for the raw and interpolated values for the IMX inlet. . . . .	412
C.197 Relative error . . . . .	413
C.198 Interpolation error for the IMX inlet - symbols show locations that are within tolerance (o), over-predicted (+), and under-predicted (-). . . . .	414
C.199 Third clocking probe position . . . . .	415
C.200 Contour plots for the raw and interpolated values for the IMX inlet. . . . .	416
C.201 Relative error . . . . .	417

C.202 Interpolation error for the IMX inlet - symbols show locations that are within tolerance (o), over-predicted (+), and under-predicted (-). . . . .	418
C.203 Fourth clocking probe position . . . . .	419
C.204 Contour plots for the raw and interpolated values for the IMX inlet. . . . .	420
C.205 Relative error . . . . .	421
C.206 Interpolation error for the IMX inlet - symbols show locations that are within tolerance (o), over-predicted (+), and under-predicted (-). . . . .	422
C.207 Fifth clocking probe position . . . . .	423
C.208 Contour plots for the raw and interpolated values for the IMX inlet. . . . .	424
C.209 Relative error . . . . .	425
C.210 Interpolation error for the IMX inlet - symbols show locations that are within tolerance (o), over-predicted (+), and under-predicted (-). . . . .	426
C.211 Sixth clocking probe position . . . . .	427
C.212 Contour plots for the raw and interpolated values for the IMX inlet. . . . .	428
C.213 Relative error . . . . .	429
C.214 Interpolation error for the IMX inlet - symbols show locations that are within tolerance (o), over-predicted (+), and under-predicted (-). . . . .	430
C.215 Seventh clocking probe position . . . . .	431
C.216 Contour plots for the raw and interpolated values for the IMX inlet. . . . .	432
C.217 Relative error . . . . .	433
C.218 Interpolation error for the IMX inlet - symbols show locations that are within tolerance (o), over-predicted (+), and under-predicted (-). . . . .	434

## Nomenclature

$A$	Area
$a$	Interpolation coefficients
$a$	Speed of sound
$A_i$	Placeholder variable in $K_\theta$
$b$	Interpolation coefficients
$B_i$	Placeholder variable in $K_\theta$
$C$	Spline interpolation cubic function
$c$	Interpolation coefficient
$C_d$	Coefficient of discharge
$CI$	Confidence interval
$D$	Dummy variable indicating any distortion index
$D$	General distortion index
$d$	Interpolation coefficient
$fit$	Linear regression fit
$g_c$	gravitational correction factor
$I_{sp}$	Specific Impulse (s)
$IDC$	Circumferential Distortion Index
$IDC_i$	Ring Circumferential Distortion Index
$IDT$	Combined Distortion Index
$K_\theta$	Circumferential Distortion Index

$K_a$	Combined Distortion Index
$K_r$	Radial Distortion Index
$K_{\theta,i}$	Ring Circumferential Distortion Index
$K_{r_i}$	Ring Radial Distortion Index
$l$	Length
$M$	Mach number
$M$	Mach number
$M$	Mach number
$n\Delta S$	Normalized change in the sensitivity function between probe sets
$nS$	Normalized sensitivity function
$NP$	Number of probes per ring
$NR$	Number of rakes
$p$	Interpolation results
$P_{t_{i,j}}$	Pressure reading at rake i, ring j, psi
$q$	Dynamic pressure
$q_2$	Dynamic pressure at the AIP, psi
$R$	Specific gas constant
$r$	Radius, in
$R^2$	Goodness of fit for the sensitivity regression line
$R_i$	Ring radius, in
$S$	Sensitivity function
$s$	Data point size
$T$	Temperature
$V$	Velocity
$v$	Velocity
$W$	weight flow
psi	pounds per square inch

## Symbols

$\Delta\theta_j$	Angular distance between rakes, deg
$\Delta S$	Change in the sensitivity function between probe sets
$\delta$	Pressure error
$\epsilon$	Derived quantity error
$\Gamma$	Relative error in IDT
$\gamma$	Ratio of specific heats (1.4 for air)
$\lambda$	Variogram function for Kriging interpolation
$\rho$	Density
$\tau$	Error in picked data points, psi
$\theta$	Angle, deg

## Subscripts

1	First order polynomial interpolation
2	Readings at the AIP
320	Full 320 probe set
40	Result from the 40-probe, ARP1420 layout
$\infty$	Freestream conditions
$k$	index
$s$	Static
<i>air</i>	Value for air
<i>axis</i>	Figure axis
<i>bleed</i>	bleed air
<i>corr</i>	Corrected
<i>LS</i>	low speed inlet - for the IMX, this is the turbojet inlet
<i>max</i>	Maximum
<i>min</i>	Minimum



<i>pipe</i>	Cold pipe
<i>plug</i>	Mass flow plug
<i>t</i>	Total
<i>abs</i>	Absolute
<i>exact</i>	Result from the full data set
<i>i</i>	Probe ring
<i>int</i>	Interpolated value
<i>j</i>	Probe rake
<i>k</i>	Kriging interpolation
<i>lower</i>	Lower confidence interval
<i>n</i>	Number of unknowns
<i>rel</i>	Relative
<i>sampled</i>	Result from the Monte Carlo sampled results
<i>upper</i>	Upper confidence interval
11	Two dimensional first order polynomial interpolation
3	Third order polynomial interpolation

### Conventions

'	First derivative
"	Second derivative
-	Average
·	flow rate
$f(\dots)$	function of

### Acronyms

AIP	aerodynamic interface plane
CBO	Congressional Budget Office
CFD	computational fluid dynamics

CIA Central Intelligence Agency  
DARPA Defense Advanced Research Projects Agency  
FaCET Falcon Combined Cycle Engine Test  
GRC NASA Glenn Research Center  
GUI Graphical User Interface  
HiSTED High Speed Turbine Engine Demonstration  
IMX Small Scale Inlet Mode Transition Experiment  
LACE liquid air cycle engine  
LIMX Large Scale Inlet Mode Transition Experiment  
NASA National Aeronautics and Space Administration  
NASP National Aerospace Plane  
PDF Probability density function  
RBCC Rocket Based Combined Cycle  
RLV reusable launch vehicle  
SABRE Synergistic Air-Breathing Rocket Engine  
SSTO single stage to orbit  
TBCC Turbine Based Combined Cycle  
TSTO two stage to orbit  
USAF United States Air Force  
VSTOL vertical and short take-off and landing

# Chapter 1

## Introduction

### 1.1 Historical Context

In today's aerospace environment, with ever dwindling budgets and stop-and-go timelines, it is important to find ways to cut down on design cycle time and cost. At present, designing an inlet for supersonic aircraft requires multiple iterations of sophisticated software platforms on supercomputers to predict the vehicle's performance. In the initial design phase, many of the specifications and parameters are fluid, solidifying as decisions are made and technology limitations become clear. During subsequent phases, it is not uncommon for a vehicle's mission to change; this impacts specifications and design parameters which travel downstream, back to the analysts who run and re-run the computer simulations. Each vehicle design iteration takes time, increasing proportionally with how many parameters are set. The computational cost per iteration is high, even on a supercomputer. The results of the simulation must also be validated. Validation usually requires experimental data. This data is gathered from various scales of experiments, ranging from component rigs to prototypes to full-size vehicles or a combination thereof. These tests produce large data sets which must be reduced into a set of easily understood parameters to judge the relative effectiveness of a design. The team has to decide if design changes are required by comparing these parameters to customer specifications. Upstream, during the modeling and proof-of-concept stages, changes are cheap and easy to implement. The further downstream the design is, the more difficult and expensive changes become. Additionally, work stoppages due to lack of funding can force engineers to return to designs weeks, months, or years after suddenly having to abandon

projects. Therefore, any reduction in cycle time becomes imperative to a vehicle's successful design.

This iterative, stop-and-go design work is a reality in particular for exotic, high speed vehicle designs. A program such as the National Aerospace Plane was barely getting off the ground before major components of the program were modified, reduced, or canceled. Its legacy lives on in smaller-scope projects, such as the X-43 and X-51 vehicles and rig tests, but they are merely tendrils of the original concept. One additional design iteration may not have saved the program, but could have been a launching off point for future programs such as the Blackswift hypersonic vehicle.

These programs fail for various reasons, including political pressures and cost overruns. One reason for cost overruns that engineers have control over is the lack of technology readiness. This deficiency includes the technology to combust at supersonic speeds, availability of heat-resistant materials, the lack of robust, ultra-responsive sensors, and insufficient computational efficiency to analyze complicated flow fields. In the 1970s, NASA researchers dreamed of pressure sensors that could capture dynamic pressure fluctuations at rates of 600 hertz. Today, we have easily surpassed this sampling rate with piezoelectric sensors which can sample at rates in the hundreds of kilohertz. Supercomputers and parallel processing have enabled us to analyze complicated geometries in extreme flow regimes. However, in order to advance technology readiness levels overall, computational and experimental methods must build upon each other. As a consequence of previous programs falling short of this bar, the interest in providing resources necessary for these vehicles to succeed has waned. The future of high-speed, air-breathing vehicles thus lies in assuring sufficient readiness levels can be met.

Many areas of improvements are needed for such an assurance. It can hardly be undertaken by a single person. Instead, the overarching problem must to be broken up into many smaller, solvable problems. This work is one attempt at solving a small part of the problem, namely to address the issues associated with the inlet-engine integration, specifically with respect to how we determine inlet flow distortion.

## 1.2 Problem Statement

Highly integrated propulsion systems designed for supersonic and hypersonic vehicles are exceedingly complex. This work will focus on one part of the system: the characterization of flow distortion at the interface plane of the inlet and the engine. These inlets divert air from the freestream to the engine. The inlet must deliver the right amount of airflow to the engine, at the correct speed, and in a relatively uniform manner. Due to the shock systems that form on the vehicle, the shape of the inlet, and a growing boundary layer the airflow is usually not uniform. All engines are designed to withstand some amount of non-uniformity, but too much flow irregularity can damage or even shut-off the engine.

This flow irregularity is measured by changes in total pressure at the inlet-engine interface. Engineers use both computational models and experimental investigations to capture how the total pressure changes throughout the flight envelope. This work specifically seeks to bridge these two fields by finding accurate ways to convert discrete experimental data points into continuous pressure contours and using the computational model to sample the flow in the areas of interest.

In order to address these questions, two inlets are studied – an axisymmetric inlet for a supersonic stealth vehicle and a two-dimensional inlet for an access-to-space vehicle. For the supersonic inlet, only experimental data exists. This inlet was tested at NASA in the 1970s where the interface plane between the inlet and engine was instrumented with 320 probes. However, only three test cases were run and there is limited information about the inlet parameters for each test case. For the access-to-space vehicle, a full set of computational results exists and limited experimental data. The computational results are Reynolds Averaged Navier-Stokes and the experimental data is limited to 9 probes at the inlet-engine interface.

With these data sets, this work will investigate how interpolation methods of discrete data points impact the continuous solution, how simulation methods can help optimize sampling locations, and how sensitive simulation results are to the number of sampling points.

### 1.3 Assumptions

Flow distortion has two major components in inlets: dynamic and steady state fluctuations. Dynamic distortion cannot be feasibly evaluated via computational methods as they require a full resolution of the turbulence scales. Dynamic pressure fluctuations, which lead to dynamic distortion, can be captured via dynamic pressure transducers that sample the flow at rates of several thousand hertz. Steady state distortion can be solved with three dimensional computational fluid dynamics and common pressure transducers to measure the static pressure field. Since only standard computational results and steady state sensor data exists, dynamic distortion will not be considered in this work.

Only supersonic inlets are studied in this work. Subsonic inlets are prone to different sources of inlet flow distortion. These sources produce separate flow distortion mechanics which impact the engine in distinct ways from supersonic flow irregularities. Similarly, no hypersonic inlet is directly studied in this work. Hypersonic inlets have many added challenges to resolve flow perturbations which are not studied in this work.

Lastly, the assumption is made that researchers have a relatively high level of confidence in the computational and experimental results. Computational codes used in this work are verified and have been validated against various experimental results. The experimental data from this work comes from official NASA reports and is assumed to be properly calibrated.

### 1.4 Overview

The context, motivation, and assumptions of this problem have been discussed above. In Chapter 2, the background and pedigree of the vehicles studied will be discussed, as well as what advancements have been made in the area of inlet flow distortion. This chapter features a full literature review on the field and the parameters used to describe inlet flow distortion. In Chapter 3, the inlets that were used for this work are introduced along with the existing data sets. This chapter also features information about how the data was obtained and the limitations on the data.

Chapters 4 and 5 discuss how different interpolation schemes impact the data analysis for inlet flow distortion, first using surrogate modeling followed by using existing data sets. Chapter 6 outlines a method to optimize probe placement to maximize the data gathered during experiments for a given parameter. Lastly, Chapter 7 features further analysis of the sensitivity each additional probe has on capturing distortion. Conclusions – including the contributions to the field, limitations of this dissertation, and potential future work – can be found in chapter 8.

There are several appendices to this work. Appendix A on page 206 examines the error in the supersonic vehicle's data set, which was obtained from the original report. Appendix B on page 211 shows a graphical user interface based on the data analysis in Section 3.1.2 on page 53 created for research engineers at NASA. Chapter 5 on page 112 represents only one test case for each inlet and presents the rest of the data using statistical methods. The individual results of all test cases and subsets can be found in Appendix C on page 213.

# Chapter 2

## Background

In the first chapter, the problems faced by engineers tasked with designing exotic, high-speed vehicles were presented. A brief historical context was given along with what questions this work seeks to address. This chapter will introduce some commonly used terms, such as what constitutes a combined cycle engine. It will give examples of such vehicles and their predecessors. Most of these programs did not achieve flight; this chapter will go into some of the reasons why. A literature review is presented on the topic of flow distortion. This section explains what flow distortion is, why it matters, how it is measured, and what has been discovered about the phenomena to date. Lastly, the parameters used to determine the amount of flow distortion are introduced.

In the first chapter, the problems faced by engineers tasked with designing exotic, high-speed vehicles were presented. A brief historical context was given along with what questions this work seeks to address. This chapter will introduce some commonly used terms, such as what constitutes a combined cycle engine. It will give examples of such vehicles and their predecessors. Most of these programs did not achieve flight; this chapter will go into some of the reasons why. A literature review is presented on the topic of flow distortion. This section explains what flow distortion is, why it matters, how it is measured, and what has been discovered about the phenomena to date. Lastly, the parameters used to determine the amount of flow distortion are introduced.



## 2.1 Combined Cycle Engine Definition

The term "combined cycle" is broad and a bit misleading term that can lead to the inclusion of all sorts of different power plant types. Any power generation method in which more than one cycle is utilized, including those used in electrical power plants to generate electricity, can be called a "combined cycle" power plant. In that case, electricity is often generated in a power plant by a process where water is evaporated and turned into steam to power turbines which drive generators. "Combined cycles", in this setting, refers to the heat of the turbine exhaust gas being used to evaporate the water, creating the steam that will eventually drive the turbine[2]. While essential for our everyday life, these forms of "combined cycle" power plants will not be considered in this work.

In the same vein, all afterburning turbojets could be considered as "combined cycle" engines if the afterburner can operate on the same principle as a ramjet, meaning without the turbojet compressing, combusting, and expanding the air prior to it being re-heated in the afterburner. While afterburning turbojets are interesting, they are rarely included under the heading of "turbine based combined cycle" engines.

What sets the "combined cycle" engines apart from single cycle engines is that they must have two or more distinct modes that must be able to operate in tandem and independently from each other. Only engines that meet this classification will be considered as a "turbine based combined cycle" engine. Thus, a regular afterburning turbojet cannot be considered a "combined cycle" engine in this work, since the turbojet has to operate for most afterburners to function. The re-heat cycle in a generator cannot operate without the generator running. There are engines out there, however, that do meet this independent cycle requirement, such as the Pratt & Whitney J58 engine which powered the SR-71 Blackbird[3]. This engine would be considered a combined cycle engine since the afterburner could operate independently of the turbojet as a ramjet. This would be considered a Turbine Based Combined Cycle (TBCC) engine.

A TBCC powered vehicle can be in any configuration, although it is most commonly in either an in-line or over-under configuration. An in-line configuration, as shown in figure 2.1, was

used for the Pratt & Whitney J58 afterburning turbojet used in the SR-71 Blackbird. The J58 features a translating spike which moves inward to close the airflow to the turbojet and redirects it to the afterburner, which starts to operate as a ramjet. The other configuration, an over-under configuration, features two distinct flowpaths. One is a "low speed" flowpath for the turbojet. The other is a "high speed" flowpath for the ramjet, scramjet, or dual mode scramjet. The National Aerospace Plane (NASP) was designed to use an over-under configuration, as shown in figure 2.2, where the flow is directed to the appropriate flowpath via cowls which open and close depending on the flight speed. Both configurations feature a maneuver called a "mode transition", where the vehicle transitions from one thrust source to the other. This transition is extremely important to the successful operation of the vehicle and will be discussed extensively later on.

A Rocket Based Combined Cycle (RBCC) engine is a combined cycle engine consisting of a rocket stage and another, usually air-breathing, engine. Each engine can operate independently, though concept designs also have them operating in tandem[4]. An example of a RBCC program was the NASA GTX[5]. The GTX vehicle would have taken off vertically using a rocket motor, then the vehicle would have tipped over and transitioned to a ejector ramjet engine and eventually tip back vertically and achieve orbit via the rocket motor[6]. A major problem with the GTX and RBCC engines in general is that in order to achieve the propellant savings via the ramjet engine, the vehicle has to cruise for a relatively long time in the atmosphere before ascending to orbit. At present, due to the complexities associated with the technology and the development cost, RBCC engines are not economically feasible. International RBCC programs include the SABRE (Synergistic Air-Breathing Rocket Engine) - shown in figure 2.4 - which includes a liquid air cycle engine (LACE) pre-cooler for the combustion air[7]. Work on the SABRE started in the 1980s with the British HOTOL (Horizontal Take-Off and Landing) single stage to orbit (SSTO), unmanned reusable launch vehicle (RLV), but the program was eventually canceled. SABRE development was put on hold until the engine company, Reaction Engines Limited, announced plans to develop its own vehicle called the Skylon.

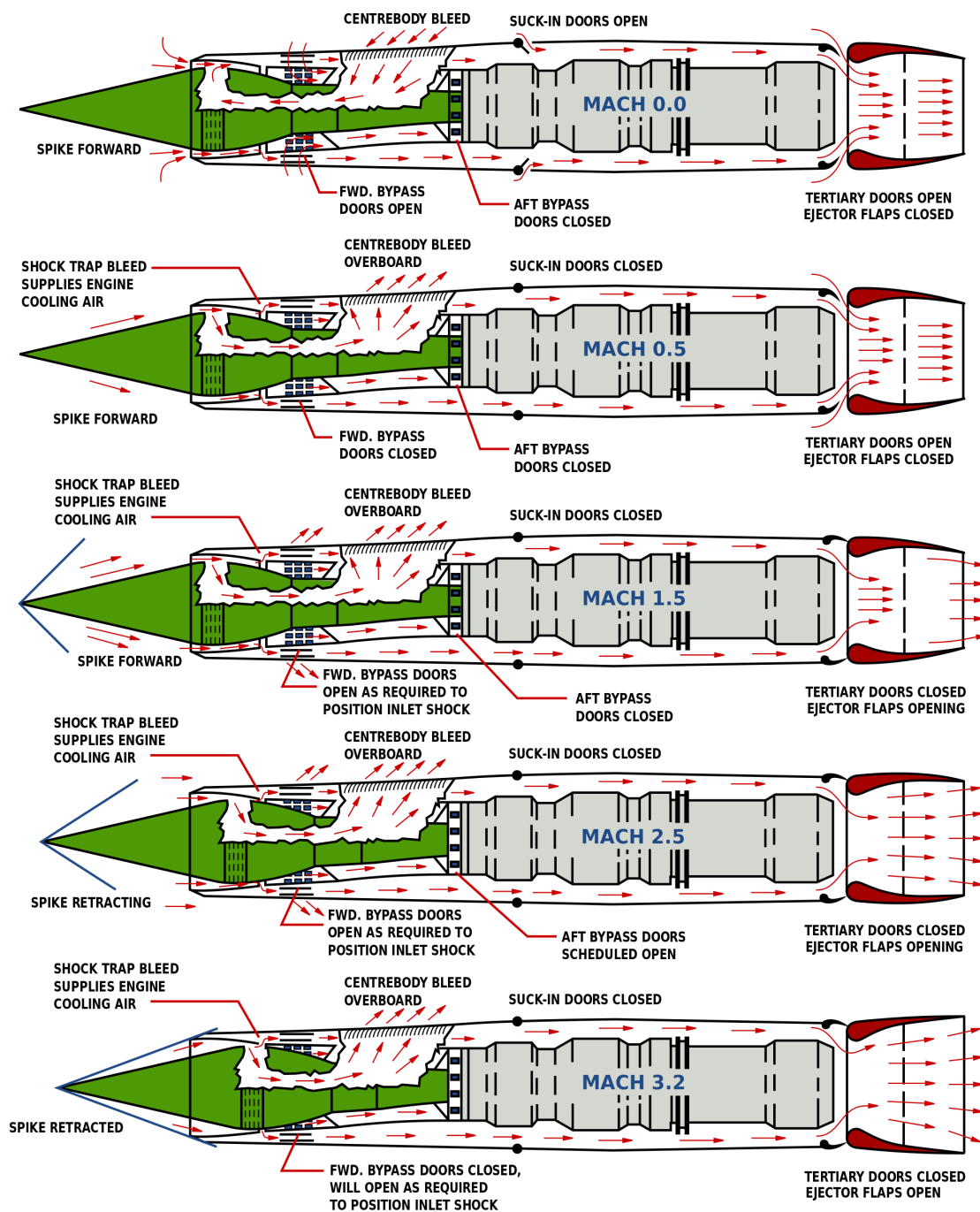


Figure 2.1: Different configurations through the flight envelope of the SR71 Blackbird's engine, the J58. An example of an in-line configuration of a TBCC engine[3].

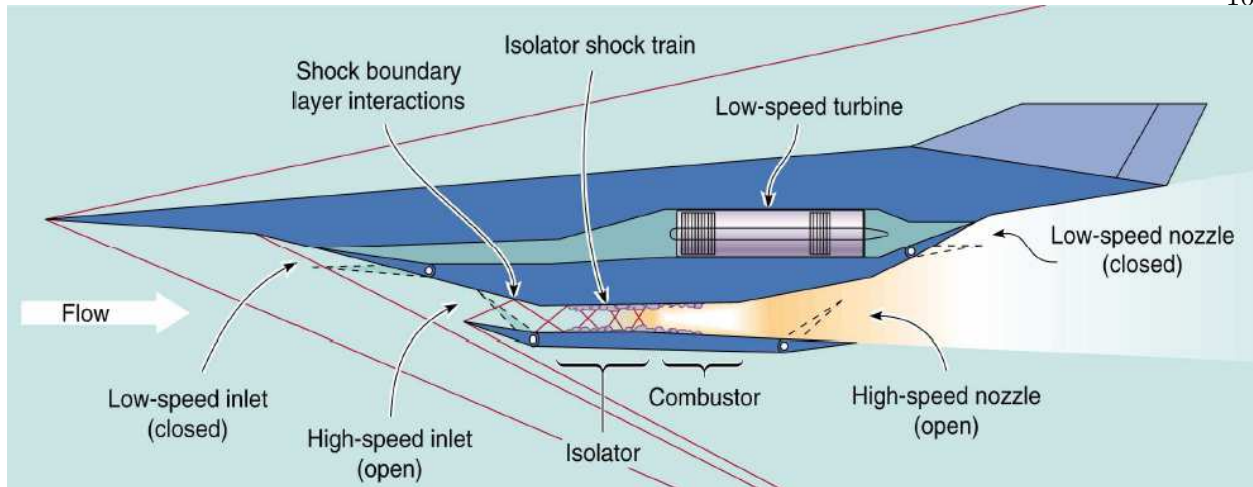


Figure 2.2: An example of an over-under configuration of a TBCC powered vehicle[8]. Image courtesy of NASA.

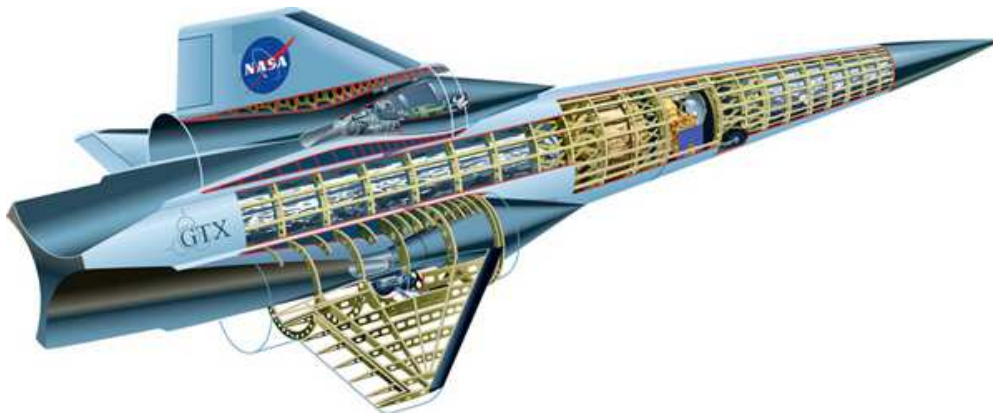


Figure 2.3: Artist's concept of the NASA GTX vehicle[6]. Image courtesy of NASA.

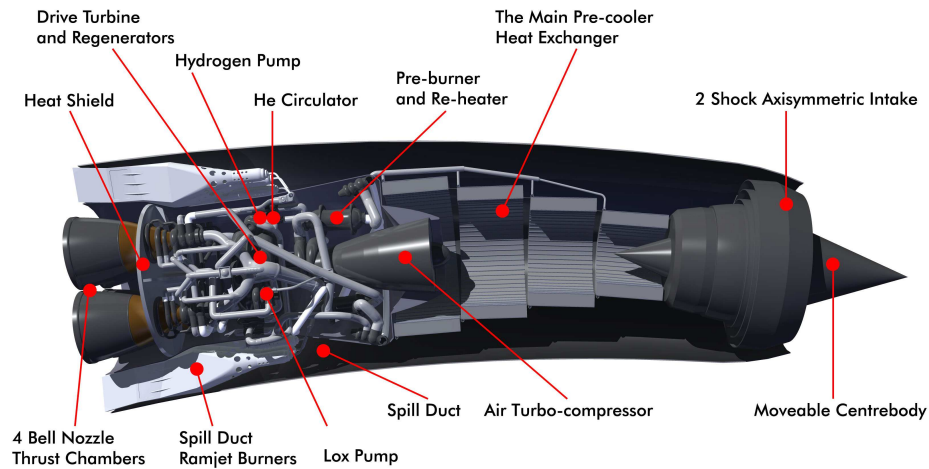


Figure 2.4: Artist's concept of the SABRE engine. Image reproduced with permission of Reaction Engines Limited[9].

## 2.2 Air Breathing Reusable Launch Vehicle Engine Work to Date

Since the 1950s, a small section of the aerospace world has been working to develop an air-breathing RLV. Hailed as the "holy grail" of space access by some, an air-breathing RLV uses air as the oxidizer to reach the outer limits of our atmosphere instead of carrying oxidizer tanks on-board like a rocket does. This saves weight, leading to a higher specific impulse ( $I_{sp}$ ) as shown in figure 2.5 - a figure adapted from Chuck Trefny at NASA - and increases the payload mass fraction. The reusable launch vehicle would reduce cost by reducing the number of models that have to be produced to access space since the engine is not jettisoned during launch. The vehicle can take off and land horizontally on a regular runway like a commercial airplane instead of a special launch pad[10]. In addition, horizontal take-off allows for much wider launch windows than vertical take-off[10]. The NASA and the USAF have been working together since NASA's inception on various projects to realize the goal of an air-breathing RLV.

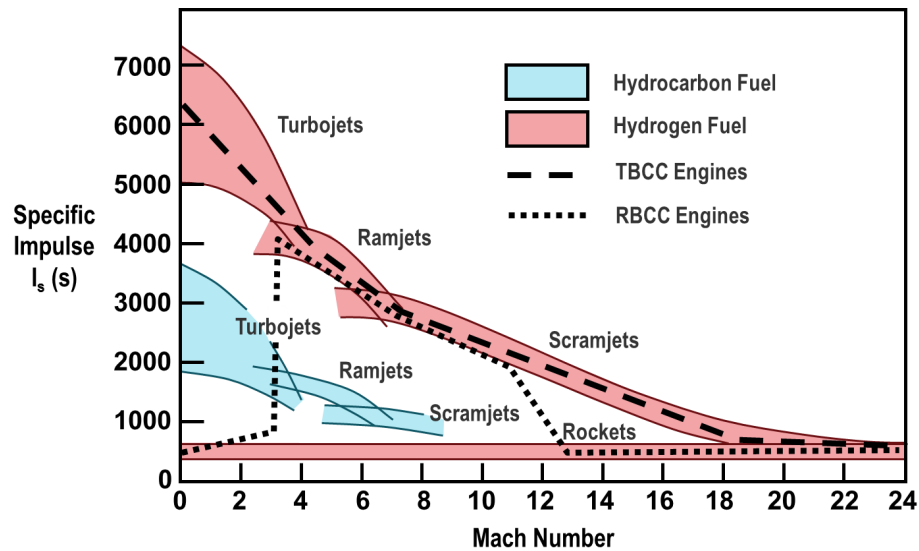


Figure 2.5: Engine efficiency of various engine types with predicted performance for TBCC and RBCC engines. Image courtesy of Chuck Trefny, NASA.

The engine architecture that enables an air-breathing RLV is generally considered to be a TBCC engine. As discussed in section 2.1, this is an engine that has a turbojet along with another, separate engine to provide thrust. The US has been working on and off on a TBCC vehicle for almost seven decades and several other nations, including Germany, France, and Japan, have started and ended their own projects. The majority of these projects have waxed and waned as public interest and perceptions changed. Figure 2.6 shows a sampling of the major projects that were meaningful either in the RLV or TBCC technologies.

### 2.2.1 Sänger I and II

Sänger I refers to the first spaceplane, named after its designer Eugen Sänger[11]. The vehicle, called "Sibler Vogel" (Silver bird) in German, was meant to be a rocket-powered, rail-launched spaceplane, also often called a "Raketenbomber", which translates to "rocket bomber"[11]. It wasn't a combined cycle powered vehicle, but it is important to include it as it would be the jumping off point for Sänger II. The mission the Sänger I would fly would be the one to bomb America during

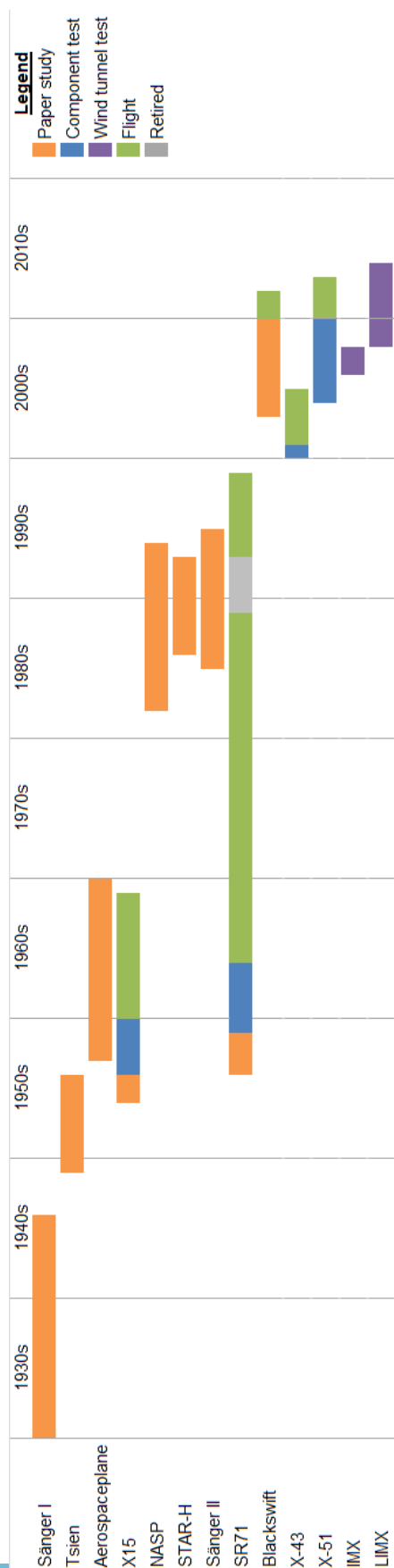


Figure 2.6: Timeline of various engine programs with their relative, estimated progress.

World War II, by heading to the edge of our atmosphere via the rocket engine, descend down to the stratosphere where the lifting body would generate lift again. This would cause the vehicle to climb in altitude again, then descend, etc, in a series of ever smaller "hops" until it reached its destination, drop a large bomb, and then head to Japan to land[12]. Sänger's spaceplane was considered too expensive and technologically out-of-reach at the time to be researched, designed, and built[12]. It was a good choice by the Germans, as Sänger had made a few mistakes in the re-entry calculations and the plane would have most certainly burned up in the atmosphere with the first hop[12].

Work on Sänger II, shown in figure 2.7, started in the 1980s during the height of the TBCC frenzy. The vehicle went through many design iterations and was proposed for many missions. The vehicle was designed to be a reusable launch vehicle which would rendezvous with a space station, drop off up to 36 passengers, then glide back down to earth to be refurbished[12, 13, 14, 15]. The vehicle would be developed to have two stages: an air-breathing stage and a rocket stage[14]. The air-breathing stage would be powered by a turbojet until the vehicle reached ramjet capable velocities, transition to the ramjet, and bring the vehicle close to the edge of the atmosphere[13, 14]. The second stage would separate from the air-breathing vehicle - which would return to port - and be powered via rocket to space[14]. It was hailed as a huge potential cost savings due to the air-breathing engines that would bring the rocket and payload closer to the edge of the atmosphere, decreasing the costs of launches, and that the air-breathing stage could maybe even be used as a hypersonic transport[13, 15]. However, the project ended in the mid 1990s as a paper study with very limited ramjet feasibility component testing[16], cited as being too expensive and technologically unfeasible[17].





Figure 2.7: Artist's concept of the Sänger II spaceplane[13].

### 2.2.2 Tsien Spaceplane

Hsue-Shen Tsien, a student of von Karman and one of the founders of NASA's Jet Propulsion Laboratory, was the mastermind behind this particular vehicle[12]. Again, while the vehicle was not a combined cycle engine, the advancements made through Tsien's work are substantial to spaceplane technology and reusable launch vehicles. Tsien was one of the many American scientists who flew to Germany at the tail end of World War II to meet and debrief German scientists, including Wernher von Braun[18, 12]. In addition to interviewing the scientists, Tsien was able to study Sänger's research, which was brought to the US after the war and translated from German into English[12]. Tsien collected all the information in a report which would become the so-called "bible" for many future aircraft and rocket engineers and cemented his place as the "father of the Dyna-soar"[12]. Tsien also went beyond Sänger's work and developed his own rocket powered transport vehicle, able to transport 10 people from New York to Los Angeles in 45 minutes[12]. The study never made it far, as Tsien's security clearance was revoked as he was under suspicion of harboring communist sympathies in the mid-50s[12]. Tsien eventually emigrated to China, where he became one of the founding fathers of the Chinese aerospace sector. Even though the Tsien spaceplane itself would

never fly, his research led to the Dyna-Star which would lead to the Space Shuttle, which was arguably the first semi-reusable launch vehicle.

### 2.2.3 X15

At the same time as the United States Air Force (USAF) and industry partners were working on the Aerospaceplane - discussed in subsection 2.2.4 - work had begun on the North American X-15 research plane, a joint venture between the USAF and NASA. Initially planned as an "orbital air-launched hypersonic boost-glide winged vehicle" [12], this vehicle is also not true combined cycle engine, but the data gathered from the X-15 at hypersonic speeds would pave the way for NASP. Although the initial goal for the X-15 was what the X-20 would eventually address, it was quickly realized those goals were too ambitious and the project scope was reduced to a flying test bed for new technology[18, 12]. Unlike previous aerospace projects, the X-15 quickly moved from pure paper studies to component studies, with wind tunnel tests starting as early as 1956[12]. The X-15, shown in figure 2.8 with one of its pilots - Neil Armstrong - broke altitude and speed records for the time. The X-15 proved that a vehicle could be engineered to go to enormous speeds. With this proof of concept, the United States started working on the largest hypersonic undertaking yet - the National Aerospace Plane.

### 2.2.4 The Aerospaceplane and NASP

The Aerospaceplane was the precursor to the NASP[19]. The Aerospaceplane was a collection of paper studies but was the first instance where someone suggested using a scramjet as the main engine for cruise on a vehicle, propelling it to Mach 5+ speeds and setting the tone for TBCC powered vehicles in the future. Ramjets and scramjets rely on the incoming freestream air to move at supersonic speeds so shocks form ahead of the combustion chamber in order to compress the air. Ramjets then slow down the flow to subsonic speeds for combustion, but scramjets keep the flow supersonic through the combustion chamber. Thus, in order to use a ramjet or scramjet for cruising speeds, a rocket or turbine engine has to be utilized to bring the vehicle up to supersonic speeds.



Figure 2.8: Neil Armstrong with the X-15 rocket plane, for which he served as a test pilot. Image courtesy of NASA.

The Aerospaceplane vehicle mission would be to take off horizontally, using a LACE - which is an air-breathing turbojet or turbofan where the air is cooled to a temperature where it liquefies and then pumped to the desired pressure, instead of running it through a compressor. To remove the nitrogen, which makes up almost 80% of the air we breathe but also is not combustible, a pair of ACES would essentially remove the nitrogen from the air through a centrifuging process[18]. If this sounds like science fiction by today's standards, it was ruled completely impossible at the time of design. The project never even attempted to leave the realm of paper. However, the theory behind the vehicle was a driving force behind the development of NASP.

NASP would have been the first combined cycle RLV. Also known as the X-30, it was meant to be a single stage to orbit, reusable launch vehicle which could take off from and land at a conventional runway[20]. The design featured an afterburning turbojet with a dual-mode scramjet in a separate inlet. The goals for the program were lofty, as were the projections by NASA and the USAF. Computational fluid dynamics (CFD) was to be used to cut down on wind tunnel testing and thus on the development cost of the program. Materials had to be invented to be able to withstand

the extreme temperatures when the vehicle would travel at hypersonic speeds. And the power plant would be the crown jewel of the vehicle. The announcement of NASP by President Ronald Reagan in his 1986 State of the Union address sparked international interest in a similar RLV[20]. The French company Dassault announced that same year they would develop the STAR-H, an air-breathing, horizontal take-off, combined cycle reusable launch vehicle[21]. The Germans got back in the spaceplane game by announcing the Sänger II, a turbojet-ramjet combined cycle powered vehicle to be used as a two stage to orbit (TSTO) RLV which had a separate orbiter (Horus) and launch vehicle (Cargus)[14].

The NASP vehicle would be initially powered by a turbojet to Mach 3 or 4, at which point a dual mode ramjet would take over and push the vehicle to Mach 6 and beyond, where the dual mode ramjet would essentially operate as a scramjet. The vehicle would then accelerate further and head upwards to orbit, where two rockets would blast the vehicle into space, making it a "single stage" that reached orbit. This vehicle would be able to launch at any time from any runway. Unlike rockets, which require specific take off windows and cannot return to their launch pad once in the air, the NASP vehicle would have made bringing cargo and astronauts to orbit much more convenient. The vehicle would have been larger than the space shuttle: 200 ft long and weighing in at 300,000 lbs at take off[22]. The inlets, as seen in figure 2.9, were designed to be two dimensional with an over-under configuration of the turbojet and dual mode scramjet.

The program hoped to lower the cost of reaching orbit and replace the space shuttle after its retirement. The program office believed launch costs would be reduced because the design would allow faster turn-around, usage of commercial runways and crew, minimal refurbishment between launches, no loss of major components, and a greater payload fraction due to the lack of oxidizer and oxidizer tanks[20]. Initially, there was a great deal of excitement around the program, even achieving a mention in the State of the Union Message by Ronald Reagan in 1986. Reagan hailed the NASP program as a cheaper way to reach low Earth orbit or, alternatively, travel to Tokyo from Washington DC in under 2 hours. He dubbed it the 'Orient Express'. This led to some confusion, as there was no plan to develop the 'Orient Express'[20].



Figure 2.9: Artist concept of the National Aerospace Vehicle, showing the two dimensional inlets. Image courtesy of NASA.

However, despite all the hype, the NASP vehicle never materialized. Marred by overly rosy projections, constant budget cuts, and technology roadblocks, it never got beyond the subscale testing stage. The program was essentially divided into three phases. Phase I preceded the actual NASP program and consisted of a comprehensive feasibility study, lasting from 1982 to 1985[23]. Phase II, starting in 1985, was meant to be the technology development and maturation stage. Phase II was projected to be completed in 1994 and would lead to the decision whether Phase III, consisting of a full-scale X-30 vehicle, should even be attempted[23]. In fact, the Congressional Budget Office (CBO) started suggesting as early as 1989, four years into the ten year program, that funding be slowed down. The CBO was concerned that the "outlook was overly optimistic" and that the program was striving for technology beyond the state of the art[24]. While acknowledging that US engineers had accomplished such feats in the past, specifically citing the B-1A and XB-70 bombers, the NASP program also had an aggressive timeline. While it took the XB-70 bomber 69 months from their equivalent of NASP's Phase II stage to test and the B-1A took 53 months, the

NASP program had scheduled 40 months of work between the end of Phase II and a flight test of the full vehicle[24]. By 1991, the CBO was calling for cancellation of the program, citing that the program had no real purpose beyond developing hypersonic technology, as payloads could be brought to orbit via rockets and the Strategic Defense Initiative could be used for strategic attack missions[25, 26, 27].

Another major factor for the cancellation of the NASP program was the cost. By 1993, the government had spent over \$2.5 billion with an additional \$1 billion of funding coming from various industry partners[27], but the program had only reached 25% of its critical events and tests[23]. In addition, the estimated cost of the program, originally projected for \$3.1 billion in 1986[23] ballooned to \$15 billion by 1992[18]. As the program was competing with other programs for limited federal funding, it needed to satisfy a clear need instead of existing as a technology development program. While the cost of the program is staggering, the projection was much lower than what was spent on the Space Shuttle prior to its first launch in 1981, which cost \$35 billion in 2013\$[28, 29] from 1972 to 1980.

It would be remiss to classify the whole program as a failure, despite not realizing a flight-ready vehicle. NASP brought about major changes to hypersonic system design, CFD, materials science, and scramjet propulsion. NASP was on the right track with its lifting body shape, called a wave rider[30]. NASP helped focus the CFD community on real world application rather than on the numerical integration schemes to use[31] while also highlighting the limitations of the tool[32]. On the materials side, the NASP program helped develop graphite/epoxy liquid hydrogen tanks, titanium matrix composites for the wing and tail, and carbon-carbon materials for the elevons[30]. With the funding from NASP, NASA Langley tested several flowpath models and compiled a database from the resulting data[30]. Additionally, there were several programs that spawned from NASP, including the X-43 (scale model test seen in figure 2.10) and X-51 test vehicles, the Small Scale Inlet Mode Transition Experiment (IMX) and the Large Scale Inlet Mode Transition Experiment (LIMX), and development of a high Mach turbojet[33]. All these vehicles have helped us understand the unique challenges associated with hypersonic travel.

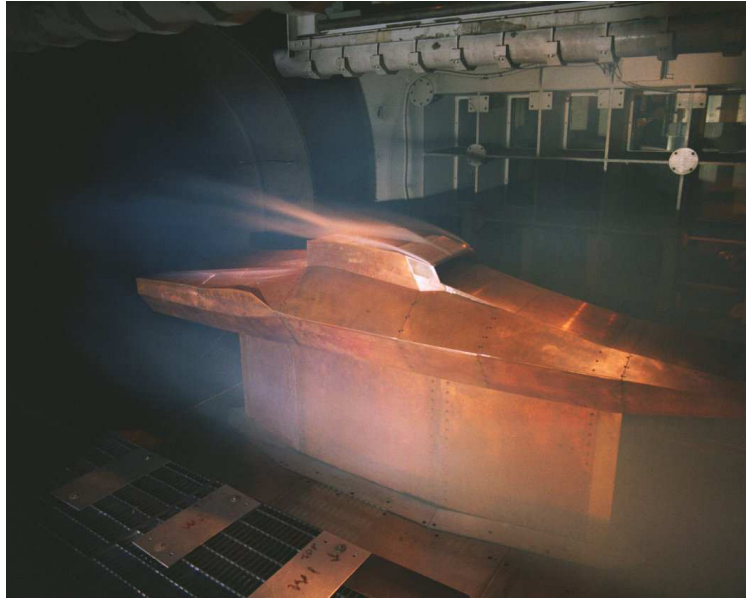


Figure 2.10: Scale model of the X-43 tested in the NASA Langley Hypersonic Wind Tunnel. Image courtesy of NASA.

### 2.2.5 SR-71 Blackbird Program

While the NASP vehicle would have been the first TBCC powered RLV, it is fair to say the first TBCC-like vehicle was the J58 powered SR71 Blackbird, shown in figure 2.11. The J58 engine, pictured in figure 2.1, is an afterburning turbojet. However, unlike a normal afterburning turbojet, this engine can operate as a ramjet at high speeds. It does this through a translating spike which serves as a device to keep the shock on the lip of the engine as well as redirecting the airflow at high Mach number.

At low Mach numbers, the translating spike is all the way forward and the side doors are open, allowing the maximum amount of air to travel to and around the engine. The side doors close as soon as the SR71 begins to move to reduce the drag on the engine. As the operating Mach number increases, the spike retracts, partially obstructing the airflow to the turbojet and redirects it towards the afterburner, allowing the afterburner to act like a ramjet[3]. The J58 is considered a TBCC-like engine due to its ability to operate as a turbojet, as an afterburning turbojet, and

almost like a pure ramjet when the majority of the air is redirected to just the afterburner. It is not considered a pure TBCC engine as the turbojet never completely shuts off, even at high speeds.

The SR71 was an impressive feat for its time. Starting in 1959 with funding from the Central Intelligence Agency (CIA), the aircraft was meant to be an intimidating spy plane[34]. The vehicle went through several iterations, starting with the A-12, which was exclusively a CIA reconnaissance plane, then became a fighter plane with the development of the YF-12A for the USAF in 1963[34]. In 1964, the SR-71 entered service. It would become the most famous of all the Blackbird variants. The various Blackbirds flew for several years before the Secretary of Defense decided to cancel the YF-12 program in 1968, mostly citing budgetary concerns as the vehicles were expensive to maintain between flights. The SR-71 was officially cancelled in 1997 by the USAF[34]. After the cancellation of the YF-12, NASA worked with the USAF to continue flying three Blackbirds as flying test-beds until 1998[34]. The research accomplished with the flying test-beds ranged from landing research for the space shuttle to inlet studies to validate wind tunnel data on, among other things, inlet distortion and inlet unstart[34].

The Blackbird program was highly successful and ahead of its time. While the maintenance and refurbishing of the aircraft turned out to be cost prohibitive, the program was overall a success. The Blackbird family flew for over 50,000 hours, almost 12,000 of those hours at Mach 3+. It proved to engineers everywhere that TBCC-powered vehicles were possible, although posing a difficult engineering challenge.

### 2.2.6 Falcon Program

The Falcon program, funded by Defense Advanced Research Projects Agency (DARPA) and the USAF, is meant as a means to design and test hypersonic technologies enabling global reach [35]. The program consisted of three major thrusts (two remain at present).





Figure 2.11: SR71 taking off. Image courtesy of NASA[36].

The first part of the program is the High Speed Turbine Engine Demonstration (HiSTED), which is aiming to develop a Mach 4 capable turbojet [37]. As stated earlier, the fastest a turbojet has ever propelled a vehicle was the SR-71, which topped out at Mach 3.2. The HiSTED program aims to improve individual turbine components in order to reach the goal of Mach 4 flight [35]. At present, only component tests have been completed.

The second part is the Falcon Combined Cycle Engine Test (FaCET) project. This is working to validate operational limits of a TBCC engine and its components. The individual components being tested are the inlet, combustor, and static nozzle. For the inlet, FaCET is looking at the integration of the low speed and high speed flowpath and testing the properties of these inlets. Wind tunnel tests have been completed as of 2008 [35]. The combustor test program is looking at using one dimensional codes as predictors of the combustor's performance as well as finding ways to create continuous, stable combustion in a dual mode ramjet [37]. Lastly, the static nozzle tests are to enable a variable geometry aft cowl nozzle and determine its effects on engine performance as well as validating the CFD [35]. All of these tests seek to complete a "freejet test", which would integrate a TBCC propulsion system and its components into a demonstrator vehicle, the HTV-3X, capable of taking off and landing on its own and achieve Mach 6 flight [37].



Figure 2.12: Artist's concept of the Blackswift vehicle[38].

The last part was the Blackswift, shown in figure 2.12, which was canceled in 2008 [35]. Blackswift would have been a vehicle that would be accelerated to Mach 6+, cruise for about a minute, before landing autonomously. The vehicle was meant as a demonstrator for a global reach intelligence, surveillance, and reconnaissance vehicle with a secondary mission as a launch vehicle [37]. Although \$10 million was appropriated in 2008, which was not estimated to be nearly enough funding to achieve a demonstrator vehicle, the project was ultimately canceled all together[35].

The Falcon program continues as FaCET and HiSTED today, working to improve individual components and validate design codes.

### 2.3 Inlet Distortion

All the above programs have recurring themes: the development costs are too high, the technology readiness level is not high enough, and to be successful both computational and experimental methods have to be employed. It is a monumental task to tackle all of these problems and it would be well beyond the scope of a PhD dissertation. This work seeks to contribute to the problem of inlet flow distortion - how computational and experimental methods can work together to bring down the overall cost and cycle time.

### 2.3.1 What is Flow Distortion?

Flow distortion refers to any flow that deviates from a uniform profile in space and time[39]. These flows will deviate from a uniform flow (shown on the far left of figure 2.13) and idealized flow because the profile will no longer be uniform and stable. Distortion can occur due to fluctuations in velocity, total pressure, or total temperature across a slice of the inlet[40]. This fluctuation can be caused by various sources, including internal sources such as shock wave and boundary layer interactions, boundary layer separation, and vortices traveling down the inlet[40] and external sources such as "armament firing, flight maneuvers, thrust reversal, inlet unstart, inlet buzz"[41].

Distortion is usually subdivided into radial and circumferential directions. Radial distortion refers to the velocity, total pressure, or total temperature profile varying from tip to hub, as seen in figure 2.14(a). In the example given, it shows a large amount of low pressure distortion in the center and high pressure distortion near the tip. Radial distortion tends to be more benign[40].

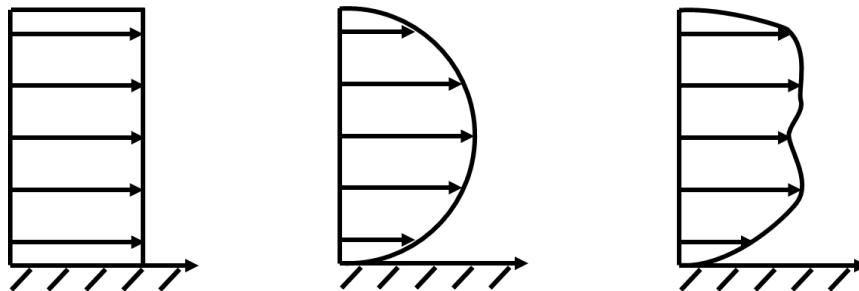
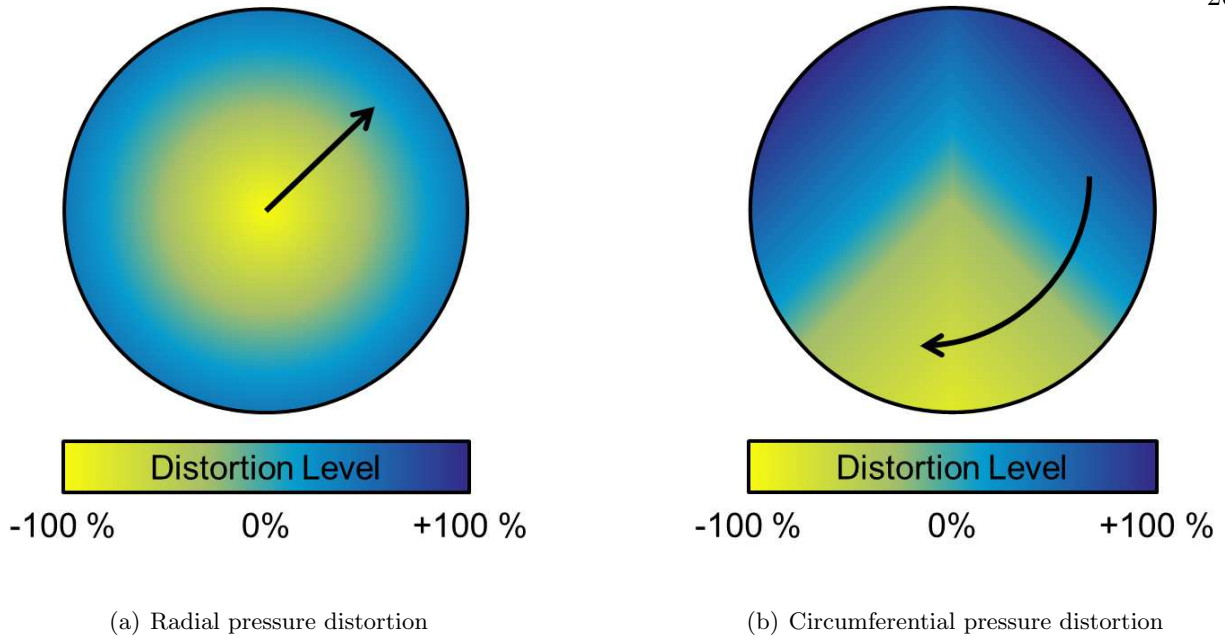


Figure 2.13: Example of a velocity profile for uniform flow, an ideal Poiseuille flow, and distorted flow in two dimensions.

The other type of distortion, the circumferential type, varies as one moves around the inlet. In the example shown in figure 2.14(b), it shows high pressure distortion in the 9 o'clock to 12 o'clock and 3 o'clock position, with an area of low pressure distortion between the 5 and 7 o'clock positions. Circumferential distortion tends to be a much bigger factor in distortion than radial. However, all distortion encountered by real inlets are a combination of radial and circumferential distortion[40].



There is also a differentiation between static and dynamic distortion. Static distortion refers to flow distortion that can be captured with steady-state instrumentation while dynamic distortion can only be captured with dynamic sensors[42]. A cartoon drawing of such a reading for one sensor can be seen in figure 2.14. Realistically, an engine sees both types of distortion. However, like radial and circumferential distortion, one is more benign than the other. It has been widely documented, including in the standard governing inlet face distortion, that dynamic distortion has a much greater impact on stall margins[42, 43].

### 2.3.2 Why is Characterizing Flow Distortion Important?

Flow distortion can cause major problems for the engine. While all engines can handle some flow distortions, they all have a limit. If the flow distortion exceeds this limit, it can lead to engine stall or inlet unstart. In fact, one way to think of the stall margin of an engine is to think of how much distortion an engine can tolerate[40, 44].

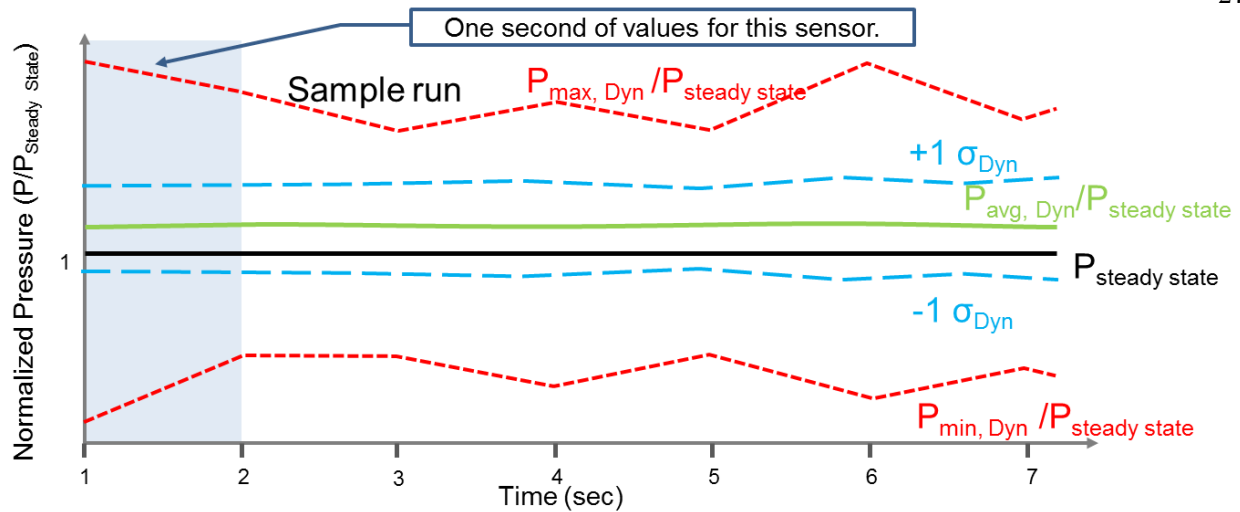


Figure 2.14: Comparison of normalized steady state versus dynamic pressure readings. The black line shows the reading of a normal, steady state pressure transducer. The dashed red line shows the extrema of the dynamic pressure transducer readings.

The main way inlet distortion leads to engine stall is through a lack of mass capture or mass flow delivered to the engine[39] and a lower total pressure recovery[44]. When there is less mass capture and a lower pressure recovery, we're moving down the stall line towards the origin of the plot, as shown in figure 2.15. That means the vehicle has a much smaller operating range.

The literature review in section 2.3.4 will go more into detail on this point, but as more advanced aircraft have been developed, the overall stall margin has been reduced. As this trend developed, so did research into flow distortion.

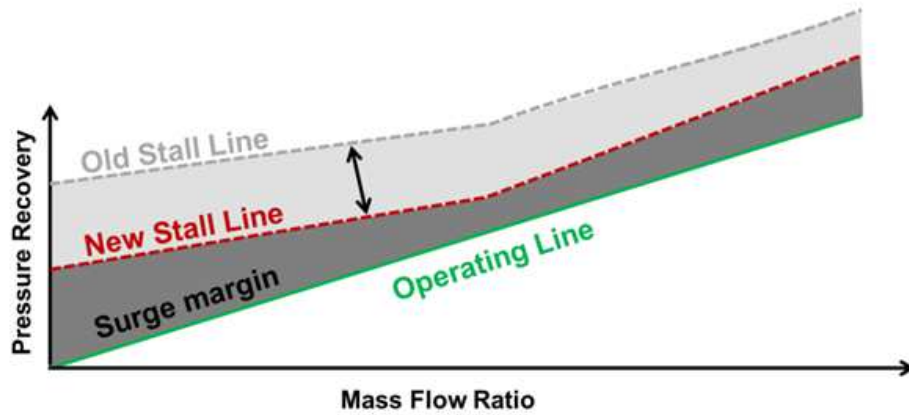


Figure 2.15: Sample compressor stall margin with the effects of distorted flow.

### 2.3.3 How is Flow Distortion Defined?

Flow distortion is based on a non-uniform flow. It is however difficult to quantify exactly how much it is distorted because it needs to be related to something. In the most general terms, distortion is quantified by the following relation, shown in equation 2.1.

$$D = \frac{P_{t,max} - P_{t,min}}{\bar{P}_t} \quad (2.1)$$

This relation simply states that at the particular slice of the inlet, we subtract the minimum from the maximum total pressure in that area and divide by the average in that slice. A value of 0 means there is no flow distortion and a positive or negative number would indicate there is some distortion.

Flow distortion is generally measured via an "index" or "distortion descriptor". These terms are used interchangeably. The index refers to the normalized deviation of flow from the bulk of the flow, usually measured in total pressure. There are many distortion indices, generated through extensive testing at the engine manufacturer; for the purpose of this work, the distortion indices used by Stoll et al [1]. will be used. These indices are classified into circumferential, radial, and overall distortion indices. The definition of these indices can be found in section 2.3.5.

### 2.3.4 Work to Date on Flow Distortion

Flow distortion in general has been an important topic for engine developers[45]. The specific topic of the inlet's contribution to flow distortion has been coming to the forefront of the field as jet engines were pushed to the limits of their capabilities. Designs that included Vertical and Short Take-Off and Landing (VSTOL) capabilities[46] and highly integrated engine designs such as the XB-70[47] made researchers take note of the inlet's contribution to flow distortion. It was in this era that researchers first started to tie pressure fluctuations in the inlet to engine performance[45, 47]. Other programs saw opportunity to squeeze more performance out of the vehicle in general or the engine specifically by reducing inlet flow distortion. The field is vast but can be roughly categorized into four major sectors:

- (1) Flow distortion mechanics & experimental set-up
- (2) Steady state versus dynamic distortion effects
- (3) Distortion effects on the propulsion system
- (4) Distortion through fan and compressor stages

Each one of these areas will be discussed separately in the following sections. It should be noted that, as with all research, none of the sources listed below generally only studied one of these sectors at a time and there is some overlap, but individual pieces of the research as it relates to the above thrusts have been parsed out to give a complete overview of each sector.

#### 2.3.4.1 Basic Mechanics & Experimentation

In the mid-1960s, researchers at the USAF and NASA started looking into various inlet designs and found that some caused a phenomena called "inlet unstart" or "engine stall". Inlet unstart refers to an event where the inlet back-pressures and has to expel captured air, usually in the form of a normal shock and the shock systems have to be re-established for the inlet to properly compress the air. Engine stall refers to a similar event, but inside the turbojet. These

are often violent - in the case of SR71 and XB70 pilots, deadly - events. There are many causes of unstart and stall, but in highly integrated inlets, a major factor can be inlet distortion. The research into the flow mechanics and experimentation within the field is lengthy and broad, with engineers investigating many different avenues.

In 1965, NASA researchers were experimenting with two side by side inlets and they wanted to see if there was an interaction between the two shock systems[48]. The goal of the testing was to find the likelihood of the inlet unstating or being on the verge of unstating - called "inlet buzz" - based on the shape of the inlet. That same decade, wind tunnel testing in NASA Glenn Research Center's (GRC) supersonic 10 foot by 10 foot supersonic wind tunnel led NASA to conclude that the magnitude of the pressure fluctuations could vary with the location of the terminal shock[48]. Preliminary data suggested that installing bleed holes could decrease the magnitude of pressure fluctuations at the design point and vortex generators could reduce it over the full flight envelope. This discovery, that bleed and vortex generators would be beneficial to decrease distortion, would be verified by several researchers[48, 49, 50, 41, 51]. Mitchell also noted that the bleed should remain aft of the vortex generators, as otherwise it would have the opposite effect, distorting the flow further[49]. Albers and Felderman looked at design parameters that could reduce inlet distortion, especially changing the subsonic diffuser shape[52]. Latham discussed changing the shape of the whole inlet in order to reduce distortion[48, 53] instead of just redesigning individual components. His redesign resulted in a smaller, bifurcated inlet with various cowl shapes and with a blow-in door for additional airflow.

The actual causes of inlet flow distortion were investigated as well. During flight tests of the F-111, Hughes and Johnson noted that the distorted flow would propagate through the engine and seemed to be tied to the boundary layer[54, 48]. This would be later corroborated by Albers, who also found that boundary layer separation in the subsonic diffuser was a major factor in reduced stall margin[52]. Melick, whose work is extensively discussed in section 2.3.4.2, wanted to relate distortion to stall margin loss and turbulence indicators[55, 48]. He was also one of the first to step away from purely empirical relations and use actual analysis to determine inlet distortion.



He thought that detailed distortion patterns would be indicative of the loss in stall margin, but concluded that much more in terms of flight test data would be required, as wind tunnels were incapable of simulating the types of situations in which turbulence occurred[55]. Latham found that angle of attack was another major factor of inlet flow distortion, with negative angles of attack being especially bad[53].

Flight testing of the XB70 in 1970 showed that altitude, atmospheric conditions, and incoming turbulence had major effects on the performance of the inlet[56, 47]. Martin discovered in the moments leading up to engine stall on the XB70, the turbulence was very high[47]. Further, he concluded that while statistical assumptions on dynamic pressure fluctuations, discussed in section 2.3.4.2, could be used but were far from perfect. Povolny took into account flight data and wind tunnel data when he found, in 1971, that combined steady state and dynamic "oscillations" - as he called them - would have a greater impact than either did by themselves[41]. Additionally, Martin noted that as Mach number increased, the distortion in the inlet decreased, due to the decreased flow separation in the inlet[47]. External factors beyond the atmosphere could impact distortion, such as weapons fire and flight maneuvers[41].

In the realm of testing and producing distortion in wind tunnel experiments, the main guideline today is the Aerospace Recommended Practice APR1420[43]. However, the requirements we have today to produce, measure, and reduce distortion data has come a long way from 1969. Back then researchers, armed with magnetic tape and analog instruments, recorded flight and wind tunnel data from several inlet designs and compared the data to Gaussian distributions. The researchers concluded that the pressure fluctuations (steady state only at this point) could be measured with sensors available in 1969 and their statistical parameters, such as pressure recovery and fluctuations, could be indicative of inlet performance[57, 48]. They realized the limits of their work as more sophisticated sensors would be required to actively monitor the flow distortion in the inlet.

There are two main focuses on inlet distortion experimentation. One is trying to generate distortion, either in an inlet or ahead of the engine, and the other is trying to measure the distortion levels. We'll first delve into how NASA and engine companies worked a great deal on how to

generate distortion patterns. Initially, the community turned to simple distortion screens, as can be seen in figure 2.16. These screens are extremely easy to transport and install, but they are also limited. They can only test a single, steady state distortion pattern at a time and changing screens means having to stop the test, remove the engine, change the screen, and re-install the engine to the test cell[58]. VanDeusen and Mardoc at Pratt & Whitney worked on a mechanism that could create distortion. Two apparatus worked independently to create both circumferential and radial distortion, shown in figure 2.17[44, 58]. The circumferential distortion was controlled by vanes installed in four rectangular quadrants, each outfitted with ten vanes. They could be opened and closed individually. The radial distortion was controlled by four guillotine-like mechanisms that created a blockage in the inlet. This design's main limitation was that distortion could only be evaluated in 90 degree increments[58]. In the early 1970s, NASA developed a few other methods as well. Burcham at Dreyden worked on ways to create turbulence and measured distortion as it changed with Mach number, validating wind tunnel data for the F-111[59]. At the same time NASA created an air-injection system that was equipped with nine jets controlled by six valves at 60 degree intervals, as shown in figures 2.18 and 2.19[60]. The air injection test allowed researchers to simulate dynamic pressure fluctuations by controlling the strength, frequency, and duration of the six valves[60, 61, 48]. Today, work is being performed on perfecting the distortion screens that can simulate dynamic distortion, where there are various sized airfoils in different patterns, as shown in figure 2.20[58]. These screens have the benefits of the first generation screens - portable and simple - while allowing for some more advanced testing.

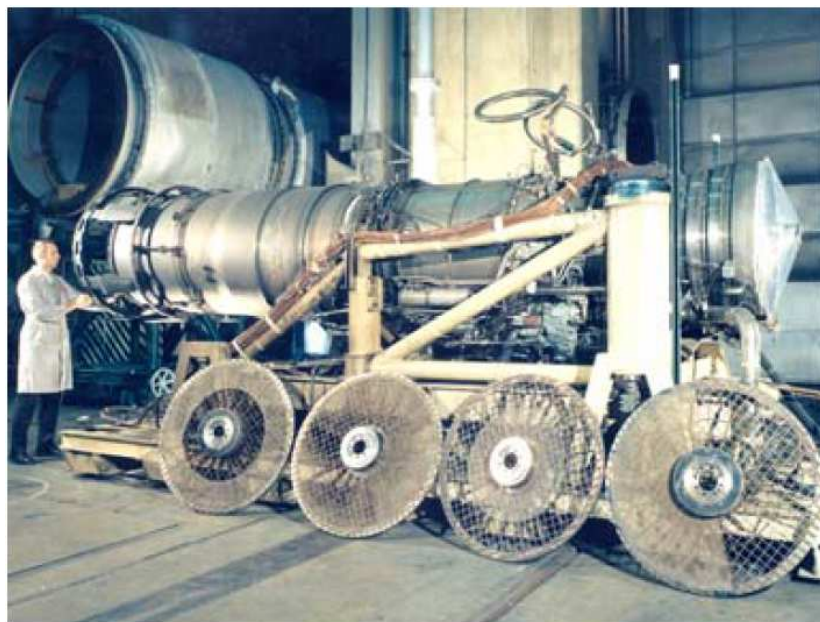


Figure 2.16: Distortion screens used to test inlet total pressure distortion. Image courtesy of Arnold Engineering Development Center[58].

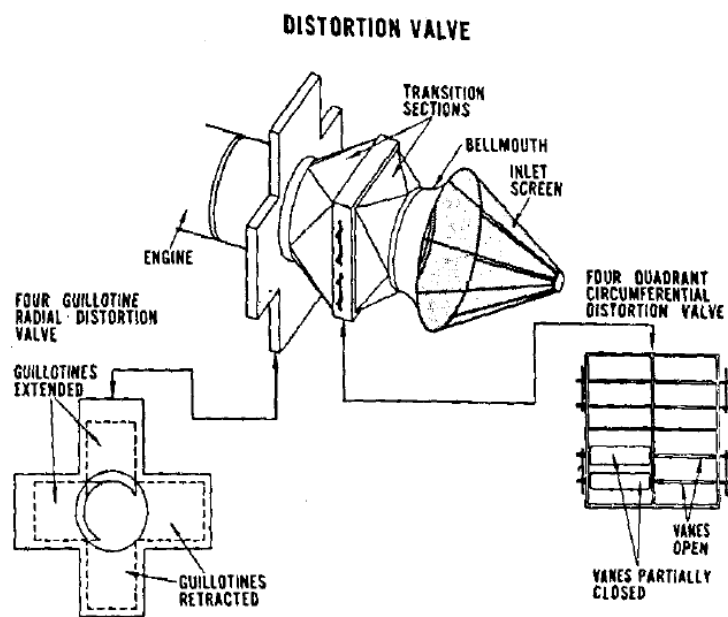


Figure 2.17: Test mechanism suggested by VanDeusen and Mardoc at Pratt & Whitney[44]. Image reproduced with permission of the rights holder, AIAA.

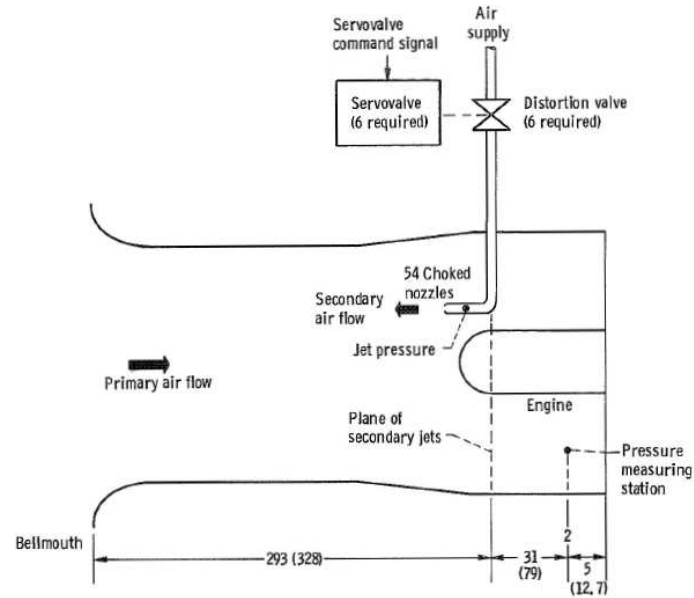


Figure 2.18: Test set-up for dynamic distortion generation. All units in inches with centimeters in parentheses. Image courtesy of NASA[60].

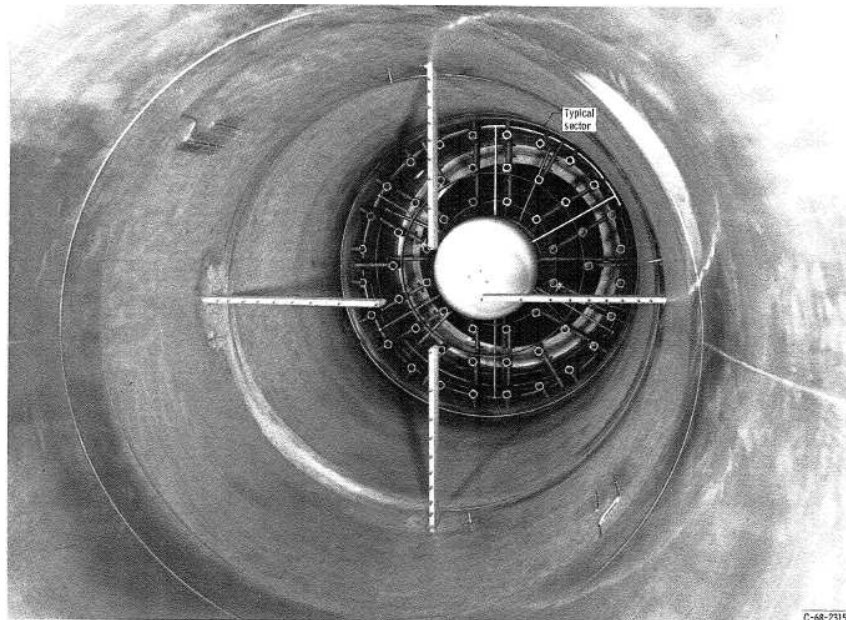


Figure 2.19: Photograph of the jet injection test apparatus installed in an engine. Image courtesy of NASA[60].



Figure 2.20: Sample of a modern distortion screen with varying vane sizes and densities. Image courtesy of Arnold Engineering Development Center[58].

To measure the distortion already in the inlet, it is nowadays common practice to use a 40 probe, five rake array at the aerodynamic interface plane (AIP)[43]. However, initially, Stoll et al ran a series of experiments in 1979 where they varied calculating various indices using the full array of 320 probes down to 20[1]. Each rake contained 5 probes. The probe number was not only reduced, but the subsets were chosen from various clocked positions, so that the optimum location could be found. In the case of the four rake, 20 probe subset, it was clocked 16 times, either by 5 or 7.5 degrees[1]. All the probes only read steady state pressure fluctuations, as dynamic pressure sensors were not available at the time. The researchers found that the distortion descriptors had errors between 20-40% from what was read with 320 probes. Having only 20 to 40 probes resulted in the 40% error, according to the research. A more lengthy discussion will follow in sections 2.3.4.2 and 3.2 on the validity of making conclusions based just on steady state pressure probes and on the experimental set-up respectively. It should be noted that most of the conclusions on the error in the index results are not applicable to today's testing. Nowadays, each one of the 40 probes -

arranged as is shown in figure 2.22 - is usually a highly sensitive, dynamic pressure probe that can sample the pressure at over 20,000 Hz.

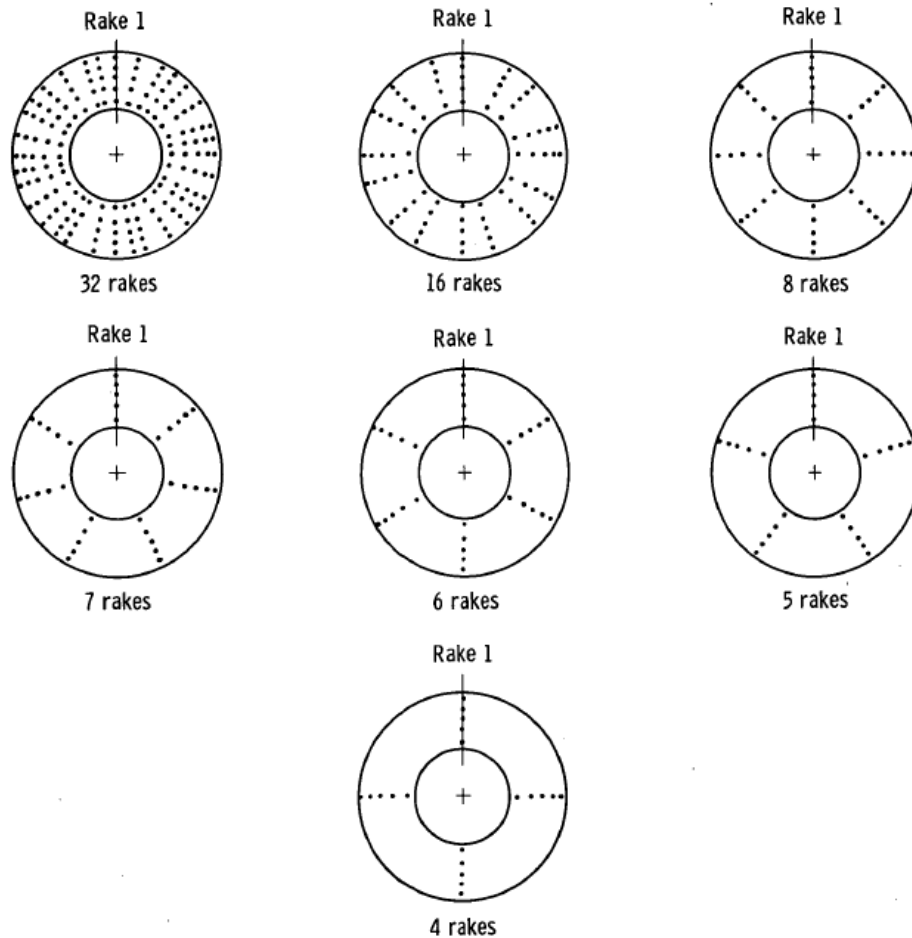


Figure 2.21: Various rake configurations used in a 1979 test to determine optimum rake configuration.

Image courtesy of NASA[1].

The main location where inlet pressure distortion is evaluated at is the Aerodynamic Interface Plane (AIP); this is where the engine face and inlet meet[45]. The majority of NASA's inlet group research is focused on this area, mainly on ensuring there is adequate total pressure recovery and reduced distortion at the engine face[62, 63, 64]. Recent research shows that it may be beneficial to track the distortion throughout the inlet, especially in highly integrated vehicles, to ensure off-design

performance[45].

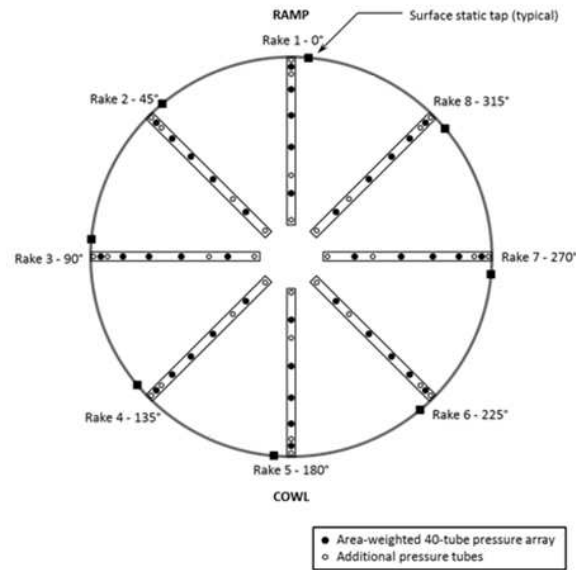


Figure 2.22: Modern rake locations, as suggested by ARP1420[43]. Image courtesy of NASA.

#### 2.3.4.2 Steady State and Dynamic Distortion

The true beginning of this thrust of study was in 1969 when engineers at NASA, using the apparatus described in reference [60], tried to quantify what different pulse durations and frequencies would do to the engine[48, 65]. They found that the amplitude of the response, meaning how the engine reacted, and the duration of the pulse, meaning how fast the air was ejected from the jet, were inversely related. A short, sharp injection was worse than a long, slow injection. This was the first hint of dynamic distortion.

With 1970s technology, it was difficult to obtain instantaneous readings. Researchers postulated that the instrumentation had to be able to sample at least at 600 Hz to capture dynamic distortion, but even that was out of reach at the time[50]. There was a confirmed relationship between steady state and dynamic distortion, though, and researchers guessed it scaled with the size of the AIP. Because of the difficulty in reading at such high rates, certain researchers concluded, incorrectly, that

even when distortion was not present, stall could occur[41]. Of course stall can occur without inlet distortion being the culprit, but Povolny had no way to know that his inlet probably experienced dynamic distortion in addition to the steady state which could easily lead to engine stall or inlet unstart. Slowly, the instrumentation developed, but in 1972 as they were trying to capture total pressure changes dynamically, a NASA researcher noted that the instrumentation was "insufficient for stability but adequate for early studies" of inlets[48, 66].

Melick, whose work would become the benchmark for years to come, created a analytical model for dynamic total pressure fluctuations that utilized statistical methods to fill the gaps[48, 55]. Melick and Ybarra went on to write a computer code based on that assumption. Calogeras at NASA looked at data from several projects tested in the GRC 10 foot by 10 foot supersonic wind tunnel at the time and found that the dynamic distortion could have huge impacts on the stability of the engine[48, 67]. He also concluded that dynamic total pressure peaks are unique and didn't necessarily follow a Gaussian distribution. Despite that, Melick and Ybarra's model would be used for years to come. In 1975, Melick and Ybarra's method was improved upon by taking into account the turbulence level and vortex core size in the fluid flow field[48].

In 1976, NASA discussed the merits of using root mean square and probability density function, arguing that the longer you ran an experiment, the more likely it was you were to capture the maximum total pressure fluctuations and thus the maximum dynamic distortion[48]. The idea that to analyze dynamic pressure distortion one had to find the maximum response using statistical methods would be studied for the next several years and be improved upon[48, 68, 69, 70, 71]. The statistical method was also compared to flight and test data and was found to be within 20% error of observed values during flight[48, 72, 73]. Wind tunnel data was considered to be accurate as well for capturing dynamic pressure fluctuations; one researcher noting that "peak distortion data from subscale inlet model wind tunnel tests are shown to be representative of full-scale flight test peak distortion" [74, 48].

In 1980, a report written by engineers at NASA looked forward to the exciting prospect of having analog/digital hybrid editing systems to monitor dynamic pressure distortion[75, 48].



Engineers longed for 600 Hz sampling rates. Today, dynamic pressure probes read at sampling rates of over 20,000 Hz. Computers can handle reading in data from hundreds of probes simultaneously and store terabytes of data locally. Our knowledge of dynamic pressure fluctuations and dynamic pressure distortion has vastly increased by testing with the technology available, and we know that dynamic pressure distortion does not follow a Gaussian distribution, as will be shown in the IMX experimental data analysis in section 3.1.2, but is rather unique as Calogeras thought in 1973. Nevertheless, the researchers were right in concluding that accurate information about steady state and dynamic distortion both played an important role in a successful engine-inlet integration.

#### 2.3.4.3 Propulsion System Impacts

With the advent of advanced fighter jets, as engines were pushed further and further, stall margins were increasingly reduced. Kostin in 1969 in fact called for the reduction of stall margins, writing that "through better definition of the statistics of the inlet engine system at any instant", we should be able to reduce the stall margin to the minimum required[57]. Kostin may or may not have been aware that inlet distortion would be one of the factors that would require engineers to keep some stall margin. That same year at GRC in the 10 foot by 10 foot supersonic wind tunnel, engineers tested various inlets with and without the engine to see if the pressure field was impacted[48]. It was not.

In 1971, Povolny saw in experiments that flow conditions in the inlet could impact the operating limits of the engine[41]. He concluded it was inlet pressure distortion. NASA agreed and in 1973 published a report that defined how steady state circumferential total pressure impacted the engine's stall margin[48, 55].

As is mentioned in section 2.3.4.4, the TF30 engine was extensively studied, but so was the J85. In 1974, an axisymmetric inlet was put before a J85 engine to see the distortion response and four instantaneous distortion indices were created to describe the phenomenon[48, 76]. In addition, the author wished to create a universal index to describe inlet distortion. It may have been due to the fact that at the same time, NASA engineers looked at all available results, be they

theoretical, analytical, or experimental in nature, to find a way to characterize their impact on the engine[48, 77]. They found that the TF30 and J85, extensively studied at this point, response to inlet distortion could be predicted to some measure of accuracy. It seemed like a universal index would be possible. However, engine technology would drastically change over the next half century and experts nowadays agree that a universal index, applicable to all engines, would be impossible.

With everyone in agreement that the main impact of inlet distortion on the propulsion system was reduced stall margin, engineers and scientists started to try and investigate what specifically about inlet distortion caused the reduced stall margin. While today it is understood that it causes uneven loading on the fan and compressor blades, at the time, NASA had some ingenious ways to try and determine what exactly caused the reduction in stall margin. NASA investigated a simple two dimensional inlet, attached to both a cold pipe and a J85 engine, to see how the inlet handled an ingested wing tip vortex[48, 78]. The vortex did cause a reduction in stall margin, but it was solely due to the vortex location and rotation, not the inlet distortion. The location of the support struts also had an impact on stall margin and that a variable exhaust nozzle could increase the stall margin of the engine to offset the effects of inlet distortion[48, 42].

#### **2.3.4.4 Propagation Through Fans and Compressors**

The last thrust of distortion research in the past has dealt with how inlet distortion affects fan and compressor stages and the rest of the engine. This research is coupled with that mentioned in section 2.3.4.3 but goes beyond engine performance.

In 1970, as the community became aware of the existence of dynamic distortion and that it reduced stall margins, NASA started looking at how this impacted the fan and compressor individually. McAulay found that while steady state distortion can change the transient of an engine, it didn't seem to impact stall margin greatly. However, dynamic distortion did reduce the stall margin of the compressor of a turbofan engine[48, 79]. McAulay stressed early on that it would become critical in the field for engineers to find ways to prevent compressor stall due to inlet distortion.

A year later, Povolny looked further into the impacts of distortion on compressors. He found that although the compressor's stall margin was decreased, the first stage of blades to see the distortion was hardly ever the "weak link", but rather the stall margin reduction came further down the row[41]. He also noted that the fluid flow interactions between blade rows had a much larger impact on stall margins.

At the Naval Postgraduate School, Farmer started investigating if there was a way to analyze the inlet distortion traveling through an axial compressor stage. Using simple relations, he found that distortion could be modeled as vorticity[40]. The goal of his thesis was to create a more comprehensive and reliable method to determine how much of the inlet distortion propagated through the compressor. A year later, Melick at NASA Ames used a simple compressor-turbine work balance over the whole compressor to see if inlet distortion affected the engine[48, 55]. This was considered "sufficient" at the time being for an analysis.

Components beyond the fan and compressor were also investigated. In 1974, NASA investigated distortion data gathered through a whole engine, including the fan, low pressure compressor, high pressure compressor, as well as the afterburner. Velocity was measured at the inlet and exit of the compressor with and without distortion, but no significant changes were detected[48, 80]. The researchers tried to find the location in the engine when distortion did become an issue, but were unsuccessful.

In 1975, NASA again looked at a whole engine, this time the TF30. Researchers measured the effects of distortion on the internal workings of the engine, specifically how it impacted velocity, temperature, and pressure[81, 48]. The inlet distortion created in the test was circumferential in nature, using an air jet device discussed in reference [60], but inside the engine it became circumferential and radial, which makes sense as the rotor blades would add a radial component. The researchers also noted specifically that velocity did not change with or without distortion present, nor did it seem to impact overall performance, other than stall margin. The following year, the engine was again investigated using the air jet device to create dynamic distortion for the engine[48, 82] while steady state distortion was created in the inlet. The researchers were now able

to pinpoint that the stall was initiated near the front stages of the low pressure compressor when the engine did eventually stall. That same year, the engine was instrumented to find a relation between the rotating and surge stall margins[48, 83]. The team confirmed that the low pressure compressor was most important to maintain stable thrust output from the engine as distortion was present.

As it became clear now that the low pressure compressor and fan were clearly the main focus when inlet distortion was present, researchers set off trying to quantify "how bad" it was when distortion hit the fan. A paper presented at Pennsylvania State University shared that when a fan stage was subjected to steady state distortion from an inlet, there were pressure and velocity effects and it could lead to a cascade effect[48]. A journal paper discussed NASA's work in trying to predict how the distortion eventually dissipated through an axial compressor subjected to steady state inlet distortion[48]. Burstadt et al also presented in 1976 that even small perturbations in the steady state distortion entering a compressor stage could have a major impact on compressor stall margin[48, 84]. Impellers were also investigated and theoretically inlet distortion traveling into the engine would be even less of a problem there than with axial compressors[48]. However, while inlet distortion did not seem to impact a whole compressor module, researchers did find that it changed the flow field locally at the airfoil[48].

When computational capabilities increased, the research started to turn away from looking at just stall margin and instead look at how ingested distortion impacted the flow field overall. In 1980, NASA theorized that non-uniform, swirled flow would translate through the engine and could cause the flow to be different downstream than if distortion was not present[48]. There was also a push to define what parameters inside the compressor could aid the designers in reducing the swirl and improve the flow field[48].

In modern times, we know that the combination of steady state inlet distortion and swirl in the flow can cause problems for fan blades[39]. Swirled flow is more pronounced, as it will cause a drop in performance, while steady state inlet distortion will be benign. However, when swirl is present in the flow, it can cause the distortion to amplify. There is still research on whole compressor modules, but at a much slower rate than in the mid to late 1970s, and usually much more focused.

In 1998, Boller looked at how a wake ingested in an inlet would impact the distortion and thus the compressor [85]. He found that as wake thickness increased, the inlet distortion increased. The amplified distortion still did not seem to cause a propagation through the blade rows, leaving the dynamic response between blade stages unchanged.

### 2.3.5 Distortion Index Definition

The above section went into detail about what research has been performed in the field of inlet flow distortion. However, this is only a partial picture. In section 2.3.3 it was alluded that the level of distortion is measured via an index. In the following section, various indices that are used in this work are described.

#### 2.3.5.1 Circumferential Distortion Index

Circumferential distortion indices quantify the likelihood of distortion occurs as one sweeps through the angles of the AIP, as is shown in figure 2.23. The impact of circumferential distortion on the surge margin is shown in this figure. What is most interesting to note is that four areas of  $45^\circ$  have less of an impact on the surge margin than one area of  $180^\circ$ .

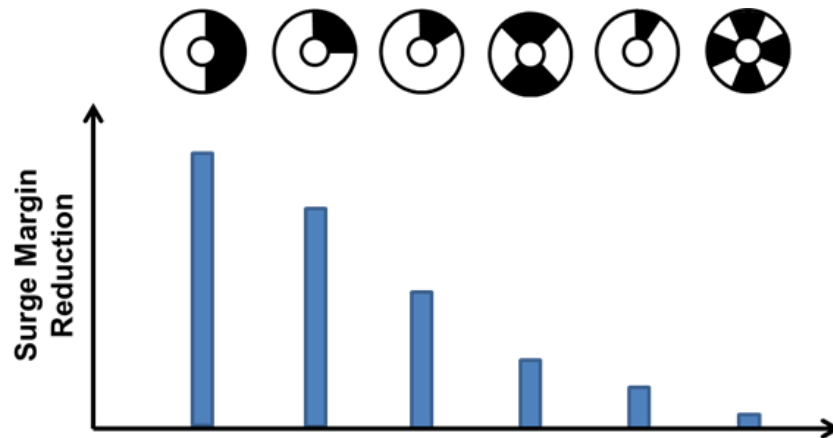


Figure 2.23: Reduction in surge margin based on various circumferential distortion patterns tested, based on reference [86].

This work used two different indices,  $K_\theta$  and IDC, to describe the circumferential distortion.  $K_\theta$  is based on the summation of the pressure tangentially, at constant radius. The calculations to obtain the overall ( $K_\theta$ ) and ring ( $K_{\theta,i}$ ) distortion are shown in Eq. (2.2). A full derivation of  $K_\theta$  can be found in reference [87].

$$\begin{aligned}
 K_\theta &= \frac{\sum_{i=1}^{NP} \frac{K_{\theta,i}}{R_i}}{\sum_{i=1}^{NP} \frac{1}{R_i}} \\
 K_{\theta,i} &= \frac{1}{q_2} \sqrt{A_i^2 + B_i^2} \\
 A_i &= \frac{1}{180} \sum_{j=1}^{NP} P_{t_{i,j}} \Delta\theta_j \cos\theta_j \\
 B_i &= \frac{1}{180} \sum_{j=1}^{NP} P_{t_{i,j}} \Delta\theta_j \sin\theta_j
 \end{aligned} \tag{2.2}$$

On first glance, it appears that Eq. (2.2) has dimensions of degrees. However, as the derivation of the equation in reference [87] shows, the  $\frac{\pi}{180}$  term is the conversion from degrees to radians. The  $\pi$  term in the conversion cancels out with the initial derivation of  $A_i$  and  $B_i$ , leaving just  $\frac{1}{180}$ .

IDC is a simpler calculation, shown in Eq. (2.3). The overall distortion is the larger value of the average of the inner two rings and the outer two rings. The ring distortion is a ratio of the average pressure minus the minimum pressure to the average pressure.

$$\begin{aligned}
 IDC &= \left[ \frac{1}{2} (IDC_1 + IDC_2), (IDC_4 + IDC_5) \right] \\
 IDC_i &= \frac{\overline{P}_{t_j} - \min(P_{t_{i,j}})}{\overline{P}_t}
 \end{aligned} \tag{2.3}$$

It should be noted that having a single 180 degree section of distortion caused more of a surge margin reduction than four 45 degree sections, as can be see in figure 2.23. The difference

between the two circumferential indices studied is that the  $K_\theta$  index takes into consideration the contribution of each individual probe to the overall ring distortion and then averages together all the ring distortions to get a final distortion number. This index does not focus on minimum or maximum values but rather focuses on comparing area-weighted averages of measurements at one radius to the next. *IDC* on the other hand tries to first find the lowest pressure value per ring and then finds the maximum average pressure of the two tip and two hub rings, completely ignoring the middle ring of probes. This method is more focused on how much the average ring pressure deviates from the overall face average pressure.

### 2.3.5.2 Radial Distortion Index

Radial distortion indices describe the distortion as one steps from the center outwards towards the perimeter of the AIP, as is shown in figure 2.24. It should be noted that there is a greater reduction in surge margin if there are areas of low pressure at both the hub and the tip - more so than if an area of low pressure only exists at the hub. This is because low pressure areas on the fan blade tip leads to uneven loading of the fan blade[86].

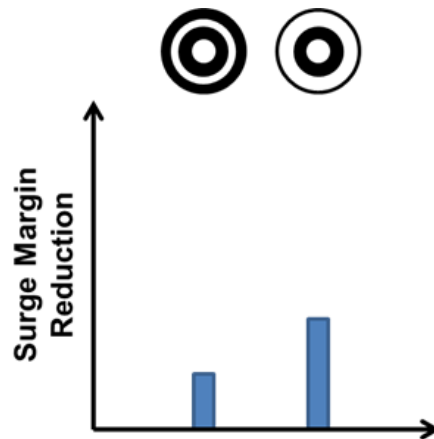


Figure 2.24: Reduction in surge margin based on various radial distortion patterns tested, based on reference [86].

Only one radial distortion index was used. It is related to the circumferential distortion index  $K_\theta$ . In this case, the radial ring average is the absolute difference between the overall average and the ring average.

$$K_r = \frac{\sum_{i=1}^{NP} \frac{K_{r_i}}{R_i^{2.8}}}{\sum_{i=1}^{NP} \frac{1}{R_i^{2.8}}} \quad (2.4)$$

$$K_{r_i} = \frac{1}{q_2} |\overline{P}_t - \overline{P}_{t_i}|$$

### 2.3.5.3 Combined Distortion Index

The combined distortion index is used to determine overall distortion without regard to contributions angularly or along radius. Two different combined indices were used in this work, related to  $K_\theta$  and  $K_r$ , named  $K_a$  (Eq. (2.5), the other related to IDC.

$$K_a = K_\theta + K_r \quad (2.5)$$

The final index that was evaluated in the paper was IDT. It is defined in Eq. (2.6) below.

$$IDT = \frac{\max(P_{t_{i,j}}) - \min(P_{t_{i,j}})}{\overline{P}_{t_2}} \quad (2.6)$$

These indices are useful in comparing different distortion levels. However, as they are not tied to any engine limits, they do not indicate the overall "goodness" of a design.

## 2.4 Summary of Findings

In this chapter, much of the background of the field was discussed. The initial interest in inlet distortion came from an investigation into why so many combined cycle engine powered vehicles do



not move beyond the initial design and prototype stage even though these engine types could be very powerful in the development of reusable launch vehicles and supersonic transportation. The causes for cancellation vary, but all involve the cost and required budget to realize the designs. One way in which cost can be reduced is by reducing the number of required iterations in the design, which can be achieved through various means, including more cost-effective experimentation and cross-talk between engineers running computational simulations and those performing prototype testing.

This research focuses on one part of the vehicle design, namely the inlet, and specifically on one aspect of the design, namely how we capture how distorted the flow is by the time it reaches the AIP. To understand the state of the art and how distortion is calculated at present, a literature study was completed. Four main aspects were considered: the mechanics of flow distortion and how experimentation was developed to study the mechanics, the difference in steady state and dynamic distortion, the effects distortion has on the propulsion system, and what happens to distortion as the flow moves through the fan and compressor. Lastly, the indices that are used in this work were introduced and discussed as they pertain to this work. In the next chapter, the inlets and data sets that were used in this work will be introduced.

Hopefully the reader has seen that while this field is mature, there still are many open questions and roads for advancement. The most interesting open question this work hopes to answer is how computational results can be used in conjunction with experimental results in order to accurately estimate flow distortion in an inlet with greater confidence. In the next chapter, the inlets are presented along with the data sets that are available. The limitations of these data sets are also discussed.

# Chapter 3

## The IMX and YF12 Inlets

The motivation for this work is to advance the state of the art of combined cycle engines, particularly the inlet design of such vehicles. While most of these programs were canceled at some point in their development, they resulted in various smaller, offshoot programs. These include a study at NASA Glenn Research Center (GRC) into how the flow responded in an inlet during a mode transition based on the NASP vehicle design. This program. Another was performed in the 1970s to determine how much data was lost by reducing the number of probes in an inlet. In this chapter, these inlets are described, including the experimental and computational data available. The author collaborated in the analysis of the experimental data of the NASP-derivative inlet, thus the data reduction methodology is included in this work. Lastly, the limitations of the data sets are discussed, especially as it pertains to the rest of this research.

### 3.1 Small-Scale Inlet Mode Transition Experiment (IMX)

The Small-Scale Inlet Mode Transition Experiment (IMX) - shown in figure 3.1 - is the result of the short-lived X43b vehicle. It is an over-under configuration (example shown in 2.2) TBCC inlet. It is scaled down, but in the full-scale model, the turbojet would be located on the upper flow path while the dual mode ramjet is located in the lower flow path. A splitter cowl sits between the two flow paths and can be moved to open or close either flow path. IMX was built to specifically address the variable geometry of the mode transition - that is when the cowl closes to either flow path and the other engine takes over providing thrust to the vehicle. In addition, IMX aimed at

determining inlet performance and validating the CFD results. The inlet is a two-dimensional, rectangular inlet which transitions to circular at the AIP and at the dual mode ramjet. The final scaled up version was designed to power a X43b-type or NASP-like vehicle.

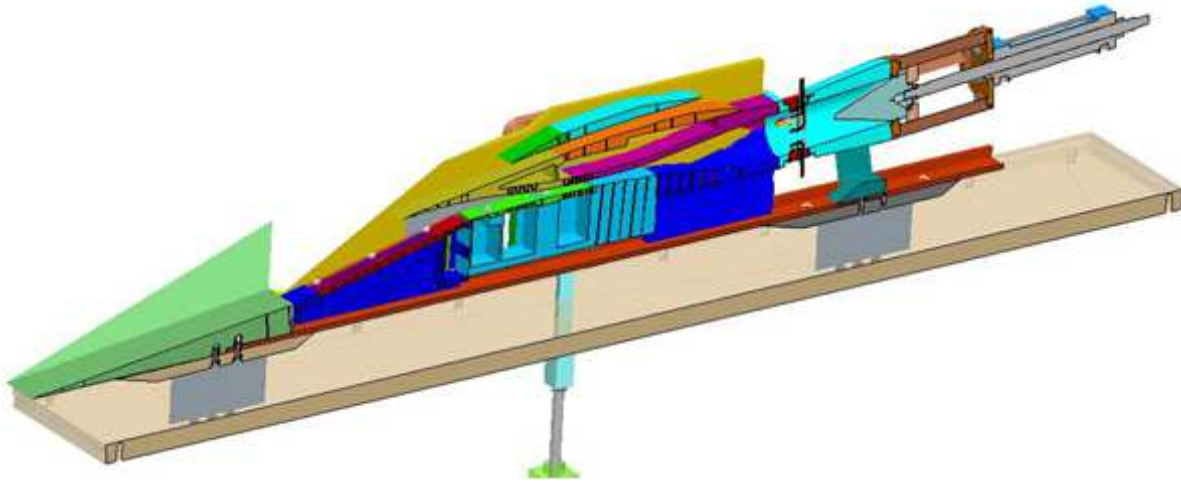


Figure 3.1: Computer rendering of the IMX model. Image courtesy of NASA.

The model also includes several bleed ports, as illustrated in figure 3.2. In this case, "SW" refers to sidewall bleeds, "C" refers to cowl bleeds and "R" refers to ramp bleeds. These bleed ports serve as a mechanism to reduce distortion. Bleed levels were calculated by measuring the pressure in the plenum chamber attached to the bleed section. As the pressure increased, more mass flow was siphoned off the core flow via bleed paths.

### 3.1.1 Experimental Set-up

The IMX inlet was tested in the GRC 1 ft by 1 ft supersonic wind tunnel starting in June 2008 until December 2008. The model was tested from Mach 2.5 to Mach 4. The model was set to a 4 degree angle of attack for simulation of the cruise flight condition. The mode transition between the turbojet and ramjet cycles was assumed to be between Mach 3 and 4, thus the cowl was opened and closed at Mach 3, 3.5, and 4 to simulate three stages of the transition. As the inlet model was

small and to keep cost down, the cowl was designed to be manually reconfigurable between tests rather than actuated during the test. The model's low-speed inlet included a forebody plate, cowl, ramp, throat, subsonic diffuser, and AIP. The AIP diameter for the IMX model was designed to be 1.821 inches (4.625 cm).

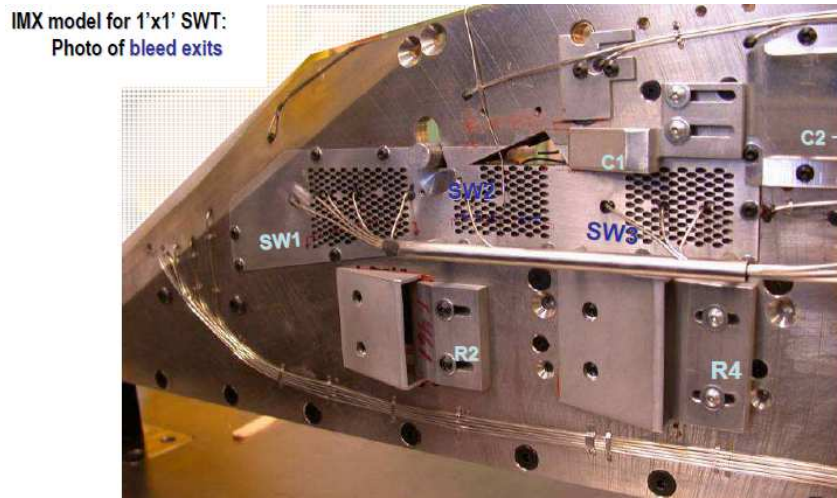


Figure 3.2: Photo showing bleed regions of the IMX model. Image courtesy of NASA.

In order to gather performance data, several sensors were set-up in the model. To measure the mass flow in the low speed inlet, a mass flow plug was used, shown in figure 3.3. The mass flow plug translated into an open position to allow more air to be captured and returned to a closed position to reduce air flow. The distance traveled by the plug was measured via a potentiometer calibrated during each run. Either fully closed or fully open was used as the zero point for calibration. The pressure at the entrance and ahead of the mass flow plug (in the case of the IMX at the AIP due to the small scale of the model) were measured to determine the mass flow.

The model was equipped with 98 static pressure taps along the centerline and along the right wall of the model (the left wall was left without instrumentation to allow access to the model). Figure 3.4 shows the location of the static pressure taps along the cowl, ramp and the sidewall. In addition, as can be see in the sidewall depiction, a series of Pitot pressure rakes were installed. The

low speed flow path had a total of eighteen tubes installed, with half located at the throat and half at the AIP. The throat's Pitot rakes were configured as three rakes with three tubes each with three static pressure taps below the total pressure taps (see 3.6).

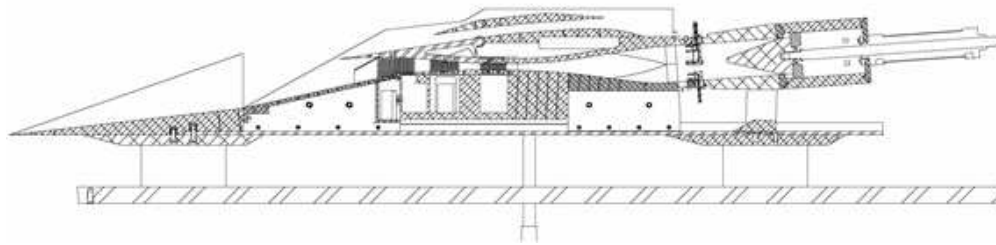


Figure 3.3: Drawing of the low speed flow path mass flow plug location in the IMX model. Image courtesy of NASA.

The AIP had a total of three rakes. Two were at the 90 and 270 degree positions (measured from the 12 o'clock position, which is defined as 0 degrees) each with two tubes. The third traversed the whole AIP from 0 degrees to 90 degrees and had five taps located on it, four at the same radial locations as the rakes at 90 and 270 degrees and one tap in the center (see figure 3.5). There were also four static pressure taps located around the circumference of the AIP. The model was instrumented with two dynamic pressure transducers in the ramp and associated wall to ensure the shocks were in the correct location and did not oscillate.

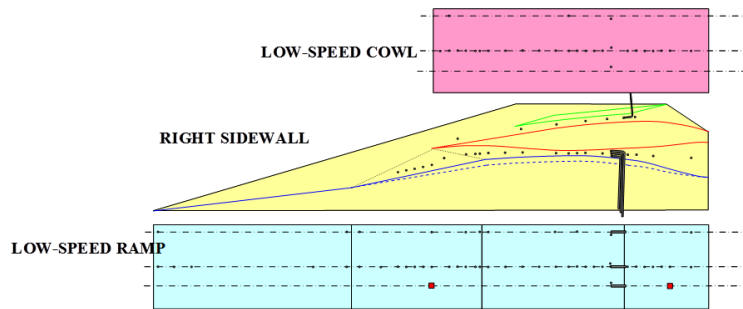


Figure 3.4: Location of the static pressure taps in the IMX model. Image courtesy of NASA.

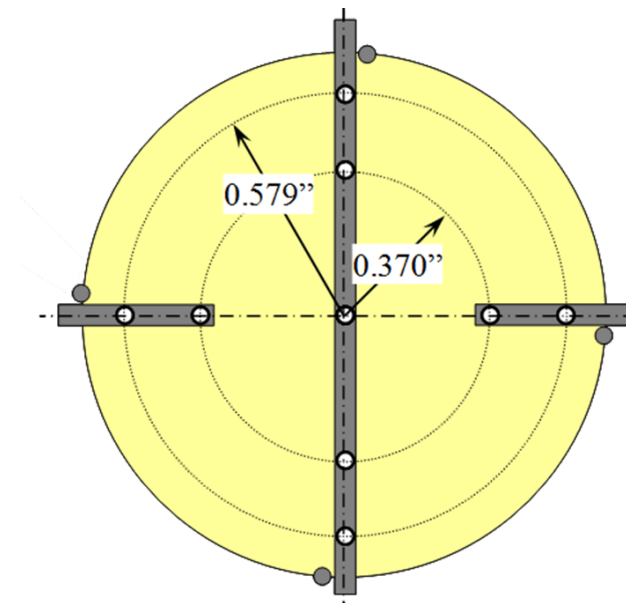


Figure 3.5: Visualization of the total pressure rakes and static taps in the IMX model's AIP. Image courtesy of NASA.

As the model was equipped with bleed ports, there were several mass flow readings for the bleed areas that were monitored throughout the test. Each bleed port had a plenum which was instrumented with one pressure sensor. Based on the known open area of the bleed holes, the area relationship between the freestream and throat, and the pressure read in the plenum, the mass flow ratio for each bleed area was determined and subtracted from the overall mass flow.

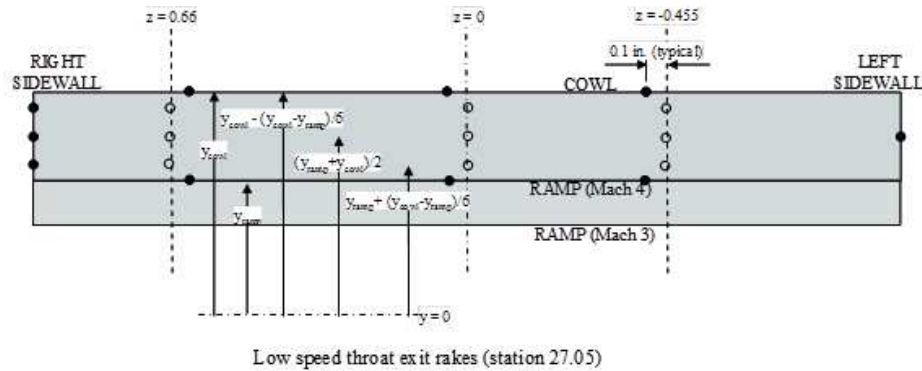


Figure 3.6: Visualization of the total pressure rakes and static taps in the IMX model's subsonic diffuser. Image courtesy of NASA.

### 3.1.2 Data Analysis

A total of 69 runs were completed between May 2007 and December 2008 with 5,341 readings generated. The tests were run from Mach 2 to Mach 4 with almost 80% of the testing completed at Mach 4. Not all of those data points are viable, as several of them are tunnel calibration tests or inadvertent inlet problems, such as unstart or buzz.

The total pressure taps are distributed over the inlet, as seen in figure 3.7. Radially, they are at 0.526 and 0.803 inches, each 90 degrees apart with the exception of the center tap, which is at 0,0. The static pressure taps are slightly offset from the total pressure rakes and on the surface. The readings are all in pounds per square inch (psi). A note on naming convention: rake 1 is located at the 12 o'clock position and the numbering then moves clockwise. Although rake 1 technically traverses the whole inlet, only the first two taps are considered to be part of rake 1, with the last two taps being considered rake 3. The center tap is not considered to be part of a rake. This conforms to the ARP1420 standard naming convention. The center tap is not used for most calculations, as ARP1420 does not utilize a center tap for the calculations.

The mass flow is measured via the mass flow plug and its position relative to a cold pipe. This can be seen in figure 3.3; the mass flow plug is the solid conical structure on the far right. The AIP pressure rakes are shown directly ahead of the cone. The channel between the cone and the

AIP rakes is what is called the cold pipe. In larger models, there would be a separate set of pressure probes inside the cold pipe, usually at several diameter-lengths behind the AIP. However, due to IMX's small size, this was impossible and the AIP rake data is used to determine the flow through the cold pipe.

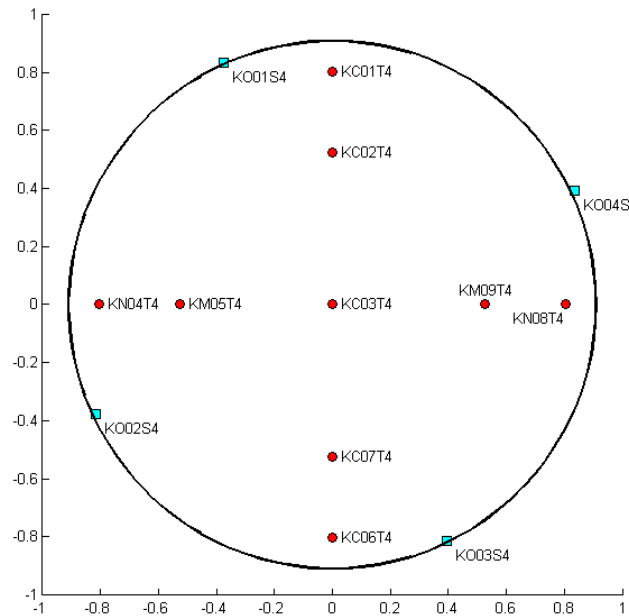


Figure 3.7: Locations of the total pressure taps (red) and static pressure taps (cyan) at the AIP.

To calculate the mass flow, a series of steps have to be solved, starting with the idealized mass flow at the plug, based on the area relation between the plug and the cold pipe:

$$\dot{m}_{plug} = \rho_{pipe} v_{pipe} \frac{A_{plug}}{A_{pipe}} A_{pipe} \quad (3.1)$$

In order to calculate the density of the air in the pipe, the ideal gas law is used:

$$\rho_{pipe} = \frac{P_{s,pipe}}{R_{air} T_{s,pipe}} \quad (3.2)$$



The Mach number can then be obtained by using the isentropic relations, solved for Mach number:

$$\frac{P_t}{P_s} = \left[ 1 + \frac{\gamma - 1}{2} M^2 \right]^{\frac{\gamma}{\gamma - 1}} \quad (3.3)$$

$$M = \sqrt{\frac{2}{\gamma - 1} \left[ \left( \frac{P_t}{P} \right)^{\frac{\gamma - 1}{\gamma}} \right]} \quad (3.4)$$

The isentropic area relation is used to get  $\frac{A_{plug}}{A_{pipe}}$ :

$$\frac{A_{plug}}{A_{pipe}} = \left( \frac{\gamma + 1}{2} \right)^{\frac{\gamma + 1}{2(\gamma - 1)}} M_{pipe} \left( 1 + \frac{\gamma - 1}{2} M_{pipe}^2 \right)^{\frac{-(\gamma + 1)}{2(\gamma - 1)}} \quad (3.5)$$

The Mach number is used to calculate the static temperature in the cold pipe using the isentropic relation:

$$T_{s,pipe} = \frac{T_{t,pipe}}{\left( 1 + \frac{\gamma - 1}{2} M_{pipe}^2 \right)} \quad (3.6)$$

Velocity is calculated using the definition of Mach number:

$$v_{pipe} = M_{pipe} \sqrt{\gamma R_{air} T_{s,pipe}} \quad (3.7)$$

All these equations, 3.2, 3.4, 3.5, 3.6, and 3.7 are substituted into Eq. (3.1) and this yields:

$$\dot{m}_{plug,ideal} = \sqrt{\frac{\gamma}{R_{air} T_{s,pipe}}} \frac{P_{t,pipe}}{A_{plug}} \left( \frac{\gamma + 1}{2} \right)^{-\frac{\gamma + 1}{2(\gamma - 1)}} \quad (3.8)$$

The final mass flow rate is obtained via:

$$\dot{m}_{pipe} = \dot{m}_{plug,ideal} * C_d \quad (3.9)$$

where  $C_d$  is the coefficient of discharge for that particular mass flow plug. The coefficient of discharge is often obtained from a geometrically similar mass flow plug. This is an area of research for GRC, as there is some debate about the accuracy of this method[88]. However, without calibration of the exact mass flow plug used in the IMX wind tunnel tests, this is the most accurate method available.

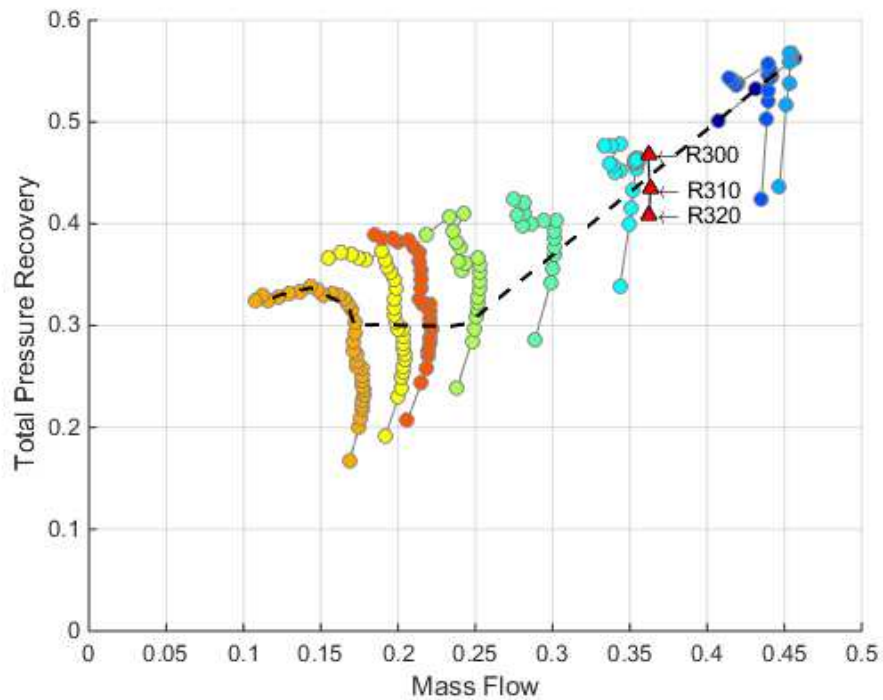


Figure 3.8: IMX cane curve with CFD conditions indicated as red triangles.

To evaluate the operating envelope of the inlet, a cane plot is generated. This plot shows total pressure recovery versus the mass flow ratio for several cowl positions. The total pressure recovery is calculated by averaging all the AIP pressures for a given run and dividing it by the freestream pressure. The mass flow ratio is calculated by dividing the measured mass flow from the plug by the total theoretical mass capture of the inlet. The result can be seen in figure 3.8. This shows the maximum total pressure recovery is around 55% at the maximum mass capture ratio. The dashed

black line shows the tested mode transition path for the inlet.

When reducing the data at the AIP, the majority of calculations stem directly from the measured pressures, such as the Mach number, the pressure recovery, and inlet distortion. In general, the Mach number is calculated at each pressure tap via the isentropic relations shown in equations 3.3 and 3.4. However, there can be issues at high Mach numbers, when the pressures are lower, due to areas of separated flow. At these conditions, the total pressure readings in the center of the flow field can be lower than the static pressure at the wall, leading to a negative term inside the radical of Eq. (3.8). In order to avoid this problem, another way to solve for the Mach number is to use the implicit relation the Mach number has to the mass flow rate by solving for the equation's roots. In this case, a Newton-Raphson method was used. This method starts with creating this function (which is equal to 0):

$$M_2 : f(M_2) = M_2 \left( 1 + \frac{\gamma - 1}{2} M_2^2 \right)^{-\frac{\gamma+1}{2(\gamma-1)}} - \frac{m_{corr,2} \sqrt{T_{t,\infty}}}{\sqrt{\frac{g_c \gamma}{R_{air}} P_{t,\infty} A_2}} = 0 \quad (3.10)$$

The derivative is then taken with respect to Mach number, yielding:

$$\frac{df}{dM} = \left( 1 + \frac{\gamma - 1}{2} M^2 \right)^{\frac{1}{1-\gamma} - \frac{3}{2}} \left[ \frac{\gamma - 1}{2} \left( 1 - \frac{\gamma + 1}{\gamma - 1} + 1 \right) M^2 + 1 \right] \quad (3.11)$$

The new Mach number is solved for by calculating:

$$M_k = M_{k-1} - \frac{f}{\frac{df}{dM}} \quad (3.12)$$

This method requires an initial guess for the Mach number, which was  $M = 0.3$ . For the data reduction, an error of  $1e - 5$  was considered acceptably small. The Mach number can be compared to the one calculated via the isentropic relation. Finally, the dynamic pressure,  $q$ , is calculated.

$$q = \frac{1}{2} \gamma P_{s,2} M_2^2 \quad (3.13)$$

After the main variables ( $P$ ,  $q_o$ , and  $M$ ) are extracted, additional parameters of interest can be calculated. These parameters include the pressure recovery, which is calculated by dividing each individual total pressure measurement by the wind tunnel's freestream total pressure measurement,  $P_{t,\infty}$ . Another is the distortion is calculated as shown in equation 2.1. Each one of these parameters is plotted as a contour and averaged over the face of the AIP. In order to make the contour, the discrete data points are interpolated to create continuous data. The interpolation method used was a bicubic spline, which creates a series of polynomials to fit the data together. A thorough discussion of what interpolation method should be used will follow in chapter 4. It should also be noted that there are not enough points to make a proper contour map of this AIP's contour.

The resultant plots generated look like figure 3.9. On the top left is the throat recovery contour plot and the top right is the AIP recovery contour plot. These plots are not considered informative plots because the data they are generated from is considered sparse, but are instead generated for completeness and comparison to other inlets. Above the contour is the average recovery at the throat and AIP respectively. On the next row are informative plots: the bar plots of pressure readings at each individual station. On the left hand side are the pressure readings at the throat. In this case, station 1 refers to the column of pressure taps at  $x = -0.6$  in, station 2 is at  $x = 0$  in, and station 3 is at  $x = 0.4$  in. The bottom and top readings denoted with an (S) in the legend are static readings, while those with a (T) are total pressure readings. The same information is provided for the AIP pressure probes.

Underneath the pressure data is a cane curve graph. The black lines show all possible cane curves that were run for the IMX. The red dot shows where this particular reading falls on the cane curve.

These compilation plots are the ultimate goal of the data analysis of the experimental data. This one figure shows the inlet's estimated pressure contours, discrete experimental readings, the probe locations, and corresponding vehicle operating point. All these pieces of information give the researchers an idea of how well the inlet is performing.

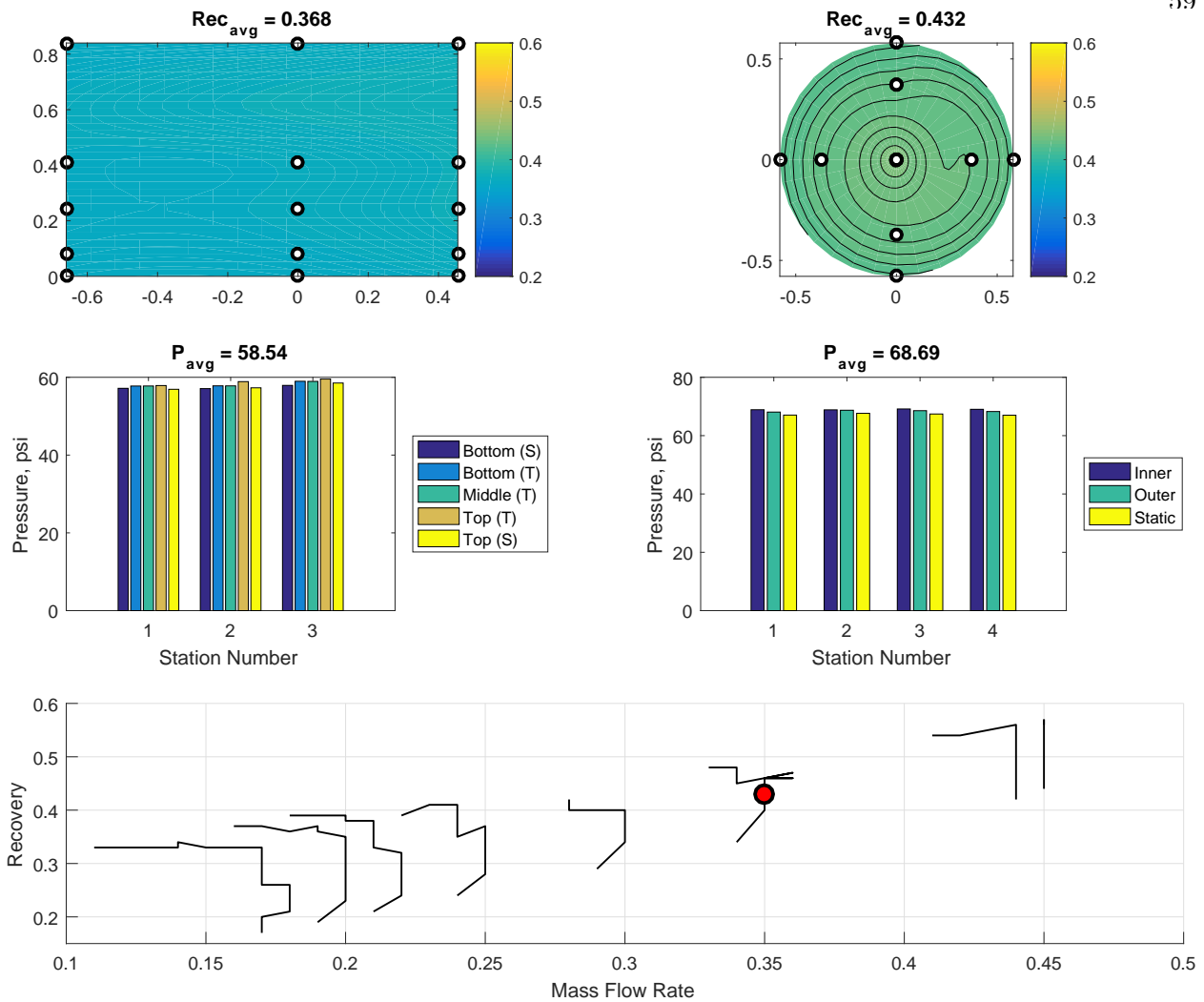


Figure 3.9: Sample IMX data analysis result. This is for run 33, reading 2333. It was a test done at Mach 3 for a cowl angle of -2 degrees.

### 3.1.3 Computational Fluid Dynamics

NASA Glenn did a full, three dimensional RANS on the IMX inlet[64]. A thorough discussion on the details of the model set-up and how it was run can be found in ref [64]. For the purpose of this work, the pressure calculated at the AIP will be shown and discussed.

The mesh at the AIP is shown in figure 3.10. The model was run using NASA Glenn’s US

Wind CFD code. The mesh is Cartesian and at a 69x35 density and cut down the center through a line of symmetry. It should be noted that figure 3.10 shows double the size - namely a 69x70 grid size - than what was run. The red dots show where a 40-probe array would be located if it were to be implemented.

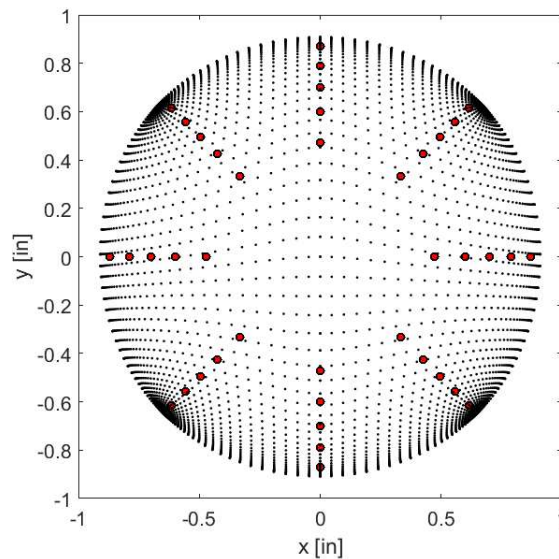


Figure 3.10: CFD mesh used for the IMX RANS CFD

The CFD was run at three different conditions, called R300, R310, and R320. The location on the cane curve relative to the overall mission can be found in fig 3.8 as red triangles. All of these runs feature a -2 degree cowl position. The bleed rate for R300 was reduced between R300 to R320 by approximately 1.5%. The full set of weight flow conditions for each run can be found in table 3.1.

Table 3.1: IMX CFD run conditions

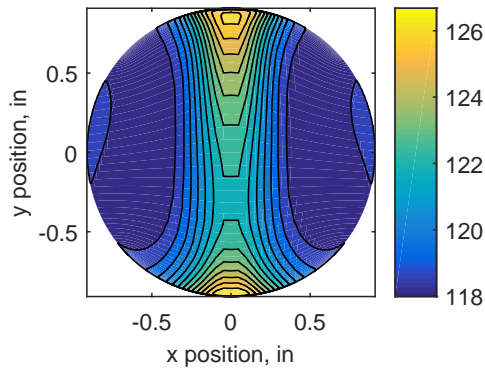
	$\frac{W_2}{W_{LS}}$	$\frac{W_{bleed}}{W_{LS}}$	$\frac{P_{t,(i,j)}}{P_{t,\infty}}$
R300	0.633	0.131	0.468
R310	0.635	0.130	0.434
R310	0.635	0.130	0.434

The freestream conditions the CFD was run at can be found in table 3.2. Both the English and SI units are shown for completeness.

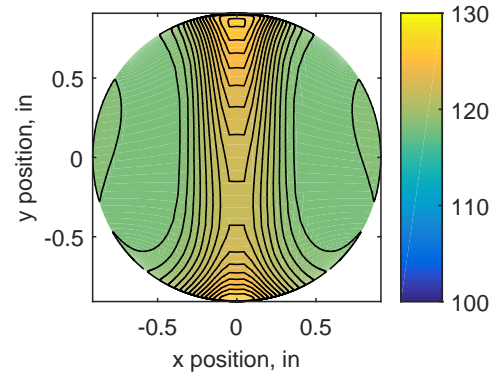
Table 3.2: Freestream conditions the CFD was run at

Parameter	Value (English units)	Value (SI units)
$M_\infty$	3.974	3.974
$P_{t,\infty}$	158.8 psi	1095 kPa
$T_{t,\infty}$	547 R	304 K
$P_{s,\infty}$	1.1 psi	7.5 kPa
$T_{s,\infty}$	132 R	73 K
$a_\infty$	563 ft/s	172 m/s
$V_\infty$	2234 ft/s	681 m/s
$\dot{W}_\infty$	0.9105 slug/s	13.3 kg/s
$\dot{W}_{LS}$	0.0276 slug/s	0.403 kg/s

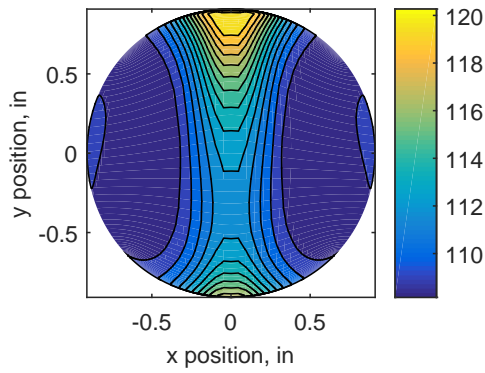
The resulting pressures can be found in figures 3.11(a), 3.11(c), and 3.11(e). It should be noted that these figures do not have the same pressure scales. The same results are presented with the same colorbar in figures 3.11(b), 3.11(d), and 3.11(f). All pressures are in psi while all dimensional units are in inches.



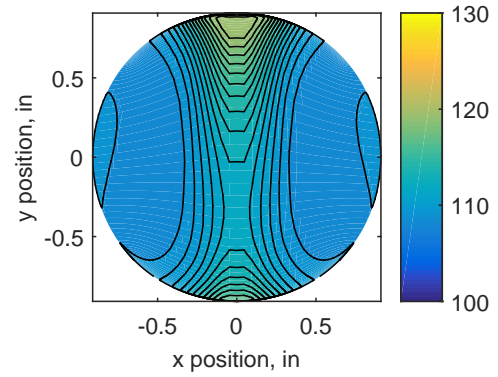
(a) R300 with individual colorbar



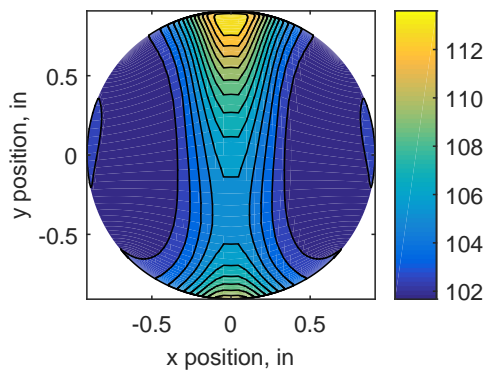
(b) R300 with an overall colorbar



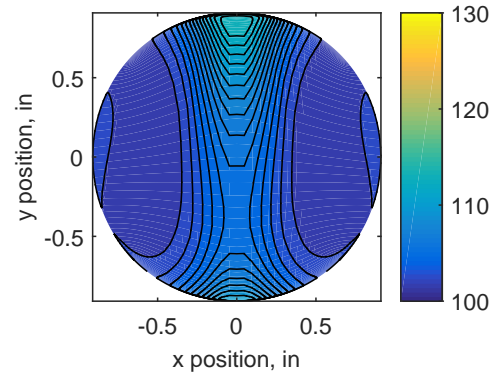
(c) R310 with individual colorbar



(d) R310 with an overall colorbar



(e) R320 with individual colorbar



(f) R320 with an overall colorbar

Figure 3.11: Pressure results for IMX CFD runs R300, R310, and R320, with individual colorbars and an overall colorbar.



### 3.1.4 Findings and Limitations

The IMX was a prototype inlet, created to gather some preliminary data to validate the CFD for the LIMX. As with all prototypes, there were several limitations in this model. The model is a scale model - about one tenth scale of the LIMX. That means that the AIP area was very small ( $A_{AIP} = 2.5930in^2$ ). The blocked area - that taken up by the probes and rakes - totaled to about  $0.273in^2$ . This is about 10% of blockage. If 8 rakes were used, the blockage would have increased to  $0.428in^2$ , which is equivalent to almost 17% blockage. Increased blockage can be a source of interference and changes in the flow. There is no set guidelines on how much blockage is too much blockage and at what point it compromises the experiment[89], though general rules of thumb place the limit of acceptable somewhere between 10 and 15%. Thus, the 8 rake configuration would have pushed the bounds of acceptable blockage in the experiment.

Another limitation was the way the computational result was obtained. In order to get accurate results, the inlet has to be modeled as a whole – including modeling the bleed air accurately. In order to achieve this level of accuracy many details of the design must be retained in the computational model, which is computationally expensive. Most of the computational expense comes from resolving the various scales of turbulent fluid flow which is handled differently by each CFD method. The most accurate method is Direct Numerical Simulation (DNS) which resolves all scales of turbulence, however this takes up a great deal of computational time[90]. On the other side of the spectrum is the industry standard Reynolds Averaged Navier Stokes (RANS), which uses statistical turbulence models, reducing the computational time[90]. In between these two methods are Large Eddy Simulation (LES) and Detached Eddy Simulation (DES) CFD codes, which attempt to resolve large-scale unsteady motions produced by eddy-like structures while using statistical models for the smaller-scale turbulent flows[91]. While this is less computationally expensive than DNS CFD, LES and DES are still limited by the complexity of the fluid flow they can resolve[90]. LES and DES are becoming more popular as computational power increases though it will take some time before inlets as detailed and complex as studied in this work can be efficiently analyzed.

Thus, only RANS CFD solutions are utilized in this research.

### 3.2 YF12 Scaled Inlet

In 1979, researchers at NASA Ames conducted an inlet experiment on a one third size YF-12 inlet (figure 3.12). The YF-12 vehicle was the precursor to the SR-71 vehicle; one of the YF-12 was obtained by NASA and used as a flying test bed[34]. The experiment conducted with this inlet was a recreation of the vehicle's inlet and scaled down for wind tunnel testing. It was run around the same time the inlet distortion testing standard[43] were written. The research was mostly focused on how much error was generated in five distortion indices based on the number of probes used to generate the index.

The inlet was run three times, labeled as "test cases", each time with 320 total pressure probes inserted into the flow at the AIP. The ambient total pressure and dynamic pressure at the AIP were reported, shown in table 3.3. Ambient total pressure remained constant throughout testing indicating the same wind tunnel conditions between test cases. However, dynamic pressure at the AIP changes with each test, suggesting an adjustment to conditions within the inlet. Adjustments that would impact the dynamic pressure at the AIP include changes to the variable geometry and bleed rates. The authors of this paper postulate that the change in dynamic pressure is the result of changes to the bleed rate and upstream variable geometry by the original researchers.

Table 3.3: Test conditions for the three YF12 test cases.[1]

Test Condition	$P_{t,0}$	$\bar{q}_2$
TC1	19.64 psi	1.847 psi
TC2	19.64 psi	0.9014 psi
TC3	19.64 psi	0.8896 psi

The inlet conditions are not specifically given, but it is likely that the second and third cases had increased bleed rates, as the distortion is overall much lower than for test case 1. The exact

dimensions of the inlet are not reported, but the AIP is estimated to be around 19 inches in diameter. This number was obtained by dividing the inlet diameter of a standard J58 engine by three.

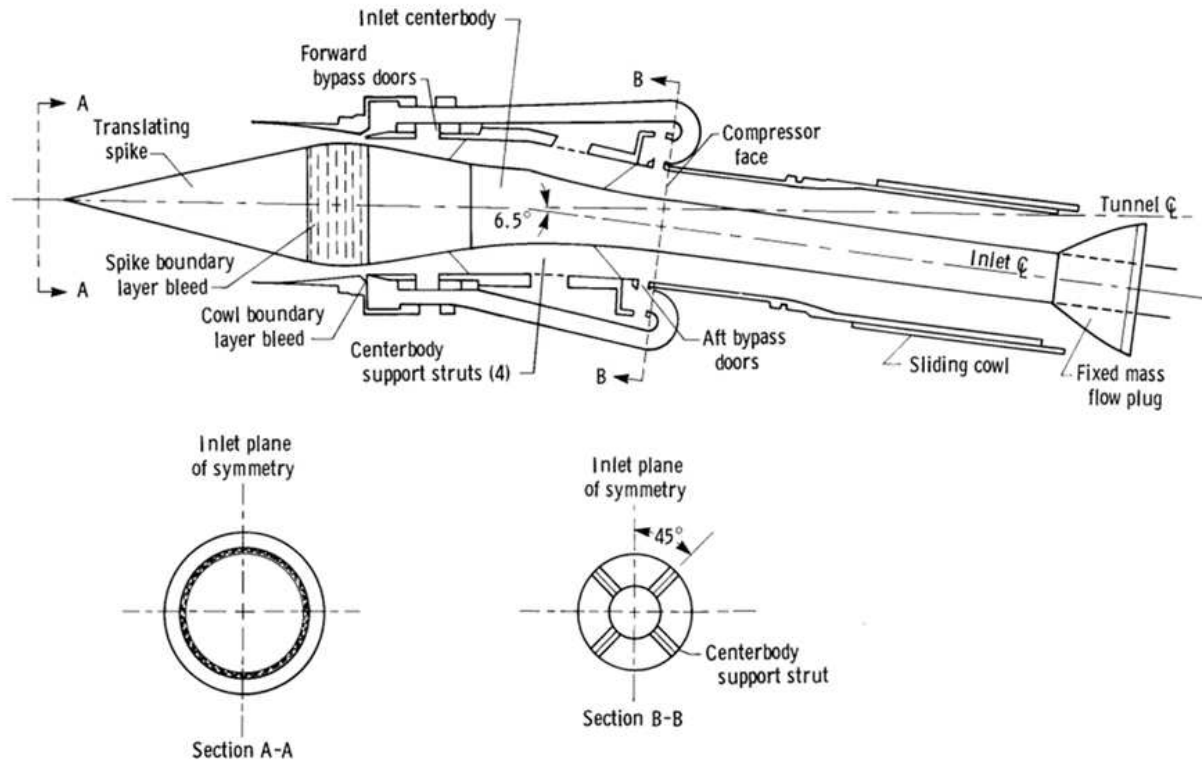


Figure 3.12: YF12 inlet used for the 320-probe experiment. Image from NASA[1]

### 3.2.1 Experimental Set-up

The original researchers selected subsets of the 320 probes after the experiment, as shown in figure 3.13. A single subset describes a set of equi-spaced rakes around the circumference of the AIP. Each chosen subset was also rotated, maintaining the original pattern, leading to various clocked positions. A zero clocking refers to the reference rake at 0 degrees pointing to the 12-o'clock position. Figure 3.14 shows an example of the first clocking.

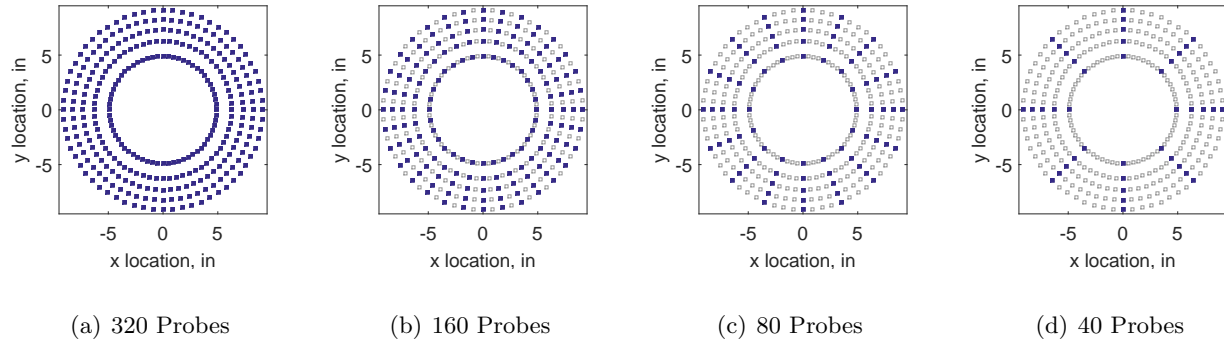


Figure 3.13: Subsets of probes chosen for analysis by the original researchers.

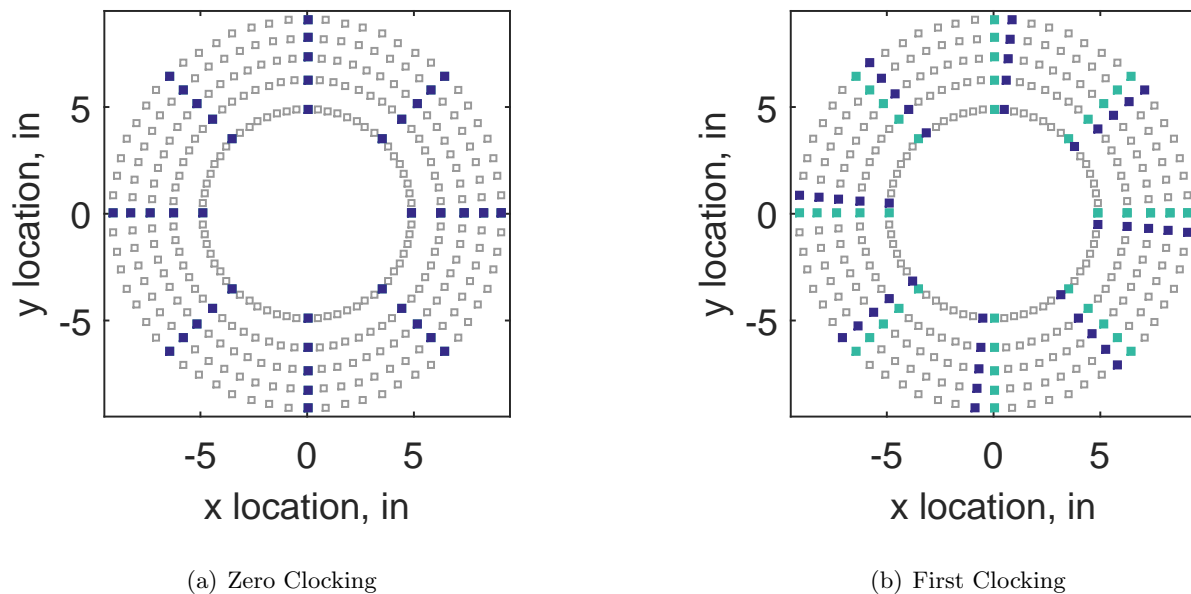


Figure 3.14: Clocking example of the 40 probe subset, with the darker color representing the clocking.

The data was only available in the form of hand drawn graphs in the electronic report, thus the program DataThief[92] was used to capture and tabulate the original data. DataThief has been proven to accurately and reliably capture data[93]. The overall error on the x-coordinate (angular probe location) was determined to be  $0.95^\circ$  and 0.325 psi on the y-coordinate. A full analysis of error can be found in Appendix A. The error was considered acceptably small, as this translates to a 0.0041% error on the x-coordinates and approximately 2% on the y-coordinates.

### 3.2.2 Data Analysis

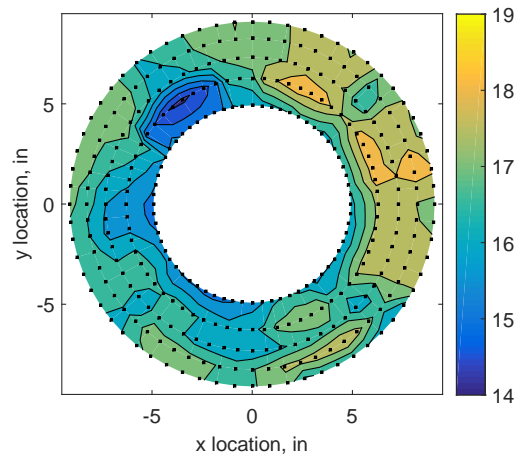
The plot of the raw data for test case 1 can be found in fig 3.2.2. The raw pressure data for test case 2 can be found in fig 3.2.2. Lastly, the raw pressure data for test case 3 can be found in fig 3.2.2.

The contours range from 14 psi to 19 psi and the black squares refer to the pressure probe locations. In test case 1, there was a fair amount of variance in the total pressure. Pressure ranged from 14.4 to 18.5 psi in this test case, with an average pressure of about 16.8 psi. In test cases 2 and 3 there was less variance in the pressure. Test case 2 had a range of 14.5 to 17.4 psi with an average of 15.3 psi while test case 3 ranged from 15 to 17 psi with an average of 15.7 psi.

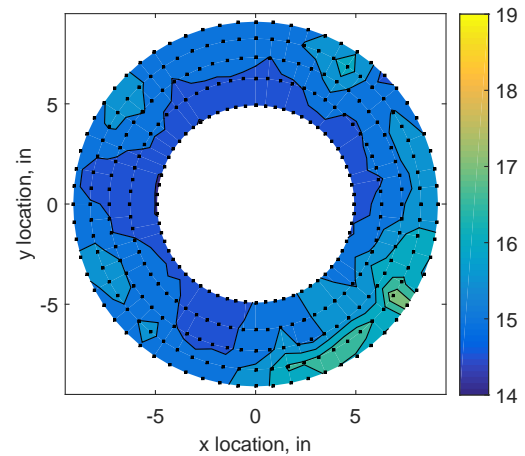
The results for the distortion indices defined in section 2.3.3 for the test cases 1 through 3 are listed in table 3.4. It should be noted that a distortion index is a dimensionless number and usually corresponds to a limit determined by each engine company through extensive testing. While the definition of the index is publicly available, the index limits are generated for a specific engine and are usually proprietary to the company. For this paper, we will assume that these limits were acceptable.

Table 3.4: Distortion index results for the experiment

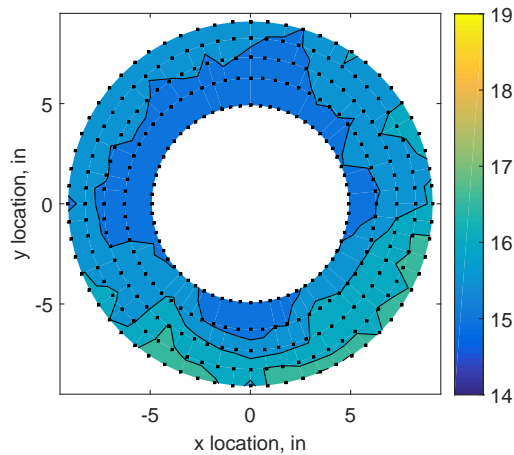
Test number	$K_\theta$	$K_r$	$K_a$	$IDC$	$IDT$
Test case 1	0.319	0.291	0.609	0.0804	0.245
Test case 2	0.411	0.368	0.779	0.0551	0.188
Test case 3	0.354	0.349	0.703	0.0321	0.130



(a) Test Case 1



(b) Test Case 2



(c) Test Case 3

Figure 3.15: Raw pressure contour plots; scatter plot indicates probe locations.

### 3.2.3 Findings and Limitations

There are several limitations to this data set. The research as reported ignored a few factors, such as how much obstruction 320 probes created on the flow. There are also several unknowns due to the inlet and report's classification. The inlet is classified, which means that the geometry is unknown. The bleed rates are not given. The researchers did not report anything about the probes, including the make and model, what their relative uncertainty was, what the Pitot diameter was,

on what system the data was gathered, nor how they ensured that all probes were functioning at the time of the test.

The inlet conditions are not specifically known, but it is likely that the second and third cases had increased bleed rates, as the distortion is much lower. The exact dimensions of the inlet are also not given in the paper, but the AIP is estimated to be around 19 inches in diameter. This number was obtained by dividing the inlet diameter of a standard J58 engine by three. Nevertheless, interesting information can still be gathered from this experiment.

In addition, the question has been raised about how much blockage there was due to the probes. The area of the YF12 inlet was approximately  $A_{AIP} = 283.5in^2$ . It is unknown what size the pressure probes were in this test, but a good assumption would be that the pitot tube was approximately a one eighth of an inch diameter. That would result in about a  $A_{320probes} = 3.93in^2$ . This equates to about 1.39% of blockage. As stated before in section 3.1.4, a general rule of thumb is that as long as the blockage area is less than about 10-15%, the flow field changes due to blockage are acceptably small.

### 3.3 Summary of Findings

The two inlets studied in this work – the IMX and YF12 – were introduced. Three data sets resulted from these projects; a sparse experimental data set for the IMX, a full computational set for the IMX, and a rich experimental set for the YF12. The IMX experimental data set is considered too sparse to confidently draw conclusions about the distortion at the AIP. The YF12 inlet is classified, thus computational data sets cannot be generated for this inlet. That leaves the author with two usable data sets: the computational IMX data and the experimental YF12 data. These data sets will be used in the coming chapters.

The IMX experiment spurred two main questions: how should discrete data points be transformed into a continuous contour map and does the way the data is interpolated matter to the final result? Secondly, especially when there is limited space and cost-constraints are a major hurdle in the program, are there ways to determine where to place the probes to ensure the maximum

amount of information is gathered? The first question will be attempted to be answered in chapter 5 and the second in chapters 6 and 7. However, as there was so little "real" data available, the authors turned to surrogate modeling to study the trends associated with transforming discrete data points into continuous data. In the next chapter, surrogate modeling will be explained and the methodology to answer the question of how to create continuous data from discrete points will be introduced.



# Chapter 4

## Interpolation of Pressure Data via Surrogate Modeling

In the previous chapters, the state of the art of combined cycle engine vehicles, inlet flow distortion, and the data sets available were presented. Now the first open question will be addressed, namely how to form continuous contour plots from discrete data points. In order to create continuous contour plots, the discrete experimental points are interpolated. This results in continuous pressure maps, which are used to evaluate the overall "goodness" of a design. Many interpolation methods are available; they each have their own pros and cons. As mentioned in the previous chapter, only a limited set of measured data was available. To isolate the effects of just the interpolation methods from errors that exist in real data sets, surrogate models were employed. These models approximate possible results based on existing data, physical bounds, and engineering experience. The surrogate models used in this work were informed by the existing YF12 inlet data presented in section 3.2.

### 4.1 Background

There is no official guidance on how total pressure distortion data should be interpolated to evaluate flow distortion at the inlet-engine interface plane. ARP1420[43] is the standard that governs how inlet experiments should be conducted in order to quantify inlet flow distortion. However, the standard does not suggest an approach for data analysis. A common visual representation of the data is in the form of a donut plot – a contour plot of the pressure, recovery, or distortion. These contour plots are formed interpolating the measured data. It is thus up to each individual researcher to determine what method to use to transform the discrete total pressure data gathered from an

experiment into a continuous contour map of pressure. A cubic spline method is popular as it is often simply assumed to be accurate.

In order to test this assumption, this work will generate data sets and use various interpolation methods to test which method is the best against various measures of success. The data sets are generated via a surrogate model. A surrogate model is meant to represent real data but is generated using a pseudo-random variable with some distribution. In this surrogate model, the results from the IMX computational fluid dynamic (CFD) data set was used to generate the model. From this full 320 point data set, the 40 points prescribed by the standard are extracted, then interpolated back to the original 320 points.

Four methods were investigated: bilinear, cubic spline, polar, and Kriging. These methods are chosen for various reasons. Bilinear is often considered a benchmark method[94], cubic spline is touted for being the best cost-to-performance method[95], polar reduces the dimensionality by holding the radius constant and only changing the angle, while Kriging takes into account spatial data into the interpolation[96]. The measures of success for each interpolation method include the error in the interpolated results as well as the visual representation of the data.

## 4.2 Methodology

For this work, the surrogate model was created based on computational inlet data and known distortion patterns of interest. The surrogate model is described in detail in section 4.2.1. Twenty-five test cases were created for three different patterns. For each model, 320 points were generated. 40-point-sets were selected as prescribed by ARP1420 although at various starting angles to sweep through all data points. The reduced point sets were then interpolated using four different methods, described in section 4.2.2. The four methods include two strictly in Cartesian space: bilinear and cubic spline. One method uses a linear interpolation method in polar coordinates, essentially only taking into account changes in the angular direction while keeping the radial position the same. The last method is a statistics-based method called Kriging. The measures of success for each method, explained in section 4.2.6, include quantitative as well as qualitative measures.

### 4.2.1 Surrogate Model

The surrogate model was created using the test data from the YF12 inlet described in section 3.2. Three different patterns were evaluated: a 180 degree low pressure pattern, four 45 degree low pressure patterns, and a hub low pressure pattern. These patterns can be found in figure 4.1. Areas of low pressure are shown in blue in these figures.

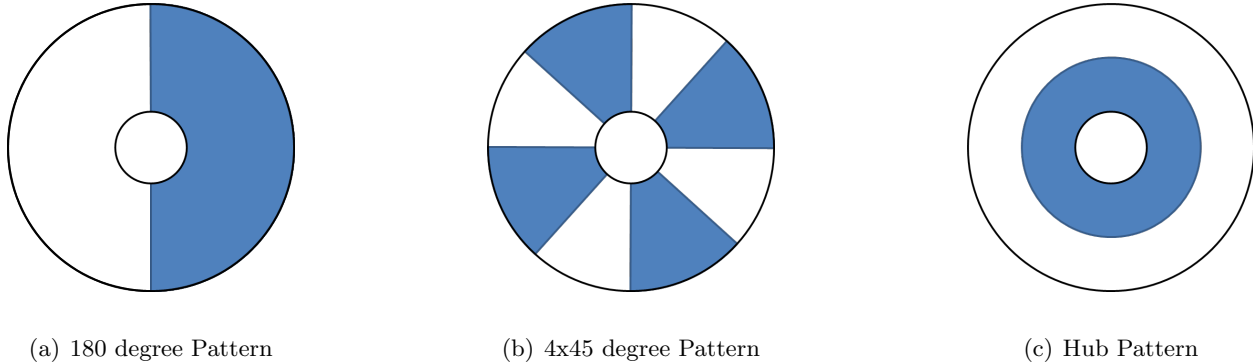


Figure 4.1: Patterns used to create the surrogate models. Areas in blue are areas of "low" pressure.

To determine what should be construed as low pressure, the original test case 1 data was sorted and the 100 lowest readings were extracted. The results for that can be found in a histogram in figure 4.2.

The mean and standard deviation for the "low" pressure area were found as well as the mean and standard deviation of the 320 probes. To create the areas of low and normal pressure, a uniform distribution was created. The upper and lower limits are based on two standard deviations from the mean.

Table 4.1: Surrogate model conditions

	Mean	Std. Dev	Lower Limit	Upper Limit
Low Pressure Area	15.9 psi	0.80 psi	14.9	16.9
Normal Pressure Area	16.8 psi	0.49 psi	15.2	18.4

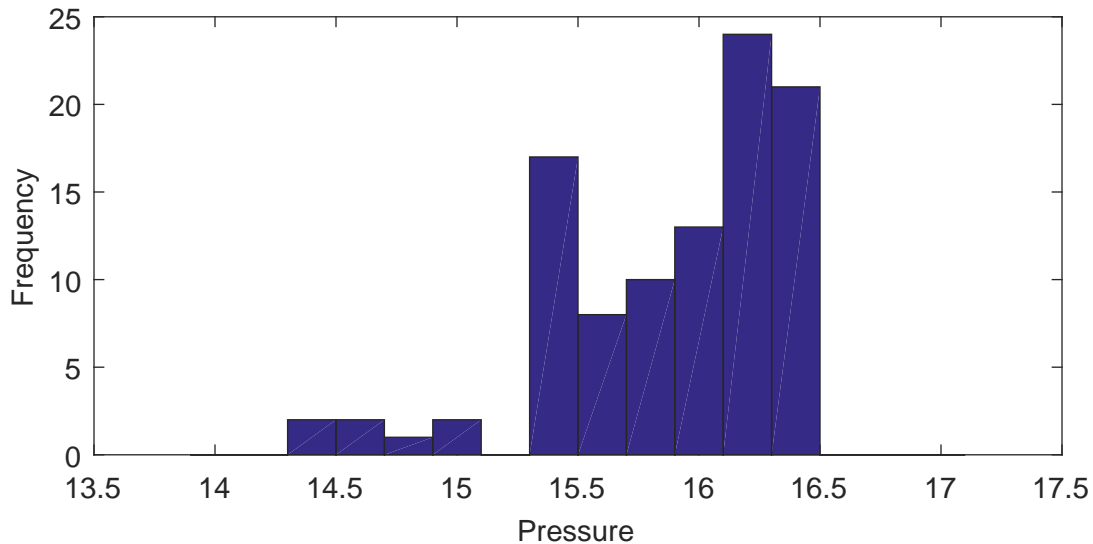
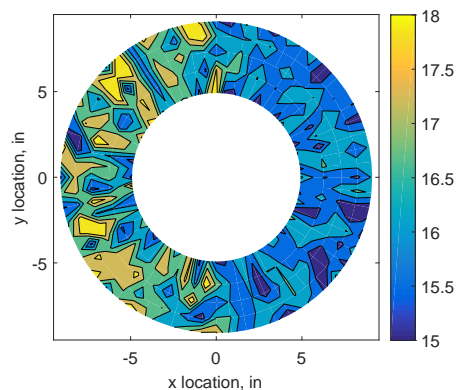


Figure 4.2: Histogram of the 100 lowest pressure readings for the YF12 experiment's test case 1

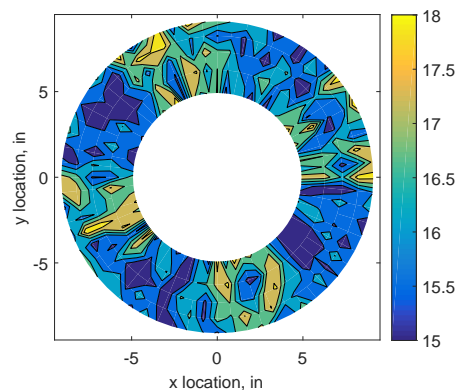
A sample for each pattern is shown in figure 4.3. The areas of lower pressure can be seen in blue while areas of higher pressure map towards yellow. The three patterns studied are clearly visible.

#### 4.2.2 Interpolation Methods

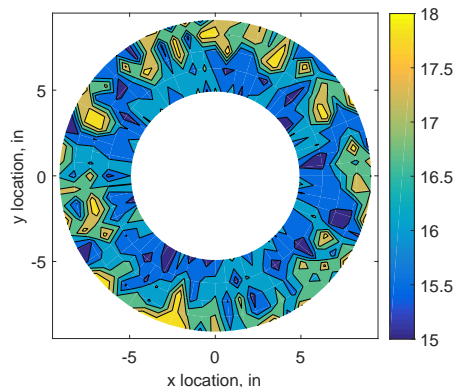
The four interpolating methods that are examined in this work are Cartesian bilinear and Cartesian cubic spline interpolation as well as polar angular and a Kriging interpolation scheme. For each interpolation method, the eight rake configuration was used as a representative subset of data. The eight rake configuration was chosen as this is what ARP1420[43] recommends, shown in figure 4.4. This subset of 40 data points was then interpolated to the produced 320 points.



(a) 180 degree Pattern



(b) 4x45 degree Pattern



(c) Hub Pattern

Figure 4.3: Sample of each of the patterns used to create the surrogate models.

Interpolation is simply a method by which one can approximate values of a function  $f(x)$  for any  $x$  where the value of  $f(x)$  may not be given[97]. A new interpolation function,  $p_n(x)$ , is created to approximate  $f(x)$ . This function can be created using various methods. Four methods – bilinear, spline, polar, and Kriging – will be described in the coming sections. However, one should note that all of these interpolation functions are merely approximations. As such, they can be better or worse depending on the function they are trying to approximate.

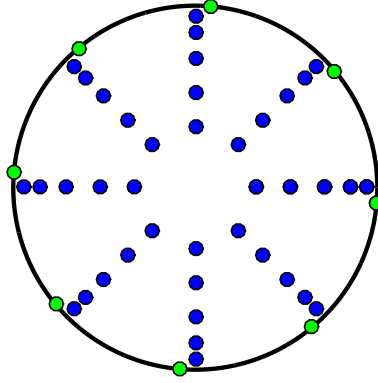


Figure 4.4: ARP1420 suggested probe layout. Blue probes indicate total pressure probes while green indicate surface static pressure taps.

### 4.2.3 Bilinear Interpolation

Linear interpolation is the oldest form of interpolation, with roots in the ancient world[98]. In its simplest terms, linear interpolation draws a straight line between the known values at  $(x_0, y_0)$  and  $(x_1, y_1)$  based on an interpolation coefficient. The interpolation function  $p_1$ , where the subscript 1 denominates that the interpolation polynomial is of the first order, can be described as in Eq. (4.1).

$$p_1(x, y) = a_0 f(x_0, y_0) + a_1 f(x_1, y_1) \quad (4.1)$$

where

$$a_0 = \frac{x - x_1}{x_0 - x_1} a_1 = \frac{x - x_0}{x_1 - x_0} \quad (4.2)$$

When expanding linear interpolation to two dimensions, it is called bilinear interpolation. Now, the coefficients are dependent on four points, each with an  $x$  and  $y$  variable. The interpolation function  $p_{11}$  – with the subscript 11 indicating that the interpolation polynomial is of the first order in all directions – is thus also more complex.

$$p_{11}(x, y) = b_{00}f(x_0, y_0) + b_{01}f(x_0, y_1) + b_{10}f(x_1, y_0) + b_{11}f(x_1, y_1) \quad (4.3)$$

As the interpolation coefficient calculation becomes more complex, it will be presented in matrix form in Eq. (4.4).

$$\begin{bmatrix} b_{00} \\ b_{01} \\ b_{10} \\ b_{11} \end{bmatrix} = \left( \begin{bmatrix} 1 & x_0 & y_0 & x_0y_0 \\ 1 & x_0 & y_1 & x_0y_1 \\ 1 & x_1 & y_0 & x_1y_0 \\ 1 & x_1 & y_1 & x_1y_1 \end{bmatrix}^{-1} \right)^T \begin{bmatrix} 1 \\ x \\ y \\ xy \end{bmatrix} \quad (4.4)$$

Bilinear interpolation is attractive because it is computationally fast[99] and only requires four points to be weighted in order to calculate the interpolated value, shown in fig. 4.5. Although it is an older method, it is still commonly used. A simple search of "bilinear interpolation" in AIAA journals shows over 500 hits with over 20 just in the year 2016 alone. Many common applications are for image processing[99, 100] and for benchmarking of other interpolation processes[94].

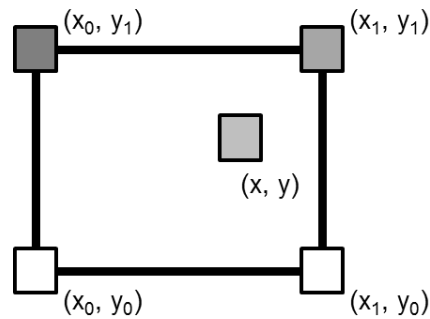


Figure 4.5: Diagram depicting bilinear interpolation points

#### 4.2.4 Spline Interpolation

Spline interpolation was first proven in 1946 by Schoenberg[101] but wasn't used extensively until the 1970s, when it showed promise in image processing[98]. This interpolation method is also a piecewise interpolation function, like the bilinear interpolation method, insofar as it fits points together with a series of curves. The curves are generated by finding the first and second derivative of the function being interpolated[102]. Imagine there are  $n$  data points, then the  $p_3(x)$  is such that

$$p_3(x) = \begin{cases} C_1(x), & x_0 \leq x \leq x_1 \\ C_i(x), & x_{i-1} \leq x \leq x_i \\ C_n(x), & x_{n-1} \leq x \leq x_n \end{cases} \quad (4.5)$$

where each  $C$  represents a cubic function. The general equation for a cubic function is

$$C_i(x) = a_i + b_i x + c_i x^2 + d_i x^3 \quad (4.6)$$

For each segment, there are four coefficients that must be determined. In order to ensure the spline curves are smooth, the solution at the nodes have to satisfy the condition in Eq. (4.7).

$$C_i(x_{i-1}) = y_{i-1} \text{ and } C_i(x_i) = y_i \quad (4.7)$$

Another way to ensure Eq. (4.7) is adhered to, it can be rewritten as in Eq. (4.8).

$$a_i + b_i x_{i-1} + c_i x_{i-1}^2 + d_i x_{i-1}^3 = y_{i-1} \text{ and } a_i + b_i x_i + c_i x_i^2 + d_i x_i^3 = y_i \quad (4.8)$$

The functions also must have the same slope of tangent lines and concavity. This is ensured through commonality of the first and second derivatives at all node points.

$$C_i(x)' = C_{i+1}(x)' \text{ and } C_i(x)'' = C_{i+1}(x)'' \quad (4.9)$$



Another way to ensure Eq. (4.9) is adhered to, it can be rewritten as in Eq. (4.10).

$$b_i + 2c_i x_i + 3d_i x_i^2 = b_{i+1} + 2c_{i+1} x_i + 3d_{i+1} x_i^2 \text{ and } 2c_i + 6d_i x_i = 2c_{i+1} + 6d_{i+1} x_i \quad (4.10)$$

There are  $2(n - 1)$  of these conditions. This still leaves two unknowns for the whole system of equations. These are satisfied by using prescribed boundary conditions. These boundary conditions can either be natural boundary conditions, where

$$C_1(x_0)'' = C_n(x_n)'' = 0 \quad (4.11)$$

or it can be a clamped boundary condition, where

$$C_1(x_0)' = C_n(x_n)' = 0 \quad (4.12)$$

Cubic spline interpolation methods are often employed in digital image processing[98] although it has other uses such as in trajectory planning[103]. While cubic spline interpolation is slower than bilinear interpolation[99]. However, in terms of computational cost-to-performance trade offs, it is the most efficient method to use[104, 105, 106].

#### 4.2.4.1 Polar Angular Interpolation

At present, interpolation in a polar or spherical space is usually reserved for fully three dimensional virtual realities, often encountered in video games[107]. However, polar interpolation schemes could be very interesting for this particular application. A feature of inlet designs is that they tend to be circular and therefore the pressure probes are usually placed along rings. By interpolating along the angle, the complexity of the problem drops from two dimensional interpolation to one dimensional interpolation.

To interpolate in angular space, the linear interpolation, Eq. (4.1) was used to derive the polar equivalent. The equation was transformed into polar coordinates using standard definitions shown in Eq. (4.13).

$$\begin{aligned}x &= r \cos \theta \\y &= r \sin \theta\end{aligned}\tag{4.13}$$

When Eq. (4.13) is plugged into Eq. (4.1), the result is:

$$f(r, \theta) = \frac{(r_2 \cos \theta_2 - r \cos \theta)}{(r_2 \cos \theta_2 - r_1 \cos \theta_1)} f(r_1, \theta_1) + \frac{(r \cos \theta - r_1 \cos \theta_1)}{(r_2 \cos \theta_2 - r_1 \cos \theta_1)} f(r_2, \theta_2)\tag{4.14}$$

In this case, the interpolation is along constant radii, thus  $r = r_1 = r_2$  and the radius term can be pulled out of the equation, resulting in Eq. (4.15):

$$f(\theta) = \frac{(\cos \theta_2 - \cos \theta)}{(\cos \theta_2 - \cos \theta_1)} f(r, \theta_1) + \frac{(\cos \theta - \cos \theta_1)}{(\cos \theta_2 - \cos \theta_1)} f(r, \theta_2)\tag{4.15}$$

This effectively reduces the dimensionality of the interpolation to one dimension. Physically speaking, unlike the bilinear interpolation which assumes that the points in between rakes are somehow related to pressures read at different radial positions, the ring between rakes has similar fluid flow at a certain radius.

#### 4.2.5 Kriging Interpolation

The Kriging method was developed in the 1950s by South African mining engineer Daniel Krige, who sought to determine the likelihood of gold deposits based on borehole samples[108, 109]. Initially, most of the applications were in geospatial applications[110, 111], although it is also used in digital image manipulation[98], a variety of aerospace applications[112, 108, 113], and computer aided design[109].

Kriging works through weighting the variance of the difference in observations between known locations[109]. The weighting is done via a function called a variogram by the mathematician

Georges Matheron, who took Krige's work and created the mathematical basis for the method[111], shown in Eq. (4.16).

$$p_k(x, y) = \sum_{i=1}^n \lambda_i f_i(x, y) \quad (4.16)$$

It should be noted that no matter how the variogram is generated, the sum of all the variogram functions over the unknown points,  $n$ , must be equal to 1. There are many different types of Kriging methods; this work will only consider ordinary Kriging for simplicity. For a more comprehensive derivation of the Kriging method the reader should consult the literature[108, 113].

Kriging is attractive as it has been shown to be very accurate, often being as or more accurate than cubic spline interpolation methods[111]. The downside of using a Kriging interpolation method is that it assumes a Gaussian distribution in the data[96], the results are highly dependent on the variogram selected[96], and the method is exceedingly complex when compared to bilinear or cubic spline interpolation methods[96, 111, 114].

#### 4.2.6 Measures of Success

There are several ways to identify the best interpolation method – it depends how "best" is measured. In this work, the measures of success that are evaluated are:

- Interpolation accuracy and precision
- Locations falling within tolerance
- Number of interpolated locations that are over-predicted
- Number of interpolated locations that are under-predicted
- Interpolation impact on derived quantities (distortion descriptors)
- Visual accuracy of the interpolation

Each of these measures is important but for different reasons. The interpolation accuracy and precision ensures that the resultant plots can be used to guide the inlet design and engine selection. The interpolation being correct for each location makes sure there are not too many artificial peaks and valleys that could lead to erroneous conclusions. The impact on derived quantities ensure the inlet is properly characterized for the chosen engine. And lastly, the visual accuracy is a qualitative check on the interpolation method.

#### 4.2.6.1 Accuracy and Precision

Once the 40 probe subset is interpolated to 320 probes, the researchers calculate an error based on the raw pressure data. The error is calculated using the following relation:

$$\delta_{rel} = \frac{P_{i,j_{int}} - P_{i,j_{320}}}{P_{i,j_{320}}} \quad (4.17)$$

Based on Eq. (4.17), histograms are created for each test case and 40 probe subset. Based on the histogram, a distribution is fitted to the error data and a probability density function is created. The accuracy of the interpolation method is how close the error mean is to 0. The precision of the interpolation method is the size of the standard deviation; a smaller standard deviation indicating a more precise results.

#### 4.2.6.2 Location Predictions

The number of interpolated locations falling within and out of tolerance is another measure of the goodness of the interpolation method. The tolerance chosen for this work is an error of 1%. This number was chosen because pressure transducers tend to have an error of about 0.25% (precision applications) to 1.25% (general applications) of range[115].

In addition to viewing how many interpolated points are within tolerance, the locations that are out of tolerance are tracked. Both under- and over-predicting can be detrimental although they can lead researchers to different conclusions and have different impacts on the derived quantities.

#### 4.2.6.3 Impact on Derived Quantities

The final measure of success is the impact on the distortion indices. It should be noted that indices are normally calculated from the measured probe locations, not interpolated values. Even if an index is calculated from computational data, it is based on where the 40 probe rake array would be positioned. However, the derived quantities are calculated from the interpolated values here for completeness to get a full understanding of the scheme's impact.

The error on the derived quantities is calculated both as an absolute error and a percent error. This is because some of the indices are very small so percent error becomes meaningless while in other cases, the percent error can be very useful. The absolute error is calculated as:

$$\epsilon_{abs} = D_{int} - D_{320} \quad (4.18)$$

Where D is a stand-in for any of the indices calculated in this work. The relative error is calculated as:

$$\epsilon_{rel} = \frac{D_{int} - D_{320}}{D_{320}} \quad (4.19)$$

#### 4.2.6.4 Visual Accuracy

The visual accuracy is a "soft" measure of success. This means that there is no clear mathematical formula that is followed to ensure the interpolation method is correct, it is merely a visual inspection of the result. It is inherently difficult to quantify this measure of success as each expert might draw a different conclusion. Thus, this measure of success should never be taken on its own and always coupled with the other, more rigorous targets.

## 4.3 Results

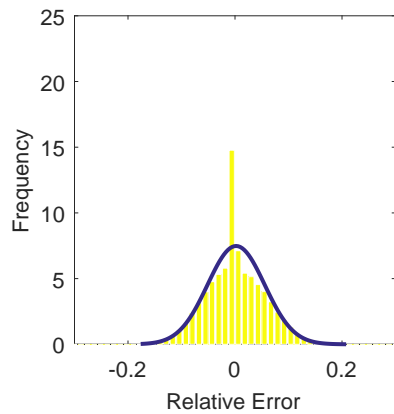
The results of the interpolation of the surrogate modeling are shown below. Twenty five test cases were run, with eight subsets of data per test case, for three patterns, and with four different interpolation schemes. This results in a total of 2,400 different results. For the sake of brevity, most results are shown using statistical analysis only. The same test case and clocking is shown throughout for all images - Test Case 2, Clocking 3. This was chosen at random.

### 4.3.1 Accuracy and Precision

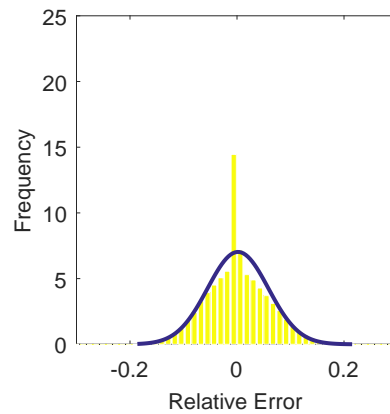
The accuracy and precision were measured in terms of the overall mean and standard deviation of the error (Eq. (4.18)), shown in figures 4.6 through 4.8. A mean closer to zero shows a more accurate result while a smaller standard deviation indicates a more precise result.

Figure 4.6 show the compiled results for the 180 degree low pressure pattern. The resultant histogram looks mostly normally distributed with a high frequency near the mean. A normal distribution confirms that the data can be treated as Gaussian and the mean and standard deviation can be calculated for a normal distribution. The polar interpolation method is the exception, with a high positive bias error.

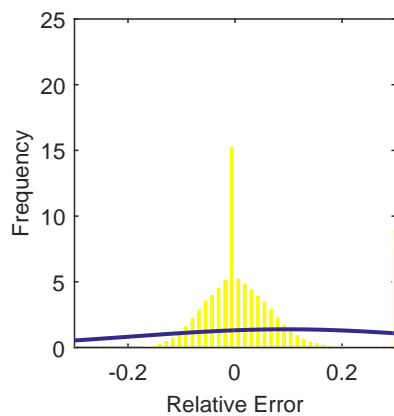
Figure 4.7 show the compiled results for the 4x45 degree low pressure pattern. The histogram looks very similar to that of the 180 degree pattern, with all methods showing largely normal results save for the polar interpolation scheme, which has again a very high error. The hub pattern, shown in figure 4.8 has a similar result, with mostly normal distributions though the polar interpolation method shows a positive skew.



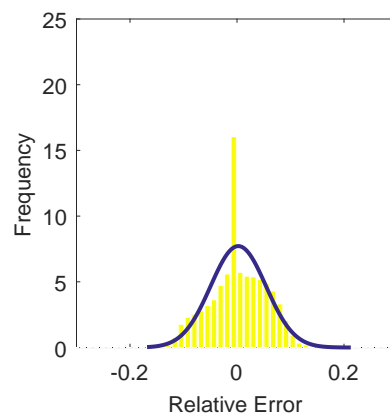
(a) Linear Interpolation Error



(b) Spline Interpolation Error

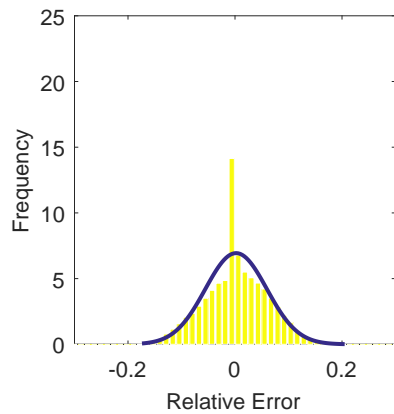


(c) Polar Interpolation Error

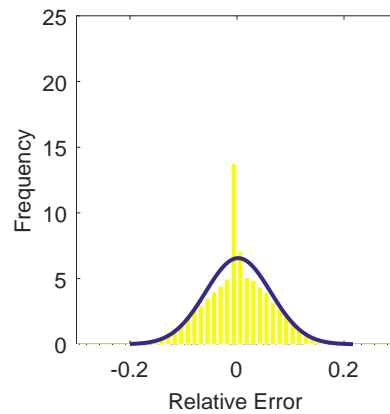


(d) Kriging Interpolation Error

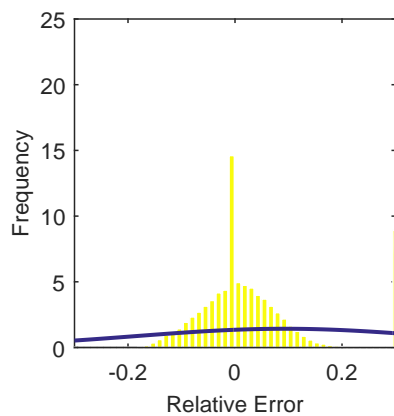
Figure 4.6: Relative error for various interpolation schemes of the 180 degree low pressure pattern.



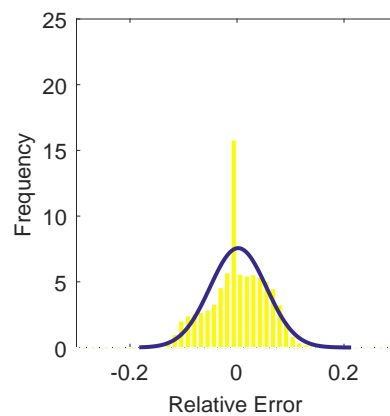
(a) Linear Interpolation Error



(b) Spline Interpolation Error



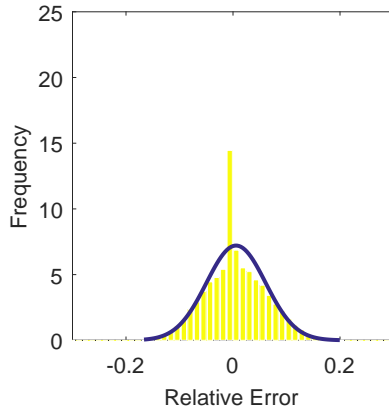
(c) Polar Interpolation Error



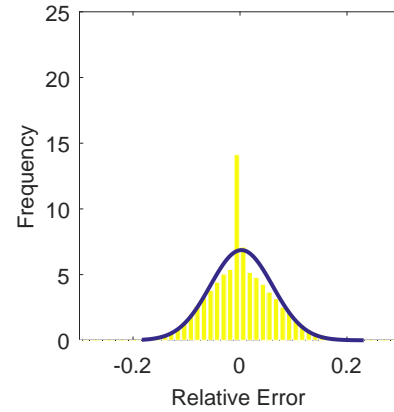
(d) Kriging Interpolation Error

Figure 4.7: Relative error for various interpolation schemes of the 4x45 degree low pressure pattern.

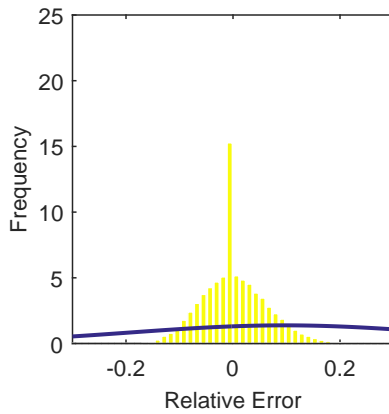




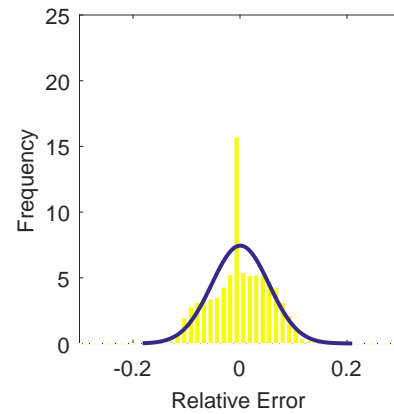
(a) Linear Interpolation Error



(b) Spline Interpolation Error



(c) Polar Interpolation Error



(d) Kriging Interpolation Error

Figure 4.8: Relative error for various interpolation schemes of the hub low pressure pattern.

A tabulation of the mean of the mean and the mean standard deviation for the methods are shown in table 4.2. As the PDFs plotted in figures 4.6 through 4.8 alluded, the polar method is clearly not accurate nor precise. The mean of the error ranges from 0.093 to 0.096, compared to an average error of 0.005 or less. The polar interpolation method also has the largest standard deviation, with a standard deviation of more than 0.280. The other methods all have standard deviations of around 0.06 or less. The most accurate method for all three patterns is the spline interpolation, with errors of 0.0026 or less and standard deviations of 0.061 or less. The linear and Kriging methods are close but have slightly higher means and standard deviations. There is no great difference in the results based on the pattern, suggesting that the results of the accuracy and

precision of the different interpolation methods are independent of the surrogate model used.

Table 4.2: Interpolation accuracy and precision for the surrogate model

	180		4x45		Hub	
	Mean	Std. Dev.	Mean	Std. Dev.	Mean	Std. Dev.
Linear	0.00206	0.0533	0.00204	0.0575	0.00568	0.0553
Spline	0.00184	0.0567	0.00214	0.0608	0.00260	0.0581
Polar	0.0960	0.288	0.0932	0.280	0.0962	0.287
Kriging	0.00242	0.0517	0.00224	0.0527	0.00065	0.0535

### 4.3.2 Location Predictions

As has been stated before, many data points were analyzed for these surrogate models. It would be exhaustive and not informative to display each and every location prediction as a plot as is shown in chapter 5. Thus, only the PDF of the location predictions will be shown as well as the mean and standard deviation in tabular form.

The overall location predictions can be found in tables 4.3, 4.4, and 4.5. From these tabulations, there does not seem to be a great difference between patterns. This again suggests that the results of the interpolation method chosen is independent of the surrogate model pattern. However, the polar method under performs greatly in this measure of success as well, having the fewest points within the tolerance and greatly over-predicting most locations. There is no great difference between the other three methods in terms of location predictions and can all be considered equally good.

The within tolerance points do not include the original 40 known points. The tolerance is  $\pm 1\%$  of the exact solution, as this is approximately the error on a standard total pressure probe. Almost all the methods had an average of around 75 of the 320 points fall within tolerance, an average of around 130 points fall above tolerance, and an average of about 115 points fall under the tolerance level. This indicates that all methods overshoot or under-predict at similar rates. The only exception is the polar method, which has higher instances of over-prediction.

Table 4.3: Mean interpolation location prediction results falling within, above, and below the tolerance band for the 180 degree low pressure pattern.

	Within			Above			Below		
	Mean	Std. Dev.	Range	Mean	Std. Dev.	Range	Mean	Std. Dev.	Range
Linear	77.2	5.8	30.0	123.0	17.6	84.0	119.7	17.5	87.0
Spline	76.6	6.20	32.0	122.4	16.9	84.0	121.0	16.9	89.0
Polar	69.3	7.4	36.0	145.0	22.5	103.0	105.7	19.1	92.0
Kriging	77.1	5.9	33.0	129.9	17.4	98.0	113.1	17.5	87.0

Table 4.4: Mean interpolation location prediction results falling within, above, and below the tolerance band for the 4x45 degree low pressure pattern.

	Within			Above			Below		
	Mean	Std. Dev.	Range	Mean	Std. Dev.	Range	Mean	Std. Dev.	Range
Linear	74.5	5.37	26.0	130.4	16.44	94.0	115.1	14.94	94.0
Spline	73.8	5.14	32.0	128.6	15.31	93.0	117.6	14.30	92.0
Polar	66.0	6.66	32.0	152.1	24.65	130.0	101.9	20.44	111.0
Kriging	75.8	5.86	34.0	133.0	16.13	98.0	111.1	16.24	92.0

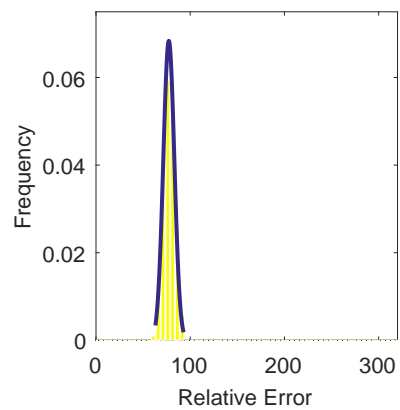
Table 4.5: Mean interpolation location prediction results falling within, above, and below the tolerance band for the hub low pressure pattern.

	Within			Above			Below		
	Mean	Std. Dev.	Range	Mean	Std. Dev.	Range	Mean	Std. Dev.	Range
Linear	75.3	6.00	33.0	132.0	15.56	71.0	112.7	16.10	71.0
Spline	75.4	6.24	43.0	124.2	14.09	72.0	120.5	14.21	61.0
Polar	68.4	8.28	42.0	143.9	24.69	105.0	107.7	20.17	85.0
Kriging	74.9	5.96	34.0	128.2	14.31	68.0	116.9	14.25	68.0

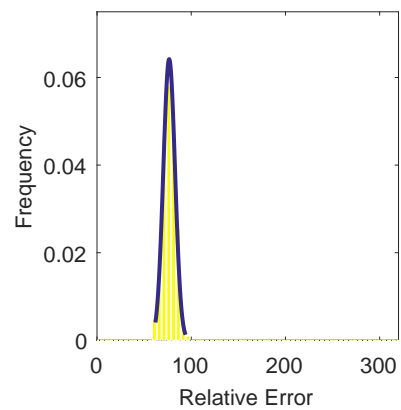
When looking at all three of these patterns, it is difficult to discern which one is overall the best. It appears that Kriging and bilinear interpolation lead to the most points falling within tolerance. To minimize the number of points that overshoot, the spline interpolation stands out while to minimize the number of points that undershoot, the polar method appears to be best. The results are inconclusive and do not suggest a single 'best' method for location prediction.

#### **4.3.2.1 Number of Locations Falling Within Tolerance**

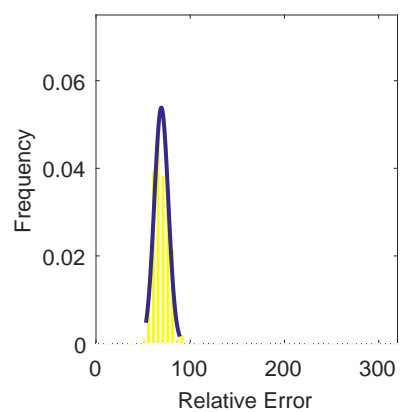
A visual guide to the tables above are shown below. These figures (4.9 through 4.11) show the PDF of how many points fall within the tolerance for each pattern and method. All four methods behave similarly, although the polar interpolation method consistently has fewer points falling within tolerance and has a larger spread of data. This confirms again that the results are independent of the pattern and depend solely on the method used. The average number of locations falling within tolerance – without counting the original 40 known points – is around 75 points with a standard deviation of about 6 points.



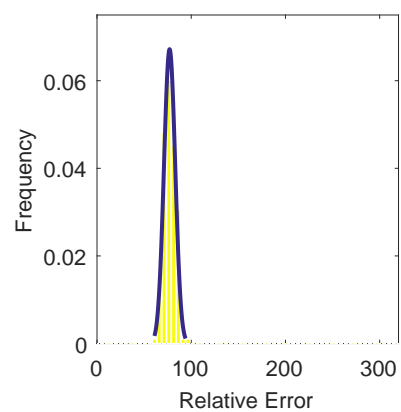
(a) Linear Interpolation



(b) Spline Interpolation

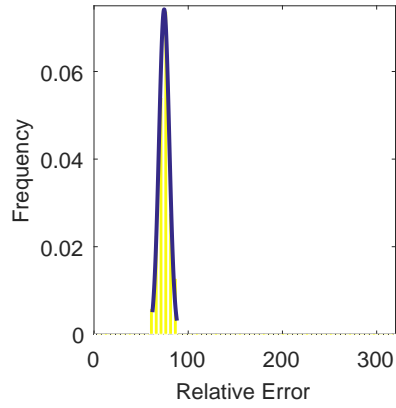


(c) Polar Interpolation

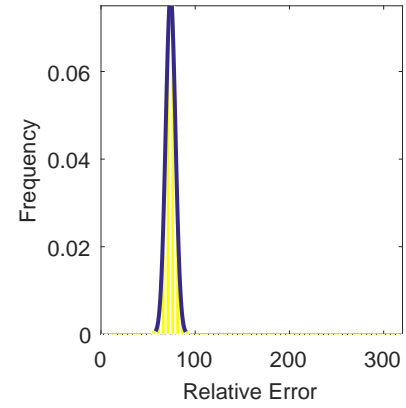


(d) Kriging Interpolation

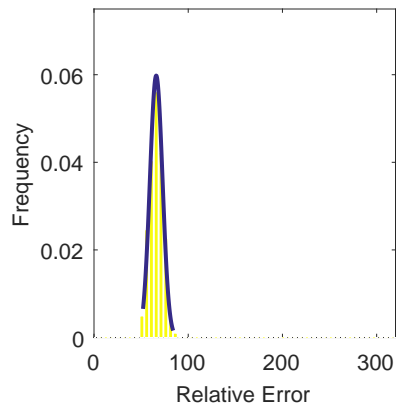
Figure 4.9: Interpolation results falling within the 1% tolerance band for the 180 degree low pressure pattern.



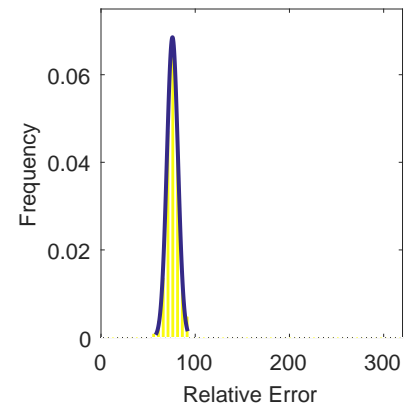
(a) Linear Interpolation



(b) Spline Interpolation

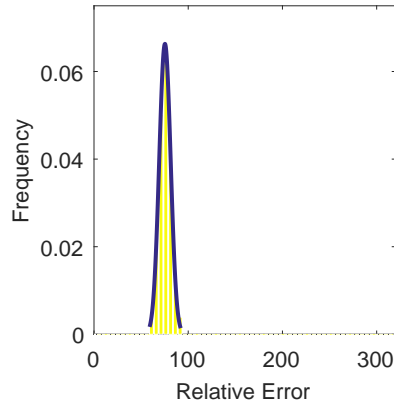


(c) Polar Interpolation

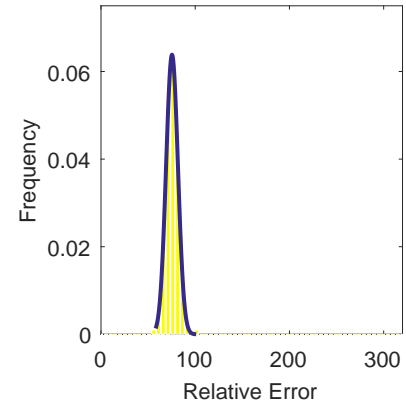


(d) Kriging Interpolation

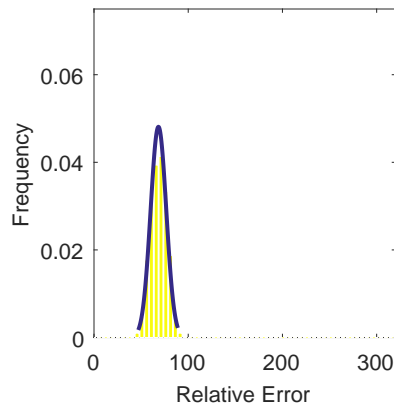
Figure 4.10: Interpolation results falling within the 1% tolerance band for the 4x45 degree low pressure pattern.



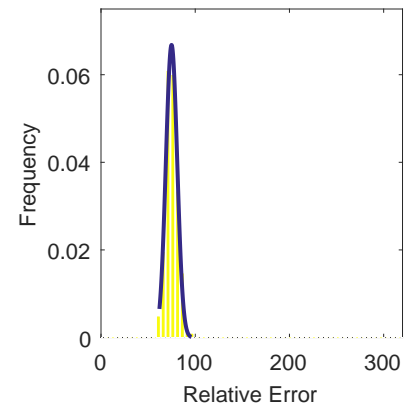
(a) Linear Interpolation



(b) Spline Interpolation



(c) Polar Interpolation

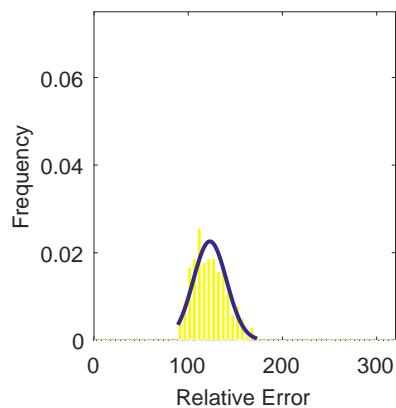


(d) Kriging Interpolation

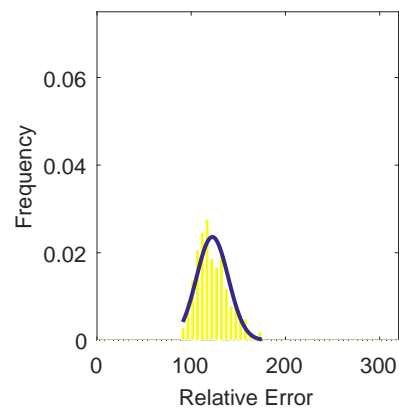
Figure 4.11: Interpolation results falling within the 1% tolerance band for the hub low pressure pattern.

#### 4.3.2.2 Number of Locations Falling Above Tolerance

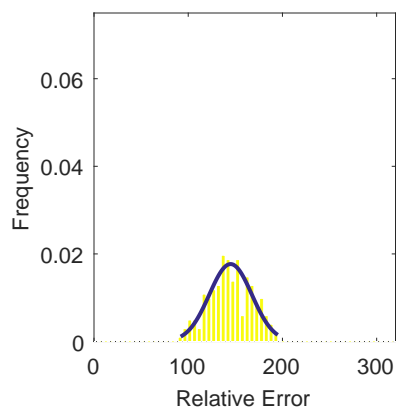
Similarly to the section above, these figures (4.12 through 4.14) show the PDF of how many points fall above the tolerance for each pattern and method. The average number of locations falling above the tolerance is around 115 points with an average standard deviation of about 19 points.



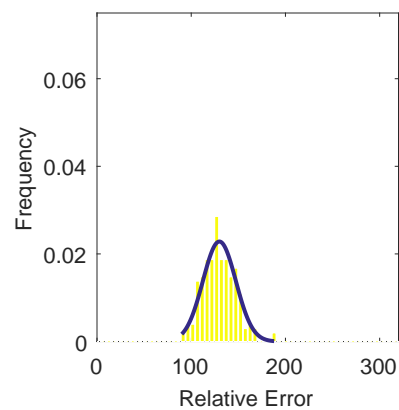
(a) Linear Interpolation



(b) Spline Interpolation



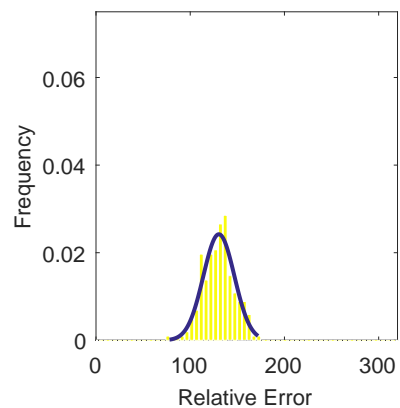
(c) Polar Interpolation



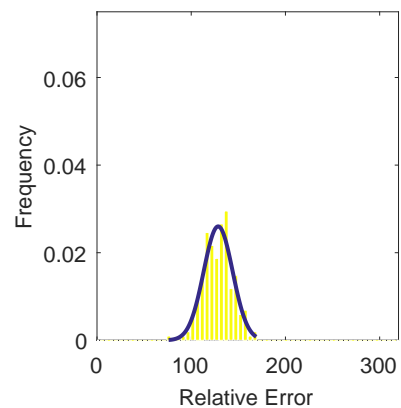
(d) Kriging Interpolation

Figure 4.12: Interpolation results falling above the 1% tolerance band for the 180 degree low pressure pattern.

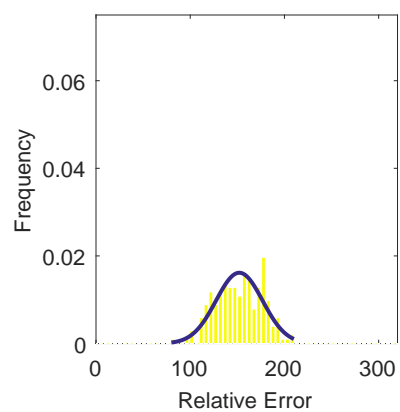




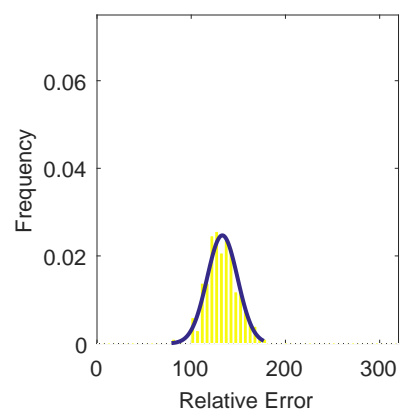
(a) Linear Interpolation



(b) Spline Interpolation

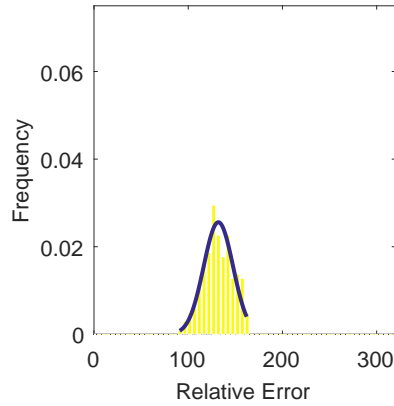


(c) Polar Interpolation

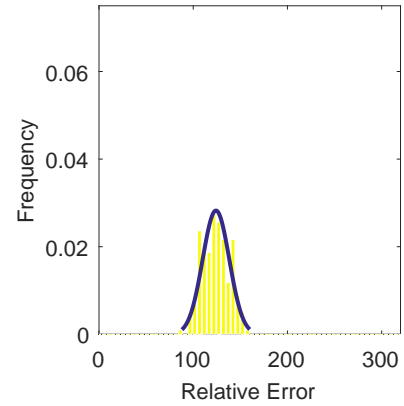


(d) Kriging Interpolation

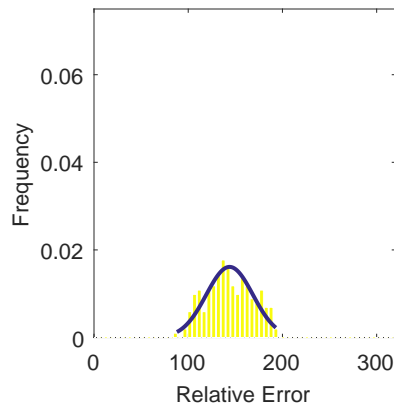
Figure 4.13: Interpolation results falling above the 1% tolerance band for the 4x45 degree low pressure pattern.



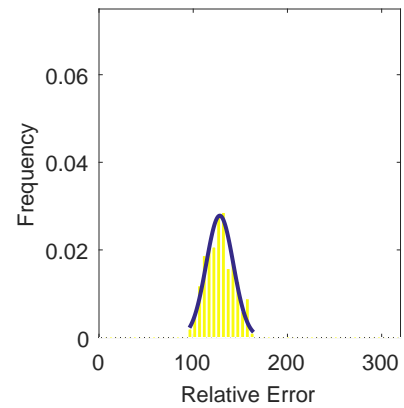
(a) Linear Interpolation



(b) Spline Interpolation



(c) Polar Interpolation

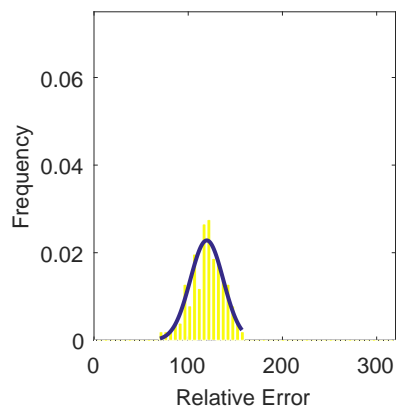


(d) Kriging Interpolation

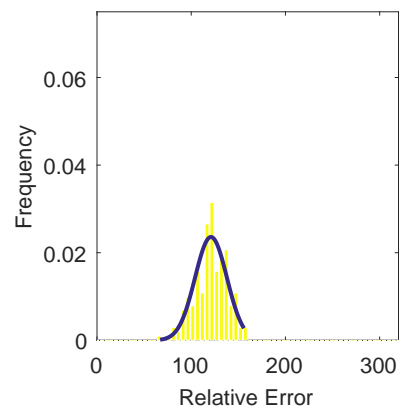
Figure 4.14: Interpolation results falling above the 1% tolerance band for the hub low pressure pattern.

#### 4.3.2.3 Number of Locations Falling Below Tolerance

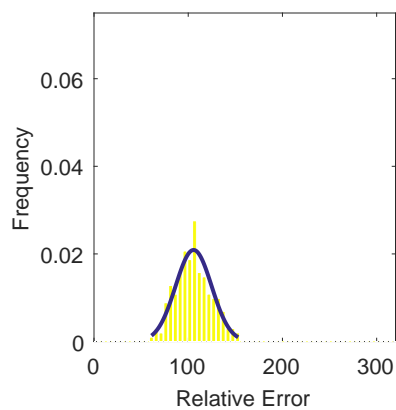
These figures (4.15 through 4.17) show the PDF of how many points fall below the tolerance for each pattern and method. The average number of points under-predicted is about 130, with an average standard deviation of 18.



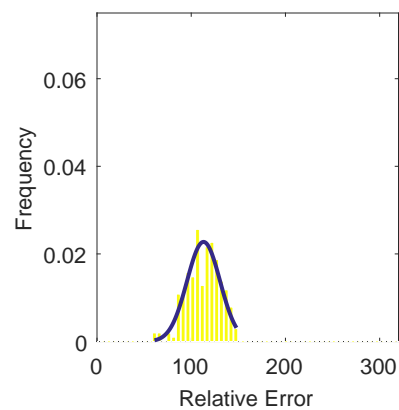
(a) Linear Interpolation



(b) Spline Interpolation

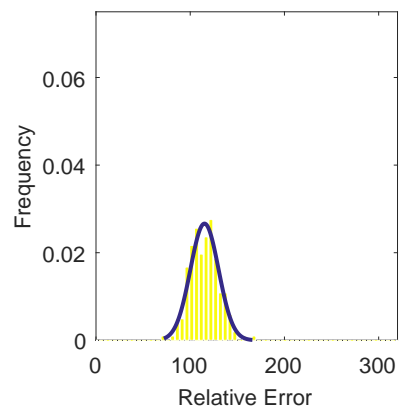


(c) Polar Interpolation

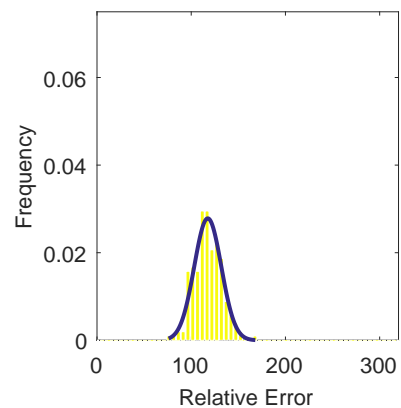


(d) Kriging Interpolation

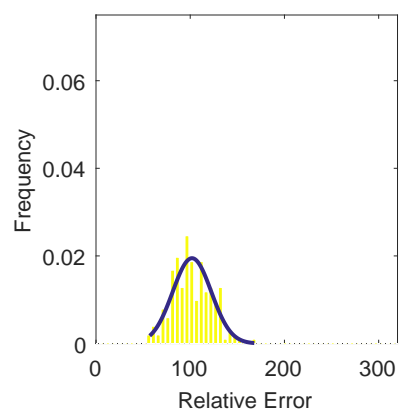
Figure 4.15: Interpolation results falling below the 1% tolerance band for the 180 degree low pressure pattern.



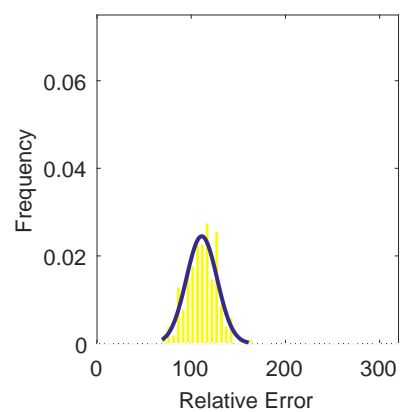
(a) Linear Interpolation



(b) Spline Interpolation

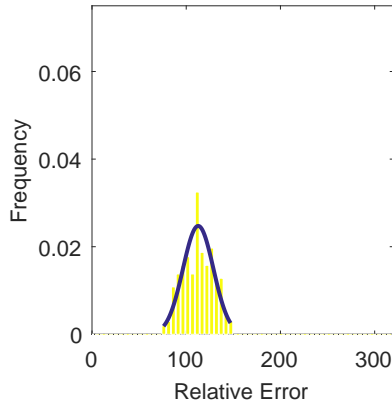


(c) Polar Interpolation

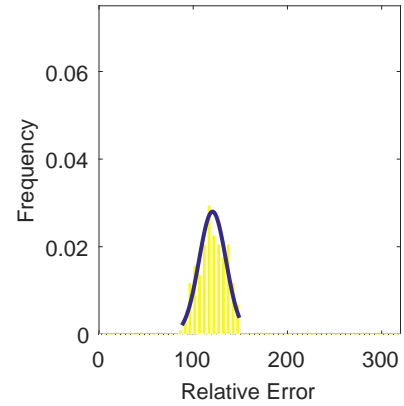


(d) Kriging Interpolation

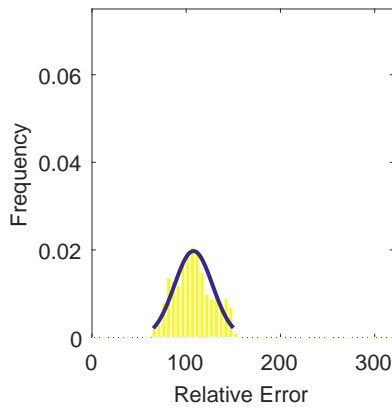
Figure 4.16: Interpolation results falling below the 1% tolerance band for the 4x45 degree low pressure pattern.



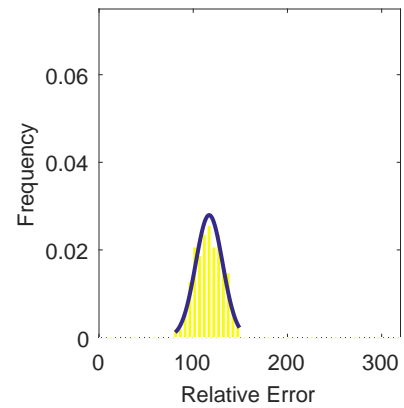
(a) Linear Interpolation



(b) Spline Interpolation



(c) Polar Interpolation

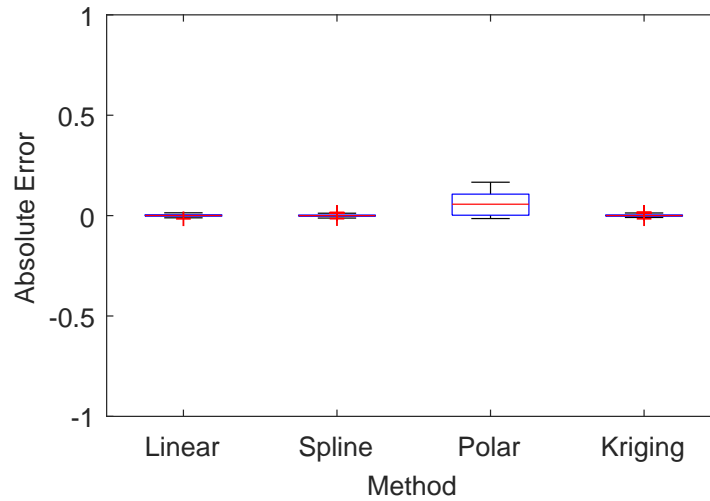


(d) Kriging Interpolation

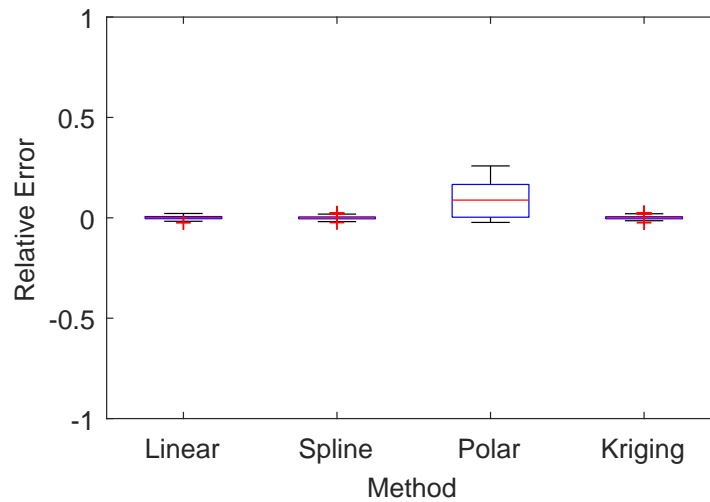
Figure 4.17: Interpolation results falling below the 1% tolerance band for the hub low pressure pattern.

### 4.3.3 Impact on Derived Quantities

The final quantitative measure of success is how the interpolation methods impact the derived quantities. It should be noted that in real world applications, the derived quantities are calculated solely based on the measured experimental data or based on nodes closest to the experimental probes from the computational results. However, for the sake of completeness of the analysis, this section is included.



(a) Absolute Error



(b) Relative Error

Figure 4.18: Absolute and relative error of each interpolation method for the  $K_\theta$  index

Both the absolute error and relative error are calculated and presented as a box plot in fig. 4.18 through 4.21. It should be noted that  $K_a$ , the total distortion index based on  $K_\theta$  and  $K_r$ , is omitted, as it merely is a summation of those two distortion indices.

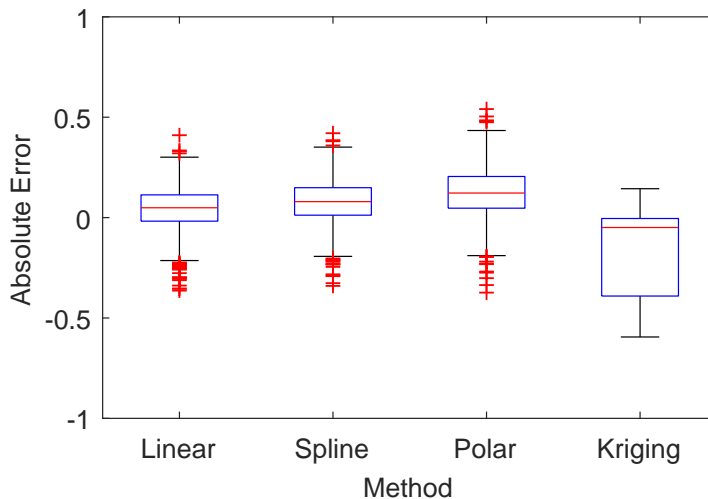
The results in the derived quantities are not shown broken down by pattern as previous results have shown the pattern chosen for the surrogate model does not affect the interpolation results.

The red line near the center of the box represents the sample median of the distortion indices. The

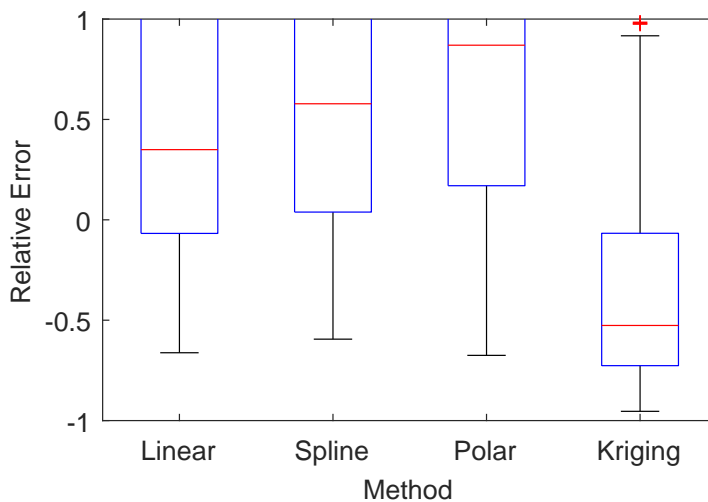
blue box surrounding the red line represents the 25th and 75th percentiles of the samples. The black lines extending above and below the box represent the full interquartile range. The red data points extending beyond the black line represents the outliers.

Fig. 4.18 shows the absolute and relative errors of the calculation of the circumferential K-index for each interpolation method. The largest absolute error is in the polar method, with a mean absolute error of 0.060 and a standard deviation of 0.057. The other three methods are comparable with mean absolute errors below 0.001 and standard deviations of about 0.005. The largest relative error is also in the polar method, with a mean relative error of 0.93 and a standard deviation of 0.090. The other three methods have mean relative errors of less than 0.001 with standard deviations of about 0.007. This indicates all methods are about equally as accurate at predicting  $K_\theta$  other than the polar method, which is not adequate.

Fig. 4.19 shows the absolute and relative errors of the calculation of the radial K-index for each interpolation method. The largest absolute error is in the Kriging method, with a mean absolute error of -0.16 and a standard deviation of 0.21. The other three methods are comparable, though the polar method is more positively skewed. The standard deviation of the absolute error for the remaining three methods - polar, linear, and spline - are on the order of 0.1. The relative errors for  $K_r$  are deceptively large when compared to  $K_\theta$ . This is due to the values of  $K_r$  being relatively small.



(a) Absolute Error



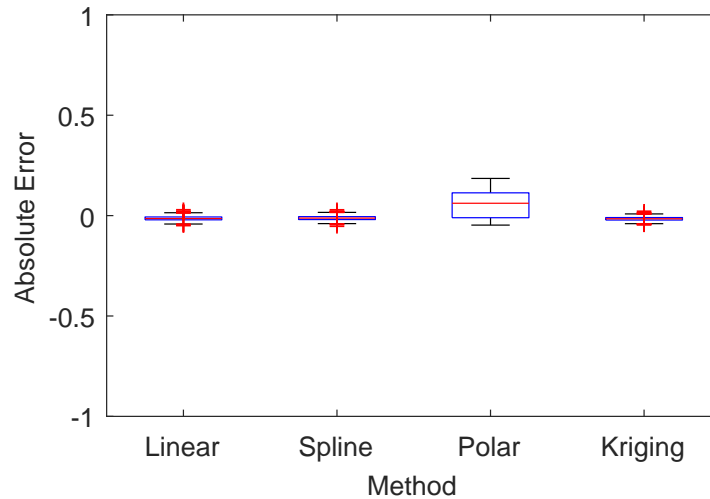
(b) Relative Error

Figure 4.19: Absolute and relative error of each interpolation method for the  $K_r$  index

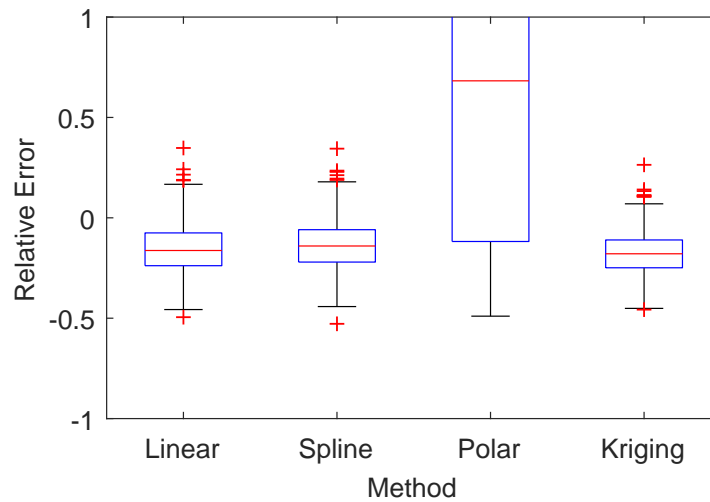
The largest relative error is in the polar method, with a mean relative error of around 1.9 and a standard deviation of 2.89. The smallest relative error is surprisingly in the Kriging method, with a mean relative error of -0.21 and a standard deviation of 0.86. The other two methods have mean relative errors around 1.2 with standard deviations of about 2.

This indicates that none of the methods are particularly good at resolving a value for  $K_r$ .





(a) Absolute Error

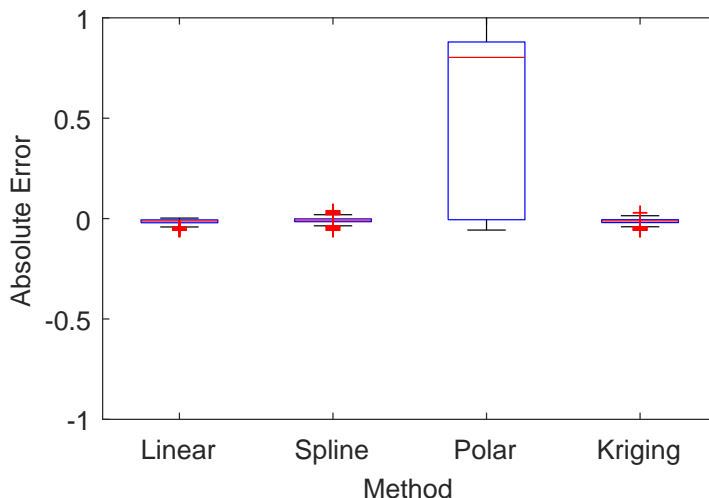


(b) Relative Error

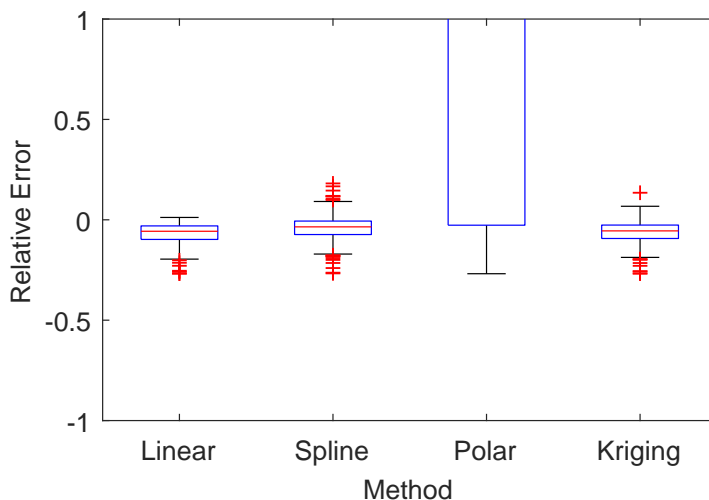
Figure 4.20: Absolute and relative error of each interpolation method for the *IDC* index

Fig. 4.20 shows the absolute and relative errors of the calculation of the circumferential ID-index for each interpolation method. The largest absolute error is in the polar method, with a mean absolute error of 0.059 and a standard deviation of 0.069. The other three methods are comparable with mean absolute errors below -0.01 (all the methods show a negative skew) and standard deviations of about 0.01. The largest relative error is also in the polar method, with a mean relative error of 0.67 and a standard deviation of 0.78. The other three methods all have

relative mean errors of around -0.15 with standard deviations of around 0.12. As with the other distortion indices, the results indicate all methods save the polar method predict *IDC* equally well.



(a) Absolute Error



(b) Relative Error

Figure 4.21: Absolute and relative error of each interpolation method for the *IDT* index

Fig. 4.21 shows the absolute and relative errors of the calculation of the combined ID-index for each interpolation method. The largest absolute error is in the polar method, with a mean absolute error of 0.54 and a standard deviation of 0.42. The other three methods are comparable with mean

absolute errors around -0.010 – again indicating a negative skew – and standard deviations of about 0.01. The largest relative error is also in the polar method, with a mean relative error of 2.53 and a standard deviation of 2.0. The other three methods have a general negative skew in the relative error average, though all are about -0.05 and with standard deviations of 0.05. For this last method, it again appears that all interpolation methods are approximately the same except for the polar method, which greatly overestimates *IDT*.

#### 4.3.4 Visual Accuracy

The final measure of success is the visual accuracy of the interpolation methods. As it is much easier to visualize data than it is to look at tables of information, these plots are usually what most decisions are based on. Therefore, the plots should be accurate representations of the data for researchers to make informed decisions.

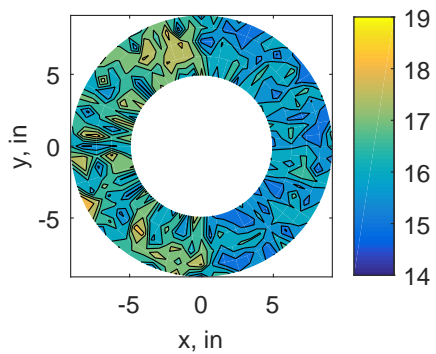
For all these visual plots, a randomly selected test case and clocking was used for the sake of brevity, although the same test case and clocking was used for all these images. The researchers have reviewed all test cases and clockings and found no striking difference between test cases and clockings, thus this one singular data point is representative of all the data.

The 180 degree patten contour plots can be found in fig. 4.22. One thing that is immediately striking is that all the interpolation methods smooth the data. None of the interpolated results show the granularity and intricacy of the original data. It should be noted as this is a surrogate model, it is far more granular and chaotic than a real AIP pattern would be. However, one can immediately see that the Kriging method does not capture any of the chaos except for at the known node points. The other three methods look similar, though the polar method does tend to create a swirl-type pattern that is likely not realistic. However, in terms of visual accuracy, all but the Kriging method appear to be acceptable.

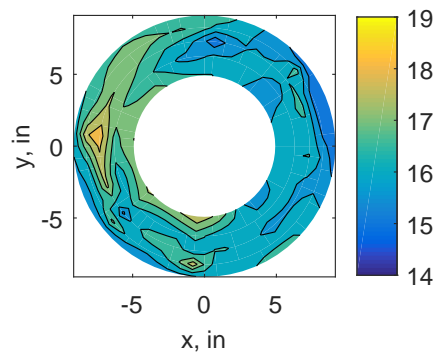
Next is the 4-by-45 degree patten contour plots, shown in fig. 4.23. Similar to the 180 degree model, the pattern is quite chaotic and the Kriging method only shows accurate results at and around the known points. The linear, spline, and polar methods look very similar, though the polar

method shows an add pattern between the 8 and 10 o'clock positions. None of the interpolations capture the high point at the 8 o'clock and 6 o'clock positions, though there is an artificial high point near the 5 o'clock position. It is safe to say that while none of the remaining three methods are perfect, they are all much closer to the original result than the Kriging method.

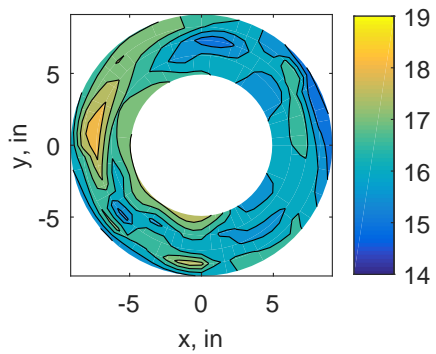
Lastly is the hub-to-tip pattern contour plots, shown in fig. 4.24. The Kriging method again shows the face-average pressure at all points except at the known node points. The other three methods all show exaggerated areas of high pressure between the 2 and 4 o'clock positions, with the polar method showing the most exaggerated and the spline method the least exaggerated. This again leads to the conclusion that while none of the remaining three methods are ideal, they are much better visual representations than the Kriging method.



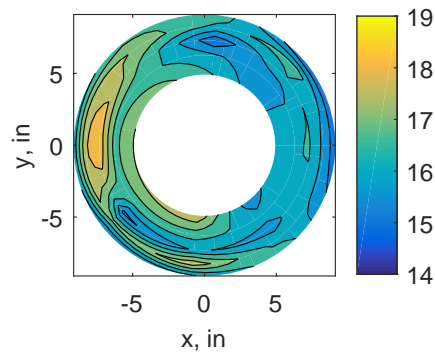
(a) Raw Data



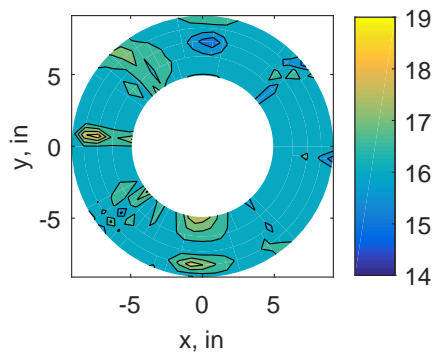
(b) Linear Interpolation



(c) Spline Interpolation

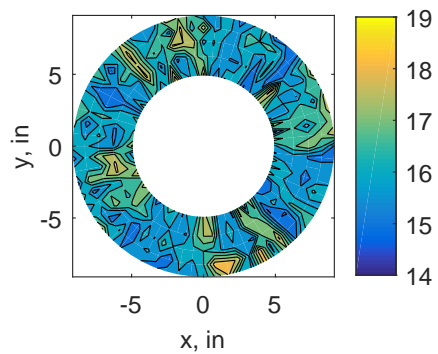


(d) Polar Interpolation

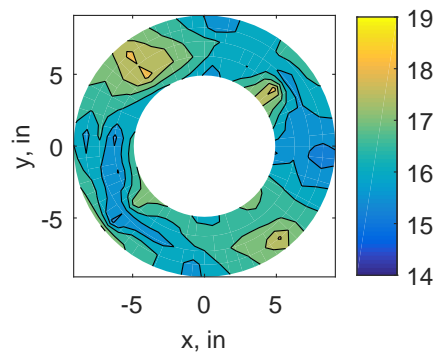


(e) Kriging Interpolation

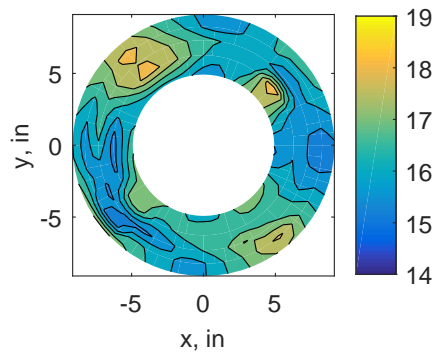
Figure 4.22: Visual accuracy of interpolation methods for the 180 degree pattern



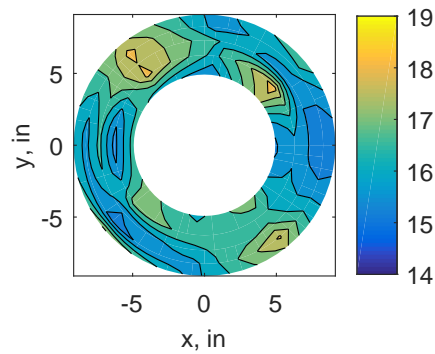
(a) Raw Data



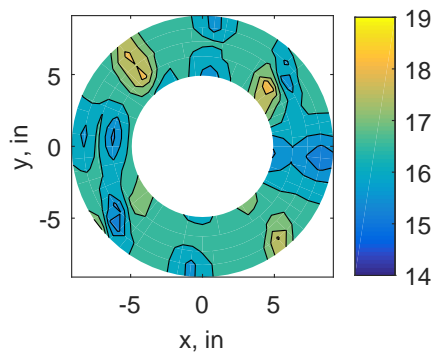
(b) Linear Interpolation



(c) Spline Interpolation

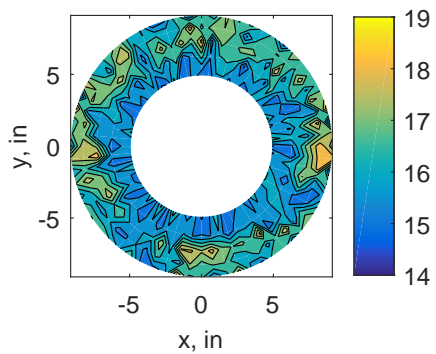


(d) Polar Interpolation

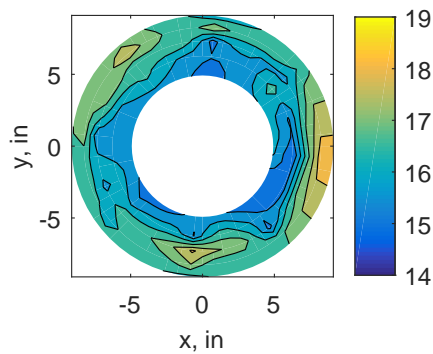


(e) Kriging Interpolation

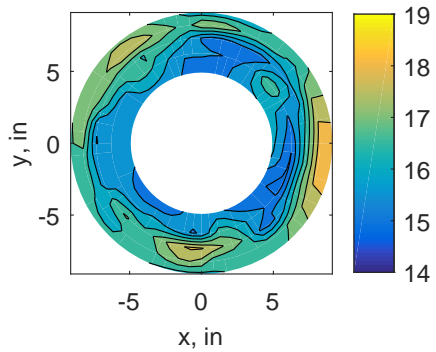
Figure 4.23: Visual accuracy of interpolation methods for the 45 degree pattern



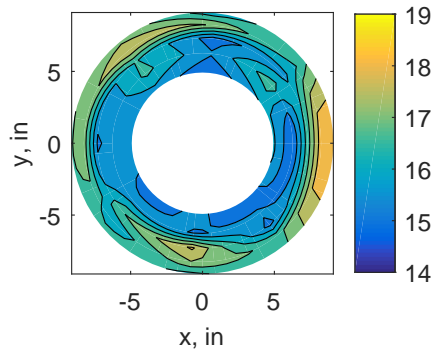
(a) Raw Data



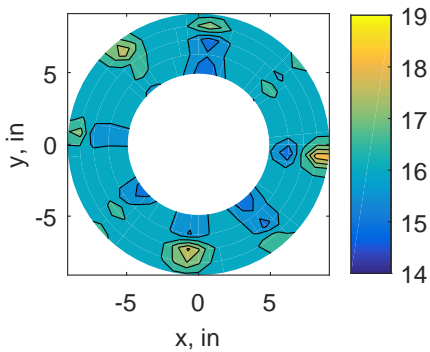
(b) Linear Interpolation



(c) Spline Interpolation



(d) Polar Interpolation



(e) Kriging Interpolation

Figure 4.24: Visual accuracy of interpolation methods for the hub to tip pattern

#### 4.4 Conclusions

This research aimed at determining if there was an optimum way to transform discrete experimental data points into a continuous contour plot. For this initial work, a surrogate model was created based on real experimental data. Various subsets of data were chosen in accordance with how the standard suggests pressure probes should be distributed and those subsets were interpolated back to the full data set using four different methods. The interpolated results were compared both quantitatively and qualitatively to the original data.

The results show that various methods work, but only the spline method scored high in most categories. In terms of accuracy and precision, the spline interpolation method had consistently the smallest mean error and standard deviation. For the location prediction, the spline method was good at not over-predicting the points, though the Kriging method was better at getting more points within tolerance and the polar interpolation method better for ensuring the fewest points were under-predicted. If under-prediction is a concern or the most points must be within tolerance, the spline method may not be best. In terms of the derived quantities, anything other than the polar method can be used while for the visual accuracy, all but the Kriging method show good results. Thus, the spline method is likely the best overall method based on this study.

There are some known uncertainties in the results. These can be partially attributed to the data set. As with all surrogate modeling, the model is not perfect. The way the surrogate model is created has a large impact on the results down the road, meaning that the random variable used has its proverbial thumb on the scale. Another part of the lack of clear "best" method from the data is due to the fact that each interpolation method has its own strengths and weaknesses. Linear interpolation is easy to implement and computationally cost effective, but it assumes that there is a certain relationship between data points. Kriging may be more difficult to implement but takes into account spatial data, which could help with unevenly distributed data points.

Overall, the results show that a spline method satisfies the most measures of success based on this model. This work also confirms one fundamental inquiry – that the interpolation method



used to transform discrete data points into a contour map has an effect on the results. Different methods lend themselves better to achieve various measures of success. In this case the spline method appeared to come out on top; the question remains if this is true when it is applied to real data. In the next chapter, this additional uncertainty is added to the study to determine if the initial results hold true.

# Chapter 5

## Interpolation of Experimental and Computational Pressure Data

An attempt was made in chapter 4 to determine if the interpolation method used to transform discrete data into continuous pressure maps was significant and if so, which method was most accurate. The results showed that the method used can be significant, but depends partially on what is considered a success. To get accurate, precise results, the spline interpolation method consistently outperformed the other methods. However, it was not the best when it came to predicting the results at each and every location.

Part of the uncertainty in the results could be due to the nature of surrogate modeling; in the end, the model is heavily dependent on what assumptions go into the random variable used to create the model. These assumptions include the probability distribution of the random variable that is used to generate the surrogate model and the bounds applied to the random variable. A Gaussian random variable will create a different surrogate model from a uniformly distributed random variable, as will a more tightly bounded variable versus a large range variable. As the relationship between various points in the flow of real data is much more complex than most random variables can capture, experimental data will be used in this chapter, though the methodology remains largely the same as in chapter 4.

### 5.1 Background

Two inlets were studied for this work – a one third YF12 inlet and a one tenth scale TBCC inlet. The YF-12 was the prototype vehicle for the SR-71 Blackbird that was later used by NASA

and the US Air Force as a flying test bed [34]. The YF12 inlet is an axisymmetric inlet with a translating spike which can close off the airflow to the main turbojet engine and divert the airflow to the afterburner. This lets the engine operate as a de-facto ramjet, thus making it a TBCC-like engine. Only the exact, 320 probe data is available for this inlet. The inlet geometry is still classified and thus no computational results can be generated. The TBCC inlet on the other hand was created for a NASP-like vehicle. In order to study the transition from turbojet to ramjet and vice versa, NASA started the Inlet Mode Transition Experiment, called IMX for short. This inlet is a two-dimensional inlet with an over-under configuration. While limited, sparse test data exists for the IMX, it was not enough data to generate accurate contour plots by the author. Computational results were generated by John Slater at NASA Glenn. For this work, only the CFD data for the IMX will be utilized.

More information on the inlets and the data available can be found in chapter 3, specifically in section 3.2 for the YF12 inlet and section 3.1.3 for the IMX inlet.

## 5.2 Methodology

The methodology used is the same as that used for the surrogate model discussed in chapter 4. This work will look at how interpolating subsets of data from a down-selected 40 probe set compare to the full probe set. The four interpolation methods examined in this paper are Cartesian bilinear interpolation, Cartesian spline interpolation, polar angular interpolation, and Kriging interpolation. The measure of success for each of these methods is evaluated against the full 320 pressure data as well as the impact it has on the flow distortion descriptors, which are derived from the engine manufacturers based on the fan and compressor behavior. Further reading on the methodology can be found in section 4.2.2.

There are several ways to assess interpolation methods against the measures of success. In this work, the measures of success that are evaluated are the interpolation accuracy and precision, how well each location is predicted, and the impact on the derived quantities. A more thorough discussion can be found in section 4.2.6. A tolerance level of 1% was applied, meaning that all

interpolated results that fall within 1% of the exact solution are considered good.

Inlet flow distortion is generally measured via an "index" or "distortion descriptor". These terms are used interchangeably. The index refers to the normalized deviation of flow from the bulk of the flow, usually measured in total pressure. There are many distortion indices, generated through extensive testing at the engine manufacturer; for the purpose of this work, the distortion indices used by Stoll[1] are used. These indices are classified into circumferential, radial, and overall distortion indices. Two sets of indices were used in this work, the K-indices and the ID-indices. K-indices include the circumferential index  $K_\theta$ , radial index  $K_r$ , and combined index  $K_a$ . The ID-indices include the circumferential index  $IDC$  and combined index  $IDT$ . A more thorough explanation of these indices can be found in section 2.3.3.

### 5.3 Results

For the YF12, all three test cases and several subsets of 40 probes were evaluated, as described in figure 5.1. However, for the sake of brevity, only the first test case and zero clocking position will be shown in this chapter. Similarly, for the IMX CFD data, all three CFD runs and the 8 possible positions for the 40 probes were evaluated but only run 300 and the zero clocking position will be shown. The complete results can be found in Appendix C.



Figure 5.1: Clocking example of the 40 probe subset, with the darker color representing the clocking.

### 5.3.1 Interpolation Accuracy and Precision

The interpolation accuracy and precision are measured in terms of how close each interpolated value got to the exact, 320 probe solution. The error is determined by eq. 5.1, which was previously presented in chapter 4 as eq. (4.17). The accuracy of the method is determined by taking the mean of the error; good accuracy means the mean error is close to zero.

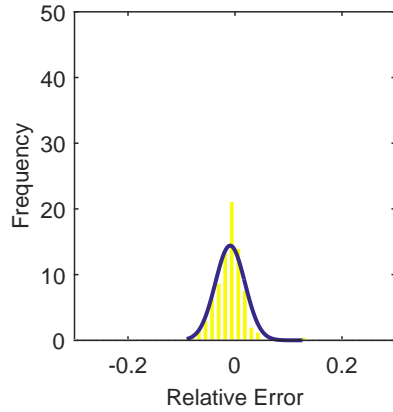
$$\delta_{rel} = \frac{P_{i,j_{int}} - P_{i,j_{320}}}{P_{i,j_{320}}} \quad (5.1)$$

Precision is measured in terms of the standard deviation of the error. A larger standard deviation implies that the method is less precise. The results are presented in the form of histograms with probability density curves shown.

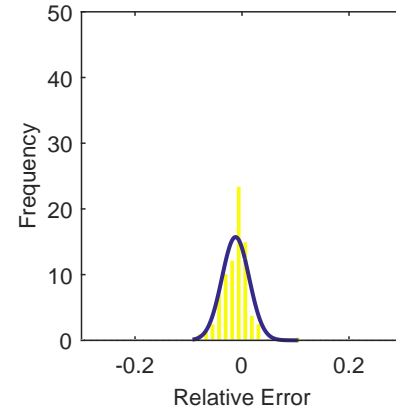
#### 5.3.1.1 YF12

The histogram for the YF12 inlet test case 1, zero clocking interpolation error is shown in figure 5.2. The distribution is approximately normal. The aggregate YF12 results for the mean error of all test cases and clocking positions are shown numerically in table 5.1.

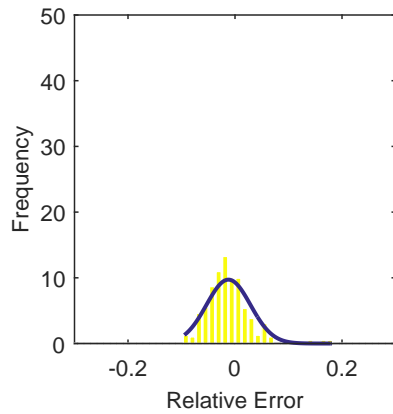
The most accurate method for this test case and clocking subset is the spline interpolation, which has a mean error of 0.077. The Kriging interpolation was the least accurate, with a mean error of 0.101. The range on the error represents how much difference there was in the mean error between all the methods. The linear interpolation method has consistently the smallest mean error; the mean error, 0.098, is higher than all but the Kriging method but the range of the mean error, 0.168, and the maximum mean error, 0.192, are the smallest. This indicates that while in terms of only the mean error the spline method comes out ahead, the linear method gives a more consistently accurate result.



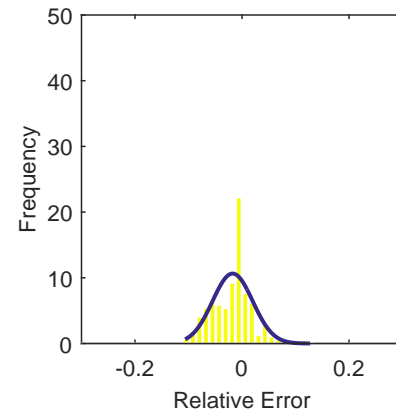
(a) Linear Interpolation Error



(b) Spline Interpolation Error



(c) Polar Interpolation Error



(d) Kriging Interpolation Error

Figure 5.2: Relative error for various interpolation schemes of test case 1, zeroth clocking for the YF12 inlet.

Table 5.1: Range and mean results for the mean error for all test cases and all clockings for the YF12 inlet.

	Min	Mean	Max	Range
Linear	0.023	0.098	0.192	0.168
Spline	0.004	0.077	0.212	0.315
Polar	0.008	0.084	0.225	0.207
Kriging	0.002	0.101	0.317	0.216

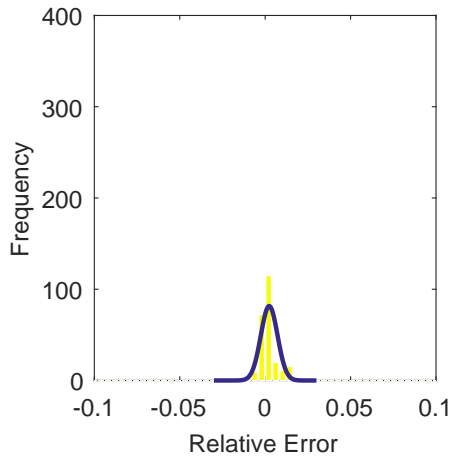
In terms of precision, the standard deviation is evaluated. The standard deviation is shown visually by the width of the probability density curve in figure 5.2. The overall standard deviation in the error was compiled in the across all test cases and clocking positions in table 5.2. The most precise methods were the spline and polar methods.

Table 5.2: Range and mean results for the standard deviation of the error for all test cases and all clockings for the YF12 inlet.

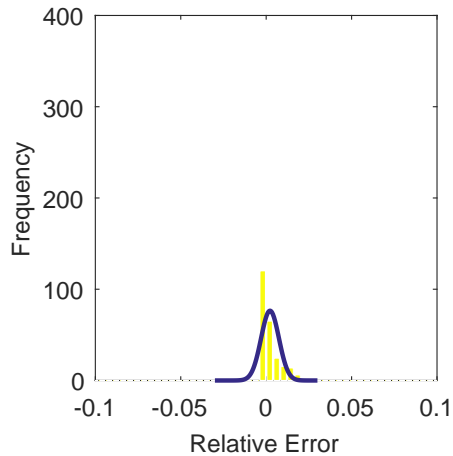
	Min	Mean Std. Dev.	Max	Range
Linear	0.076	0.142	0.215	0.139
Spline	0.081	0.133	0.208	0.127
Polar	0.072	0.131	0.197	0.124
Kriging	0.111	0.203	0.357	0.246

### 5.3.1.2 IMX

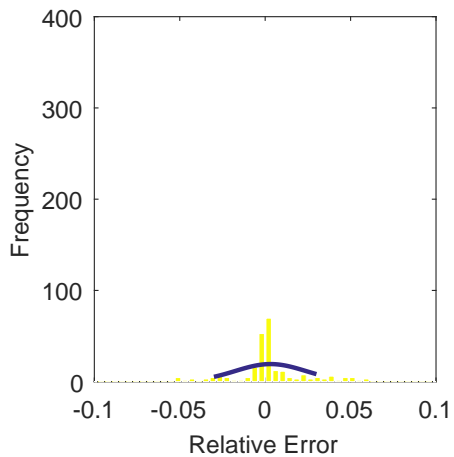
A similar analysis was performed on the IMX CFD. The histogram for the IMX inlet CFD run 300, zero clocking is shown in figure 5.3. As with the YF12 inlet, the distribution of the relative error of interpolation is approximately normal. The aggregate results are shown in table 5.3. The results do not delineate a superior method in this case. All four of the methods are about equally accurate, with a mean error of less than 0.002. The range on the accuracy is also similar, ranging from 0 to 0.004. Based on this information, there is no preferred method to get consistently accurate interpolation results.



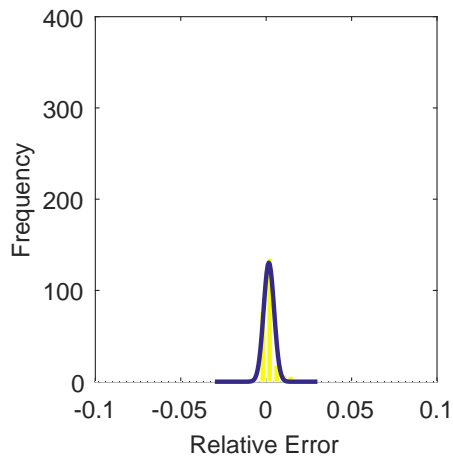
(a) Linear Interpolation Error



(b) Spline Interpolation Error



(c) Polar Interpolation Error



(d) Kriging Interpolation Error

Figure 5.3: Relative error for various interpolation schemes of run number R300, zeroth clocking for the IMX inlet.



Table 5.3: Range and mean results for the mean error for all test cases and all clockings for the IMX inlet.

	Min	Mean	Max	Range
Linear	0.0005	0.0018	0.0031	0.0026
Kriging	0.0002	0.0016	0.0027	0.0024
Spline	0.0007	0.0018	0.0040	0.0033
Polar	0.0000	0.0013	0.0041	0.0040

The aggregate results for the precision is shown in table 5.4. The average standard deviation ranges from 0.002 for the polar method to 0.0046 for the spline method, with the linear and Kriging methods falling roughly in the middle. This shows that the polar method is the most precise in the aggregate. In terms of consistency, the standard deviation range is evaluated. The most consistent precise method are the linear and spline methods, with ranges of about 0.0026. When looking at all the data for precision, it can be argued that the linear interpolation method is consistently the most precise. It has the lowest maximum standard deviation, the range is the smallest, and the mean is about in the middle. Thus, for the most consistently precise results, a linear interpolation method should be employed.

Table 5.4: Range and mean results for the standard deviation error for all test cases and all clockings for the IMX inlet.

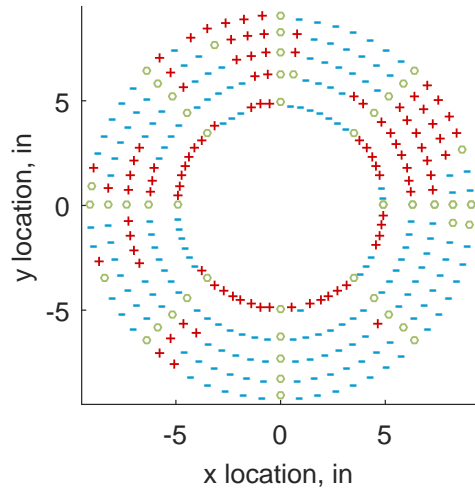
	Min	Mean	Max	Range
Linear	0.0024	0.0033	0.0050	0.0026
Spline	0.0033	0.0046	0.0061	0.0028
Polar	0.0009	0.0021	0.0067	0.0058
Kriging	0.0021	0.0032	0.0053	0.0032

### 5.3.2 Location Predictions

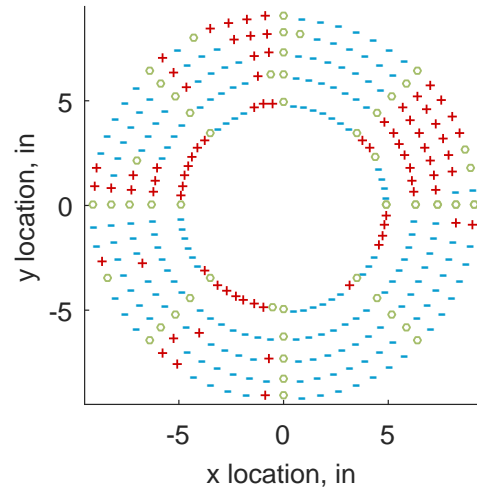
The location predictions evaluate how well each interpolation method succeeds at every coordinate. This can help researchers determine if a method is prone to under-prediction or over-prediction. Under-prediction implies that the real pressure is higher at those locations than what the interpolation method indicates. An over-prediction would mean that the real pressure at that location actually reads lower than what the interpolated value shows. Both can lead to incorrect conclusions about the pressure field. The preferred result is that points fall within a given tolerance band of the exact result. In this case, a 1% tolerance band is applied. This means that if the interpolated value is within 1% of the experimental reading for the YF12 inlet or of the computational result for the IMX inlet, it is considered "in tolerance".

#### 5.3.2.1 YF12

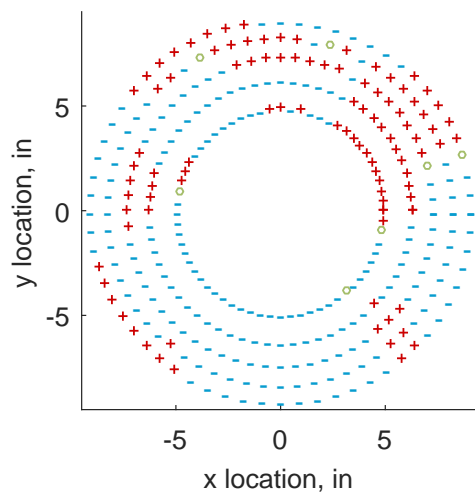
The location prediction for the YF12 inlet is shown graphically in figure 5.4 for test case 1, zero clockings. Locations that fell within tolerance (1% of the experimental reading) are shown as green circles while over-predicted locations are marked as red pluses and under-predicted locations as blue minuses. This visual representation can help determine if certain areas of the interpolation method is prone to under- or over-prediction. The 2 to 3 o'clock position appears to be consistently over-predicted, though the rest of the area is largely under-predicted. The results close to the hub (the inner-most locations) seem to suffer from high over-prediction rates for this particular test case and clocking.



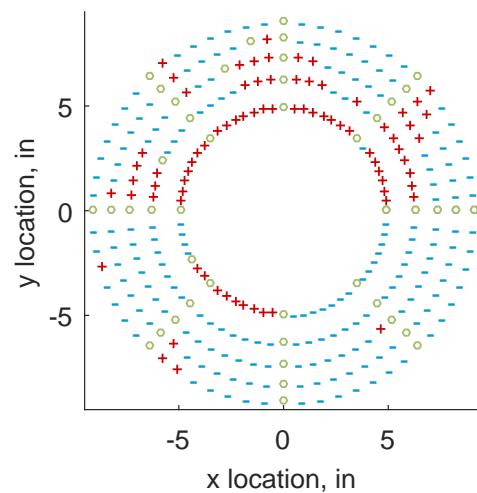
(a) Linear Interpolation



(b) Spline Interpolation



(c) Polar Interpolation



(d) Kriging Interpolation

Figure 5.4: Interpolation error for the YF12 inlet - symbols show locations that are within tolerance (o), over-predicted (+), and under-predicted (-).

Tables 5.5, 5.6, and 5.7 tabulate the location prediction results for all the test cases and clockings. The goal for location prediction results is to maximize the number of probes that fall in tolerance (table 5.5) while minimizing the number of probes that fall outside of the tolerance band (tables 5.6 and 5.7). For the YF12, to maximize the number of probes that fell within tolerance on average was the polar method, with 14 points in addition to the known points falling within

tolerance. It is also the least consistent method to get points within tolerance, with the largest range of results: a 50 point difference from the minimum to the maximum in tolerance points. When taking into account consistency, meaning maximizing the average number of points falling within tolerance while maintaining a smaller range, the linear and Kriging methods look more attractive. The mean number of points falling in tolerance are 9 and 8, respectively, though both have the smallest range of 14. Thus, to ensure the location predictions get most points within tolerance, the linear or Kriging methods would be best suited.

Table 5.5: Range and mean results for the in-tolerance locations for all test cases and all clockings for the YF12 inlet. These numbers do not include the 40 probes used for interpolation.

	Min	Mean	Max	Range
Linear	3	9	17	14
Spline	2	10	25	23
Polar	2	14	52	50
Kriging	2	8	16	14

To ensure that the most locations are accurately predicted, the number of points falling outside of the tolerance band should also be minimized. Table 5.6 is the aggregate result of the four interpolation methods for the YF12 inlet. On average, the linear method has the fewest locations that are under-shot, with 108 locations. In terms of consistency, the Kriging and polar methods methods have the smallest range, with 96 and 100 point ranges respectively. To minimize the mean and the range, the spline method seems better suited, with a mean of 127 points falling under tolerance and with a range of 121. Thus, the spline method is likely best to minimize the number of under-shot locations consistently.

Table 5.6: Range and mean results for the under-shot locations for all test cases and all clockings for the YF12 inlet.

	Min	Mean	Max	Range
Linear	54	108	182	128
Spline	76	127	197	121
Polar	115	147	215	100
Kriging	111	151	207	96

The number of locations that are over-predicted, meaning the interpolated result predicts a higher pressure than the exact solution, is shown in table 5.7. This result is more clear-cut. The spline method has the fewest number of points that are over-shot on average with a 20 point lead over the other methods. It also has the most consistent results, with a range of 90 points. Thus, the spline method is clearly best for this particular measure of success.

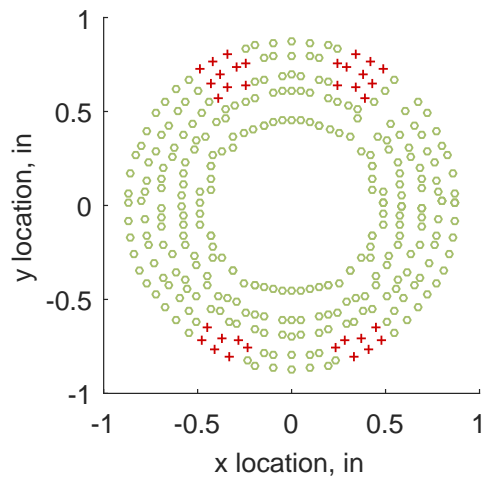
Table 5.7: Range and mean results for the over-shot locations for all test cases and all clockings for the YF12 inlet.

	Min	Mean	Max	Range
Linear	90	163	218	128
Spline	69	121	159	90
Polar	66	143	191	125
Kriging	77	160	200	123

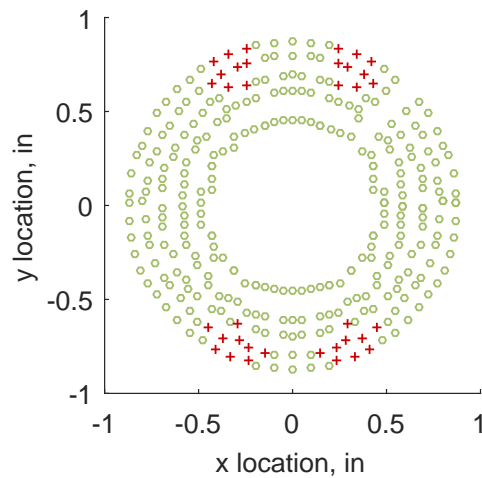
### 5.3.2.2 IMX

The location prediction for the IMX inlet is shown graphically in figure 5.5 for Run 300, zero clockings. Locations that fell within tolerance (1% of the computational result) are shown as green circles while over-predicted locations are marked as red pluses and under-predicted locations as blue minuses. It is a striking contrast to the YF12 location predictions (figure 5.4). Almost all the points fall within tolerance, with problem locations only showing up from the 11 to 11:30 o'clock positions

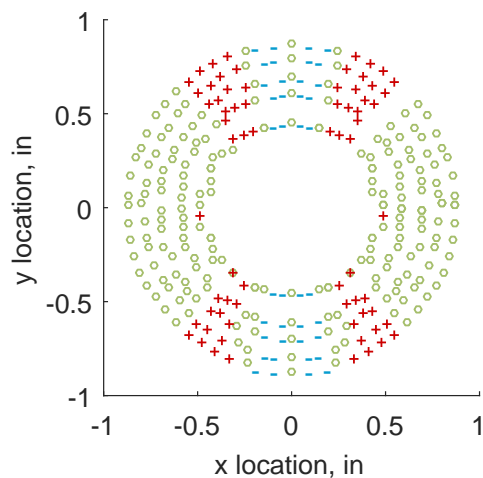
and from the 0:30 to 1 o'clock positions being consistently over-predicted. This is largely due to the smoother, continuous data associated with computational results.



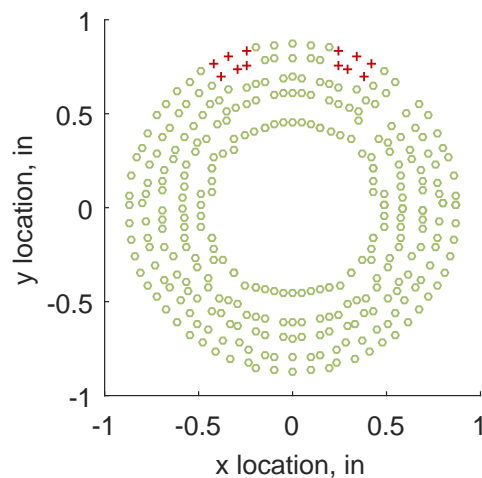
(a) Linear Interpolation



(b) Spline Interpolation



(c) Polar Interpolation



(d) Kriging Interpolation

Figure 5.5: Interpolation error for the IMX inlet - symbols show locations that are within tolerance (o), over-predicted (+), and under-predicted (-).

Tables 5.8, 5.9, and 5.10 show the location predictions in the aggregate for all of the IMX CFD runs. The Kriging method has the highest average points falling within tolerance, with 250

points. It also does so least consistently, with a range of 182 points. The spline method seems to be better suited to maximize the number of points within tolerance, with 213 average points falling within tolerance and a range of 68.

Table 5.8: Range and mean results for the in-tolerance locations for all test cases and all clockings for the IMX inlet. These numbers do not include the 40 probes used for interpolation.

	Min	Mean	Max	Range
Linear	170	207	246	76
Spline	177	213	245	68
Polar	124	153	170	46
Kriging	98	250	280	182

Table 5.9 shows the number of locations that fall under the tolerance band. The Kriging method does the best, with 9 points falling under the tolerance on average and a range of 58. All the methods save the polar method (which has the highest average number of points falling under tolerance) have a similar range to the Kriging method.

Table 5.9: Range and mean results for the under-shot locations for all test cases and all clockings for the IMX inlet.

	Min	Mean	Max	Range
Linear	0	34	59	59
Spline	0	30	56	56
Polar	40	56	74	34
Kriging	0	9	58	58

Looking at the number of points falling above the tolerance (table 5.10), the Kriging method is again the best on average with a mean of 21 points exceeding the tolerance. However, it also has the largest range with 127. The spline method instead should be used as it has a mean of 37 and a

range of 24.

Table 5.10: Range and mean results for the over-shot locations for all test cases and all clockings for the IMX inlet.

	Min	Mean	Max	Range
Linear	17	39	52	35
Spline	23	37	47	24
Polar	62	71	83	21
Kriging	0	21	127	127

### 5.3.3 Visual Accuracy

A visual representation of the contour plots – also called donut plots – are of special interest to researchers. As it is often easier to visualize results in this manner, having accurate contour plots ensures correct conclusions are drawn from the data. These plots make it easy to compare between flight conditions and inlet configurations; it is important that the interpolation method does not distort the result qualitatively.

#### 5.3.3.1 YF12

The results for the YF12 can be found in figure 5.6. Figure 5.6(a) is the full 320 data from the 320 probes, while figures 5.6(b) through 5.6(e) show the interpolated results. The linear and spline interpolations are visually very similar although they miss details from the full data set. While the interpolated contour plots capture some of the high and low pressure areas if that area is instrumented, they imply the flow is more uniform in areas without instrumentation. The polar interpolation captures more of the high pressure and low pressure areas, but also inserts an artificial area of lower pressure in the high pressure zone at the 3 o'clock position. The Kriging interpolation method does not generate an accurate visual plots, relying too heavily on the average pressure at the AIP. The zones of higher and lower pressure on the Kriging plot are where the probes are located,



which is why there is a series of islands of high or low pressure, but the remainder of the contour show mostly mean pressure. This is due to the weighting the Kriging method uses to interpolate between points, as was explained in section 4.2.5.

Thus, in order to ensure an accurate visual representation of the results, the linear and spline methods are better suited than the Kriging or polar methods.

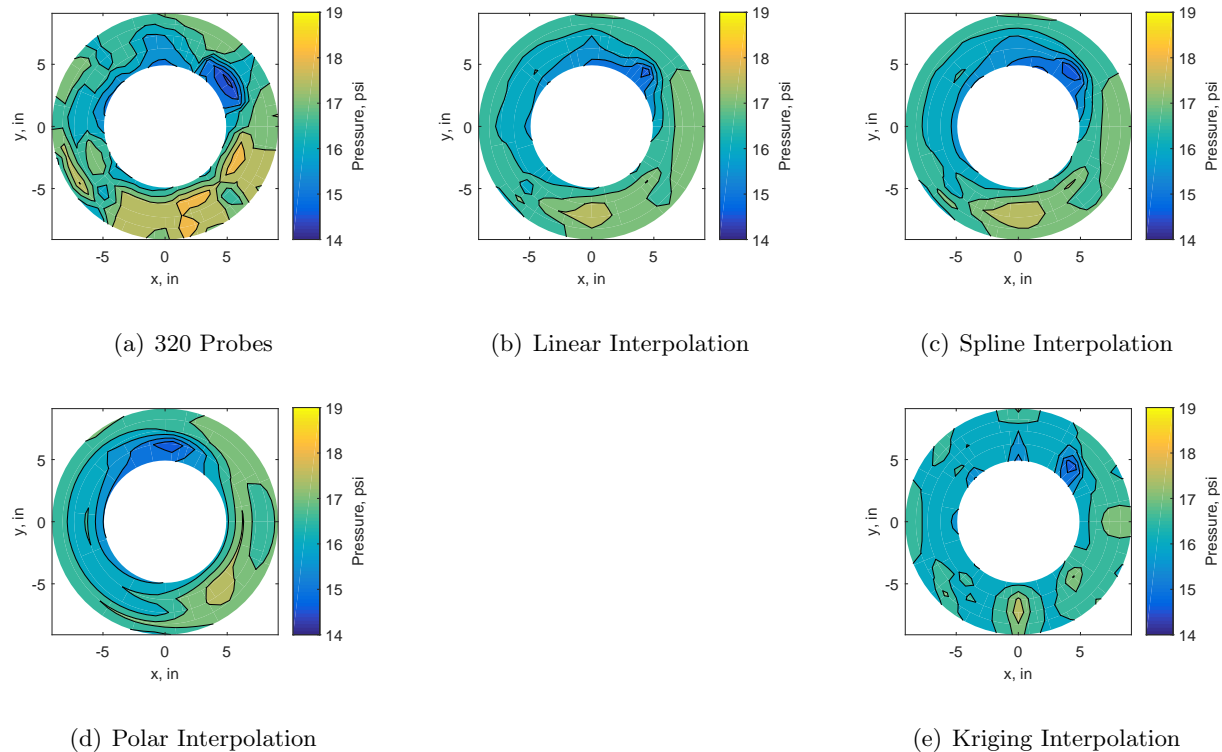


Figure 5.6: Contour plots for the full 320 and interpolated values for the YF12 inlet.

### 5.3.3.2 IMX

Similarly, for the IMX inlet, the contour plots are shown in figure 5.7. In this case, the Kriging interpolation (figure 5.7(e)) is very similar to the spline and linear interpolation methods. This is due to the fact that much of the area between data points was relatively uniform and the areas of high activity were sampled by all the data subsets. These three methods show relatively good agreement with the full 320 point data set. The polar interpolation, shown in figure 5.7(d), does not show a good representation for the raw data set (figure 5.7(a)). This method could not resolve

the areas of high activity, as it relies only on angular data and is not influenced by radial changes. Thus, all but the polar method are suited to create accurate visual representations of the data.

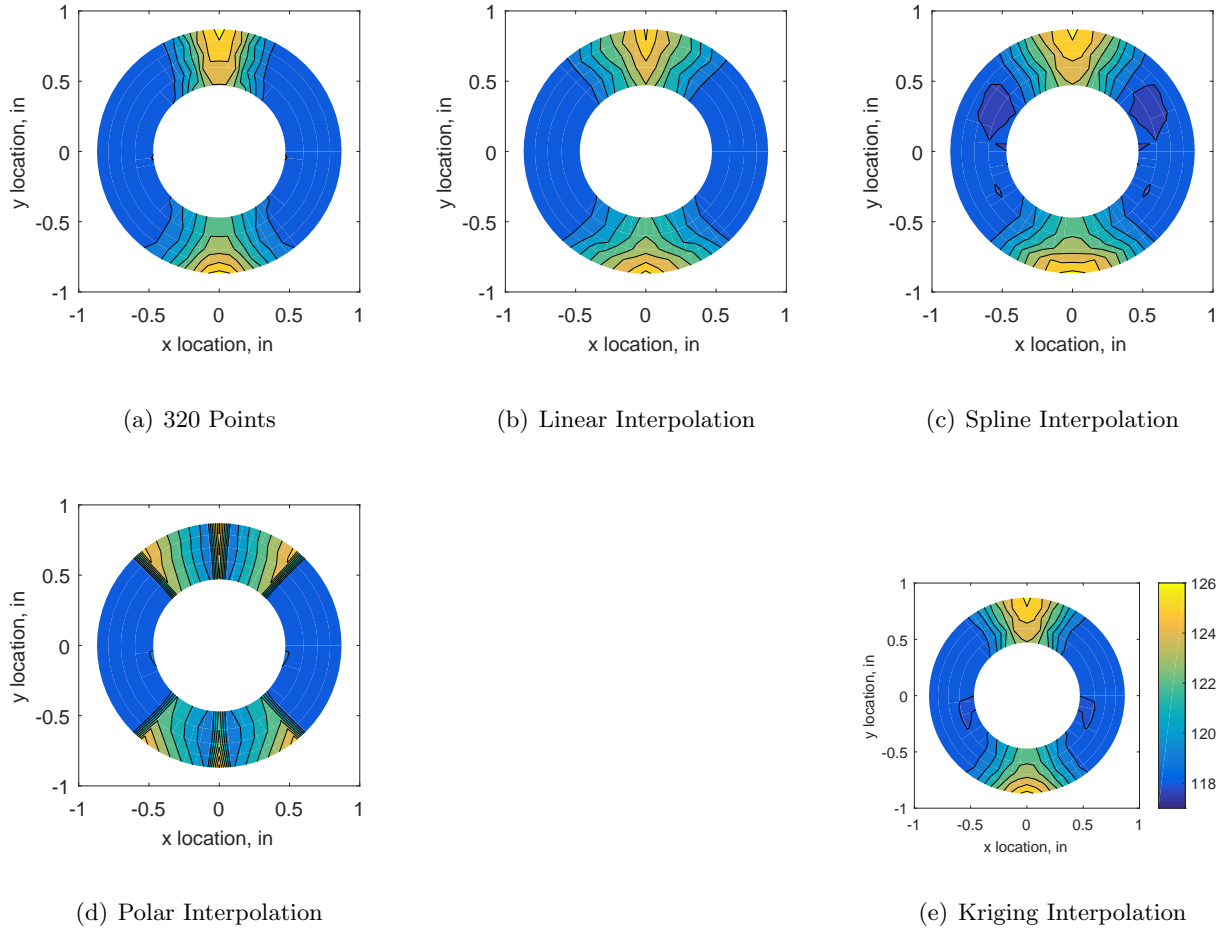


Figure 5.7: Contour plots for the full 320 and interpolated values for the IMX inlet.

### 5.3.4 Derived Quantities Results

The derived quantities are, much like the visual donut plots, a key metric researchers use. These singular numbers describe the pressure variations at the AIP to determine if the inlet design is acceptable for a given engine. In this work, five indices were assessed. It should be noted that these results are necessarily how researchers use the indices; usually only the locations described in the standard[43] (see figure 4.4) are sampled and those locations are used to determine the distortion. However, for the sake of completeness of this study, the results of all the interpolated values are

used and compared to the exact, 320 probe set solution.

It should be noted that a distortion index is a dimensionless number and usually corresponds to a limit determined by each engine company through extensive testing. While the definition of the index is publicly available, the index limits are generated for a specific engine and are usually proprietary to the company. For this work, the assumption is that these limits were acceptable.

#### 5.3.4.1 YF12

Before delving into how the interpolation methods affect the distortion indices, it is beneficial to discuss the indices with respect to each other. In order to do this, the 320 probe, exact solution is used. These results are tabulated in table 5.11. At first glance, one can see that the indices are each on very different scales. The K-indices are in the 0.2 to almost 1 range.  $K_\theta$  almost doubles between test case 1 and 3, subsequently so does  $K_a$  (as it simply is the sum of the other two K-indices).  $K_r$  increases between test case 1 and 2, but then slightly decreases from test case 2 to 3. The ID-indices behave quite differently, with  $IDC$  and  $IDT$  steadily decreasing from test case 1 to 3. To reiterate, it is interesting to note how different these indices are from one another but it does not speak to the relative goodness of the design as that remains an unknown.

Table 5.11: Results for the YF12 exact distortion indices

	$K_\theta$	$K_r$	$K_a$	$IDC$	$IDT$
Test Case 1	0.321	0.255	0.576	0.092	0.243
Test Case 2	0.599	0.370	0.969	0.064	0.192
Test Case 3	0.625	0.337	0.962	0.038	0.132

One last look at the exact indices is in figure 5.8. This shows how the indices vary from hub (ring1) to tip (ring 5). It is interesting to note that there are no definite patterns between test cases. This shows that the maximum and minimum distortion indices move to different areas of the AIP between test cases, sometimes in a predictable fashion and other times seemingly at random. A more thorough look at the distortion indices can be found in section 2.3.3.

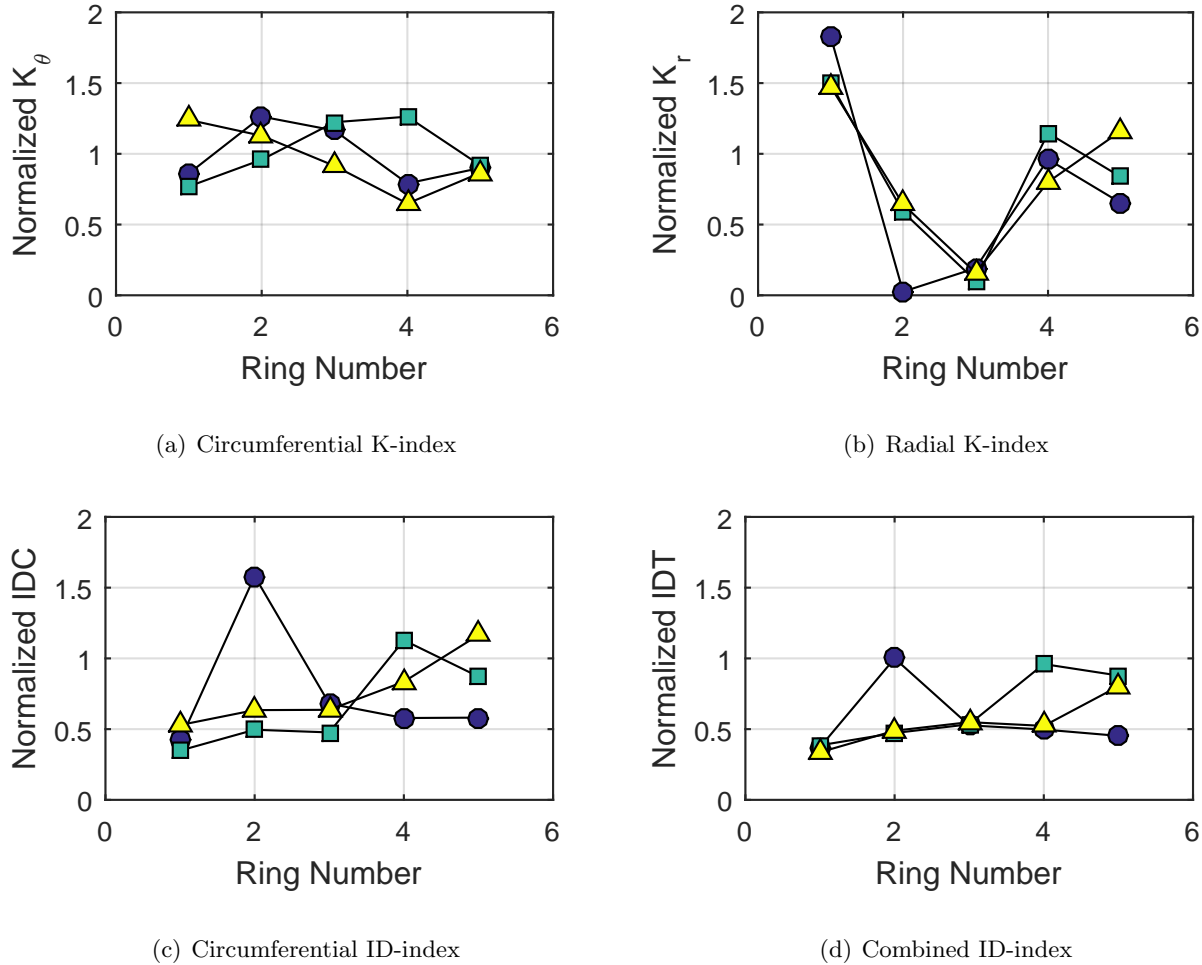


Figure 5.8: Ring distortion indices, normalized by the overall index (see table 5.12). Circles represent test case 1, squares represent test case 2, and triangles represent test case 3.

Returning to the interpolation methods, the distortion indices for test case 1 are listed in table 5.12 and plotted as a series of bar graphs (figure 5.9). One thing to note again is the relative scale of each index. While errors in  $IDC$  might seem very large, one should keep in mind the absolute value of the index is small, so even minor perturbations appear as a large relative error. In terms of how well the interpolated data sets resolve the indices, polar predicts a substantially lower  $K_r$  than any of the other methods, which also translates into a lower  $K_a$  since that is a summation of  $K_r$  and  $K_\theta$ . There is almost no difference in the calculation of  $IDT$  and  $K_\theta$  between the methods, though  $IDT$  is under-predicted at a higher rate for all methods. The circumferential distortion indices  $K_\theta$  and  $IDC$  show little difference between each interpolation method used. The combined

indices vary more as well, but mostly due to the impact of the radial distortion prediction. It is worth noting that all the interpolated distortion indices under-predict the distortion. This implies that a distortion index calculated from an interpolated data set might show a more positive result than a real inlet will provide.

Table 5.12: Interpolation effects on the derived quantities for the YF12 inlet test case 1, clocking C1.

	$K_\theta$	$K_r$	$K_a$	$IDC$	$IDT$
320 Probes	0.321	0.255	0.576	0.092	0.243
Linear	0.318	0.222	0.539	0.084	0.200
Spline	0.317	0.238	0.555	0.087	0.201
Polar	0.317	0.221	0.537	0.076	0.201
Kriging	0.316	0.108	0.423	0.082	0.202

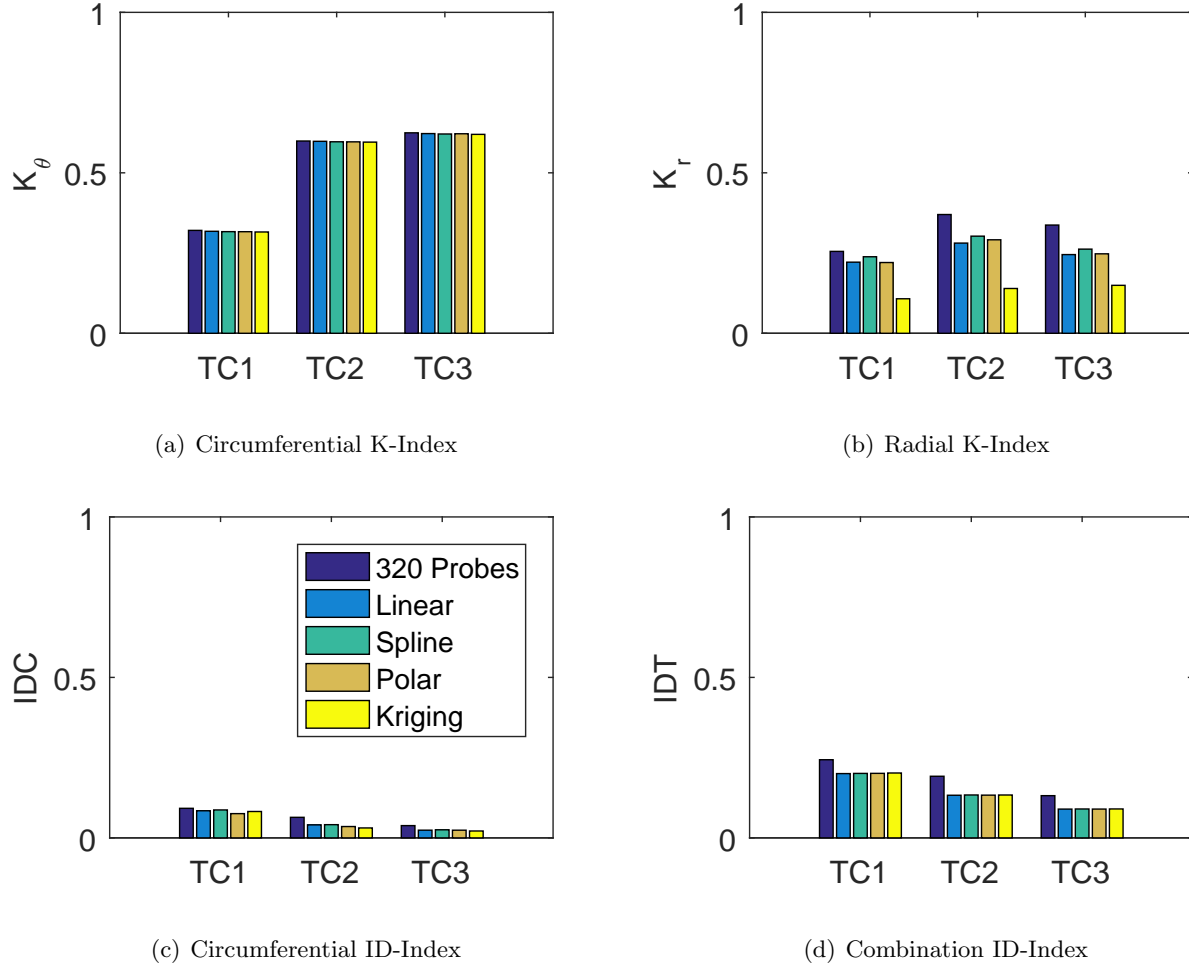


Figure 5.9: Barplots of the distortion indices for the zeroth clocking for the YF12 inlet.

The error in the individual distortion indices can be found in figures 5.10 through 5.13. These boxplots show the absolute and relative errors, calculated via (4.18) and (4.19) discussed in chapter 4, for all test cases and clockings; they only differentiate by the interpolation method used.

The error in the individual distortion indices can be found in figures 5.10 through 5.13. These boxplots show the absolute and relative errors, calculated via (4.18) and (4.19) discussed in chapter 4, for all test cases and clockings; they only differentiate by the interpolation method used.

Figure 5.10 shows the results for the circumferential index  $K_\theta$ . The absolute and relative errors do not change by much for this index. The errors are all well below 1% with no significant difference between the methods. Thus, no method is superior in this case to estimate  $K_\theta$ .

Figure 5.11 shows the results for the radial index  $K_r$ . The absolute error in this case is much

smaller than the relative errors, since the denominator is a relatively small number. The average absolute error ranges from -14% for the Kriging method, to less than 0.3% for the spline method. In terms of relative error, this increases to -45% for the Kriging method and about 0.6% for the spline method, indicating the spline method is better at estimating  $K_r$  than the others.

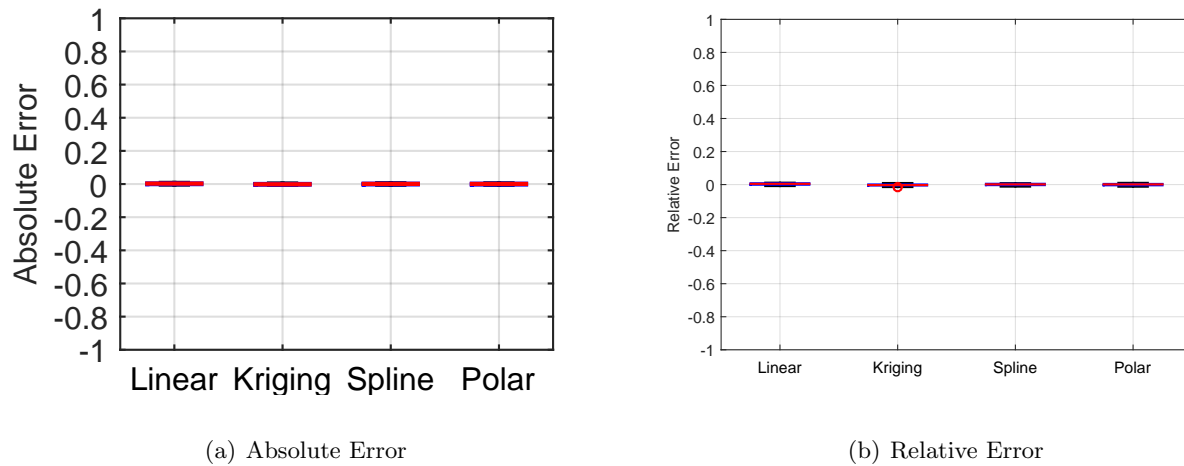


Figure 5.10: Absolute and relative error of each interpolation method for the  $K_\theta$  index for the YF12 inlet.

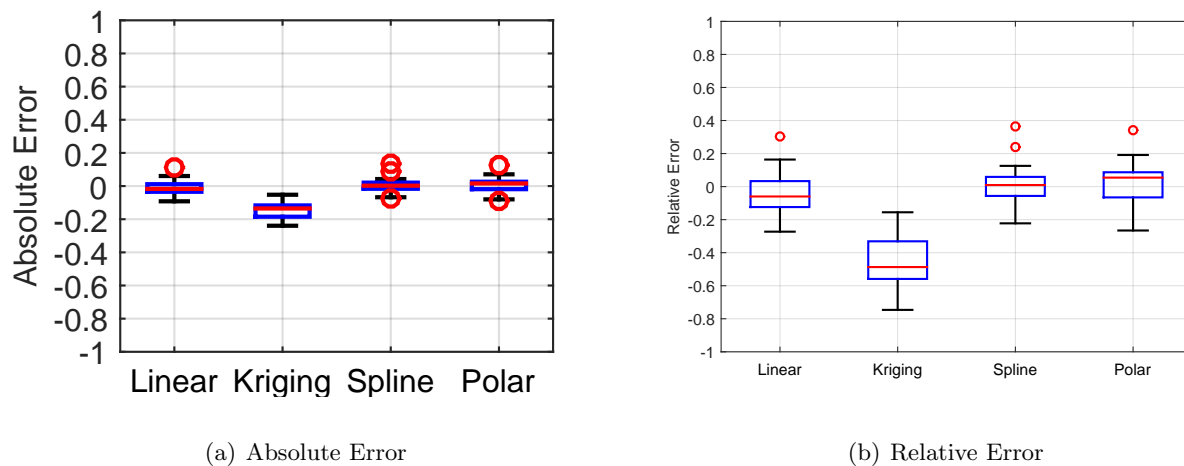


Figure 5.11: Absolute and relative error of each interpolation method for the  $K_r$  index for the YF12 inlet.

Figure 5.12 shows the results for the circumferential index  $IDC$ . The average absolute error

ranges from -1.3 to -1.7%, with not much difference between the methods. The relative error shows a larger range for the Kriging method, but all the mean errors are around -20 to -30%. Thus, none of the methods are suited to calculate *IDC*.



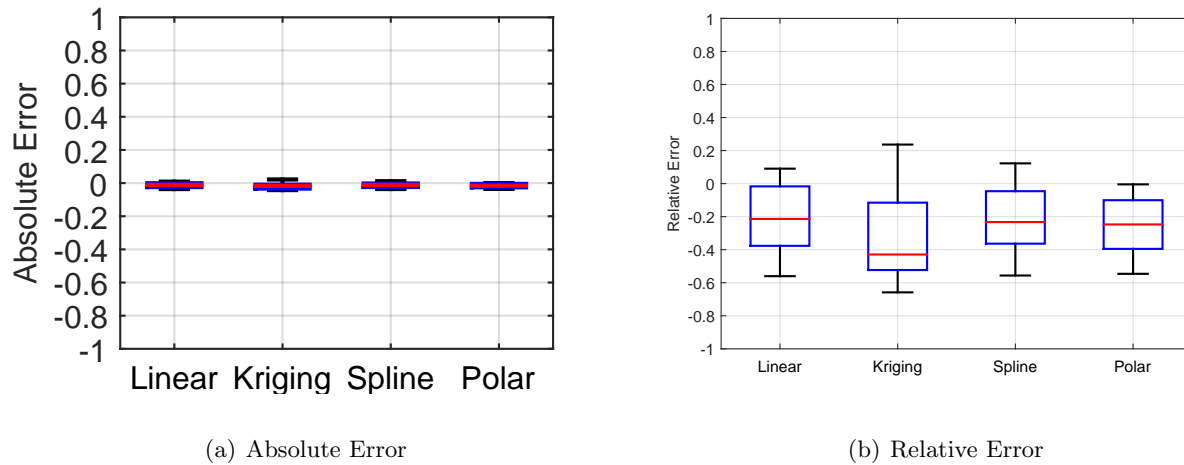


Figure 5.12: Absolute and relative error of each interpolation method for the *IDC* index for the YF12 inlet.

Figure 5.13 shows the results for the combined index *IDT*. The absolute error is again much smaller than the relative errors, since the denominator is a relatively small number. The average absolute error ranges from -3.5 to -4%, with not much difference between the methods. The relative error shows similar ranges with mean errors or about -20%. Thus, none of the methods are suited to calculate *IDT*.

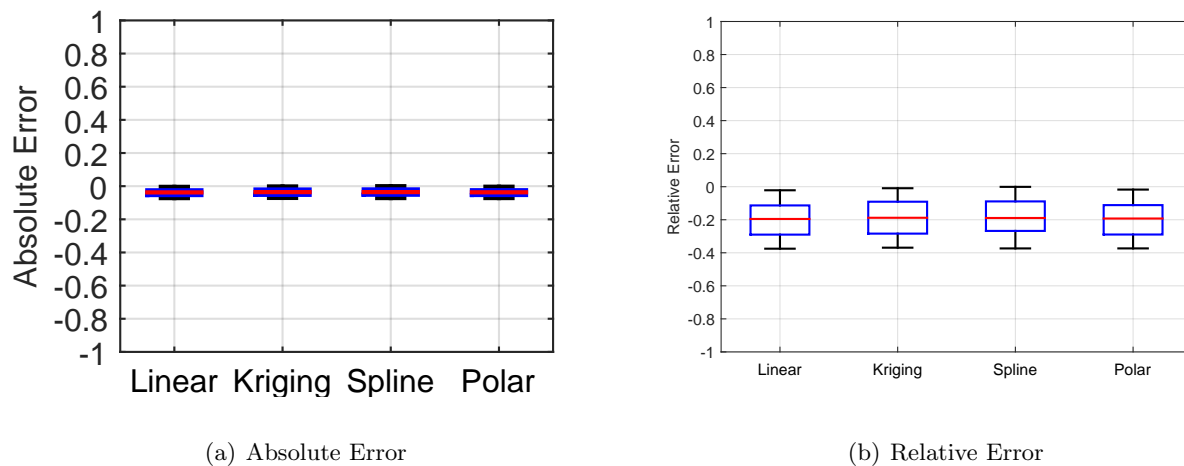


Figure 5.13: Absolute and relative error of each interpolation method for the *IDT* index for the YF12 inlet.

### 5.3.4.2 IMX

As with the YF12 inlet, the IMX distortion indices were evaluated for the full, 320 data set as well as for the 320 point interpolated data set. These results of the full data set can be found in table 5.13. Similarly to the YF12 data, the indices do not seem to follow any specific pattern.  $K_\theta$  decreases from Run 300 to Run 320.  $K_r$  on the other hand increases from Run 300 to Run 310, but then decreases from Run 310 to Run 320.  $IDC$  increases slightly from Run 300 to Run 310, but then remains the same while  $IDT$  increases steadily again.

Table 5.13: Results for the IMX exact distortion indices

	$K_\theta$	$K_r$	$K_a$	$IDC$	$IDT$
Run 300	0.432	0.010	0.442	0.015	0.070
Run 310	0.398	0.022	0.419	0.020	0.108
Run 320	0.374	0.017	0.391	0.020	0.113

To visualize what happens to the indices, figure 5.14 shows how the indices vary from hub (ring1) to tip (ring 5).  $K_\theta$  varies some for Run 300 between hub and tip but Run 310 and 320 hardly vary at all.  $K_r$  does create a zig-zag pattern between rings, but all three run numbers follow that pattern. There is no discernable difference between rings for any of the runs for the ID-indices.

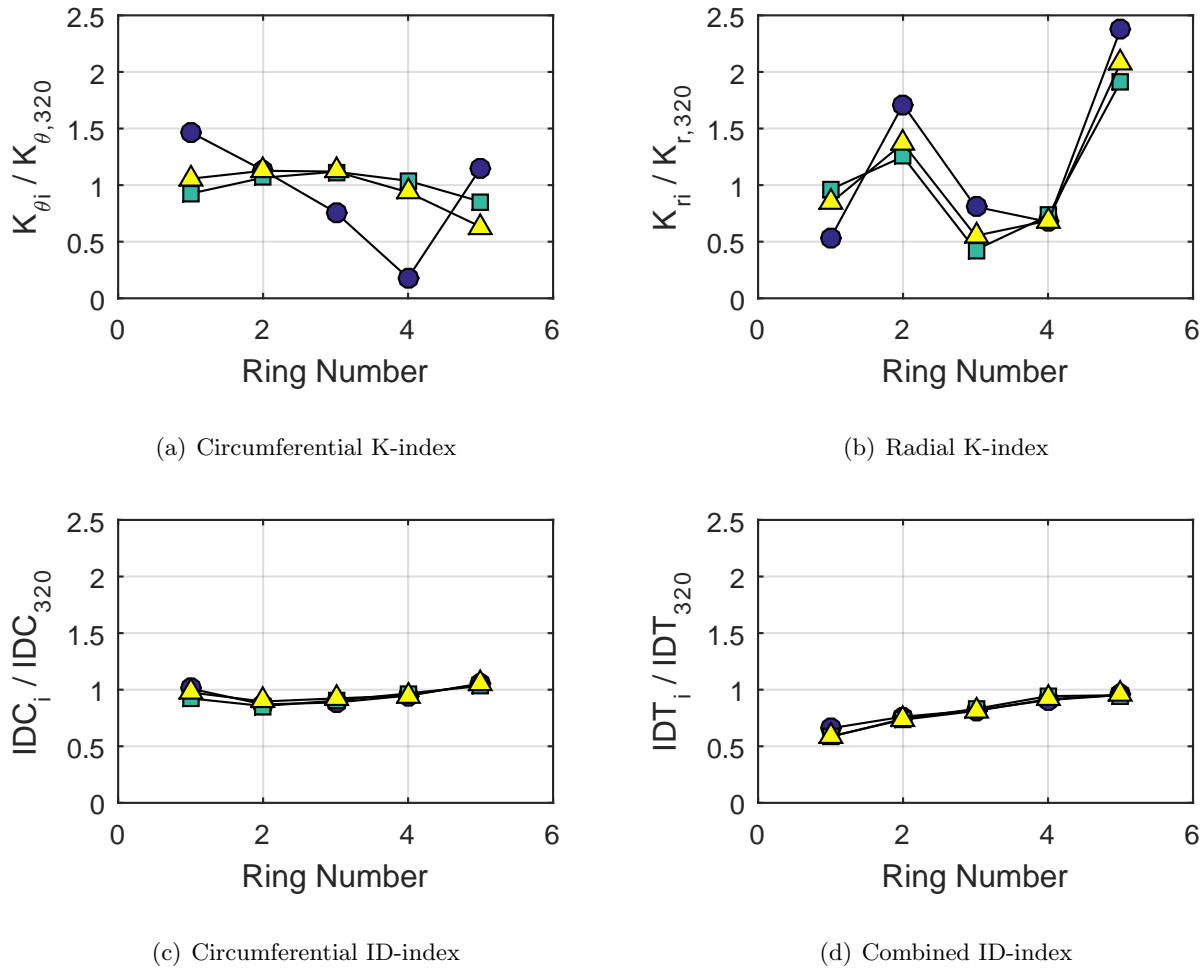


Figure 5.14: Ring distortion indices, normalized by the overall index (see table 5.14). Circles represent Run 300, squares represent Run 310, and triangles represent Run 320.

The distortion indices for Run 300 are listed in table 5.14 and plotted as a series of bar graphs (figure 5.15). One thing to note again is the relative scale of each index. While errors in all the indices save  $K_\theta$  and  $K_a$  might seem very large, one should keep in mind the absolute value of the remaining indices are small, so even minor perturbations appear as a large relative error. In terms of how well the interpolated data sets resolve the indices, the linear method is the only one that comes close to the real value for  $K_\theta$ .  $K_r$  is over-predicted by all the methods except for the Kriging and Linear methods. The linear method is also closest to the real value of  $IDC$ , and all methods seem to be able to predict  $IDT$ . Overall, this indicates that the best interpolation method to resolve the distortion indices is the linear method.

Table 5.14: Interpolation effects on the derived quantities for the IMX inlet run number R300, clocking C1.

	$K_\theta$	$K_r$	$K_a$	$IDC$	$IDT$
320 Probes	0.432	0.010	0.442	0.015	0.070
Linear	0.393	0.019	0.412	0.016	0.070
Spline	0.350	0.025	0.375	0.018	0.070
Polar	0.350	0.026	0.375	0.020	0.072
Kriging	0.350	0.017	0.367	0.018	0.070

As with the YF12, the indices were plotted in bar graphs in figure 5.15 for just Run 300, zero clockings. In this case, the interpolated distortion indices fall short of predicting  $K_\theta$  for all methods.  $K_r$  is such a small value, it is difficult to discern anything from the data, although polar interpolation comes closes to the full 320, exact probe value. For  $IDC$ , polar and Kriging are both close in predicting the indices. For  $IDT$ , all methods fare well in predicting the index, though the spline interpolation tends to overshoot the index.

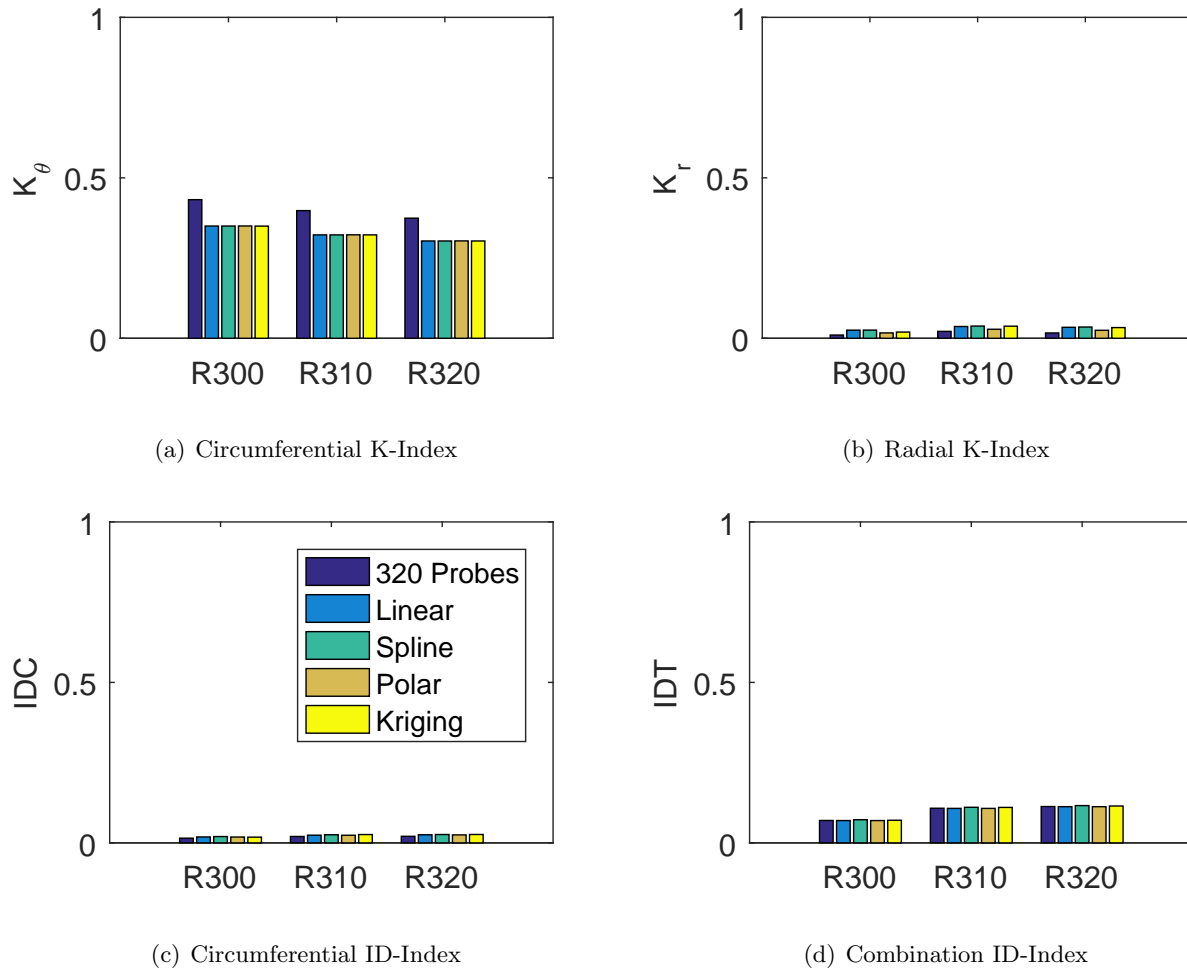


Figure 5.15: Barplots of the distortion indices for the zeroth clocking for the IMX inlet.

To compare the methods overall without regard for run number and clockings, a series of boxplots were created. The boxplots show the absolute and relative error – with the reference value being the 320 probe distortion index value – for each index. The error in the individual distortion indices can be found in figures 5.16 through 5.19. These boxplots show the absolute and relative errors, calculated via (4.18) and (4.19) discussed in chapter 4, for all test cases and clockings.

Figure 5.16 shows the results for the circumferential index  $K_\theta$ . The absolute and relative errors do not change by much for this index. The errors are all around -7% and -19% respectively with no significant difference between the methods. Thus, no method is superior in this case to estimate  $K_\theta$ .

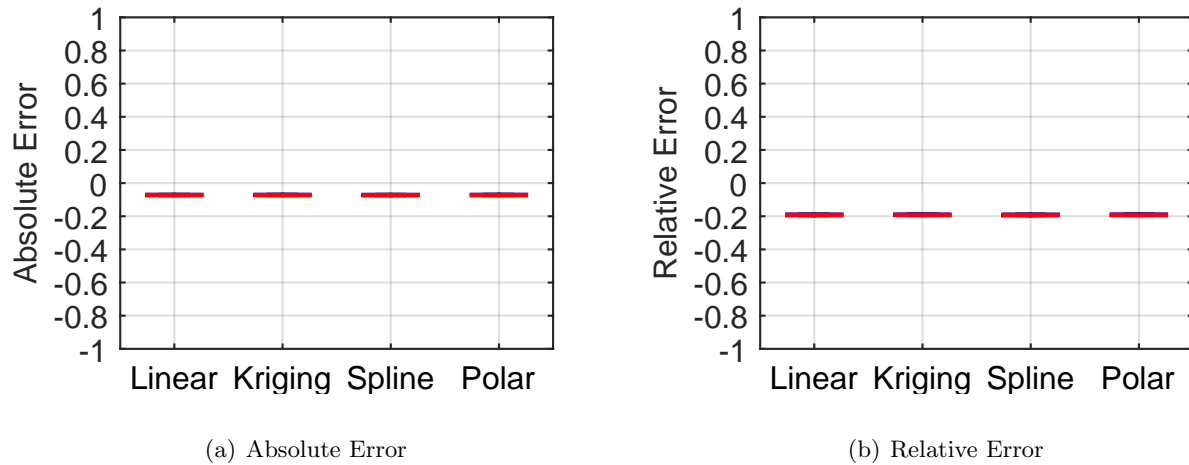


Figure 5.16: Absolute and relative error of each interpolation method for the  $K_\theta$  index for the IMX inlet.

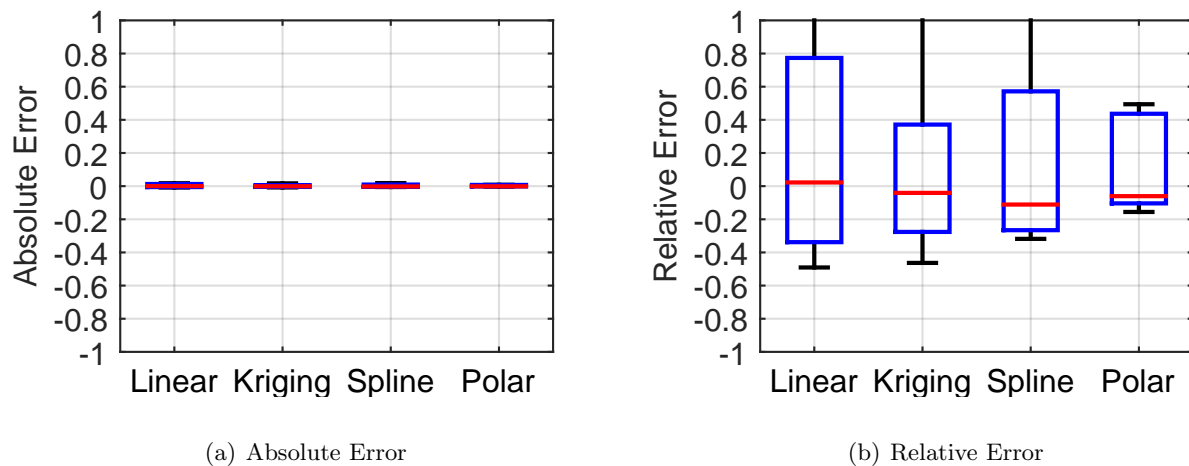


Figure 5.17: Absolute and relative error of each interpolation method for the  $K_\gamma$  index for the IMX inlet.

Figure 5.17 shows the results for the radial index  $K_\gamma$ . The absolute error in this case is much smaller than the relative errors, since the denominator is a relatively small number. The average absolute error is less than 1% for all methods. In terms of relative error, this increases to 8 % for the Kriging method to more than twice that for the linear method. However, the range of the index obtained by using the Kriging interpolation is much larger than 100%. The polar method appears to be better suited, with an absolute error of 0.2% and a 12% relative error, although no method is

ideal.

Figure 5.18 shows the results for the circumferential index  $IDC$ . The absolute error is much smaller than the relative errors, since the denominator is a relatively small number. The average absolute error ranges from 0 to 0.07%, with not much difference between the methods. The relative error shows a larger range for the Kriging method, but all the mean errors are around -1 to 12%. Thus, Kriging is the best method to consistently determine  $IDC$ .

Figure 5.19 shows the results for the combined index  $IDT$ . The absolute error is again is much smaller than the relative errors, since the denominator is a relatively small number. The average absolute error ranges from -3.5 to -4%, with not much difference between the methods. The relative error shows similar ranges with mean errors or about -20% with the exception of Kriging, which has a mean absolute error of less than -0.5% and a relative error of less than -4%. Thus, Kriging would be the most suited to determine  $IDT$ .

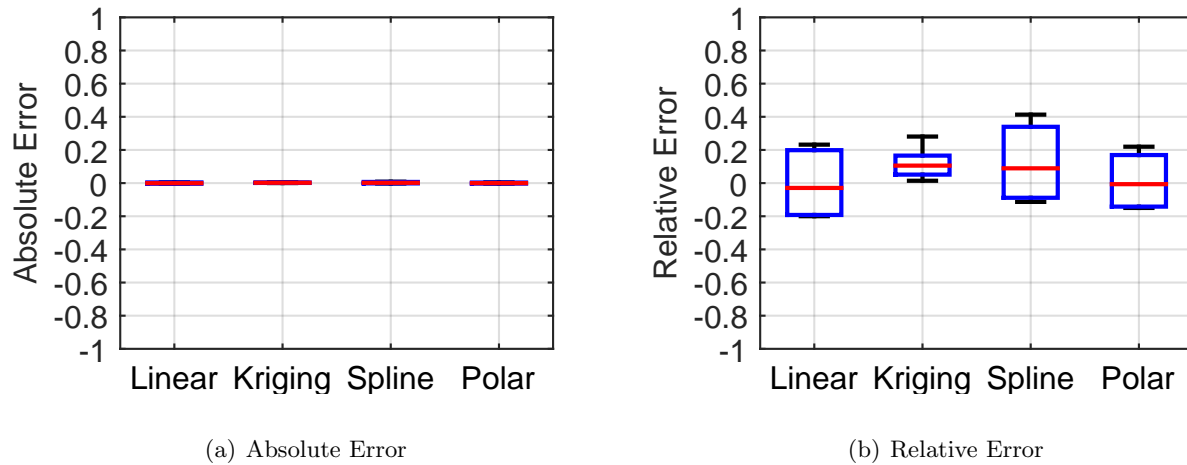


Figure 5.18: Absolute and relative error of each interpolation method for the *IDC* index for the IMX inlet.

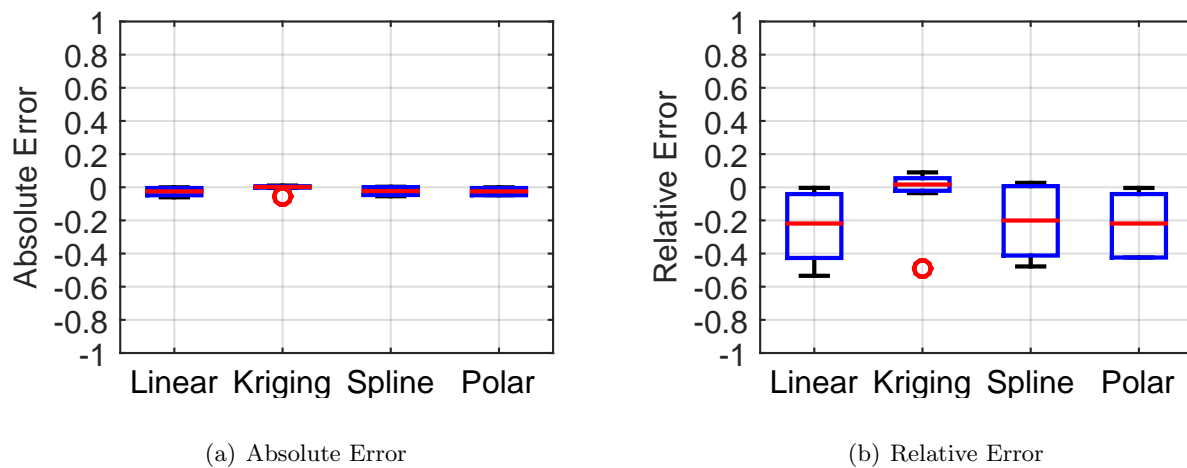


Figure 5.19: Absolute and relative error of each interpolation method for the *IDT* index for the IMX inlet.

#### 5.3.4.3 Summary of Results for the Derived Quantities

A summary of the various best interpolation methods for the distortion indices is shown in table 5.15. For the YF12 inlet, none of the methods show promise other than determining  $K_\theta$ . The spline method is the best in terms of minimizing the error due to interpolation while the Kriging method is the best in terms of location prediction. For the IMX inlet, the Kriging method is best



for estimating all distortion descriptors.

Table 5.15: Summary of best interpolation method results for distortion indices

	YF12	IMX
$K_\theta$	All methods	All methods
$K_r$	Spline, Polar	Kriging
$IDC$	None	Kriging
$IDT$	None	Kriging

### 5.3.5 Summary of Results

A summary of the various best interpolation methods for accuracy, precision, and location prediction is shown in table 5.16. The results do not show one clear interpolation method to be best for all metrics. Rather, different interpolation methods are better for various metrics. In terms of overall performance, the spline method is best suited for the YF12 inlet, as it may not get the most points within tolerance or be the most accurate, but it does well for all the other metrics. For the IMX the results are even less clear. Spline and Kriging interpolation methods have their strengths with accuracy, location predictions, and calculating derived quantities, but sacrifices in the area of precision.

Table 5.16: Summary of best interpolation method results for accuracy, precision, and location prediction

	YF12	IMX
Accuracy	Linear	All
Precision	Spline, Polar	Linear
Fewest under-shot	Spline	Kriging
Most in tolerance	Linear, Kriging	Spline
Fewest over-shot	Spline	Spline
Visual Accuracy	Linear, Spline	All but Polar
Derived Quantities	None	Kriging

#### 5.4 A Note on The Tolerance Level

A tolerance level of 1% was chosen for the majority of this work – therefore any point falling within 1% of the exact value was considered ”in tolerance” and thus acceptable. This is based on the notion that most pressure transducers have about a 1% error on readings – although more precise equipment exists.

When the tolerance level is decreased, fewer points fall in tolerance, as one would expect. Since the computational analysis for the IMX was much less prone to variations than the experimental YF12 data, the 1% tolerance level loses some of the granularity of the results. Similarly, if the tolerance level is decreased to a level where it becomes more applicable to the computational results, only the original points used in the interpolation end up within tolerance.

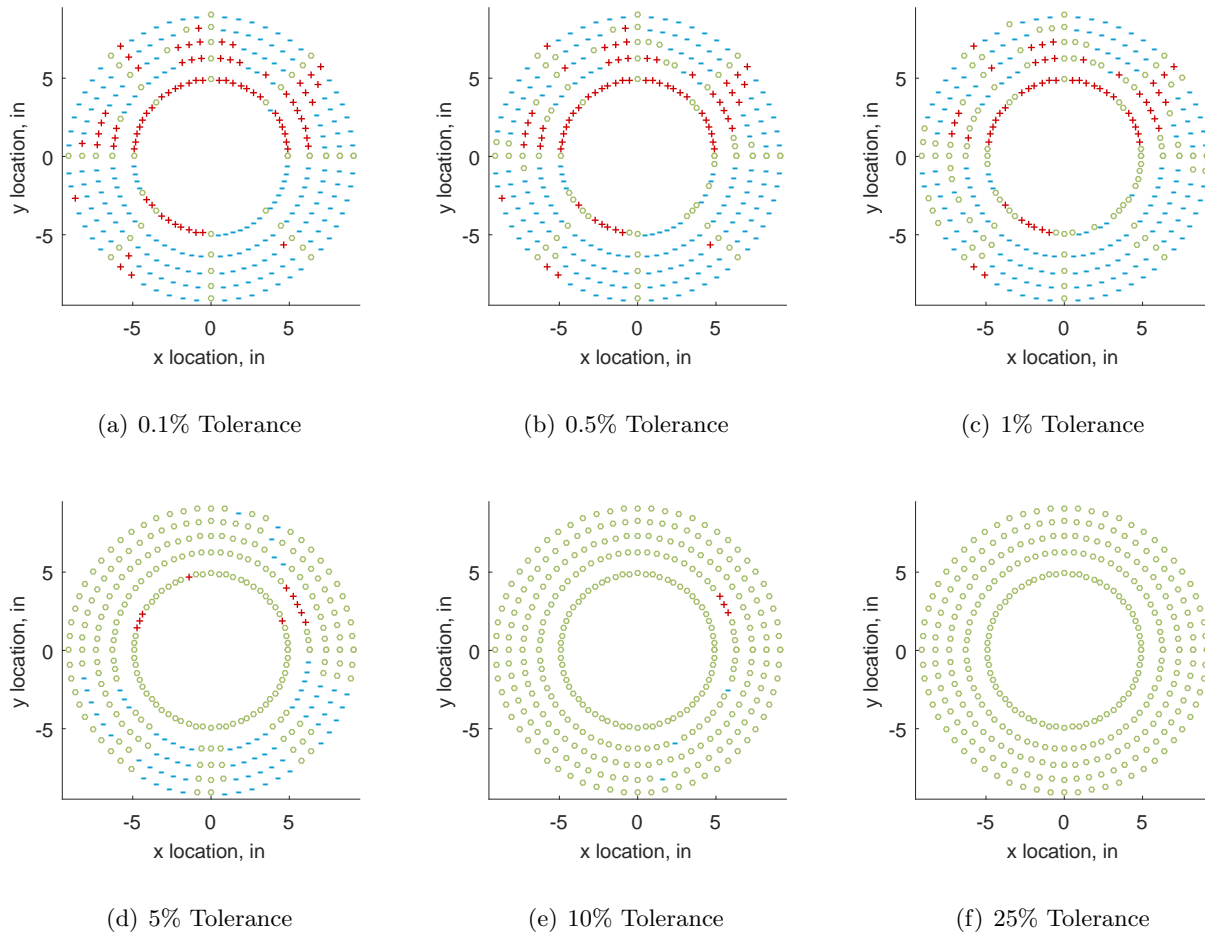


Figure 5.20: Interpolation error for various tolerance levels for the YF12 inlet using the Kriging method - symbols show locations that are within tolerance (o), over-predicted (+), and under-predicted (-).

Figures 5.20 and 5.21 illustrate this point. At a tolerance level of 0.1%, only 4 points (excluding interpolation basis locations) fall within tolerance for the Y-12 inlet, compared to 136 for the IMX. With a 5% tolerance level, all points fall within tolerance for the IMX while only about 70% of the points are in tolerance for the YF-12.

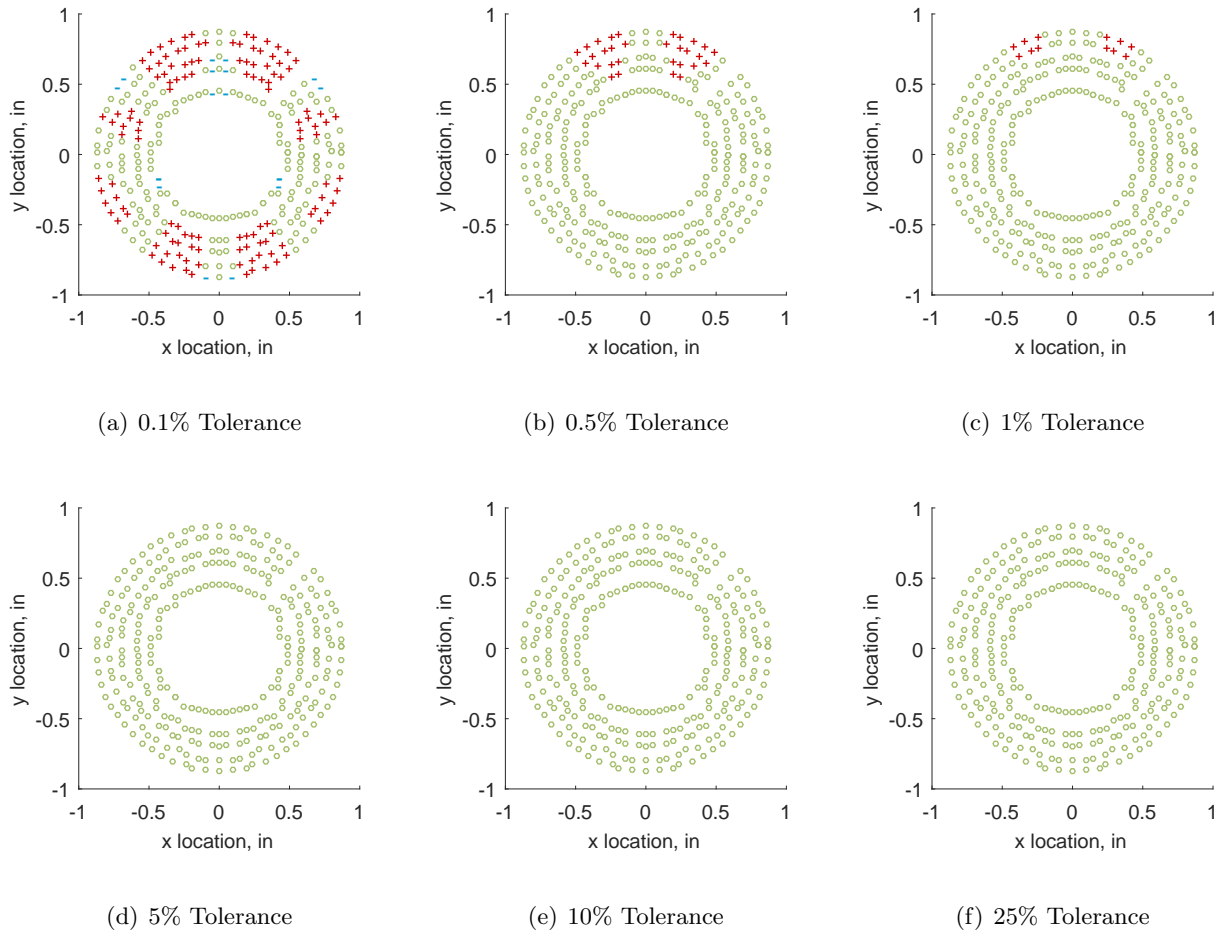


Figure 5.21: Interpolation error for various tolerance levels for the IMX inlet using the Kriging method - symbols show locations that are within tolerance (o), over-predicted (+), and under-predicted (-).

It is thus important that the right tolerance level be applied. In the case of this work, the 1% is appropriate based on the error tolerance for the experimental data. The level was kept the same for the computational data in order to compare and contrast results. However, when looking at computational data, a tighter tolerance level might be appropriate.

## 5.5 Conclusions

Inlet flow distortion can greatly reduce the operating envelope of a vehicle. Thus, it is important that investigators have the needed tools and techniques available to model and analyze

the data obtained to characterize the flow distortion. As of now, the inlet is modeled using CFD and then prototypes are tested using a 40 probe rake. Distortion indices are calculated based on measurements made with those 40 probes. The research done at NASA in the 1970s showed that pressure outliers and distributions are lost when only 40 probes are used – resulting in up to 50% error in indices. This work confirmed this and also established that interpolation methods can change the visual representation of the flow field.

As was discovered in the previous section, each interpolation method has its own strengths and weaknesses. In the aggregate, the spline and Kriging interpolation schemes were the best for the quantitative measures of success used in this work, although the spline interpolation method also does quite well with the qualitative measure of success. This indicates that a spline interpolation might be the best suited method to satisfy most of the measures of success. This is consistent with the results obtained in chapter 4.

One major aspect missing from this work to date is tying the computational data to the experimental data. An interesting future aspect of this work would be to move away from interpolation methods all together. The interpolation method on the discrete data points can have major impacts on the overall pressure contour plot. It would be interesting to move towards creating basis functions of the flow pattern based on the computational results and overlay the experimental data. Researchers would need high confidence in the computational results, but it could solve the problem of not capturing the full flow field with experimental data. To that end, one would have to know the areas of interest of the fluid flow to get the most accurate result for the parameters of interest. In the next section, a method to find these high impact areas will be discussed.

# Chapter 6

## Optimizing Probe Placement

So far, the problem of how to make continuous data out of discrete points was discussed. Different ways of interpolating the experimental data into a continuous set can impact the qualitative and quantitative results. In the conclusions, it was hypothesized that using computational results as a map, with experimental data as guideposts could help move researchers away from using interpolation methods all together and instead use real fluid flow patterns. One major question with this approach is – where should the experimental probes be placed to properly guide the computational map?

In this chapter, the notion that equi-spaced pressure probes provide the best coverage to validate a design is challenged. Random sampling of probes is undertaken and results are compared in the aggregate to find which probes have the most impact on the results. This can lead researchers to reevaluate how experiments for inlet flow distortion are conducted and can reduce the overall cost of an experiment by getting the same data with fewer probes or maximize information with the same number of probes.

### 6.1 Background

The current standard that gives guidance on how inlet flow distortion should be measured and calculated is ARP1420[43]. The probe layout the standard recommends has been discussed elsewhere, but for completeness it is shown again in figure 6.1. The blue circles represent total pressure probes and the green circles represent static pressure probes. The static pressure probes

are slightly offset from the total pressure probes as the rakes which hold in place the total pressure probes have to be bolted to the structure. Thus, the static pressure ports are slightly offset to accommodate this design. The standard essentially recommends 8 rakes at 45 degree intervals with 5 area-weighted probes per rake.

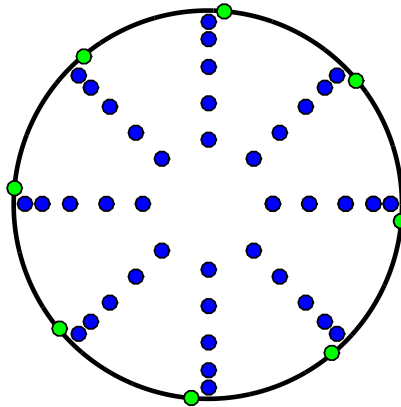


Figure 6.1: ARP1420 suggested probe layout. Blue probes indicate total pressure probes while green indicate surface static pressure taps.

Instead of using this static probe placement, the researchers aim to use random sampling and Monte Carlo simulations to determine optimal probe placement. Random sampling is a method to pick a certain number of variables randomly from a given set. The likelihood that a variable is chosen based on its probability distribution function. The probability density function can be based on knowledge, experience, or likely distribution. In this work, the variable is the probe number and the distribution is assumed to be uniform, meaning each probe has an equally likely chance of being picked. This set of points is extracted and parameters are calculated. In this case, the distortion index  $IDT$  is calculated. This extraction and calculation is the simulation. The simulation is completed many different times so that trends can be discovered in the results. This is one way in which engineering problems can be optimized.

The motivation for this work stems from the IMX experimental data. Since the AIP is small, only a limited number of probes could physically fit into the inlet without causing significant blockage. However, these probes were aligned in a sparse pattern, as can be seen in figure 6.2. This makes it difficult to validate the CFD as well as to generate distortion maps because the data points are simply too spread out. This work seeks to find better ways to place probes in optimum locations to gather the most information from an experiment. More information on the inlet studied and the data available can be found in chapter 3, section 3.1.3.

This work will focus on only one parameter of interest – the distortion index  $IDT$ . Any parameter could be chosen – pressure recovery, any other index, or a combination of these parameters. However, for the sake of simplicity and to investigate the method, only one distortion index will be used.

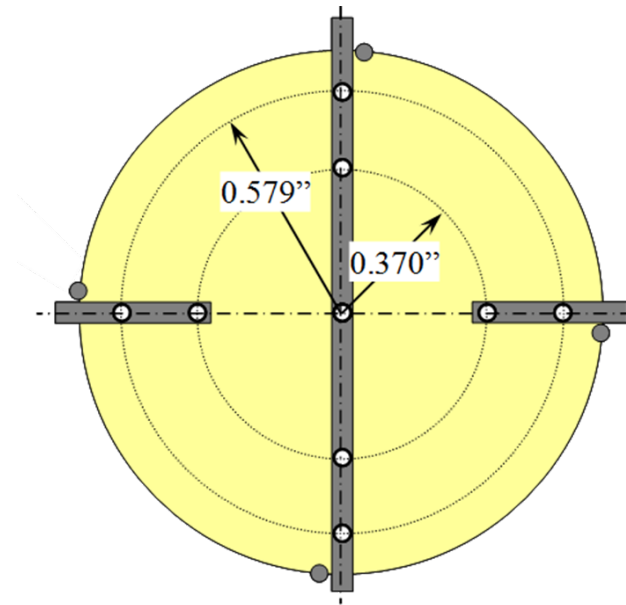


Figure 6.2: AIP instrumentation for the IMX.



## 6.2 Methodology

The goal of this work is to determine how many probes are required – and where their optimum position is – to calculate inlet flow distortion. This work assumes that computational data for the inlet is available and that the computational results are considered valid. To get an idea of the ”ideal” or exact solution, the distortion index (discussed in section 2.3.3) for the full, 320 probe data set is calculated. This is considered the ”true” answer. The index chosen for this work was the *IDT* combined distortion index, seen in Eq. (6.1). The *IDT* index was chosen as there was the most computationally cost effective and allowed for more samples to be run. Any parameter – or combination of parameters – could be used.

$$IDT = \frac{\max(P_{t_i,j}) - \min(P_{t_i,j})}{P_{t_2}} \quad (6.1)$$

From the raw data – the pressure results at each location – a number of probes are selected. The number of points selected varies from as few as 20 probes to as many as 200 probes. Each probe has a uniform distribution as shown in Eq. (6.2) and visually in fig. 6.3. That means every probe has the same probability to be selected in any given set. A uniform distribution is useful when little a priori information is known about the uncertainty of the variable of interest[116].

$$f(x) = \frac{1}{b-a}, a < x < b \quad (6.2)$$

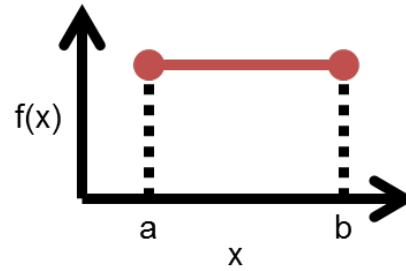


Figure 6.3: Uniform distribution of  $f(x)$  for  $a < x < b$ .

A Monte Carlo simulation is created based on the probe selection. The Monte Carlo simulation, named after the famed casino in Monaco, is a brute force statistical sampling method. Enrico Fermi first used the method in the 1930s to estimate neutron diffusion, though he did not publish on the method[117]. The method, often referred to as "statistical sampling", was developed as a tool to estimate integrals[117]. The method was further developed and named by Stanislaw Ulam, John von Neumann, and Nicholas Metropolis at Los Alamos National Laboratories for the development of nuclear weapons[117]. The method spread to many other applications as computational power of computers increased[117].

The principle behind the Monte Carlo method is the generation of independent realizations of  $x$ , based on the probability of  $x$ ,  $p(x)$ , using a pseudo-random number generator[118]. In this case,  $x$  is the probe number ranging from 1 to 320 and the probability density function,  $p(x)$ , is that described in Eq. (6.2). There then is a deterministic computation of the inputs, which in this case means calculating  $IDT$  from the given set of probes. This is the main reason Monte Carlo methods are slow[118], as the function must be computed as many times as inputs are generated. The final step is to get an aggregate of the results from which general trends can be found. In this work, the aggregate of the results are all the calculations of  $IDT$ , presented in a histogram and PDF of all the results.

Only certain solutions are of interest. The research focuses on probe sets that result in an index close to the "ideal" index calculated from the full set of probes. In order to determine which

probes are "good", a relative error is calculated using Eq. (6.3).

$$\Gamma_{rel} = \frac{IDT_{sampled} - IDT_{exact}}{IDT_{exact}} \quad (6.3)$$

Based on the relative error, sample sets that are equal or less than 10% of the exact solution are selected. This number is chosen to ensure there are enough test cases to capture all the probes from the original set. The number of times each probe occurs within the given tolerance level is counted within the cases that result in a solution within 10% error of the exact solution and the frequently occurring probes are highlighted.

The top occurring probes are chosen as the final configuration. The number of probes for this final configuration range from 20 to 200 probes. Clearly, one would not instrument an inlet in this day and age with 100 or 160 or 200 probes. These sets are included in order to see how the optimized probe patterns fill out. The index  $IDT$  is calculated based on these probes for all three test cases and the solution is compared to the exact solution for the three original test cases for the YF12.

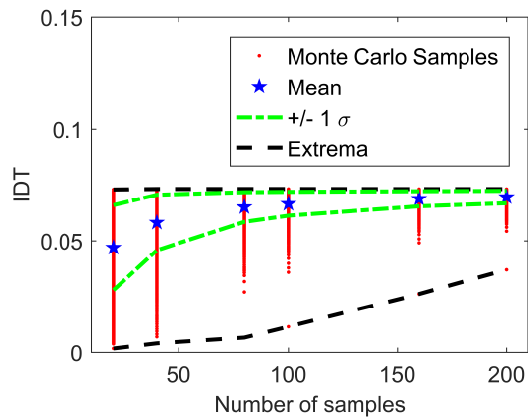
### 6.3 Results

The above described methodology was applied to the two inlets discussed in chapter 3. The number of probes investigated were 20, 40, 80, 100, 160, and 200. One million Monte Carlo simulations were run for each probe number set and for each test case for the experimental data and each run number for the computational data. One set of five million points was run for one of the YF12 test cases.

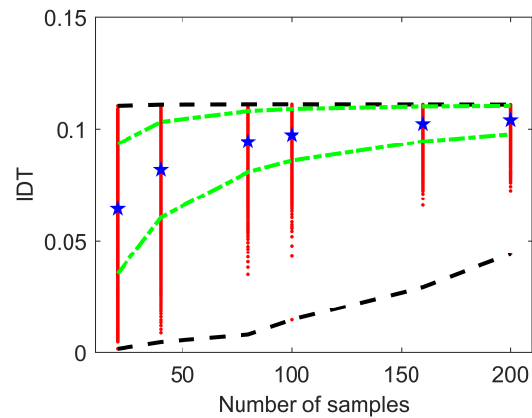
#### 6.3.1 Computational Data – IMX

As the node spacing on the IMX computational data was very dense which would lead to probe overlap, the grid of the interpolation methods discussed in chapter 5 was used. In other words, instead of all the probes, the 320 probes from the interpolation method chapter were used.

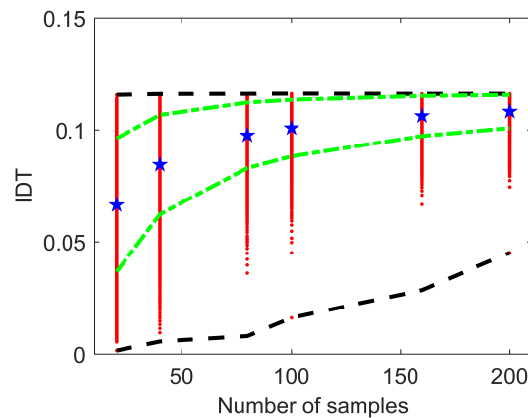
The results for *IDT* the IMX Monte Carlo sampling is shown in figure 6.4. These figures show the results of the sampling as red points, the means as blue pentagrams, one standard deviation as green lines, and the extrema in black lines. As expected, the more probes utilized in the sampling, the smaller the spread in the results.



(a) Run 300



(b) Run 310



(c) Run 320

Figure 6.4: Results of the Monte Carlo sampling of the IMX CFD data. Red points show the resultant *IDT* calculation for a sampled set. The blue pentagram shows the mean of all samples. The green lines are one standard deviation from the mean. The black dashed lines show the minimum and maximum results.

The average for *IDT* for Run 300 ranges from 0.0576 for 20 probes to 0.0689 for 200 probes,

compared to an "exact" result of 0.0698. This corresponds to an error of roughly 17.5% for 20 probes, down to less than 1.5% for 200 probes. Similarly, the range decreases from 0.0640 for 20 probes down to 0.013, almost a five-fold reduction.

The average for *IDT* for Run 310 ranges from 0.085 for 20 probes to 0.107 for 200 probes, compared to a result of 0.108 for the 320 probes. This corresponds to an error of roughly 21% for 20 probes, down to less than 1% for 200 probes. Similarly, the range decreases from 0.10 for 20 probes down to 0.02, again about a five-fold reduction.

For Run 320, the average result in *IDT* ranges from 0.088 for 20 probes to 0.112 for 200 probes, compared to a result of 0.113 for the 320 probes. This corresponds to an error of roughly 23% for 20 probes, down to less than 1% for 200 probes. Similarly, the range decreases from 0.10 for 20 probes down to 0.02, which is roughly a four-fold reduction in range.

These results confirm that as the number of probes is increased, the results converge to the exact solution – the 320 probe calculation for *IDT*. The three runs converge to different values of *IDT*, as is expected, since they represent three different data sets.

A PDF of the error in the *IDT* distortion index can be found in figures 6.5, 6.6, and 6.7. This is simply looking at the full Monte Carlo results to determine how far the results deviate from the exact solution. It is not surprising that the same trends occur: as more probes are used, the standard deviation (spread of the distribution) of the error becomes smaller. The mean also shifts closer to the true value. This further shows that the results converge to the exact solution. With fewer probes, the error appears to be all over the place; more probes show that the error eventually smooths out into a normal distribution.

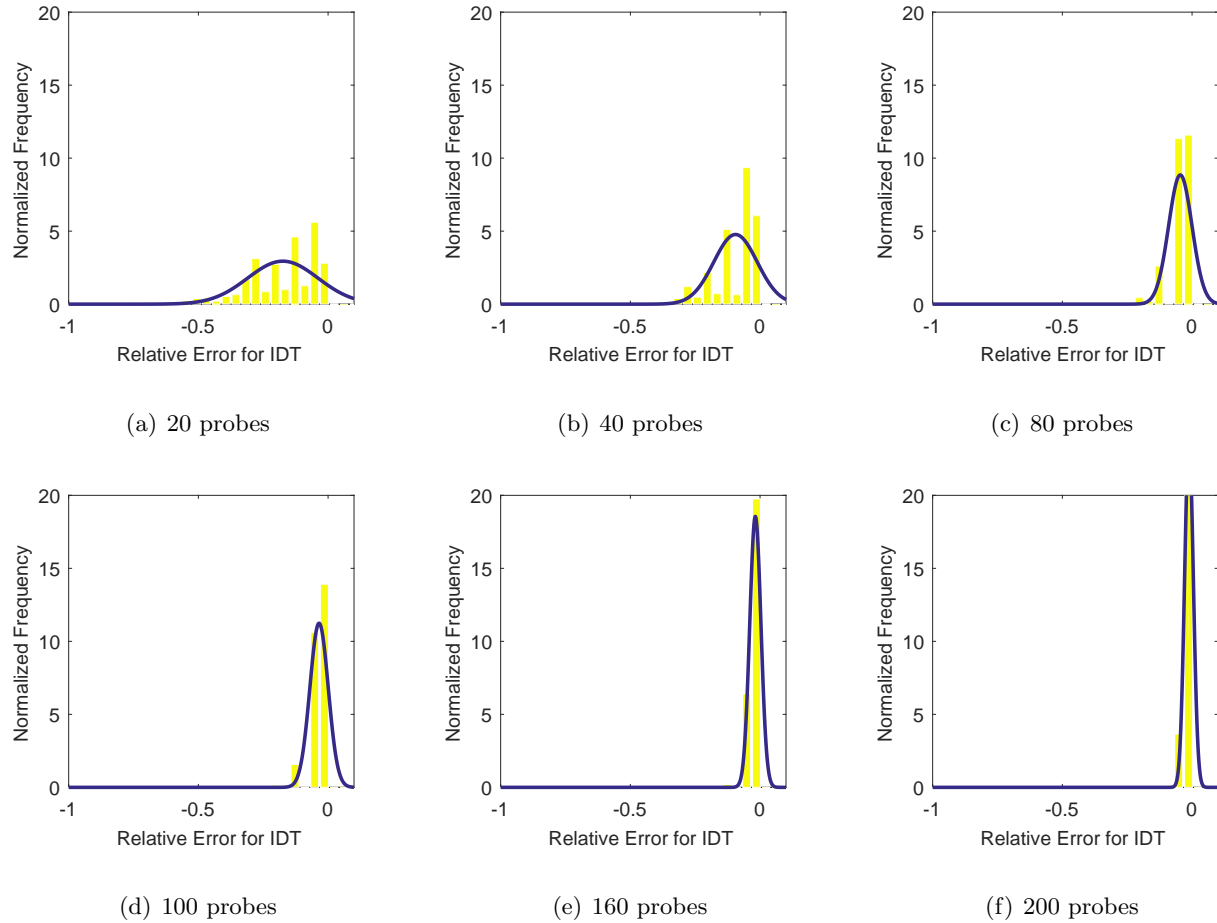
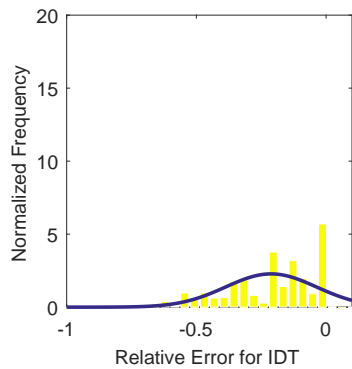
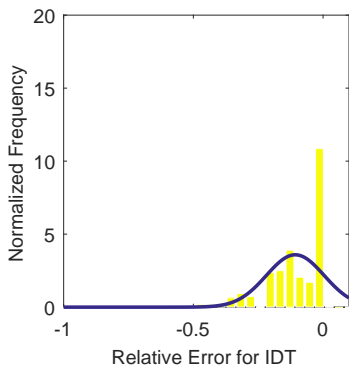


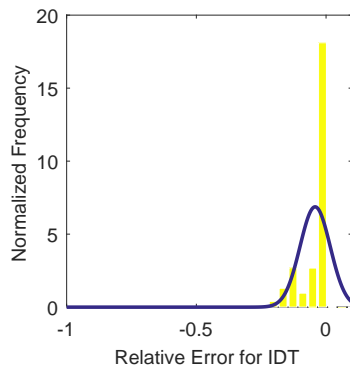
Figure 6.5: Probability density function for the error in  $IDT$  for run number R300.



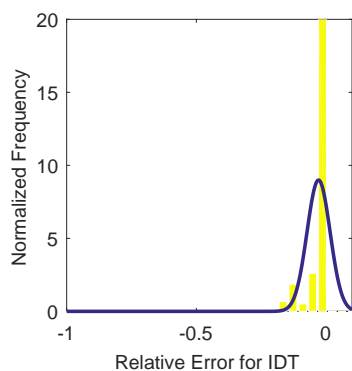
(a) 20 probes



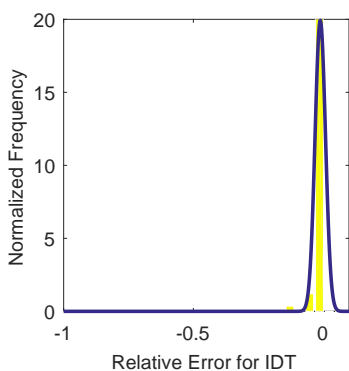
(b) 40 probes



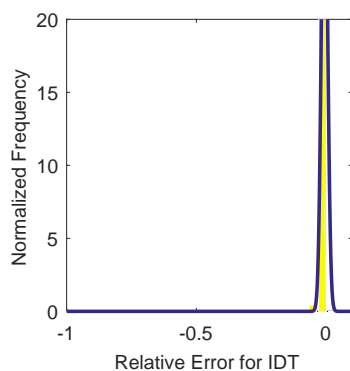
(c) 80 probes



(d) 100 probes



(e) 160 probes



(f) 200 probes

Figure 6.6: Probability density function for the error in *IDT* for run number R310.

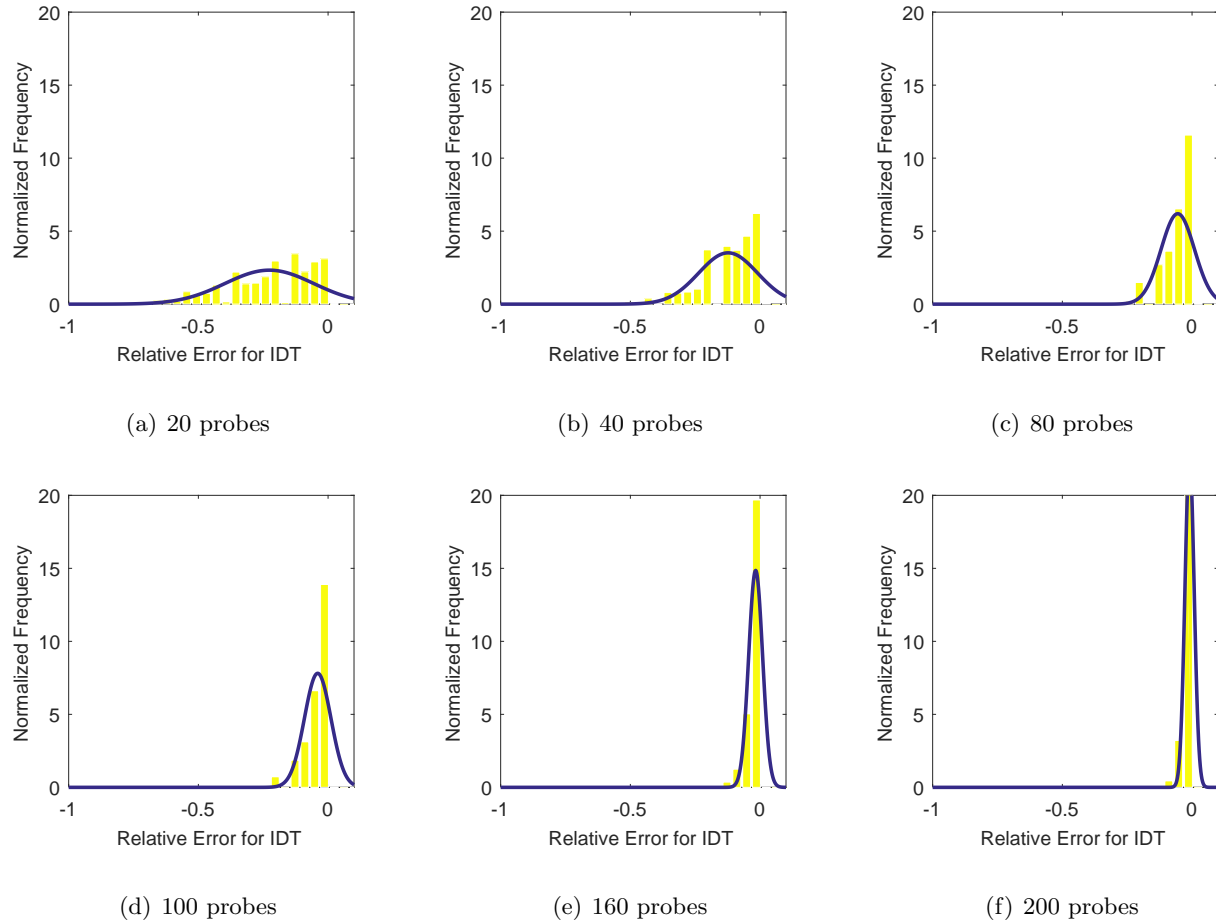


Figure 6.7: Probability density function for the error in *IDT* for run number R320.

A tabulation of the means and standard deviations of the error can be found in table 6.1. The mean of the error is reduced from over -30 % with 20 probes to less than -5% with 200 probes. The standard deviation similarly drops from more than 0.2 to less than 0.07 when increasing the number of probes from 20 to 200.

One interesting aspect of these results is that the results converge exponentially, not linearly. The gains by increasing the number of probes from 20 to 40 reduces the mean error by about half, but from 40 to 80 probes it ranges from a 2.5 fold increase in accuracy for Run 300 to a 1.8 fold increase in accuracy for Run R320. The number of probes that should be used thus becomes a cost-benefit trade off between how many probes the project can afford and how much error is acceptable.



Table 6.1: Tabulation of the mean and standard deviation in the error for  $IDT$  from the IMX CFD for all run numbers with respect to the 320 probe result.

	R300		R310		R320	
	Mean	Std. Dev.	Mean	Std. Dev.	Mean	Std. Dev.
20 Probes	-0.326	0.271	-0.404	0.269	-0.413	0.263
40 Probes	-0.166	0.177	-0.242	0.198	-0.254	0.196
80 Probes	-0.067	0.095	-0.126	0.126	-0.138	0.129
100 Probes	-0.046	0.076	-0.098	0.107	-0.110	0.111
160 Probes	-0.014	0.048	-0.053	0.072	-0.062	0.079
200 Probes	-0.003	0.039	-0.037	0.058	-0.045	0.065

It should be stressed the numbers presented in table 6.1 are in relation to the calculated  $IDT$  index for 320 probes. Another interesting way to look at these results is by comparing it to what a 40 probe set-up as described in ARP1420 would show. That is, calculating what the relative error is by the following formula:

$$\Gamma_{40} = \frac{IDT_{sampled} - IDT_{40}}{IDT_{40}} \quad (6.4)$$

For the IMX, these results of the 40 probe, ARP1420 probe layout are very close to the full 320 probe data set. This is due to the fact that the locations of interest, which will be discussed a bit further down, are covered by the 40 probe layout. The results of the mean error in  $IDT$  values are shown in table 6.2.

Table 6.2: Tabulation of the mean error in  $IDT$  from the IMX CFD for all run numbers with respect to the ARP1420 suggested, 40 probe layout.

	R300	R310	R320
20 Probe	-0.419	-0.467	-0.482
40 Probe	-0.350	-0.380	-0.398
80 Probe	-0.316	-0.326	-0.343
100 Probe	-0.310	-0.314	-0.331
160 Probe	-0.301	-0.297	-0.312
200 Probe	-0.298	-0.292	-0.306

An acceptable error of 1% in the distortion parameter  $IDT$  was chosen. This is related to the error chosen for the interpolation scheme investigation in chapters 4 and 5. When analyzing all the probe samples that lead to an  $IDT$  distortion index within 1% of the full data set by the number of occurrences, certain probes start to stand out. As can be seen in figure 6.8, the same probes show up even when the overall sample size is increased.

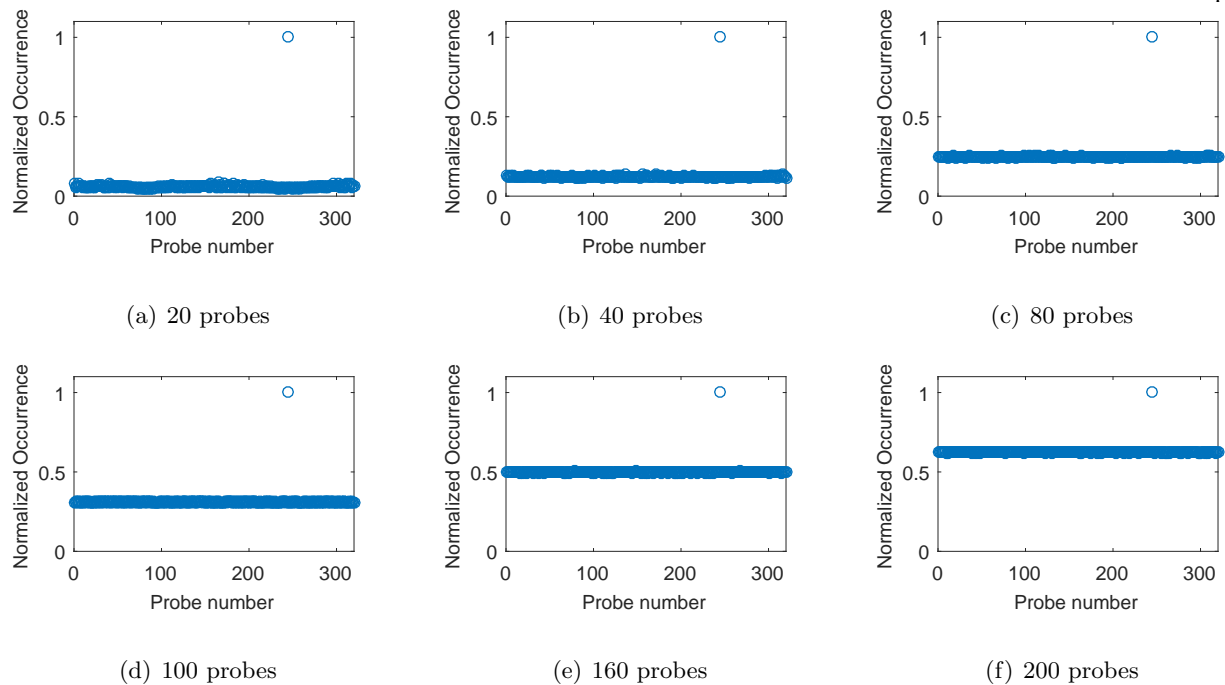


Figure 6.8: Number of occurrences for each probe over all the samples that fell within 1% error of  $IdT$  for run number 300.

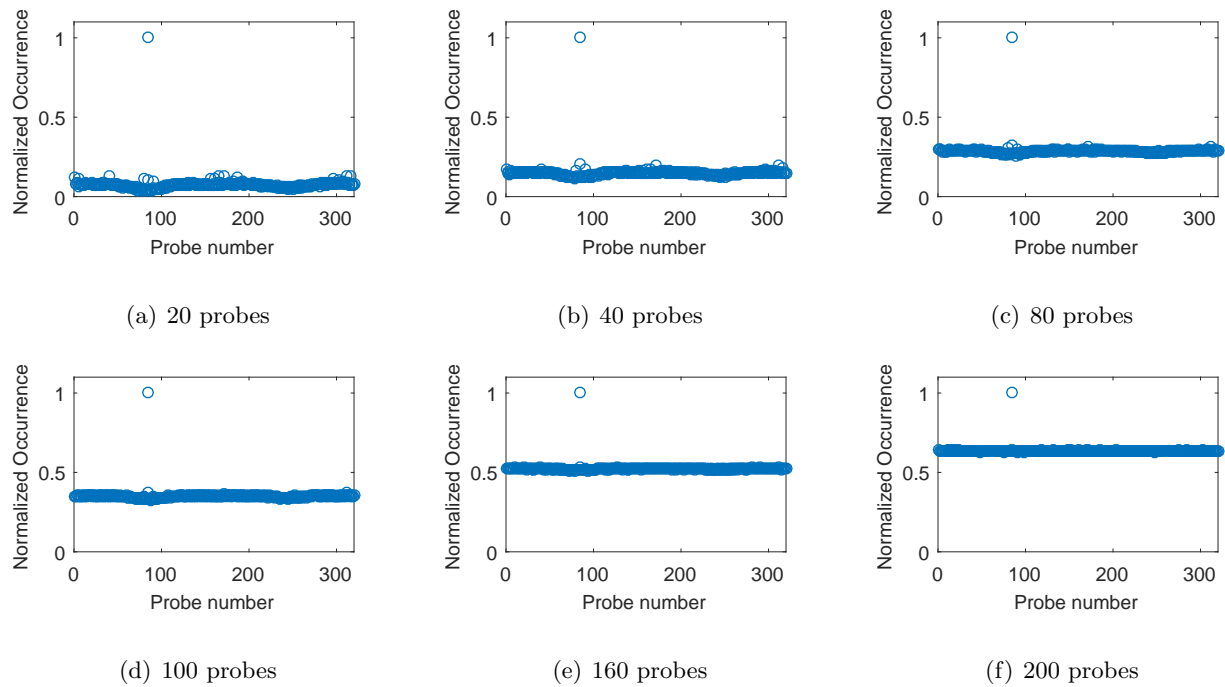


Figure 6.9: Number of occurrences for each probe over all the samples that fell within 1% error of  $IdT$  for run number 300.

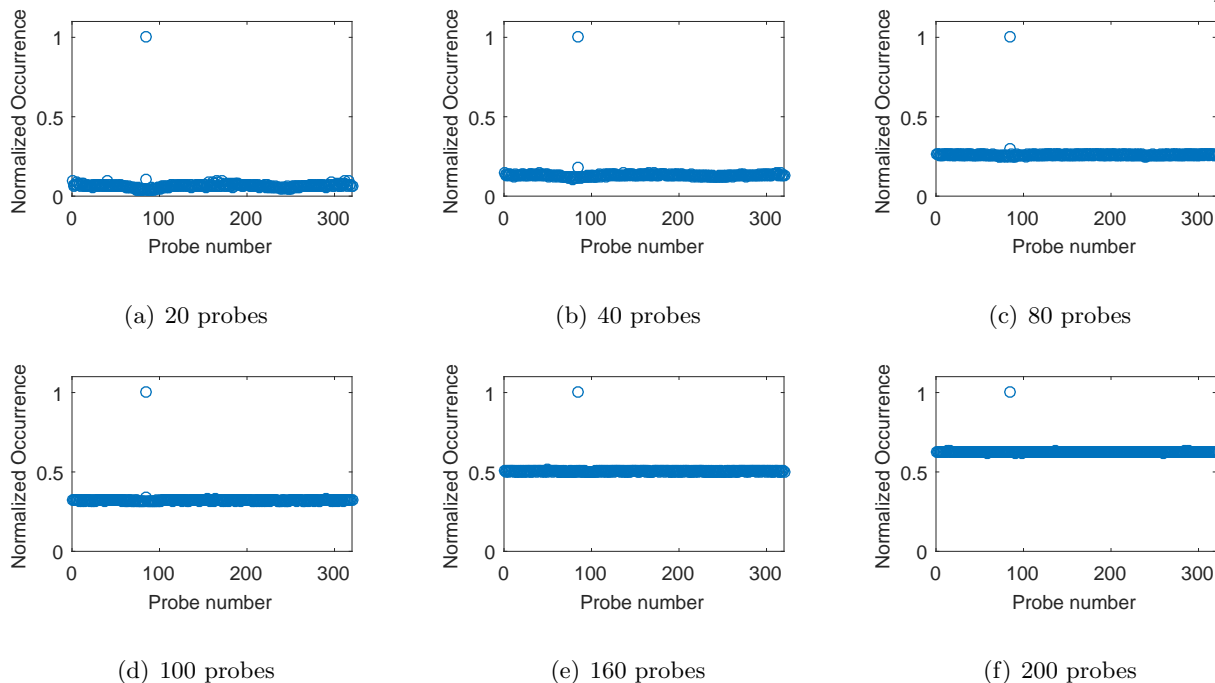
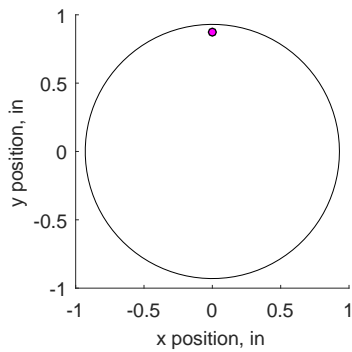
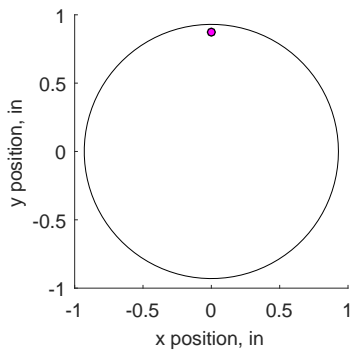


Figure 6.10: Number of occurrences for each probe over all the samples that fell within 1% error of  $IdT$  for run number 300.

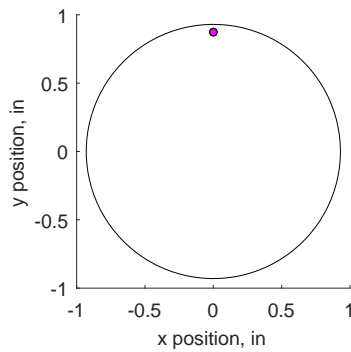
What is of note in the probe occurrence plots is that relatively few probes are in common between all the solutions that fall within 1% of the exact solution. The probes that occur the most are shown graphically in figures 6.11, 6.12, and 6.13.



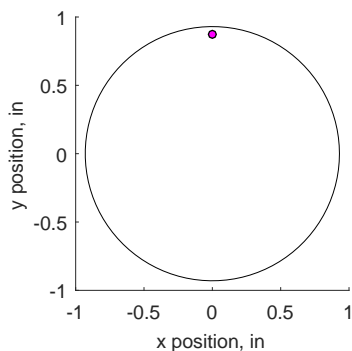
(a) 20 probes



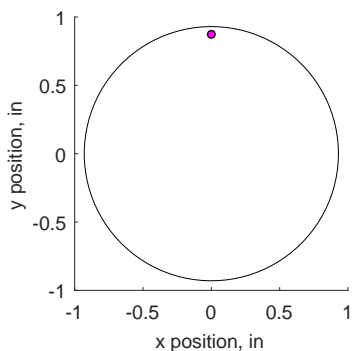
(b) 40 probes



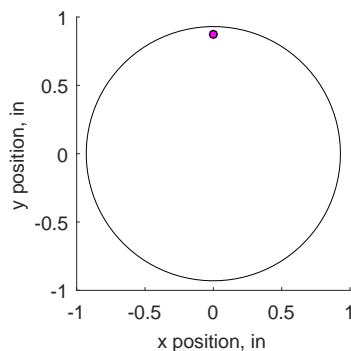
(c) 80 probes



(d) 100 probes



(e) 160 probes



(f) 200 probes

Figure 6.11: Probe locations that occur the majority of times to land within 1% of the exact *IDT* value for IMX run number R300.

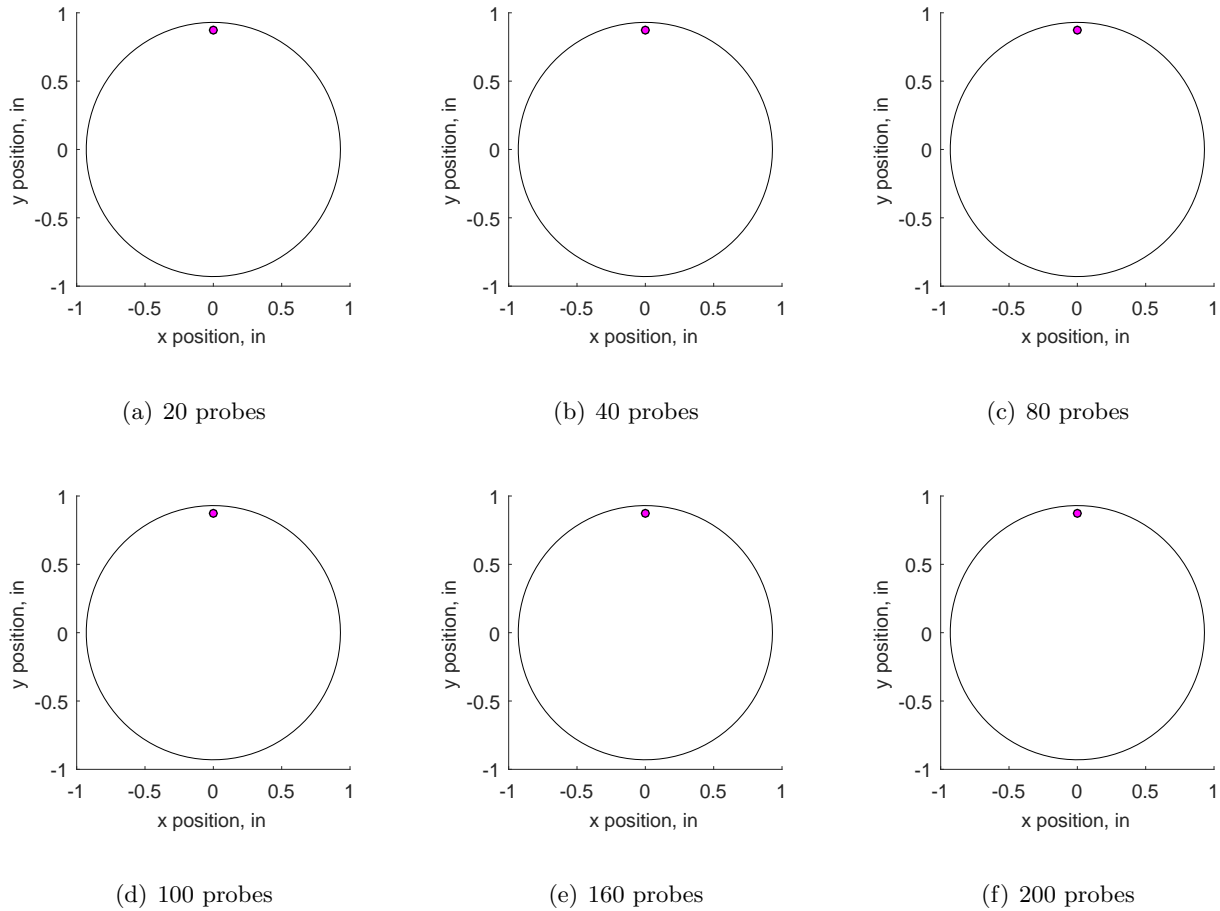


Figure 6.12: Probe locations that occur the majority of times to land within 1% of the exact *IDT* value for IMX run number R310.

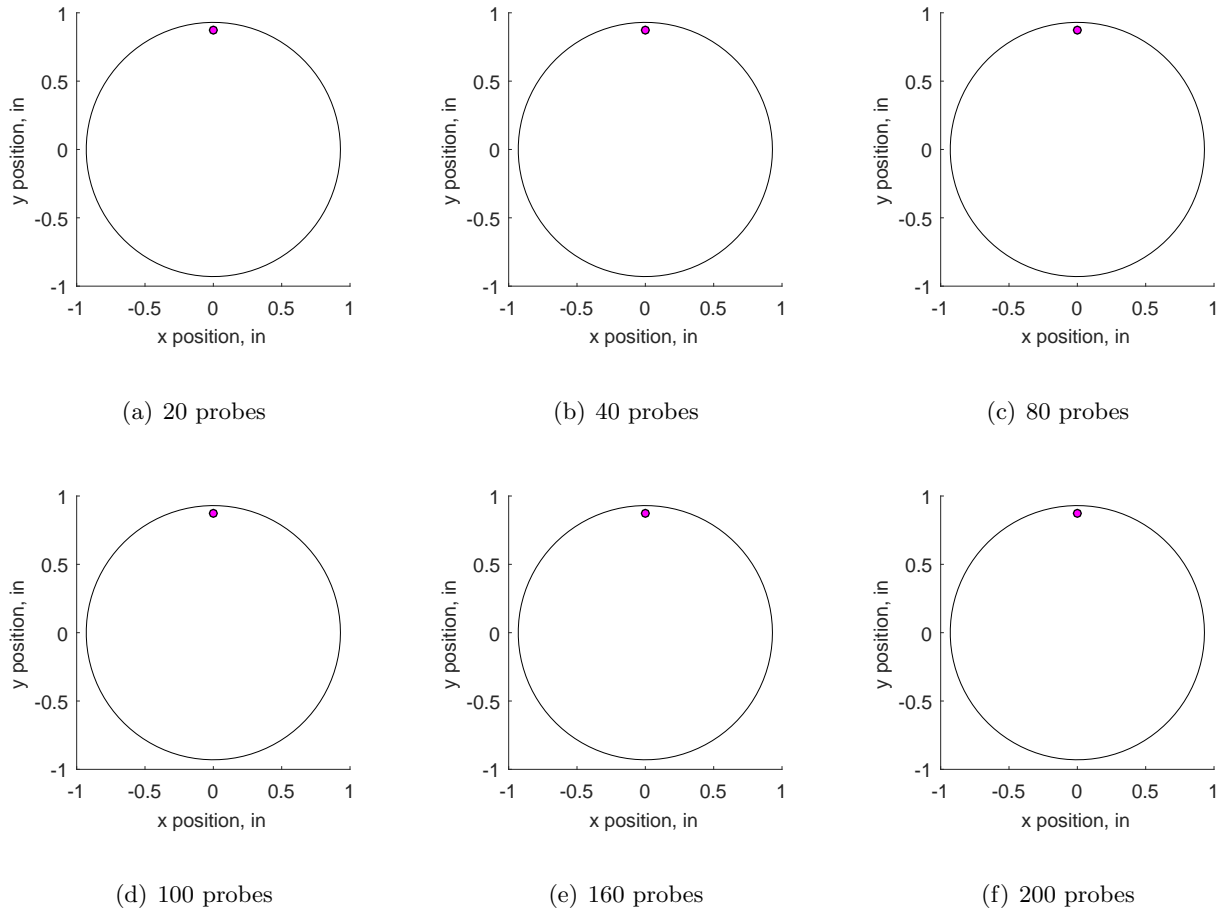


Figure 6.13: Probe locations that occur the majority of times to land within 1% of the exact *IDT* value for IMX run number R320.

All three run numbers were analyzed and the top recurring probes were selected. When compiled in the aggregate, the plots in figure 6.14 emerge.

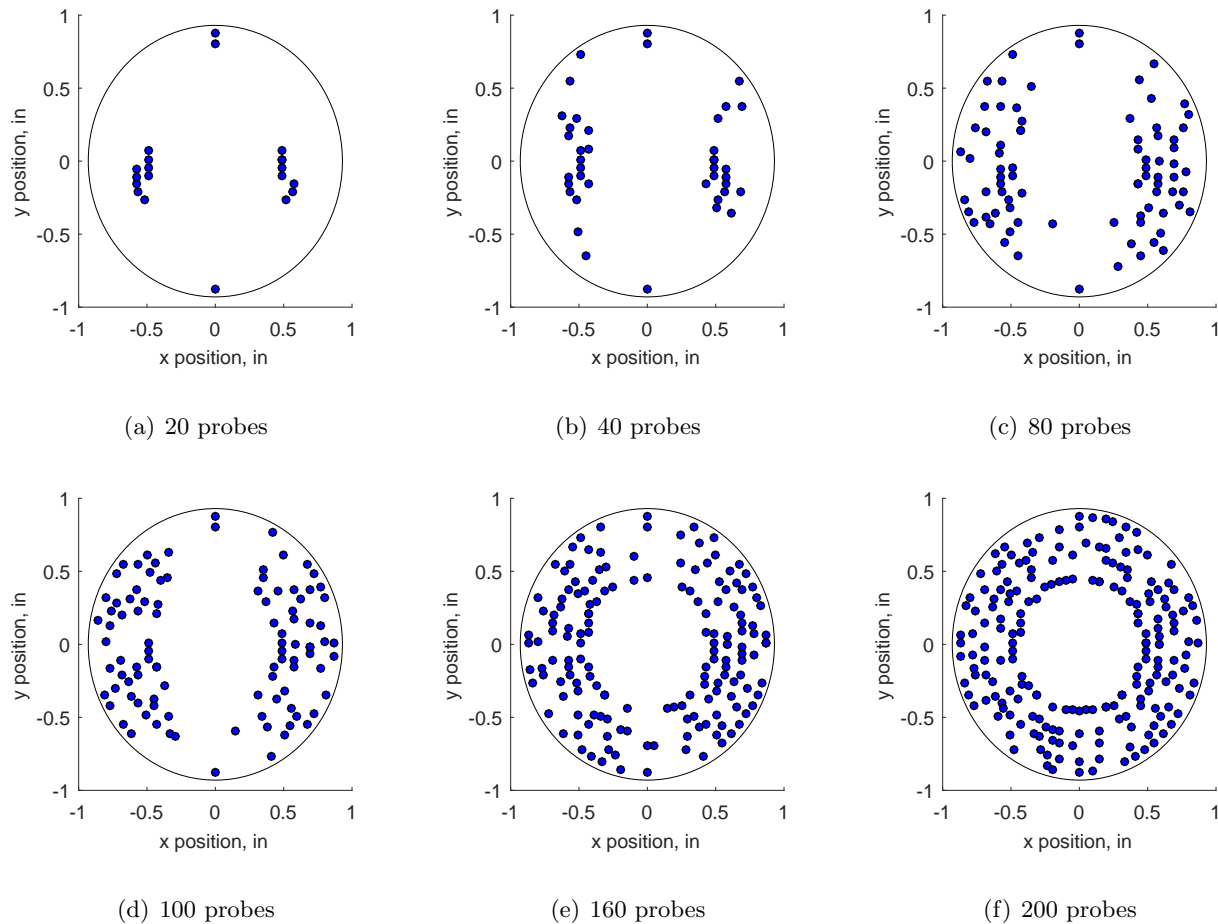


Figure 6.14: Final configuration of probes to optimize detecting *IDT* for the IMX inlet.

The distortion was calculated based on the sample sets for each of the runs. As it is not desirable to change the probe pattern each time a different set of inlet and freestream parameters are to be tested, the probe pattern should instead be able to capture the points of interest of all the different runs. In order to achieve this, the probes of interest are combined into a new set of 20, 40, etc probes. The readings at the locations of interest are extracted and *IDT* is calculated from those probes. The results of the *IDT* distortion can be found in table 6.3 and the relative error can be found in table 6.4.



Table 6.3: Results for the *IDT* distortion index for the three IMX run numbers based on the sampled probes.

	R300	R310	R320
20 Probes	0.070	0.108	0.013
40 Probes	0.065	0.077	0.072
80 Probes	0.071	0.108	0.110
100 Probes	0.071	0.108	0.112
160 Probes	0.070	0.107	0.113
200 Probes	0.071	0.108	0.111

Table 6.4: Relative error in the *IDT* distortion index for the three IMX run numbers based on the sampled probes.

	Run 300	Run 310	Run 320
20 Probes	0.004	-0.007	-0.885
40 Probes	-0.063	0.004	-0.361
80 Probes	0.013	-0.007	-0.027
100 Probes	0.011	-0.002	-0.009
160 Probes	0.001	-0.012	-0.002
200 Probes	0.016	-0.001	-0.023

The relative error does not necessarily decrease linearly and the probe lay-out has different impacts on various run numbers. The relative error jumps from less than 1% for Run 300 with 20 probes, to -6.3% for 40 probes. This is due to the way *IDT* is calculated: it is based on resolving the minimum, the maximum, and the average. In order to achieve the smallest error, all three of these parameters have to be captured. The largest source of error in this particular run is the average.

The 80 probe distribution was the least amount of probes that led to an acceptable relative error (less than 10% on *IDT*); this leads to the conclusion that in order to be within 1% of the

exact solution for all three runs, 80 probes should be used. Alternatively, these results can inform researchers that 20 probes can be arranged in such a way that the resultant parameter will be within 1% of the exact solution for Run 300 and Run 310, though a different pattern should be used for Run 320.

### 6.3.2 Experimental Data – YF12

The same analysis was conducted on the experimental data from the YF12 inlet. The results of for the PDF for three test cases are shown in figure 6.15, 6.16, and 6.17.

The average for *IDT* for test case 1 ranges from 0.171 for 20 probes to 0.237 for 200 probes, compared to an "exact" result of 0.243. This corresponds to an error of roughly 30% for 20 probes, down to less than 3% for 200 probes. Similarly, the range decreases from 0.183 for 20 probes down to 0.970, about a 2.5-fold reduction.

The average for *IDT* for Run 310 ranges from 0.124 for 20 probes to 0.184 for 200 probes, compared to a result of 0.192 for the 320 probes. This corresponds to an error of roughly 35% for 20 probes, down to less than 4% for 200 probes. Similarly, the range decreases from 0.154 for 20 probes down to 0.061, again about a five-fold reduction.

For Run 320, the average result in *IDT* ranges from 0.035 for 20 probes to 0.125 for 200 probes, compared to a result of 0.132 for the 320 probes. This corresponds to an error of roughly 30% for 20 probes, down to less than 5% for 200 probes. Similarly, the range decreases from 0.096 for 20 probes down to 0.039, which is roughly a four-fold reduction in range.

These results confirm that as the number of probes is increased, the results converge to the exact solution – the 320 probe calculation for *IDT*. The three runs converge to different values of *IDT*, as is expected, since they represent three different data sets.

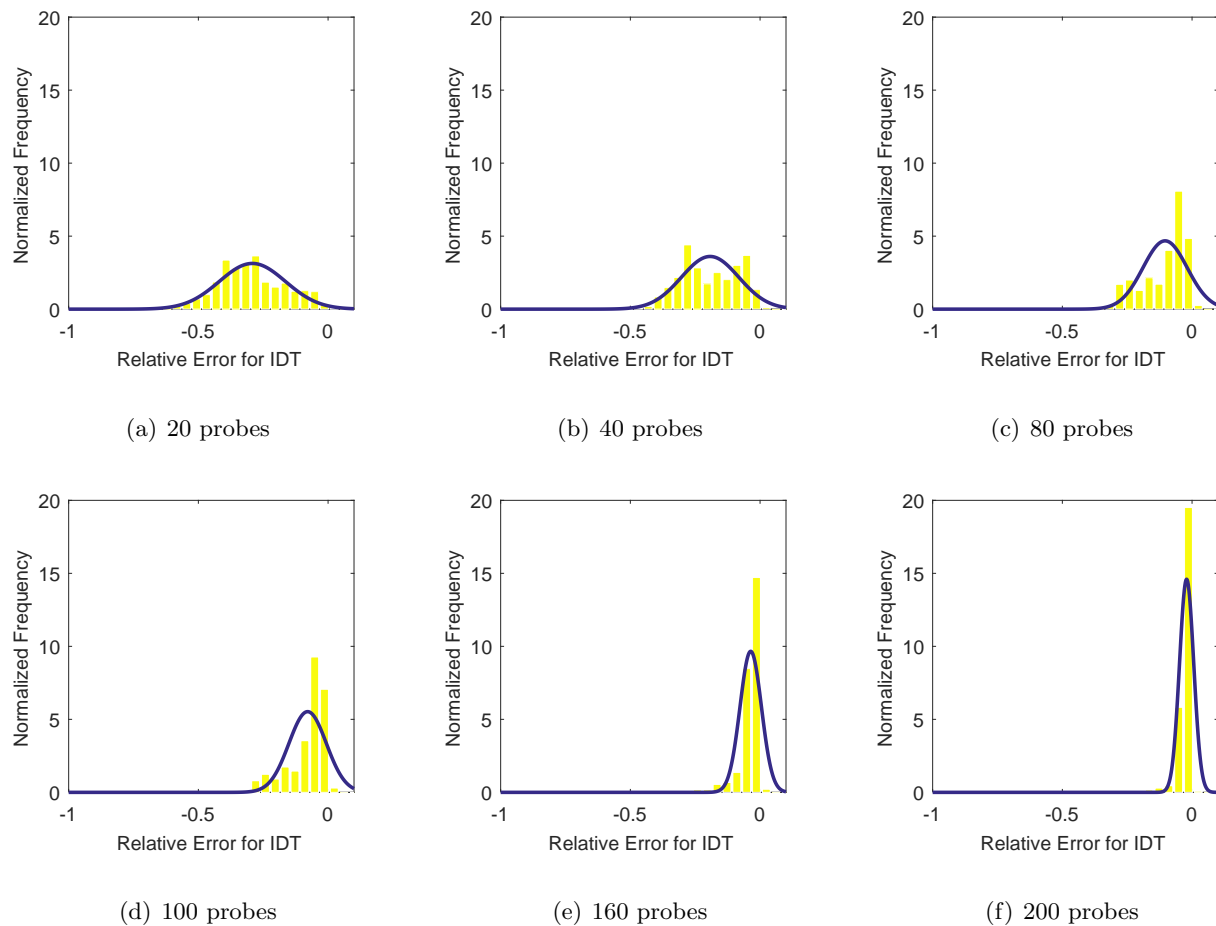


Figure 6.15: Probability density function for the error in  $IDT$  for test case 1.

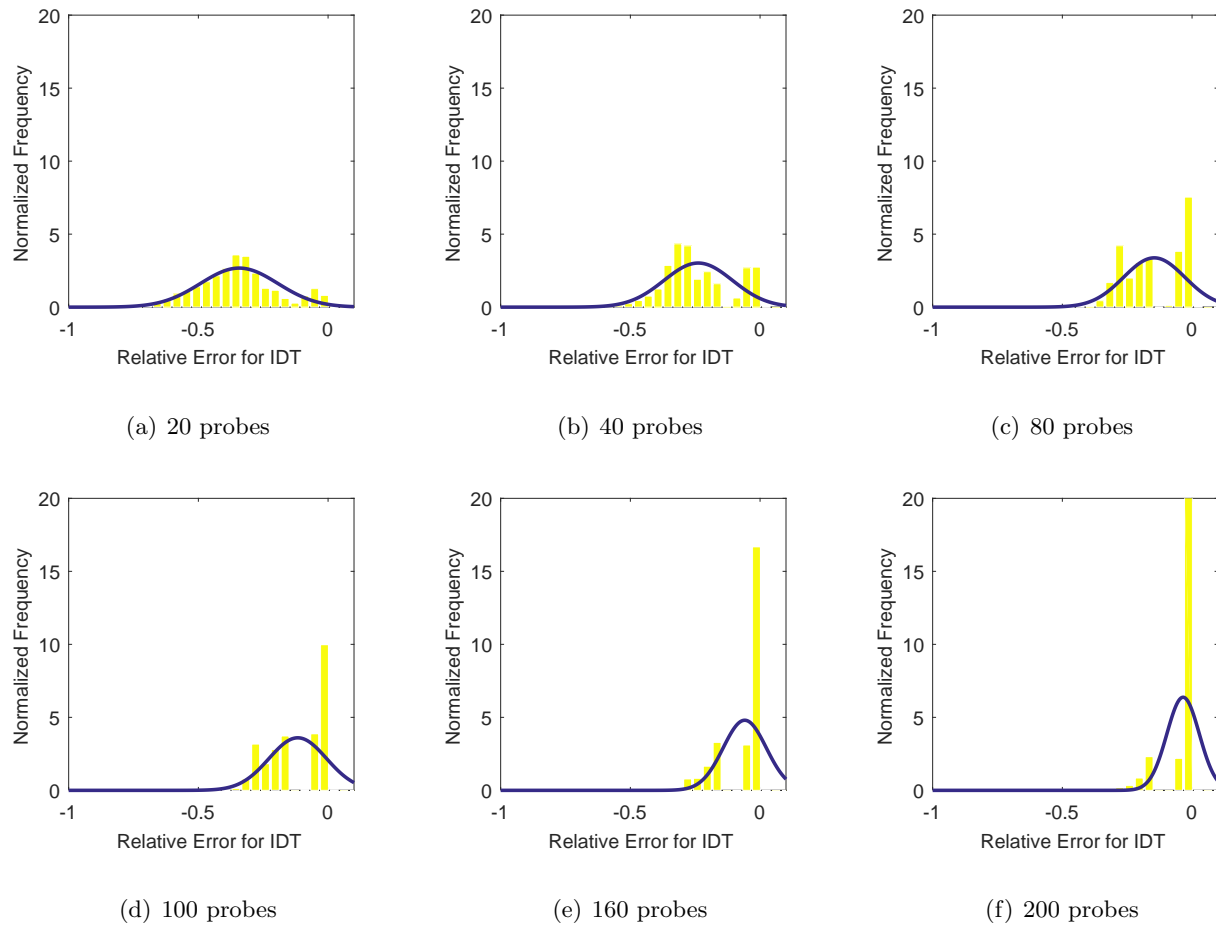


Figure 6.16: Probability density function for the error in  $IDT$  for test case 2.

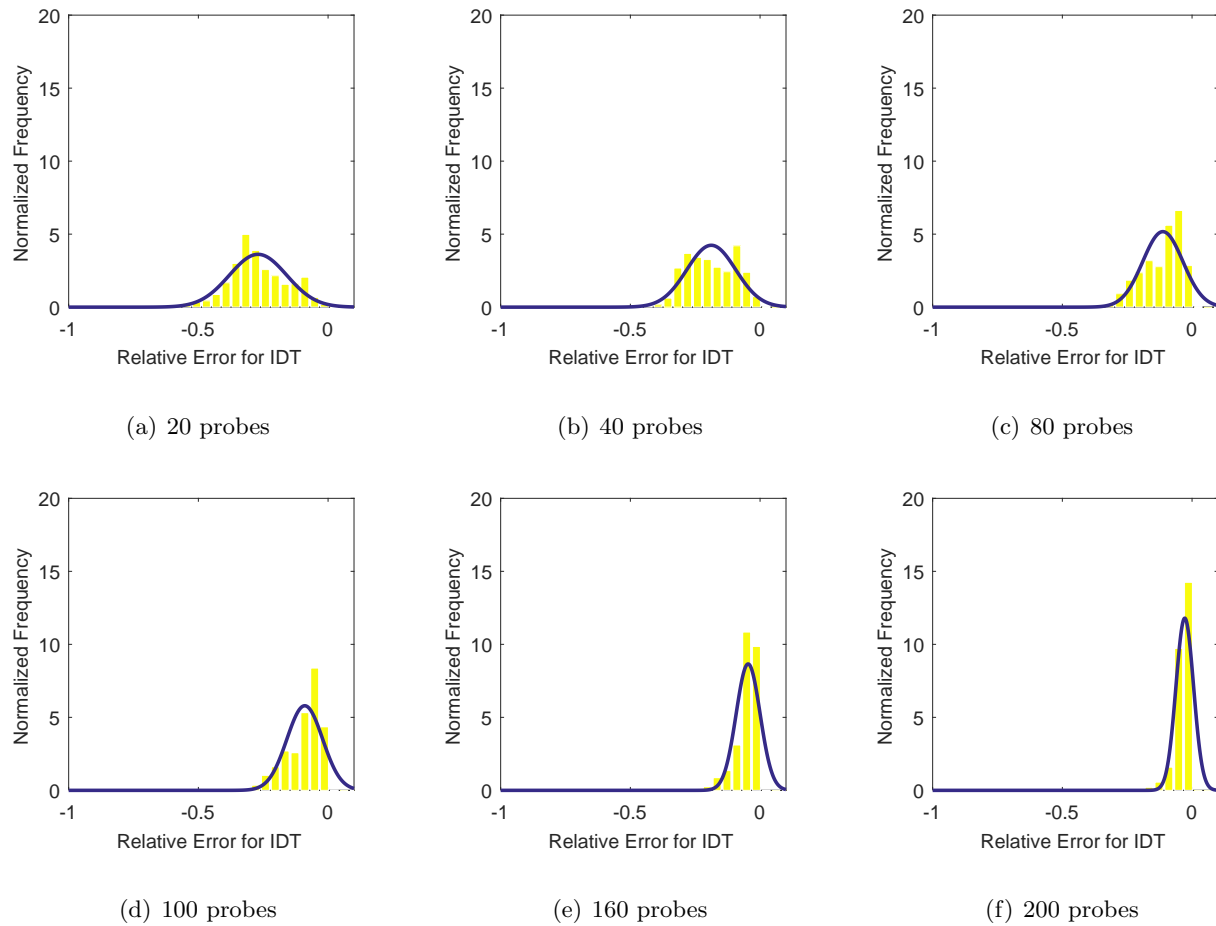


Figure 6.17: Probability density function for the error in  $IDT$  for test case 3.

A tabulation of the results can be found in table 6.5. Just as with the IMX results, the mean error and standard deviation was decreased as more probes sets were sampled.

Table 6.5: Tabulation of the mean and standard deviation in the error for  $IDT$  from the YF12 inlet for all test cases.

	Test Case 1		Test Case 2		Test Case 3	
	Mean	Std. Dev.	Mean	Std. Dev.	Mean	Std. Dev.
20 Probes	-0.292	0.128	-0.343	0.149	-0.270	0.110
40 Probes	-0.193	0.111	-0.238	0.132	-0.188	0.094
80 Probes	-0.104	0.085	-0.146	0.118	-0.113	0.077
100 Probes	-0.079	0.072	-0.117	0.111	-0.090	0.069
160 Probes	-0.036	0.041	-0.059	0.083	-0.046	0.046
200 Probes	-0.021	0.027	-0.035	0.063	-0.028	0.034

As with the IMX before, the numbers presented in table 6.5 are in relation to the calculated  $IDT$  index for 320 probes. Another interesting way to look at these results is by comparing it to what a 40 probe set-up as described in ARP1420 would show, as was discussed in eq. 6.4. For the IMX, the results between the 40 probe layout and the 320 "exact" solution was very close. For the experimental TF12 data, this does not hold true. The results of the mean error in  $IDT$  values are shown in table 6.6.

Table 6.6: Tabulation of the mean error in  $IDT$  from the YF12 experimental data for all run numbers with respect to the ARP1420 suggested, 40 probe layout.

	Test case 1	Test case 2	Test case 3
20 Probe	-0.143	-0.052	0.069
40 Probe	-0.023	0.100	0.189
80 Probe	0.085	0.233	0.299
100 Probe	0.115	0.275	0.333
160 Probe	0.167	0.358	0.397
200 Probe	0.186	0.393	0.423

While for the IMX, the difference between the exact and 40, ARP1420 recommended probe locations was small, this does not hold true for the YF12 inlet. For this inlet, the error ranges from 17% to 32%. From table 6.6, it can be seen that the error is much more erratic and much larger when compared to the 320 "exact" solution shown in table 6.5, where the errors were mostly less than 1%. The gains of using this method are much greater as the original 40 probes did not capture all of the important values associated with *IDT*.

The probe occurrences are shown in figures 6.18, 6.19, and 6.20. Unlike the computational data, where the nodes are spaced much closer together, there are fewer impacting probes. As more probe sets are sampled, the overall occurrence to fall within 1% of the "exact" solution of probes increases, but a few probes stand out.

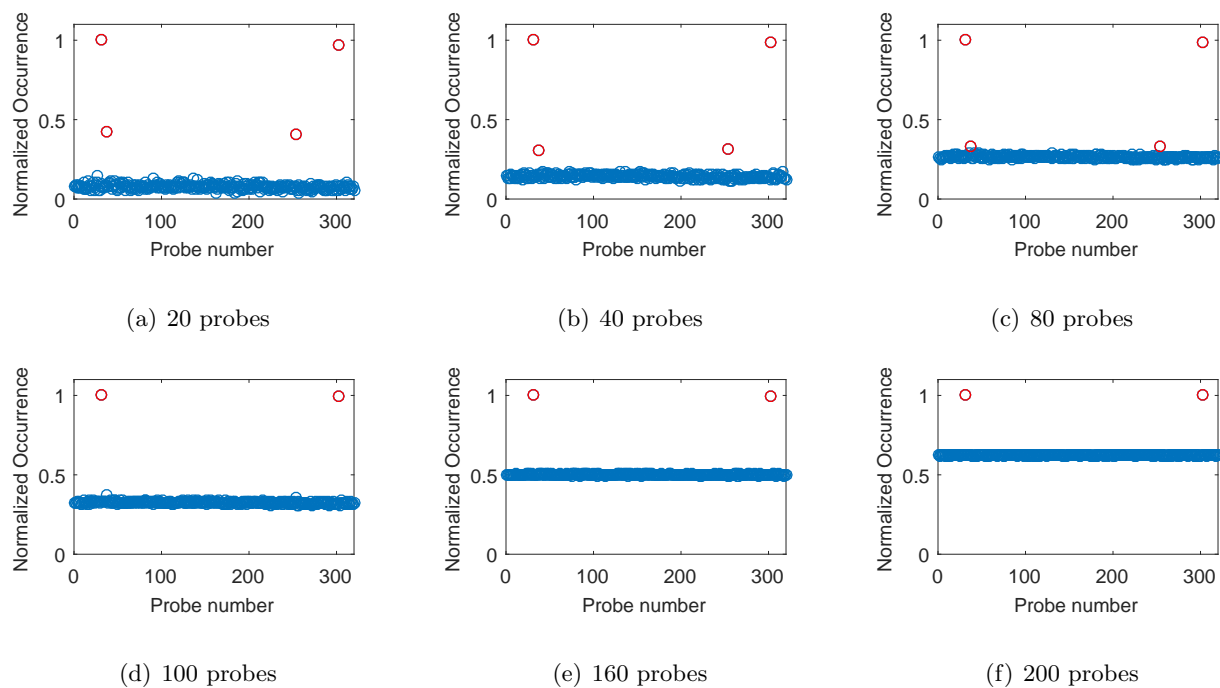


Figure 6.18: Number of occurrences for each probe over all the samples that fell within 1% error of *IdT* for test case 1.

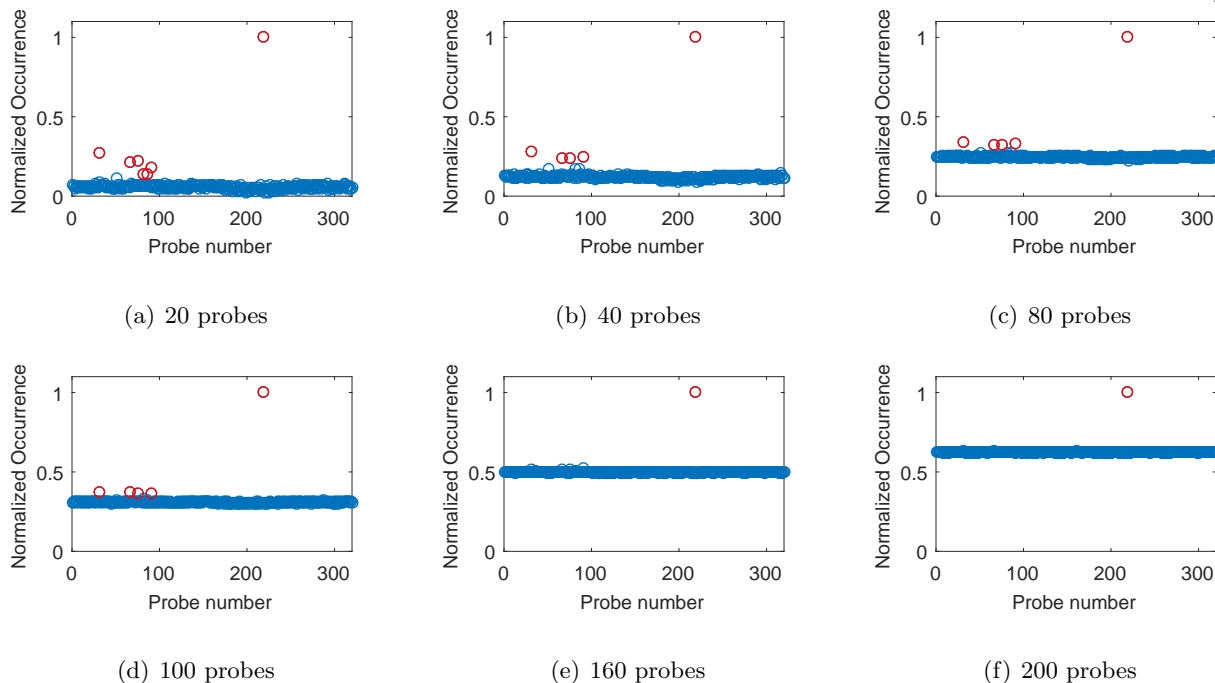


Figure 6.19: Number of occurrences for each probe over all the samples that fell within 1% error of  $IdT$  for test case 2.

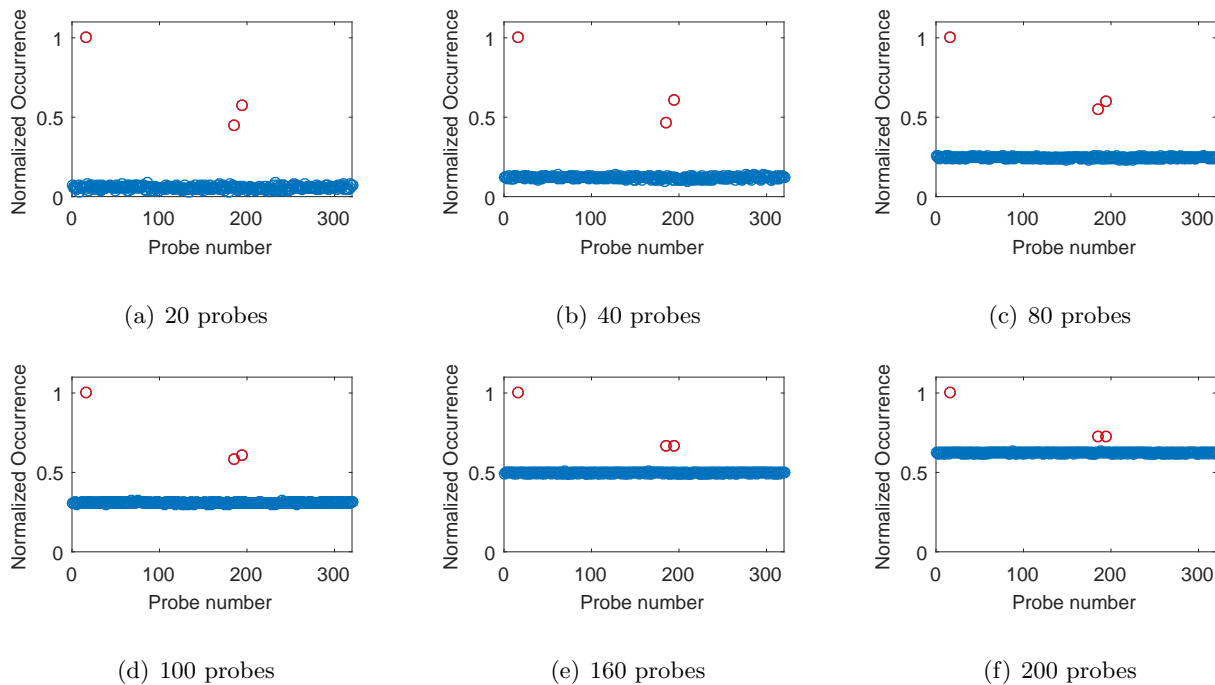


Figure 6.20: Number of occurrences for each probe over all the samples that fell within 1% error of  $IdT$  for test case 3.



The probes that occur the most are shown graphically in figures 6.21, 6.22, and 6.23. Unlike the computational results, the probes are fairly spaced out in this case, indicating that more of the flow field must be sampled to get accurate results.

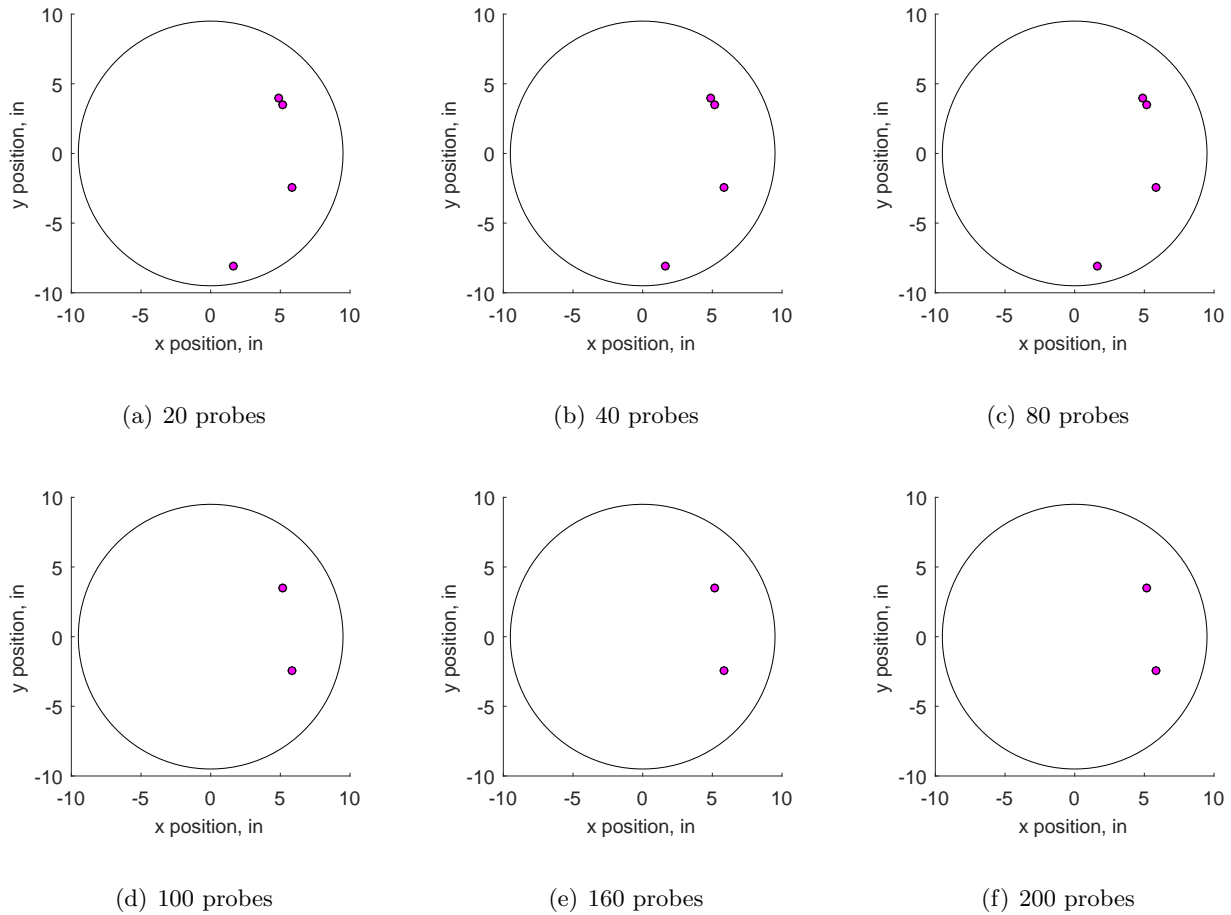
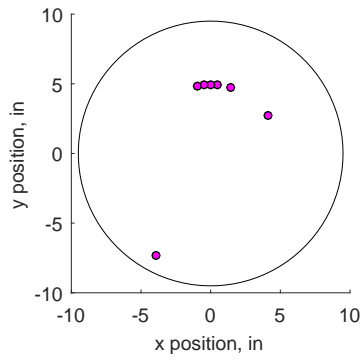
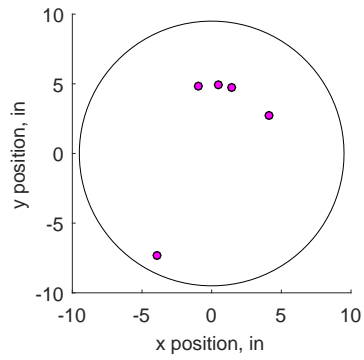


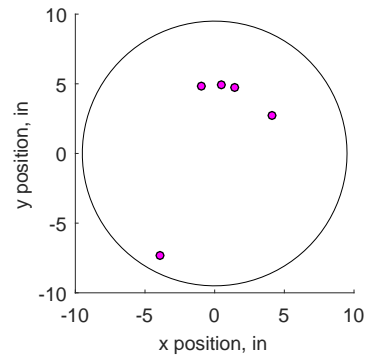
Figure 6.21: Probe locations that occur the majority of times to land within 1% of the exact *IDT* value for YF12 test case TC1.



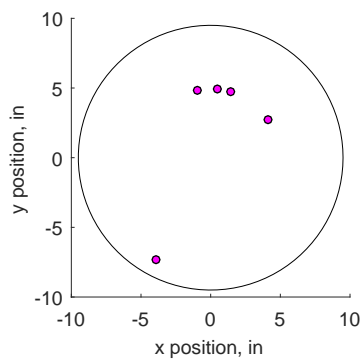
(a) 20 probes



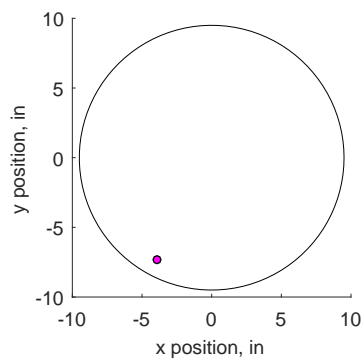
(b) 40 probes



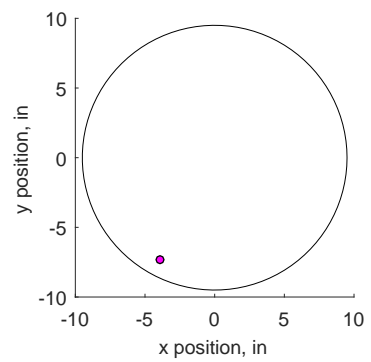
(c) 80 probes



(d) 100 probes



(e) 160 probes



(f) 200 probes

Figure 6.22: Probe locations that occur the majority of times to land within 1% of the exact *IDT* value for YF12 test case TC2.

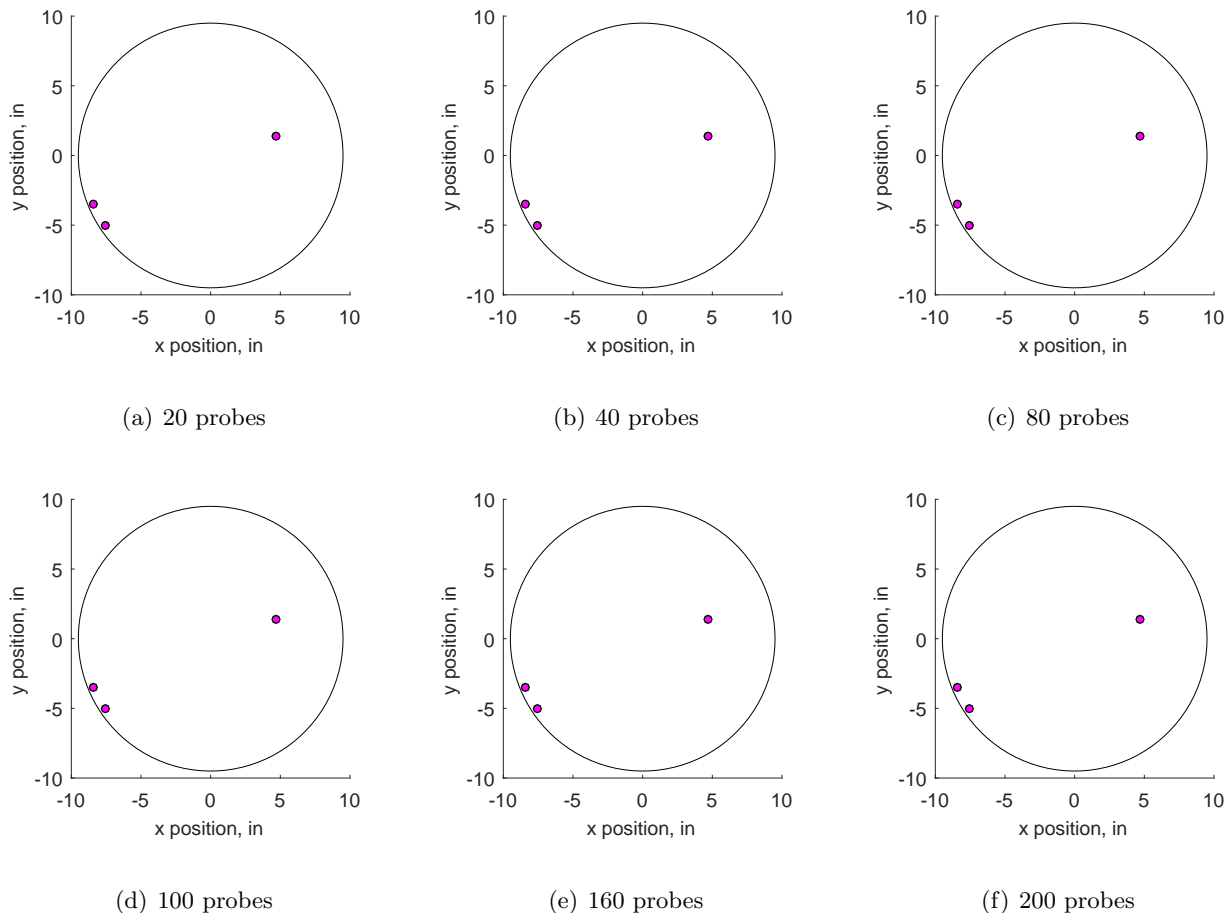


Figure 6.23: Probe locations that occur the majority of times to land within 1% of the exact *IDT* value for YF12 test case TC3.

All three test cases were analyzed and the top recurring probes were selected. When compiled in the aggregate, similarly as was done for the IMX, the plots in figure 6.24 emerge. The probes are largely clustered together for this data set.

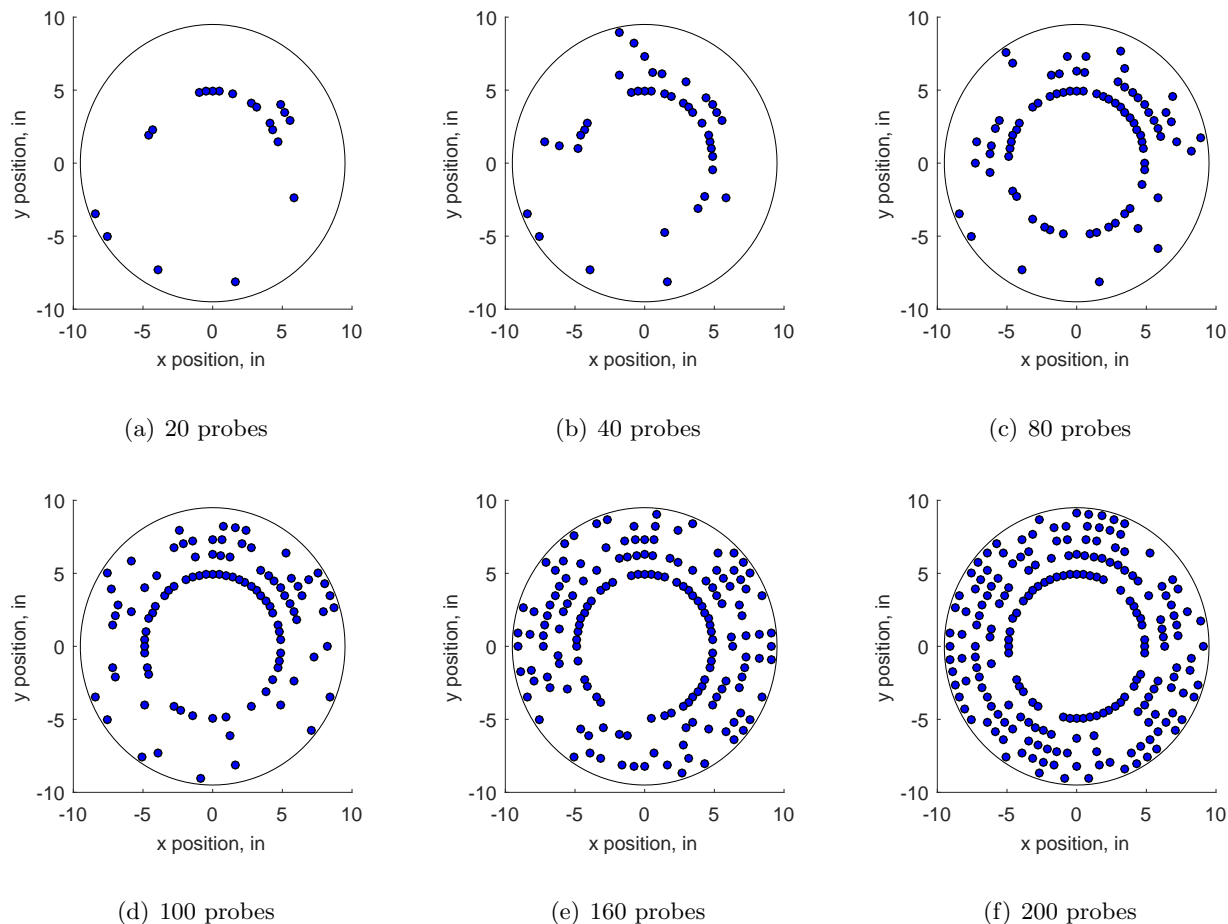


Figure 6.24: Final configuration of probes to optimize detecting *IDT* for the YF12 inlet.

The distortion was also calculated based on the sample sets for each of the runs. The results of the *IDT* distortion can be found in table 6.7 and the relative error can be found in tabel 6.8. The 40 probe distribution has an acceptable rate of error (less than 10% on *IDT*) for all of the test cases.

Table 6.7: Results for the *IDT* distortion index for the three YF12 run numbers based on the sampled probes.

	TC1	TC2	TC3
20 Probes	0.245	0.191	0.115
40 Probes	0.246	0.190	0.121
80 Probes	0.236	0.192	0.131
100 Probes	0.242	0.137	0.131
160 Probes	0.243	0.192	0.131
200 Probes	0.244	0.161	0.131

Table 6.8: Relative error in the *IDT* distortion index for the three YF12 run numbers based on the sampled probes.

	TC1	TC2	TC3
20 Probes	0.006	-0.007	-0.123
40 Probes	0.012	-0.010	-0.081
80 Probes	-0.030	-0.002	-0.007
100 Probes	-0.005	-0.286	-0.002
160 Probes	-0.002	-0.002	-0.006
200 Probes	0.001	-0.163	-0.003

For all probe numbers, with a few outliers, the parameter *IDT* can be accurately predicted. The outliers are the 20 probe layout for test case 3, 100 probe layout for test case 2, and 200 probes for test case 2. This is again due to the difficulty in resolving the mean properly. The absolute value of *IDT* decreases significantly from test case 1 to test case 3, thus even small changes can cause large fluctuations in the relative error. The raw value of the 20 probe layout for test case 3 for *IDT* is 0.115, compared to an exact value of 0.132, which may not be a significant difference. For the 100 probe layout of test case 2, the solution calculated 0.137 and 0.161 for the 200 probe layout. This

should be compared to 0.192 for the exact solution. While this is under-predicting the result, it also shows that the differences may not be as dramatic as the relative error shows.

The results are also much better when placed in context of the ARP1420 results, as is shown in table 6.9. The error, with respect to the ARP1420 layout, range from 17-22% for test case 1, 3-45% for test case 2, and 28-46% for test case 3. The method described in this chapter can reduce this error ten-fold.

Table 6.9: Relative error in the *IDT* distortion index with respect to the ARP1420 layout for the three YF12 run numbers.

	TC1	TC2	TC3
20 Probe	0.219	0.436	0.281
40 Probe	0.224	0.429	0.347
80 Probe	0.174	0.444	0.459
100 Probe	0.204	0.030	0.459
160 Probe	0.209	0.444	0.459
200 Probe	0.214	0.211	0.459

## 6.4 Conclusions

The standard, ARP1420[43], gives guidance on how to place probes to determine inlet flow distortion. The standard recommends 8 equispaced rakes, 45 degrees apart, each with 5 probes. However, the standard was written at a time when there were no computational models. With the use of the computing power available today, there are better ways to place the probes in areas of high impact.

For this work two inlets – an axisymmetric YF12 inlet and a two dimensional NASP-like inlet – were studied. The data, both computational and experimental, were sampled using a Monte Carlo method to determine if probes could be placed in more effective ways.

For the axisymmetric inlet based on experimental data, placing 40 probes in select locations

could get the results for *IDT* within less than 10% of the exact solution for almost all cases. This is much better than what the equi-spaced 40 probes were able to resolve (see chapter 5). For the two dimensional inlet, the results were not as clear. 80 probes were required to get within 10% of the exact solution for all run numbers, although this is largely due to the small value of the exact result.

While this method has its issues, it also offers a solution to how researchers can reduce the number of probes without necessarily sacrificing accuracy. This method depends on having accurate computational results in order to implement it with confidence. It can also be used to get more accurate results for an equal number of probes or be specified for accurate results of particular wind tunnel and inlet conditions.

# Chapter 7

## Probe Placement Sensitivity Analysis

In chapters 4, 5 and 6 methods on how to analyze discrete experimental data and how to optimize probe placement in general were discussed. This chapter delves more in depth on the previous work, analyzing the sensitivity of each probe added to the experiment. Instead of looking at the overall pattern established by optimizing probe placements, the focus is on varying the number of sampled probes from 20 to 40.

### 7.1 Background

The previous chapter outlined a methodology that can help optimize probe placement via sampling and simulation. Errors in the parameter of interest could be reduced almost ten-fold if using 40 probes. Alternatively, the results showed that with half as many probes as the current standard, ARP1420[43], suggests one can get within 10% of the exact solution.

One of the main drawbacks of this method is that the probes must be arranged in ways that can be difficult to implement. If a probe pattern does not lend itself to easily place 25 probes but only allows for 22, how much does that impact the final solution? This section aims to answer that question by evaluating the sensitivity of the solution in the area of interest.

As with the previous chapter, only one parameter of interest is addressed, the combined distortion index  $IDT$ . Various parameters of interest can be modeled using this method and it is not exclusive to distortion indices. Pressure recovery is another possible parameter of interest that could be investigated. This work also assumes that there is confidence in the computational and



experimental results for the inlets studied.

## 7.2 Methodology

The work done in this chapter closely follows what was presented in chapter 6 and expands on it. The work in the previous chapter focused on optimization by evaluating big increases in the number of probes selected. In this section, the area of interest is between 20 and 40 probes to determine how sensitive the solution is to the addition of extra probes.

The parameter of interest was again the total distortion index *IDT*. The exact solution was the value of *IDT* for the full, 320 probe data set. The probes are sampled using the same uniform sampling technique discussed in the previous chapter. *IDT* is calculated for that sampled set. The number of samples is incremented by 1 from 20 to 40. Millions of these samples are taken for each sample size in what is called a Monte Carlo simulation. This is a direct, brute force simulation of the data and thus becomes computationally intensive. Only solutions that fall within 10% of the exact solution are saved while the others are discarded. These are called good points.

This is where the similarities of the last chapter and this chapter end. Instead of evaluating what probes appear, the number of good points are counted with respect to how many simulations were run. The sensitivity thus is evaluated based on the ratio of good points, *S*, with respect to the total samples (eq. (7.1)).

$$S = \frac{\text{Number of Good Samples}}{\text{Number of Total Samples}} \quad (7.1)$$

The three experimental test cases of the YF12 inlet and the computational runs of the IMX inlet are used in this work. Since the solutions vary in scale by quite a bit between these inlets, it is useful to normalize the results to compare them to each other. In order to do so, *nS* (eq. (7.2)) is calculated, which is a normalization with respect to the maximum ratio of good samples to total samples.

$$nS = \frac{S}{S_{max}} \quad (7.2)$$

The sensitivity function  $S$  shows how the accuracy increases as more points are added. A different way to observe this is to evaluate how the accuracy increases between probe sample sizes. The relative ratio of good points,  $\Delta S$ , is shown in eq. (7.3).

$$\Delta S = S_{i+1} - S_i \quad (7.3)$$

Again, the different data sets have different scales, the  $\Delta S$  function is also normalized by the maximum difference between probes. It may seem counter-intuitive to the reader, but a result of 1 for  $n\Delta S$  indicates no change in sensitivity, as this indicates the maximum number of good points has been reached. On the other hand, a smaller value for  $n\Delta S$  indicates that the result is more sensitive to the addition of a probe.

$$n\Delta S = \frac{\Delta S}{\Delta S_{max}} \quad (7.4)$$

A linear regression is then performed on the normalized change in the sensitivity function,  $n\Delta S$ . This linear regression represents the overall solution sensitivity to the results. Confidence intervals of 95% are also applied to the linear regression and the goodness of fit,  $R^2$ , is calculated. More information on linear regression can be found in the references[97, 102].

### 7.3 Results

Six data sets in total were studied for this work and are presented in the aggregate. These data sets include the three test cases for the YF12 inlet (section 3.2) and the three computational

runs for the IMX inlet (section 3.1.3). A total of one million simulations were run per data set, per sample set. Good points, namely those within 10% of the exact solution, were extracted and saved.

The results for the ratio of good points,  $S$ , and the normalized ratio,  $nS$ , are shown in figure 7.1. TC1, TC2, and TC3 represent the three YF12 test cases. R300, R310, and R320 represent the three IMX computational runs. In terms of trends, all of these ratios of good points appear to be largely linear, though TC2 does show somewhat of a parabolic fit and appears to converge faster. When normalized to the maximum however, these trends disappear and there is much less variation between the data sets. This implies that sensitivity is likely not dependent on the underlying data set.

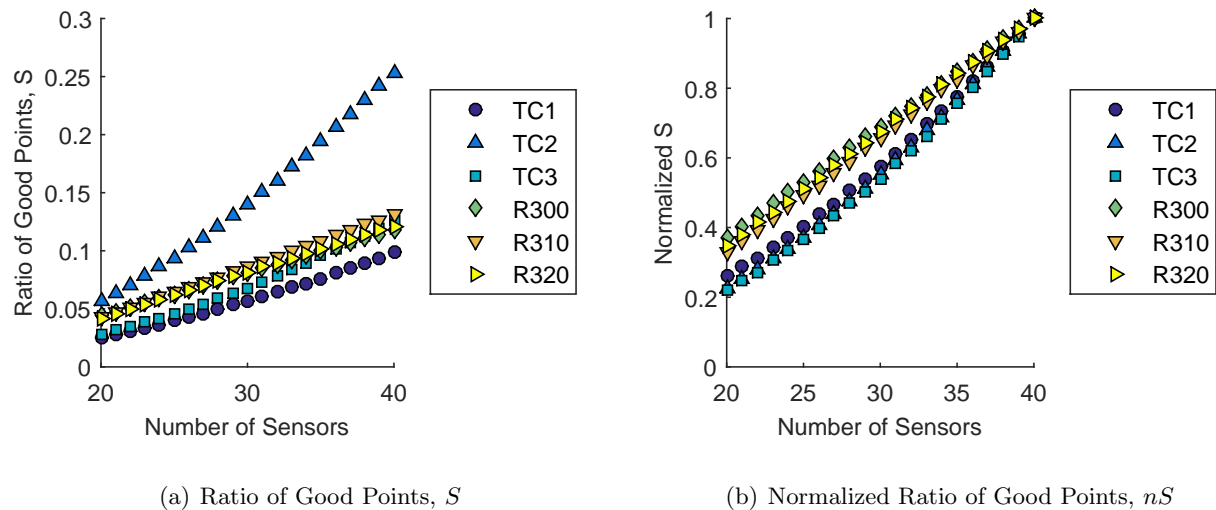


Figure 7.1: Ratio of good results for *IDT* with respect to the number of probes.

The ratio of good points show how the sensitivity changes as more probes are added overall. The change in ratio  $\Delta S$  on the other hand shows how much of a difference there is as one probe is added. This result is shown in figure 7.2. Again, the TC-labeled points are  $\Delta S$  calculated from the YF12 data while the R-labeled points are  $\Delta S$  calculated from the IMX data. The second test case of the YF12 shows higher change in probes for the regular  $\Delta S$  while the others show about half the change. When normalized (figure 7.3) this trend again disappears. There is no clear pattern that can be gleaned.

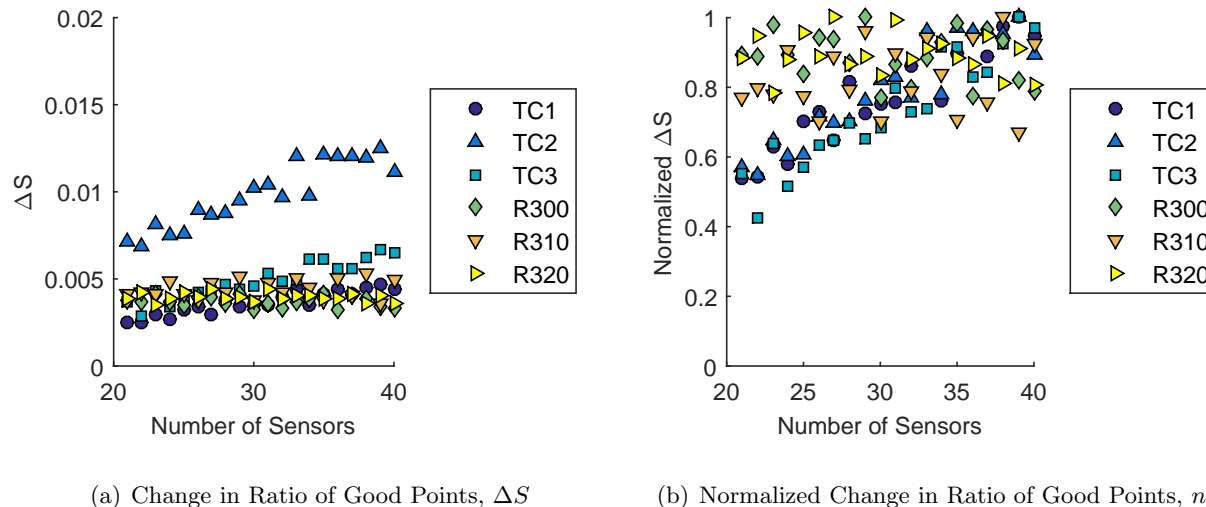


Figure 7.2: Change in ratio of good results for *IDT* with respect to the number of probes.

The mean of the normalized change in ratio of good points is tabulated (table 7.1) for further analysis. There is a trend of increasing  $n\Delta S$  as the number of probes increases. This indicates that the result becomes less sensitive as more probes are added as a result of 1 indicates the bounds of the normalization. To further illustrate the point, the increase in sensitivity is shown, which is simply  $1 - n\Delta S$ .

Table 7.1: Average change in  $n\Delta S$ 

$\Delta$ Probes	Average $n\Delta S$	Increase in Sensitivity
20-21	0.702	0.298
21-22	0.692	0.308
22-23	0.744	0.256
23-24	0.730	0.270
24-25	0.743	0.257
25-26	0.768	0.232
26-27	0.803	0.197
27-28	0.791	0.209
28-29	0.832	0.168
29-30	0.761	0.239
30-31	0.857	0.143
31-32	0.805	0.195
32-33	0.898	0.102
33-34	0.858	0.142
34-35	0.893	0.107
35-36	0.888	0.112
36-37	0.893	0.107
37-38	0.933	0.068
38-39	0.900	0.100
39-40	0.888	0.112

A linear regression was applied to the  $n\Delta S$ . This linear regression represents the average increase in sensitivity (figure 7.3).

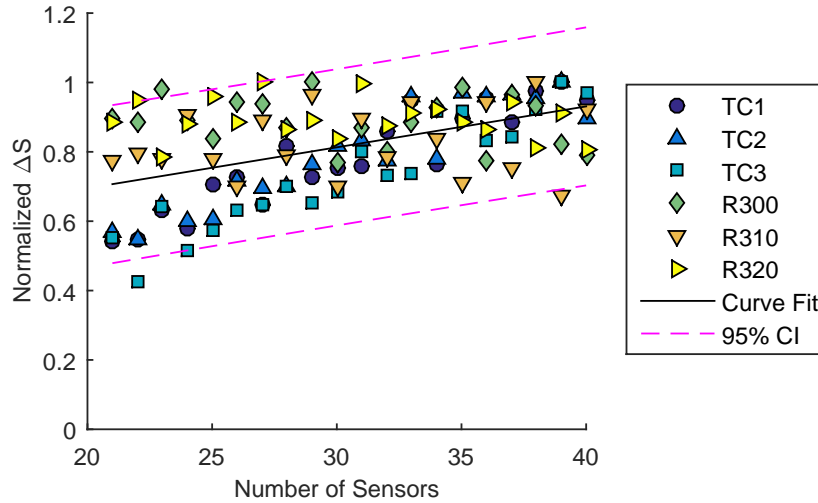


Figure 7.3: Linear regression of the normalized sensitivity function for *IDT* with 95% confidence intervals

The equation for the linear regression ends up as eq. (7.5) with an  $R^2$  value of approximately 0.3.

$$n\Delta S_{fit} = 0.012NP + 0.459 \quad (7.5)$$

The confidence interval of 95% is shown in eq. (7.6).

$$CI_{upper} = 0.015NP + 0.569CI_{lower} = 0.008NP + 0.349 \quad (7.6)$$

A total of six points fall outside of the 95% confidence interval, which is approximately 5% of all results. The sensitivity of the number of probes added thus decreases. Adding more probes early on increases the number of good results far more than adding probes towards the bounds of the solution at 40 points. From 20 to 21 probes, the average increase in sensitivity (table 7.1) is approximately 30%. However, from 30 to 31 probes, the increase is only about half that, 15%.

In the scenario given in the background section of this section, where researchers were trying to determine how much sensitivity is lost from losing 3 probes, from 25 to 22 points, the answer can be obtained by using eq. (7.9), approximately 3.6% in the final solution if this linear regression is used.

$$n\Delta S_{25} - n\Delta S_{22} \quad (7.7)$$

$$= (0.012(25) + 0.459) - (0.012(22) + 0.459) \quad (7.8)$$

$$= 0.036 \quad (7.9)$$

Another way to look at this is how sensitive each data set is to the difference between 25 and 22 probes. For this, changes in  $n\Delta S$  can be obtained directly by calculating the solution at 25 and 22 points and subtracting the difference. The results are shown in table 7.2.

Table 7.2: Individual results for  $n\Delta S$  of the 25-to-22 probe reduction scenario

Data Set	$n\Delta S$
TC1	0.0089
TC2	0.0232
TC3	0.0115
R300	0.0113
R310	0.0131
R320	0.0116

In this case, it can be seen that for the YF12, the sensitivity ranges from less than 1% to approximately 2.5%. For the computational result, the changes were all around 1%.

## 7.4 Conclusions

In chapter 6, probe locations were optimized for the parameter  $IDT$ , potentially increasing the accuracy and precision of the experimental determination of the parameter ten fold. However,

that chapter looked at macro-scale changes between probe numbers. This chapter focused on the area of interest between 20 and 40 probes to determine how much sensitivity is lost by adding or removing probes.

A general sensitivity function was found to determine the increase in number of good points are gained by adding more probes. A linear regression was used to generalize the results for all data sets used in this work. However, they can be used by directly comparing the number of good points obtained with various numbers of probes as well.

The sensitivity in the results is higher when fewer probes are used and gradually tapers off near 40 probes. There is a bigger gain in good points when the number of probes is increased from 20 to 21 probes than from 39 to 40 probes.

This result is based on the method of sampling and optimizing discussed in chapter 6. Different sampling and simulation techniques can yield different results, thus this result is only valid for the analysis done in the previous chapter. Future advancement for this particular work must also include a revisiting of the previous chapter's work.



# Chapter 8

## Conclusions

Supersonic and hypersonic propulsion systems are highly complex in their design. There are many areas of research when it comes to these propulsion systems; this work was focused on flow distortion at the aerodynamic interface plane of the inlet. This work evaluated how interpolation methods of discrete data points impacted the continuous solution, how sampling methods could help optimize probing of the flow, and how sensitive the results were to the number of sampled locations. To answer these questions, surrogate, experimental, and computational data sets were consulted.

One motivation of this research was to integrate computational and experimental methods. Currently, CFD is run in series with experiments and experimental data is used to validate the computational results. The two methods do not overlap much beyond limited predictions from validated CFD. Instead, the researchers suggest computation and experimentation should be done in parallel. Computational results should drive how the experiment is instrumented and how the data gathered should be analyzed. In turn, experimental results can validate computational models beyond narrowly defined cruise conditions.

### 8.1 Summary of Contributions

The contributions to the field are in three areas: the analysis of experimental data, the instrumentation of the AIP, and on-the-fly analysis of test data.

Experimental data comes in discrete points but this data is easier to digest as a visual plot. These plots are generated by interpolating the discrete points into continuous pressure contours.

Different interpolation methods give various solutions but no study had been conducted on which one was the most effective. Four methods were evaluated across various quantitative and qualitative measures. The spline interpolation method was found to be the most consistent method to satisfy the majority of these measures. This result was first found with surrogate models based on experimental data and repeated with experimental and computational data. Only two inlets were studied for this work and further analysis is suggested to make claims on which interpolation method is best for all inlet types. It is advised future researchers move away from prescribed interpolation methods and instead focus on methods that utilize computational data to analyze the relationship between discrete points. Basis functions can be created and scaled according to experimental results.

The governing standard suggest that the AIP be instrumented with 40, equispaced pressure probes to sample the flow. Instead, probes can be placed in more optimum locations during experiments using a uniformly sampled, Monte Carlo simulation. This method includes selecting a prescribed number of probes from the full set. Each probe has the same likelihood of being chosen, making it uniformly sampled. Monte Carlo simulations describe that this sampling is done many times over, until interesting trends appear in the solution. With as few as half the probes that the standard recommends, the distortion index could be resolved to within 10% of the exact solution. By optimizing the sampling location of the standard-recommended 40 probes, the solution could be improved ten-fold in accuracy for the parameter of interest. However, consideration must be given for physical limitations on probe placements. Too many probes in one location can lead to under-sampling of the flow for other test runs and increase the error in parameters, even when more probes are used.

Furthermore, the uniformly sampled, Monte Carlo simulated results were investigated for sensitivity along with optimization. The area of focus was between 20 and 40 probes. All experimental and computational data sets were used for this sensitivity analysis. A general sensitivity function was found using a linear regression to determine the increase in number of points falling within the 10% tolerance band of the exact solution as more probes are added. It was found that there are bigger gains in sensitivity near the lower bound than near the upper bound. This method can

also be used for the individual data sets or inlets to determine how much is gained by adding more sampling points at key locations.

In situ analysis of test data can reduce the cost and timeline of experiments. In order to facilitate on-the-fly analysis, a graphical user interface was created to help researchers reduce test data of inlet flow as soon as it is captured. The interface was created specifically for the LIMX inlet for use in the NASA Glenn 10 foot by 10 foot supersonic wind tunnel. The GUI can easily be modified to analyze alternative data sets collected from different inlets. The GUI has since been modified to adapt to the needs of experimentalists at NASA Glenn.

The contributions made to the state of the art were in an effort to bring analysts and experimentalists closer together. While there is little overlap currently between when models are tested and simulations are run, this work makes headway in how these two disciplines can benefit from one another. If computation and experimentation are done in parallel, it could reduce iteration time and leave engineers with more robust designs.

## 8.2 Dissertation Overview

In chapter 1, the problem was defined and the assumptions were given. Details of the current state of the art were covered in chapter 2. This chapter gave an overview of various high speed vehicles and their ultimate fates. A discussion ensued on what inlet flow distortion was, how it was characterized, and what work had been done to date. It also included the definitions of all the indices used in this work. Chapter 3 delved into the inlets studied in this work – the IMX and YF12 inlets – and what data was available, how this data was analyzed, and what was and was not learned from the investigation. The following work, chapters 4 and 5, looked at how pressure data should be interpolated in order to make the best predictions. Optimizing how to collect the data was discussed in chapter 6 and the sensitivity of the results to the number of probes chosen discussed in chapter 7.

Three appendices are included in this work. Appendix A highlighted the limitations (also discussed below) in how the YF12 data was gathered from the original source. Appendix B had

information about the GUI created for NASA based on the analysis shown in chapter 3 to analyze experimental inlet flow distortion in real time. As a lot of data was analyzed in chapter 5, only one subset of data was shown for each inlet in the chapter. The full set of charts and tables can be found in appendix C.

### 8.3 Research Limitations

The scope of this work was limited to two high speed air-breathing inlets for which data was published. The IMX inlet only had computational results and sparse experimental data points available. The YF12 inlet had plenty of experimental data available, but the inlet geometry and specific test conditions remain unknown. Based on this, only limited conclusions can be drawn from the work presented here.

The computational results were all based on RANS CFD because that is what was run at NASA. It is considered the state of the art for design work in industry. DES methods could prove to be more accurate for predicting inlet flow distortion behavior, but this is computationally expensive.

The experimental results for the YF12 inlet were reported in a NASA technical report and were not available electronically. The data points were hand drawn onto graph paper at the time. The data had to be obtained using a pixel-measuring program called DataThief. Analysis showed that the error from doing this was acceptably small, but errors exist both from how the data points were drawn and how the data was collected.

For the interpolation schemes, only four methods were analyzed. More complex and possibly more accurate methods exist, such as co-Kriging. However, the interpolation schemes analyzed were the most common suggestions from fellow researchers.

Additionally, the distortion indices used were limited to the ones reported in the work of Stoll et al[1]. The limits of these indices vary from engine to engine and are considered proprietary. No judgment was made on the relative goodness of inlet design based on these indices.

The probe placement optimization was done using a Monte Carlo method. Monte Carlo methods are computationally expensive and require many runs to yield accurate results. However,

this method is very easy to implement and was chosen for this reason.

#### 8.4 Future Work

Many sections of this work can be expanded upon. The main aspect that would be of interest is to study more inlet data sets. Comparing interpolation schemes on experimental data based on RANS and DES computational results would help solidify the methodology presented in this work. Having excellent computational and experimental sets could help create the methodology of scalable basis functions to reduce the reliance on interpolation methods.

Instead of utilizing Monte Carlo simulations for the probe placement optimization and sensitivity analysis, different techniques should be investigated. Monte Carlo is easy to implement and will converge to a result, but many simulations are required to get to a solution. More advanced models exist for simulating results and they should be investigated for faster convergence. Different parameters of interest should be included in the study. Overall pressure recovery and different distortion indices could be added to the optimization algorithm to see if multi-variate solutions also show improvement over the standard.

The field of inlet flow distortion is not new, but it has been largely dormant in recent years. Many efforts have gone into reducing and controlling inlet flow distortion, but these efforts are for naught if the phenomenon is not carefully measured and analyzed. Great strides can be made by advancing computational and experimental methods, but they must inform one another to truly advance the field. The promise of advanced computational fluid dynamics, more accurate sampling techniques, and the ability to manipulate huge data sets can and will propel advanced inlets into the next stage of development. The author hopes to have laid down the first few bricks of this path with regards to how these two sides of the same coin can help each other succeed.

## Bibliography

- [1] Stoll, F., Tremback, J. W., and Arnaiz, H. H., "Effect of number of probes and their orientation on the calculation of several compressor face distortion descriptors," Tech. Rep. NASA TM-72859, May, 1979.
- [2] McGovern, J. A., The Essence of Engineering Thermodynamics, Prentice Hall, 1st ed., 1996.
- [3] Goodall, J. C., SR-71 Pilot's Manual : the Official US Air Force SR-71A Flight Manual, Motorbooks International, Osceola, WI, 1992.
- [4] Nelson, D., Bradford, J., and Olds, J., "Abortability Metrics: Quantifying Intact Abort Mode Availability for Reusable Launch Vehicles," in "Space 2006," American Institute of Aeronautics and Astronautics, Reston, Virginia, SPACE Conferences & Exposition, 2006, doi:[10.2514/6.2006-7293](https://doi.org/10.2514/6.2006-7293).
- [5] Thomas, S. R., Palac, D. T., Trefny, C. J., and Roche, J. M., "Performance Evaluation of the NASA GTX RBCC Flowpath," Tech. Rep. NASA TM 2001-210953, July, 2001.
- [6] Trefny, C. J. and Roche, J. M., "Performance Validation Approach Vehicle for the Launch," Tech. Rep. NASA TM 2002-211495, April, 2002.
- [7] Musielak, D., "AIAA High Speed Air Breathing Propulsion ( HSABP ) Technical Committee," 2010.
- [8] McDaniel, J., Goynes, C., Edwards, J., Chelliah, H., Cutler, A., and Givi, P., "US National Center for Hypersonic Combined Cycle Propulsion: An Overview," in "16th AIAA/DLR/DGLR International Space Planes and Hypersonic Systems and Technologies Conference," American Institute of Aeronautics and Astronautics, Reston, Virginia, 2009, pp. 1-18, doi:[10.2514/6.2009-7280](https://doi.org/10.2514/6.2009-7280).
- [9] Reaction Engines Ltd, "The SABRE Engine - annotated".
- [10] Thomas, S. R., "TBCC Discipline Overview," in "2011 Technical Conference," NASA, Cleveland, OH, December, 2011.
- [11] Hallion, R. P., The Hypersonic Revolution: Case Studies in the History of Hypersonic Technology. Volume 1: From Max Valier to Project PRIME (1924-1967), United States Air Force, 1995.
- [12] Hallion, R. P., The Hypersonic Revolution. Volume 2. From Scramjet to the National Aero-Space Plane, United States Air Force, 1998.

- [13] Furniss, T., "Sanger aerospaceplane gains momentum," 1989.
- [14] Hogenhauer, E. and Koelle, D., "Saenger - The German aerospace vehicle program," in "National Aerospace Plane Conference," American Institute of Aeronautics and Astronautics, Reston, Virginia, July, 1989,  
doi:[10.2514/6.1989-5007](https://doi.org/10.2514/6.1989-5007).
- [15] Furniss, T., "Sanger aims for 1999 demonstration," 1989.
- [16] "Aerospaceplane Nations Meet in USA," Flight International, August, 1989, p. 41.
- [17] Andrews, D. and Andrews, J., "Air Collection and Enrichment System (ACES) for advanced 2nd generation RLVs," in "37th Joint Propulsion Conference and Exhibit," American Institute of Aeronautics and Astronautics, Reston, Virginia, Joint Propulsion Conferences, 2001,  
doi:[10.2514/6.2001-3702](https://doi.org/10.2514/6.2001-3702).
- [18] Heppenheimer, T. A., "Facing the heat barrier a history of hypersonics," Tech. Rep. NASA SP 2007-4232, April, 2007.
- [19] Launius, R. D. and Jenkins, D. R., To Reach the High Frontier: A History of U.S. Launch Vehicles, University Press of Kentucky, 2002.
- [20] Woodcock, G. R., "The National Aerospace Plane," Science, Vol. 241, No. 4865, 1988, pp. 518–518.  
doi:[10.1126/science.241.4865.518-c](https://doi.org/10.1126/science.241.4865.518-c).
- [21] Cazin, P., "French space plane research, from Hermes to transatmospheric vehicles," in "National Aerospace Plane Conference," American Institute of Aeronautics and Astronautics, Reston, Virginia, Meeting Paper Archive, 1989,  
doi:[10.2514/6.1989-5020](https://doi.org/10.2514/6.1989-5020).
- [22] Dissel, A. F., Comparative System Analysis of Reusable Rocket and Air-Breathing Launch Vehicles, Ph.D. thesis, University of Maryland, College Park, 2005,  
doi:[1903/2939](https://doi.org/10.1126/science.241.4865.518-c).
- [23] United States General Accounting Office, "National Aero-Space Plane: Restructuring Future Research and Development Efforts," Tech. rep. GEO/NSTAD-93-71, United States General Accounting Office, Washington, DC, 1992.
- [24] Congressional Budget Office, "Reducing the Deficit: Spending and Revenue Options. A Report to the Senate and House Committees on the Budget - Part II," Tech. rep., Congressional Budget Office, 1989.
- [25] Congressional Budget Office, "Selected Spending and Revenue Options," Tech. Rep. June, Congressional Budget Office, Washington, D.C., 1991.
- [26] Congressional Budget Office, "Reducing the Deficit: Spending and Revenue Options," Tech. rep., Congressional Budget Office, Washington, D.C., 1992.
- [27] Congressional Budget Office, "Reducing the Deficit: Spending and Revenue Options," Tech. rep., Congressional Budget Office, Washington, D.C., 1993.

- [28] Neuman Ezell, L., "NASA Historical Data Handbook: Volume III Programs and Projects 1969-1978," Tech. rep. NASA SP-4012, 1985.
- [29] Rumerman, J. A., "NASA Historical Data Books Volume V: NASA Launch Systems, Space Transportation, Human Spaceflight, and Space Science, 1979-1988," Tech. rep. NASA SP-4012, 1999.
- [30] McClinton, C., Hunt, J., Ricketts, R., Reukauf, P., and Peddie, C., "Airbreathing hypersonic technology vision vehicles and development dreams," in "9th International Space Planes and Hypersonic Systems and Technologies Conference," American Institute of Aeronautics and Astronautics, Reston, Virginia, International Space Planes and Hypersonic Systems and Technologies Conferences, 1999, doi:[10.2514/6.1999-4978](https://doi.org/10.2514/6.1999-4978).
- [31] Wilhite, A. W., Powell, R., Scotti, S., McClinton, C., Pinckney, S. Z., Cruz, C., Jackson, L. R., Hunt, J. L., Cerro, J. A., and Moses, P. L., "Concepts Leading to the National Aero-Space Plane Program," in "28th Aerospace Sciences Meeting," American Institute of Aeronautics and Astronautics, Reno, NV, 1990.
- [32] Roache, P. J., Verification and validation in computational science and engineering, Hermosa Publishers, Albuquerque, N.M., 1998.
- [33] Auslender, A., Suder, K., and Thomas, S., "An Overview of the NASA FAP Hypersonics Project Airbreathing Propulsion Research," in "16th AIAA/DLR/DGLR International Space Planes and Hypersonic Systems and Technologies Conference," American Institute of Aeronautics and Astronautics, Reston, Virginia, International Space Planes and Hypersonic Systems and Technologies Conferences, 2009, doi:[10.2514/6.2009-7277](https://doi.org/10.2514/6.2009-7277).
- [34] Merlin, P., "Design and Development of the Blackbird: Challenges and Lessons Learned," in "47th AIAA Aerospace Sciences Meeting including The New Horizons Forum and Aerospace Exposition," American Institute of Aeronautics and Astronautics, Reston, Virginia, January, 2009, pp. 1-38, doi:[10.2514/6.2009-1522](https://doi.org/10.2514/6.2009-1522).
- [35] Walker, S., Tang, M., Morris, S., and Mamplata, C., "Falcon HTV-3X - A Reusable Hypersonic Test Bed," in "15th AIAA International Space Planes and Hypersonic Systems and Technologies Conference," American Institute of Aeronautics and Astronautics, Reston, Virginia, May, 2008, pp. 1-11, doi:[10.2514/6.2008-2544](https://doi.org/10.2514/6.2008-2544).
- [36] NASA Photos, "SR-71 Takeoff with Afterburner Showing Shock Diamonds in Exhaust," 1992.
- [37] Mehta, U. B., "Hypersonic technologies and aerospace plane," Aerospace America, Vol. 46, No. 12, 2008, pp. 110-111.
- [38] Greatrix, D. R., Powered Flight, Springer London, London, 2012, doi:[10.1007/978-1-4471-2485-6](https://doi.org/10.1007/978-1-4471-2485-6).
- [39] Govardhan, M. and Viswanath, K., "Investigations on an axial flow fan stage subjected to circumferential inlet flow distortion and swirl," Journal of Thermal Science, Vol. 6, No. 4,



- 1997, pp. 241–250.  
doi:[10.1007/s11630-997-0003-8](https://doi.org/10.1007/s11630-997-0003-8).
- [40] Farmer, C. J., Inlet Distortion, Vorticity, and Stall in an Axial-Flow Compressor, Ph.D. thesis, Naval Postgraduate School, 1972.
- [41] Burcham, F. W., J., Calogeras, J. E., Meyer, C. L., Povolny, J. H., and Rudey, R. A., “Effects of engine inlet disturbances on engine stall performance,” Tech. rep. NASA SP-259, 1971.
- [42] Costakis, W. G., “Experimental Investigation Of A Simple Distortion Index Utilizing Steady-State And Dynamic Distortions In A Mach 2.5 Mixed-Compression Inlet And Turbofan Engine,” Tech. Rep. NASA TM X-3169, Cleveland, OH, January, 1975.
- [43] Society of Automotive Engineers, “Gas Turbine Engine Inlet Flow Distortion Guidelines,” Tech. rep. SAE ARP1420B, 2002.
- [44] Van Deusen, E. and Mardoc, V., “Distortion and Turbulence Interaction - A Method for Evaluating Engine Inlet Compatibility,” Journal of Aircraft, Vol. 9, No. 1, 1972, pp. 16–22.  
doi:[10.2514/3.58933](https://doi.org/10.2514/3.58933).
- [45] Cousins, W. T., “History, Philosophy, Physics, and Future Directions of Aircraft Propulsion System/Inlet Integration,” in “Volume 2: Turbo Expo 2004,” ASME, Vienna, Austria, 2004, pp. 305–320,  
doi:[10.1115/GT2004-54210](https://doi.org/10.1115/GT2004-54210).
- [46] Chalk, C. R. and Key, D. L., “Experiment Design and Data Acquisition for V/STOL Flying Qualities Simulations,” in “SAE Technical Paper,” 1969,  
doi:[10.4271/690695](https://doi.org/10.4271/690695).
- [47] Martin, R. A., “Dynamic Analysis of XB-70-1 Inlet Pressure Fluctuations During Takeoff and Prior to a Compressor Stall at Mach 2.5,” Tech. Rep. NASA TN D-5826, Washington, D.C., June, 1970.
- [48] Schweikhard, W. G. and Chen, Y.-S., “Literature Search of Publications Concerning the Prediction of Dynamic Inlet Flow Distortion and Related Topics,” Tech. rep. NASA CR-3673, Hampton, VA, 1983.
- [49] Mitchell, G. A., “Experimental Investigation of the Performance of Vortex Generators Mounted in the Supersonic Portion of a Mixed-Compression Inlet,” Tech. Rep. NASA TM X-2405, Cleveland, OH, November, 1971.
- [50] Bowdich, D. and Coltrin, R., “A survey of inlet/engine distortion compatibility,” in “19th Joint Propulsion Conference,” American Institute of Aeronautics and Astronautics, Reston, Virginia, Joint Propulsion Conferences, 1983,  
doi:[10.2514/6.1983-1166](https://doi.org/10.2514/6.1983-1166).
- [51] Ring, C., Kaldschmidt, G., and Syltebo, B., “Design and testing of new center inlet and S-duct for B-727 airplane with refanned JT8D engines,” in “13th Aerospace Sciences Meeting,” American Institute of Aeronautics and Astronautics, Reston, Virginia, 1975,  
doi:[10.2514/6.1975-59](https://doi.org/10.2514/6.1975-59).

- [52] Albers, J. A. and Stockman, N. O., "Calculation Procedures for Potential and Viscous Flow Solutions for Engine Inlets," *Journal of Engineering for Power*, Vol. 97, No. 1, 1975, p. 1.  
doi:[10.1115/1.3445903](https://doi.org/10.1115/1.3445903).
- [53] Latham, E. A., "Investigation of two bifurcated-duct inlet systems from Mach 0 to 2.0 over a wide range of angles of attack," Tech. rep. NASA TM X-73118, 1976.
- [54] Hughes, D. L. and Johnson, H. J., "Flight-determined characteristics of an air intake system on an F-111A airplane," Tech. rep. NASA TN D-6679, 1972.
- [55] Melick, H. C., "Analysis of Inlet Flow Distortion and Turbulence Effects on Compressor Stability," Tech. rep. NASA CR-114577, 1973.
- [56] Gallagher, R. J., "Investigation of a Digital Simulation of the XB-70 Inlet and Its Application to Flight-Experienced Free-Stream Disturbances at Mach Numbers of 2.4 to 2.6," Tech. rep. NASA TN D-5827, Washington, D.C., 1970.
- [57] Kostin, L. and Millstone, S., "Application of statistical parameters in defining inlet airflow dynamics," in "4th Propulsion Joint Specialist Conference," American Institute of Aeronautics and Astronautics, Reston, Virginia, 68, 1968,  
doi:[10.2514/6.1968-649](https://doi.org/10.2514/6.1968-649).
- [58] Beale, D., Wieland, S., Reed, J., and Wilhite, L., "Demonstration of a Transient Total Pressure Distortion Generator for Simulating Aircraft Inlet Distortion in Turbine Engine Ground Tests," in "Volume 1: Turbo Expo 2007," ASME, Montreal, Canada, 2007, pp. 39–50,  
doi:[10.1115/GT2007-27222](https://doi.org/10.1115/GT2007-27222).
- [59] Burcham, F. W., Hughes, D. L., and Holzman, J. K., "Steady-state and dynamic pressure phenomena in the propulsion system of an F-111A airplane," Tech. Rep. NASA TN D-7328, Edwards, CA, July, 1973.
- [60] Baumbick, R. J., "Device for Producing Dynamic Distortion Patterns at Inlets of Air-breathing Engines," Tech. rep. NASA TM X-2026, 1970.
- [61] Biesiadny, T. J., McAulay, J. E., and Meyer, C. L., "Technique for inducing controlled steady-state and dynamic inlet pressure disturbances for jet engine tests," Tech. rep. NASA TM X-1946, 1969.
- [62] Sanders, B. W. and Weir, L. J., "Aerodynamic Design of a Dual-Flow Mach 7 Hypersonic Inlet System for a Turbine-Based Combined-Cycle Hypersonic Propulsion System," Tech. Rep. NASA CR 2008-215214, June, 2008.
- [63] Foster, L., Saunders, J., Sanders, B., and Weir, L., "Highlights from a Mach 4 Experimental Demonstration of Inlet Mode Transition for Turbine-Based Combined Cycle Hypersonic Propulsion," in "48th AIAA/ASME/SAE/ASEE Joint Propulsion Conference & Exhibit," American Institute of Aeronautics and Astronautics, Reston, Virginia, Joint Propulsion Conferences, 2012,  
doi:[10.2514/6.2012-4143](https://doi.org/10.2514/6.2012-4143).
- [64] Slater, J. and Saunders, J., "CFD Simulation of Hypersonic TBCC Inlet Mode Transition," in "16th AIAA/DLR/DGLR International Space Planes and Hypersonic Systems and Technologies Conference," American Institute of Aeronautics and Astronautics, Reston, Virginia,

- International Space Planes and Hypersonic Systems and Technologies Conferences, 2009, doi:[10.2514/6.2009-7349](https://doi.org/10.2514/6.2009-7349).
- [65] Wenzel, L. M., "Experimental investigation of the effects of pulse pressure distortions imposed on the inlet of a turbofan engine," Tech. rep. NASA TM X-1928, 1969.
- [66] Ellis, S. and Brownstein, B., "A procedure for estimating maximum time-variant distortion levels with limited instrumentation," in "8th Joint Propulsion Specialist Conference," American Institute of Aeronautics and Astronautics, Reston, Virginia, 1972, doi:[10.2514/6.1972-1099](https://doi.org/10.2514/6.1972-1099).
- [67] Calogeras, J. E., "Instantaneous distortion investigation," Tech. rep. NASA TM X-68189, 1973.
- [68] Motycka, D., "Determination of maximum expected instantaneous distortion patterns from statistical properties of inlet pressure data," in "12th Propulsion Conference," American Institute of Aeronautics and Astronautics, Reston, Virginia, Joint Propulsion Conferences, 1976, doi:[10.2514/6.1976-705](https://doi.org/10.2514/6.1976-705).
- [69] Nimmen, J. V. and Bruno, C., "NASA Historical Data Book, 1958-1968," Tech. rep. NASA SP-4012, 1974.
- [70] Costakis, W. G., "Character of random inlet pressure fluctuations during flights of F-111A airplane," Tech. Rep. NASA TM X-3540, Cleveland, OH, May, 1977.
- [71] Sanders, M., "An evaluation of statistical methods for the prediction of maximum time-variant inlet total pressure distortion," in "16th Joint Propulsion Conference," American Institute of Aeronautics and Astronautics, Reston, Virginia, Joint Propulsion Conferences, 1980, doi:[10.2514/6.1980-1110](https://doi.org/10.2514/6.1980-1110).
- [72] Brilliant, H. and Bauer, C., "Comparison of estimated with measured maximum instantaneous distortion using flight data from an axisymmetric mixed compression inlet," in "13th Propulsion Conference," American Institute of Aeronautics and Astronautics, Reston, Virginia, 1977, doi:[10.2514/6.1977-876](https://doi.org/10.2514/6.1977-876).
- [73] Stevens, C., Olpivant, R., and Spong, E., "Evaluation of a statistical method for determining peak inlet flow distortion using F-15 and F-18 data," in "16th Joint Propulsion Conference," American Institute of Aeronautics and Astronautics, Reston, Virginia, 1980, doi:[10.2514/6.1980-1109](https://doi.org/10.2514/6.1980-1109).
- [74] Stevens, C., Spong, E., Nugent, J., and Neumann, H., "Reynolds number, scale and frequency content effects on F-15 inlet instantaneous distortion," in "17th Aerospace Sciences Meeting," American Institute of Aeronautics and Astronautics, Reston, Virginia, 1979, doi:[10.2514/6.1979-104](https://doi.org/10.2514/6.1979-104).
- [75] Marous, J. and Sedlock, D., "An analog editing system for inlet dynamic flow distortion, DYNADEC - Past, present and future," in "16th Joint Propulsion Conference," American Institute of Aeronautics and Astronautics, Reston, Virginia, 1980, doi:[10.2514/6.1980-1108](https://doi.org/10.2514/6.1980-1108).

- [76] Costakis, W. G., “Analog Computer Implementation of Four Instantaneous Distortion Indices,” Tech. Rep. NASA TM X-2993, Cleveland, OH, March 1974.
- [77] Graber, E. J., J. and Braithwaite, W. M., “Summary of Recent Investigations of Inlet Flow Distortion Effect on Engine Stability,” Tech. rep. NASA TM X-71505, Cleveland, OH, 1974.
- [78] Mitchell, G. A., “Effect of inlet ingestion of a wing tip vortex on compressor face flow and turbojet stall margin,” Tech. rep. NASA TM X-3246, 1975.
- [79] McAulay, J. E., “Effect of Dynamic Variations in Engine-Inlet Pressure on the Compressor System of a Twin-Spool Turbofan Engine,” Tech. rep. NASA TM X-2081, 1970.
- [80] Evans, D. G., DeBogdan, C. E., Soeder, R. H., and Pleban, E. J., “Some Comparisons of the flow Characteristics of a Turbofan Compressor System with and without Inlet Pressure Distortion,” Tech. rep. NASA TM X-71574, 1974.
- [81] Debogdan, C. E., Dicus, J. H., Evans, D. G., and Soeder, R. H., “Effect of a 180 deg-extent inlet pressure distortion on the internal flow conditions of a TF30-P-3,” Tech. Rep. NASA TM X-3267, September, 1975.
- [82] Mazzawy, R. S. and Banks, G. A., “Modeling and analysis of the TF30-P-3 compressor system with inlet pressure distortion,” Tech. rep. NASA CR-134996, 1976.
- [83] King, R. W., Schuermun, J. A., and Muller, R. G., “Analysis of distortion data from TF30-P-3 mixed compression inlet test,” Tech. Rep. NASA CR-2686, June, 1976.
- [84] Burstadt, P. L. and Wenzel, L. M., “A method to account for variation of average compressor inlet pressure during instantaneous distortion analyses,” Tech. rep. NASA TM X-73438, Cleveland, OH, 1976.
- [85] Boller, S., One-Dimensional Dynamic Wake Response in an Isolated Rotor due to Inlet Total Pressure Distortion, MS thesis, Virginia Polytechnic Institute and State University, 1998.
- [86] Cotter, H. N., “Integration of Inlet and Engine - An Engine Man’s Point of View,” in “Air Transportaion Meeting,” Society of Automotive Engineers, New York, 1968,  
doi:[10.4271/680286](https://doi.org/10.4271/680286).
- [87] Dicus, J. H., “FORTRAN program to generate engine inlet flow contour maps and distortion parameters,” Tech. rep. NASA TM X-2967, 1974.
- [88] Davis, D. O., Friedlander, D. J., Saunders, J. D., Frate, F. C., and Foster, L. E., “Calibration of the NASA GRC 16 inch Mass-Flow Plug,” in “ASME 2012 Fluids Engineering Division Summer Meeting,” ASME, Rio Grande, PR, 2012, pp. 269–277,  
doi:[10.1115/FEDSM2012-72266](https://doi.org/10.1115/FEDSM2012-72266).
- [89] Benedict, R. P., “Principles of Conventional Pressure Transducers,” in “Fundamentals of Temperature, Pressure, and Flow Measurements,” John Wiley & Sons, Inc., Hoboken, NJ, USA, pp. 322–334, 1984,  
doi:[10.1002/9780470172698.ch16](https://doi.org/10.1002/9780470172698.ch16).
- [90] Rodi, W., “Comparison of LES and RANS calculations of the flow around bluff bodies,” Journal of Wind Engineering and Industrial Aerodynamics, Vol. 69-71, 1997, pp. 55–75.  
doi:[10.1016/S0167-6105\(97\)00147-5](https://doi.org/10.1016/S0167-6105(97)00147-5).

- [91] Germano, M., Piomelli, U., Moin, P., and Cabot, W. H., "A dynamic subgrid-scale eddy viscosity model," Phys. Fluids A Fluid Dyn., Vol. 3, No. 7, 1991, p. 1760.  
doi:[10.1063/1.857955](https://doi.org/10.1063/1.857955).
- [92] Tummers, B., "DataThief," 2006.
- [93] Flower, A., McKenna, J. W., and Upreti, G., "Validity and Reliability of GraphClick and DataThief III for Data Extraction," Behavior Modification, Vol. 40, No. 3, 2016, pp. 396–413.  
doi:[10.1177/0145445515616105](https://doi.org/10.1177/0145445515616105).
- [94] Lee, K. R., Park, J. H., and Kim, K. H., "High-Order Interpolation Method for Overset Grid Based on Finite Volume Method," AIAA Journal, Vol. 49, No. 7, 2011, pp. 1387–1398.  
doi:[10.2514/1.J050620](https://doi.org/10.2514/1.J050620).
- [95] Meijering, E. H. W., Zuiderveld, K. J., and Viergever, M. A., "Image reconstruction by convolution with symmetrical piecewise nth-order polynomial kernels," IEEE Transactions on Image Processing, Vol. 8, No. 2, 1999, pp. 192–201.  
doi:[10.1109/83.743854](https://doi.org/10.1109/83.743854).
- [96] LARGUECHE, F.-Z. B., "Estimating Soil Contamination with Kriging Interpolation Method," American Journal of Applied Sciences, Vol. 3, No. 6, 2006, pp. 1894–1898.  
doi:[10.3844/ajassp.2006.1894.1898](https://doi.org/10.3844/ajassp.2006.1894.1898).
- [97] Kreyszig, E., Advanced Engineering Mathematics, John Wiley & Sons, New York, NY, 8th ed., 1999.
- [98] Meijering, E., "A chronology of interpolation: from ancient astronomy to modern signal and image processing," Proceedings of the IEEE, Vol. 90, No. 3, 2002, pp. 319–342.  
doi:[10.1109/5.993400](https://doi.org/10.1109/5.993400).
- [99] Amanatiadis, A. and Andreadis, I., "A survey on evaluation methods for image interpolation," Measurement Science and Technology, Vol. 20, No. 10, 2009, pp. 104–115.  
doi:[10.1088/0957-0233/20/10/104015](https://doi.org/10.1088/0957-0233/20/10/104015).
- [100] Jayroe, R. R., "Nearest Neighbor, Bilinear Interpolation and Bicubic Interpolation Geographic Correction Effects on LandsAT Imagery," Tech. rep. NASA TM X-73348, Huntsville, AL, 1976.
- [101] Schoenberg, I. J., "Contributions to the Problem of Approximation of Equidistant Data by Analytic Functions," in "I. J. Schoenberg Selected Papers," Birkhäuser Boston, Boston, MA, pp. 3–57, 1988.
- [102] Chapra, S. C. and Canale, R. P., Numerical Methods for Engineers, McGraw-Hill Higher Education, Boston, 5th ed., 2006.
- [103] Nelson, B., Yang, F. Y., Carlino, R., Perez, A. D., Faber, N., Henze, C., Göktu, A., Toole, C. O., Swenson, J., and Stupl, J., "Implementation of an Open-Scenario, Long-Term Space Debris Simulation Approach," in "AMOS 2015 Advanced Maui Optical and Space Surveillance Conference," Wailea, HI, 2015.

- [104] Thevenaz, P., Blu, T., and Unser, M., "Interpolation revisited [medical images application]," IEEE Transactions on Medical Imaging, Vol. 19, No. 7, 2000, pp. 739–758.  
doi:[10.1109/42.875199](https://doi.org/10.1109/42.875199).
- [105] Lehmann, T. M., Gonner, C., and Spitzer, K., "Survey: interpolation methods in medical image processing," IEEE Transactions on Medical Imaging, Vol. 18, No. 11, 1999, pp. 1049–1075.  
doi:[10.1109/42.816070](https://doi.org/10.1109/42.816070).
- [106] Meijering, E. H. W., Niessen, W. J., and Viergever, M. A., "Quantitative evaluation of convolution-based methods for medical image interpolation," Medical Image Analysis, Vol. 5, No. 2, 2001, pp. 111–126.  
doi:[10.1016/S1361-8415\(00\)00040-2](https://doi.org/10.1016/S1361-8415(00)00040-2).
- [107] Shoemake, K., "Animating rotation with quaternion curves," ACM SIGGRAPH Computer Graphics, Vol. 19, No. 3, 1985, pp. 245–254.  
doi:[10.1145/325165.325242](https://doi.org/10.1145/325165.325242).
- [108] Forrester, A. I. J., Sbester, A., and Keane, A. J., Engineering Design via Surrogate Modelling, John Wiley & Sons, Ltd, Chichester, UK, 2008,  
doi:[10.1002/9780470770801](https://doi.org/10.1002/9780470770801).
- [109] Van Beers, W. C. M., "Kriging Metamodeling in Discrete-Event Simulation: An Overview," in "Proceedings of the Winter Simulation Conference, 2005.", IEEE, Vol. 2005, 2005, pp. 202–208,  
doi:[10.1109/WSC.2005.1574252](https://doi.org/10.1109/WSC.2005.1574252).
- [110] Li, J. and Heap, A. D., "A review of comparative studies of spatial interpolation methods in environmental sciences: Performance and impact factors," Ecological Informatics, Vol. 6, No. 3-4, 2011, pp. 228–241.  
doi:[10.1016/j.ecoinf.2010.12.003](https://doi.org/10.1016/j.ecoinf.2010.12.003).
- [111] Jassim, F. A. and Altaany, F. H., "Image Interpolation Using Kriging Technique for Spatial Data," Canadian Journal on Image Processing and Computer, Vol. 4, No. 2.
- [112] Queipo, N. V., Haftka, R. T., Shyy, W., Goel, T., Vaidyanathan, R., and Kevin Tucker, P., "Surrogate-based analysis and optimization," Progress in Aerospace Sciences, Vol. 41, No. 1, 2005, pp. 1–28.  
doi:[10.1016/j.paerosci.2005.02.001](https://doi.org/10.1016/j.paerosci.2005.02.001).
- [113] Simpson, T. W., Mauery, T. M., Korte, J., and Mistree, F., "Kriging models for global approximation in simulation-based multidisciplinary design optimization," AIAA Journal, Vol. 39, No. 12, 2001, pp. 2233–2241.  
doi:[10.2514/3.15017](https://doi.org/10.2514/3.15017).
- [114] Koziel, S., Stainislav, O., and Leifsson, L., Surrogate-Based Modeling and Optimization, Springer New York, New York, NY, 2013,  
doi:[10.1007/978-1-4614-7551-4](https://doi.org/10.1007/978-1-4614-7551-4).
- [115] Hashemian, H. and Jiang, J., "Pressure transmitter accuracy," ISA Transactions, Vol. 48, No. 4, 2009, pp. 383–388.  
doi:[10.1016/j.isatra.2009.04.008](https://doi.org/10.1016/j.isatra.2009.04.008).

- [116] Barmish, B. R. and Lagoa, C. M., “The uniform distribution: A rigorous justification for its use in robustness analysis,” Mathematics of Control, Signals, and Systems, Vol. 10, No. 3, 1997, pp. 203–222.  
doi:[10.1007/BF01211503](https://doi.org/10.1007/BF01211503).
- [117] Landau, D. P. and Binder, K., A guide to Monte-Carlo simulations in statistical physics, Cambridge University Press, Cambridge, United Kingdom, 4th ed., 2015.
- [118] Le Maître, O. P. and Knio, O. M., Spectral Methods for Uncertainty Quantification, Scientific Computation, Springer Netherlands, Dordrecht, 1st ed., 2010,  
doi:[10.1007/978-90-481-3520-2](https://doi.org/10.1007/978-90-481-3520-2).
- [119] MATLAB, “MATLAB,” 2015.

# Appendix A

## Appendix I: YF12 Data Error

In order to get the YF12[1] raw pressure data, a program entitled DataThief[92] was used. DataThief works by the user selecting vertices for the axes and declaring their relative position. The user can then select individual points or a line and the program will calculate the coordinates of the data of interest.

DataThief itself has been studied recently and has been found to be reliable in estimating coordinates[93]. However, the original data is hand drawn and DataThief relies on the user to pick points when it comes to individual points.

An example of what the raw data looks like in the original paper is shown in figure A.2. In order to determine the inherent error in the hand drawn data points, the size of the data point was measured in pixels. Matlab's imtool graphical user interface was used to measure the size of various hand drawn points. The results are tabulated in table A.1

### A.1 Error on the Raw Data

The total axis size for figure A.2 is 0.2, which holds true across all the test cases and rings. The distance of the axis was measured in pixels as 195.5 pixels. To calculate the error, equation A.1 was used.  $P_{t,\infty}$  was the same for all test cases and can be found in table 3.3.

$$\tau_{abs} = \frac{max_{axis} - min_{axis}}{l_{axis}} s_{point} P_{t,\infty} \quad (A.1)$$



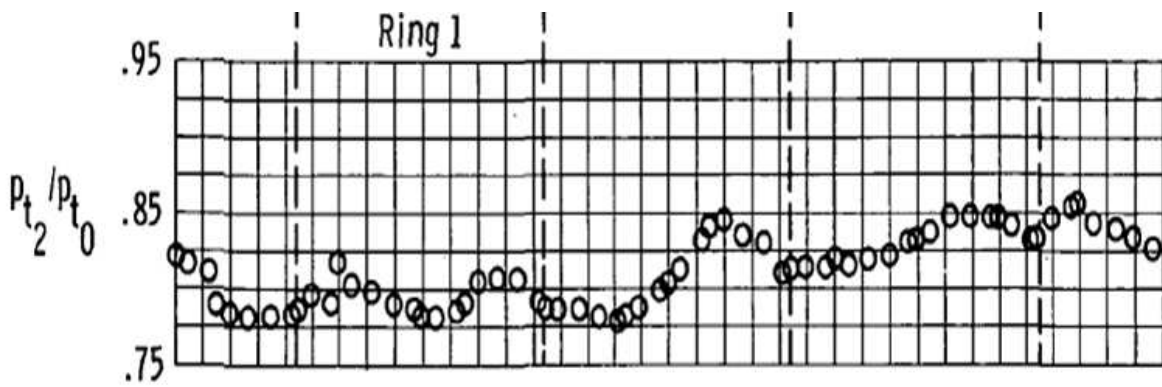


Figure A.1: YF12 raw data points for test case 1, ring 1 as shown in reference [1]. Image courtesy of NASA.

Figure A.2: YF12 raw data points for test case 1, ring 1 as shown in reference [1]. Image courtesy of NASA.

It found that the average error on the raw data was 0.264 psi. That is on the order of less than 2% of the overall pressure readings.

## A.2 Error on Picking Data Points

The other source of error was where the user placed the axis vertices as well as placing the cursor on the same point again and again. To test the former, a sample image was created with a known point, see figure A.3. The vertices were initially chosen and the captured data point cursor was placed on (0.5, 0.5) - the known exact answer. After that, the vertex points were removed from the figure and re-placed 10 times.

The results of picking vertices can be found in table A.2. Overall, there was a 0.26% mean error on the x-coordinate and a 0.55% error on the y-coordinate. This translates to a  $0.95^\circ$  on the angular location and a 0.0216 psi error on the pressure.

For the latter - picking the same point again and again - it is easier to analyze. DataThief shows the cursor coordinates, as figure A.4 shows. However, only the x-coordinate is known for the data. The y-coordinate is unknown. It is thus safe to say that there is likely a  $0.001^\circ$  (effectively

Table A.1: Pixel sizes of various sampled data points from test case 1, ring 1 from the YF12 raw data report.

Point Number	Point Size (pixels)
1	14.32
2	10.06
3	14.29
4	12.82
5	12.90
6	14.32
7	12.54
8	13.79
9	12.57
10	11.55
Average	12.92

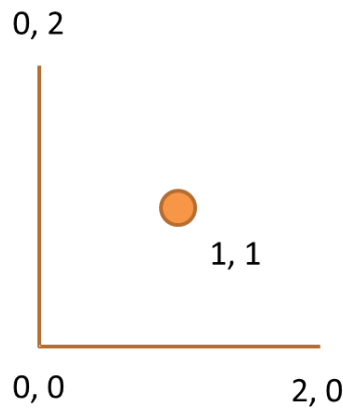


Figure A.3: Sample picture used to determine user error on picking vertices.

Table A.2: Coordinates of known point as picked by DataThief.

	x	y
1	0.5014	0.5065
2	0.5015	0.5015
3	0.5015	0.503
4	0.5031	0.503
5	0.5032	0.4998
6	0.5015	0.503
7	0.5031	0.5032
8	0.4999	0.4998
9	0.4982	0.5048
10	0.4998	0.503
Average	0.5013	0.5028

Table A.3: DataThief results for a single point being picked 10 times.

Trial	y
1	0.7734
2	0.7734
3	0.7722
4	0.7724
5	0.7728
6	0.7724
7	0.7723
8	0.7723
9	0.773
10	0.7742
Average	0.77284
Range	0.002

zero) error on the x-coordinate, but there could be a significant error on the y-coordinate. To test the y-coordinate error, the same point was picked 10 times from figure A.2.

There is a 0.002 range error on this y-coordinate. If this is multiplied by  $P_{t,\infty}$ , this results in a 0.0393 psi error.

### A.3 Overall Error

To calculate the overall error on the raw data from the YF12 experiment, the error of all the sources are added together. In this case, for the x-coordinate (the angular location), that's  $0.95^\circ$ . For the y-coordinate (the pressure), this translates to 0.325 psi error. This is around 2% error of the raw pressure data and is considered acceptably small. A sample image of test case 1, ring 1 data overlaid with the picked data can be found in figure A.5.

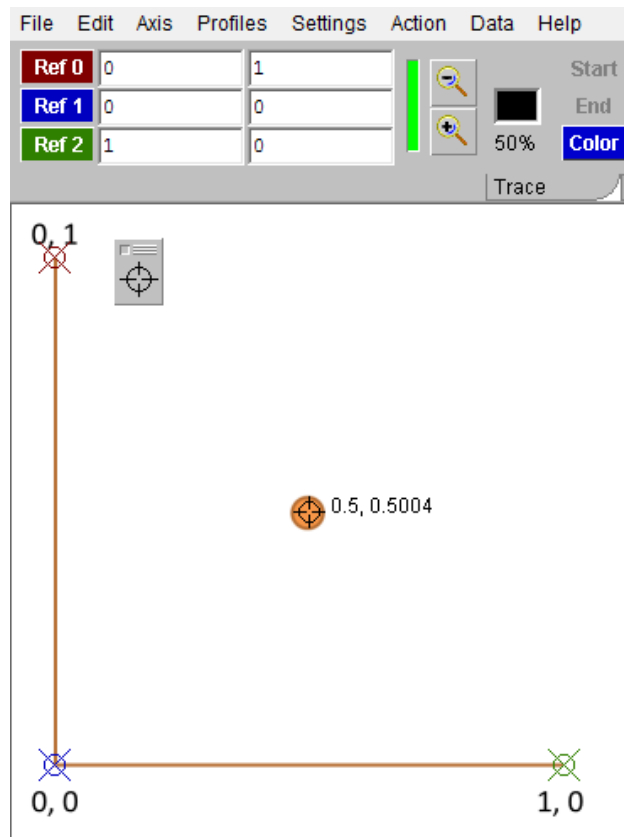


Figure A.4: Sample picture loaded in DataThief with DataThief provided coordinates displayed.

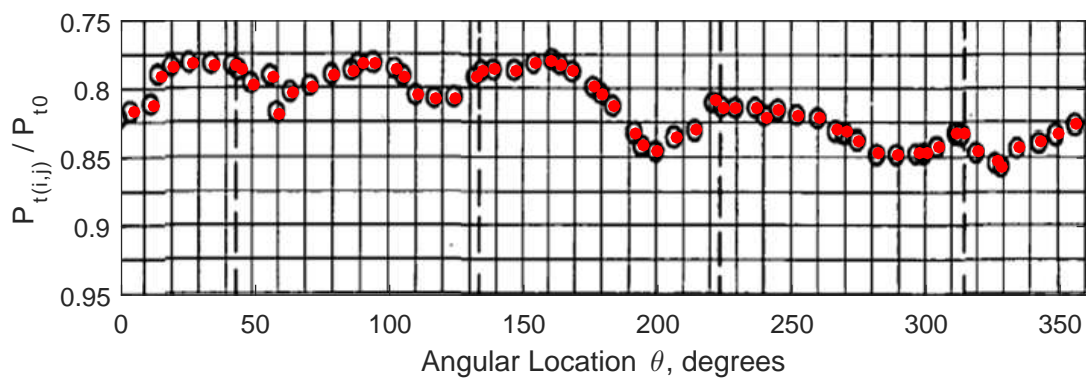


Figure A.5: The raw data from the report[1] overlaid with the points picked from DataThief in red.

# Appendix B

## Appendix II: NASA GUI

In the summer 2013 internship, a graphical user interface (GUI) was created for use in-situ in the wind tunnel during testing campaigns. As most of the wind tunnel testing in the 10 foot by 10 foot supersonic wind tunnel at GRC is done on third shift to ensure the power draw on the Cleveland power grid is not too taxing, the data reduction is usually not completed until after the testing campaign. In order to reduce cycle time, the GUI can read in data files in real time.

The LIMX resumed testing in the summer of 2015 in the 10 by 10 foot supersonic wind tunnel. In order to support NASA researchers view the distortion characteristics of the inlet in real time, the data analysis method described in section 3.1.2 on page 53 was distilled into the aforementioned GUI. Anyone in the control room can run the data reduction for each run once the data has been collected for a particular reading.

The tool, named WIDGI (see figure B.1 on the following page), can be run on any computer with the Matlab[119] application loaded onto it. WIDGI has two browse buttons, one for each file type: Dewetron to extract the dynamic readings and ESCORT to obtain the steady state measurements. In the user input panel, the user gives information about the Dewetron and ESCORT reading numbers, the associated run number, and the configuration. The user can then chose to plot the data, which generates three plots. The first is a so-called distortion cloud, which shows the user the distortion with respect to certain characteristic lines. Along with the cloud plot, the vehicle's configuration, such as angle of attack and cowl angle, are shown. Lastly, the third plot shows the Mach number of the wind tunnel and at the engine face. The plot can be saved for future reference.

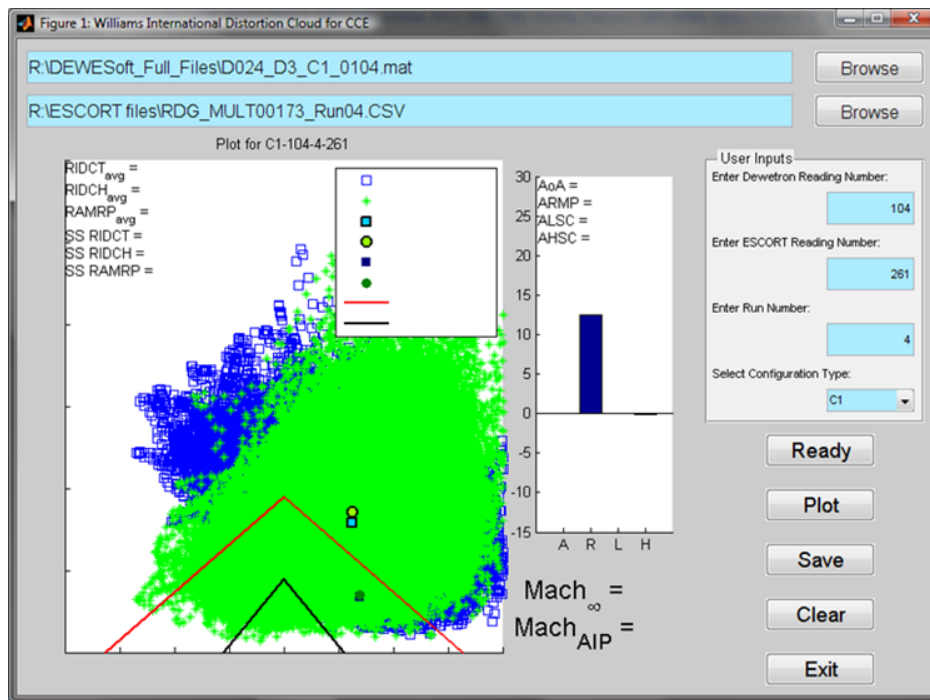


Figure B.1: The Williams International Distortion Graphical Interface (WIDGI) tool. The data is ITAR restricted and thus the results are redacted.

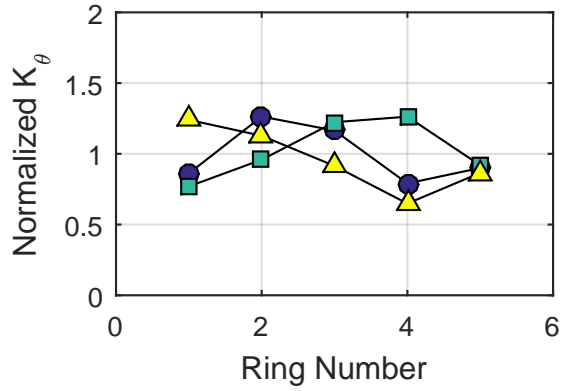
# Appendix C

## Appendix III: Full Interpolation Results

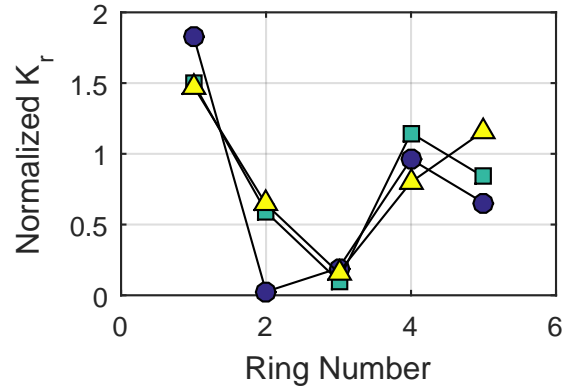
### C.1 YF12 Inlet

Table C.1: Distortion index results for the YF12 inlet

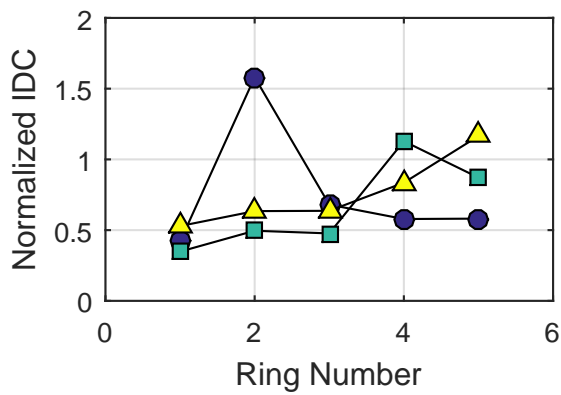
	$K_\theta$	$K_r$	$K_a$	$IDC$	$IDT$
TC1	0.512	0.255	0.767	0.0921	0.243
TC2	0.421	0.370	0.791	0.0640	0.192
TC3	0.336	0.337	0.673	0.0382	0.132



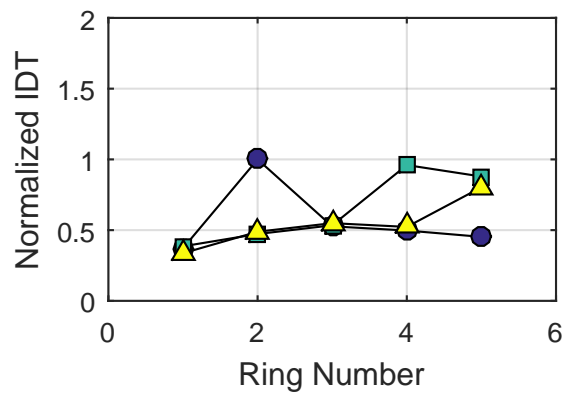
(a) Circumferential K-index



(b) Radial K-index



(c) Circumferential ID-index



(d) Combined ID-index

Figure C.1: Ring distortion indices, normalized by the overall index. Circles represent test case 1, squares represent test case 2, and triangles represent test case 3.



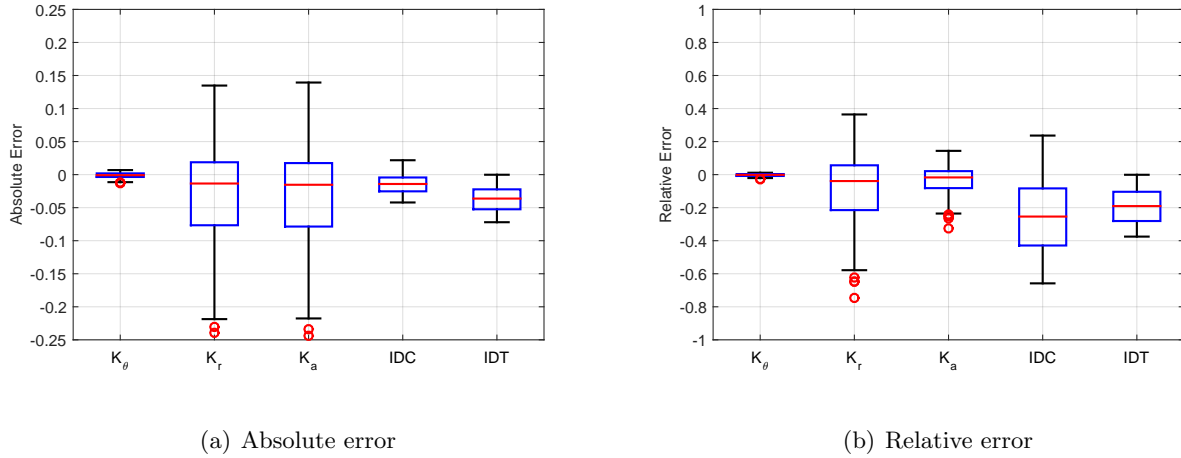


Figure C.2: Absolute and relative errors in the distortion indices for the YF12 inlet.

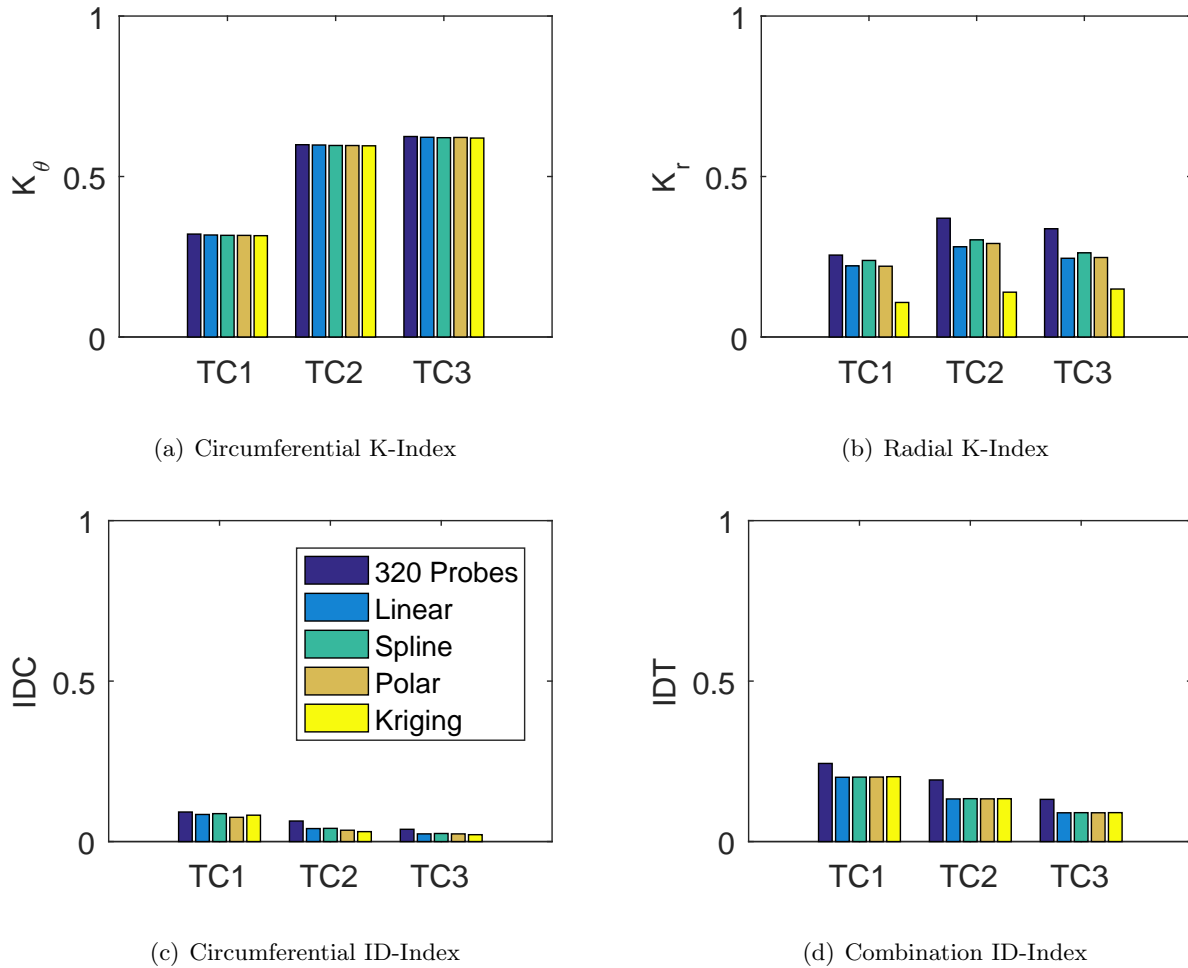
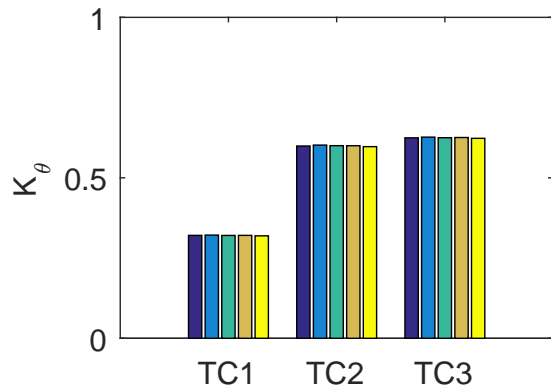
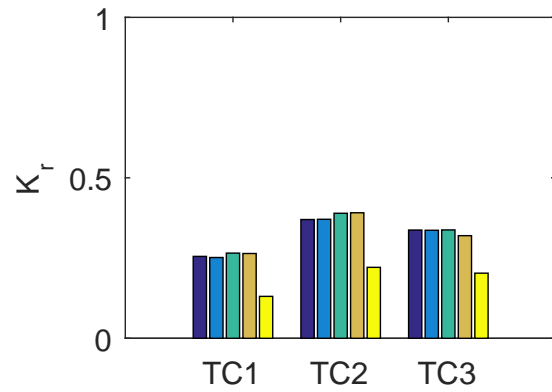


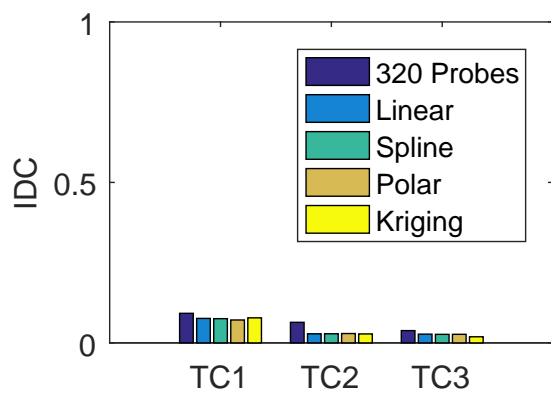
Figure C.3: Barplots of the distortion indices for the zeroth clocking for the YF12 inlet.



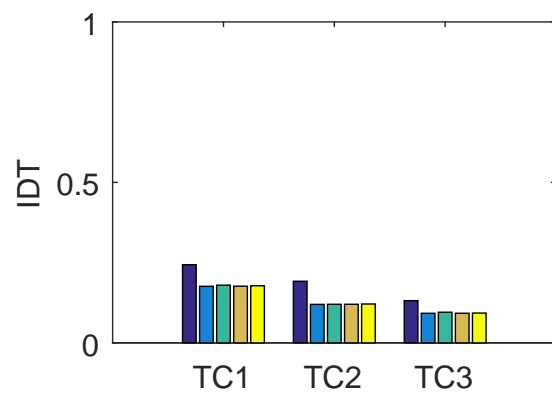
(a) Circumferential K-Index



(b) Radial K-Index



(c) Circumferential ID-Index



(d) Combination ID-Index

Figure C.4: Barplots of the distortion indices for the first clocking for the YF12 inlet.

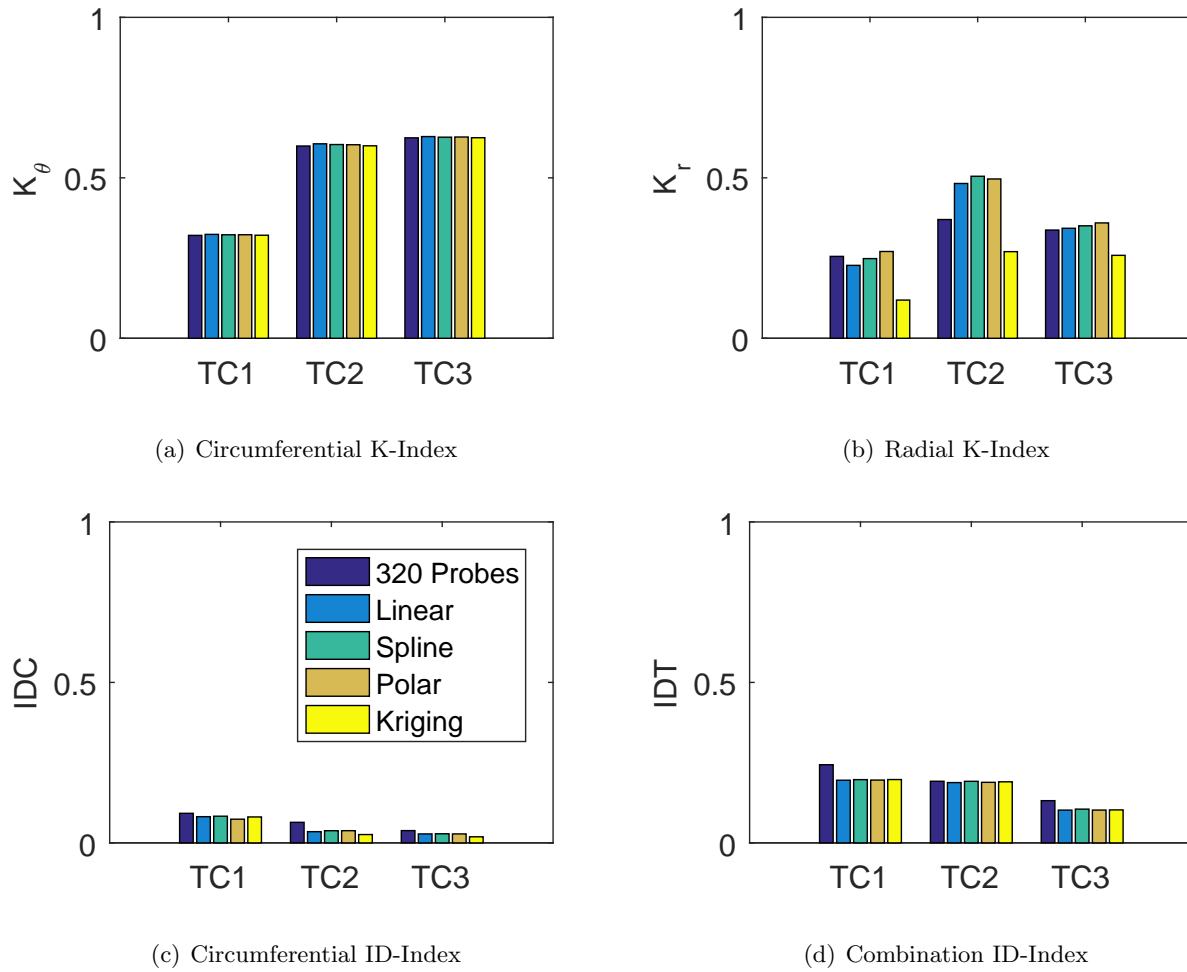
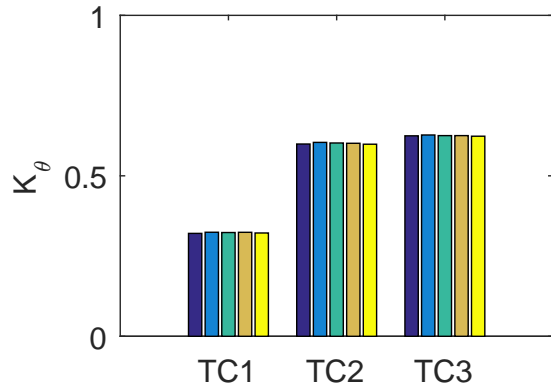
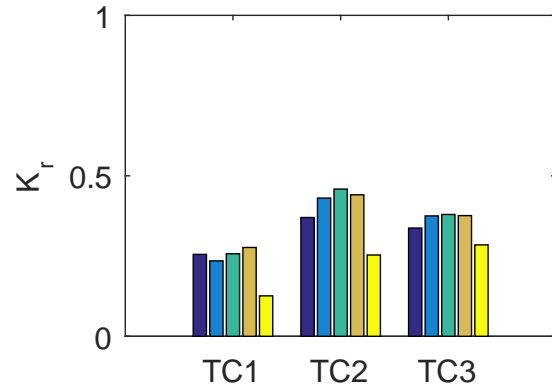


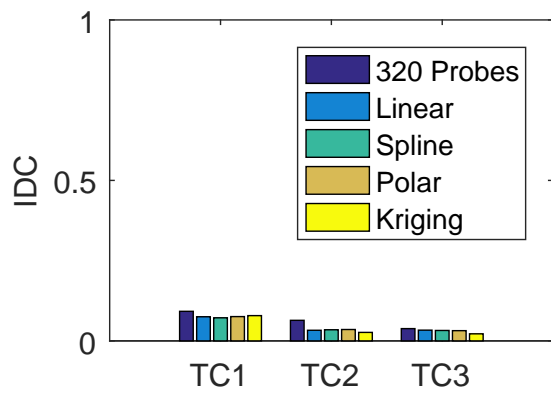
Figure C.5: Barplots of the distortion indices for the second clocking for the YF12 inlet.



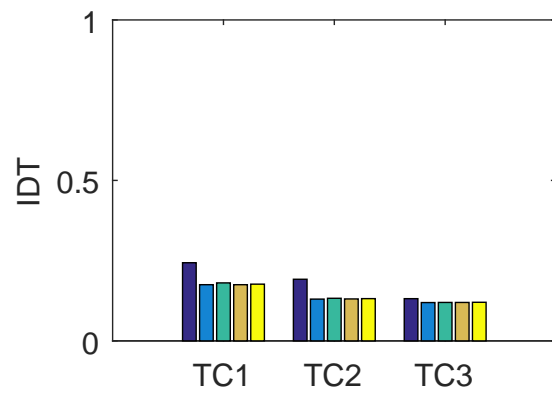
(a) Circumferential K-Index



(b) Radial K-Index

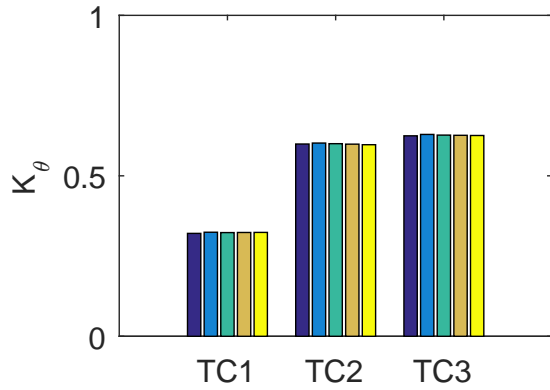


(c) Circumferential ID-Index

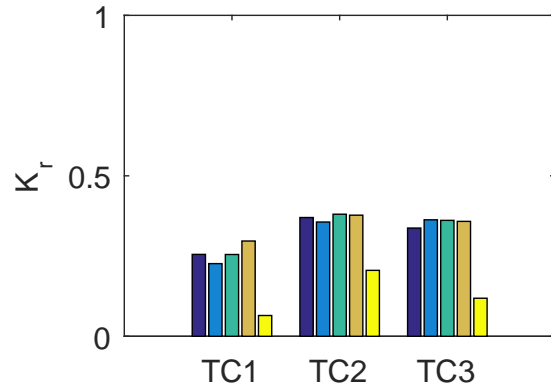


(d) Combination ID-Index

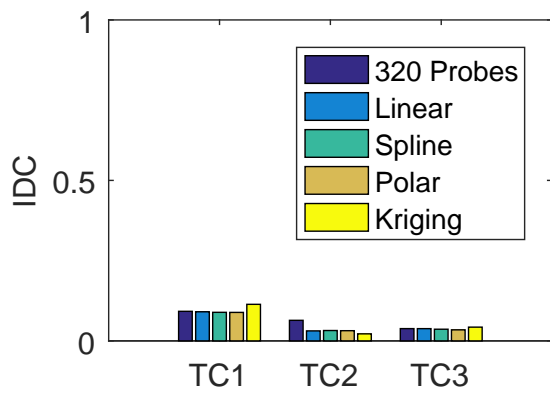
Figure C.6: Barplots of the distortion indices for the third clocking for the YF12 inlet.



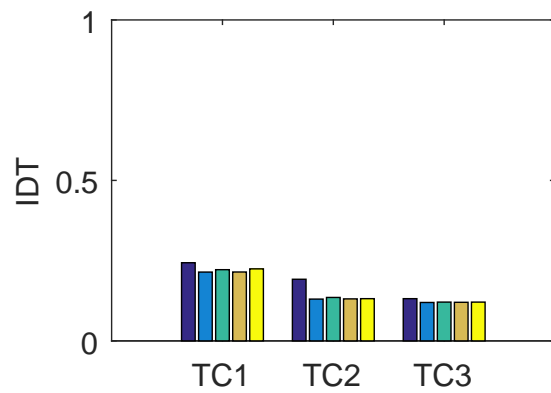
(a) Circumferential K-Index



(b) Radial K-Index

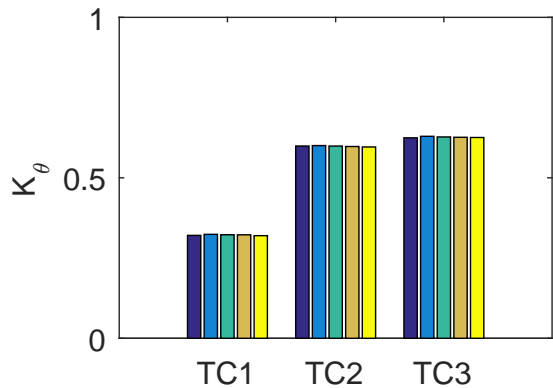


(c) Circumferential ID-Index

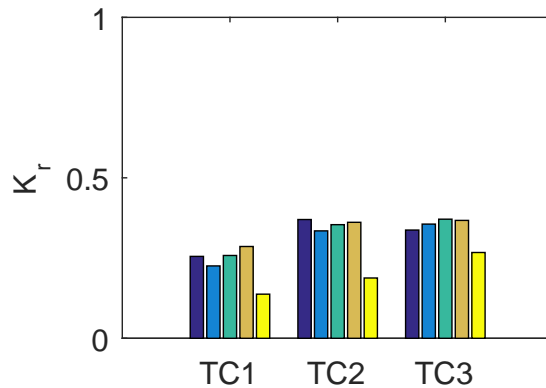


(d) Combination ID-Index

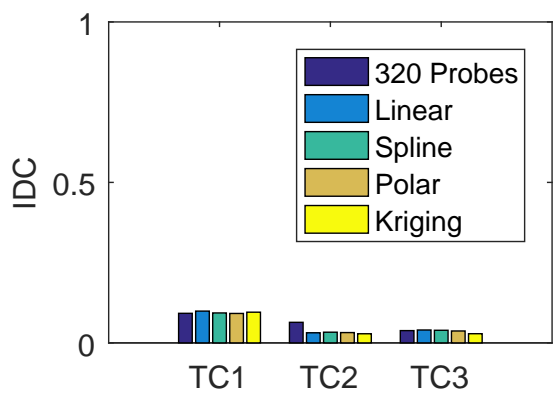
Figure C.7: Barplots of the distortion indices for the fourth clocking for the YF12 inlet.



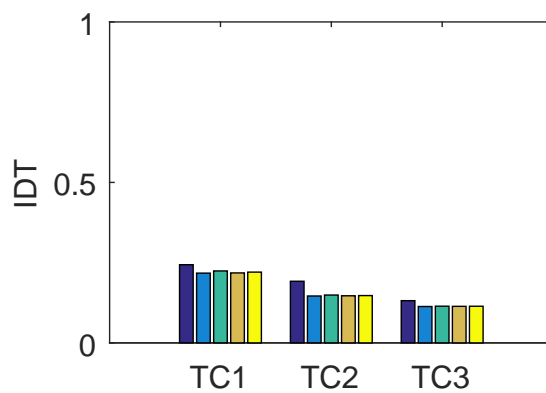
(a) Circumferential K-Index



(b) Radial K-Index

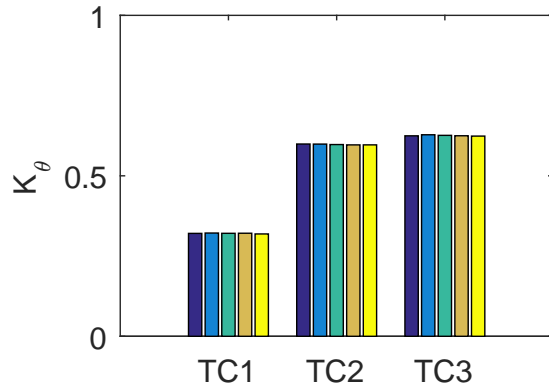


(c) Circumferential ID-Index

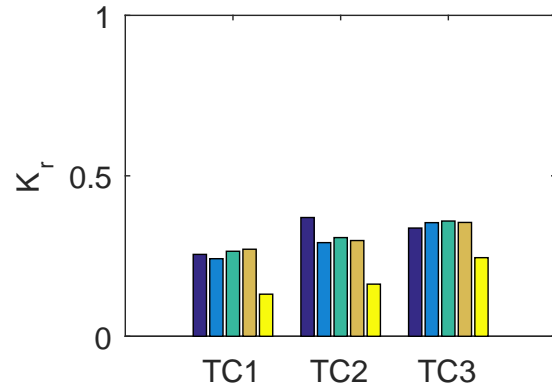


(d) Combination ID-Index

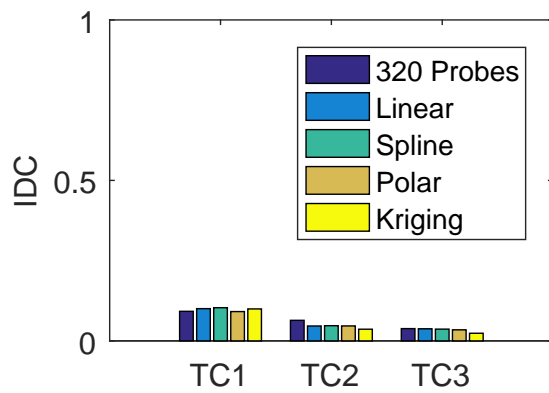
Figure C.8: Barplots of the distortion indices for the fifth clocking for the YF12 inlet.



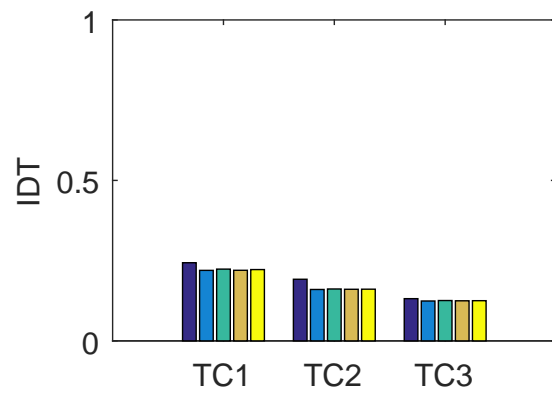
(a) Circumferential K-Index



(b) Radial K-Index

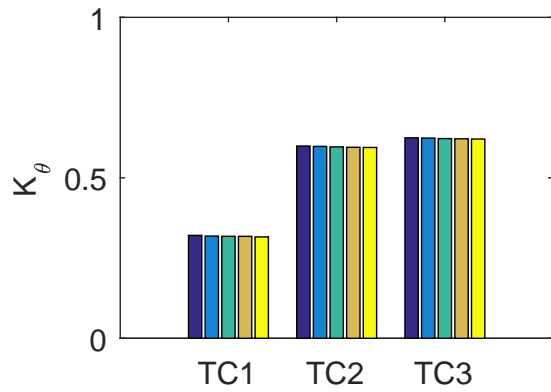


(c) Circumferential ID-Index

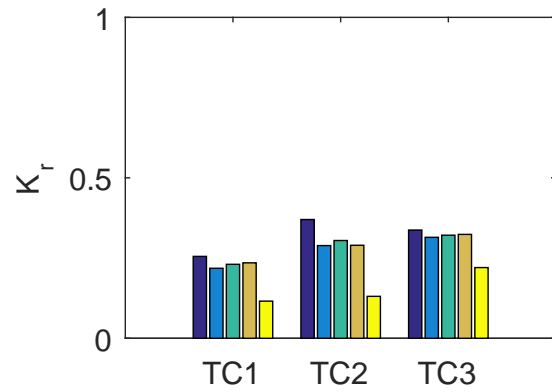


(d) Combination ID-Index

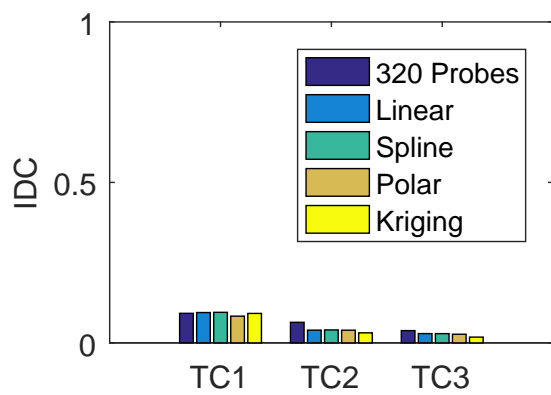
Figure C.9: Barplots of the distortion indices for the sixth clocking for the YF12 inlet.



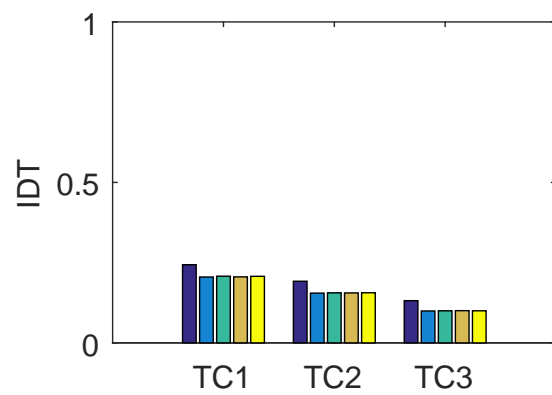
(a) Circumferential K-Index



(b) Radial K-Index



(c) Circumferential ID-Index



(d) Combination ID-Index

Figure C.10: Barplots of the distortion indices for the seventh clocking for the YF12 inlet.



## C.1.1 Test Case 1

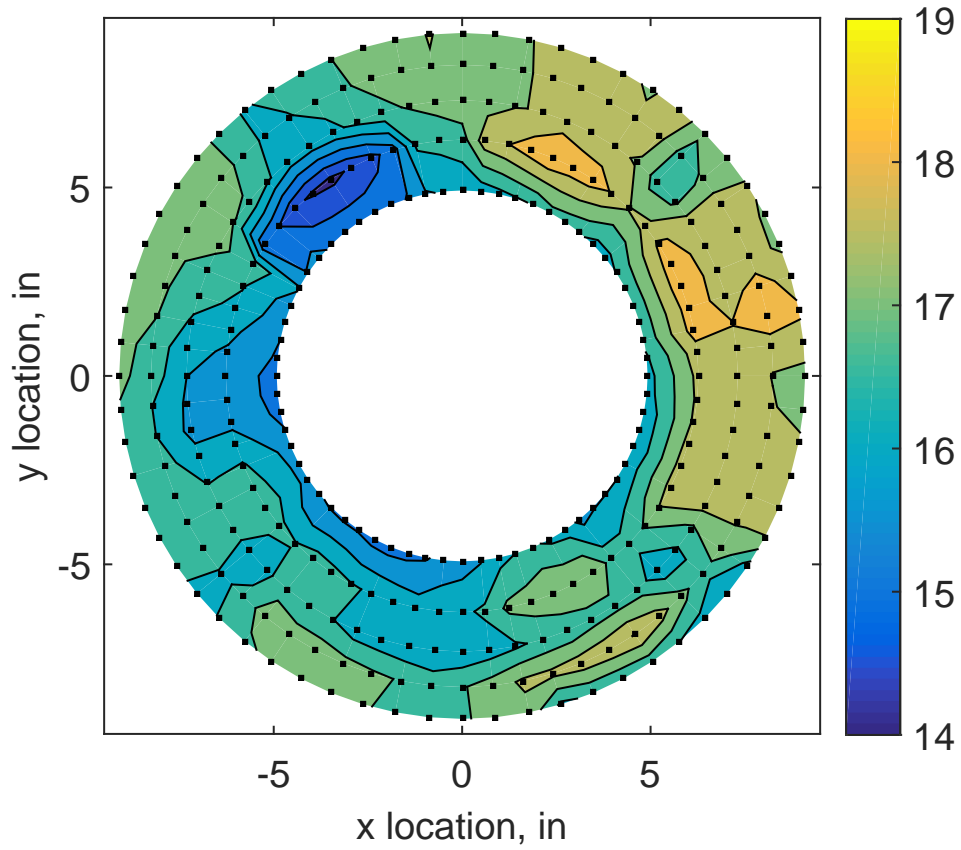


Figure C.11: YF12 test case 1 raw pressure contour created with 320 probes.

### C.1.1.1 Zeroth Clocking

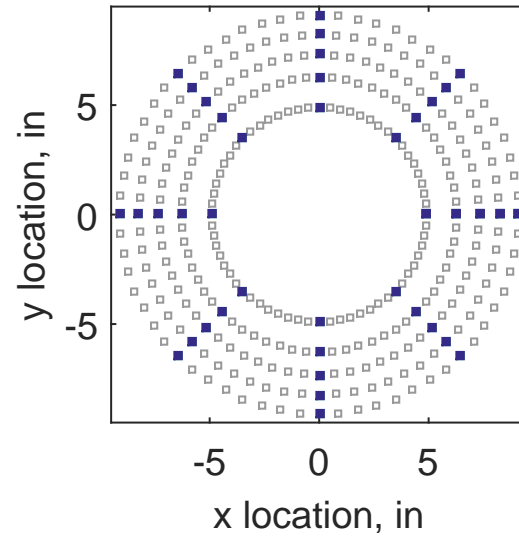


Figure C.12: Zeroth clocking probe position

Table C.2: Interpolation results for the YF12 inlet test case 1, clocking C1.

	Mean	Std. Dev.	Over-Prediction	In Tolerance	Under-Prediction
Linear	-0.166	0.204	89	22	169
Spline	-0.212	0.189	67	35	178
Polar	-0.225	0.182	94	-18	204
Kriging	-0.212	0.252	72	15	193

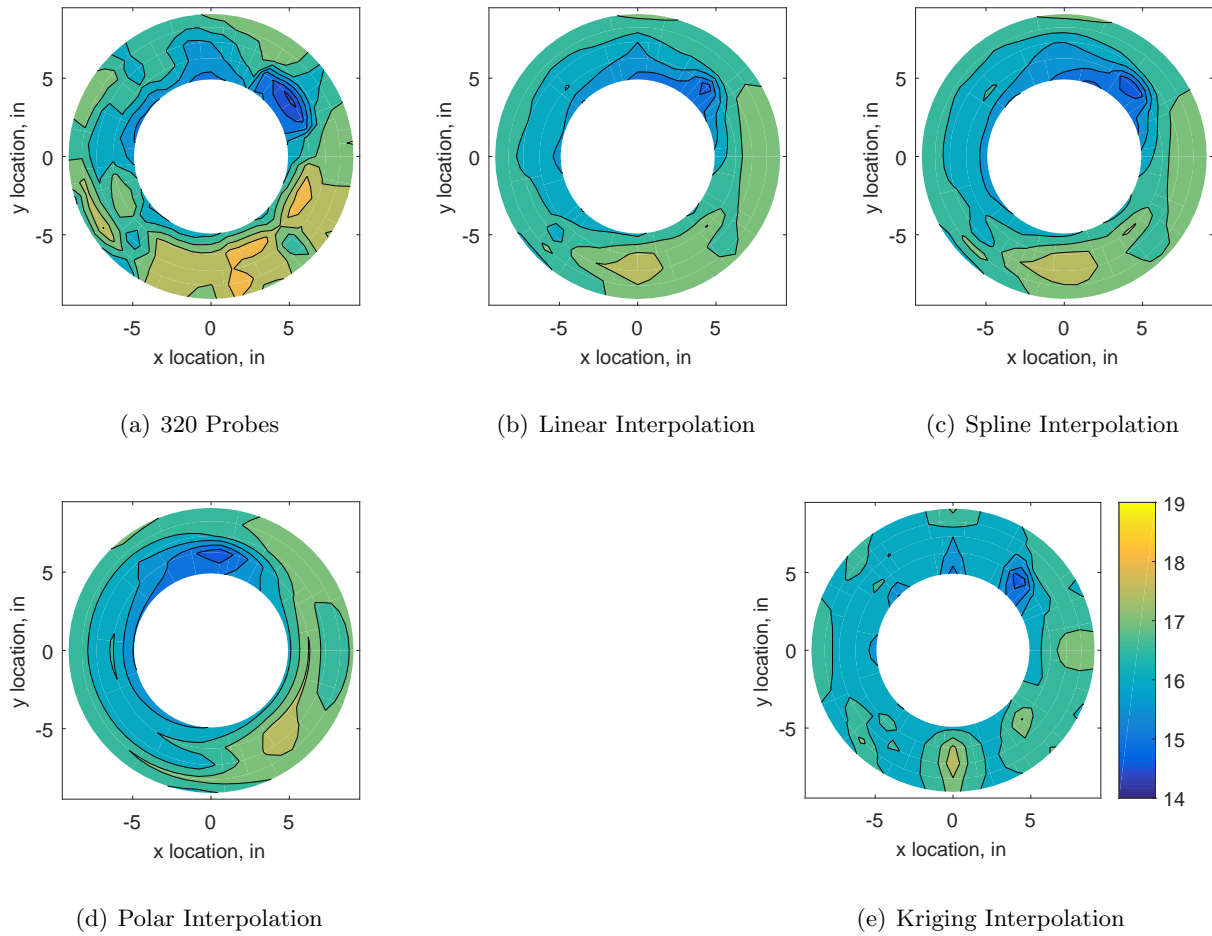
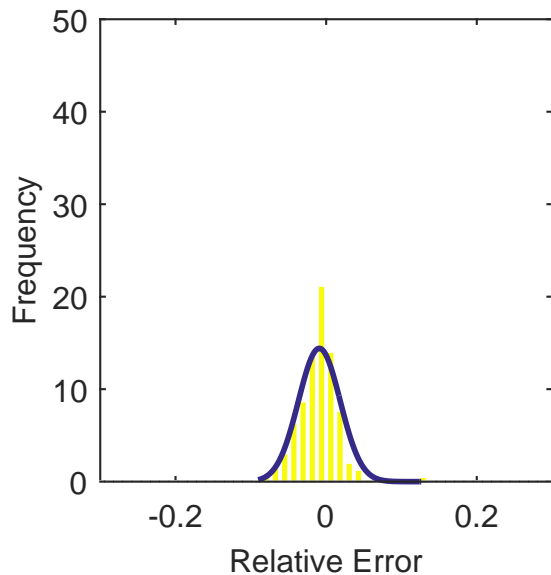
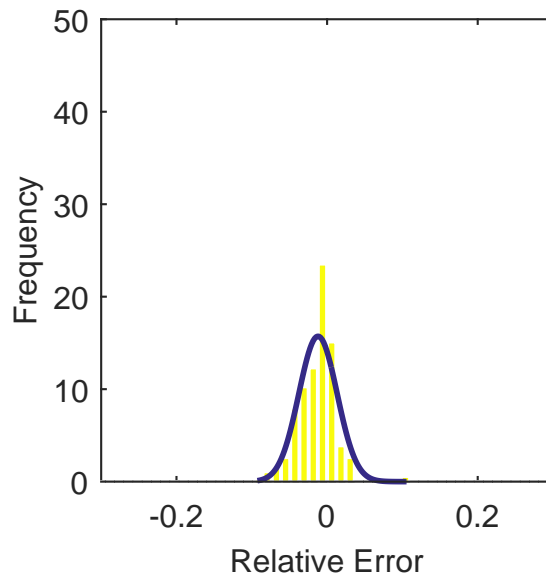


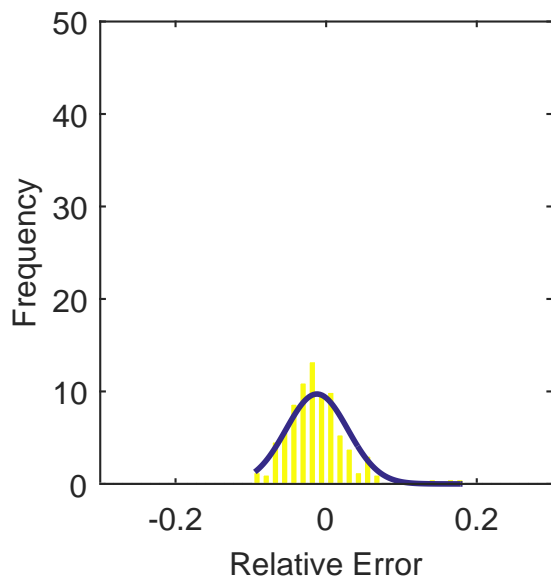
Figure C.13: Contour plots for the raw and interpolated values for the YF12 inlet.



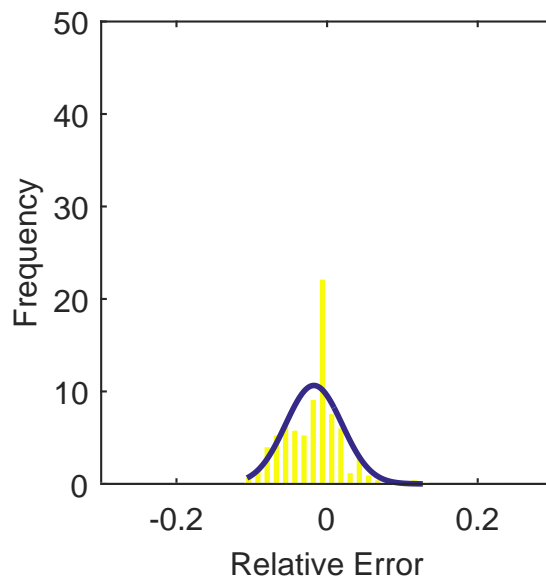
(a) Linear Interpolation Error



(b) Spline Interpolation Error

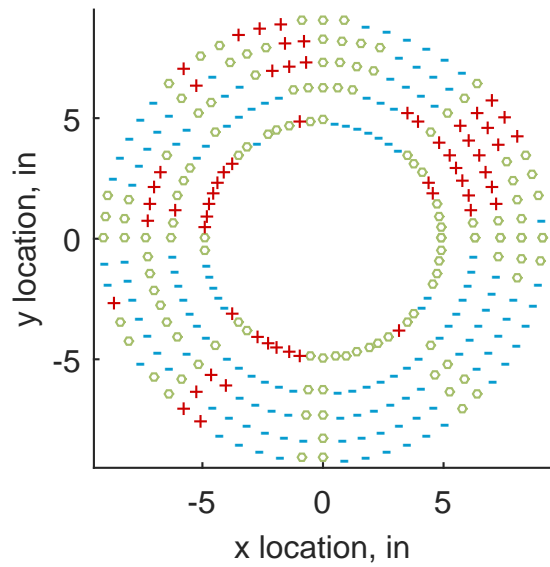


(c) Polar Interpolation Error

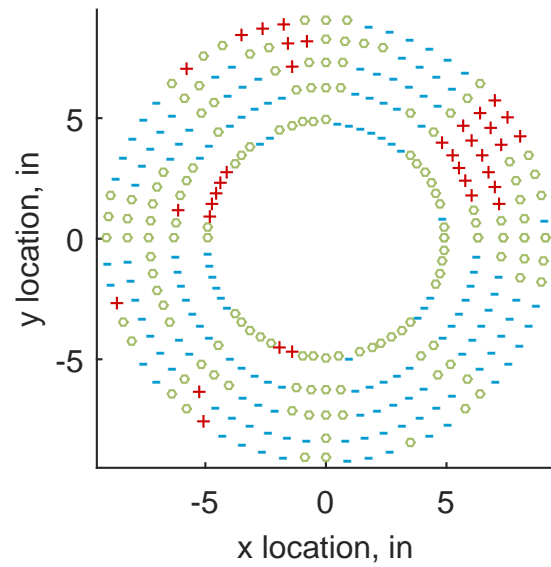


(d) Kriging Interpolation Error

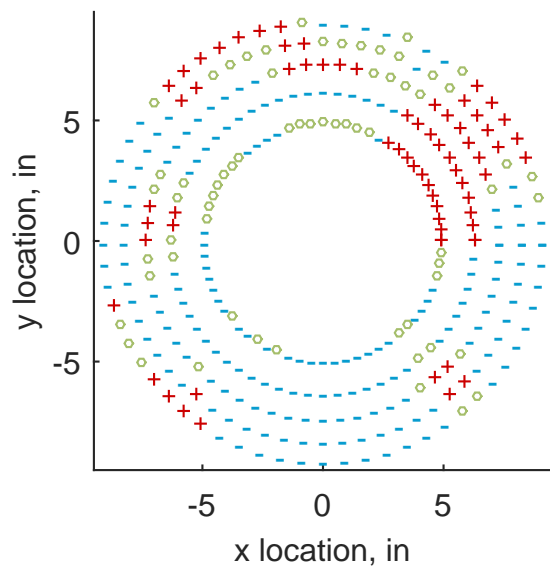
Figure C.14: Relative error for various interpolation schemes of test case 1, zeroth clocking for the YF12 inlet.



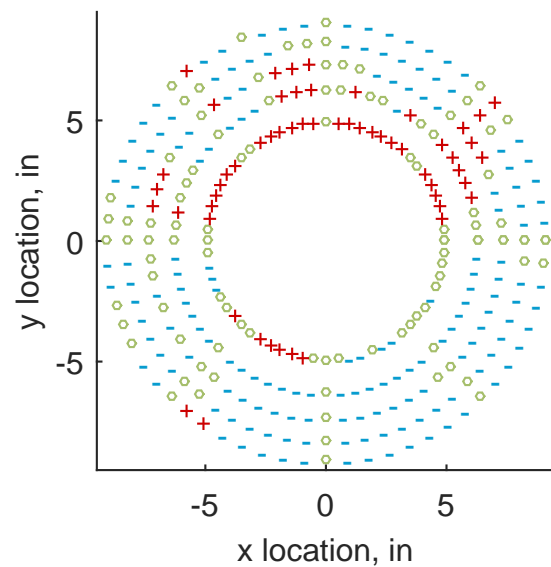
(a) Linear Interpolation



(b) Spline Interpolation



(c) Polar Interpolation



(d) Kriging Interpolation

Figure C.15: Interpolation error for the YF12 inlet - symbols show locations that are within tolerance (o), over-predicted (+), and under-predicted (-).

Table C.3: Interpolation effects on the derived quantities for the IMX inlet run number R300, clocking C1.

	$K_\theta$	$K_r$	$K_a$	$IDC$	$IDT$
Linear	0.318	0.222	0.539	0.084	0.200
Spline	0.317	0.238	0.555	0.087	0.201
Polar	0.317	0.221	0.537	0.076	0.201
Kriging	0.316	0.108	0.423	0.082	0.202

### C.1.1.2 First Clocking

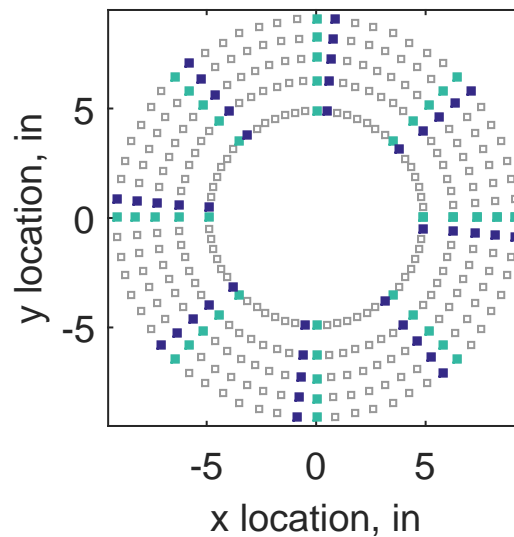
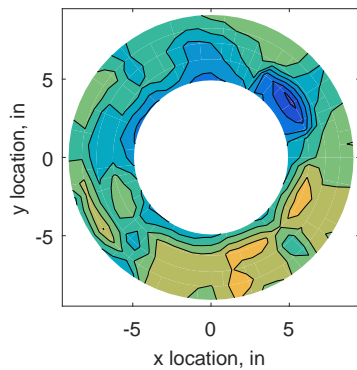


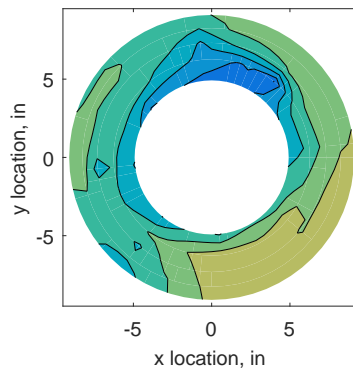
Figure C.16: First clocking probe position

Table C.4: Interpolation results for the YF12 inlet test case 1, clocking C2.

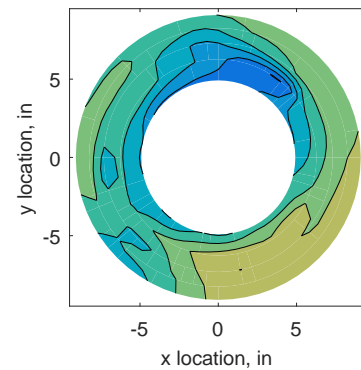
	Mean	Std. Dev.	Over-Prediction	In Tolerance	Under-Prediction
Linear	0.045	0.195	146	33	101
Spline	-0.004	0.190	129	31	120
Polar	0.008	0.160	156	-18	142
Kriging	-0.004	0.255	115	26	139



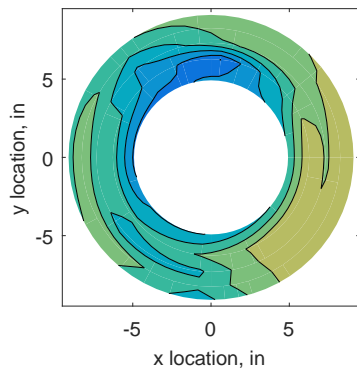
(a) 320 Probes



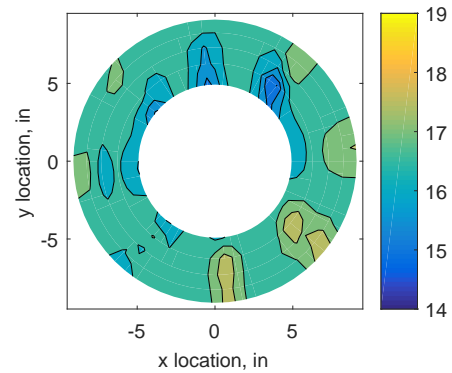
(b) Linear Interpolation



(c) Spline Interpolation

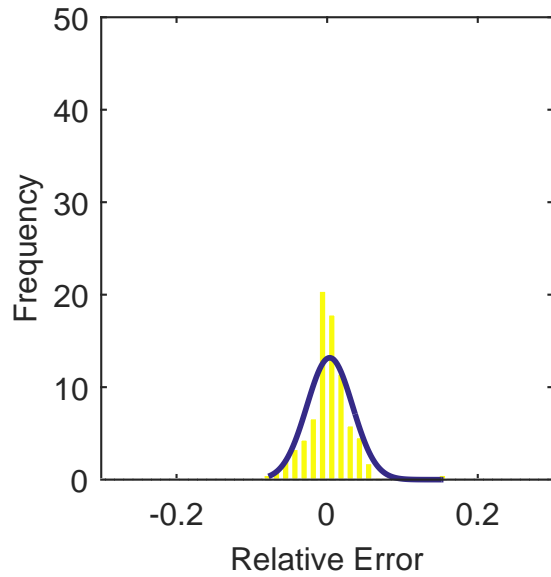


(d) Polar Interpolation

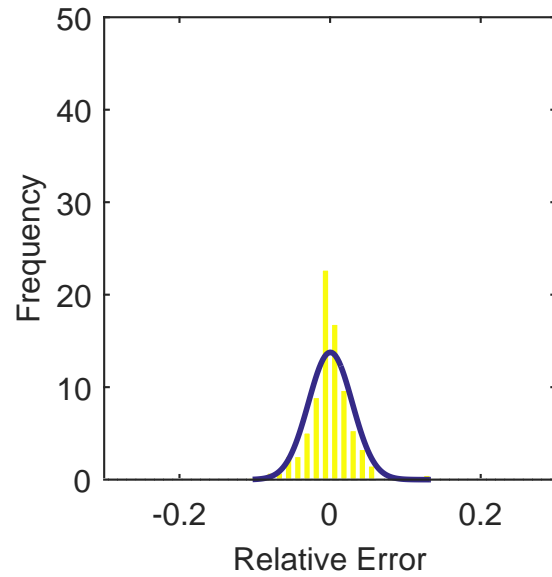


(e) Kriging Interpolation

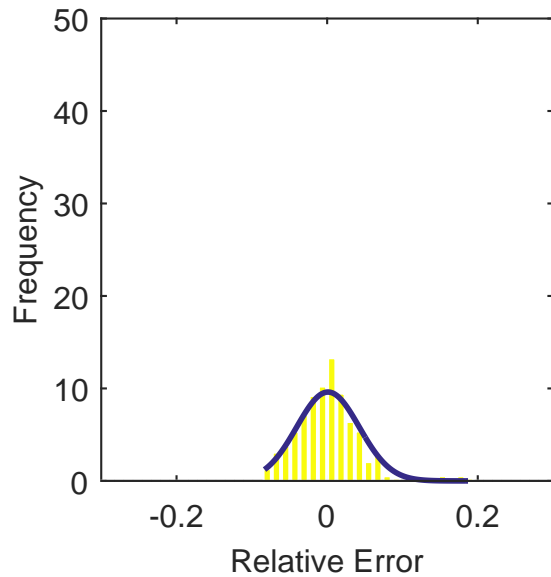
Figure C.17: Contour plots for the raw and interpolated values for the YF12 inlet.



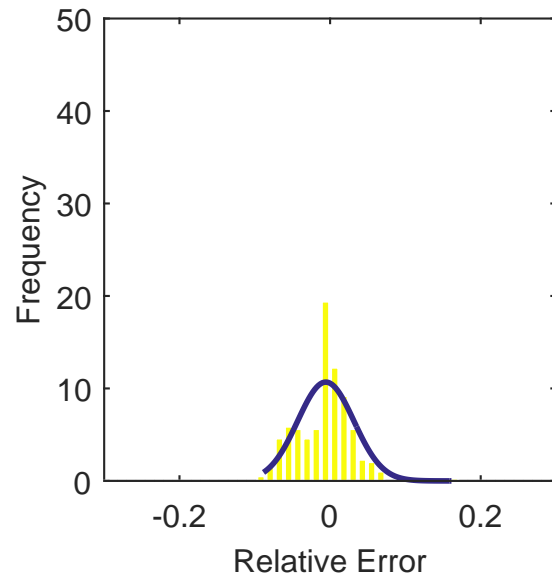
(a) Linear Interpolation Error



(b) Spline Interpolation Error



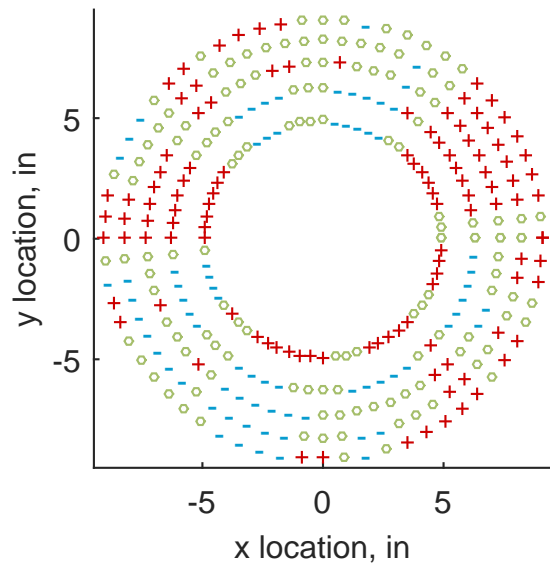
(c) Polar Interpolation Error



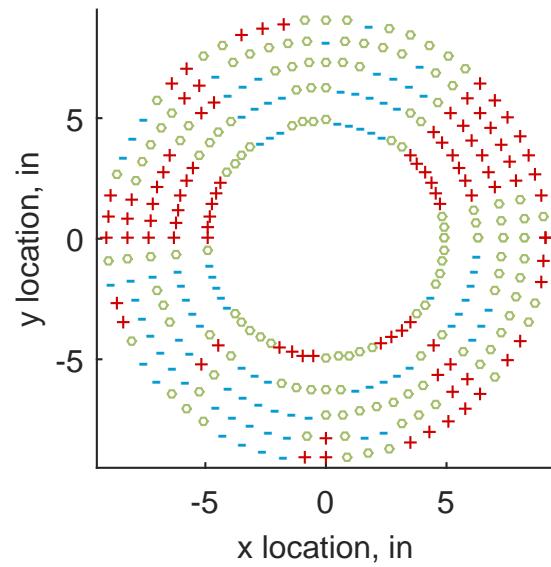
(d) Kriging Interpolation Error

Figure C.18: Relative error for various interpolation schemes of test case 1, first clocking for the YF12 inlet.

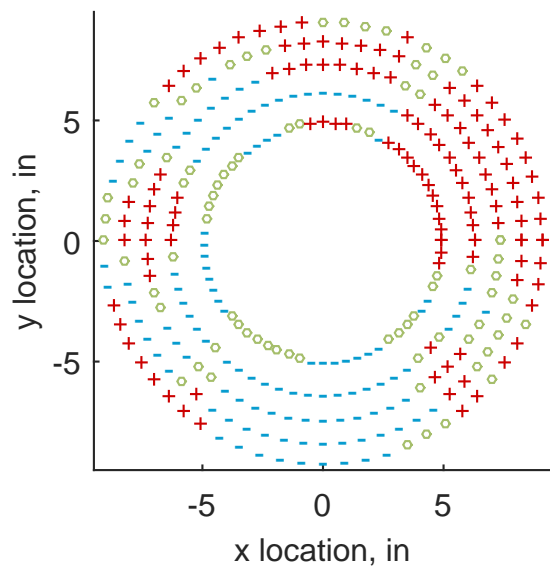




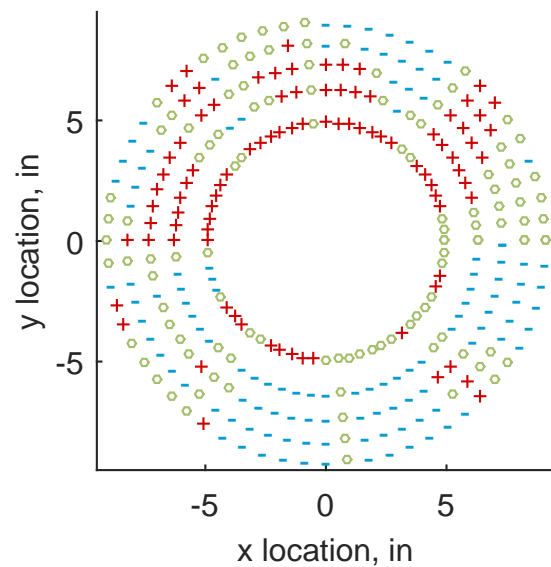
(a) Linear Interpolation



(b) Spline Interpolation



(c) Polar Interpolation



(d) Kriging Interpolation

Figure C.19: Interpolation error for the YF12 inlet - symbols show locations that are within tolerance (o), over-predicted (+), and under-predicted (-).

Table C.5: Interpolation effects on the derived quantities for the IMX inlet run number R300, clocking C2.

	$K_\theta$	$K_r$	$K_a$	$IDC$	$IDT$
Linear	0.322	0.252	0.573	0.076	0.176
Spline	0.320	0.265	0.586	0.075	0.180
Polar	0.321	0.264	0.585	0.071	0.177
Kriging	0.319	0.131	0.450	0.078	0.178

### C.1.1.3 Second Clocking

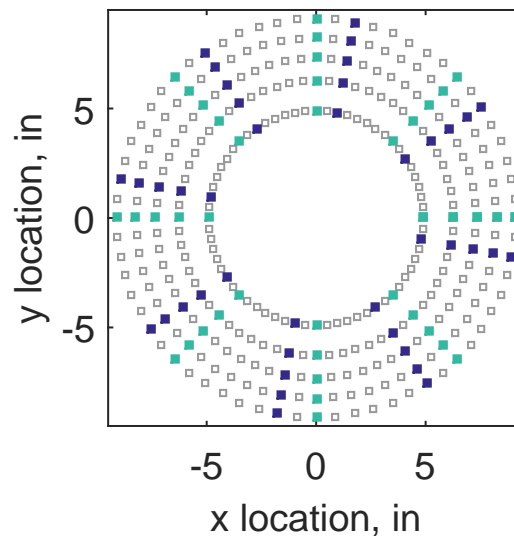
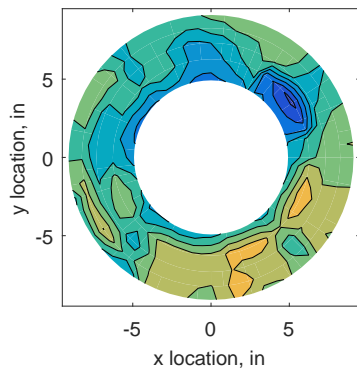


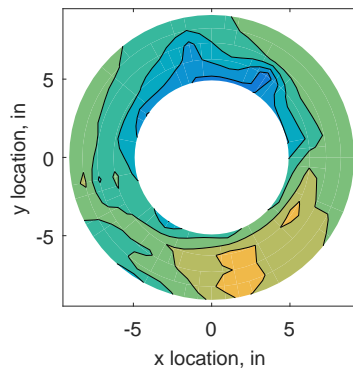
Figure C.20: Second clocking probe position

Table C.6: Interpolation results for the YF12 inlet test case 1, clocking C3.

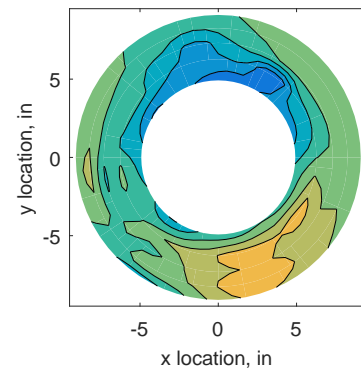
	Mean	Std. Dev.	Over-Prediction	In Tolerance	Under-Prediction
Linear	0.148	0.191	165	35	80
Spline	0.098	0.179	158	27	95
Polar	0.105	0.197	168	-13	125
Kriging	0.098	0.244	123	27	130



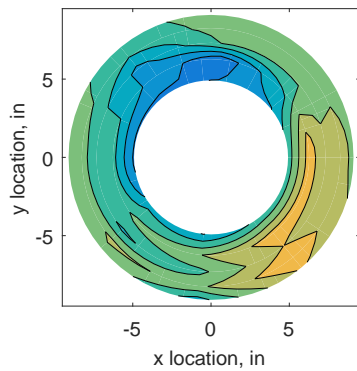
(a) 320 Probes



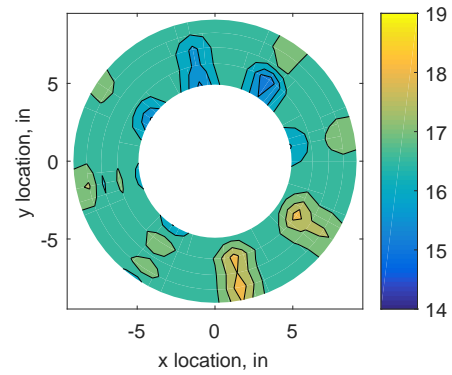
(b) Linear Interpolation



(c) Spline Interpolation

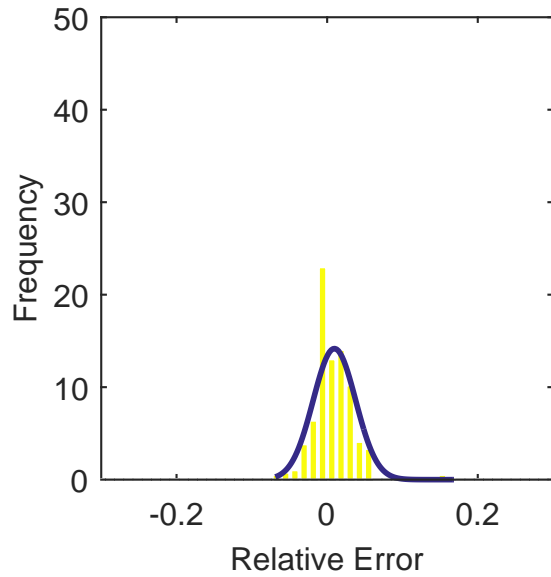


(d) Polar Interpolation

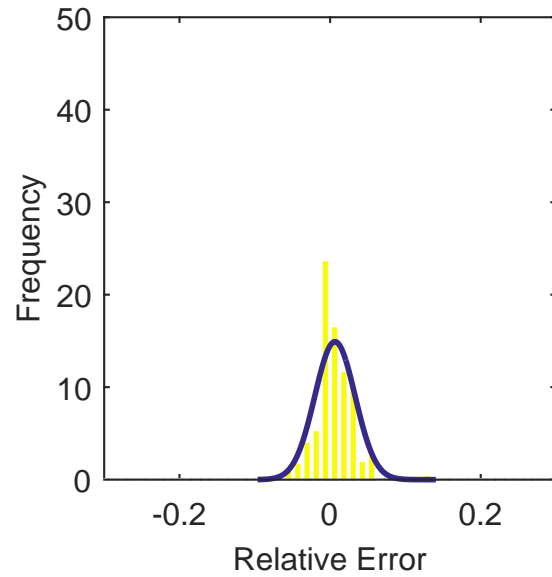


(e) Kriging Interpolation

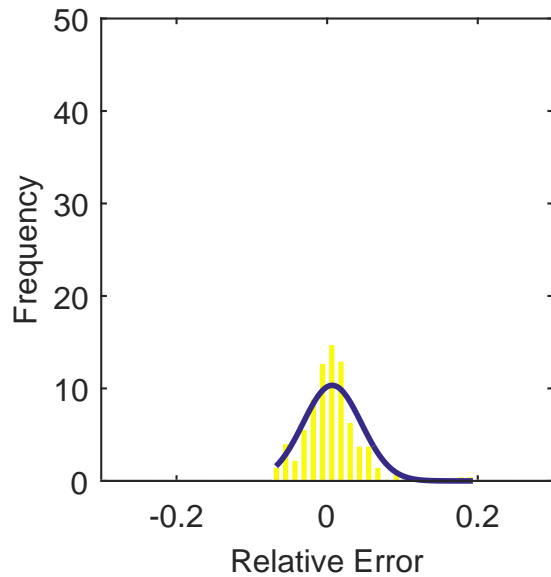
Figure C.21: Contour plots for the raw and interpolated values for the YF12 inlet.



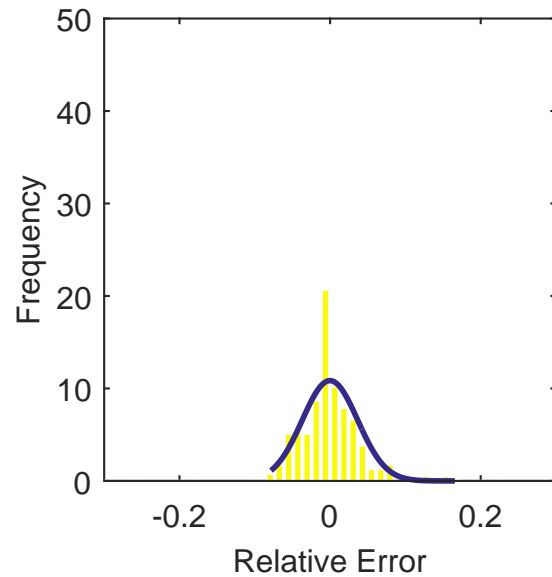
(a) Linear Interpolation Error



(b) Spline Interpolation Error

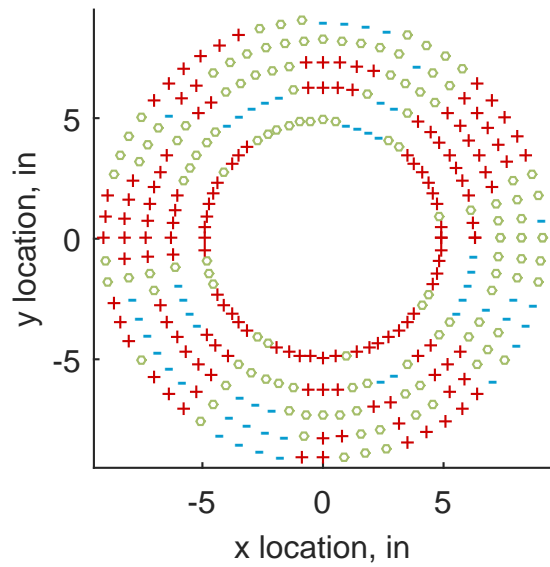


(c) Polar Interpolation Error

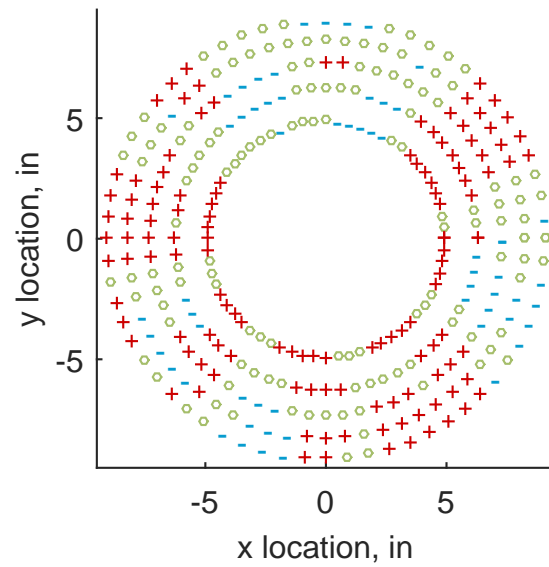


(d) Kriging Interpolation Error

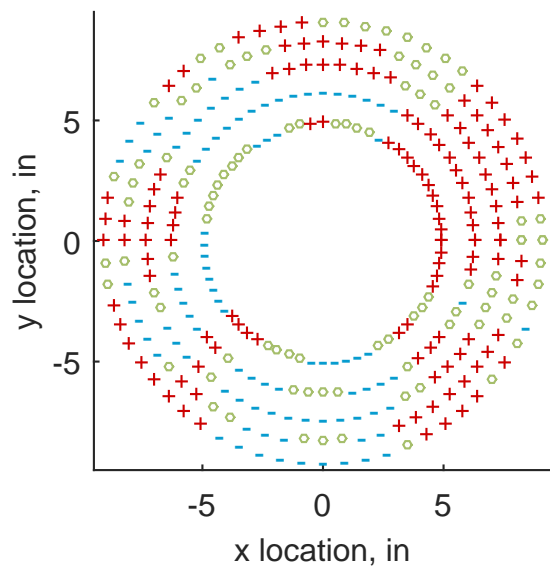
Figure C.22: Relative error for various interpolation schemes of test case 1, second clocking for the YF12 inlet.



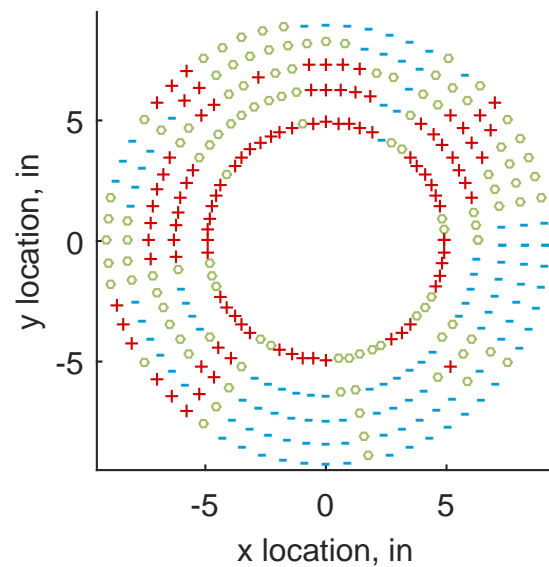
(a) Linear Interpolation



(b) Spline Interpolation



(c) Polar Interpolation



(d) Kriging Interpolation

Figure C.23: Interpolation error for the YF12 inlet - symbols show locations that are within tolerance (o), over-predicted (+), and under-predicted (-).

Table C.7: Interpolation effects on the derived quantities for the IMX inlet run number R300, clocking C3.

	$K_\theta$	$K_r$	$K_a$	$IDC$	$IDT$
Linear	0.324	0.227	0.551	0.082	0.195
Spline	0.323	0.248	0.571	0.083	0.197
Polar	0.323	0.270	0.593	0.074	0.196
Kriging	0.321	0.119	0.440	0.081	0.197

#### C.1.1.4 Third Clocking

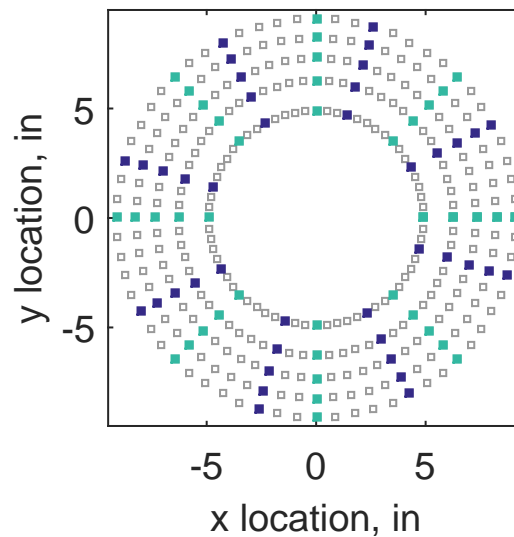
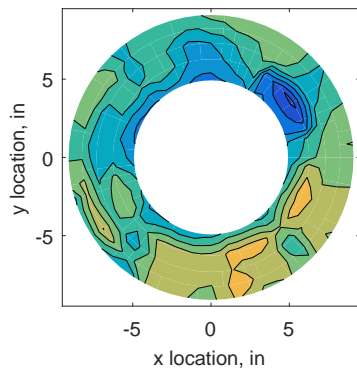


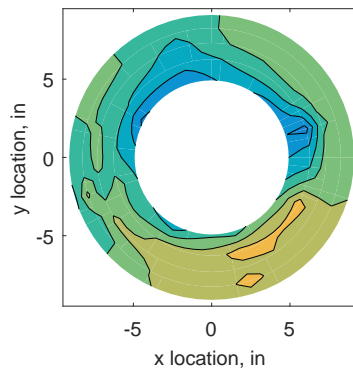
Figure C.24: Third clocking probe position

Table C.8: Interpolation results for the YF12 inlet test case 1, clocking C4.

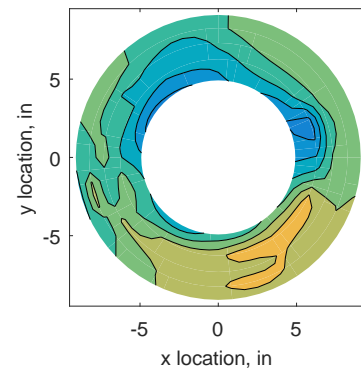
	Mean	Std. Dev.	Over-Prediction	In Tolerance	Under-Prediction
Linear	0.171	0.215	166	29	85
Spline	0.137	0.208	169	31	80
Polar	0.174	0.168	181	-9	108
Kriging	0.137	0.240	127	26	127



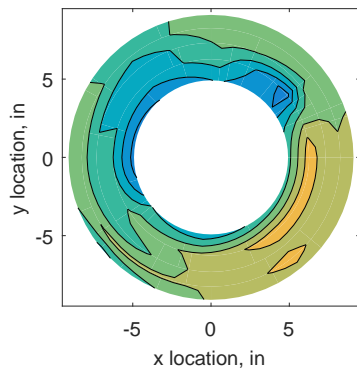
(a) 320 Probes



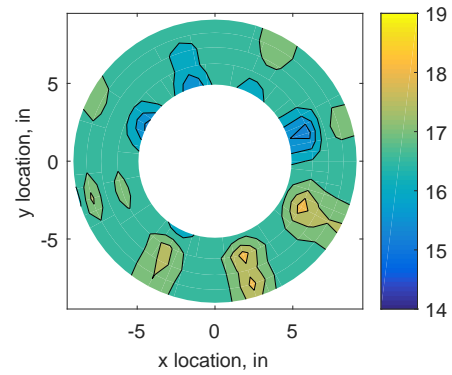
(b) Linear Interpolation



(c) Spline Interpolation

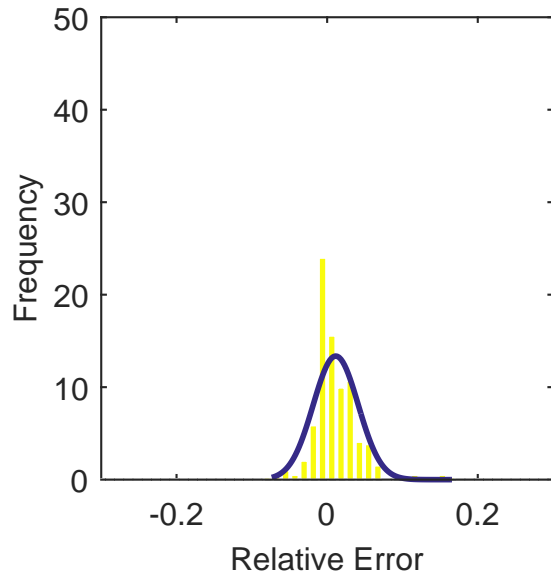


(d) Polar Interpolation

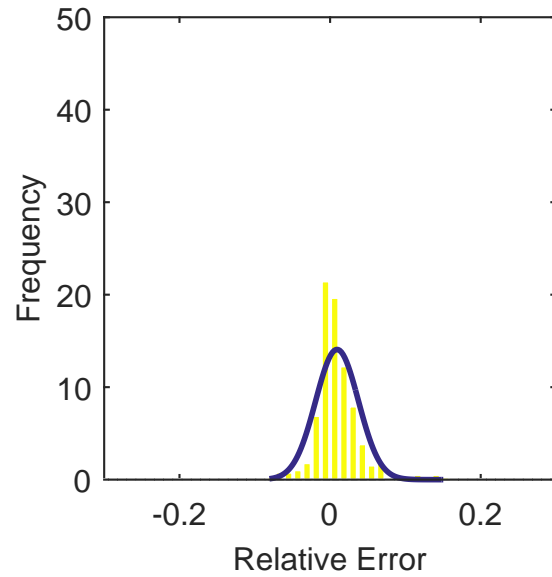


(e) Kriging Interpolation

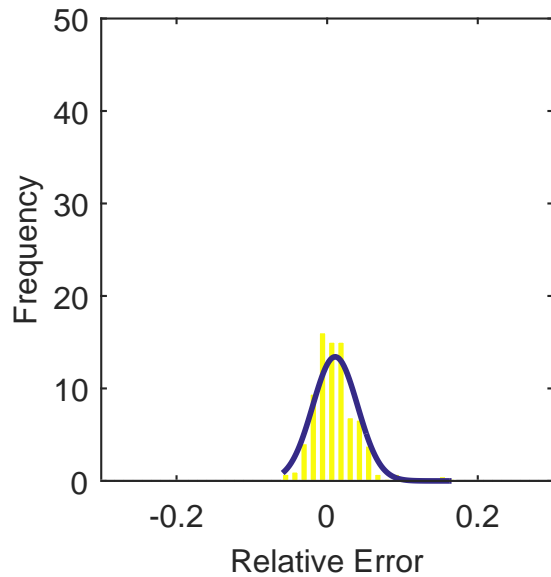
Figure C.25: Contour plots for the raw and interpolated values for the YF12 inlet.



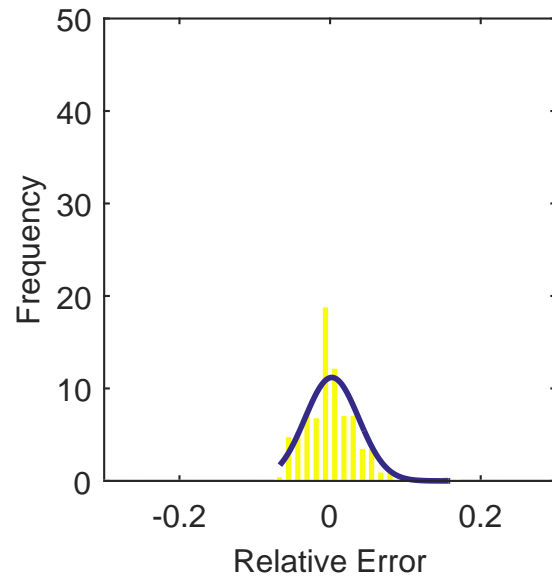
(a) Linear Interpolation Error



(b) Spline Interpolation Error



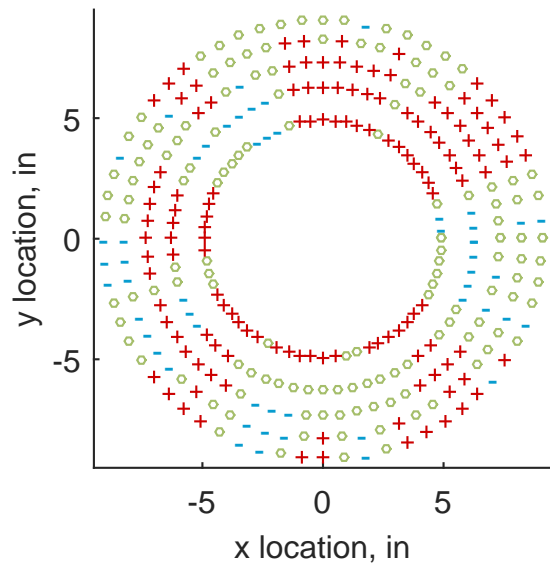
(c) Polar Interpolation Error



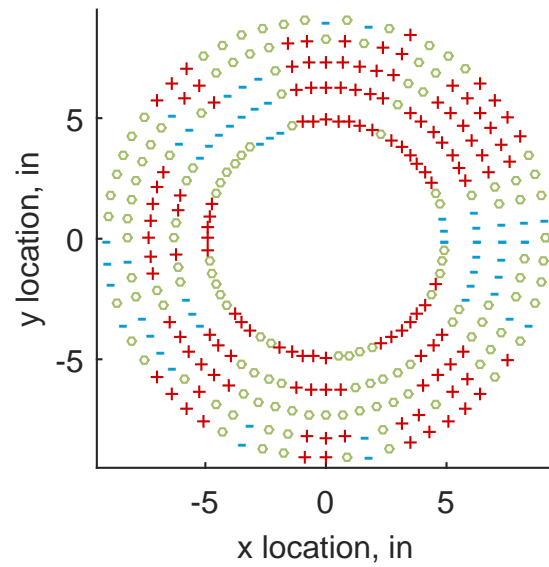
(d) Kriging Interpolation Error

Figure C.26: Relative error for various interpolation schemes of test case 1, third clocking for the YF12 inlet.

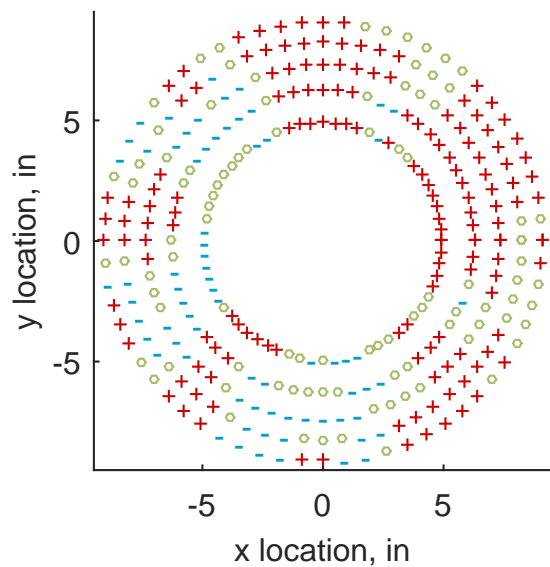




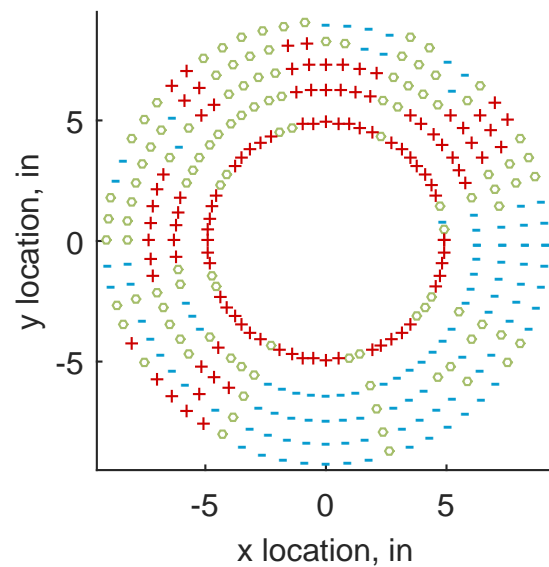
(a) Linear Interpolation



(b) Spline Interpolation



(c) Polar Interpolation



(d) Kriging Interpolation

Figure C.27: Interpolation error for the YF12 inlet - symbols show locations that are within tolerance (o), over-predicted (+), and under-predicted (-).

Table C.9: Interpolation effects on the derived quantities for the IMX inlet run number R300, clocking C4.

	$K_\theta$	$K_r$	$K_a$	$IDC$	$IDT$
Linear	0.324	0.235	0.559	0.075	0.175
Spline	0.323	0.257	0.580	0.072	0.181
Polar	0.324	0.277	0.601	0.076	0.175
Kriging	0.322	0.126	0.448	0.079	0.177

#### C.1.1.5 Fourth Clocking

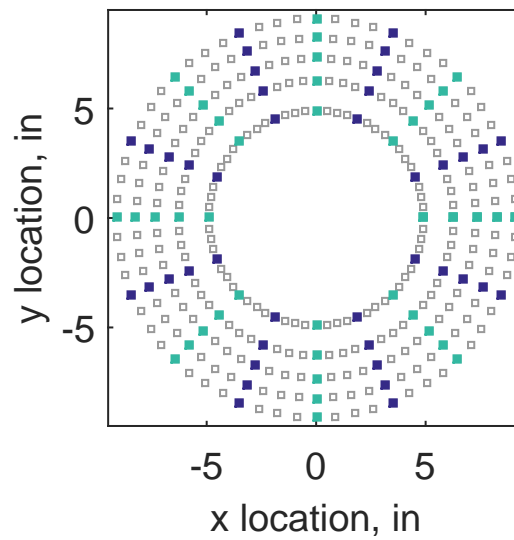
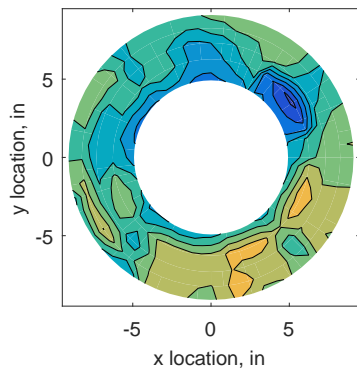


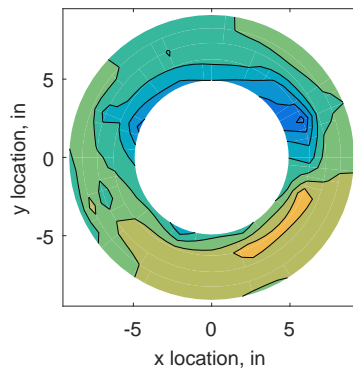
Figure C.28: Fourth clocking probe position

Table C.10: Interpolation results for the YF12 inlet test case 1, clocking C5.

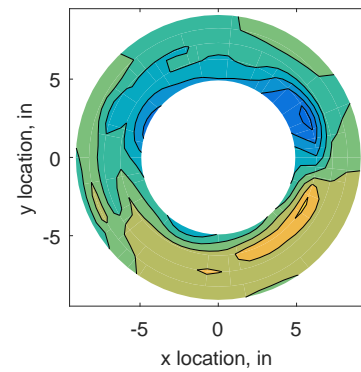
	Mean	Std. Dev.	Over-Prediction	In Tolerance	Under-Prediction
Linear	0.171	0.174	167	49	64
Spline	0.128	0.165	166	36	78
Polar	0.152	0.176	175	3	102
Kriging	0.128	0.357	139	15	126



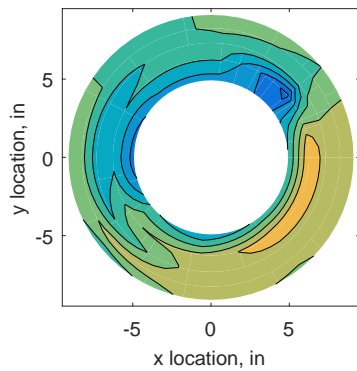
(a) 320 Probes



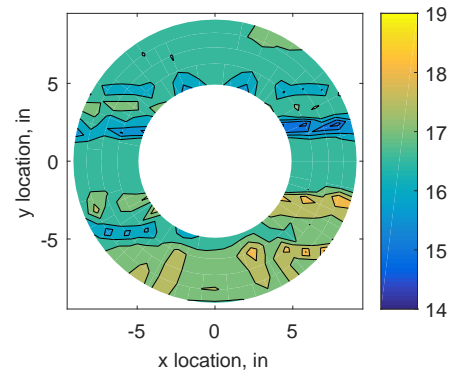
(b) Linear Interpolation



(c) Spline Interpolation

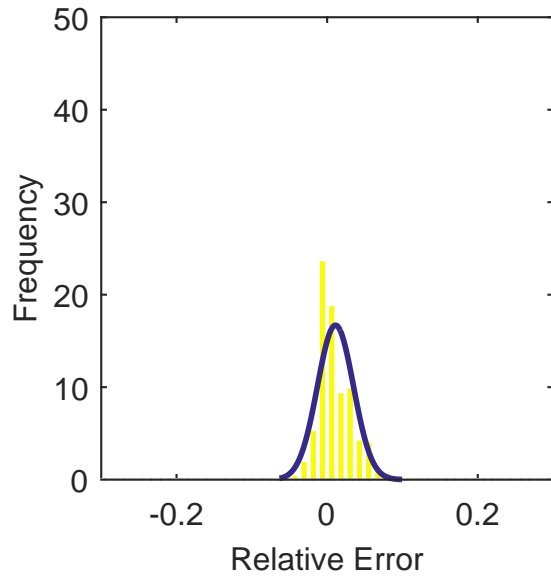


(d) Polar Interpolation

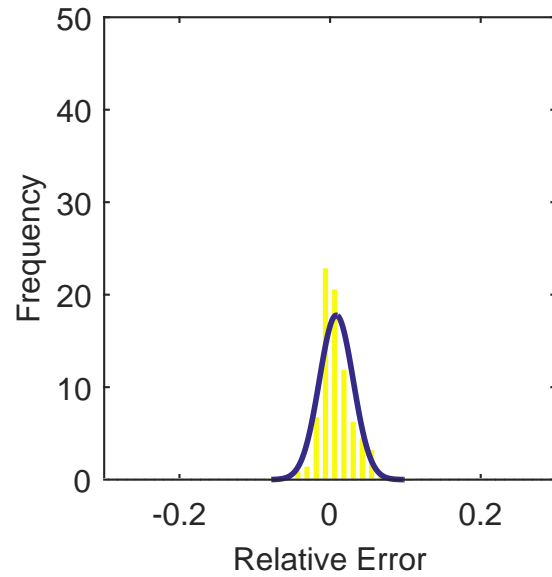


(e) Kriging Interpolation

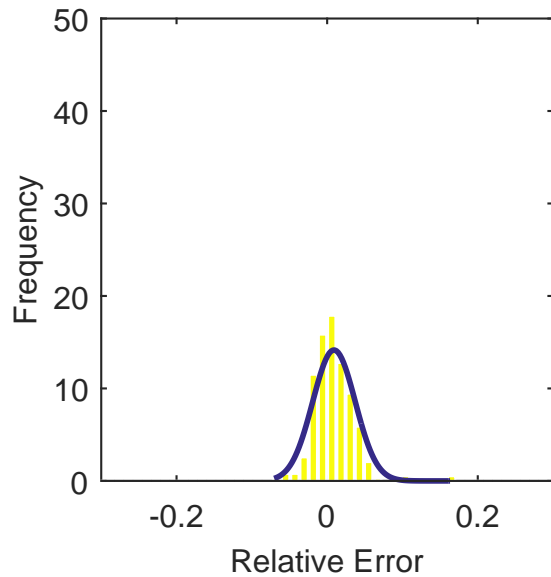
Figure C.29: Contour plots for the raw and interpolated values for the YF12 inlet.



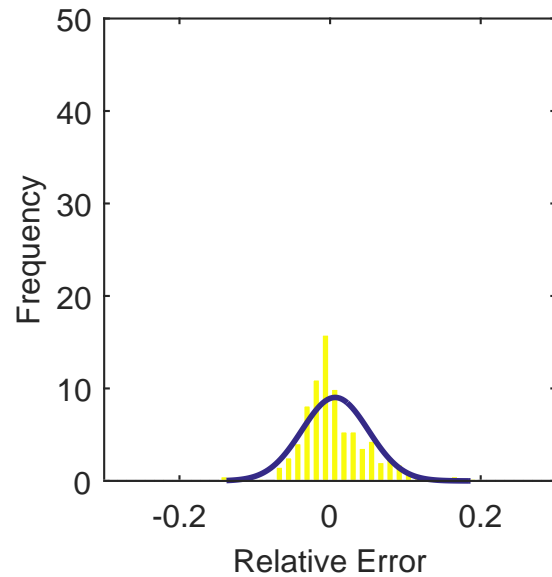
(a) Linear Interpolation Error



(b) Spline Interpolation Error

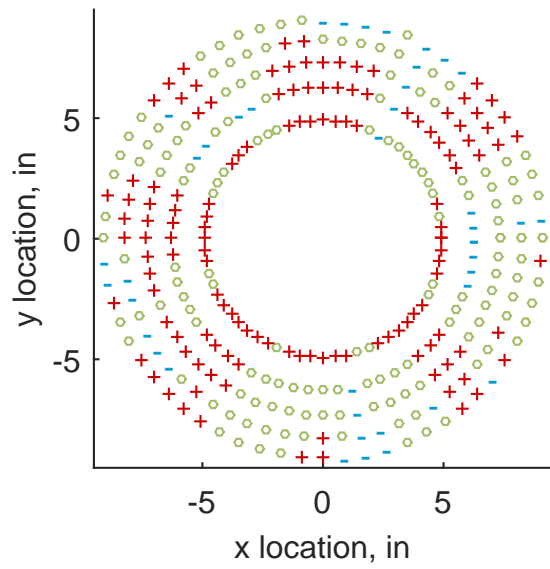


(c) Polar Interpolation Error

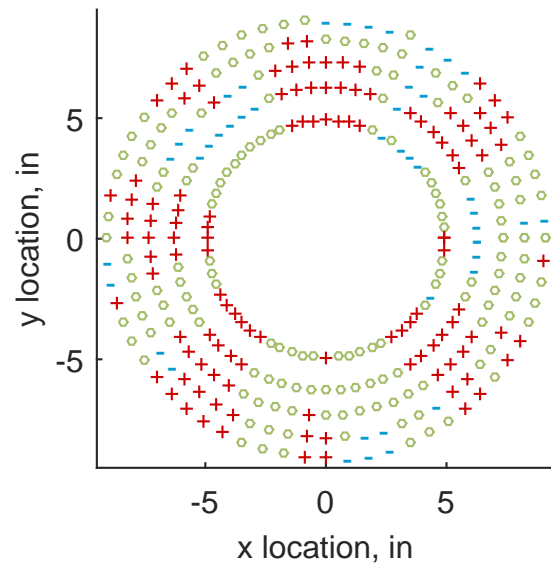


(d) Kriging Interpolation Error

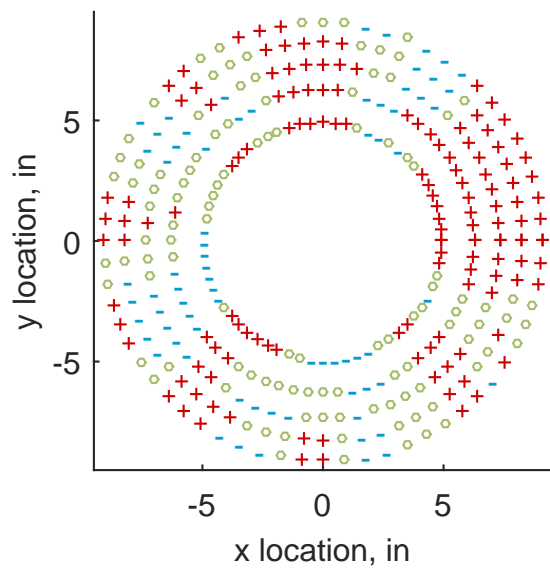
Figure C.30: Relative error for various interpolation schemes of test case 1, fourth clocking for the YF12 inlet.



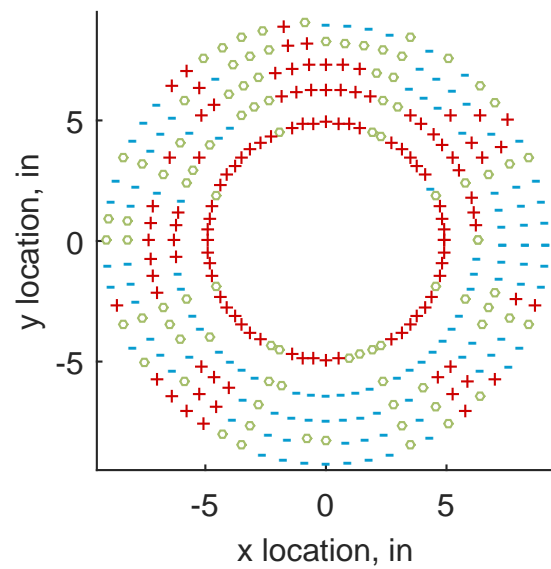
(a) Linear Interpolation



(b) Spline Interpolation



(c) Polar Interpolation



(d) Kriging Interpolation

Figure C.31: Interpolation error for the YF12 inlet - symbols show locations that are within tolerance (o), over-predicted (+), and under-predicted (-).

Table C.11: Interpolation effects on the derived quantities for the IMX inlet run number R300, clocking C5.

	$K_\theta$	$K_r$	$K_a$	$IDC$	$IDT$
Linear	0.324	0.226	0.551	0.091	0.214
Spline	0.323	0.255	0.578	0.089	0.222
Polar	0.323	0.297	0.620	0.089	0.215
Kriging	0.324	0.065	0.388	0.114	0.224

#### C.1.1.6 Fifth Clocking

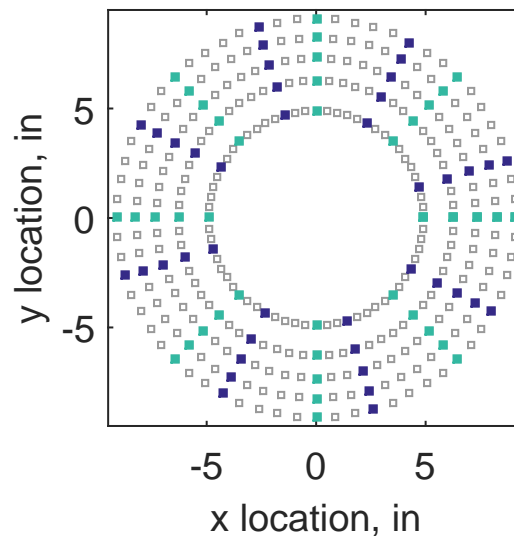
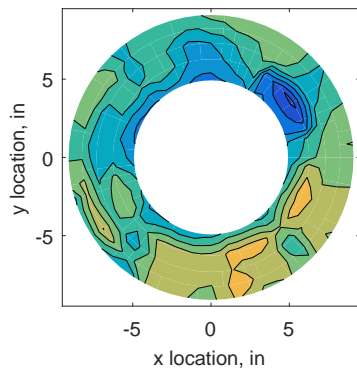


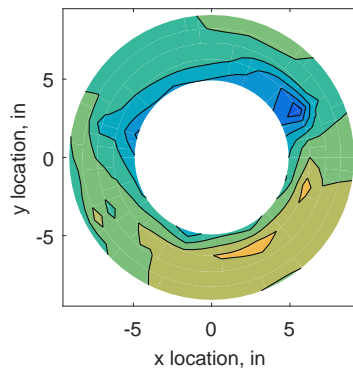
Figure C.32: Fifth clocking probe position

Table C.12: Interpolation results for the YF12 inlet test case 1, clocking C6.

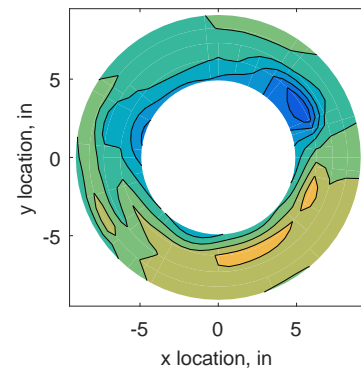
	Mean	Std. Dev.	Over-Prediction	In Tolerance	Under-Prediction
Linear	0.150	0.138	163	33	84
Spline	0.098	0.111	141	54	85
Polar	0.097	0.170	164	5	111
Kriging	0.098	0.249	103	20	157



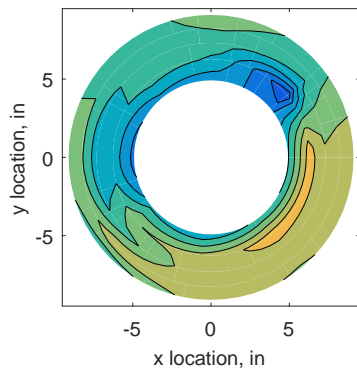
(a) 320 Probes



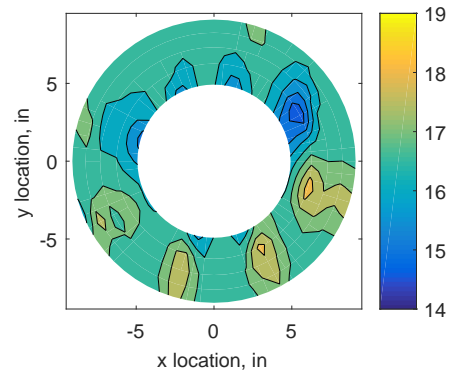
(b) Linear Interpolation



(c) Spline Interpolation

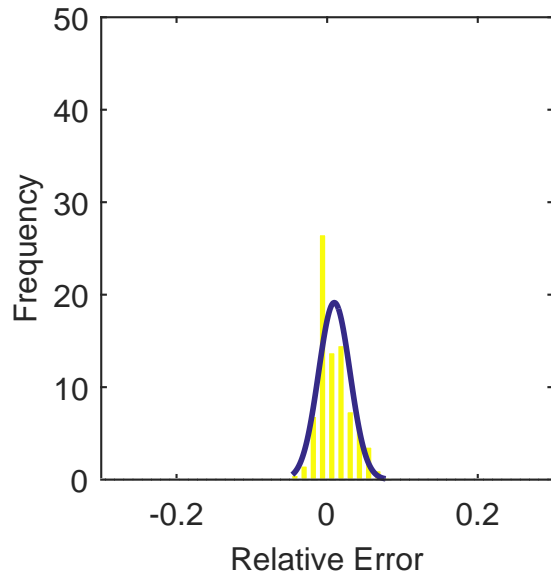


(d) Polar Interpolation

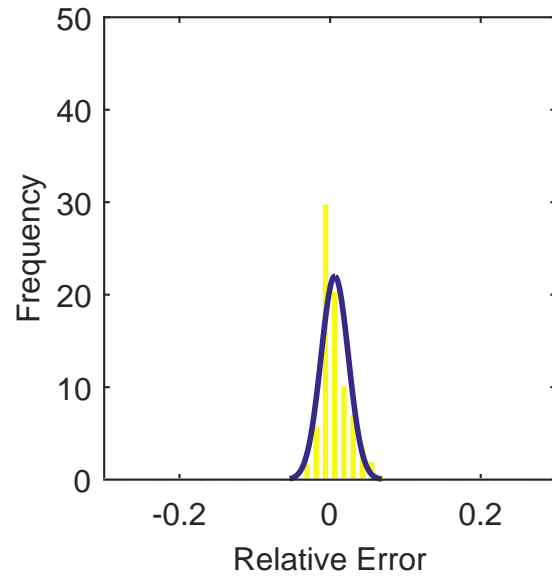


(e) Kriging Interpolation

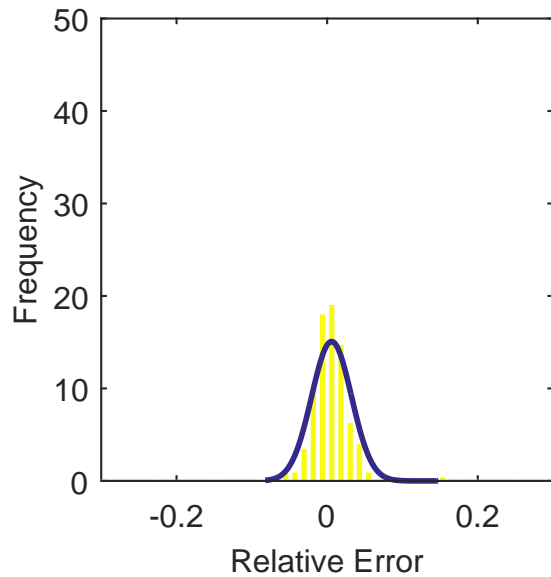
Figure C.33: Contour plots for the raw and interpolated values for the YF12 inlet.



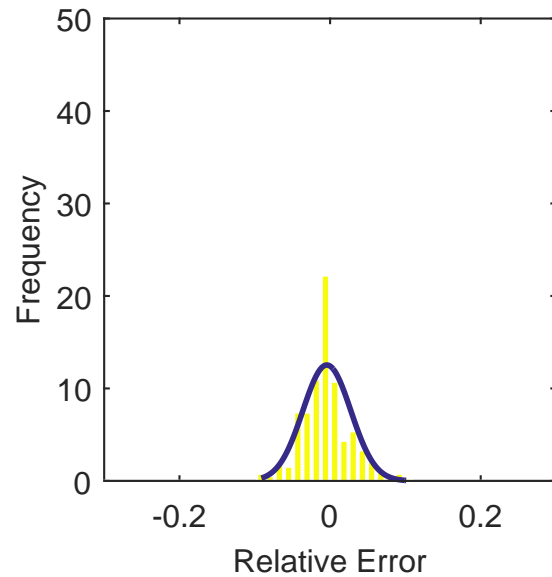
(a) Linear Interpolation Error



(b) Spline Interpolation Error



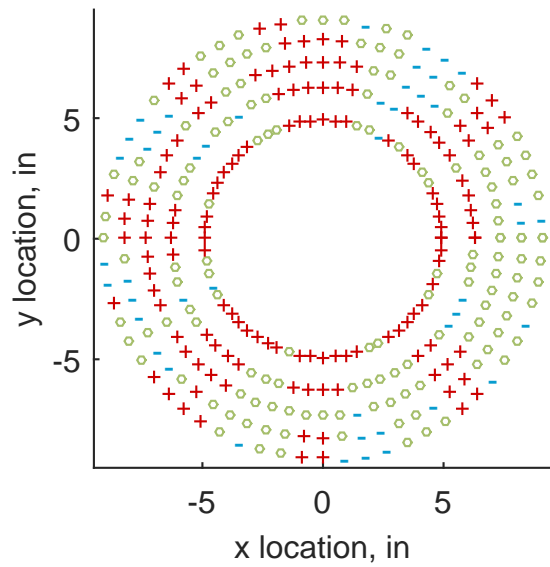
(c) Polar Interpolation Error



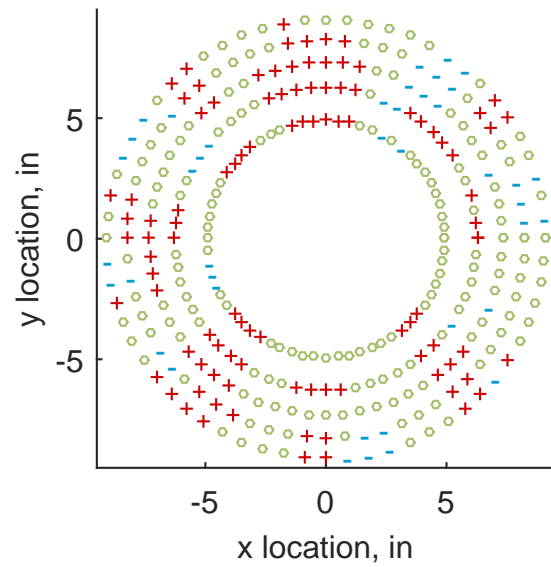
(d) Kriging Interpolation Error

Figure C.34: Relative error for various interpolation schemes of test case 1, fifth clocking for the YF12 inlet.

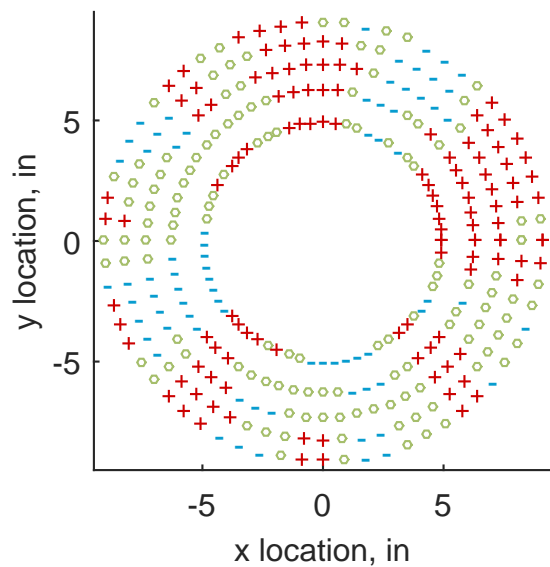




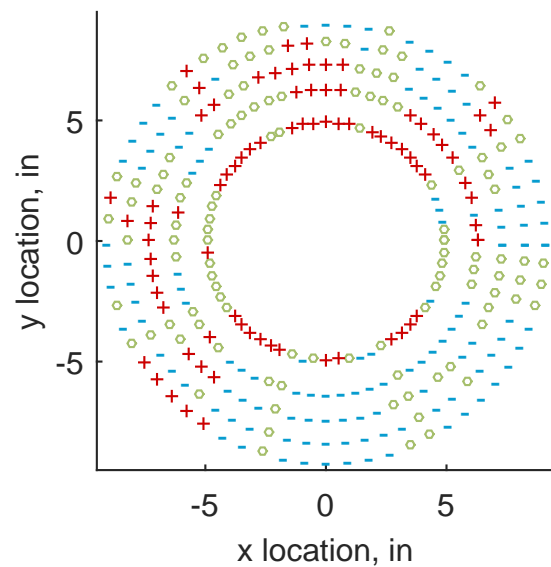
(a) Linear Interpolation



(b) Spline Interpolation



(c) Polar Interpolation



(d) Kriging Interpolation

Figure C.35: Interpolation error for the YF12 inlet - symbols show locations that are within tolerance (o), over-predicted (+), and under-predicted (-).

Table C.13: Interpolation effects on the derived quantities for the IMX inlet run number R300, clocking C6.

	$K_\theta$	$K_r$	$K_a$	$IDC$	$IDT$
Linear	0.324	0.226	0.549	0.099	0.217
Spline	0.323	0.258	0.581	0.093	0.224
Polar	0.322	0.286	0.608	0.092	0.218
Kriging	0.320	0.137	0.457	0.096	0.220

### C.1.1.7 Sixth Clocking

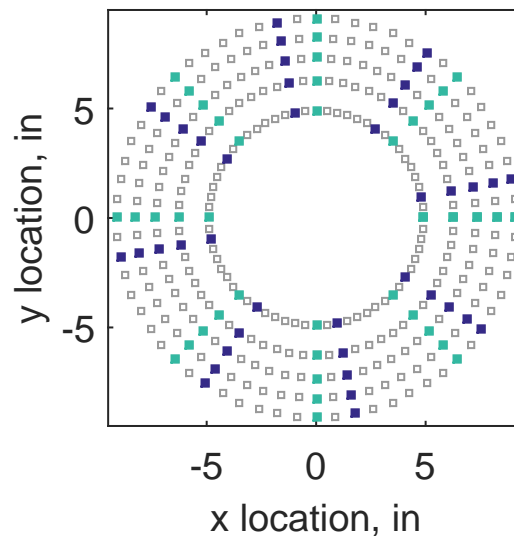


Figure C.36: Sixth clocking probe position

Table C.14: Interpolation results for the YF12 inlet test case 1, clocking C7.

	Mean	Std. Dev.	Over-Prediction	In Tolerance	Under-Prediction
Linear	0.048	0.163	128	26	126
Spline	0.013	0.141	119	34	127
Polar	0.028	0.161	136	9	135
Kriging	0.013	0.245	94	18	168

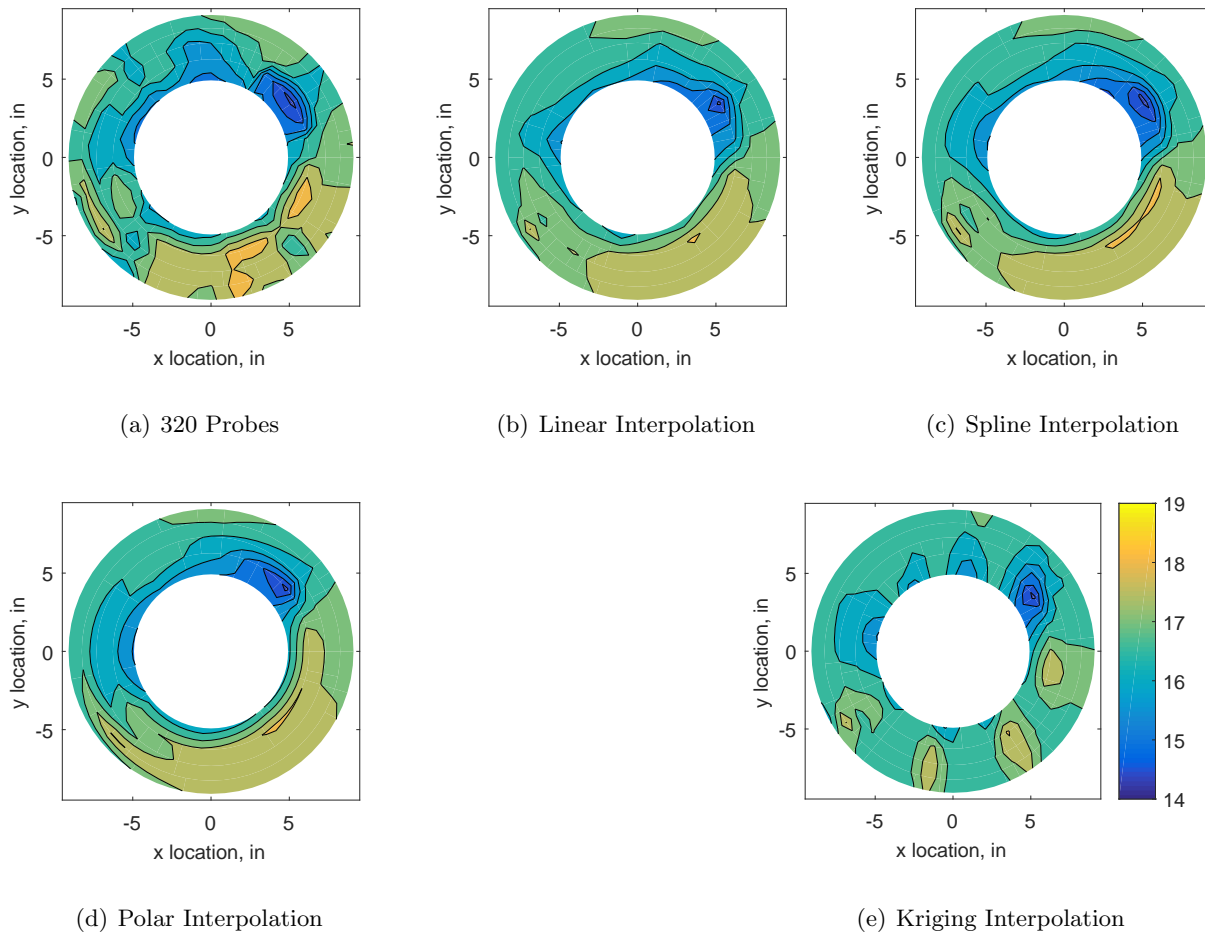
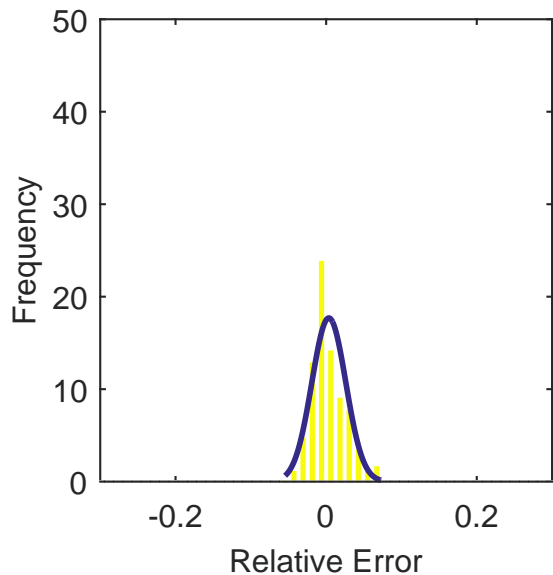
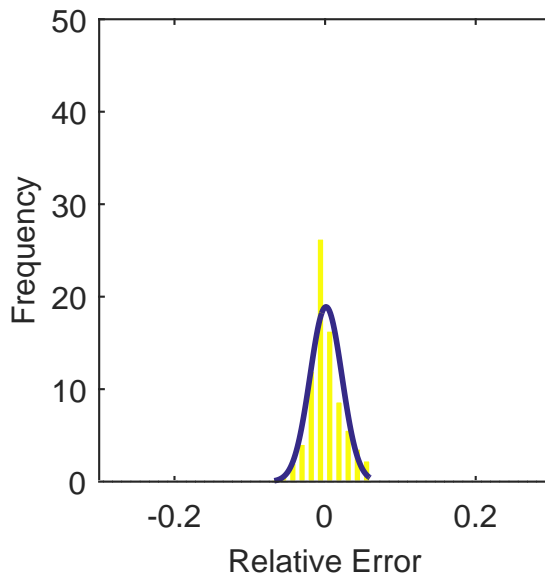


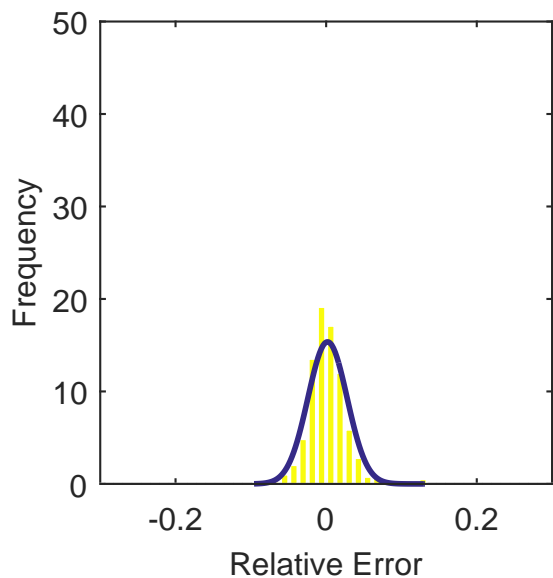
Figure C.37: Contour plots for the raw and interpolated values for the YF12 inlet.



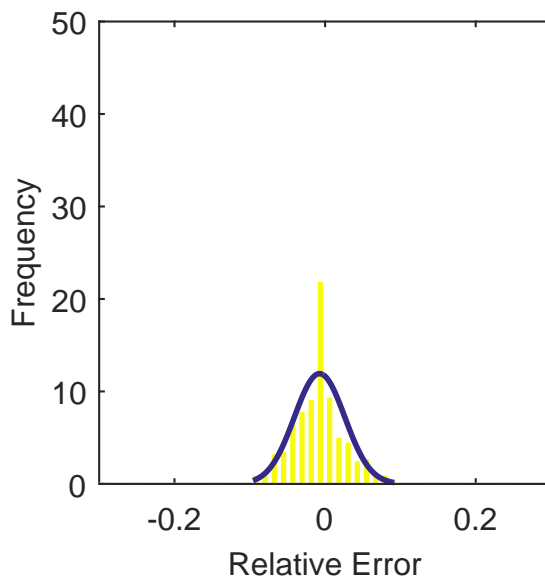
(a) Linear Interpolation Error



(b) Spline Interpolation Error

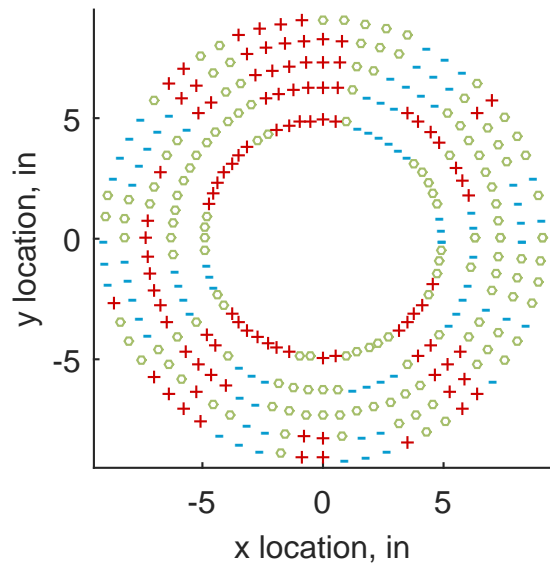


(c) Polar Interpolation Error

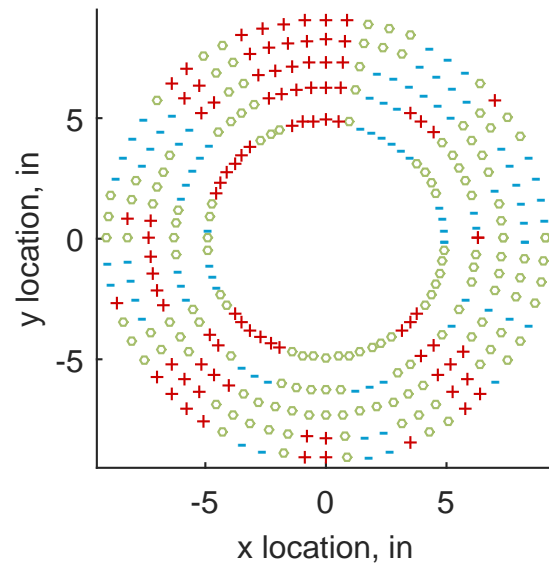


(d) Kriging Interpolation Error

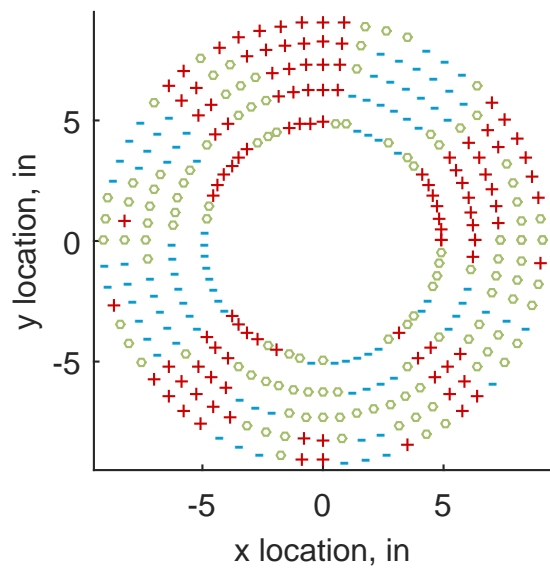
Figure C.38: Relative error for various interpolation schemes of test case 1, sixth clocking for the YF12 inlet.



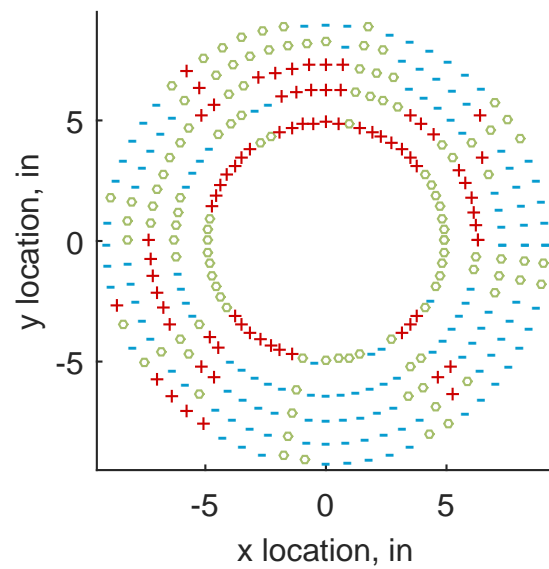
(a) Linear Interpolation



(b) Spline Interpolation



(c) Polar Interpolation



(d) Kriging Interpolation

Figure C.39: Interpolation error for the YF12 inlet - symbols show locations that are within tolerance (o), over-predicted (+), and under-predicted (-).

Table C.15: Interpolation effects on the derived quantities for the IMX inlet run number R300, clocking C7.

	$K_\theta$	$K_r$	$K_a$	$IDC$	$IDT$
Linear	0.322	0.242	0.564	0.100	0.220
Spline	0.321	0.265	0.586	0.103	0.224
Polar	0.321	0.271	0.592	0.091	0.220
Kriging	0.319	0.131	0.450	0.100	0.222

### C.1.1.8 Seventh Clocking

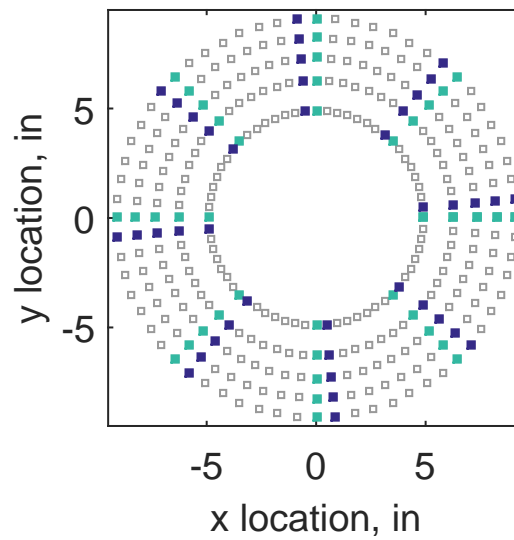
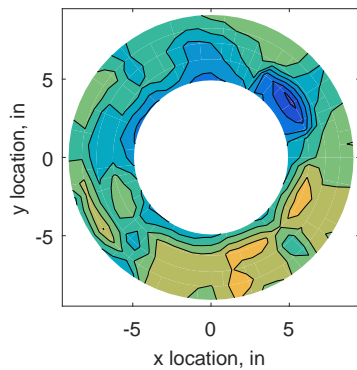


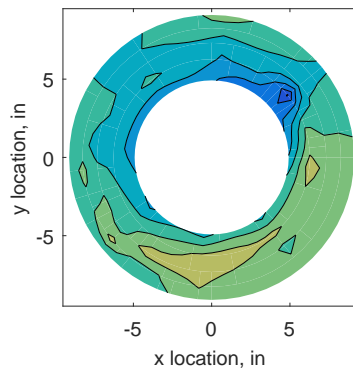
Figure C.40: Seventh clocking probe position

Table C.16: Interpolation results for the YF12 inlet test case 1, clocking C8.

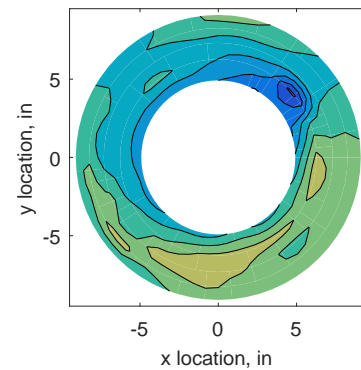
	Mean	Std. Dev.	Over-Prediction	In Tolerance	Under-Prediction
Linear	-0.133	0.208	82	25	173
Spline	-0.166	0.193	68	28	184
Polar	-0.168	0.177	67	26	187
Kriging	-0.166	0.250	67	14	199



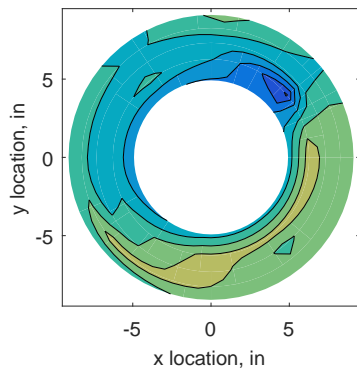
(a) 320 Probes



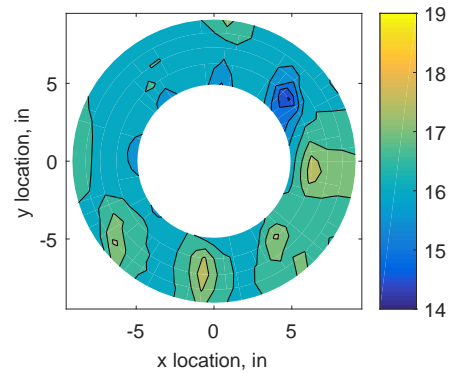
(b) Linear Interpolation



(c) Spline Interpolation

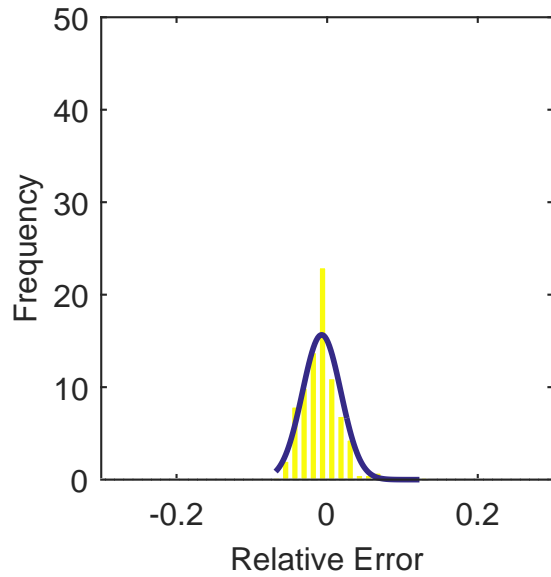


(d) Polar Interpolation

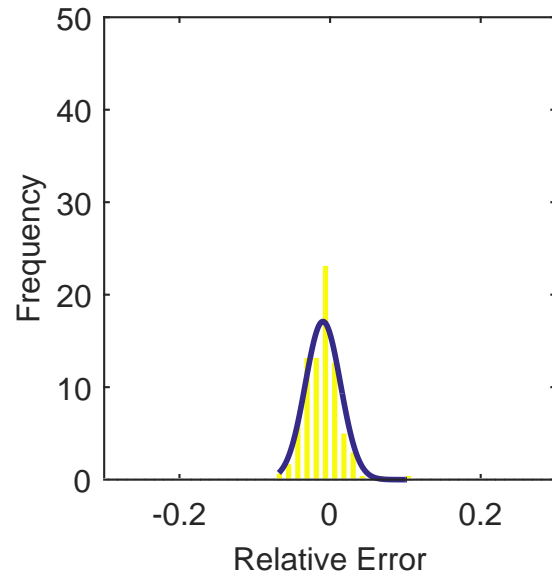


(e) Kriging Interpolation

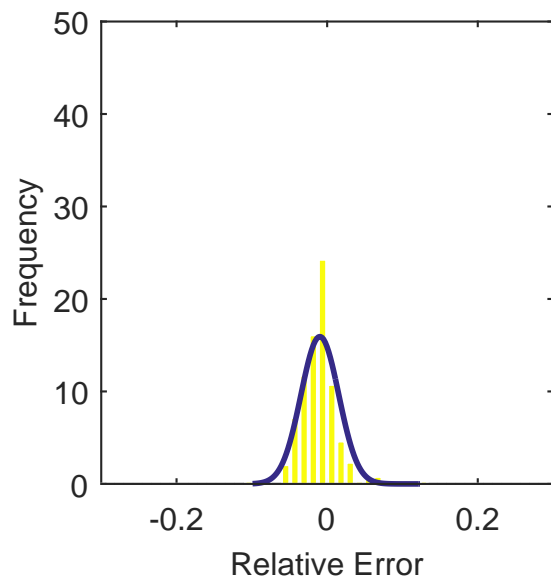
Figure C.41: Contour plots for the raw and interpolated values for the YF12 inlet.



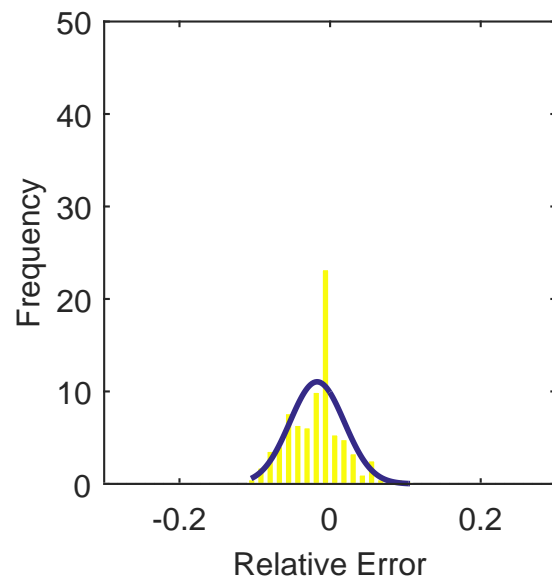
(a) Linear Interpolation Error



(b) Spline Interpolation Error



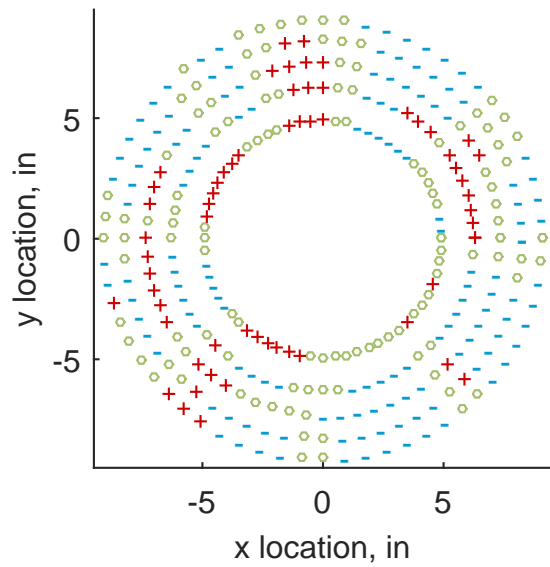
(c) Polar Interpolation Error



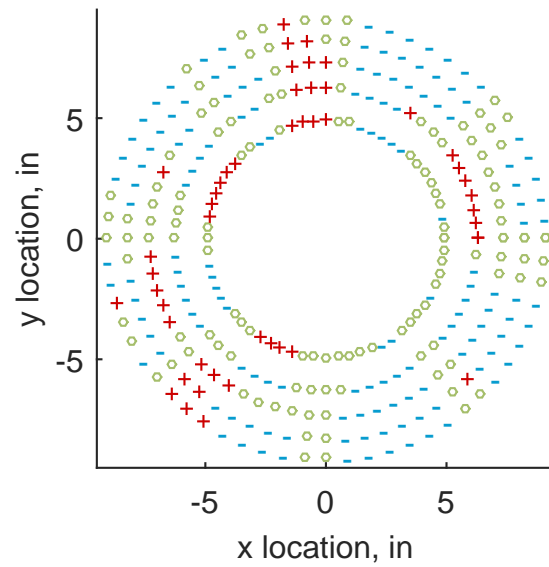
(d) Kriging Interpolation Error

Figure C.42: Relative error for various interpolation schemes of test case 1, seventh clocking for the YF12 inlet.

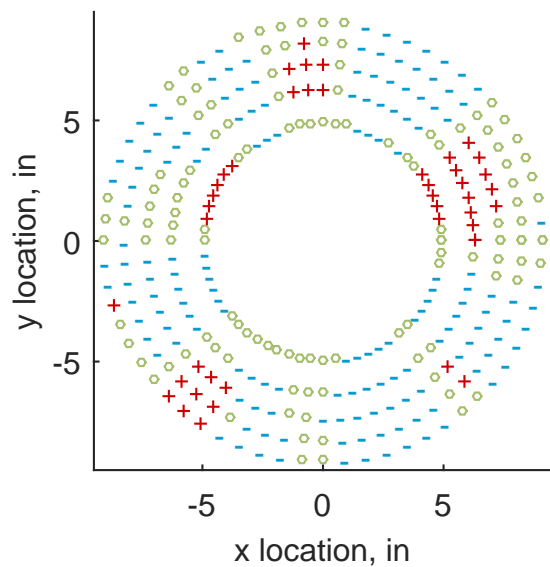




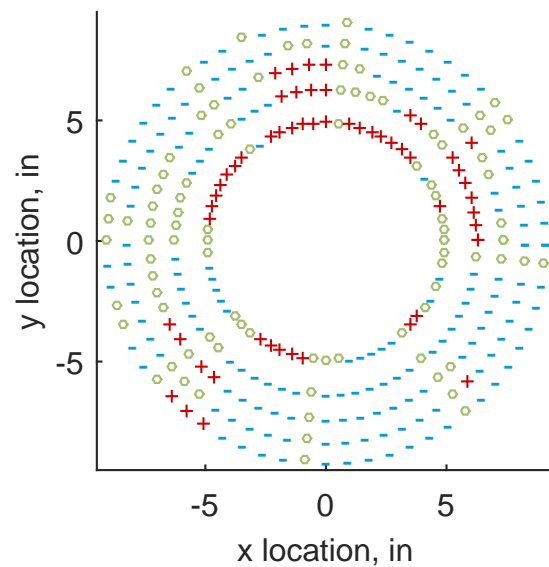
(a) Linear Interpolation



(b) Spline Interpolation



(c) Polar Interpolation



(d) Kriging Interpolation

Figure C.43: Interpolation error for the YF12 inlet - symbols show locations that are within tolerance (o), over-predicted (+), and under-predicted (-).

Table C.17: Interpolation effects on the derived quantities for the IMX inlet run number R300, clocking C8.

	$K_\theta$	$K_r$	$K_a$	$IDC$	$IDT$
Linear	0.319	0.218	0.537	0.095	0.205
Spline	0.318	0.231	0.548	0.095	0.208
Polar	0.318	0.235	0.553	0.083	0.206
Kriging	0.316	0.116	0.432	0.092	0.207

## C.1.2 Test Case 2

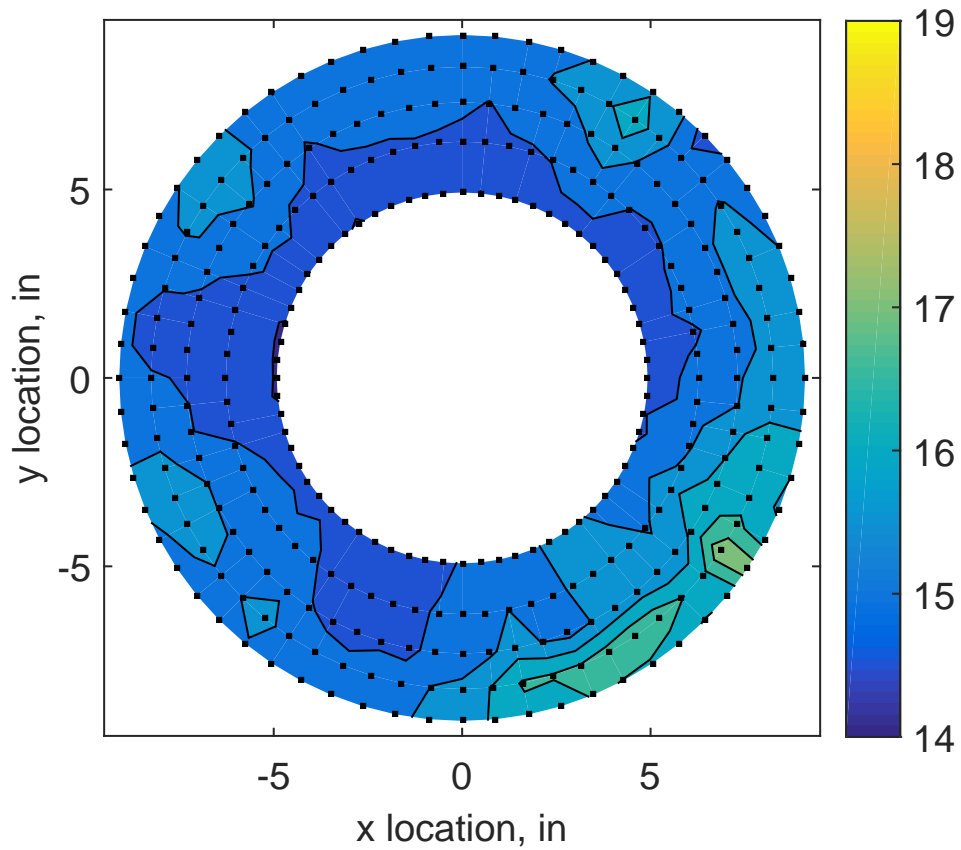


Figure C.44: YF12 test case 2 raw pressure contour created with 320 probes.

### C.1.2.1 Zeroth Clocking

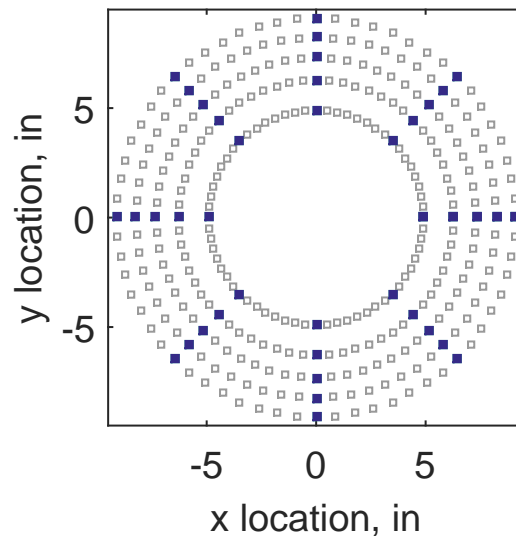


Figure C.45: Zeroth clocking probe position

Table C.18: Interpolation results for the YF12 inlet test case 2, clocking C1.

	Mean	Std. Dev.	Over-Prediction	In Tolerance	Under-Prediction
Linear	-0.044	0.161	123	45	112
Spline	-0.075	0.142	90	61	129
Polar	-0.082	0.118	133	-5	152
Kriging	-0.075	0.202	97	40	143

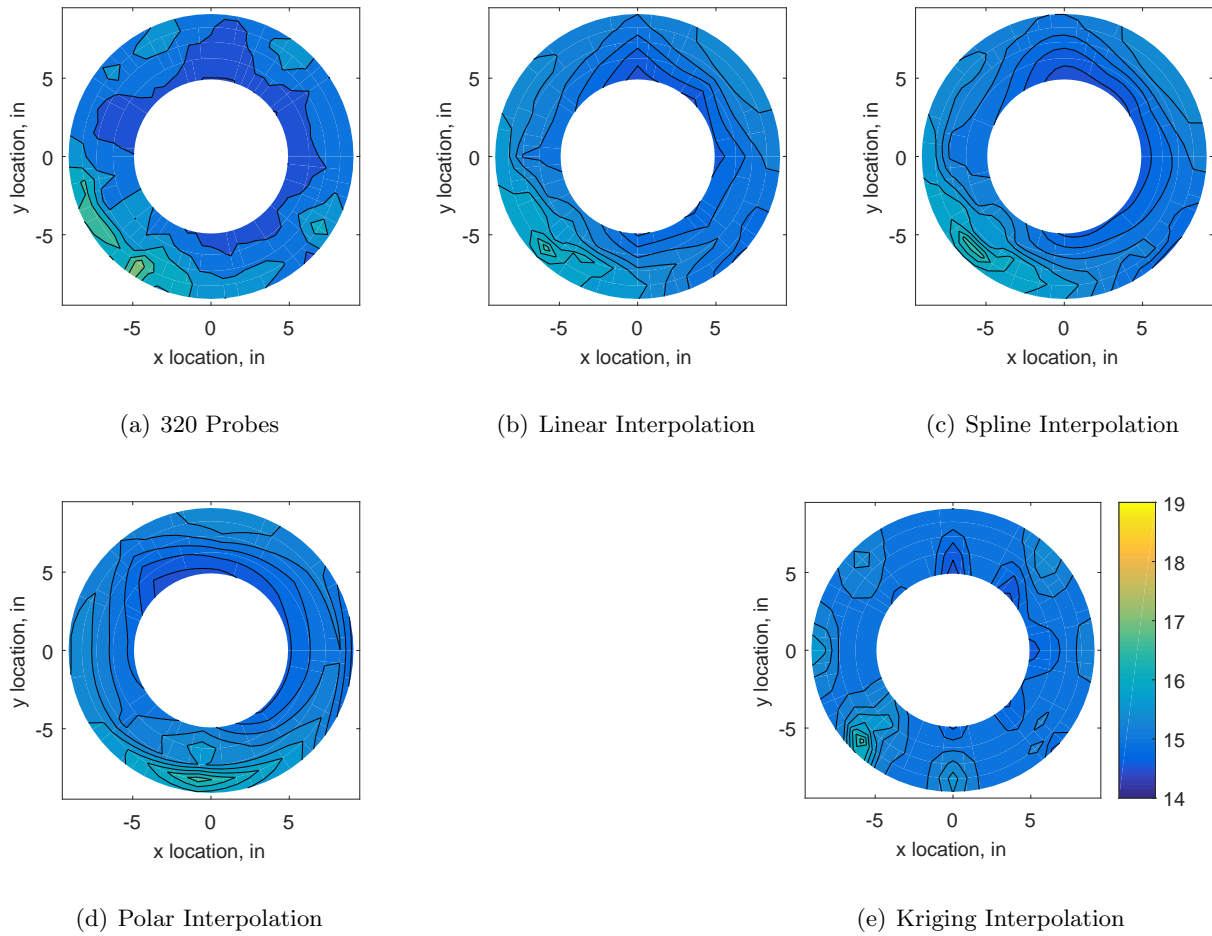
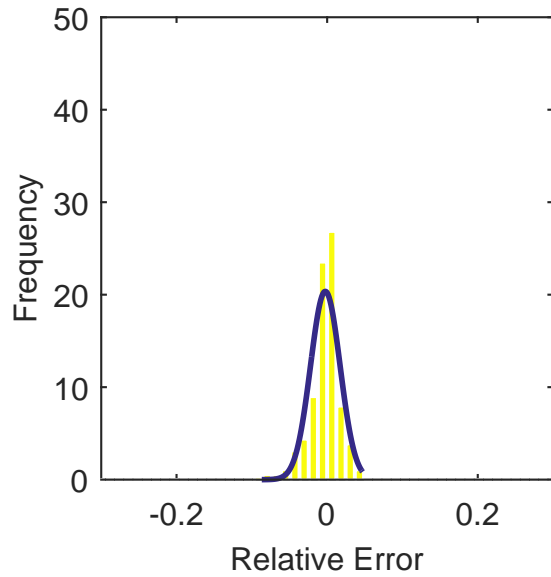
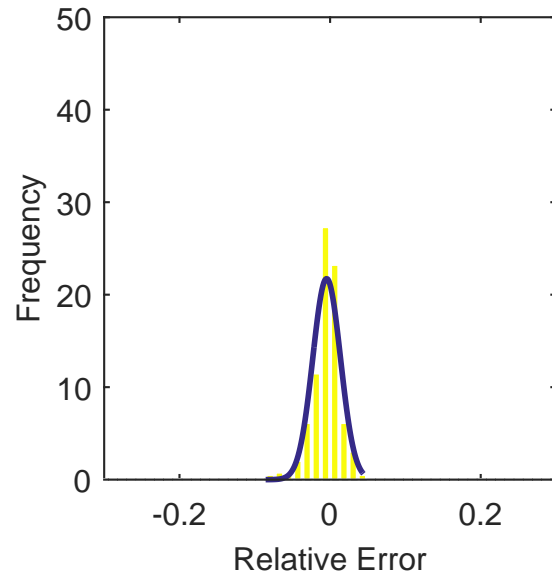


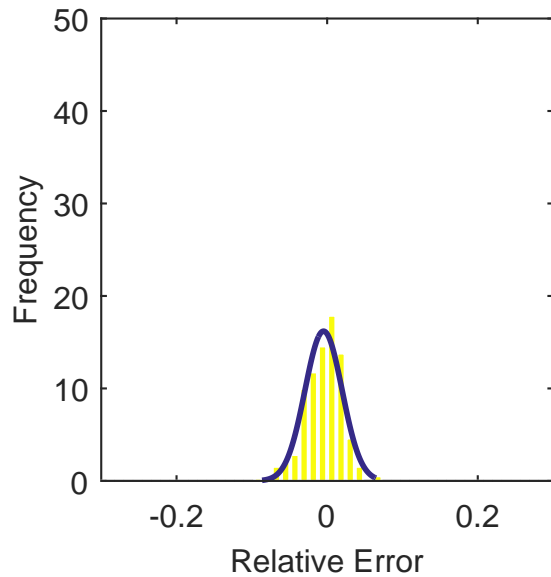
Figure C.46: Contour plots for the raw and interpolated values for the YF12 inlet.



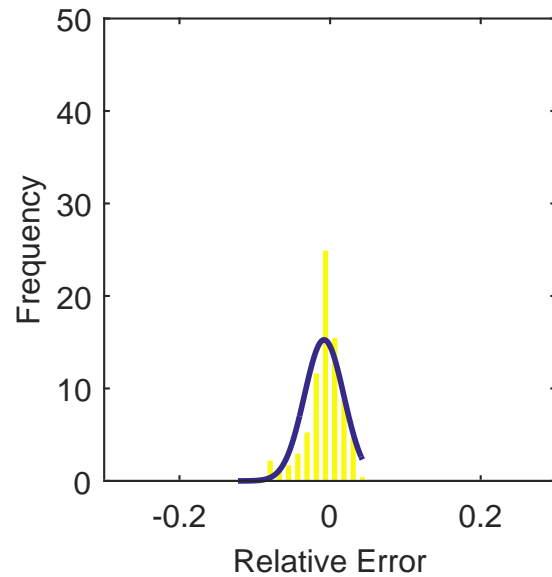
(a) Linear Interpolation Error



(b) Spline Interpolation Error

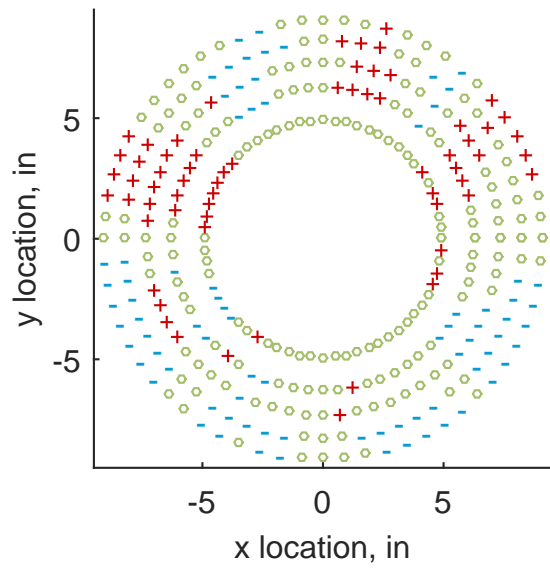


(c) Polar Interpolation Error

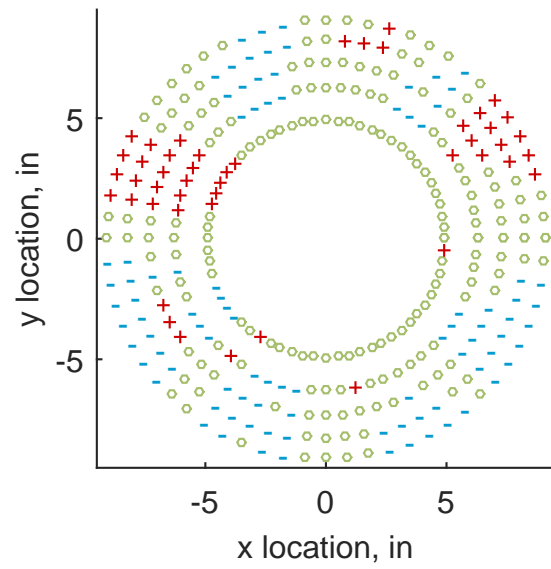


(d) Kriging Interpolation Error

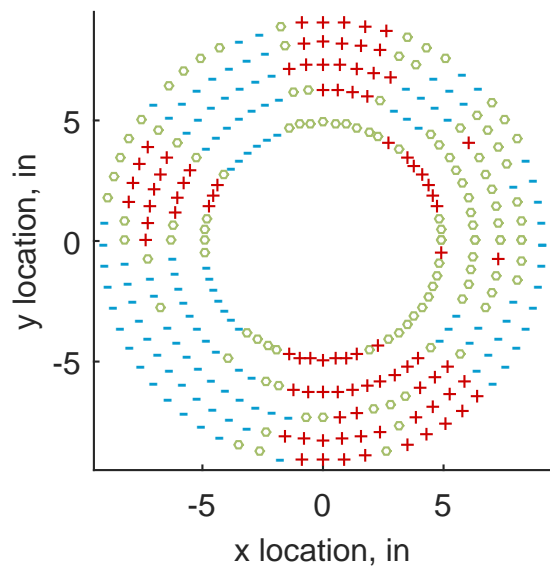
Figure C.47: Relative error for various interpolation schemes of test case 2, zeroth clocking for the YF12 inlet.



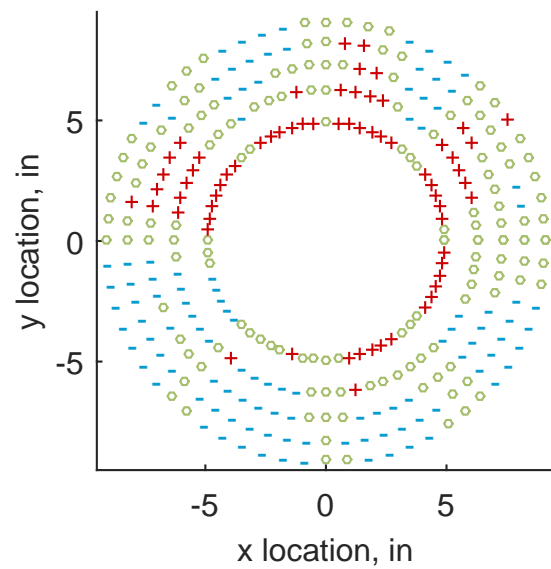
(a) Linear Interpolation



(b) Spline Interpolation



(c) Polar Interpolation



(d) Kriging Interpolation

Figure C.48: Interpolation error for the YF12 inlet - symbols show locations that are within tolerance (o), over-predicted (+), and under-predicted (-).

Table C.19: Interpolation effects on the derived quantities for the IMX inlet run number R310, clocking C1.

	$K_\theta$	$K_r$	$K_a$	$IDC$	$IDT$
Linear	0.598	0.281	0.879	0.041	0.133
Spline	0.597	0.303	0.899	0.041	0.134
Polar	0.597	0.291	0.888	0.035	0.133
Kriging	0.596	0.140	0.735	0.031	0.134

### C.1.2.2 First Clocking

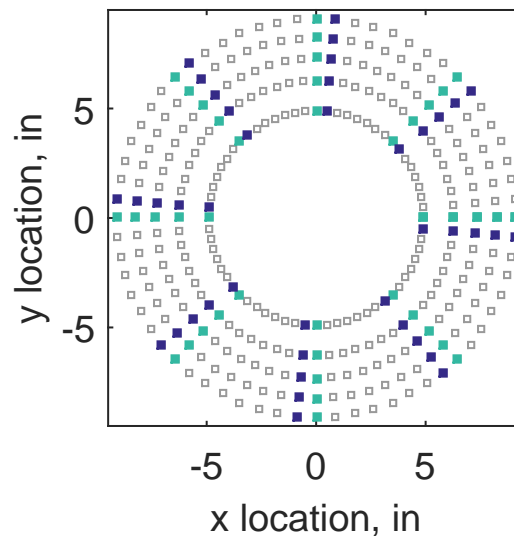


Figure C.49: First clocking probe position



Table C.20: Interpolation results for the YF12 inlet test case 2, clocking C2.

	Mean	Std. Dev.	Over-Prediction	In Tolerance	Under-Prediction
Linear	0.070	0.125	168	31	81
Spline	0.030	0.112	141	40	99
Polar	0.027	0.109	173	-12	119
Kriging	0.030	0.164	116	45	119

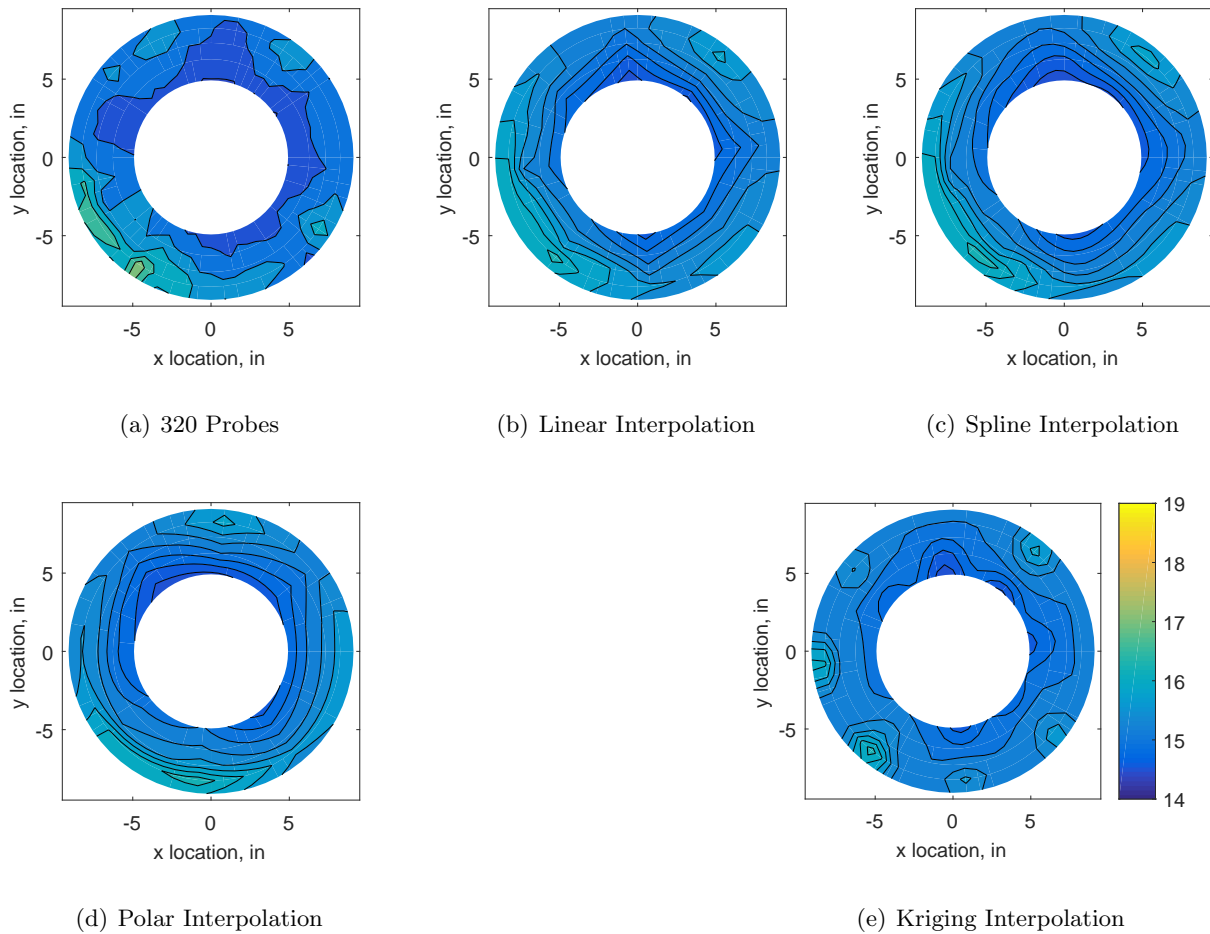
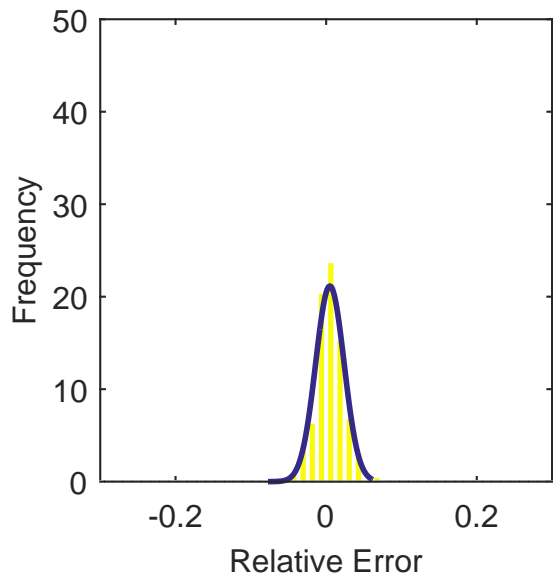
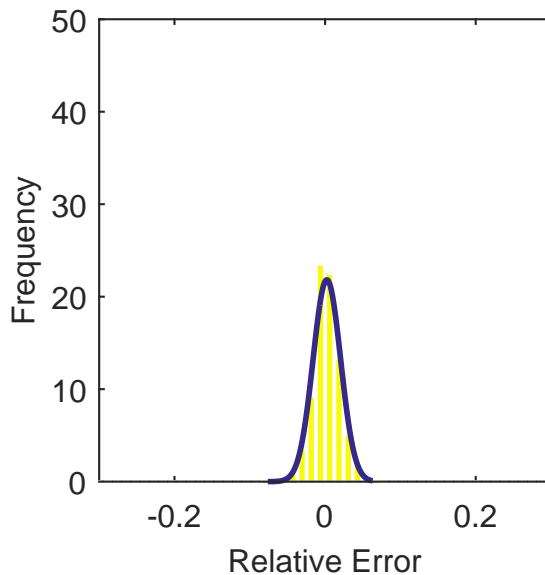


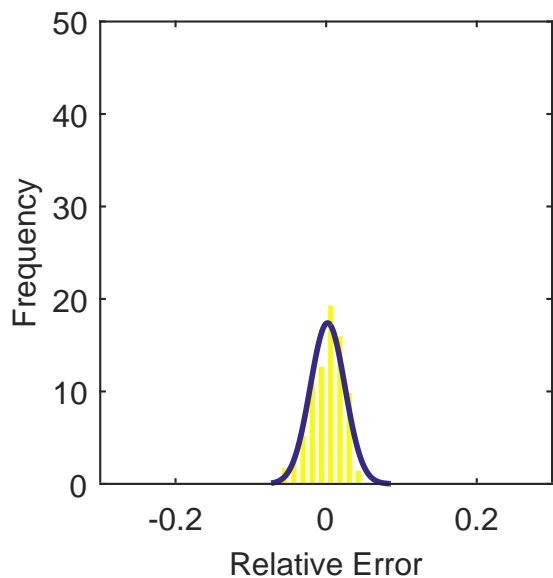
Figure C.50: Contour plots for the raw and interpolated values for the YF12 inlet.



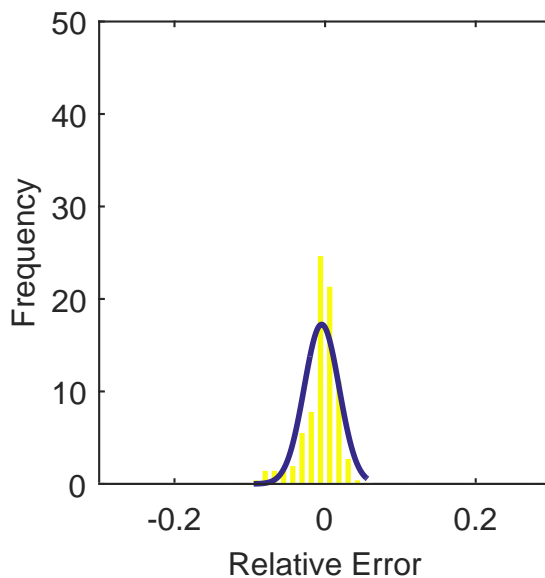
(a) Linear Interpolation Error



(b) Spline Interpolation Error

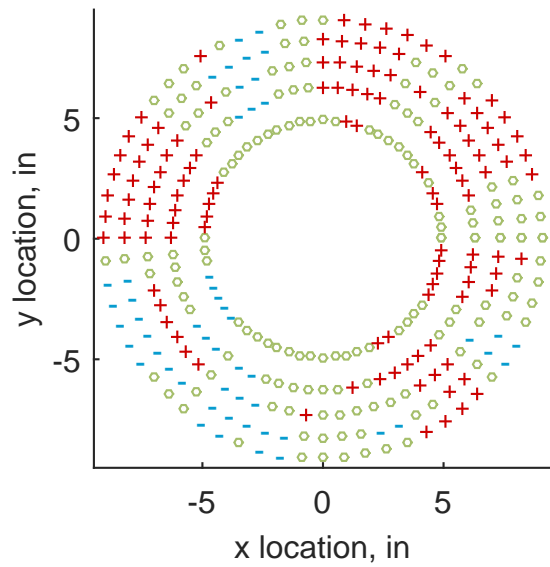


(c) Polar Interpolation Error

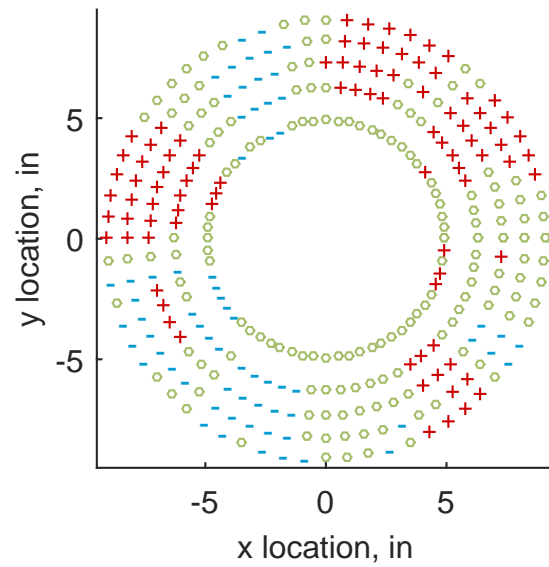


(d) Kriging Interpolation Error

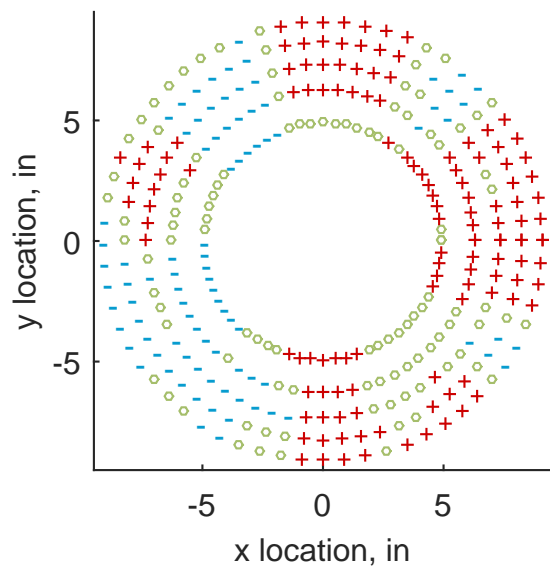
Figure C.51: Relative error for various interpolation schemes of test case 2, first clocking for the YF12 inlet.



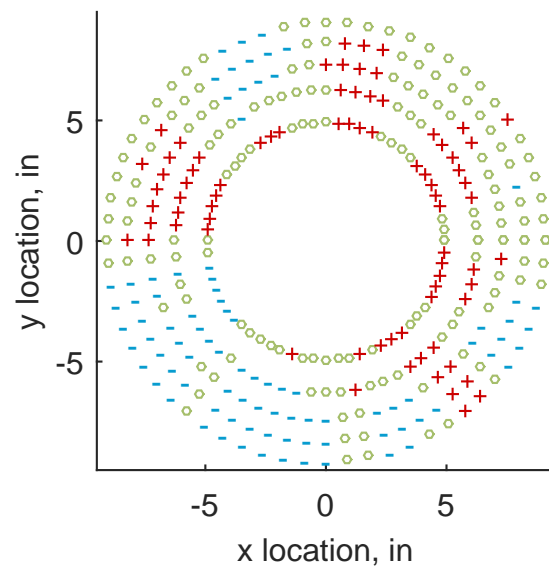
(a) Linear Interpolation



(b) Spline Interpolation



(c) Polar Interpolation



(d) Kriging Interpolation

Figure C.52: Interpolation error for the YF12 inlet - symbols show locations that are within tolerance (o), over-predicted (+), and under-predicted (-).

Table C.21: Interpolation effects on the derived quantities for the IMX inlet run number R310, clocking C2.

	$K_\theta$	$K_r$	$K_a$	$IDC$	$IDT$
Linear	0.602	0.371	0.973	0.028	0.120
Spline	0.600	0.390	0.990	0.028	0.120
Polar	0.600	0.391	0.991	0.029	0.120
Kriging	0.597	0.221	0.818	0.028	0.121

### C.1.2.3 Second Clocking

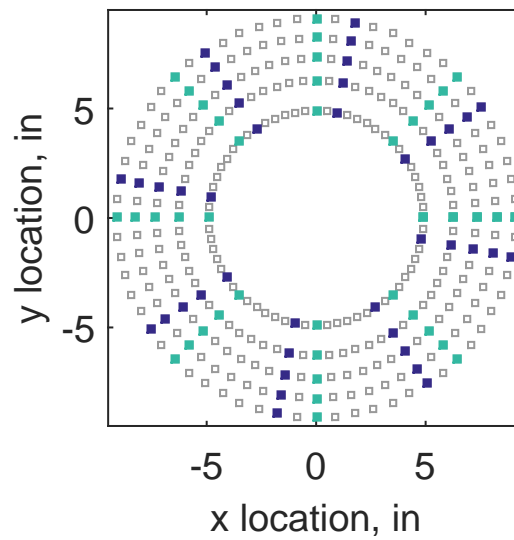
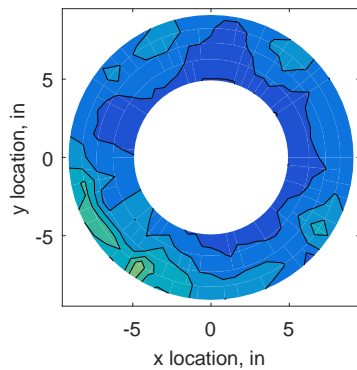


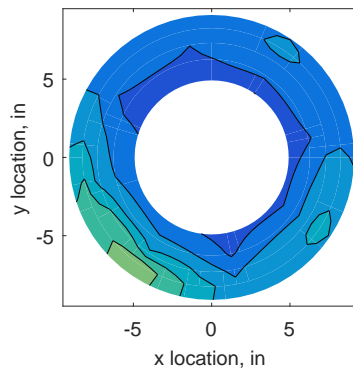
Figure C.53: Second clocking probe position

Table C.22: Interpolation results for the YF12 inlet test case 2, clocking C3.

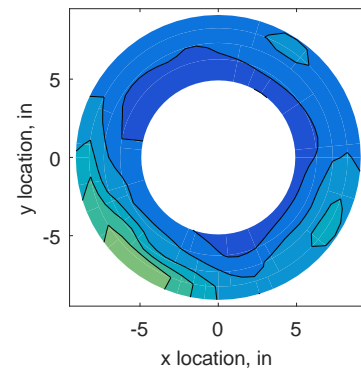
	Mean	Std. Dev.	Over-Prediction	In Tolerance	Under-Prediction
Linear	0.192	0.145	205	27	48
Spline	0.139	0.162	175	37	68
Polar	0.125	0.139	173	-3	110
Kriging	0.139	0.135	138	40	102



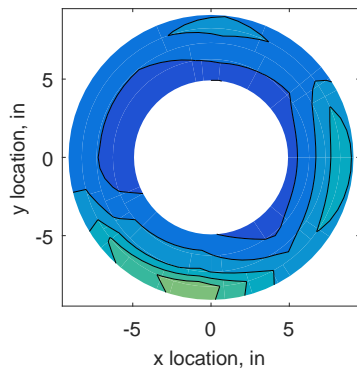
(a) 320 Probes



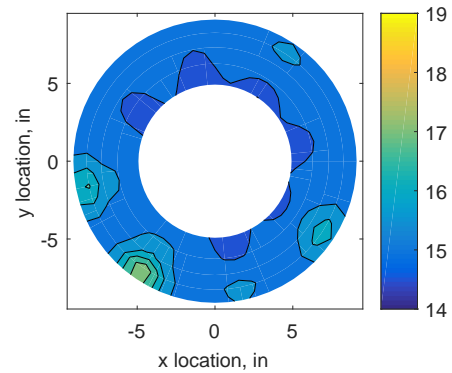
(b) Linear Interpolation



(c) Spline Interpolation

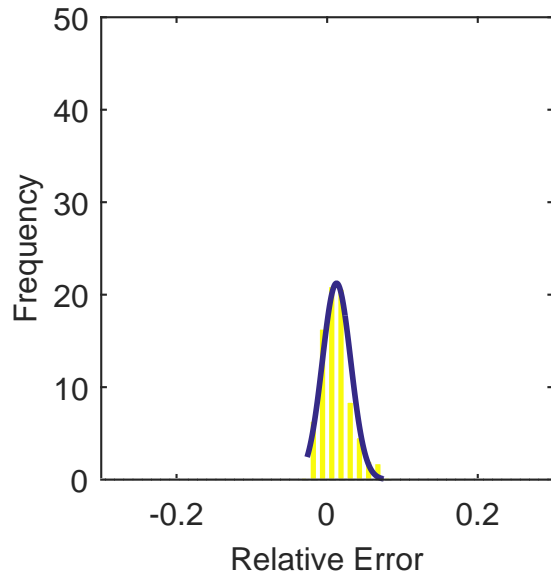


(d) Polar Interpolation

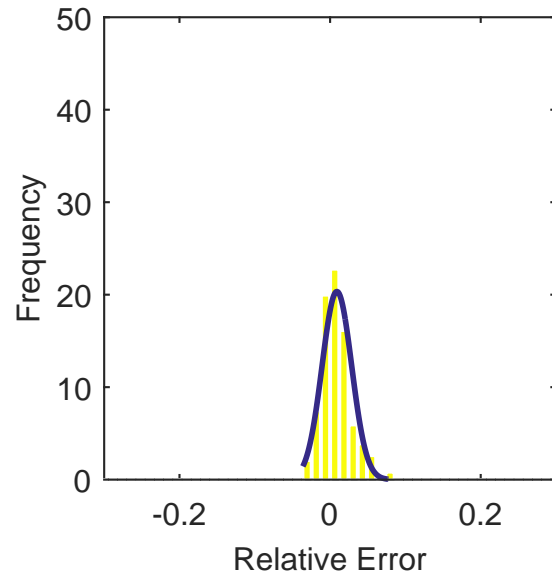


(e) Kriging Interpolation

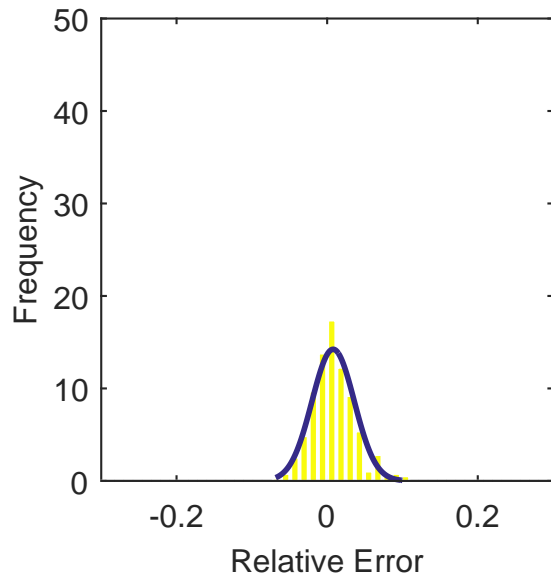
Figure C.54: Contour plots for the raw and interpolated values for the YF12 inlet.



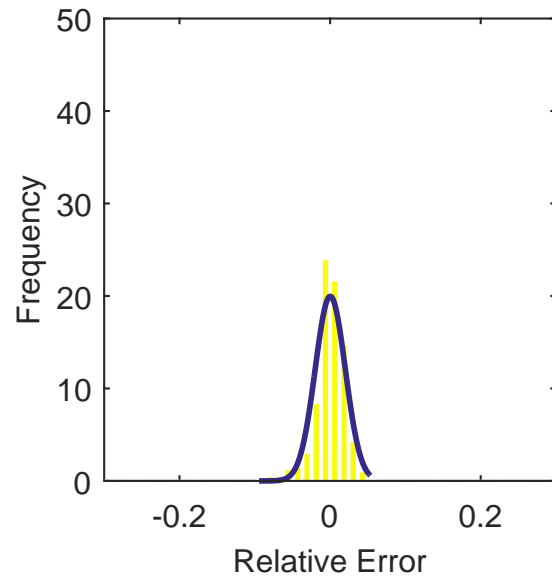
(a) Linear Interpolation Error



(b) Spline Interpolation Error

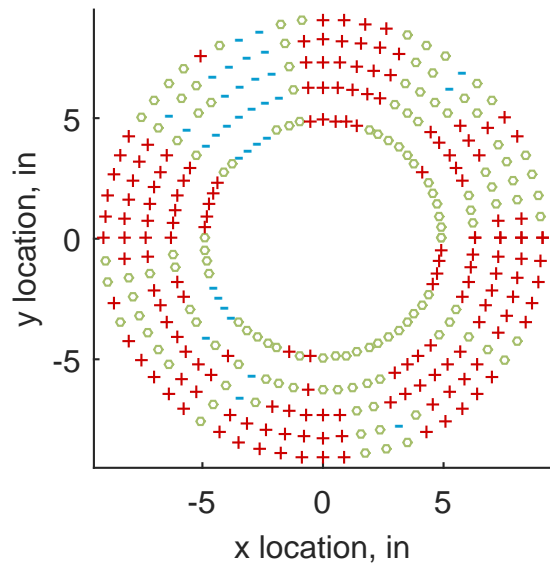


(c) Polar Interpolation Error

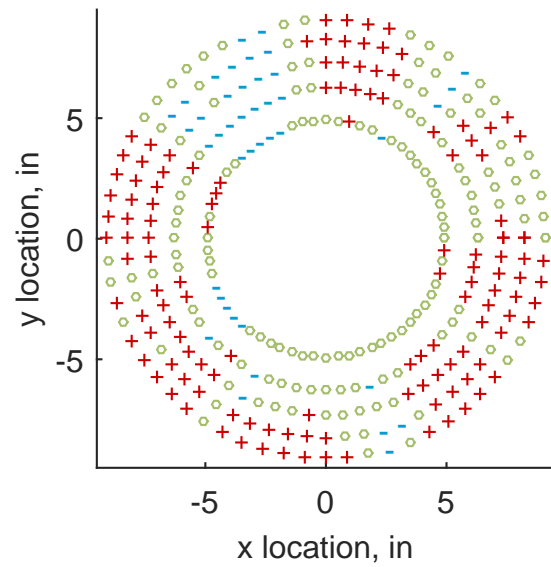


(d) Kriging Interpolation Error

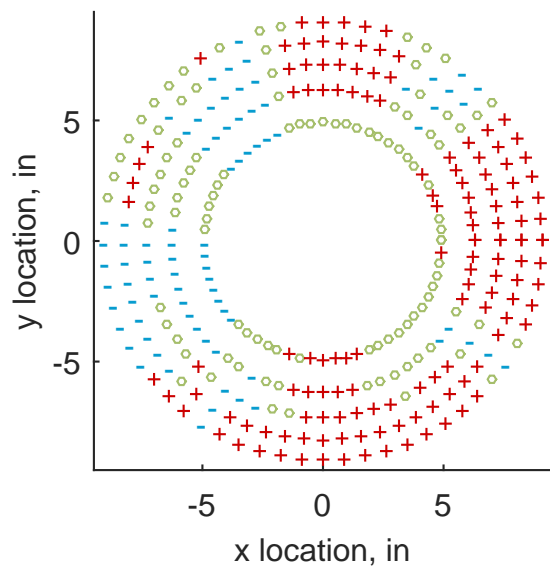
Figure C.55: Relative error for various interpolation schemes of test case 2, second clocking for the YF12 inlet.



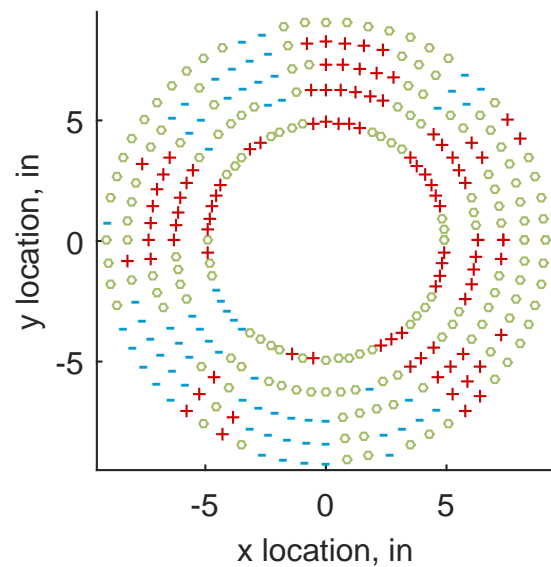
(a) Linear Interpolation



(b) Spline Interpolation



(c) Polar Interpolation



(d) Kriging Interpolation

Figure C.56: Interpolation error for the YF12 inlet - symbols show locations that are within tolerance (o), over-predicted (+), and under-predicted (-).

Table C.23: Interpolation effects on the derived quantities for the IMX inlet run number R310, clocking C3.

	$K_\theta$	$K_r$	$K_a$	$IDC$	$IDT$
Linear	0.606	0.482	1.088	0.035	0.188
Spline	0.604	0.505	1.109	0.038	0.192
Polar	0.603	0.496	1.100	0.038	0.189
Kriging	0.600	0.270	0.870	0.026	0.190

#### C.1.2.4 Third Clocking

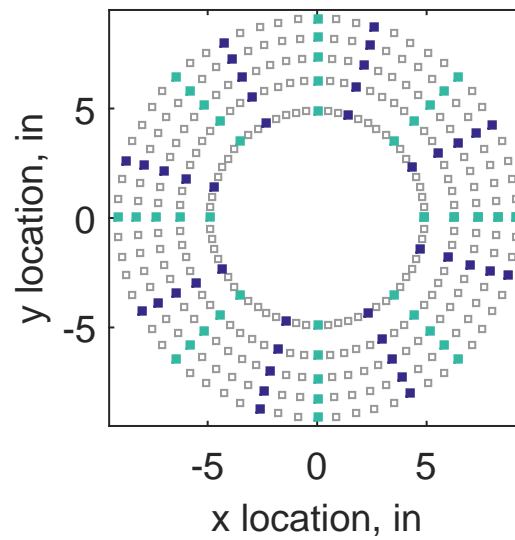


Figure C.57: Third clocking probe position



Table C.24: Interpolation results for the YF12 inlet test case 2, clocking C4.

	Mean	Std. Dev.	Over-Prediction	In Tolerance	Under-Prediction
Linear	0.135	0.136	188	29	63
Spline	0.094	0.127	167	37	76
Polar	0.071	0.090	173	1	106
Kriging	0.094	0.151	121	48	111

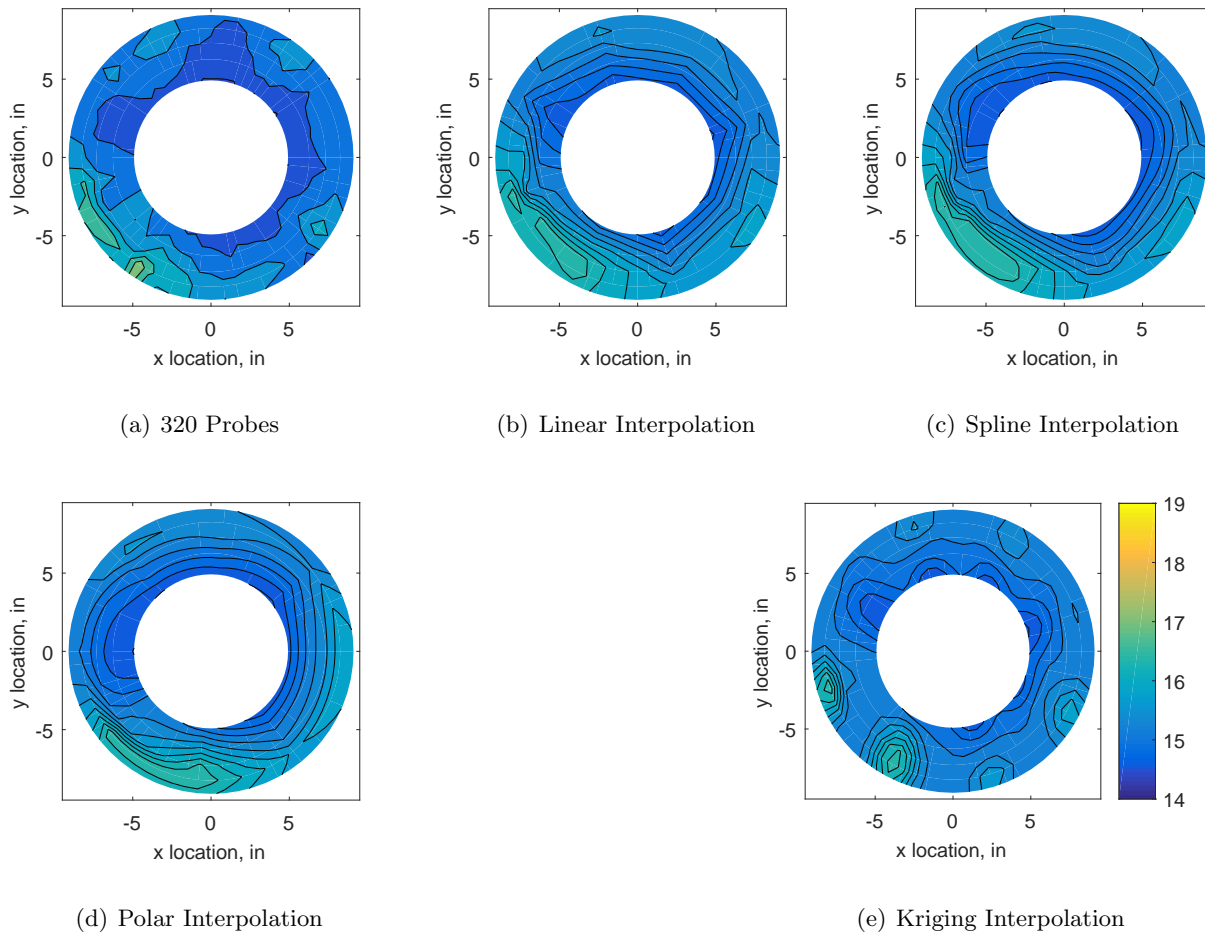
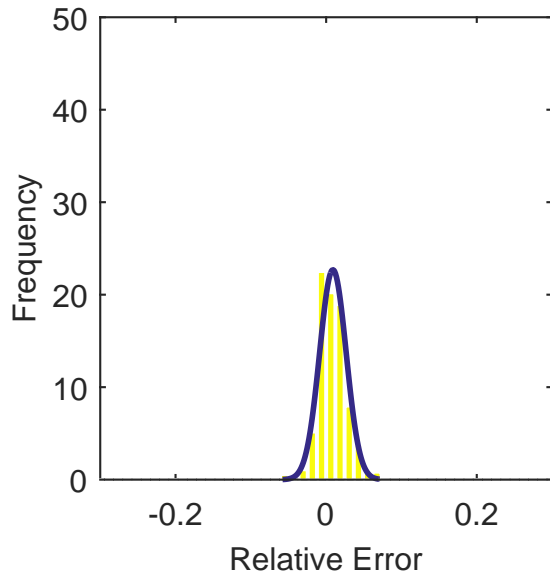
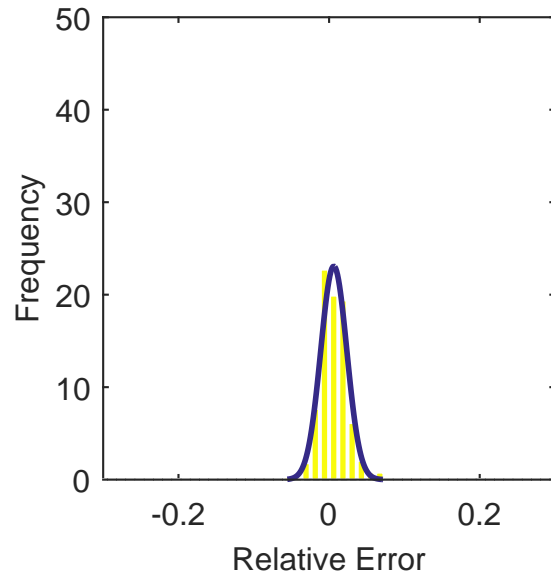


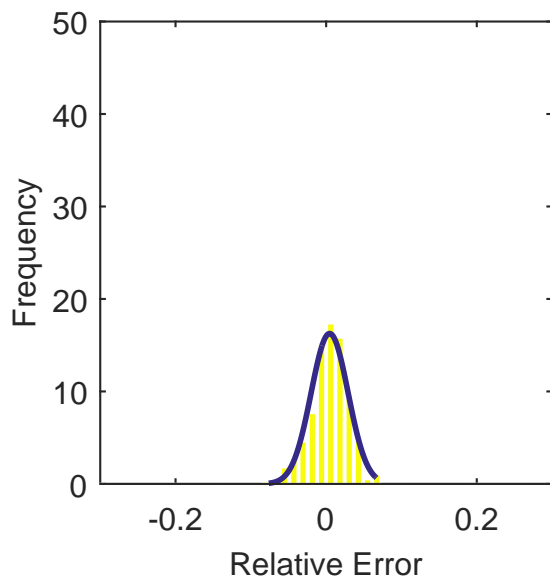
Figure C.58: Contour plots for the raw and interpolated values for the YF12 inlet.



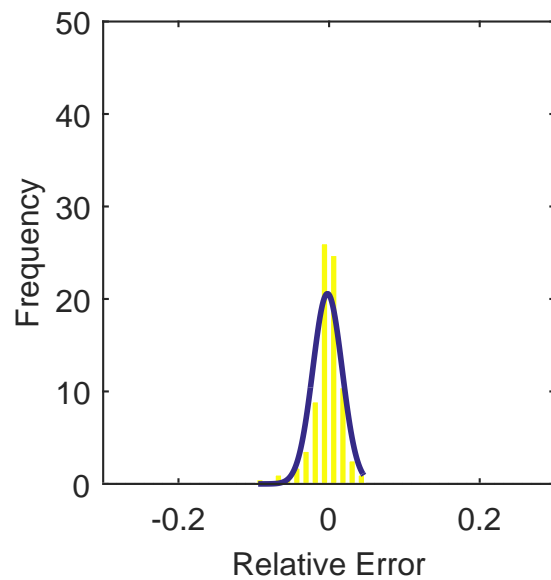
(a) Linear Interpolation Error



(b) Spline Interpolation Error

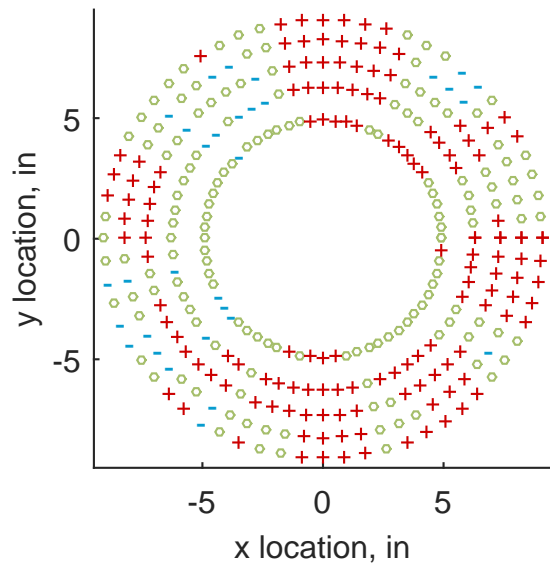


(c) Polar Interpolation Error

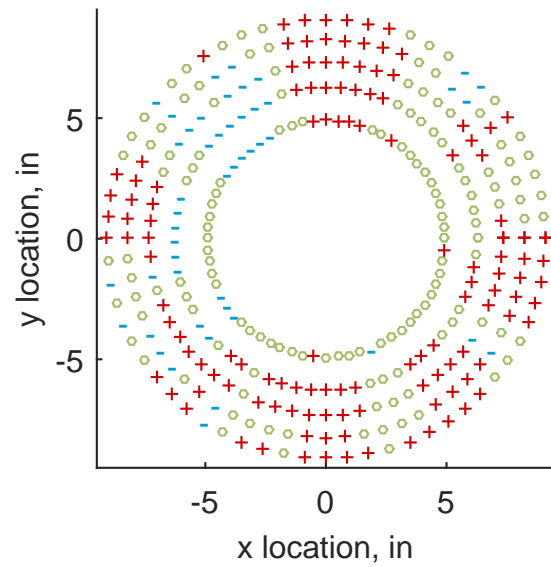


(d) Kriging Interpolation Error

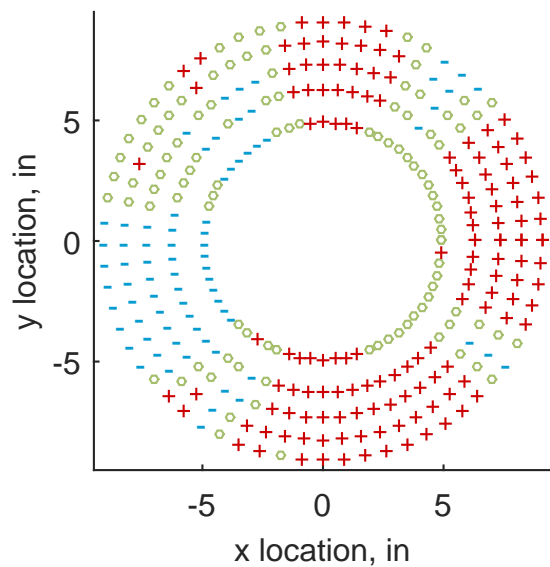
Figure C.59: Relative error for various interpolation schemes of test case 2, third clocking for the YF12 inlet.



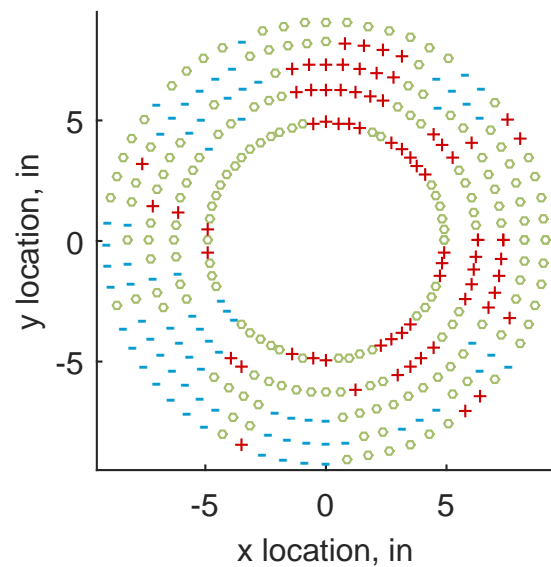
(a) Linear Interpolation



(b) Spline Interpolation



(c) Polar Interpolation



(d) Kriging Interpolation

Figure C.60: Interpolation error for the YF12 inlet - symbols show locations that are within tolerance (o), over-predicted (+), and under-predicted (-).

Table C.25: Interpolation effects on the derived quantities for the IMX inlet run number R310, clocking C4.

	$K_\theta$	$K_r$	$K_a$	$IDC$	$IDT$
Linear	0.604	0.431	1.035	0.033	0.130
Spline	0.602	0.459	1.061	0.035	0.133
Polar	0.601	0.441	1.042	0.035	0.131
Kriging	0.598	0.253	0.852	0.026	0.132

#### C.1.2.5 Fourth Clocking

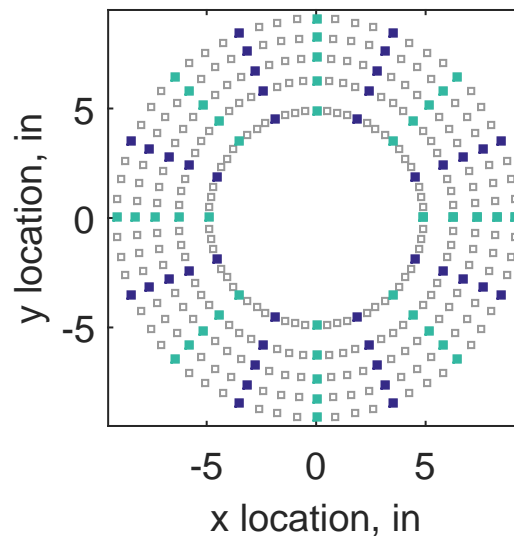
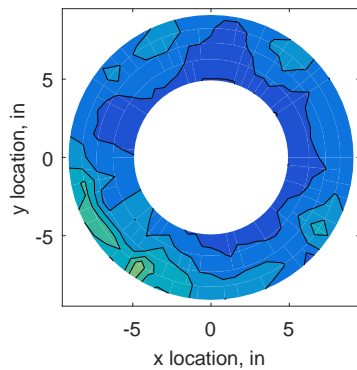


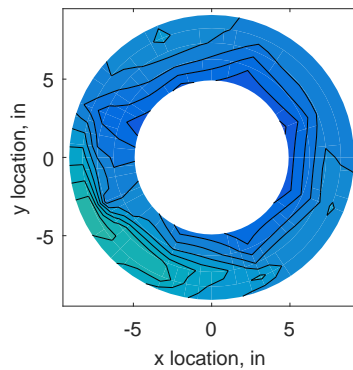
Figure C.61: Fourth clocking probe position

Table C.26: Interpolation results for the YF12 inlet test case 2, clocking C5.

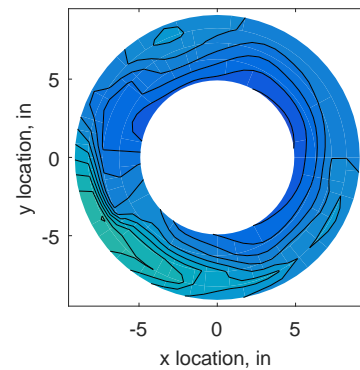
	Mean	Std. Dev.	Over-Prediction	In Tolerance	Under-Prediction
Linear	0.070	0.119	159	55	66
Spline	0.027	0.106	132	53	95
Polar	-0.010	0.101	159	8	113
Kriging	0.027	0.165	97	53	130



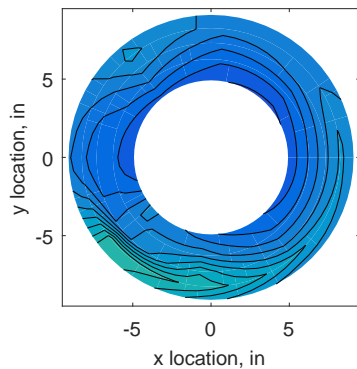
(a) 320 Probes



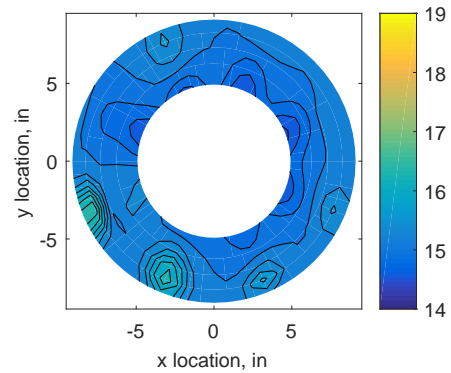
(b) Linear Interpolation



(c) Spline Interpolation

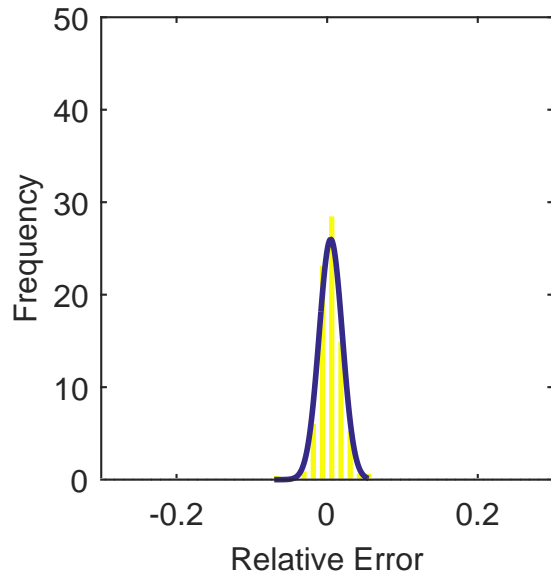


(d) Polar Interpolation

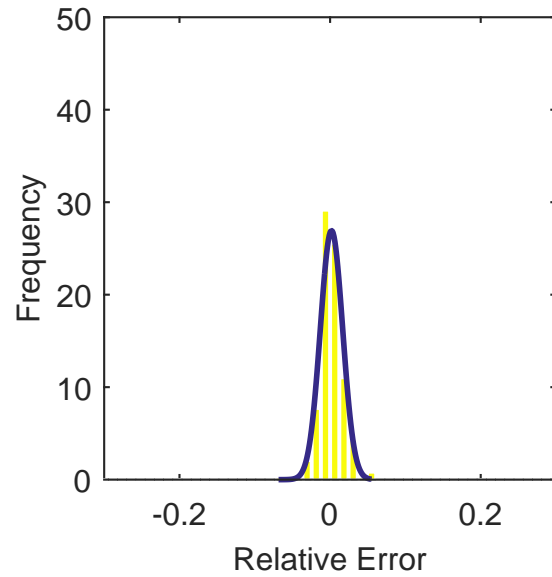


(e) Kriging Interpolation

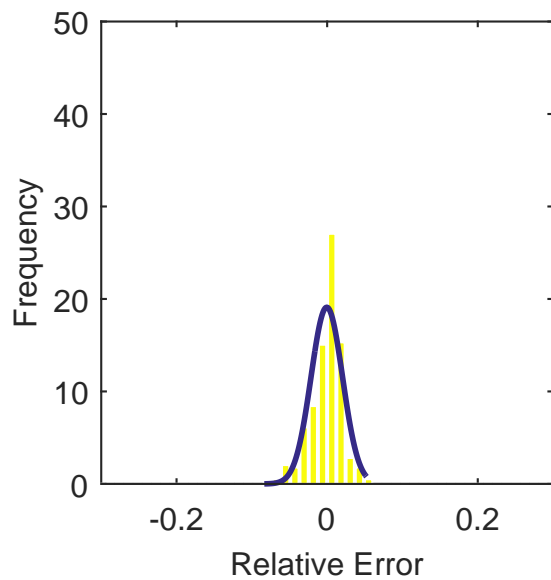
Figure C.62: Contour plots for the raw and interpolated values for the YF12 inlet.



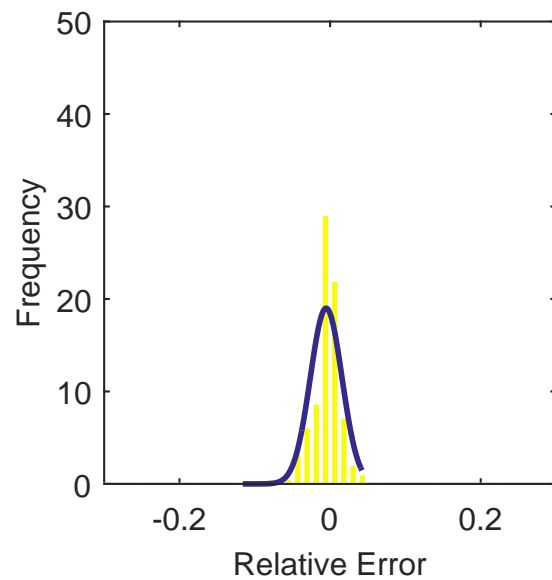
(a) Linear Interpolation Error



(b) Spline Interpolation Error

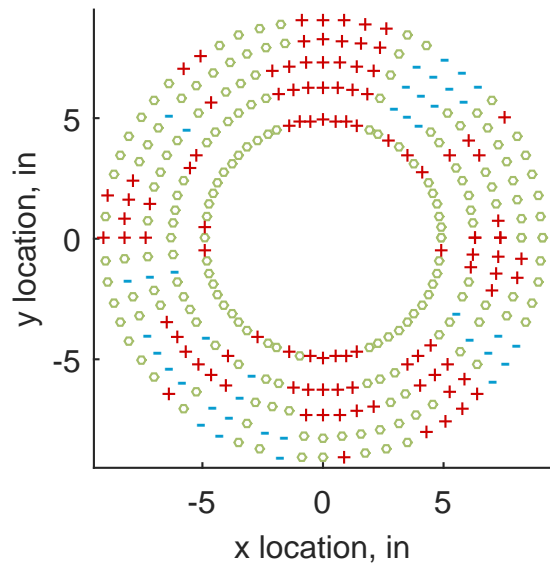


(c) Polar Interpolation Error

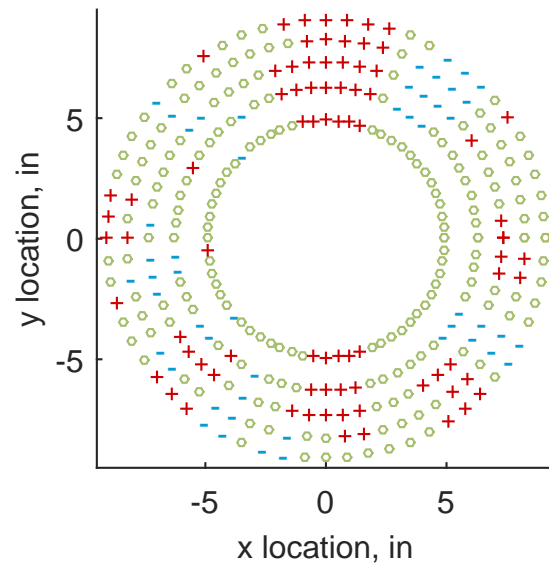


(d) Kriging Interpolation Error

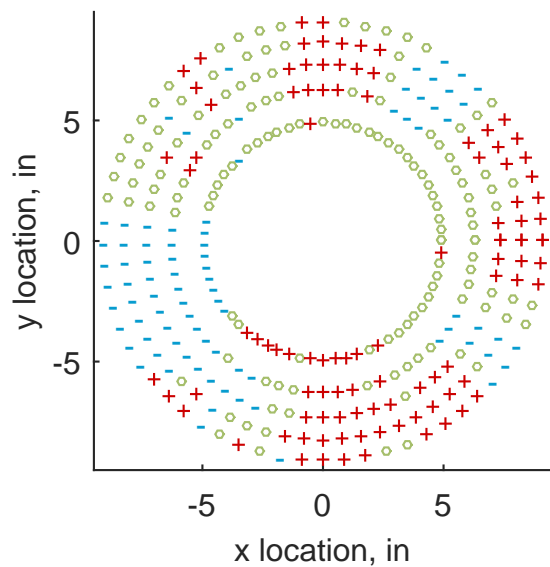
Figure C.63: Relative error for various interpolation schemes of test case 2, fourth clocking for the YF12 inlet.



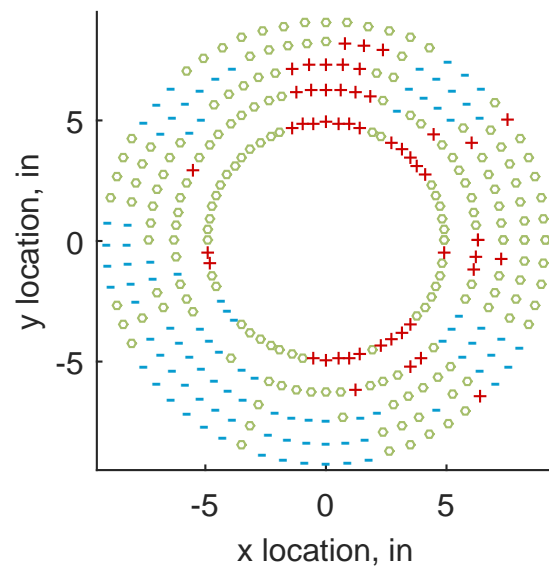
(a) Linear Interpolation



(b) Spline Interpolation



(c) Polar Interpolation



(d) Kriging Interpolation

Figure C.64: Interpolation error for the YF12 inlet - symbols show locations that are within tolerance (o), over-predicted (+), and under-predicted (-).

Table C.27: Interpolation effects on the derived quantities for the IMX inlet run number R310, clocking C5.

	$K_\theta$	$K_r$	$K_a$	$IDC$	$IDT$
Linear	0.602	0.356	0.958	0.031	0.130
Spline	0.600	0.380	0.981	0.032	0.135
Polar	0.599	0.377	0.976	0.032	0.131
Kriging	0.597	0.205	0.802	0.022	0.132

### C.1.2.6 Fifth Clocking

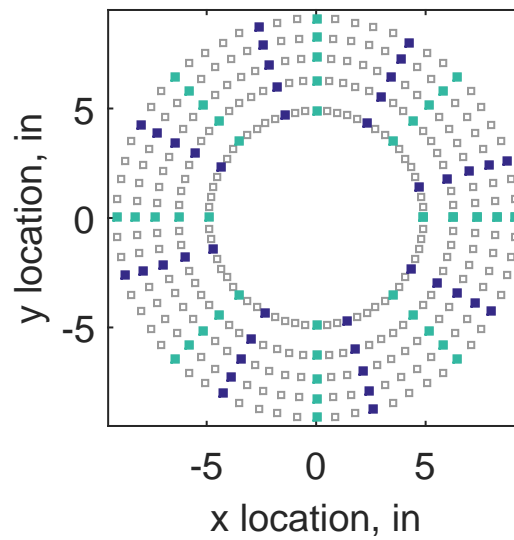
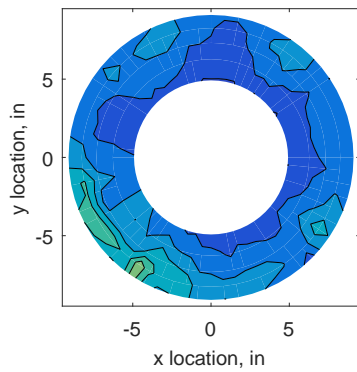


Figure C.65: Fifth clocking probe position

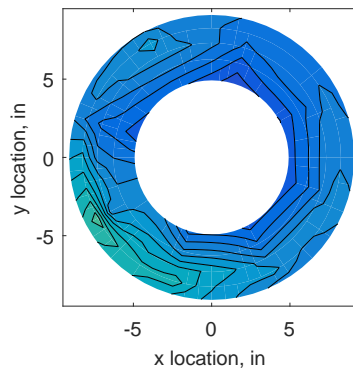


Table C.28: Interpolation results for the YF12 inlet test case 2, clocking C6.

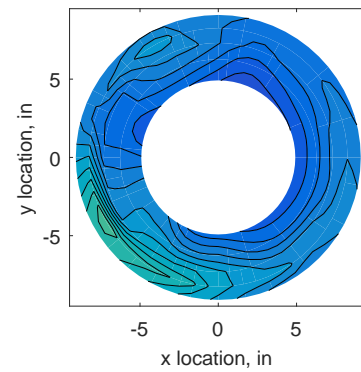
	Mean	Std. Dev.	Over-Prediction	In Tolerance	Under-Prediction
Linear	0.025	0.107	137	56	87
Spline	-0.009	0.094	112	67	101
Polar	-0.042	0.094	129	29	122
Kriging	-0.009	0.177	92	35	153



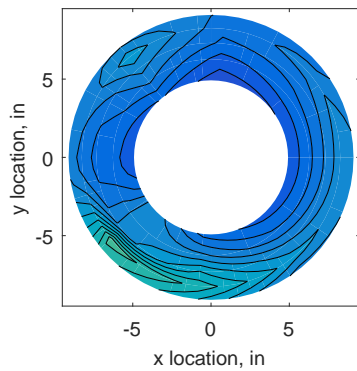
(a) 320 Probes



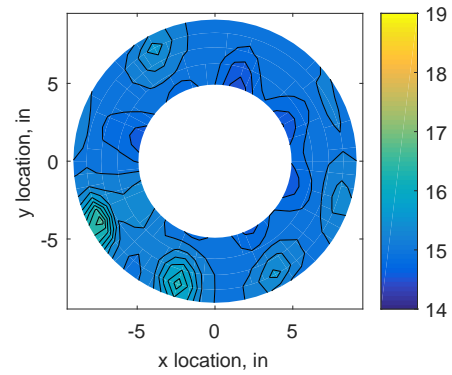
(b) Linear Interpolation



(c) Spline Interpolation

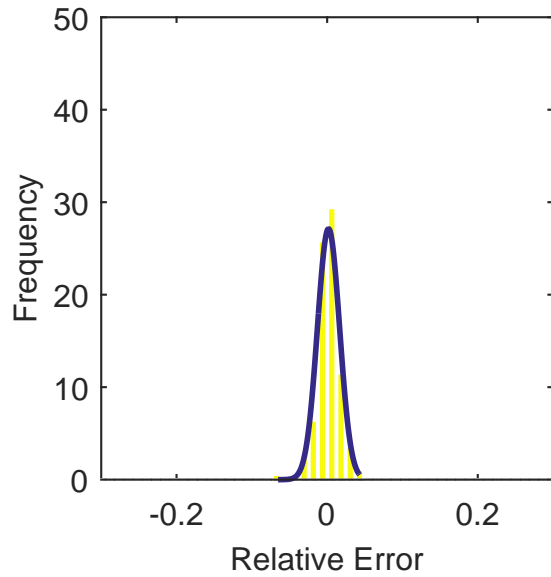


(d) Polar Interpolation

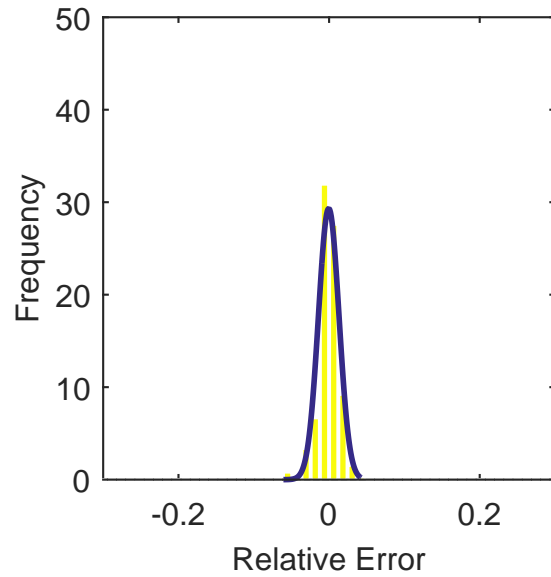


(e) Kriging Interpolation

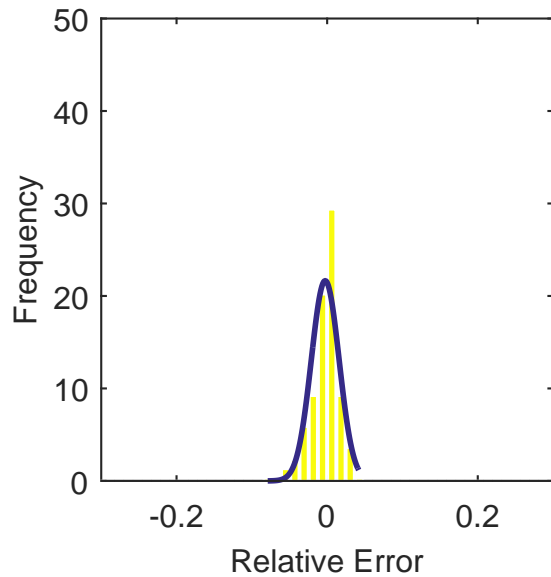
Figure C.66: Contour plots for the raw and interpolated values for the YF12 inlet.



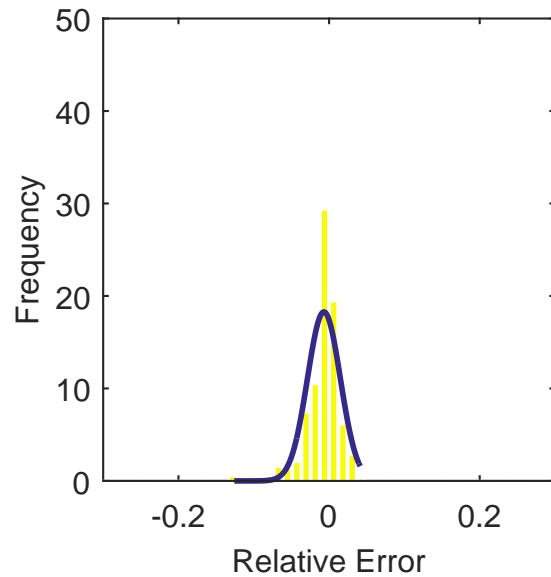
(a) Linear Interpolation Error



(b) Spline Interpolation Error

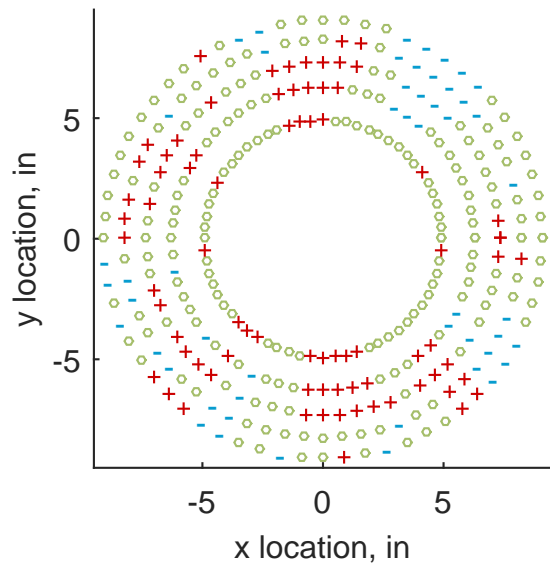


(c) Polar Interpolation Error

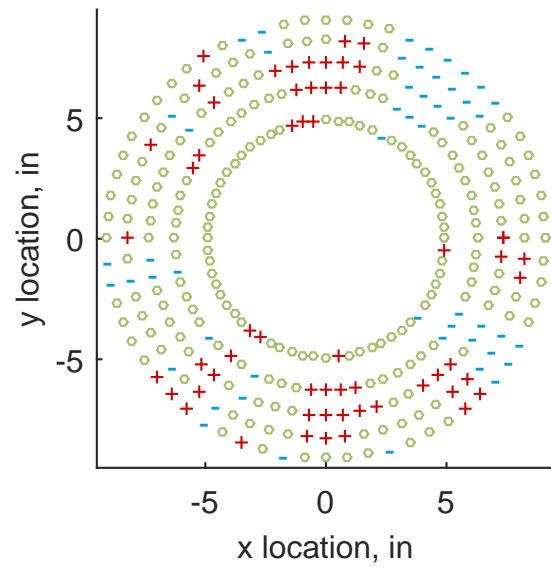


(d) Kriging Interpolation Error

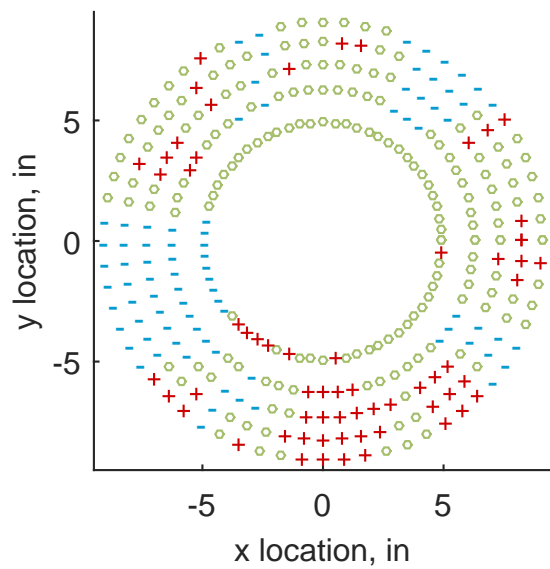
Figure C.67: Relative error for various interpolation schemes of test case 2, fifth clocking for the YF12 inlet.



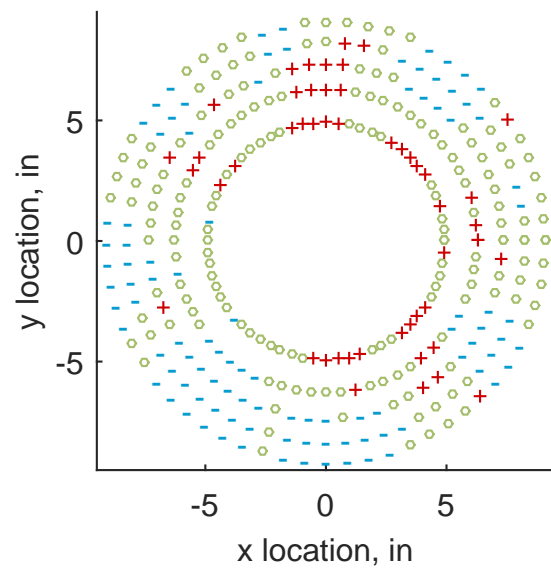
(a) Linear Interpolation



(b) Spline Interpolation



(c) Polar Interpolation



(d) Kriging Interpolation

Figure C.68: Interpolation error for the YF12 inlet - symbols show locations that are within tolerance (o), over-predicted (+), and under-predicted (-).

Table C.29: Interpolation effects on the derived quantities for the IMX inlet run number R310, clocking C6.

	$K_\theta$	$K_r$	$K_a$	$IDC$	$IDT$
Linear	0.600	0.335	0.935	0.031	0.146
Spline	0.599	0.354	0.953	0.033	0.149
Polar	0.598	0.361	0.959	0.032	0.147
Kriging	0.596	0.188	0.784	0.028	0.147

### C.1.2.7 Sixth Clocking

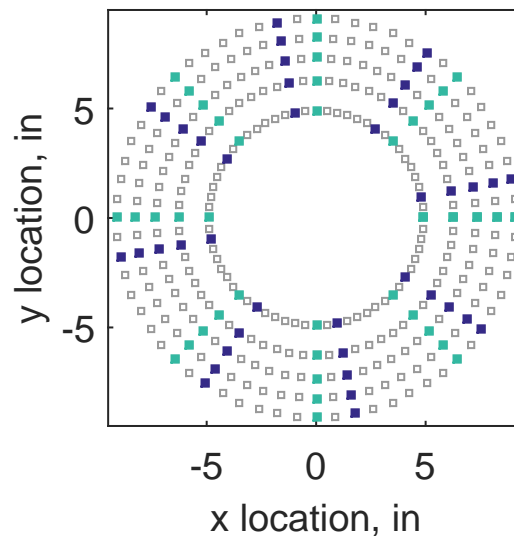
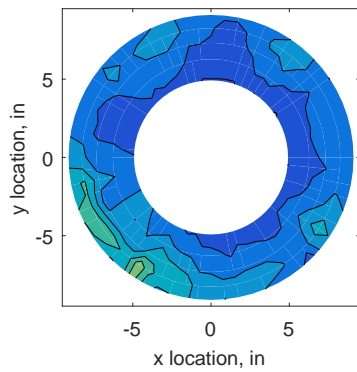


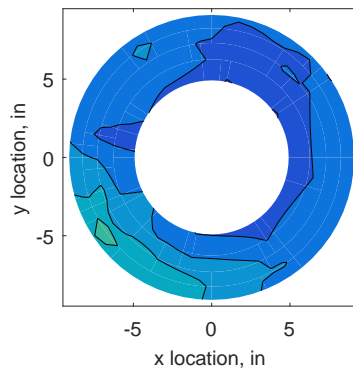
Figure C.69: Sixth clocking probe position

Table C.30: Interpolation results for the YF12 inlet test case 2, clocking C7.

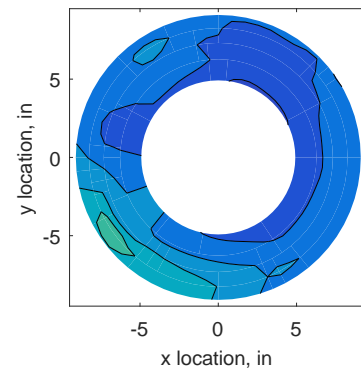
	Mean	Std. Dev.	Over-Prediction	In Tolerance	Under-Prediction
Linear	-0.023	0.121	109	57	114
Spline	-0.055	0.106	89	58	133
Polar	-0.081	0.102	96	49	135
Kriging	-0.055	0.202	101	41	138



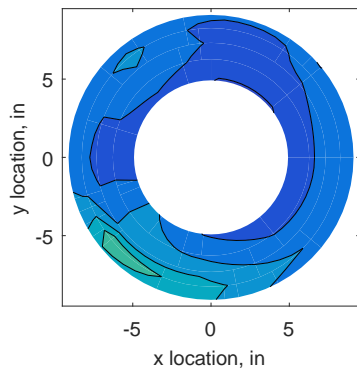
(a) 320 Probes



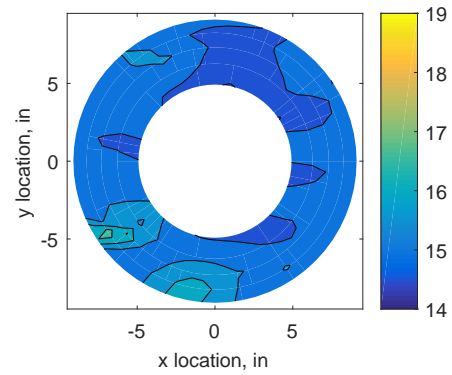
(b) Linear Interpolation



(c) Spline Interpolation

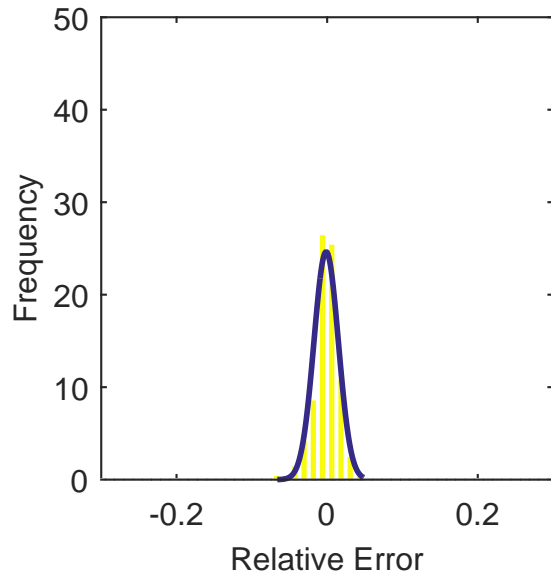


(d) Polar Interpolation

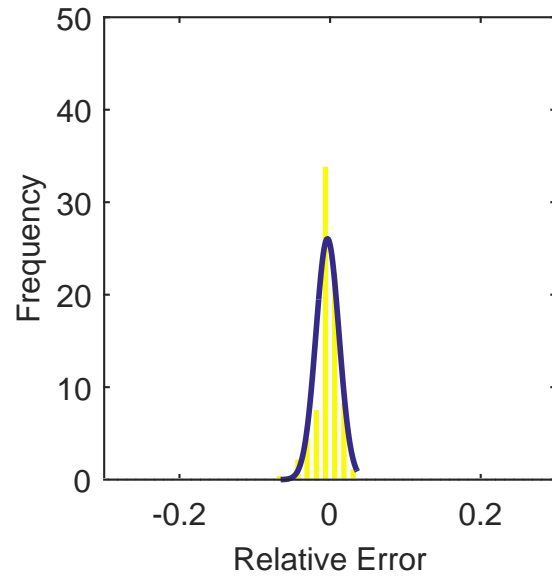


(e) Kriging Interpolation

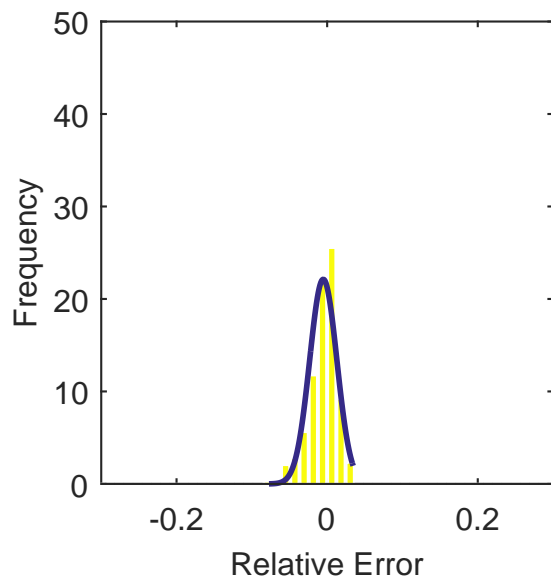
Figure C.70: Contour plots for the raw and interpolated values for the YF12 inlet.



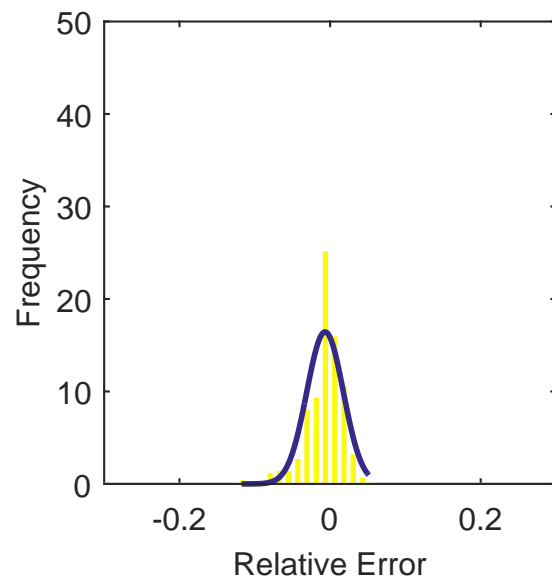
(a) Linear Interpolation Error



(b) Spline Interpolation Error

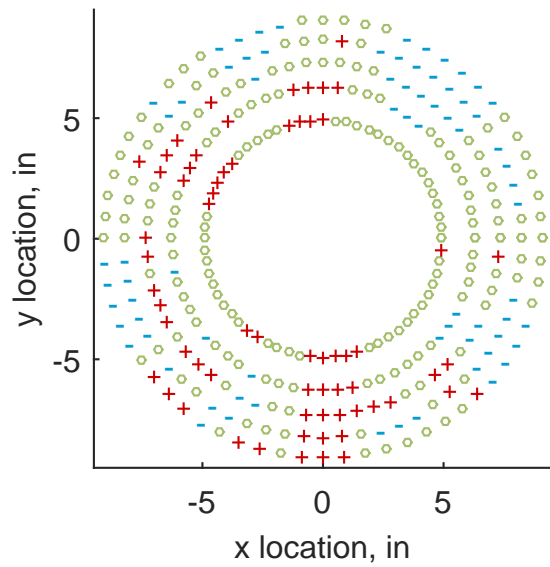


(c) Polar Interpolation Error

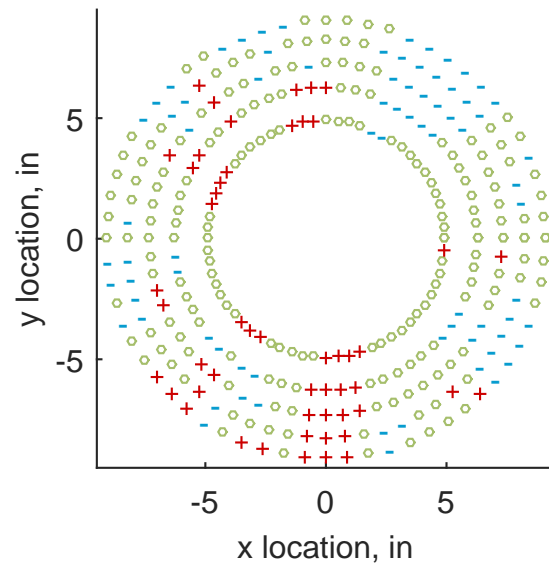


(d) Kriging Interpolation Error

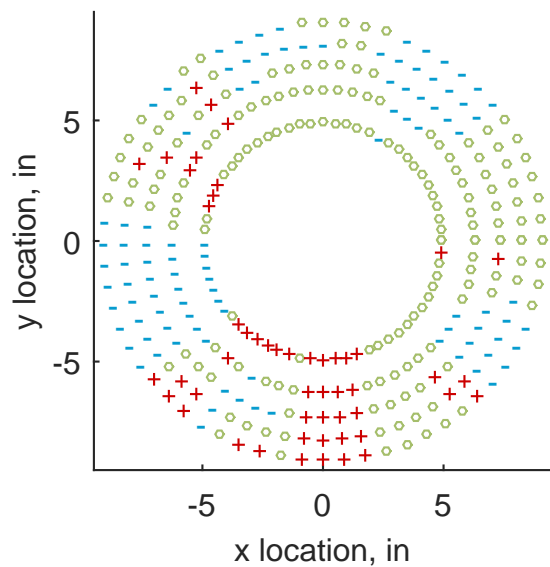
Figure C.71: Relative error for various interpolation schemes of test case 2, sixth clocking for the YF12 inlet.



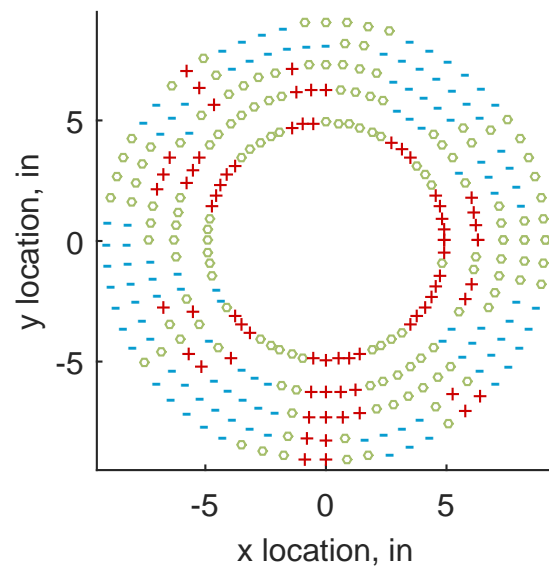
(a) Linear Interpolation



(b) Spline Interpolation



(c) Polar Interpolation



(d) Kriging Interpolation

Figure C.72: Interpolation error for the YF12 inlet - symbols show locations that are within tolerance (o), over-predicted (+), and under-predicted (-).

Table C.31: Interpolation effects on the derived quantities for the IMX inlet run number R310, clocking C7.

	$K_\theta$	$K_r$	$K_a$	$IDC$	$IDT$
Linear	0.599	0.292	0.891	0.046	0.160
Spline	0.597	0.308	0.905	0.047	0.162
Polar	0.596	0.298	0.895	0.047	0.161
Kriging	0.596	0.163	0.759	0.036	0.161

### C.1.2.8 Seventh Clocking

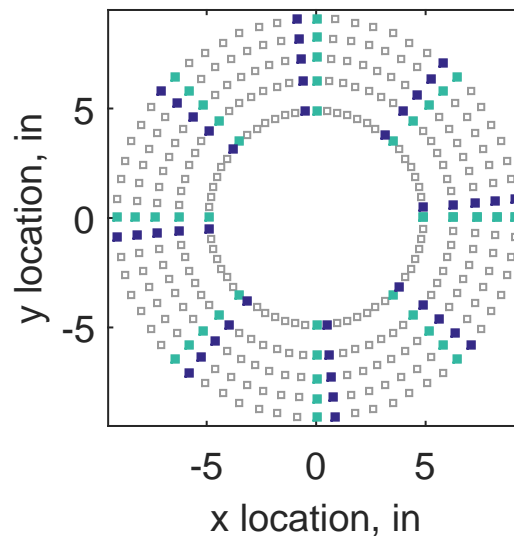


Figure C.73: Seventh clocking probe position



Table C.32: Interpolation results for the YF12 inlet test case 2, clocking C8.

	Mean	Std. Dev.	Over-Prediction	In Tolerance	Under-Prediction
Linear	-0.050	0.143	95	69	116
Spline	-0.083	0.126	68	71	141
Polar	-0.114	0.110	61	65	154
Kriging	-0.083	0.202	84	30	166

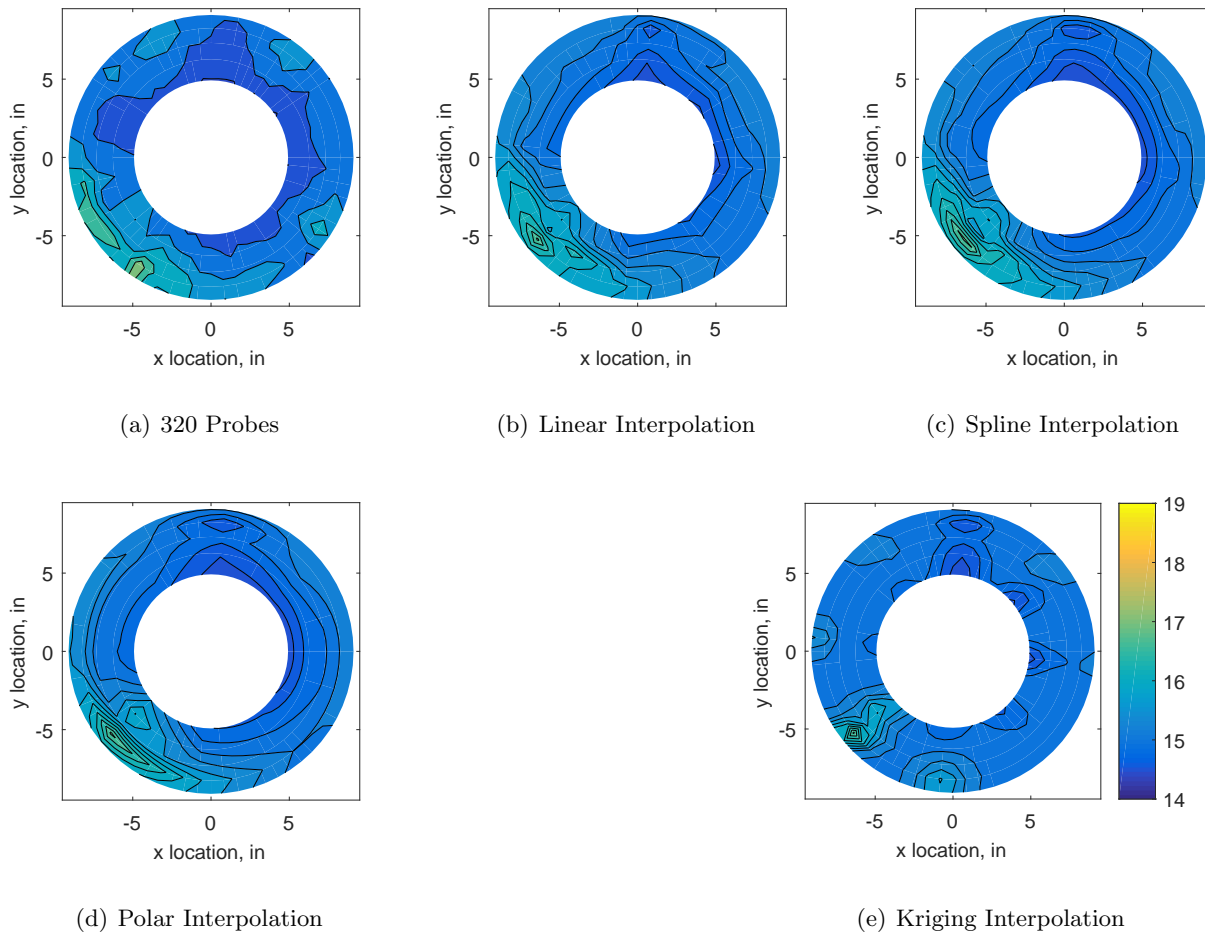
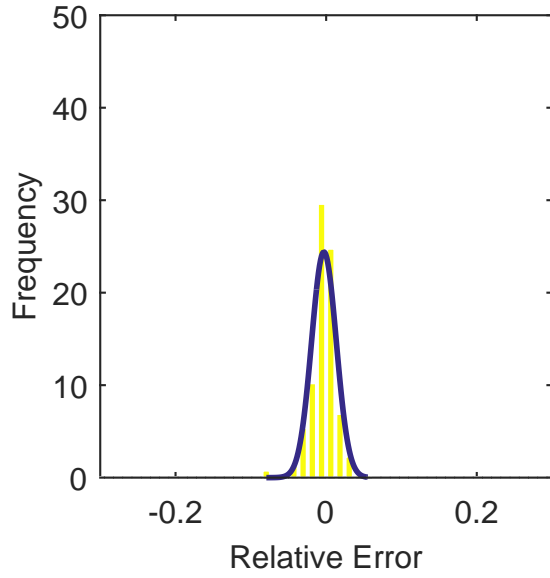
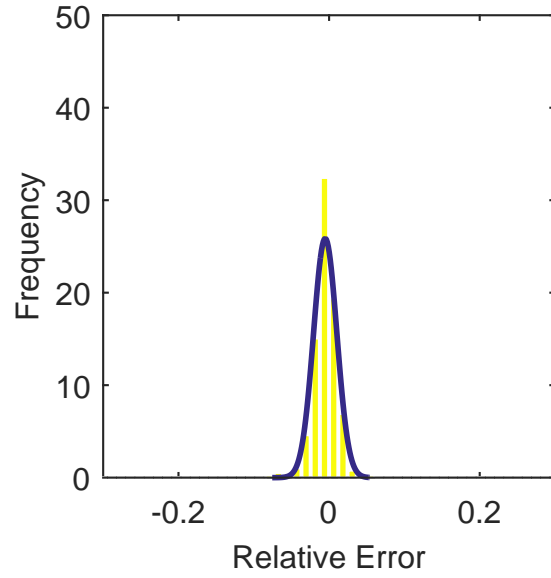


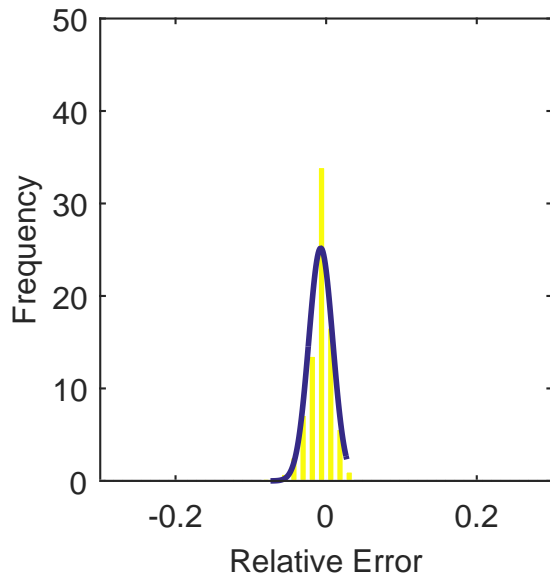
Figure C.74: Contour plots for the raw and interpolated values for the YF12 inlet.



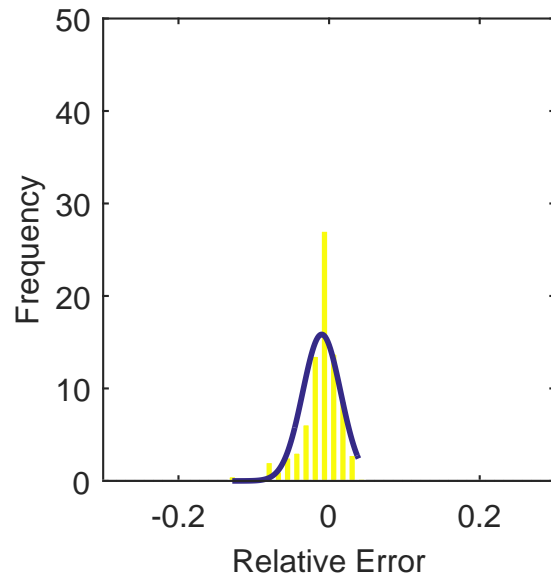
(a) Linear Interpolation Error



(b) Spline Interpolation Error

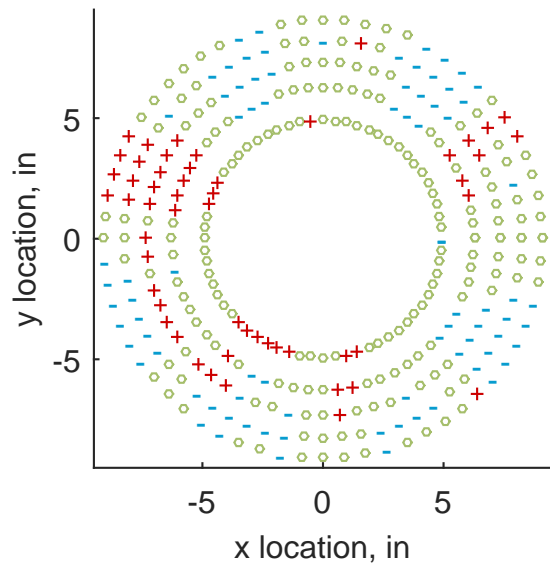


(c) Polar Interpolation Error

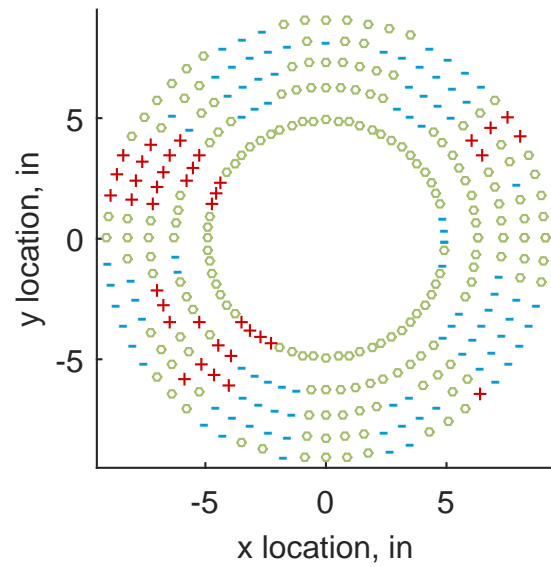


(d) Kriging Interpolation Error

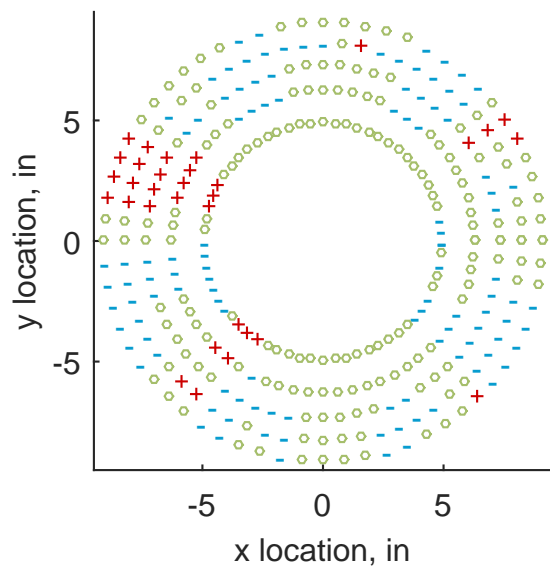
Figure C.75: Relative error for various interpolation schemes of test case 2, seventh clocking for the YF12 inlet.



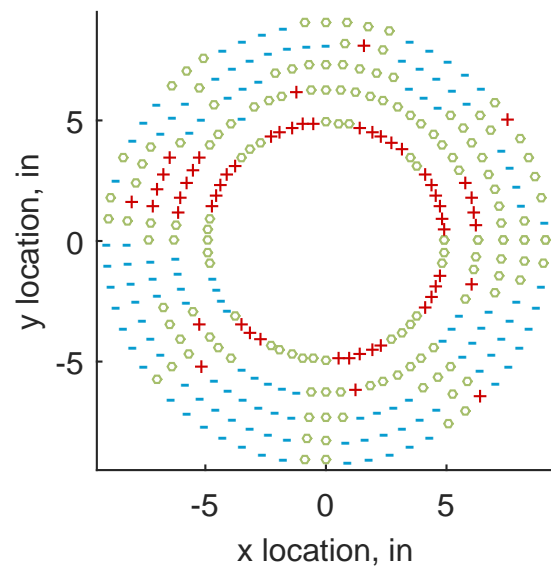
(a) Linear Interpolation



(b) Spline Interpolation



(c) Polar Interpolation



(d) Kriging Interpolation

Figure C.76: Interpolation error for the YF12 inlet - symbols show locations that are within tolerance (o), over-predicted (+), and under-predicted (-).

Table C.33: Interpolation effects on the derived quantities for the IMX inlet run number R310, clocking C8.

	$K_\theta$	$K_r$	$K_a$	$IDC$	$IDT$
Linear	0.598	0.289	0.887	0.040	0.155
Spline	0.596	0.305	0.901	0.040	0.156
Polar	0.595	0.290	0.885	0.040	0.156
Kriging	0.595	0.131	0.725	0.031	0.156

## C.1.3 Test Case 3

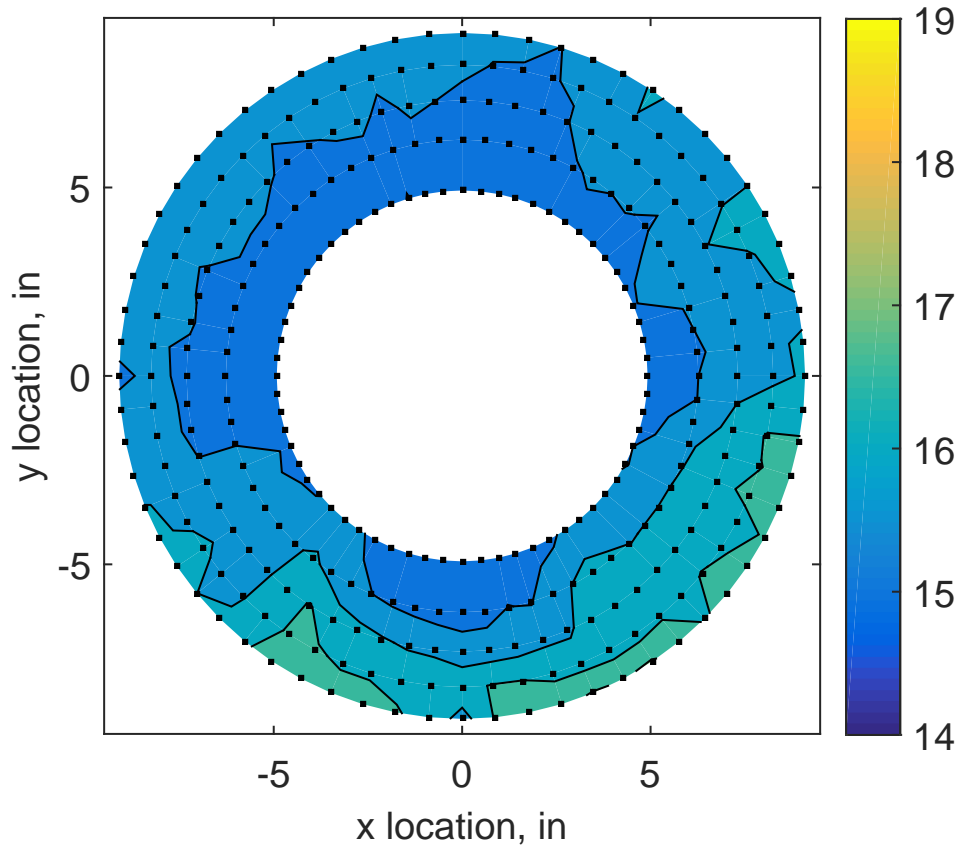


Figure C.77: YF12 test case 3 raw pressure contour created with 320 probes.

### C.1.3.1 Zeroth Clocking

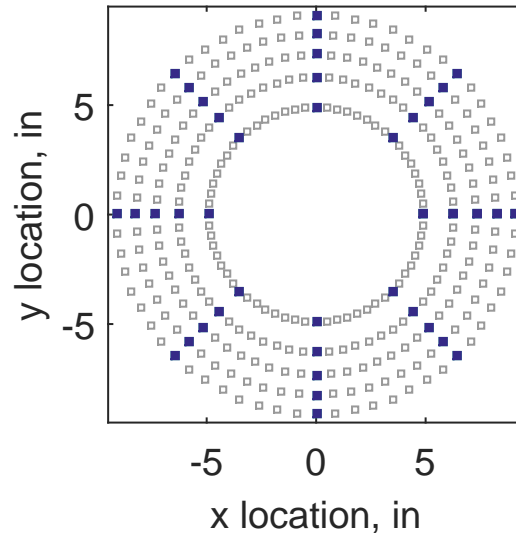
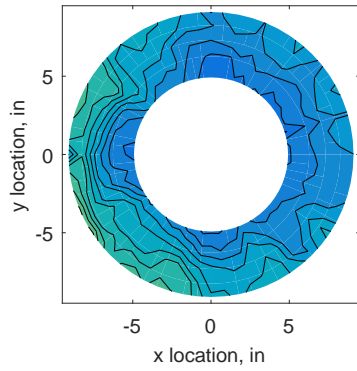


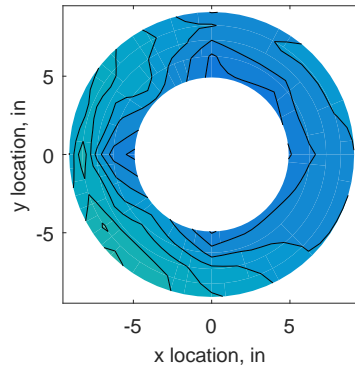
Figure C.78: Zeroth clocking probe position

Table C.34: Interpolation results for the YF12 inlet test case 3, clocking C1.

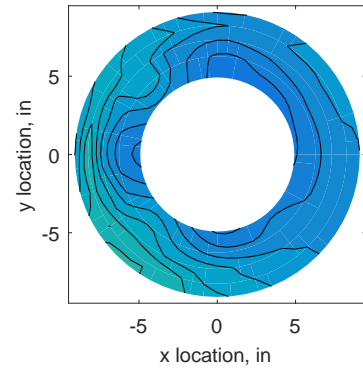
	Mean	Std. Dev.	Over-Prediction	In Tolerance	Under-Prediction
Linear	-0.081	0.122	71	74	135
Spline	-0.108	0.112	33	89	158
Polar	-0.093	0.149	108	21	151
Kriging	-0.108	0.170	74	55	151



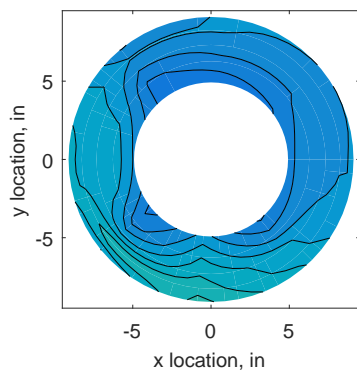
(a) 320 Probes



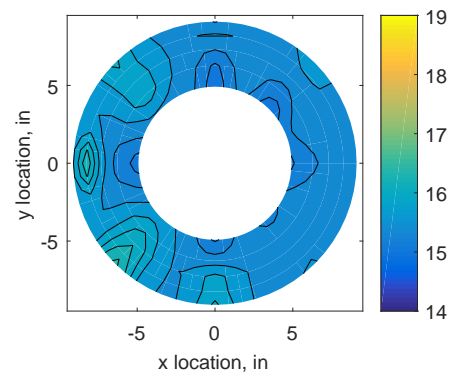
(b) Linear Interpolation



(c) Spline Interpolation

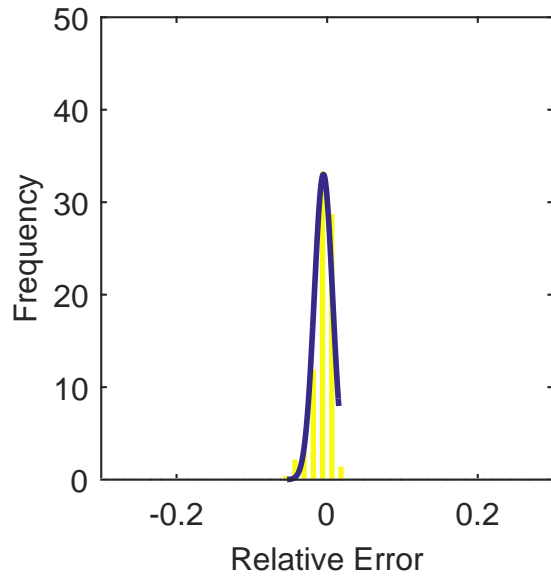


(d) Polar Interpolation

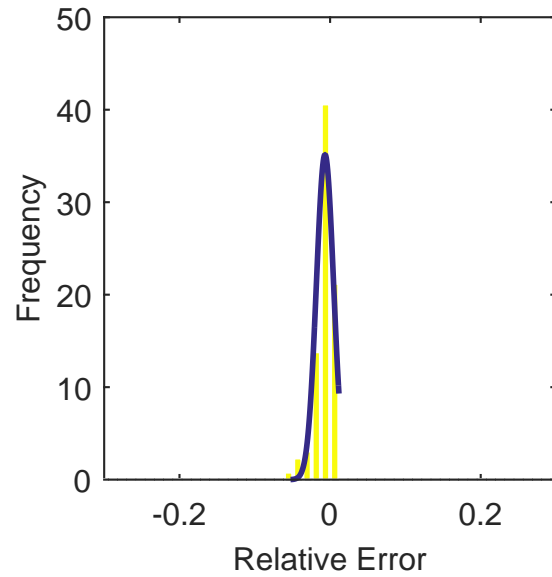


(e) Kriging Interpolation

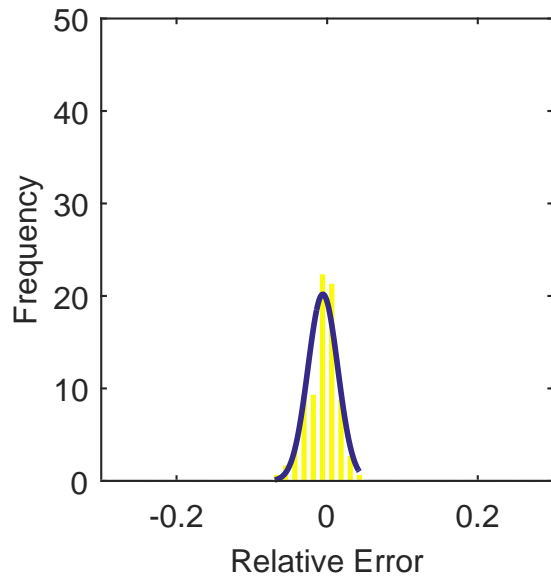
Figure C.79: Contour plots for the raw and interpolated values for the YF12 inlet.



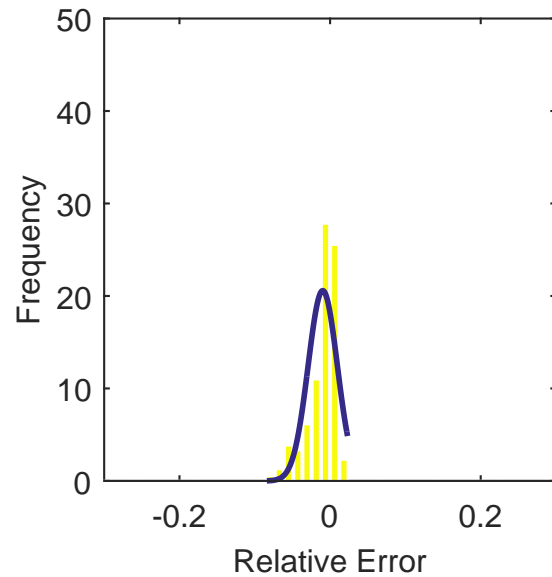
(a) Linear Interpolation Error



(b) Spline Interpolation Error



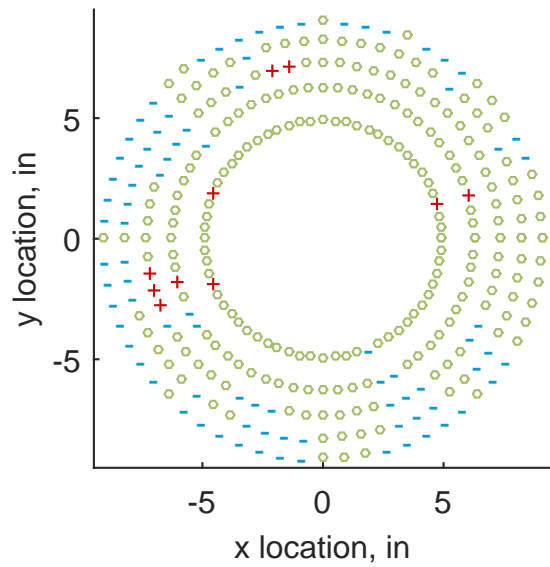
(c) Polar Interpolation Error



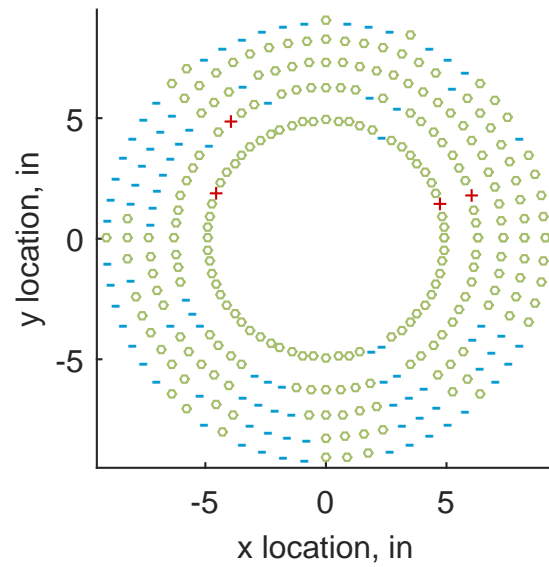
(d) Kriging Interpolation Error

Figure C.80: Relative error for various interpolation schemes of test case 3, zeroth clocking for the YF12 inlet.

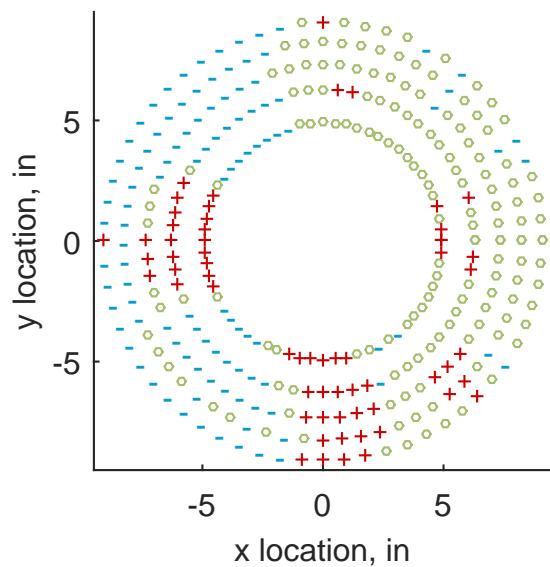




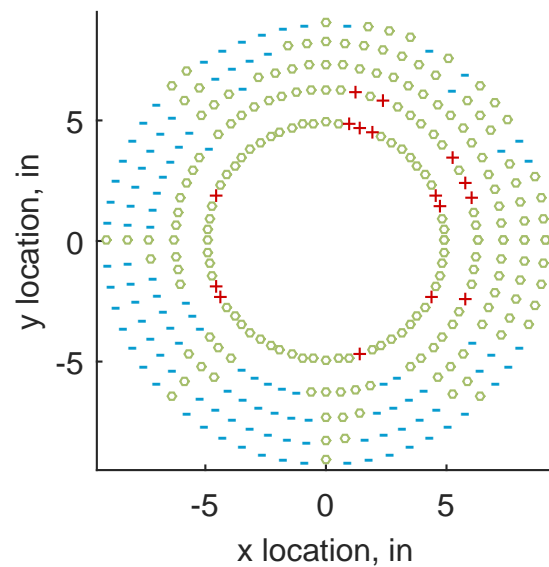
(a) Linear Interpolation



(b) Spline Interpolation



(c) Polar Interpolation



(d) Kriging Interpolation

Figure C.81: Interpolation error for the YF12 inlet - symbols show locations that are within tolerance (o), over-predicted (+), and under-predicted (-).

Table C.35: Interpolation effects on the derived quantities for the IMX inlet run number R320, clocking C1.

	$K_\theta$	$K_r$	$K_a$	$IDC$	$IDT$
Linear	0.622	0.245	0.868	0.024	0.090
Spline	0.621	0.262	0.883	0.025	0.090
Polar	0.622	0.248	0.869	0.024	0.090
Kriging	0.620	0.149	0.769	0.021	0.090

### C.1.3.2 First Clocking

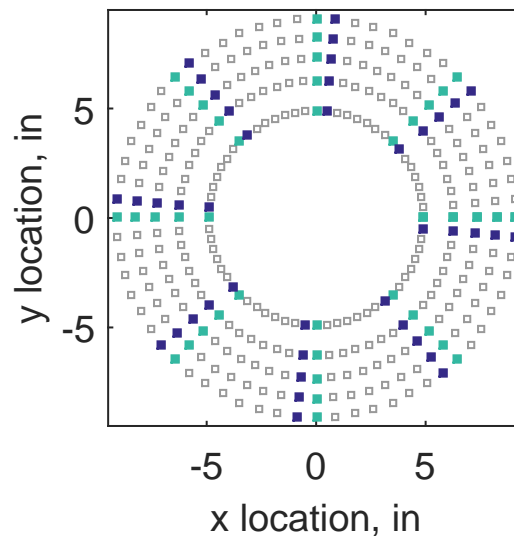
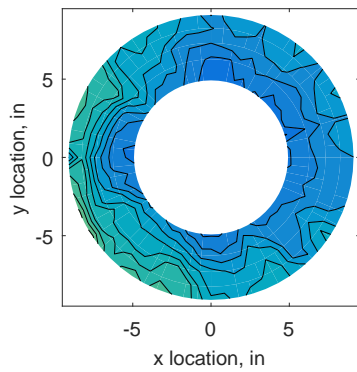


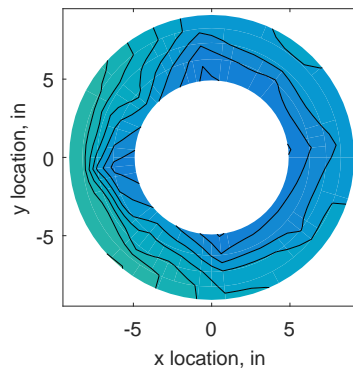
Figure C.82: First clocking probe position

Table C.36: Interpolation results for the YF12 inlet test case 3, clocking C2.

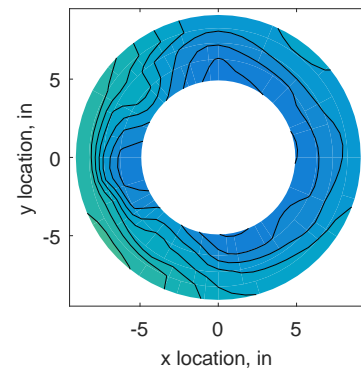
	Mean	Std. Dev.	Over-Prediction	In Tolerance	Under-Prediction
Linear	0.051	0.084	161	64	55
Spline	0.009	0.081	115	81	84
Polar	0.021	0.109	159	9	112
Kriging	0.009	0.160	114	57	109



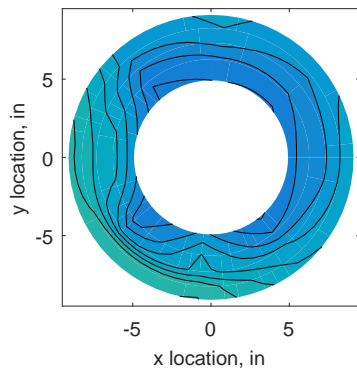
(a) 320 Probes



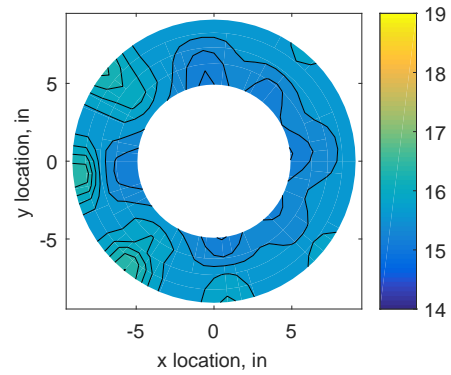
(b) Linear Interpolation



(c) Spline Interpolation

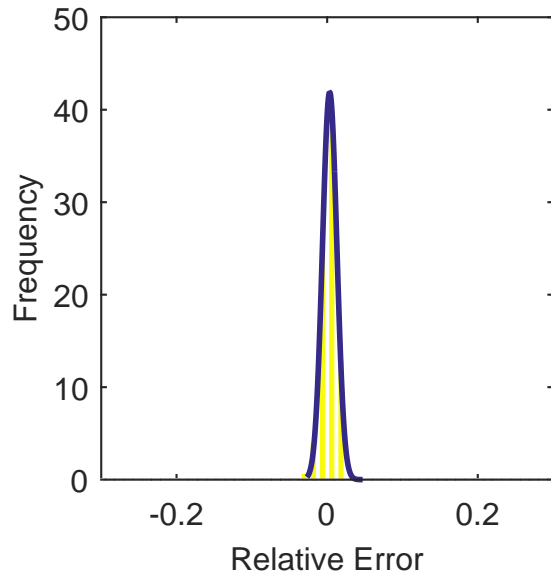


(d) Polar Interpolation

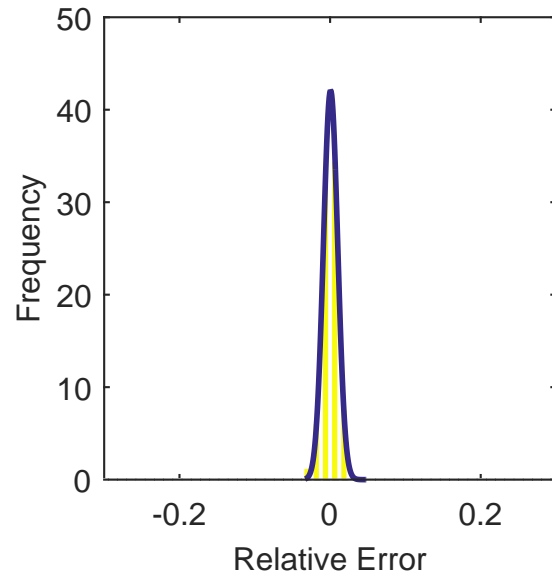


(e) Kriging Interpolation

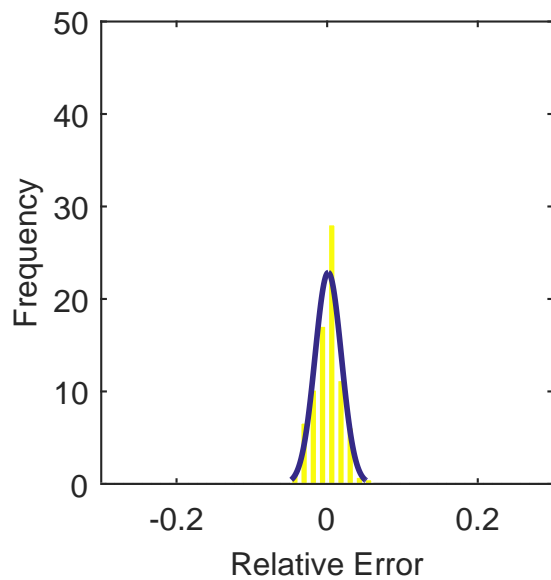
Figure C.83: Contour plots for the raw and interpolated values for the YF12 inlet.



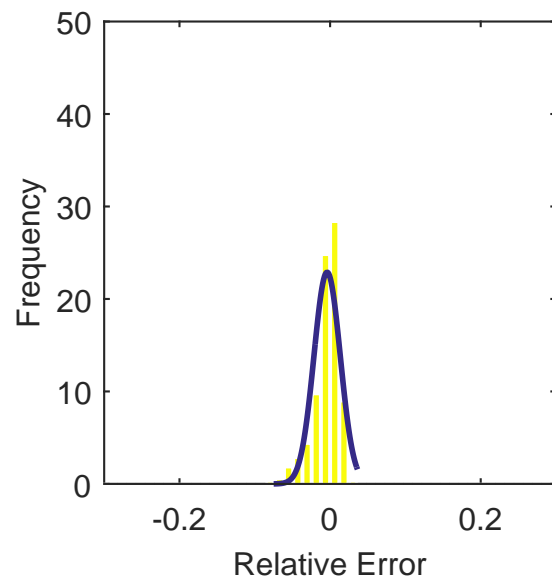
(a) Linear Interpolation Error



(b) Spline Interpolation Error

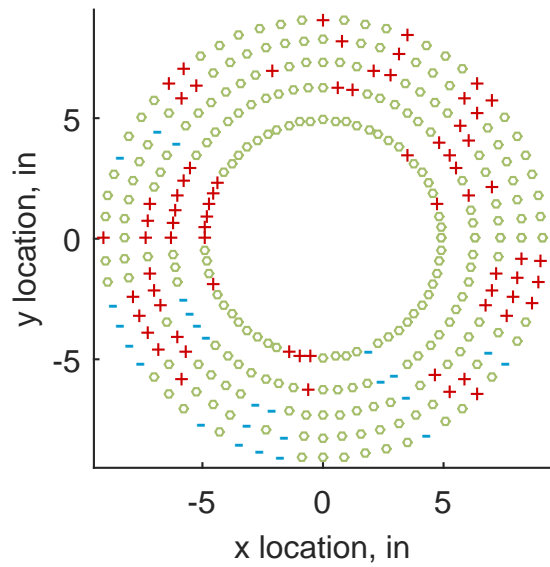


(c) Polar Interpolation Error

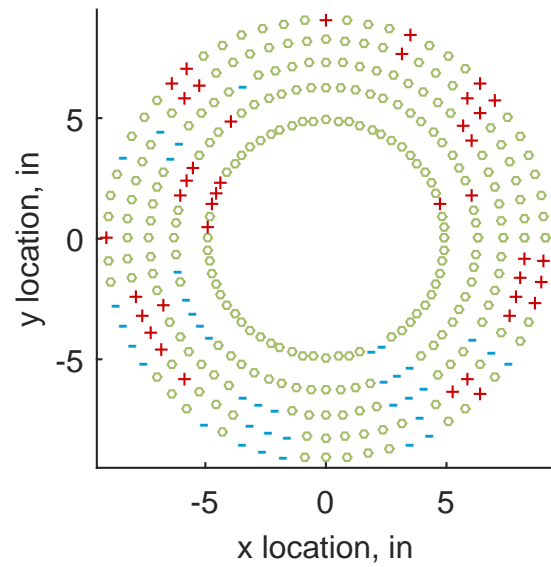


(d) Kriging Interpolation Error

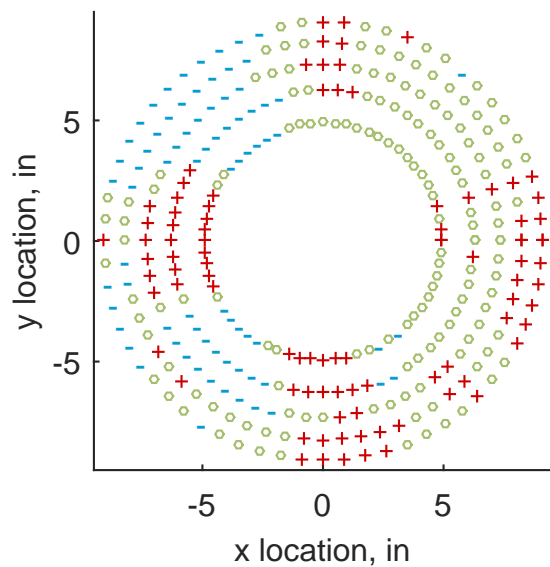
Figure C.84: Relative error for various interpolation schemes of test case 3, first clocking for the YF12 inlet.



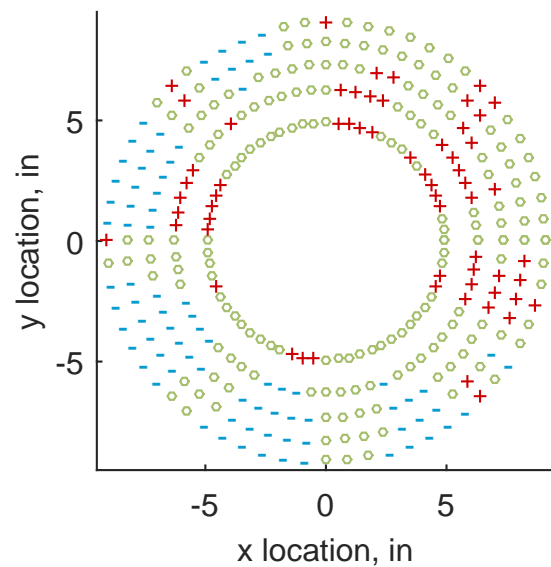
(a) Linear Interpolation



(b) Spline Interpolation



(c) Polar Interpolation



(d) Kriging Interpolation

Figure C.85: Interpolation error for the YF12 inlet - symbols show locations that are within tolerance (o), over-predicted (+), and under-predicted (-).

Table C.37: Interpolation effects on the derived quantities for the IMX inlet run number R320, clocking C2.

	$K_\theta$	$K_r$	$K_a$	$IDC$	$IDT$
Linear	0.627	0.337	0.963	0.027	0.092
Spline	0.625	0.338	0.963	0.027	0.095
Polar	0.626	0.320	0.945	0.027	0.092
Kriging	0.623	0.203	0.826	0.019	0.093

### C.1.3.3 Second Clocking

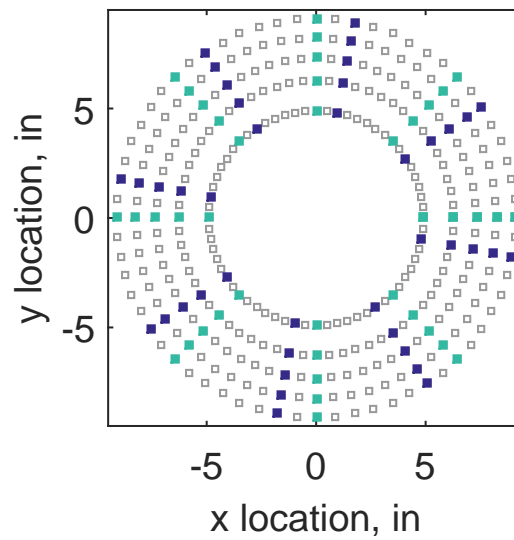
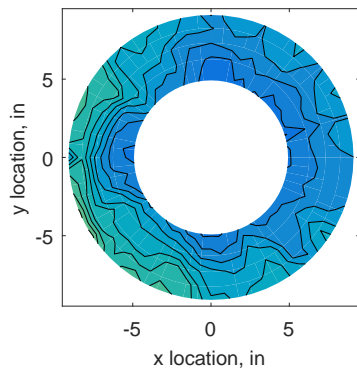


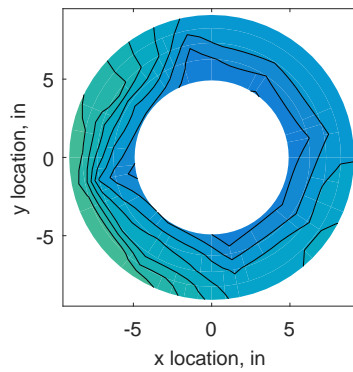
Figure C.86: Second clocking probe position

Table C.38: Interpolation results for the YF12 inlet test case 3, clocking C3.

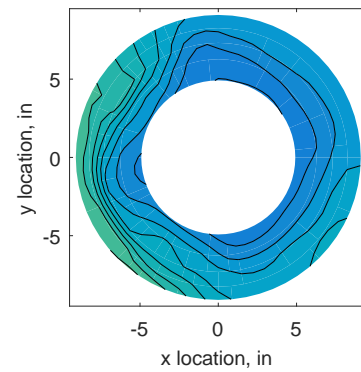
	Mean	Std. Dev.	Over-Prediction	In Tolerance	Under-Prediction
Linear	0.097	0.076	179	58	43
Spline	0.052	0.083	144	65	71
Polar	0.067	0.090	177	6	97
Kriging	0.052	0.116	136	47	97



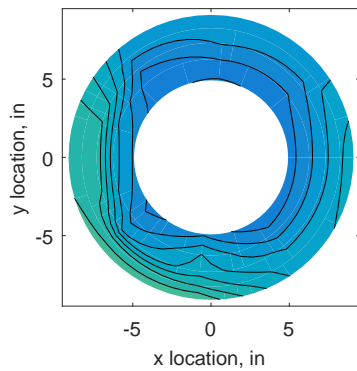
(a) 320 Probes



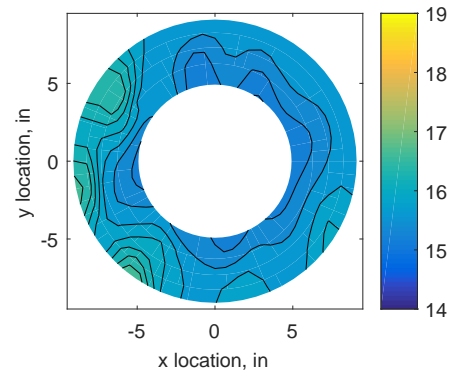
(b) Linear Interpolation



(c) Spline Interpolation

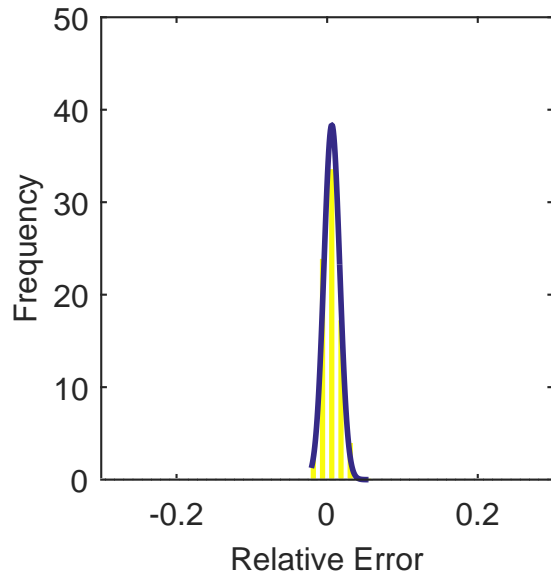


(d) Polar Interpolation

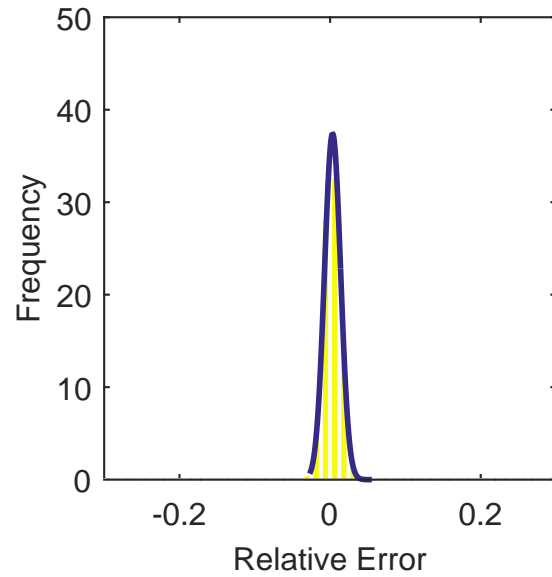


(e) Kriging Interpolation

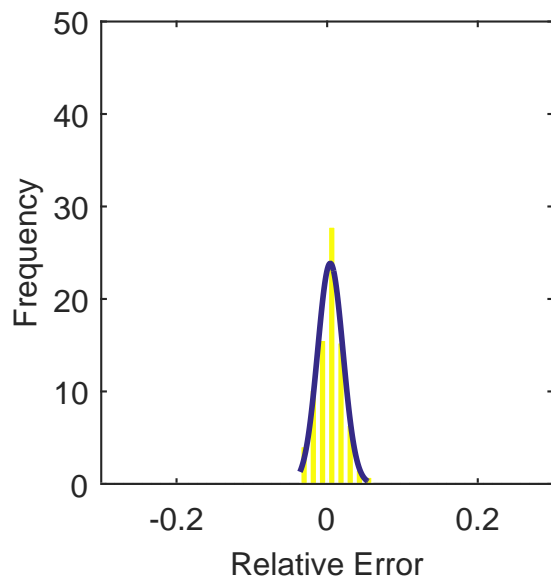
Figure C.87: Contour plots for the raw and interpolated values for the YF12 inlet.



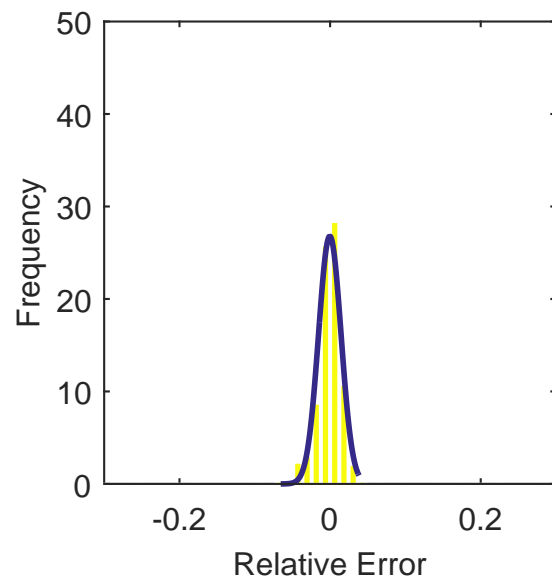
(a) Linear Interpolation Error



(b) Spline Interpolation Error



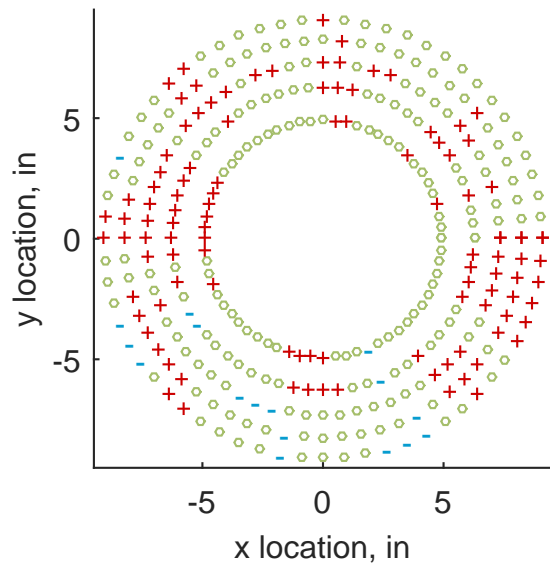
(c) Polar Interpolation Error



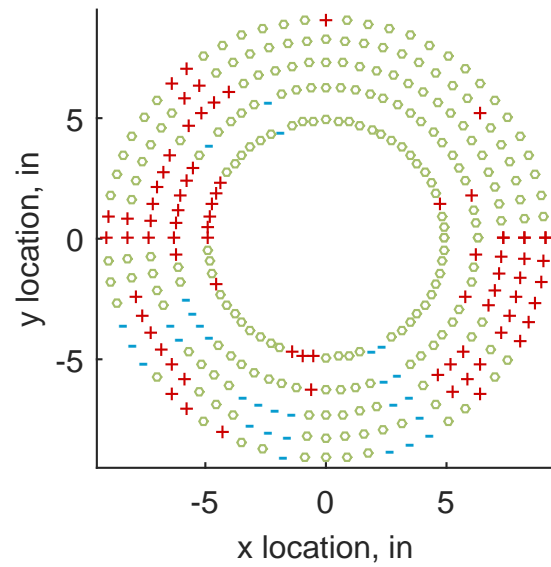
(d) Kriging Interpolation Error

Figure C.88: Relative error for various interpolation schemes of test case 3, second clocking for the YF12 inlet.

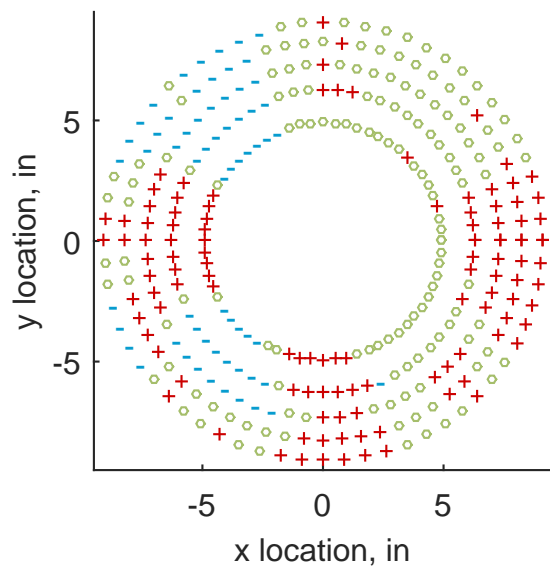




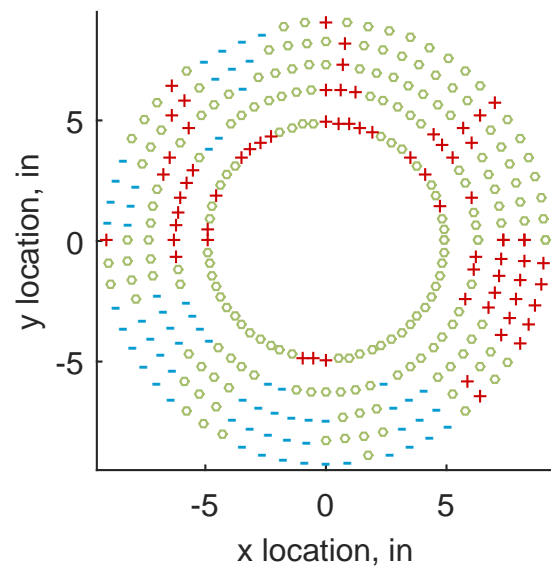
(a) Linear Interpolation



(b) Spline Interpolation



(c) Polar Interpolation



(d) Kriging Interpolation

Figure C.89: Interpolation error for the YF12 inlet - symbols show locations that are within tolerance (o), over-predicted (+), and under-predicted (-).

Table C.39: Interpolation effects on the derived quantities for the IMX inlet run number R320, clocking C3.

	$K_\theta$	$K_r$	$K_a$	$IDC$	$IDT$
Linear	0.629	0.343	0.971	0.028	0.102
Spline	0.627	0.351	0.977	0.028	0.105
Polar	0.627	0.360	0.987	0.028	0.102
Kriging	0.625	0.258	0.883	0.019	0.103

#### C.1.3.4 Third Clocking

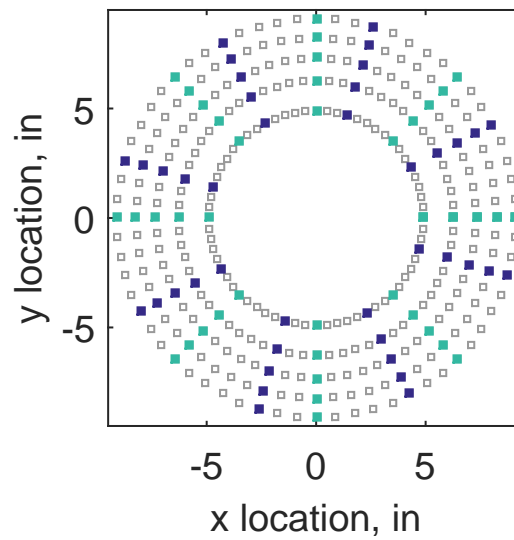
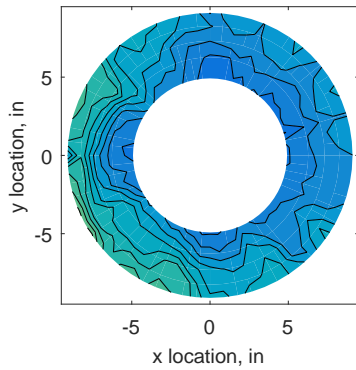


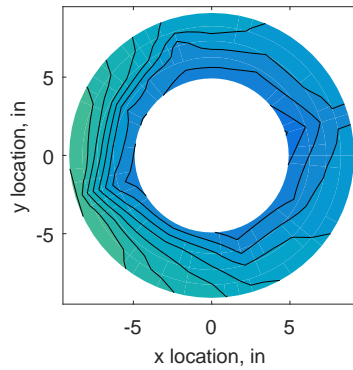
Figure C.90: Third clocking probe position

Table C.40: Interpolation results for the YF12 inlet test case 3, clocking C4.

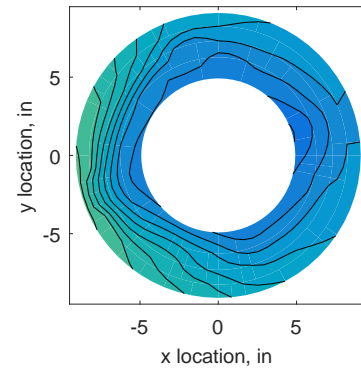
	Mean	Std. Dev.	Over-Prediction	In Tolerance	Under-Prediction
Linear	0.070	0.078	157	54	69
Spline	0.023	0.083	135	51	94
Polar	0.023	0.074	142	21	117
Kriging	0.023	0.111	106	43	131



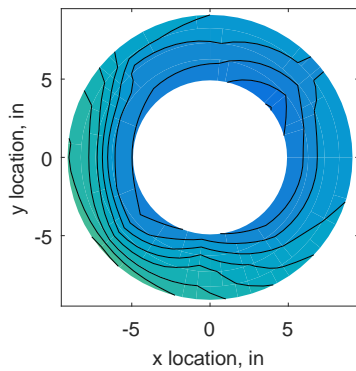
(a) 320 Probes



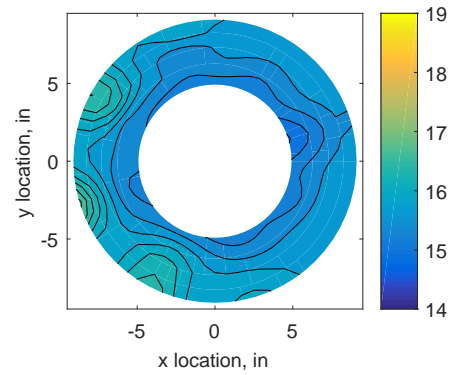
(b) Linear Interpolation



(c) Spline Interpolation

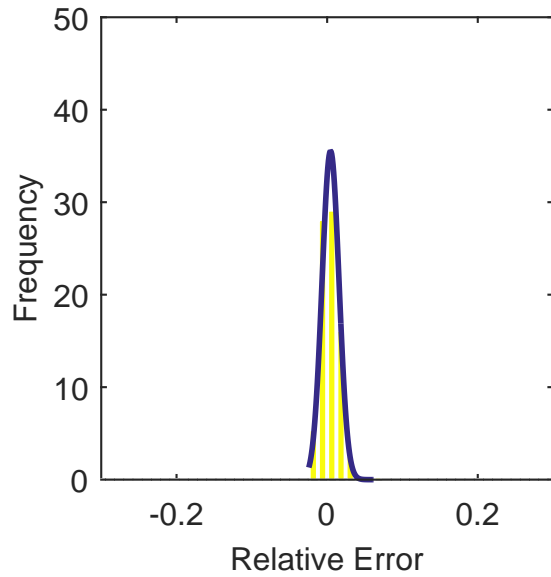


(d) Polar Interpolation

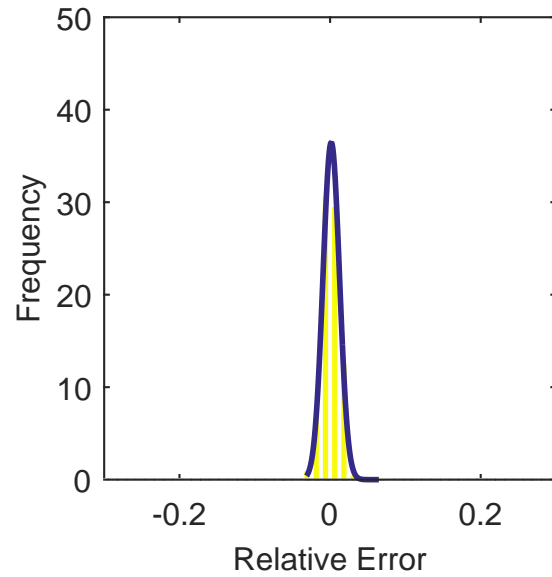


(e) Kriging Interpolation

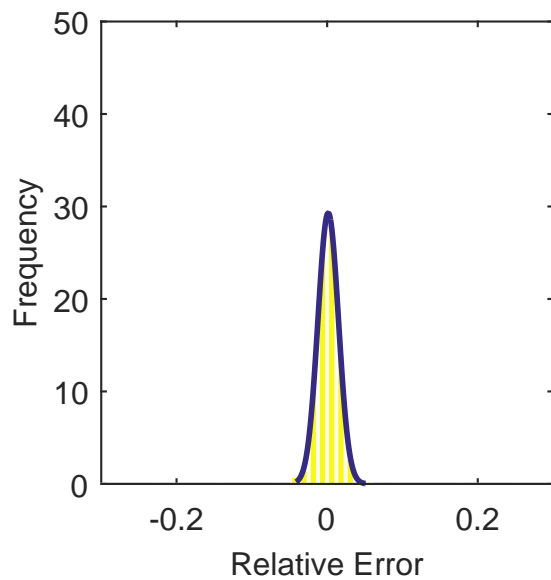
Figure C.91: Contour plots for the raw and interpolated values for the YF12 inlet.



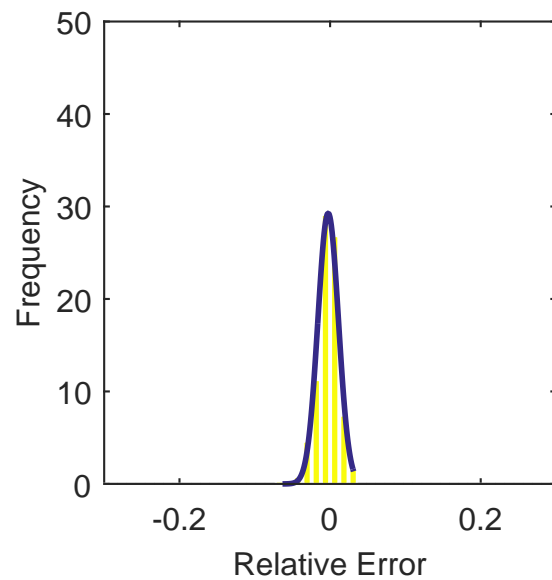
(a) Linear Interpolation Error



(b) Spline Interpolation Error

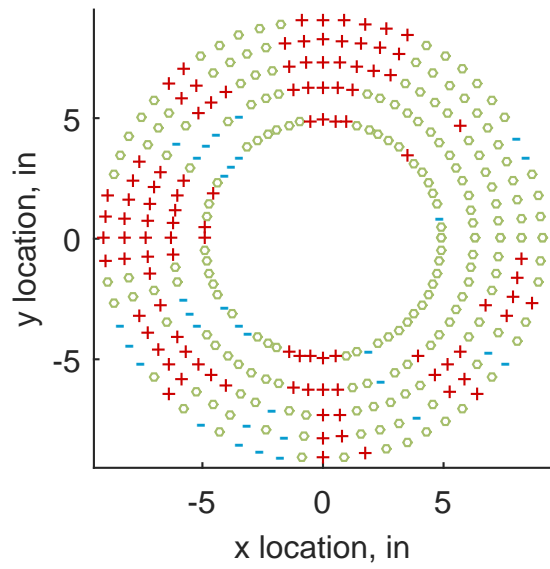


(c) Polar Interpolation Error

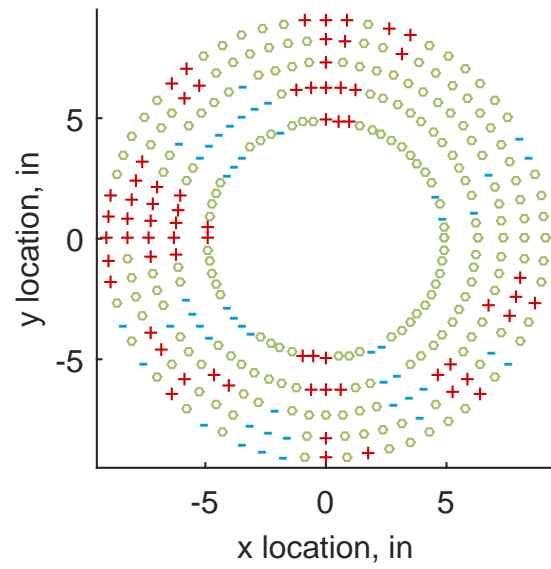


(d) Kriging Interpolation Error

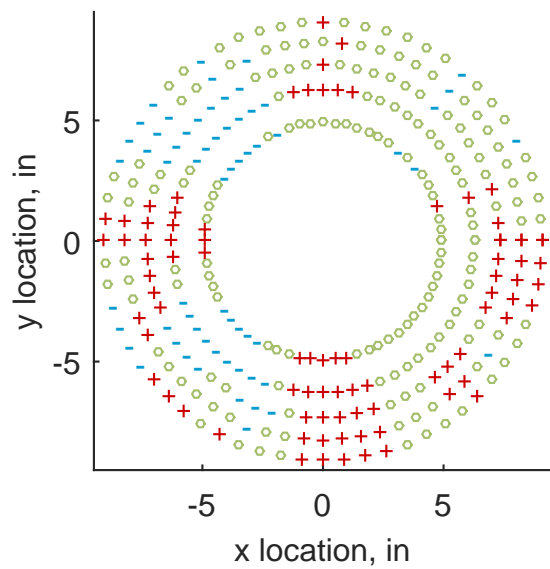
Figure C.92: Relative error for various interpolation schemes of test case 3, third clocking for the YF12 inlet.



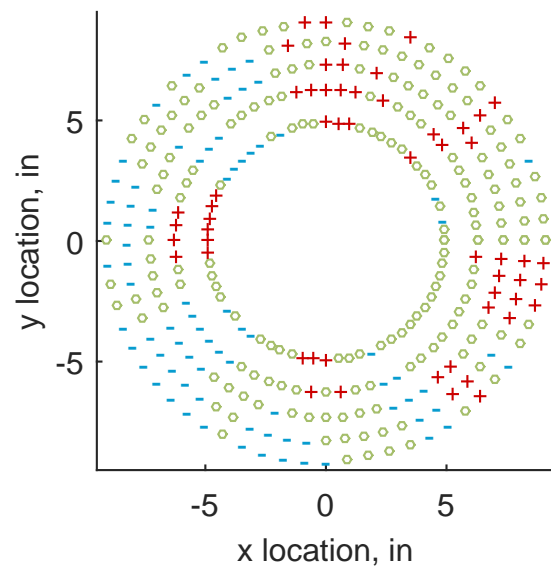
(a) Linear Interpolation



(b) Spline Interpolation



(c) Polar Interpolation



(d) Kriging Interpolation

Figure C.93: Interpolation error for the YF12 inlet - symbols show locations that are within tolerance (o), over-predicted (+), and under-predicted (-).

Table C.41: Interpolation effects on the derived quantities for the IMX inlet run number R320, clocking C4.

	$K_\theta$	$K_r$	$K_a$	$IDC$	$IDT$
Linear	0.627	0.375	1.002	0.033	0.119
Spline	0.625	0.380	1.005	0.032	0.120
Polar	0.625	0.376	1.001	0.032	0.120
Kriging	0.623	0.285	0.908	0.022	0.120

#### C.1.3.5 Fourth Clocking

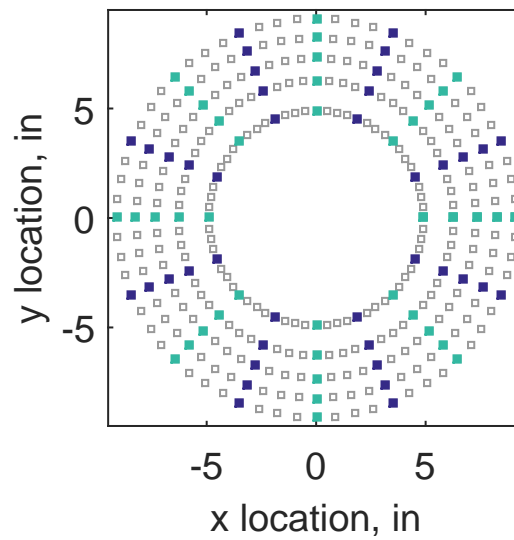
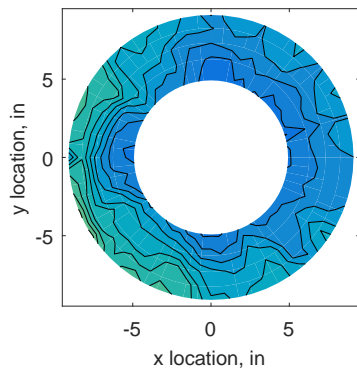


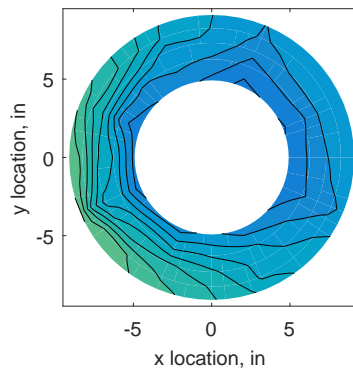
Figure C.94: Fourth clocking probe position

Table C.42: Interpolation results for the YF12 inlet test case 3, clocking C5.

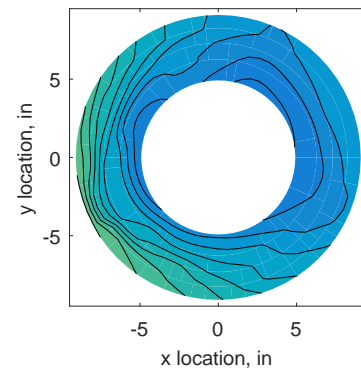
	Mean	Std. Dev.	Over-Prediction	In Tolerance	Under-Prediction
Linear	0.113	0.081	179	56	45
Spline	0.062	0.089	137	79	64
Polar	0.045	0.072	139	43	98
Kriging	0.062	0.209	126	29	125



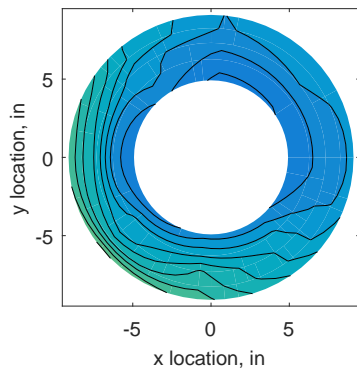
(a) 320 Probes



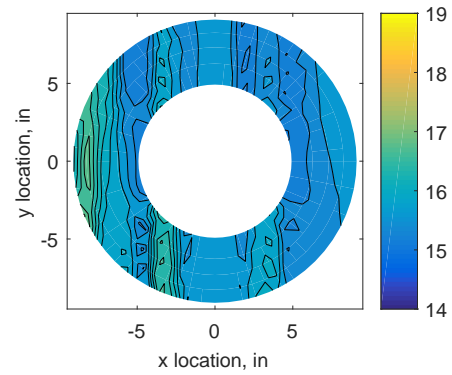
(b) Linear Interpolation



(c) Spline Interpolation

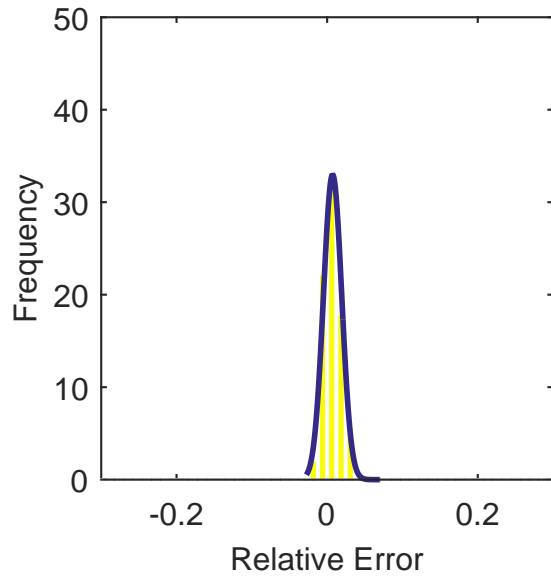


(d) Polar Interpolation

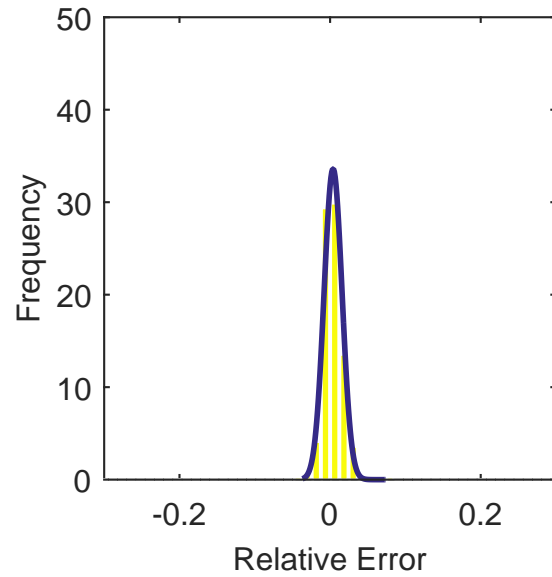


(e) Kriging Interpolation

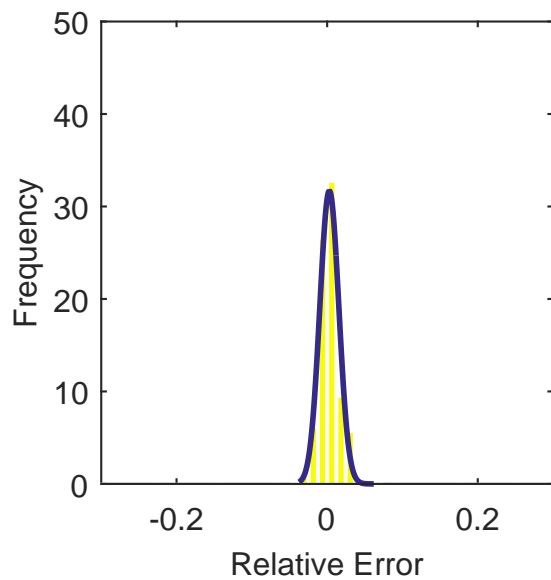
Figure C.95: Contour plots for the raw and interpolated values for the YF12 inlet.



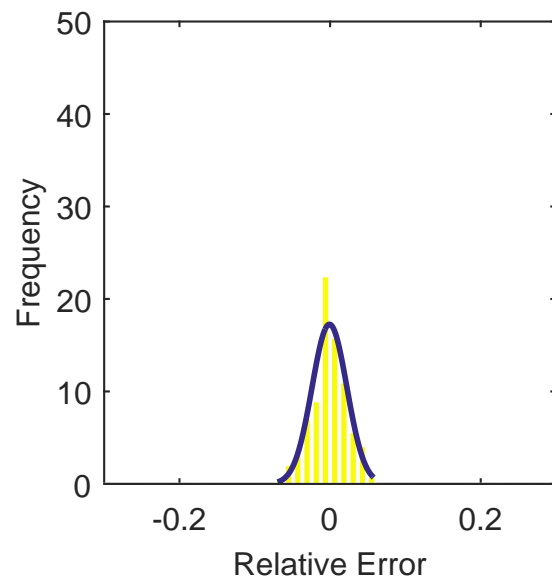
(a) Linear Interpolation Error



(b) Spline Interpolation Error



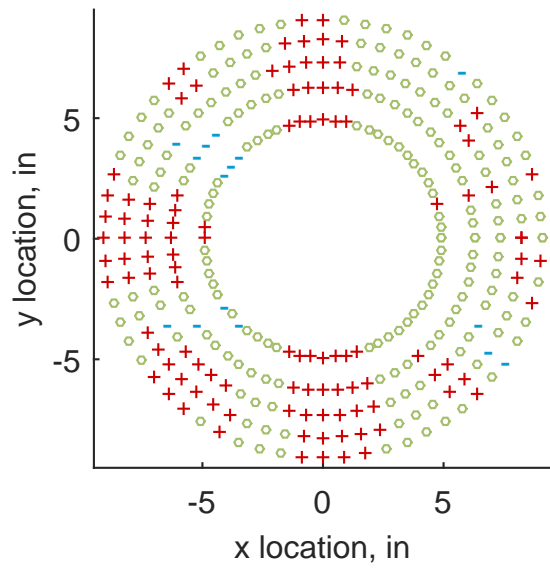
(c) Polar Interpolation Error



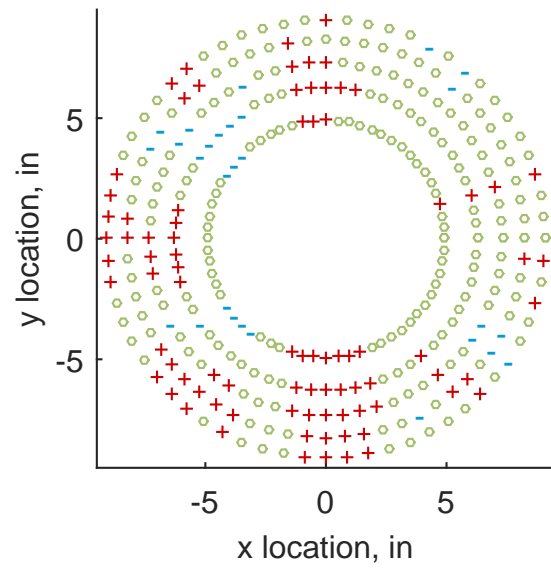
(d) Kriging Interpolation Error

Figure C.96: Relative error for various interpolation schemes of test case 3, fourth clocking for the YF12 inlet.

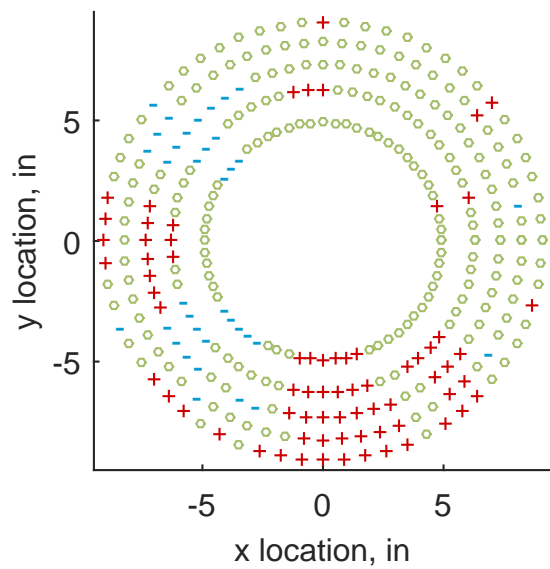




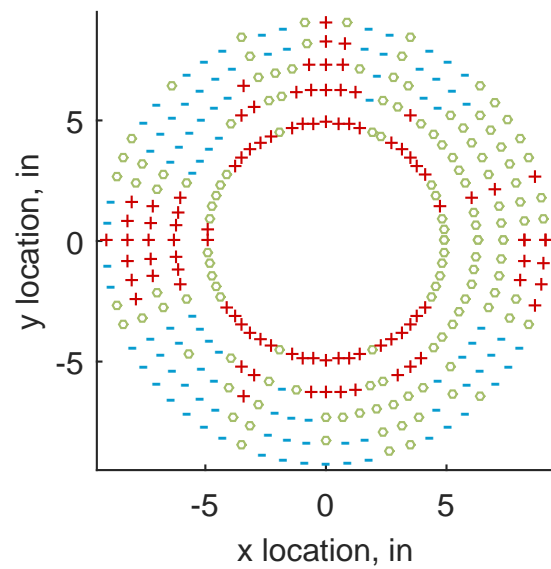
(a) Linear Interpolation



(b) Spline Interpolation



(c) Polar Interpolation



(d) Kriging Interpolation

Figure C.97: Interpolation error for the YF12 inlet - symbols show locations that are within tolerance (o), over-predicted (+), and under-predicted (-).

Table C.43: Interpolation effects on the derived quantities for the IMX inlet run number R320, clocking C5.

	$K_\theta$	$K_r$	$K_a$	$IDC$	$IDT$
Linear	0.629	0.363	0.992	0.038	0.120
Spline	0.627	0.361	0.988	0.036	0.121
Polar	0.626	0.358	0.984	0.034	0.120
Kriging	0.626	0.119	0.744	0.043	0.121

### C.1.3.6 Fifth Clocking

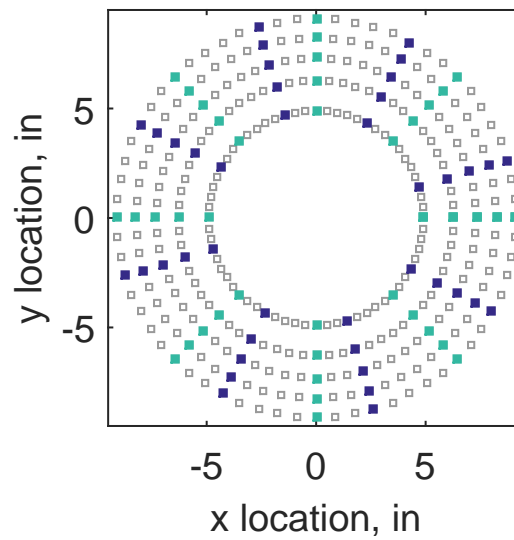
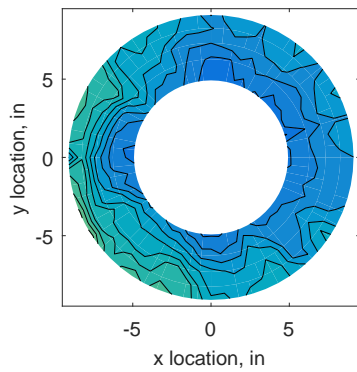


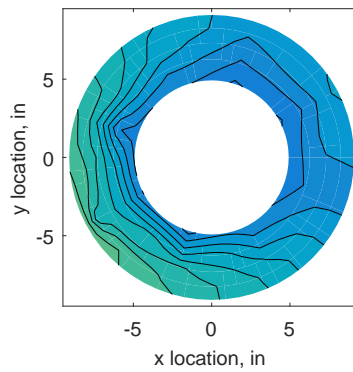
Figure C.98: Fifth clocking probe position

Table C.44: Interpolation results for the YF12 inlet test case 3, clocking C6.

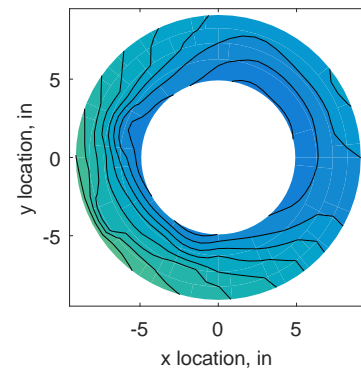
	Mean	Std. Dev.	Over-Prediction	In Tolerance	Under-Prediction
Linear	0.119	0.072	190	55	35
Spline	0.073	0.074	146	79	55
Polar	0.045	0.061	143	50	87
Kriging	0.073	0.111	144	46	90



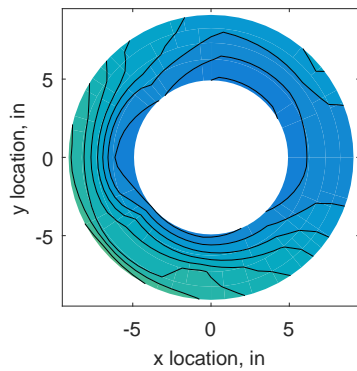
(a) 320 Probes



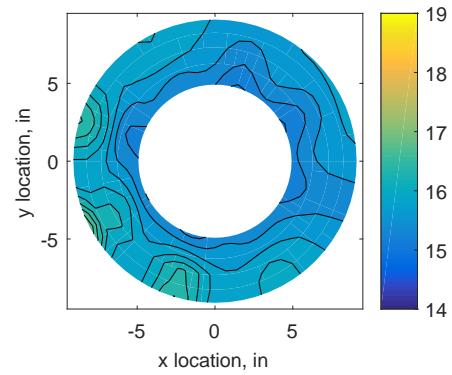
(b) Linear Interpolation



(c) Spline Interpolation

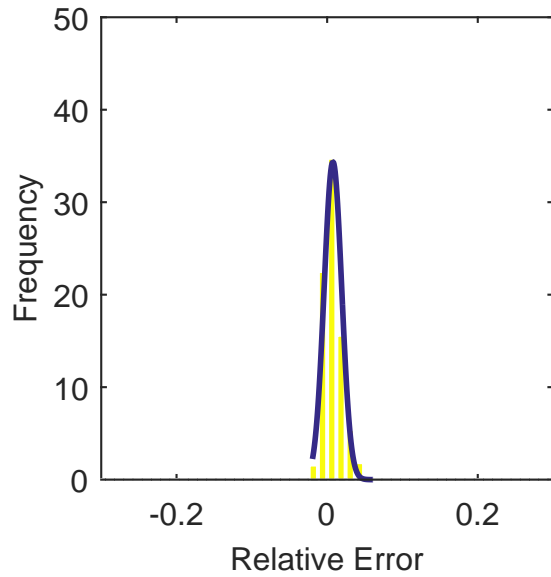


(d) Polar Interpolation

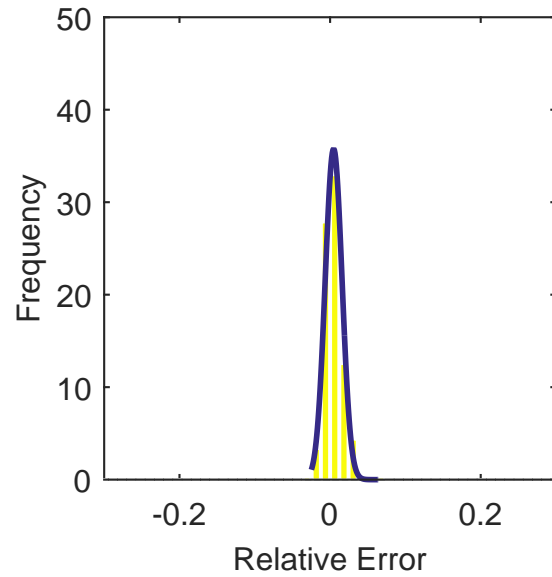


(e) Kriging Interpolation

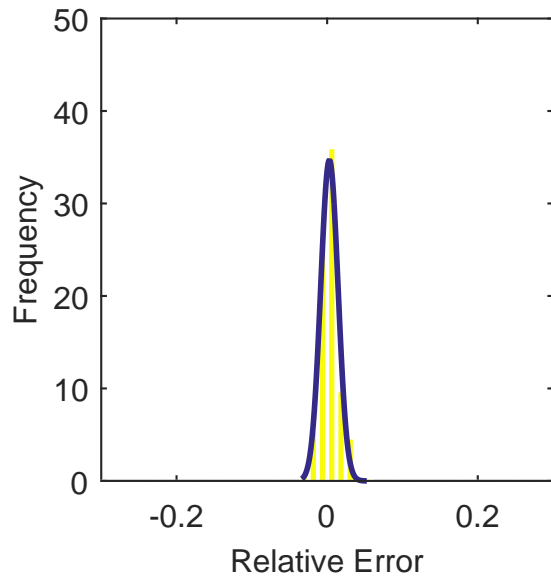
Figure C.99: Contour plots for the raw and interpolated values for the YF12 inlet.



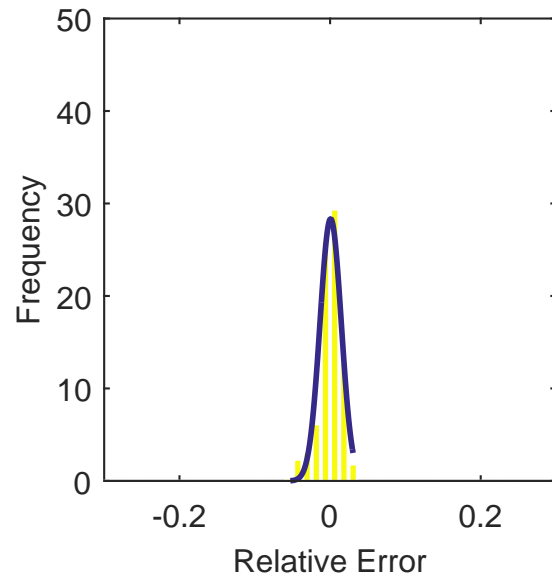
(a) Linear Interpolation Error



(b) Spline Interpolation Error

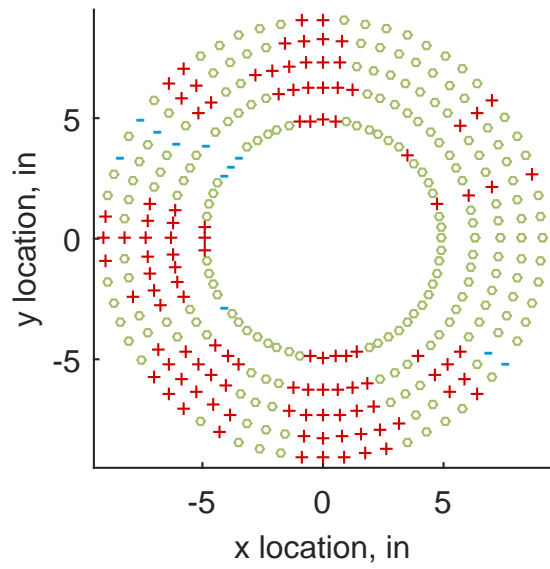


(c) Polar Interpolation Error

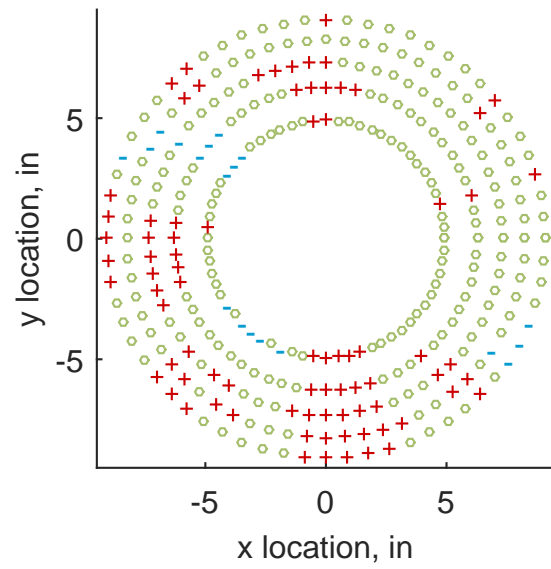


(d) Kriging Interpolation Error

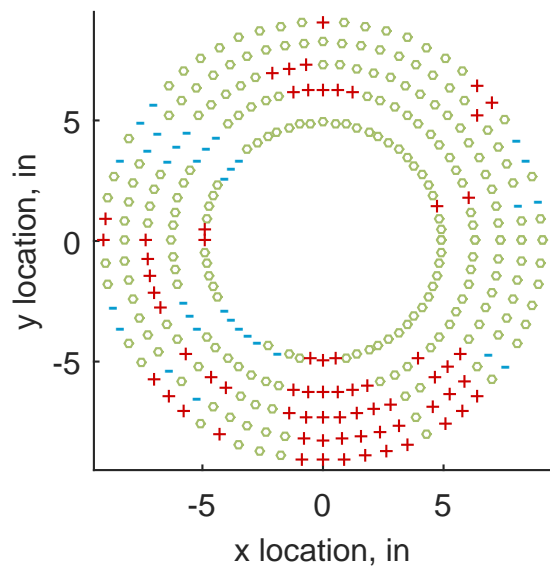
Figure C.100: Relative error for various interpolation schemes of test case 3, fifth clocking for the YF12 inlet.



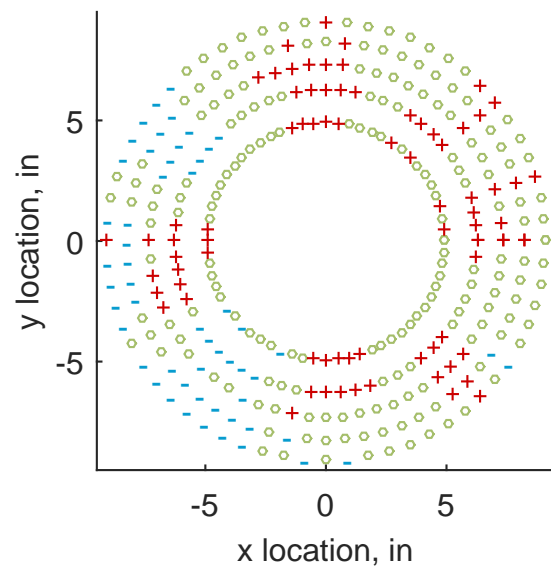
(a) Linear Interpolation



(b) Spline Interpolation



(c) Polar Interpolation



(d) Kriging Interpolation

Figure C.101: Interpolation error for the YF12 inlet - symbols show locations that are within tolerance (o), over-predicted (+), and under-predicted (-).

Table C.45: Interpolation effects on the derived quantities for the IMX inlet run number R320, clocking C6.

	$K_\theta$	$K_r$	$K_a$	$IDC$	$IDT$
Linear	0.629	0.356	0.985	0.040	0.113
Spline	0.627	0.371	0.998	0.039	0.114
Polar	0.626	0.367	0.994	0.037	0.114
Kriging	0.626	0.267	0.893	0.029	0.114

### C.1.3.7 Sixth Clocking

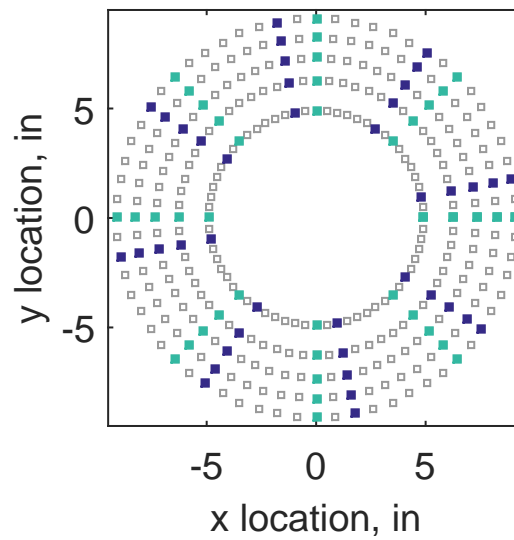
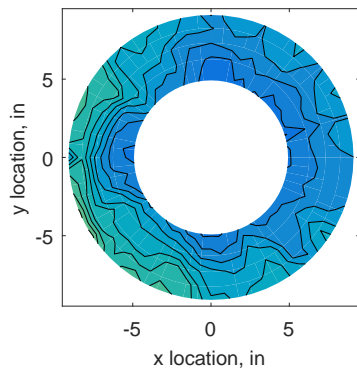


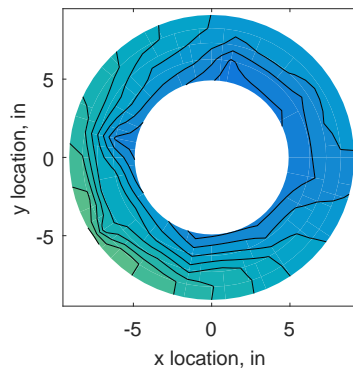
Figure C.102: Sixth clocking probe position

Table C.46: Interpolation results for the YF12 inlet test case 3, clocking C7.

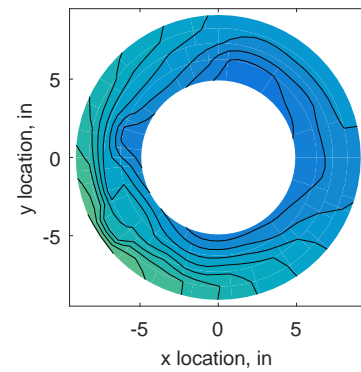
	Mean	Std. Dev.	Over-Prediction	In Tolerance	Under-Prediction
Linear	0.085	0.067	150	80	50
Spline	0.040	0.065	122	76	82
Polar	0.008	0.061	103	80	97
Kriging	0.040	0.130	109	69	102



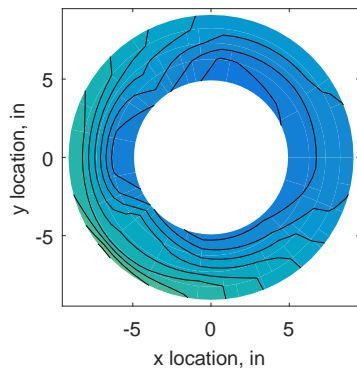
(a) 320 Probes



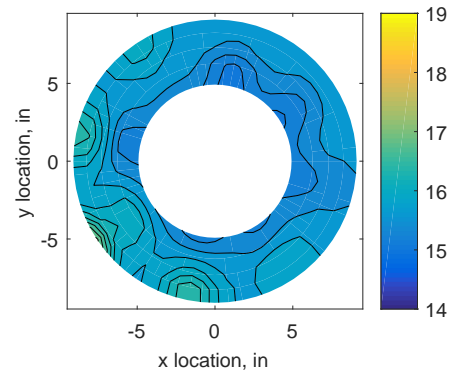
(b) Linear Interpolation



(c) Spline Interpolation

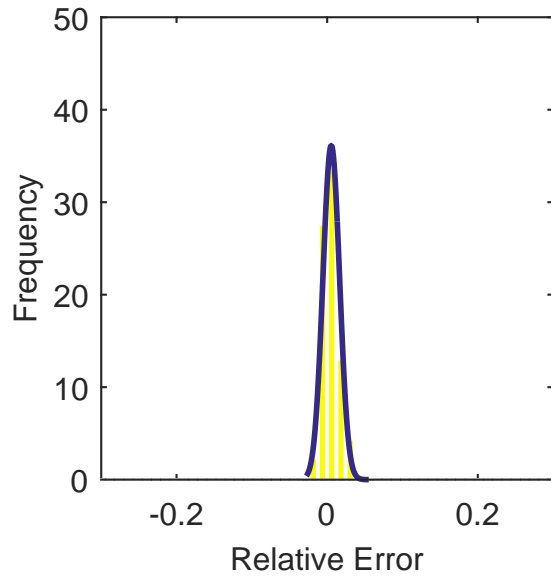


(d) Polar Interpolation

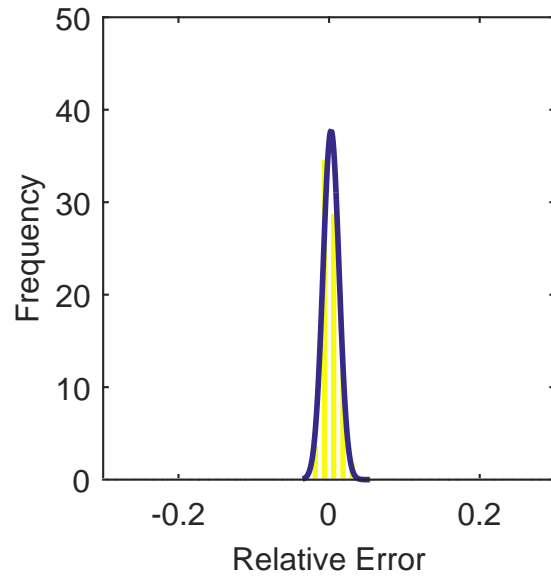


(e) Kriging Interpolation

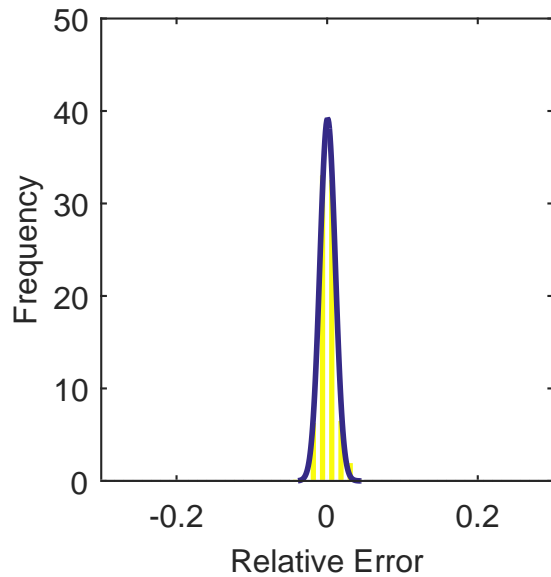
Figure C.103: Contour plots for the raw and interpolated values for the YF12 inlet.



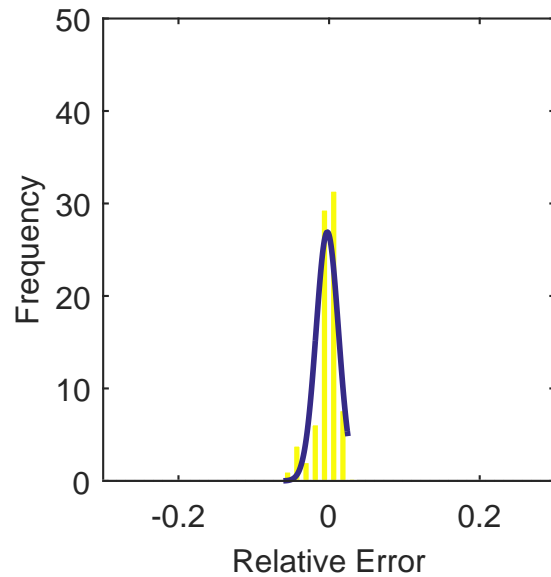
(a) Linear Interpolation Error



(b) Spline Interpolation Error



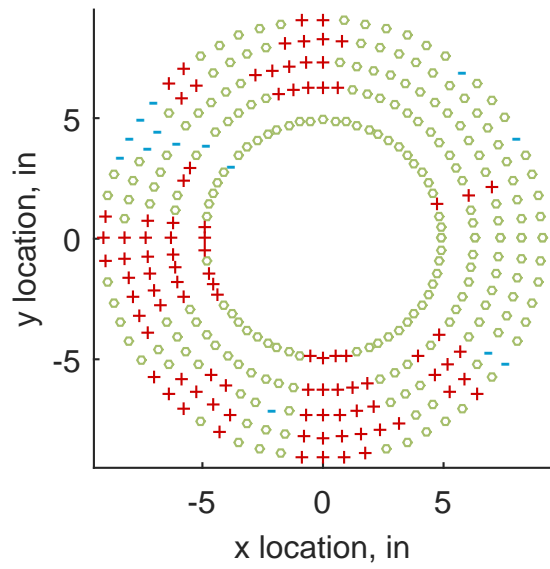
(c) Polar Interpolation Error



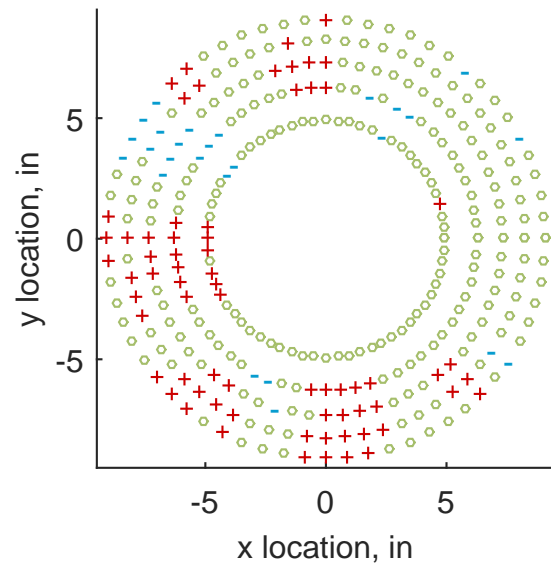
(d) Kriging Interpolation Error

Figure C.104: Relative error for various interpolation schemes of test case 3, sixth clocking for the YF12 inlet.

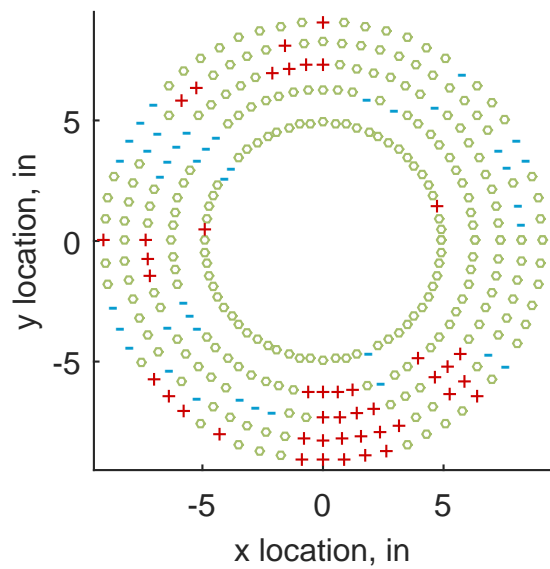




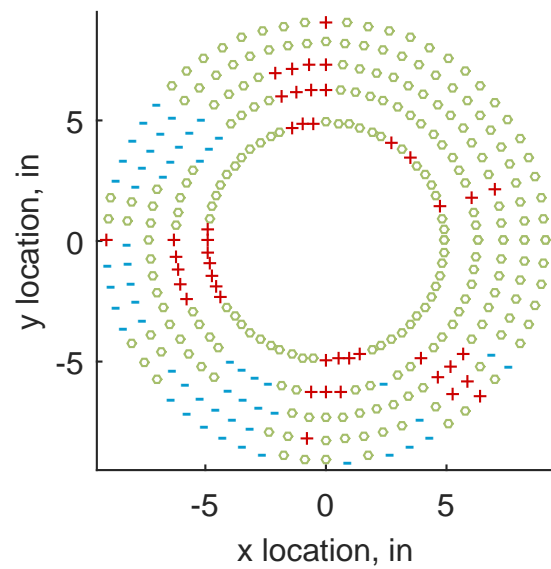
(a) Linear Interpolation



(b) Spline Interpolation



(c) Polar Interpolation



(d) Kriging Interpolation

Figure C.105: Interpolation error for the YF12 inlet - symbols show locations that are within tolerance (o), over-predicted (+), and under-predicted (-).

Table C.47: Interpolation effects on the derived quantities for the IMX inlet run number R320, clocking C7.

	$K_\theta$	$K_r$	$K_a$	$IDC$	$IDT$
Linear	0.628	0.354	0.982	0.038	0.124
Spline	0.626	0.359	0.985	0.037	0.126
Polar	0.625	0.355	0.980	0.034	0.125
Kriging	0.624	0.245	0.869	0.024	0.125

### C.1.3.8 Seventh Clocking

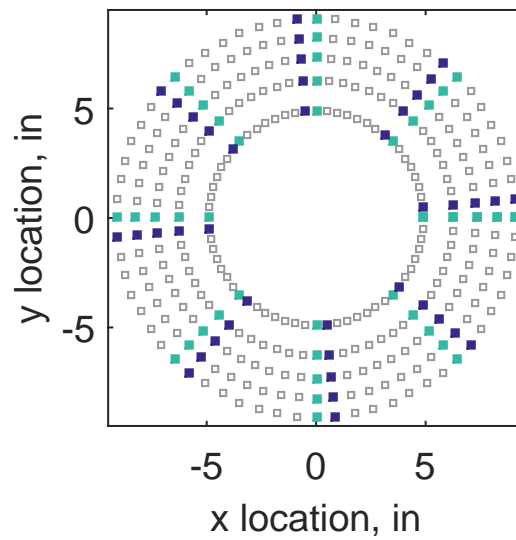
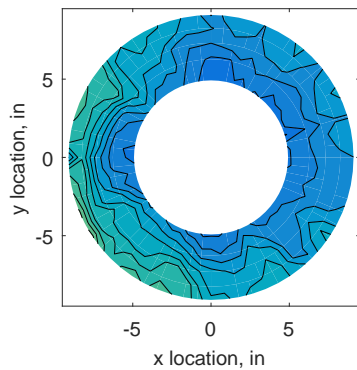


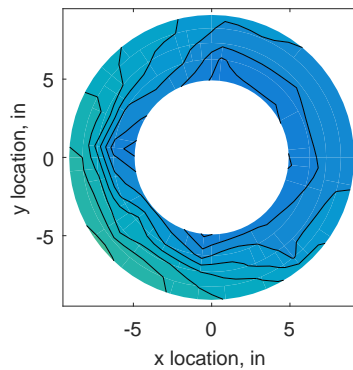
Figure C.106: Seventh clocking probe position

Table C.48: Interpolation results for the YF12 inlet test case 3, clocking C8.

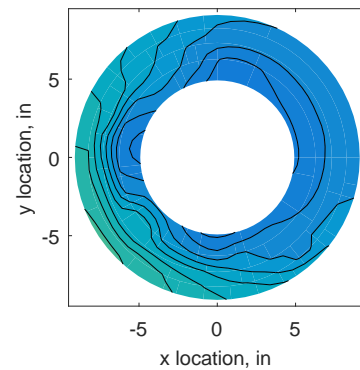
	Mean	Std. Dev.	Over-Prediction	In Tolerance	Under-Prediction
Linear	-0.026	0.075	73	93	114
Spline	-0.065	0.065	46	81	153
Polar	-0.083	0.063	36	85	159
Kriging	-0.065	0.138	61	74	145



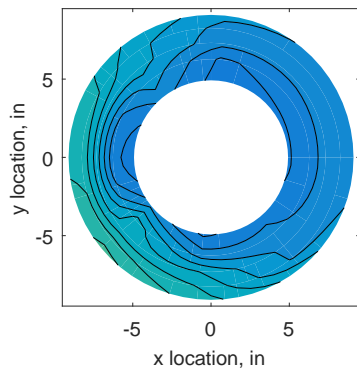
(a) 320 Probes



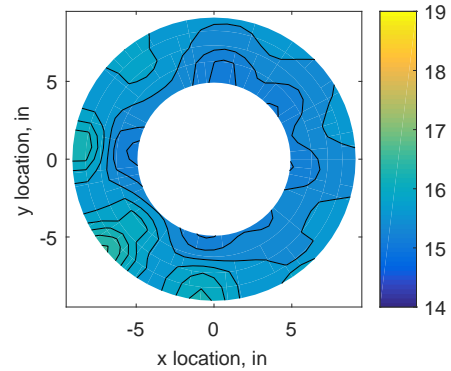
(b) Linear Interpolation



(c) Spline Interpolation

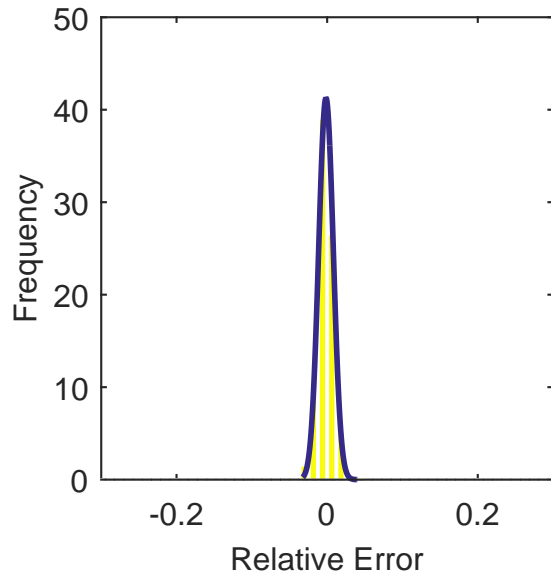


(d) Polar Interpolation

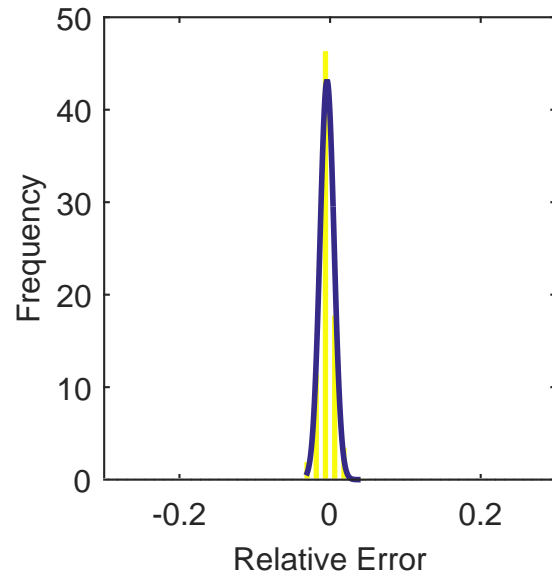


(e) Kriging Interpolation

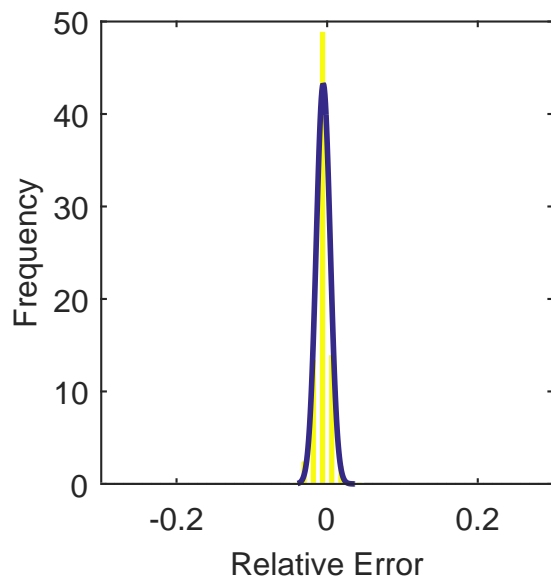
Figure C.107: Contour plots for the raw and interpolated values for the YF12 inlet.



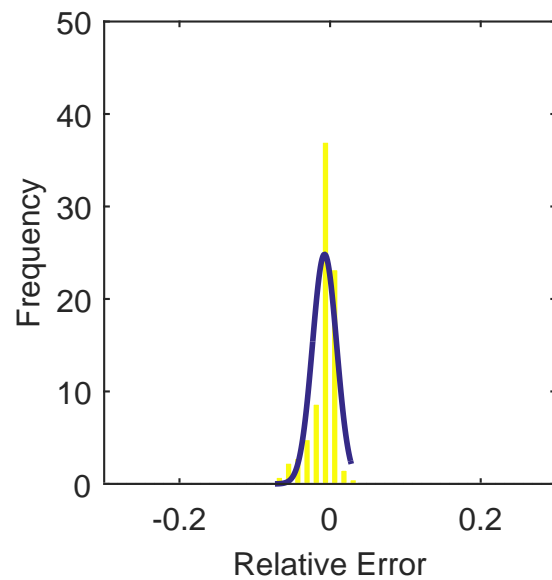
(a) Linear Interpolation Error



(b) Spline Interpolation Error

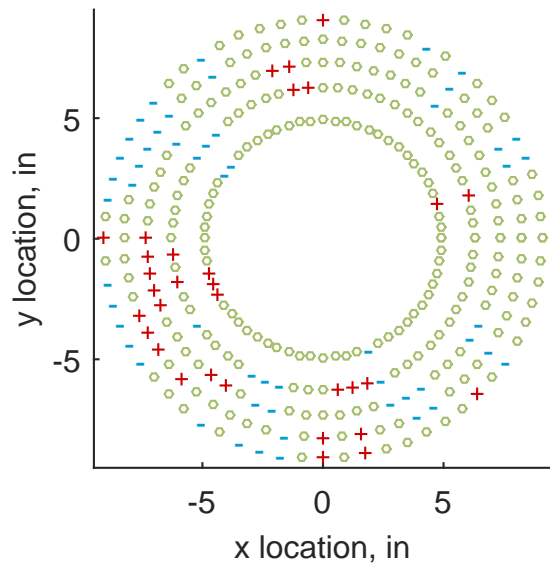


(c) Polar Interpolation Error

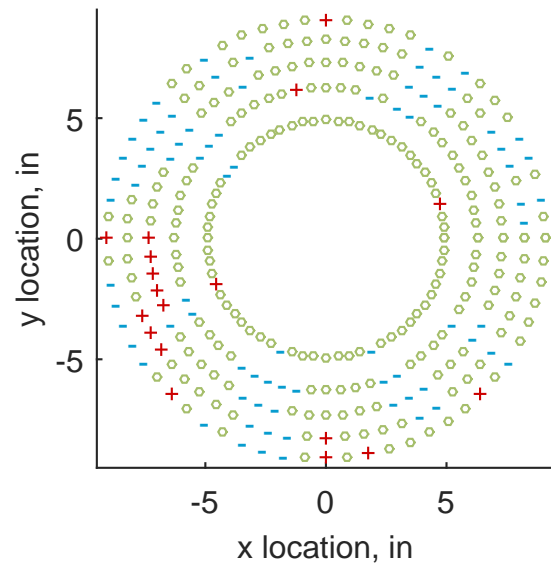


(d) Kriging Interpolation Error

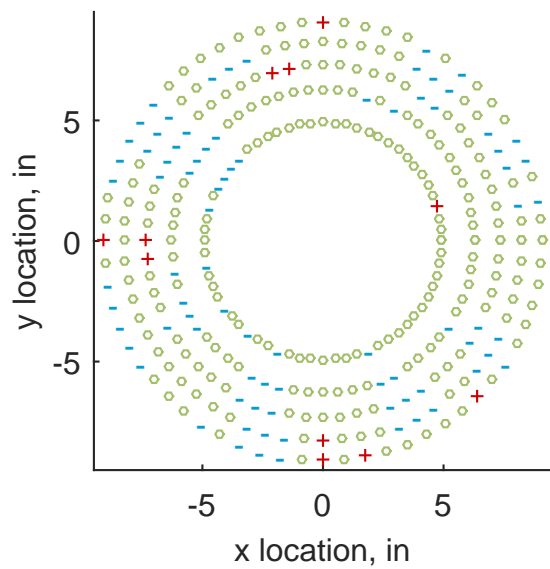
Figure C.108: Relative error for various interpolation schemes of test case 3, seventh clocking for the YF12 inlet.



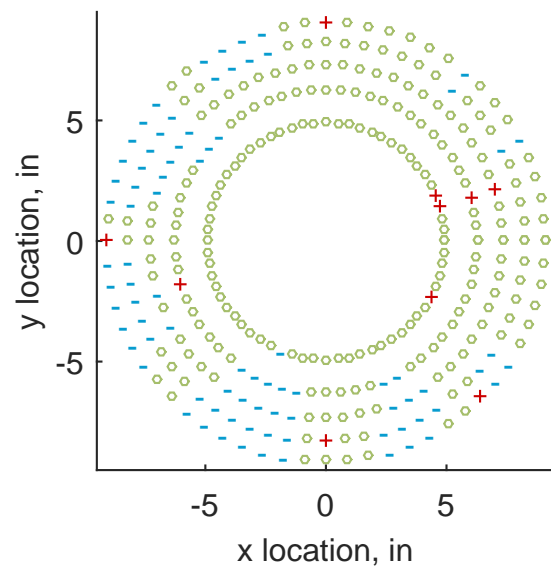
(a) Linear Interpolation



(b) Spline Interpolation



(c) Polar Interpolation



(d) Kriging Interpolation

Figure C.109: Interpolation error for the YF12 inlet - symbols show locations that are within tolerance (o), over-predicted (+), and under-predicted (-).

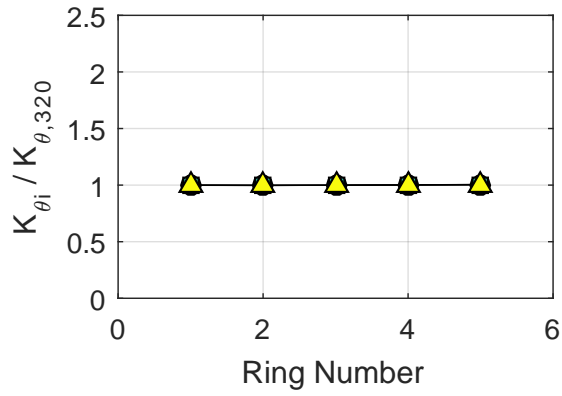
Table C.49: Interpolation effects on the derived quantities for the IMX inlet run number R320, clocking C8.

	$K_\theta$	$K_r$	$K_a$	$IDC$	$IDT$
Linear	0.624	0.315	0.938	0.029	0.099
Spline	0.622	0.321	0.943	0.029	0.100
Polar	0.621	0.324	0.945	0.027	0.100
Kriging	0.621	0.220	0.841	0.018	0.100

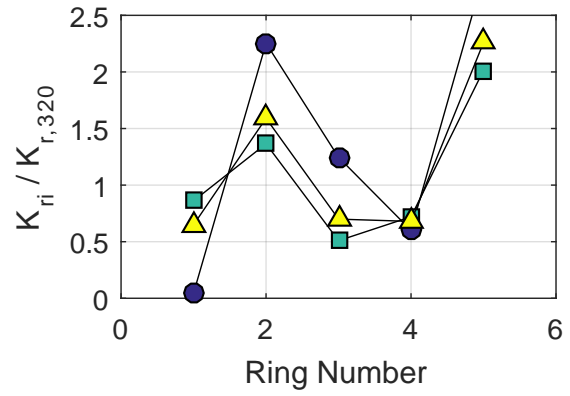
## C.2 IMX Inlet

Table C.50: Distortion index results for the IMX inlet

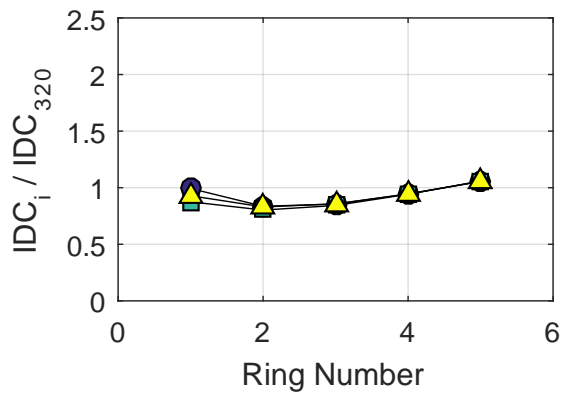
	$K_\theta$	$K_r$	$K_a$	$IDC$	$IDT$
R300	0.432	0.010	0.442	0.015	0.070
R310	0.398	0.022	0.419	0.020	0.108
R320	0.374	0.017	0.391	0.020	0.113



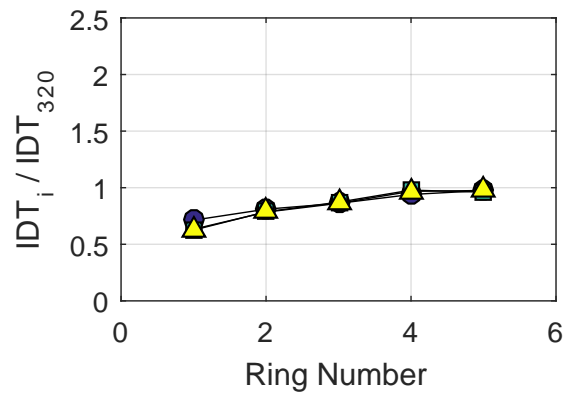
(a) Circumferential K-index



(b) Radial K-index



(c) Circumferential ID-index



(d) Combined ID-index

Figure C.110: Ring distortion indices, normalized by the overall index. Circles represent run number R300, squares represent run number R310, and triangles represent run number R320.

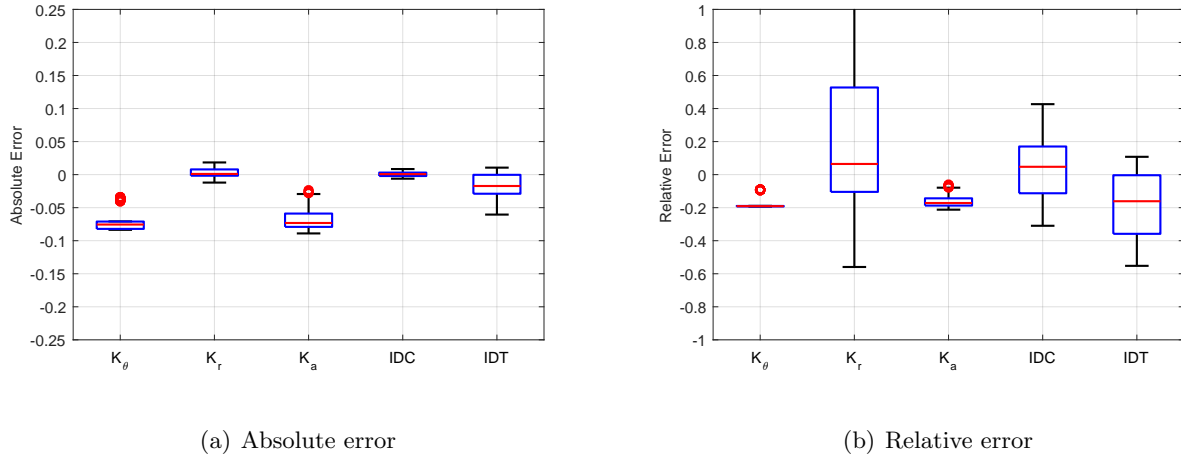


Figure C.111: Absolute and relative errors in the distortion indices for the IMX inlet.

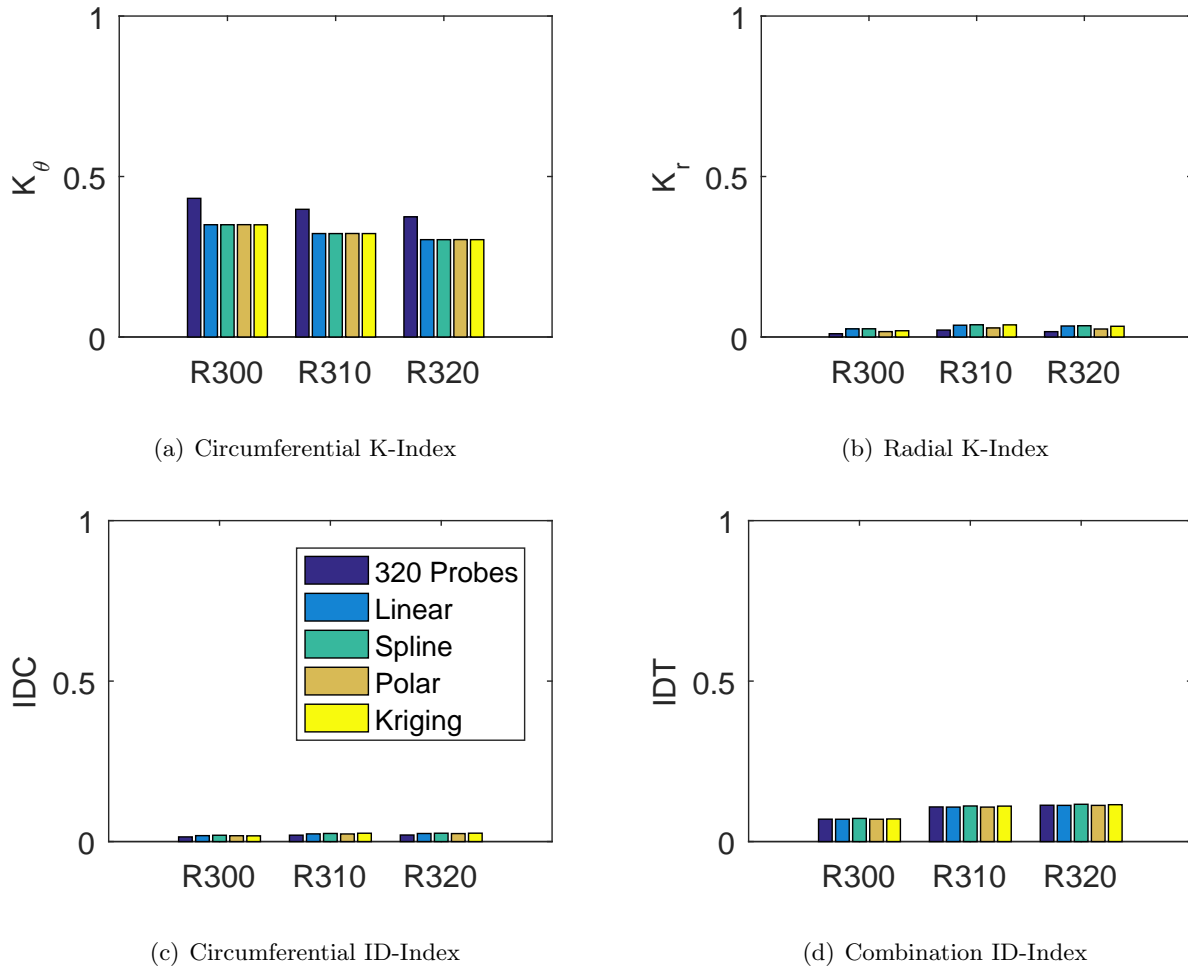
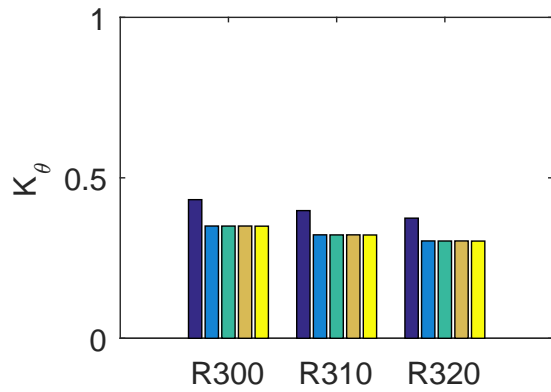
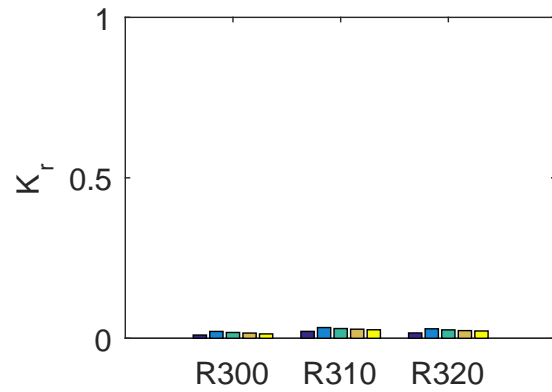


Figure C.112: Barplots of the distortion indices for the zeroth clocking for the IMX inlet.

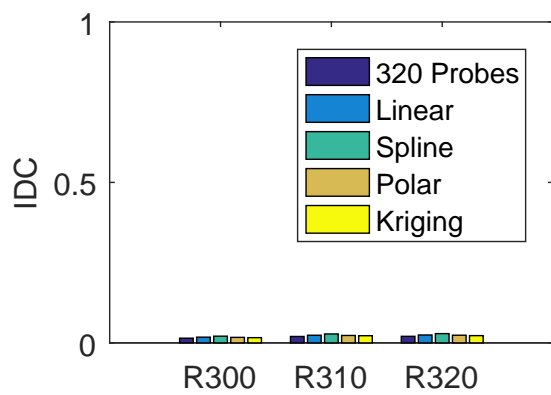




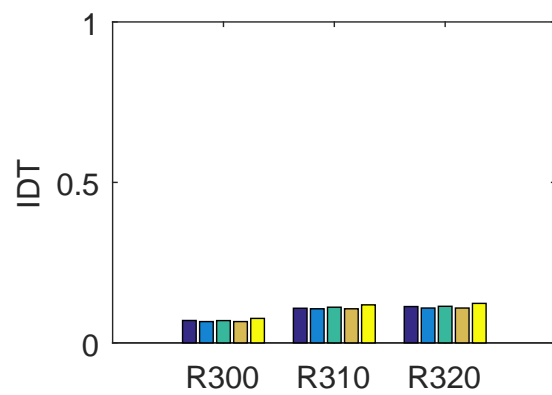
(a) Circumferential K-Index



(b) Radial K-Index



(c) Circumferential ID-Index



(d) Combination ID-Index

Figure C.113: Barplots of the distortion indices for the first clocking for the IMX inlet.

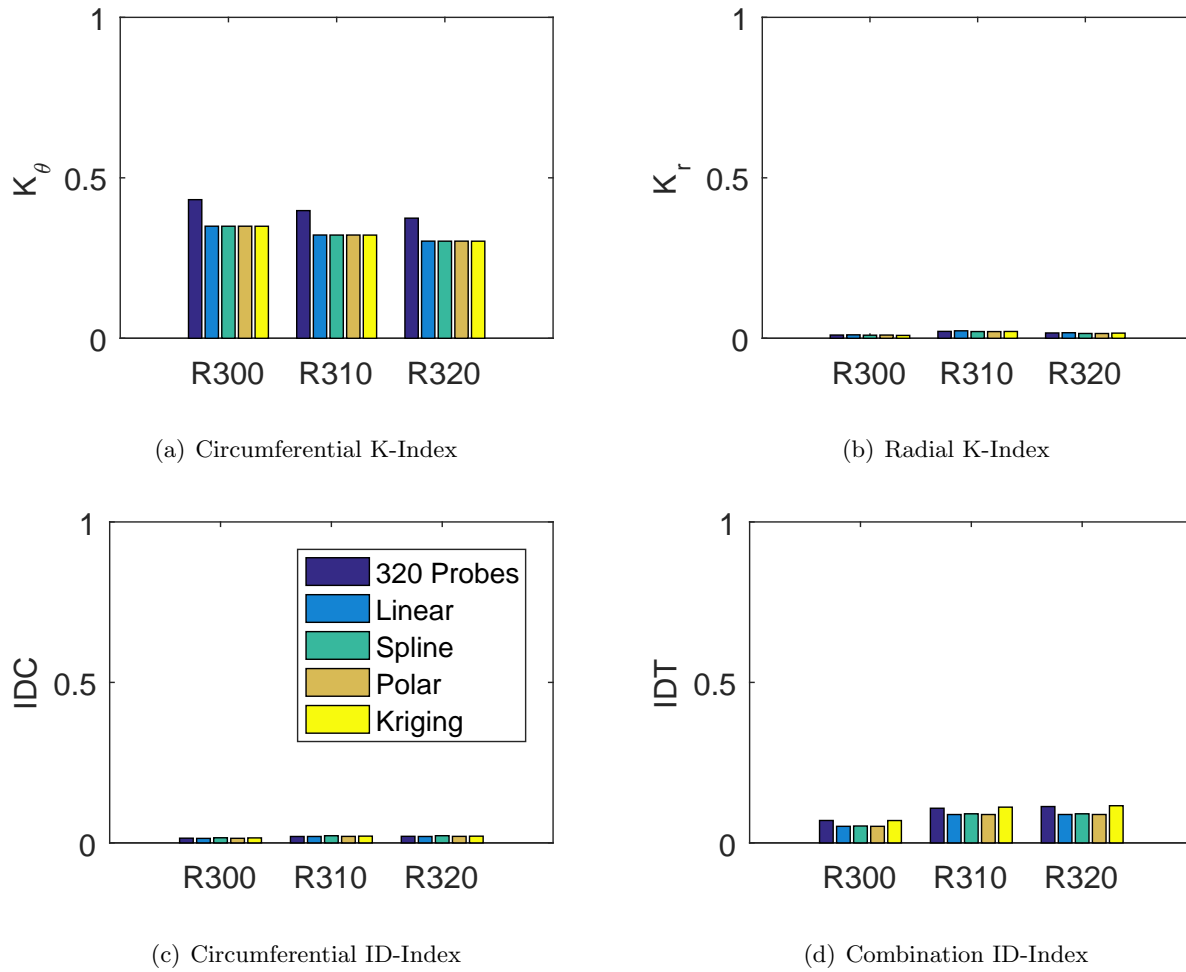
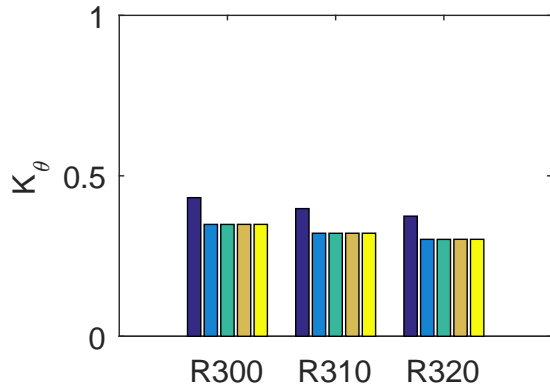
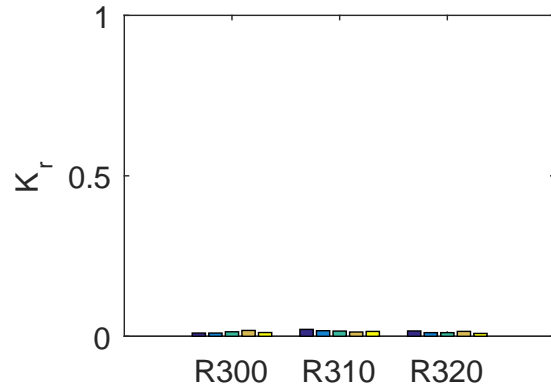


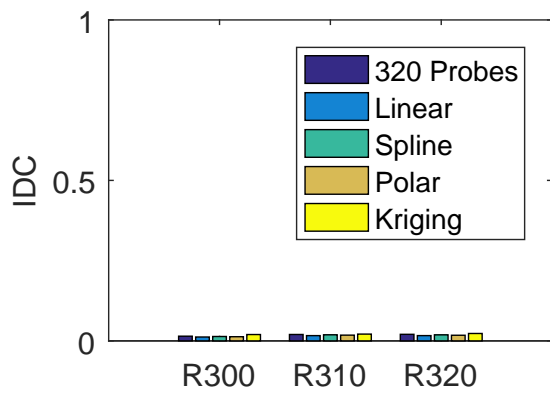
Figure C.114: Barplots of the distortion indices for the second clocking for the IMX inlet.



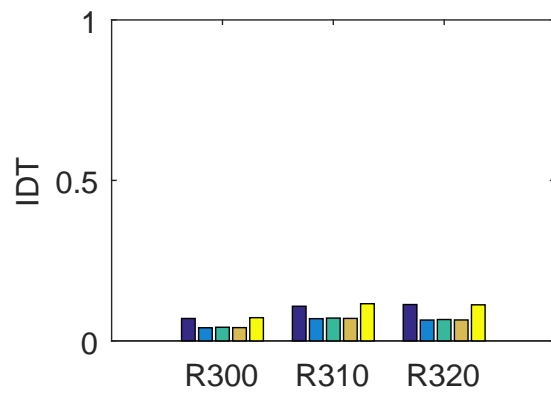
(a) Circumferential K-Index



(b) Radial K-Index

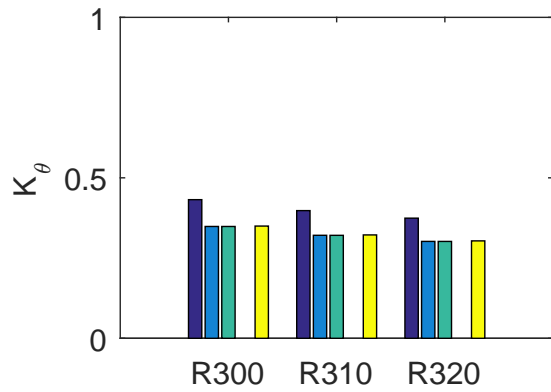


(c) Circumferential ID-Index

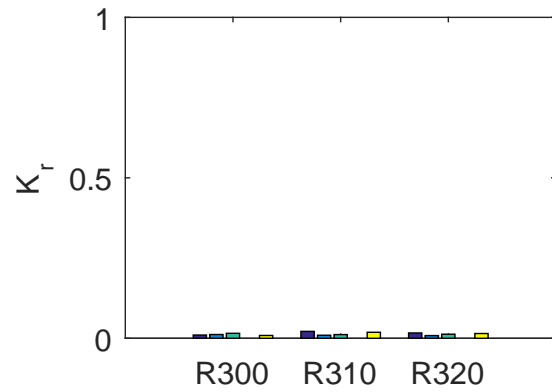


(d) Combination ID-Index

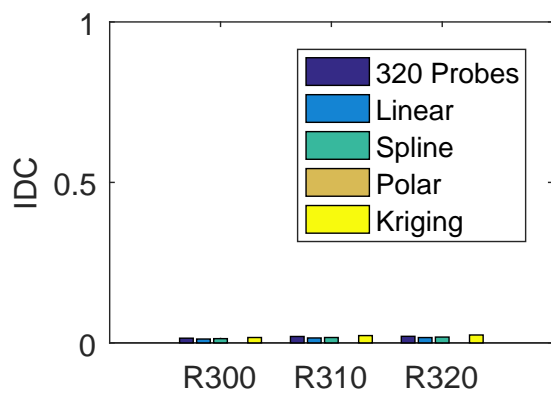
Figure C.115: Barplots of the distortion indices for the third clocking for the IMX inlet.



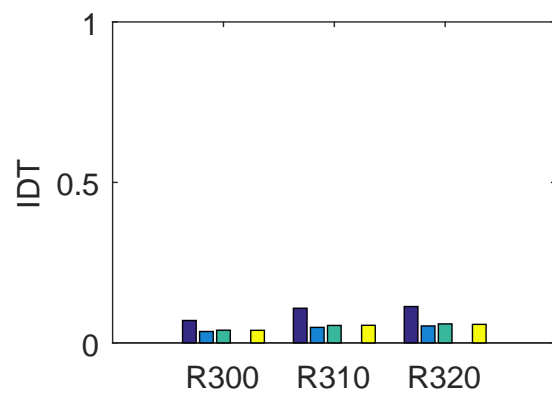
(a) Circumferential K-Index



(b) Radial K-Index

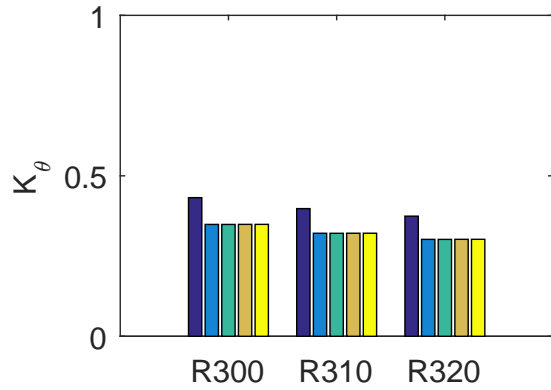


(c) Circumferential ID-Index

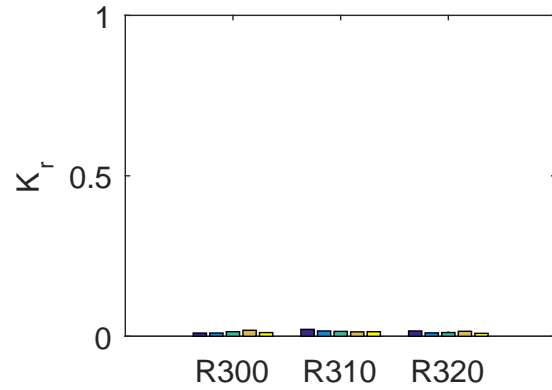


(d) Combination ID-Index

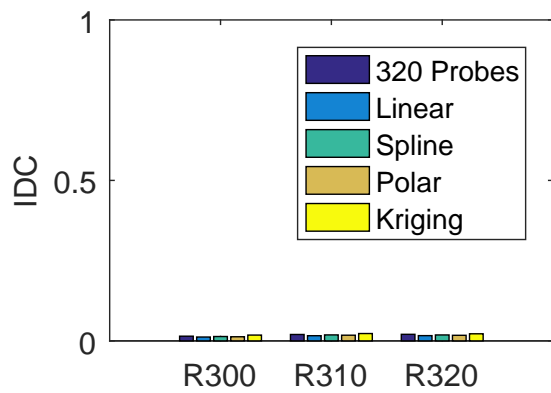
Figure C.116: Barplots of the distortion indices for the fourth clocking for the IMX inlet.



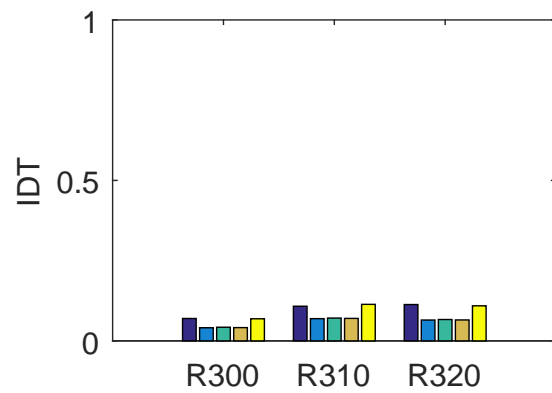
(a) Circumferential K-Index



(b) Radial K-Index



(c) Circumferential ID-Index



(d) Combination ID-Index

Figure C.117: Barplots of the distortion indices for the fifth clocking for the IMX inlet.

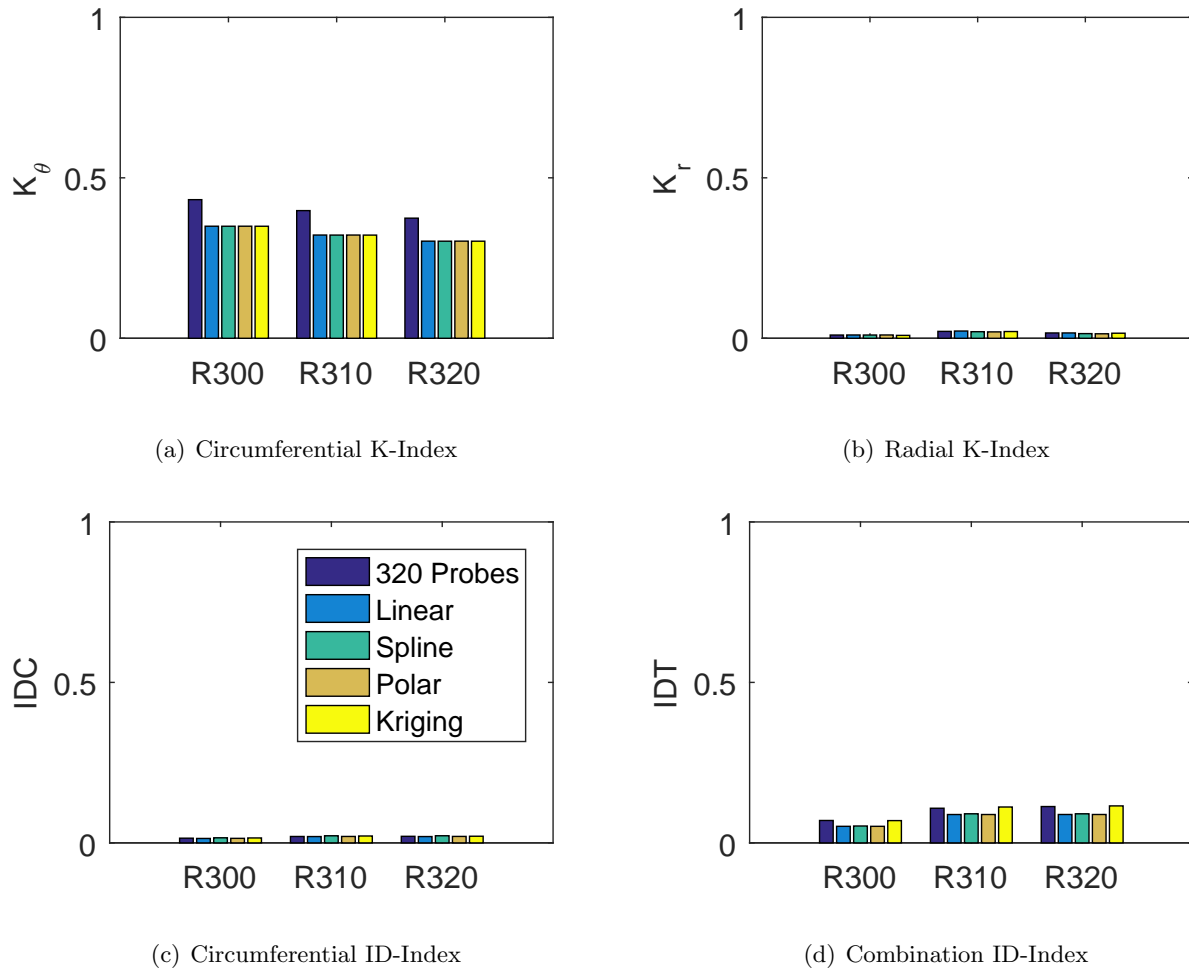
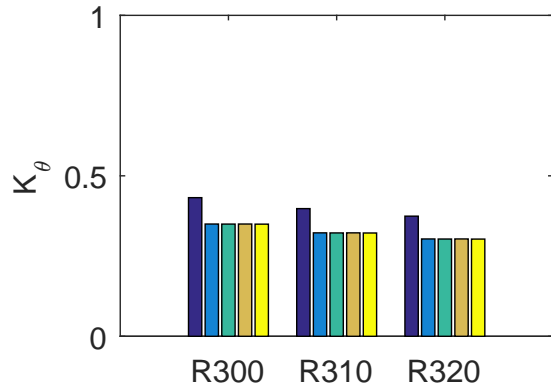
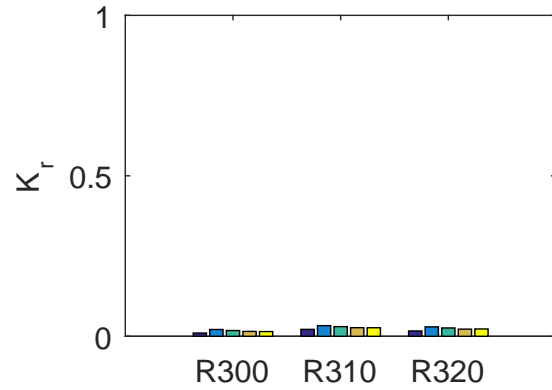


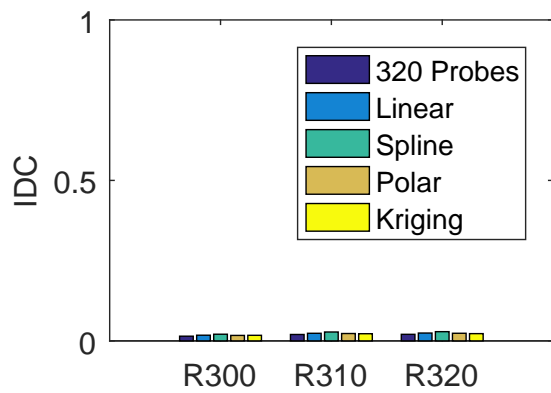
Figure C.118: Barplots of the distortion indices for the sixth clocking for the IMX inlet.



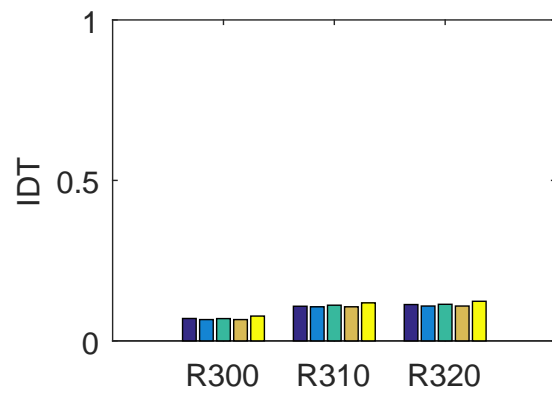
(a) Circumferential K-Index



(b) Radial K-Index



(c) Circumferential ID-Index



(d) Combination ID-Index

Figure C.119: Barplots of the distortion indices for the seventh clocking for the IMX inlet.

C.2.1 Run Number R300

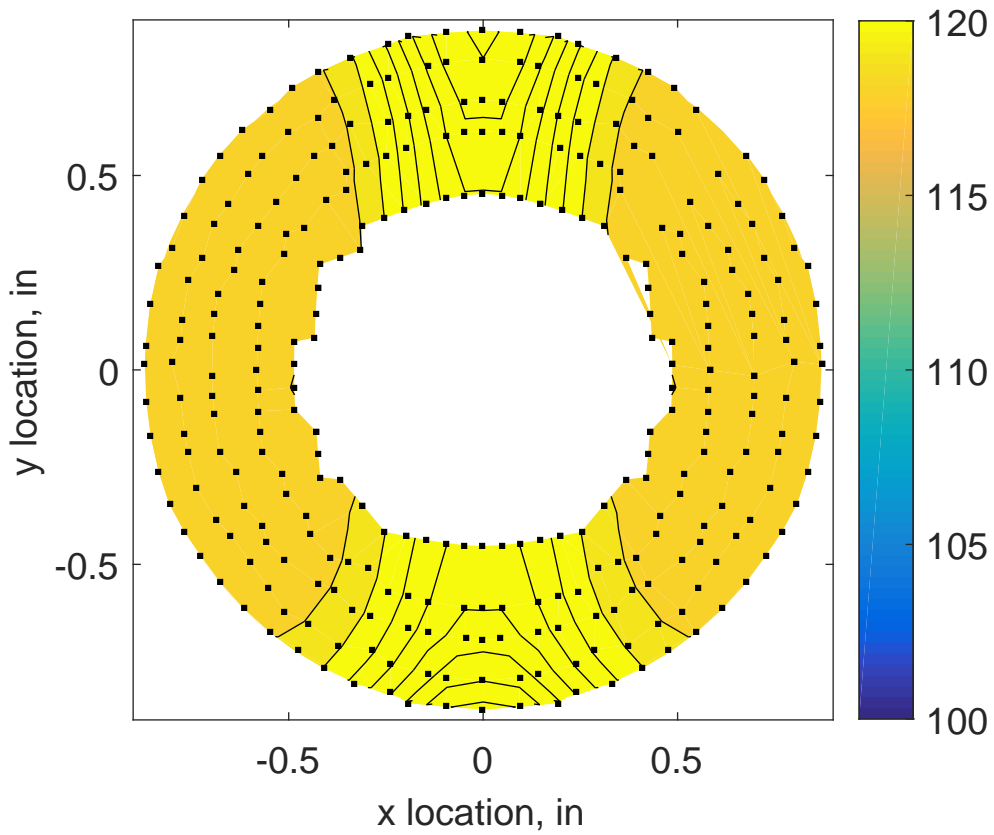


Figure C.120: IMX run number R300 raw pressure contour created with 320 probes.



### C.2.1.1 Zeroth Clocking

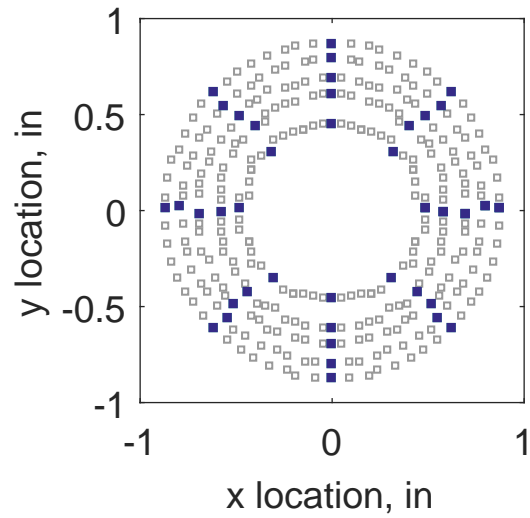
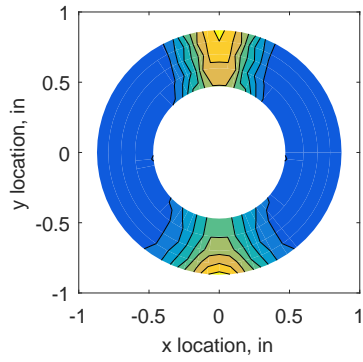


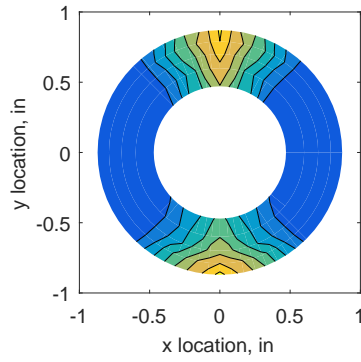
Figure C.121: Zeroth clocking probe position

Table C.51: Interpolation results for the IMX inlet run number R300, clocking C1.

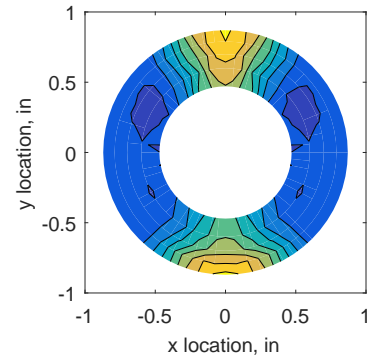
	Mean	Std. Dev.	Over-Prediction	In Tolerance	Under-Prediction
Linear	0.0023	0.0026	34	246	0
Spline	0.0022	0.0025	36	244	0
Polar	0.0031	0.0040	70	170	40
Kriging	0.0022	0.0016	12	268	0



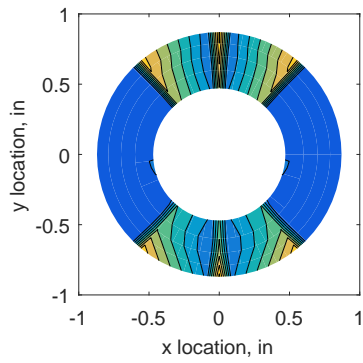
(a) 320 Probes



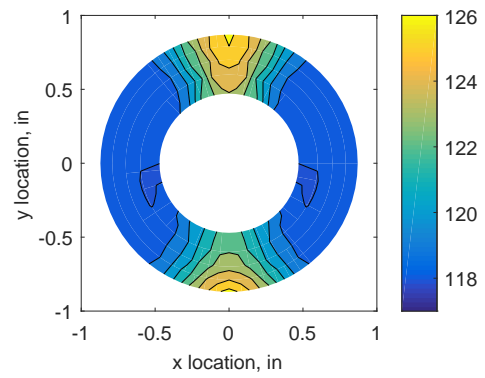
(b) Linear Interpolation



(c) Spline Interpolation

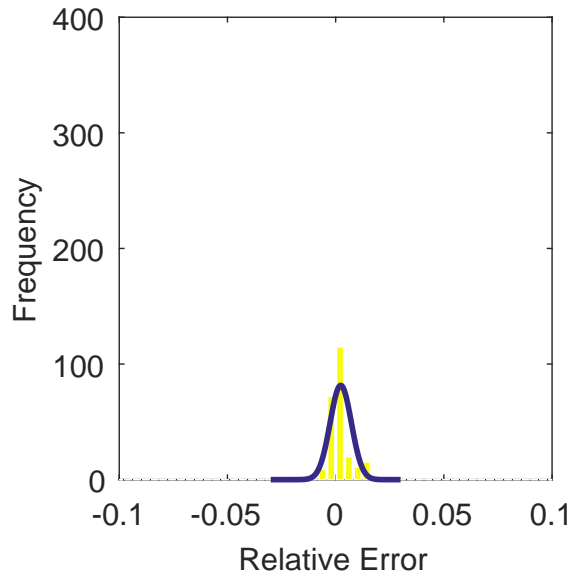


(d) Polar Interpolation

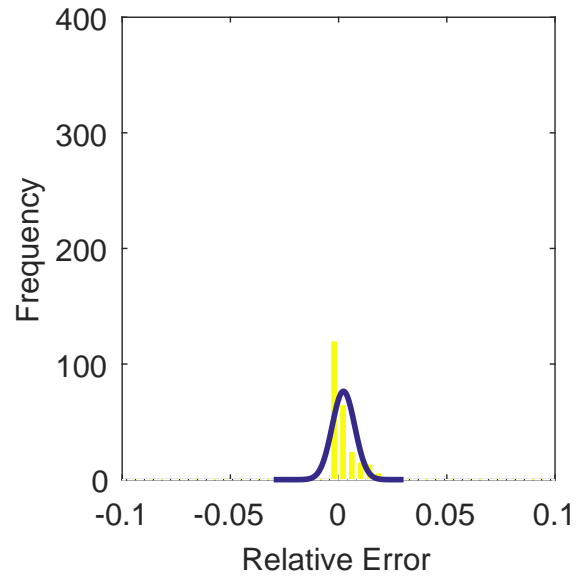


(e) Kriging Interpolation

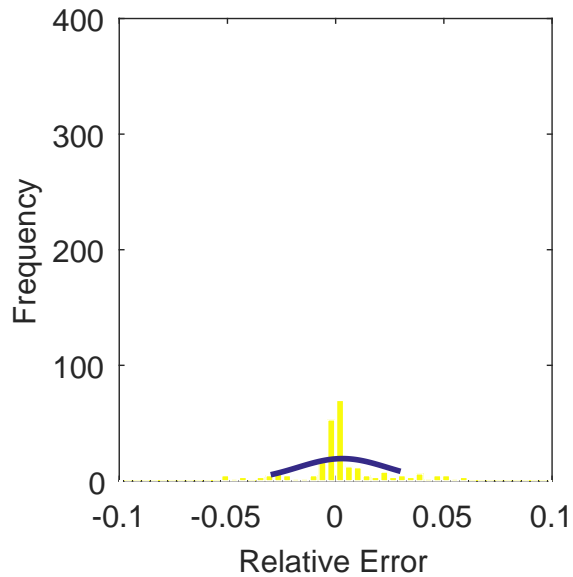
Figure C.122: Contour plots for the raw and interpolated values for the IMX inlet.



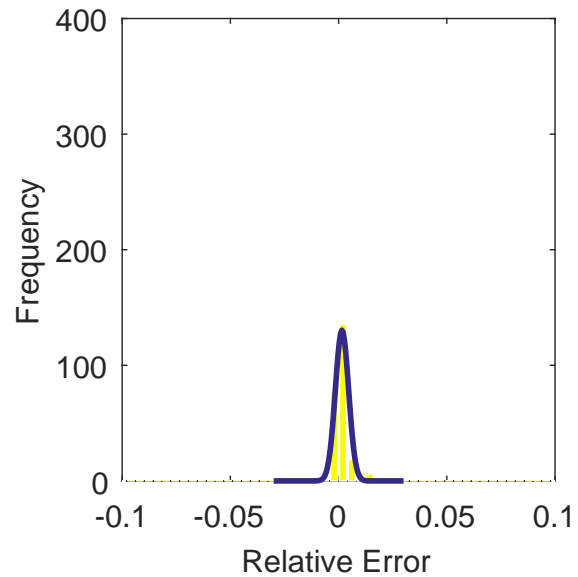
(a) Linear Interpolation Error



(b) Spline Interpolation Error

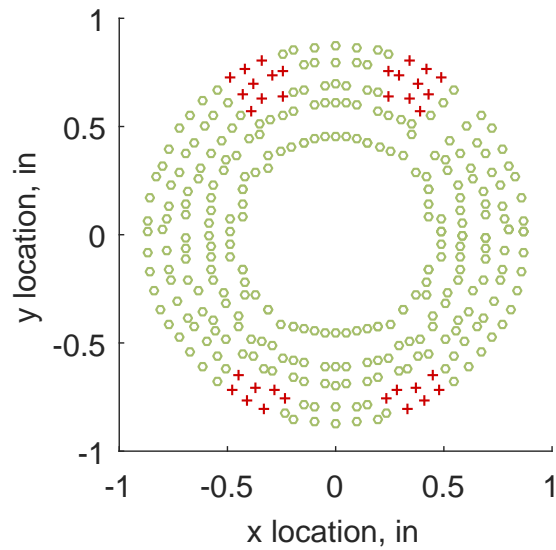


(c) Polar Interpolation Error

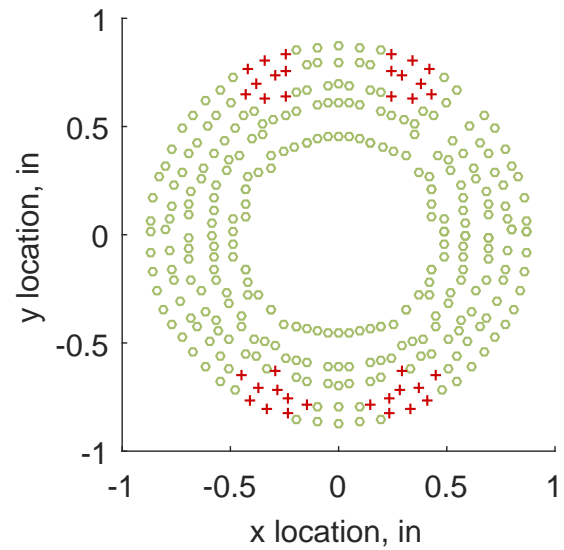


(d) Kriging Interpolation Error

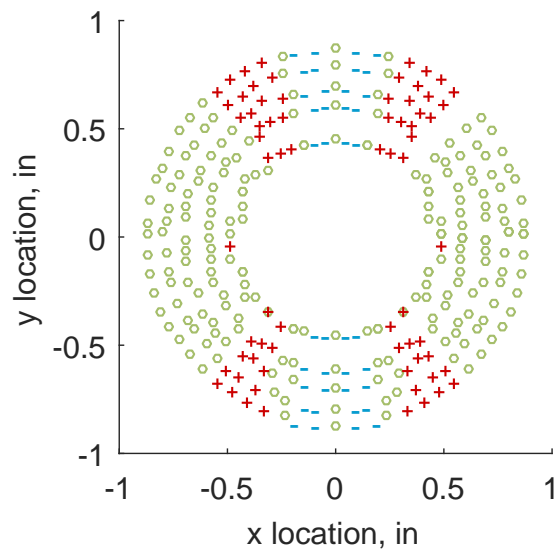
Figure C.123: Relative error for various interpolation schemes of run number R300, zeroth clocking for the IMX inlet.



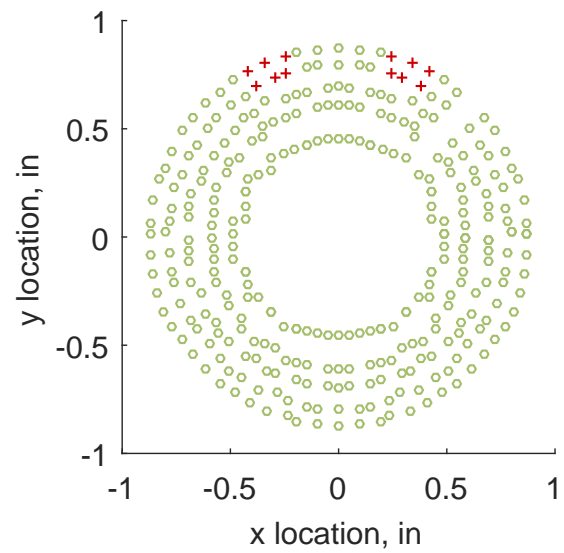
(a) Linear Interpolation



(b) Spline Interpolation



(c) Polar Interpolation



(d) Kriging Interpolation

Figure C.124: Interpolation error for the IMX inlet - symbols show locations that are within tolerance (o), over-predicted (+), and under-predicted (-).

Table C.52: Interpolation effects on the derived quantities for the IMX inlet run number R300, clocking C1.

	$K_\theta$	$K_r$	$K_a$	$IDC$	$IDT$
Linear	0.393	0.019	0.412	0.016	0.070
Spline	0.350	0.025	0.375	0.018	0.070
Polar	0.350	0.026	0.375	0.020	0.072
Kriging	0.350	0.017	0.367	0.018	0.070

### C.2.1.2 First Clocking

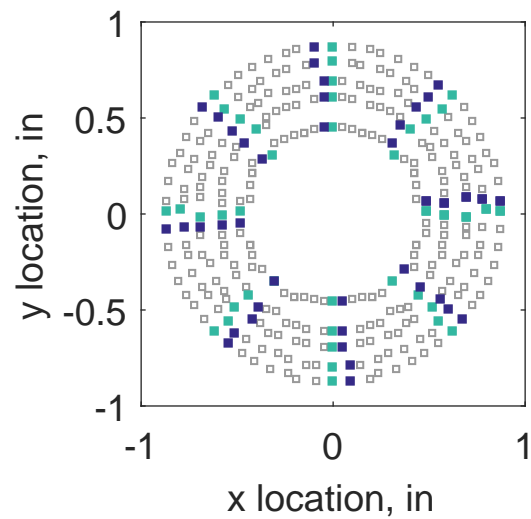


Figure C.125: First clocking probe position

Table C.53: Interpolation results for the IMX inlet run number R300, clocking C2.

	Mean	Std. Dev.	Over-Prediction	In Tolerance	Under-Prediction
Linear	0.0024	0.0024	37	238	5
Spline	0.0019	0.0021	35	245	0
Polar	0.0027	0.0039	64	166	50
Kriging	0.0019	0.0010	6	274	0

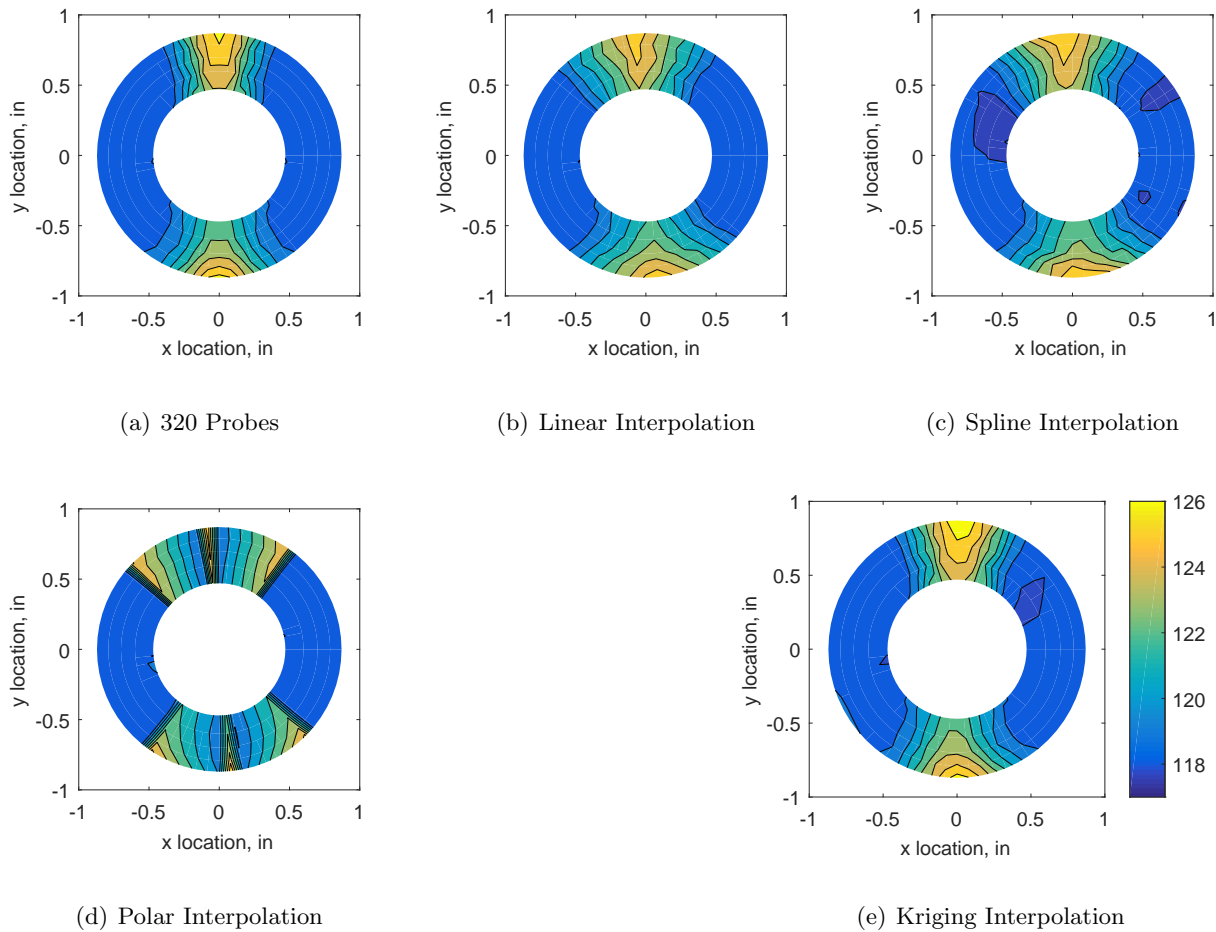
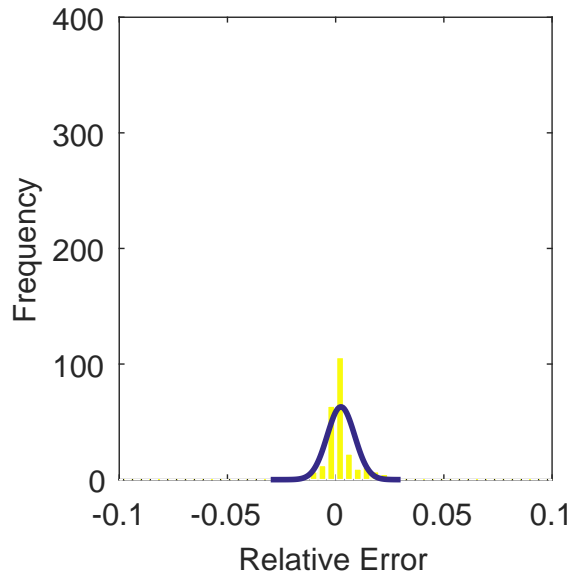
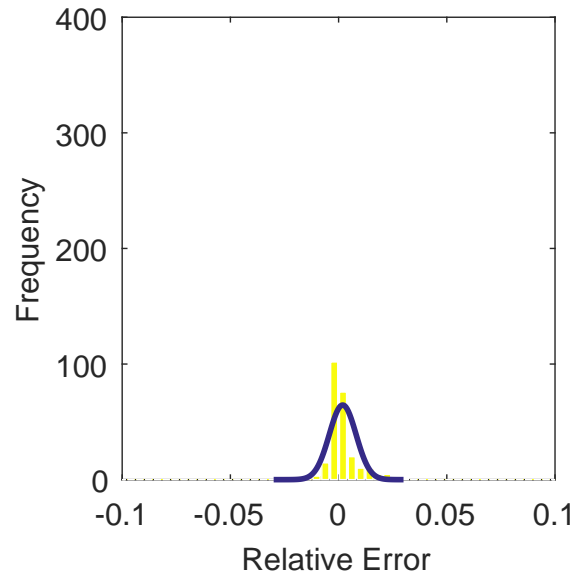


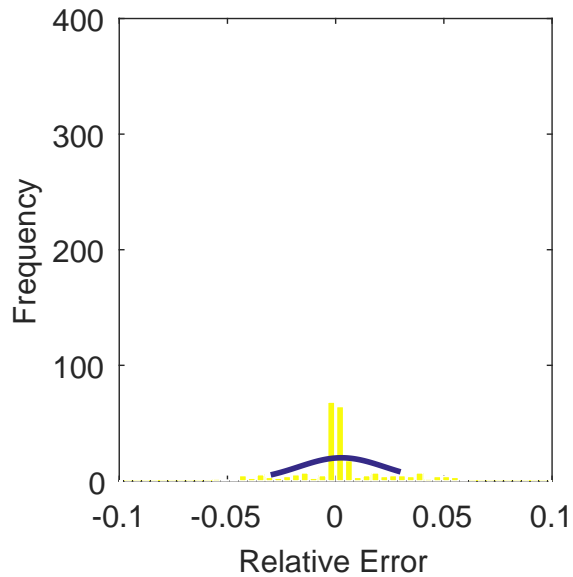
Figure C.126: Contour plots for the raw and interpolated values for the IMX inlet.



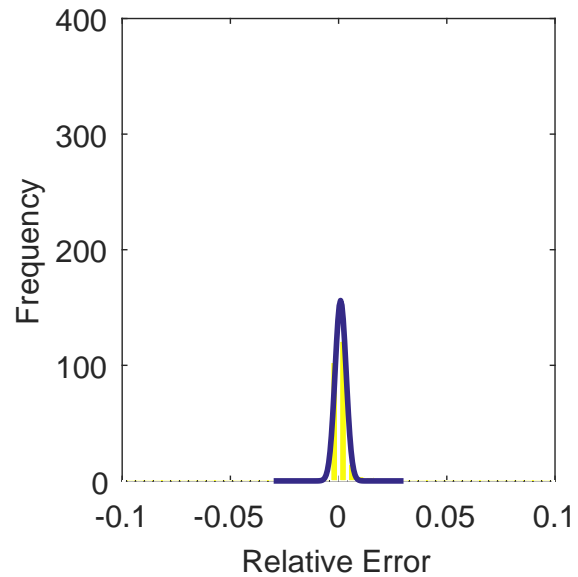
(a) Linear Interpolation Error



(b) Spline Interpolation Error

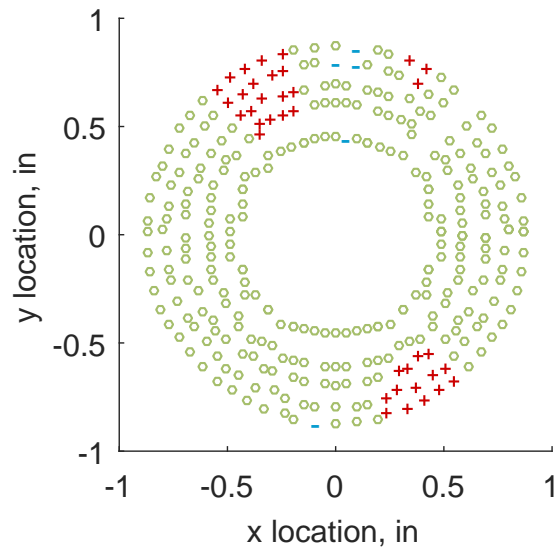


(c) Polar Interpolation Error

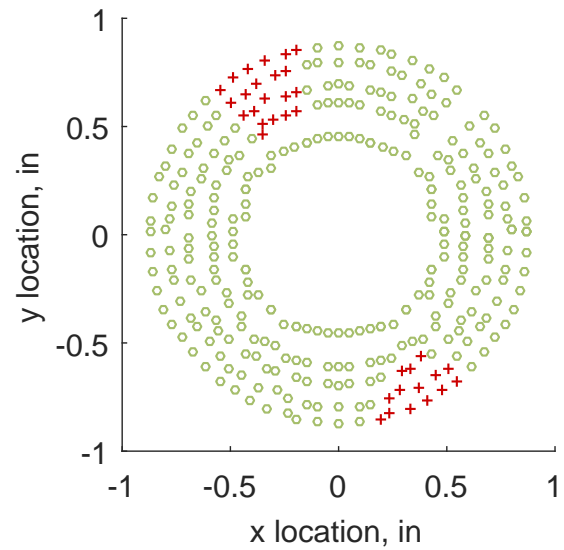


(d) Kriging Interpolation Error

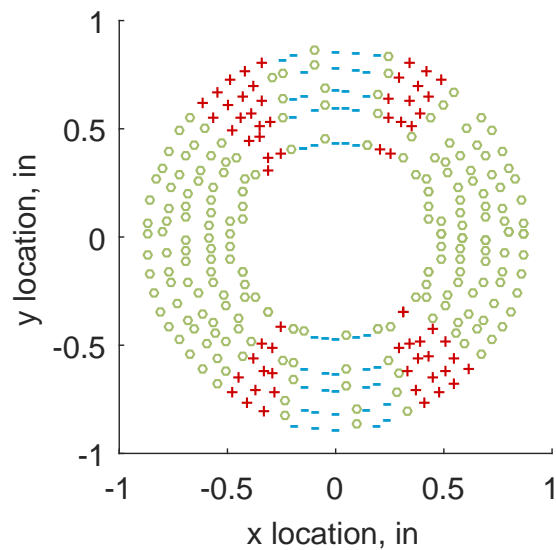
Figure C.127: Relative error for various interpolation schemes of run number R300, first clocking for the IMX inlet.



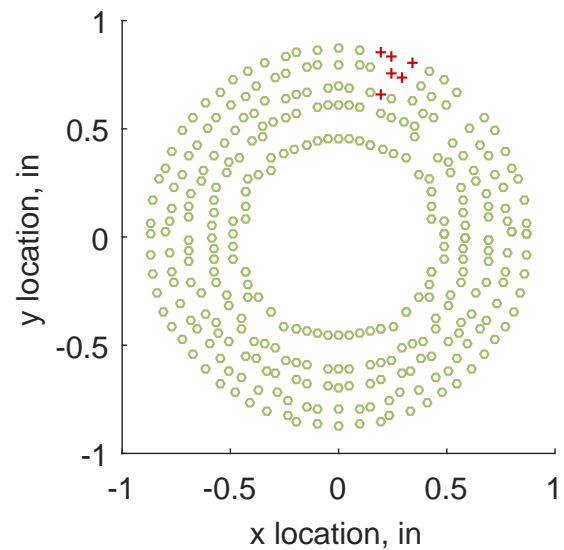
(a) Linear Interpolation



(b) Spline Interpolation



(c) Polar Interpolation



(d) Kriging Interpolation

Figure C.128: Interpolation error for the IMX inlet - symbols show locations that are within tolerance (o), over-predicted (+), and under-predicted (-).



Table C.54: Interpolation effects on the derived quantities for the IMX inlet run number R300, clocking C2.

	$K_\theta$	$K_r$	$K_a$	$IDC$	$IDT$
Linear	0.393	0.018	0.411	0.015	0.066
Spline	0.350	0.021	0.371	0.018	0.066
Polar	0.350	0.018	0.368	0.021	0.069
Kriging	0.350	0.016	0.366	0.017	0.066

### C.2.1.3 Second Clocking

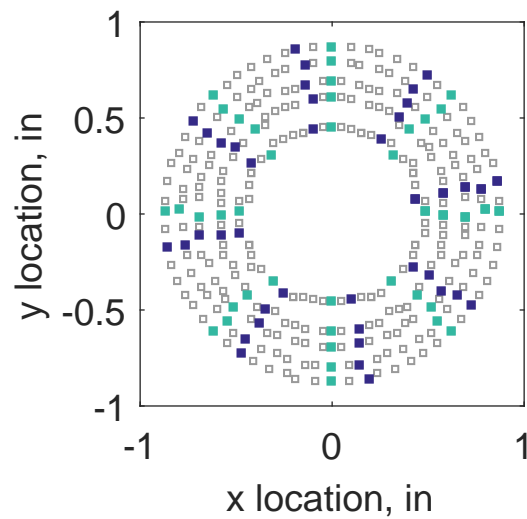


Figure C.129: Second clocking probe position

Table C.55: Interpolation results for the IMX inlet run number R300, clocking C3.

	Mean	Std. Dev.	Over-Prediction	In Tolerance	Under-Prediction
Linear	0.0007	0.0024	36	209	35
Spline	0.0004	0.0025	39	208	33
Polar	0.0009	0.0034	63	165	52
Kriging	0.0004	0.0010	0	280	0

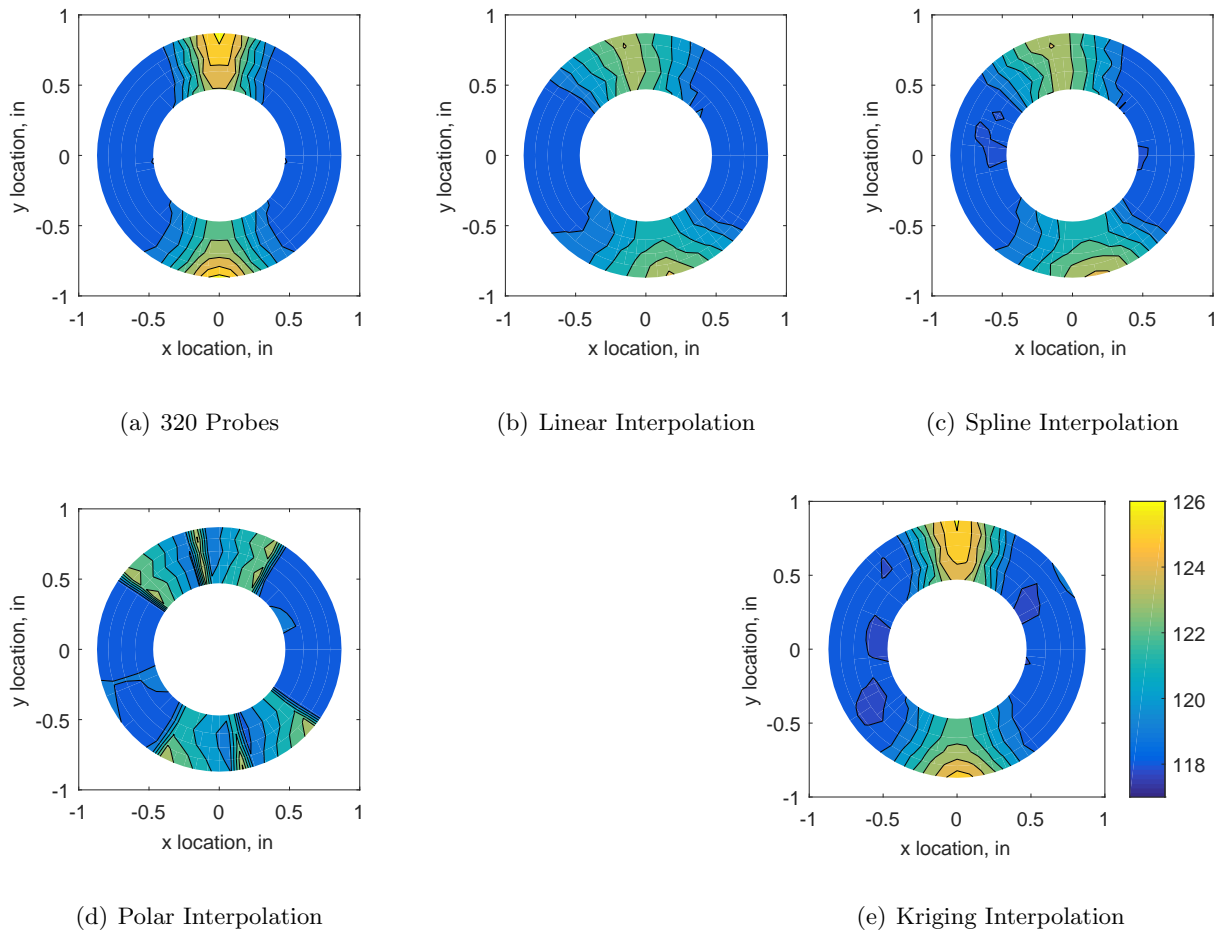
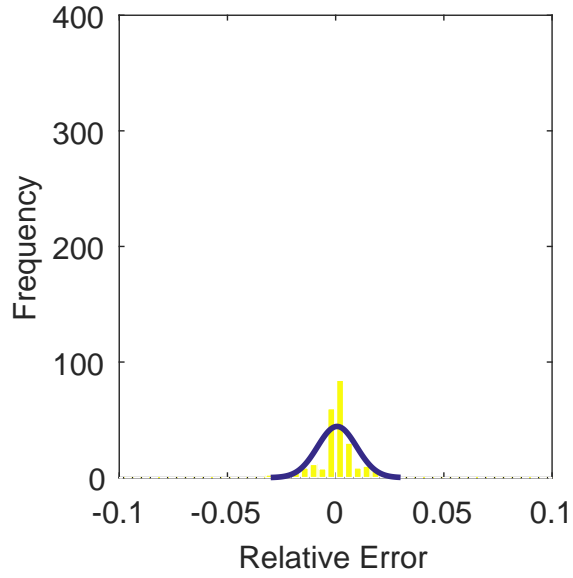
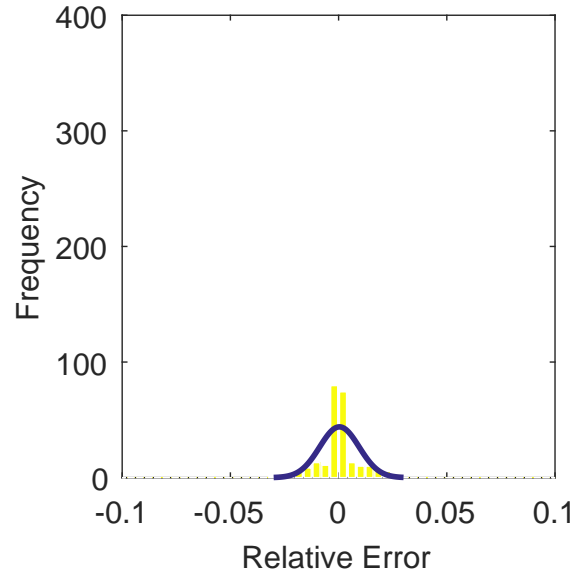


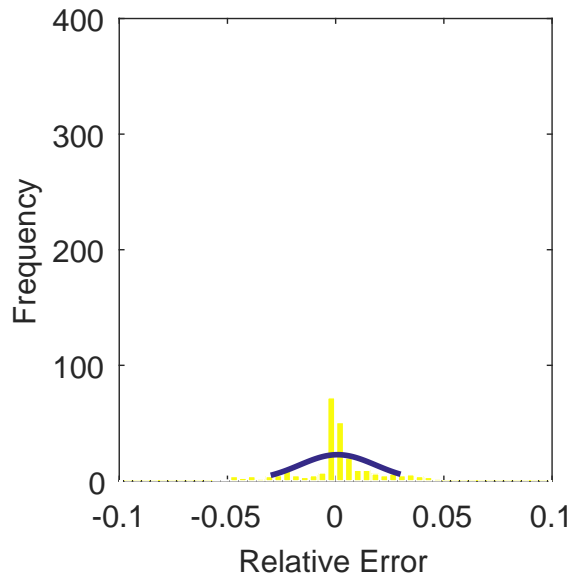
Figure C.130: Contour plots for the raw and interpolated values for the IMX inlet.



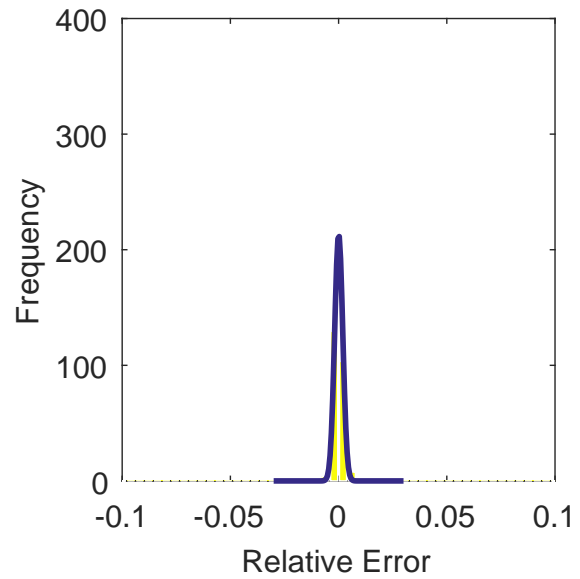
(a) Linear Interpolation Error



(b) Spline Interpolation Error

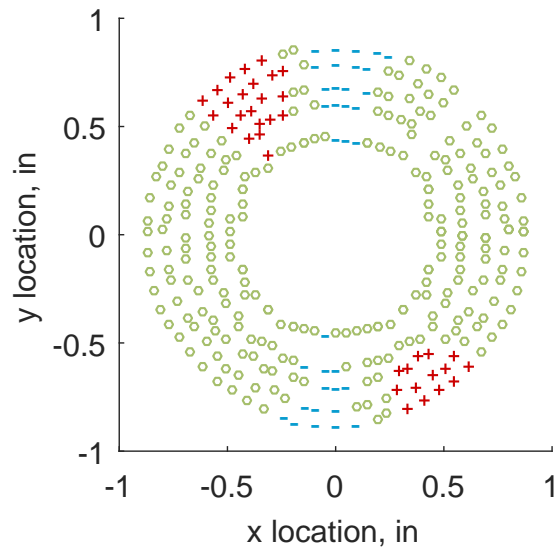


(c) Polar Interpolation Error

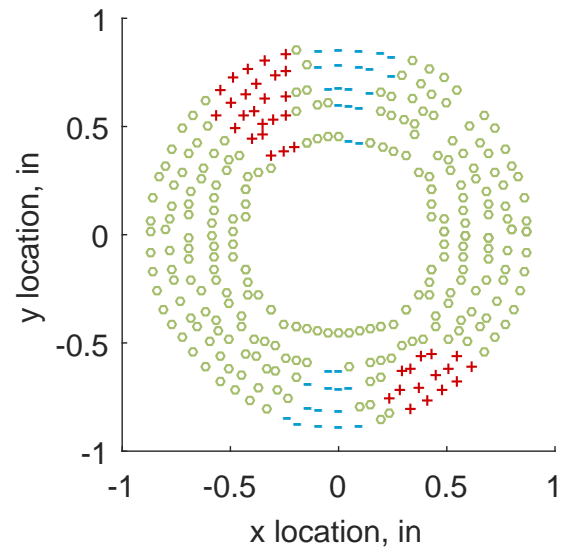


(d) Kriging Interpolation Error

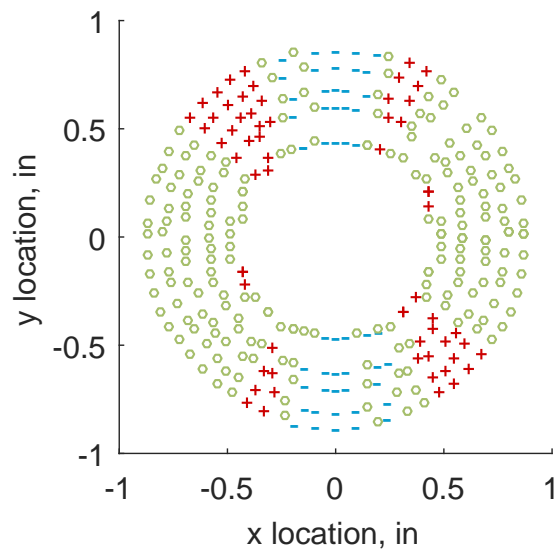
Figure C.131: Relative error for various interpolation schemes of run number R300, second clocking for the IMX inlet.



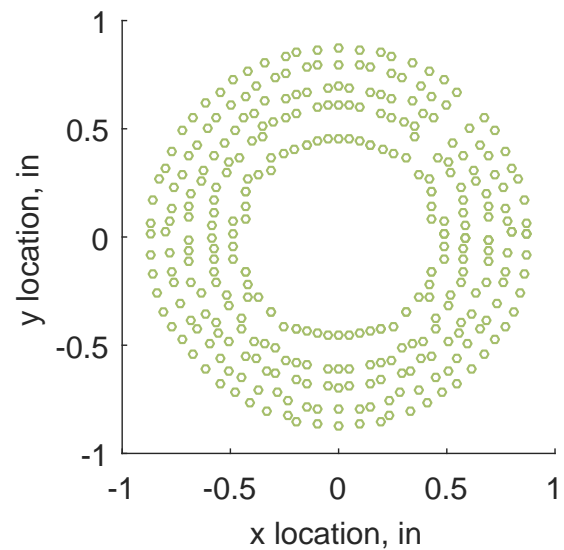
(a) Linear Interpolation



(b) Spline Interpolation



(c) Polar Interpolation



(d) Kriging Interpolation

Figure C.132: Interpolation error for the IMX inlet - symbols show locations that are within tolerance (o), over-predicted (+), and under-predicted (-).

Table C.56: Interpolation effects on the derived quantities for the IMX inlet run number R300, clocking C3.

	$K_\theta$	$K_r$	$K_a$	$IDC$	$IDT$
Linear	0.392	0.011	0.403	0.012	0.052
Spline	0.349	0.011	0.360	0.014	0.052
Polar	0.349	0.010	0.359	0.016	0.053
Kriging	0.349	0.010	0.359	0.014	0.052

#### C.2.1.4 Third Clocking

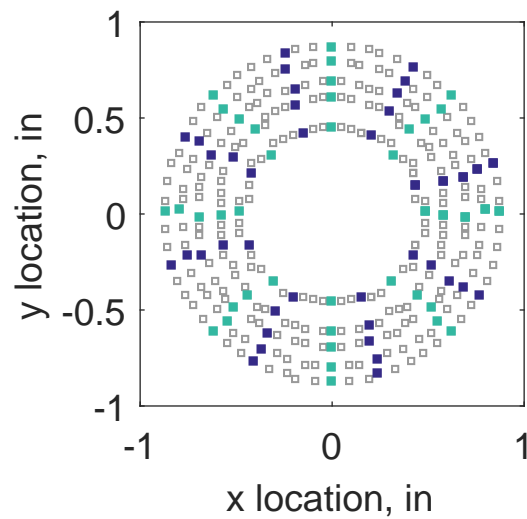


Figure C.133: Third clocking probe position

Table C.57: Interpolation results for the IMX inlet run number R300, clocking C4.

	Mean	Std. Dev.	Over-Prediction	In Tolerance	Under-Prediction
Linear	-0.0012	0.0026	30	198	52
Spline	-0.0014	0.0027	27	205	48
Polar	-0.0008	0.0034	63	156	61
Kriging	-0.0014	0.0012	0	278	2

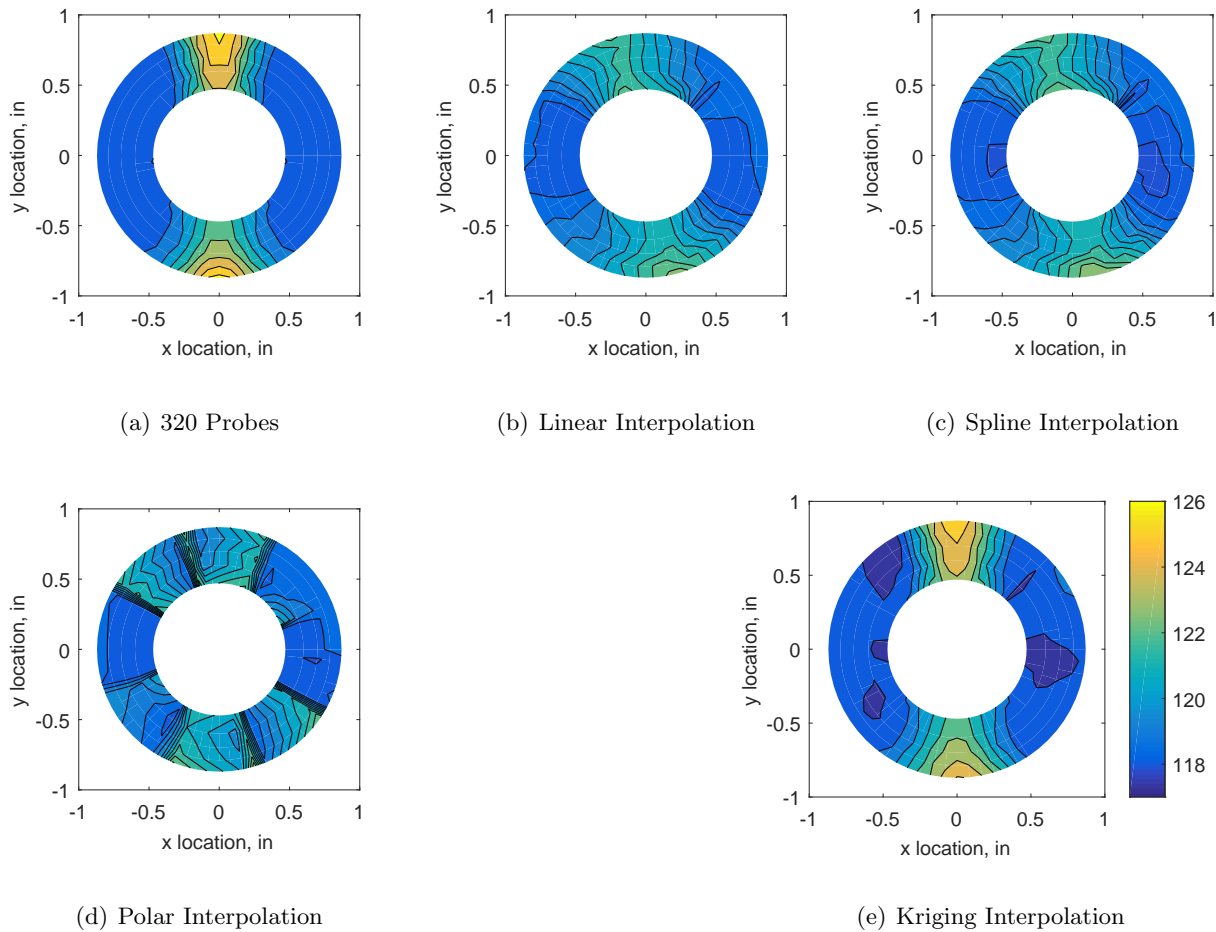
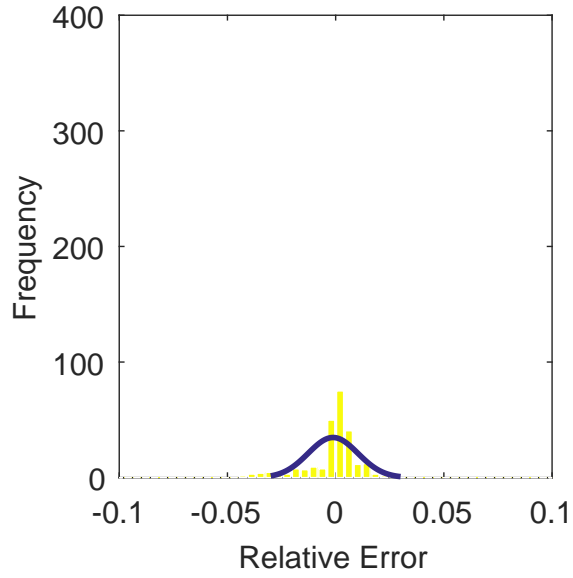
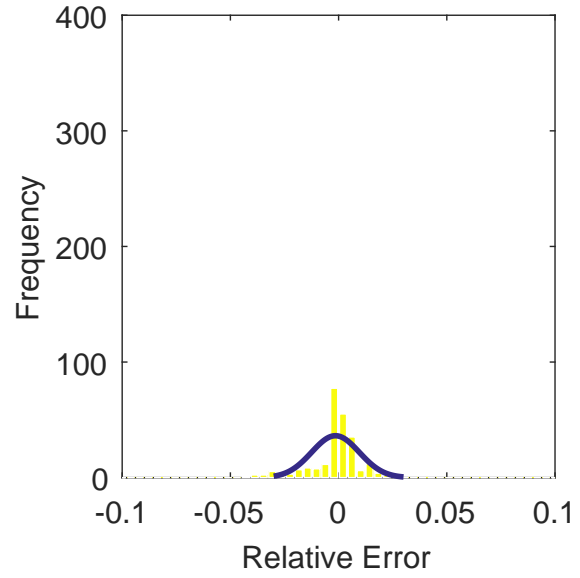


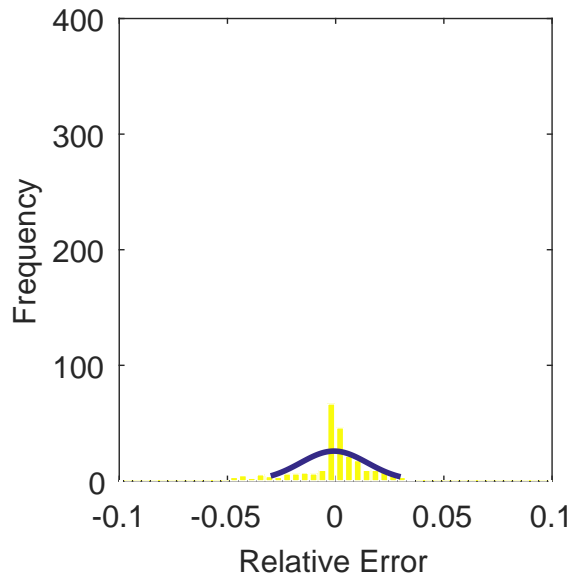
Figure C.134: Contour plots for the raw and interpolated values for the IMX inlet.



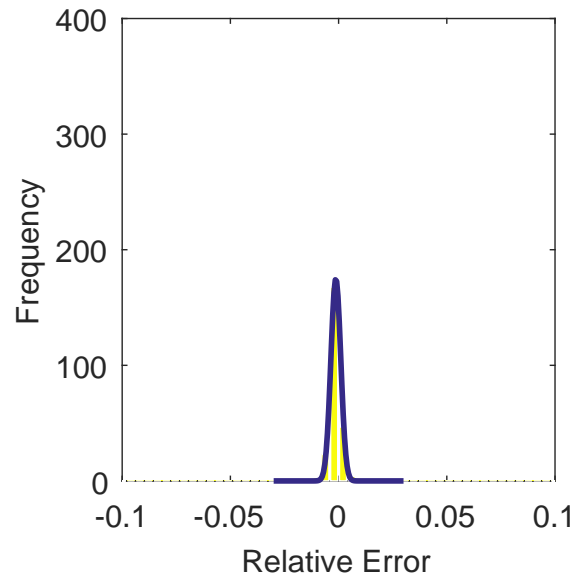
(a) Linear Interpolation Error



(b) Spline Interpolation Error

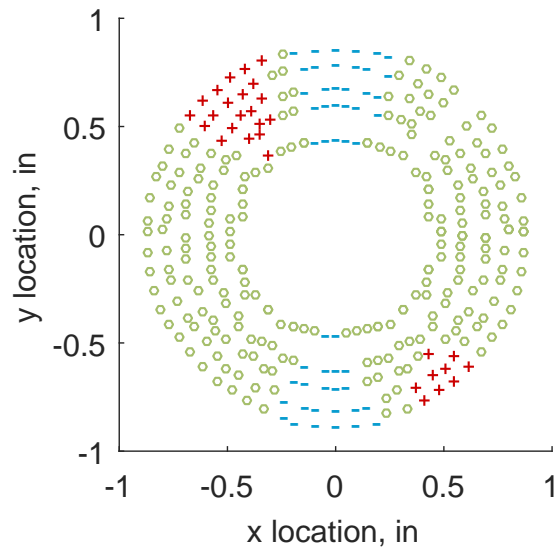


(c) Polar Interpolation Error

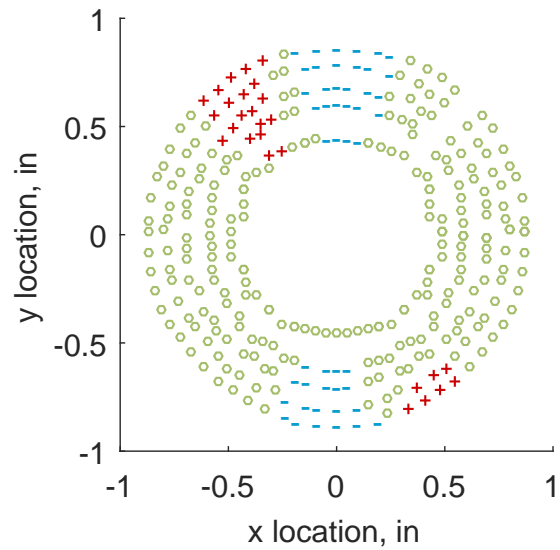


(d) Kriging Interpolation Error

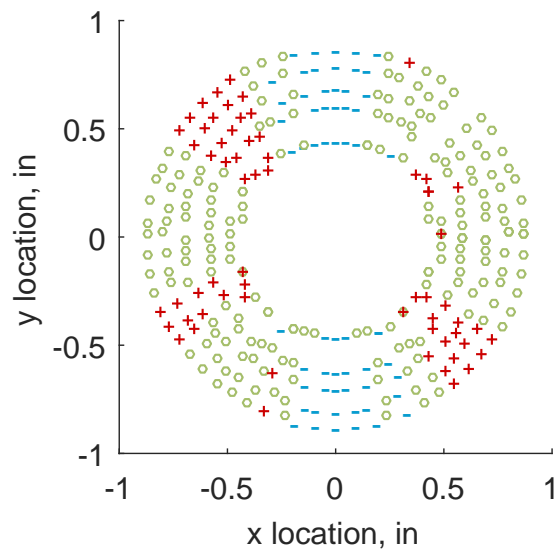
Figure C.135: Relative error for various interpolation schemes of run number R300, third clocking for the IMX inlet.



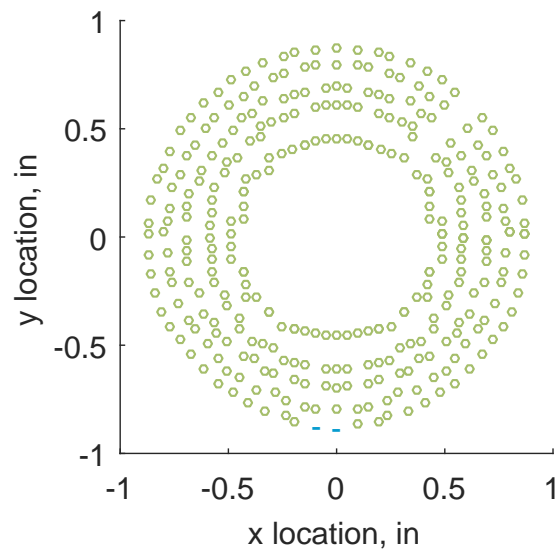
(a) Linear Interpolation



(b) Spline Interpolation



(c) Polar Interpolation



(d) Kriging Interpolation

Figure C.136: Interpolation error for the IMX inlet - symbols show locations that are within tolerance (o), over-predicted (+), and under-predicted (-).



Table C.58: Interpolation effects on the derived quantities for the IMX inlet run number R300, clocking C4.

	$K_\theta$	$K_r$	$K_a$	$IDC$	$IDT$
Linear	0.392	0.015	0.407	0.011	0.041
Spline	0.349	0.010	0.359	0.012	0.041
Polar	0.349	0.014	0.363	0.014	0.042
Kriging	0.349	0.018	0.367	0.013	0.041

#### C.2.1.5 Fourth Clocking

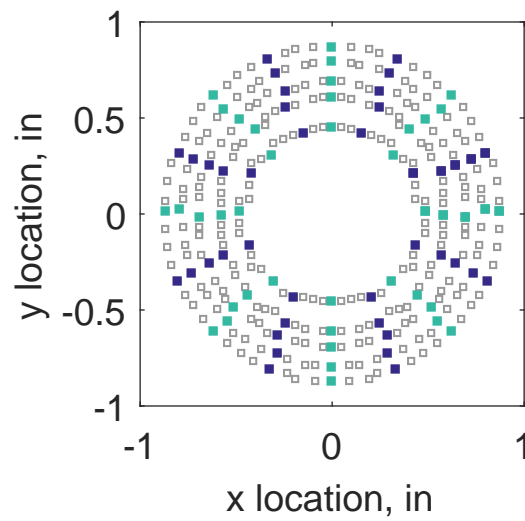


Figure C.137: Fourth clocking probe position

Table C.59: Interpolation results for the IMX inlet run number R300, clocking C5.

	Mean	Std. Dev.	Over-Prediction	In Tolerance	Under-Prediction
Linear	-0.0018	0.0034	17	209	54
Spline	-0.0020	0.0037	24	204	52
Polar	-0.0011	0.0037	71	145	64
Kriging	-0.0020	0.0048	101	126	53

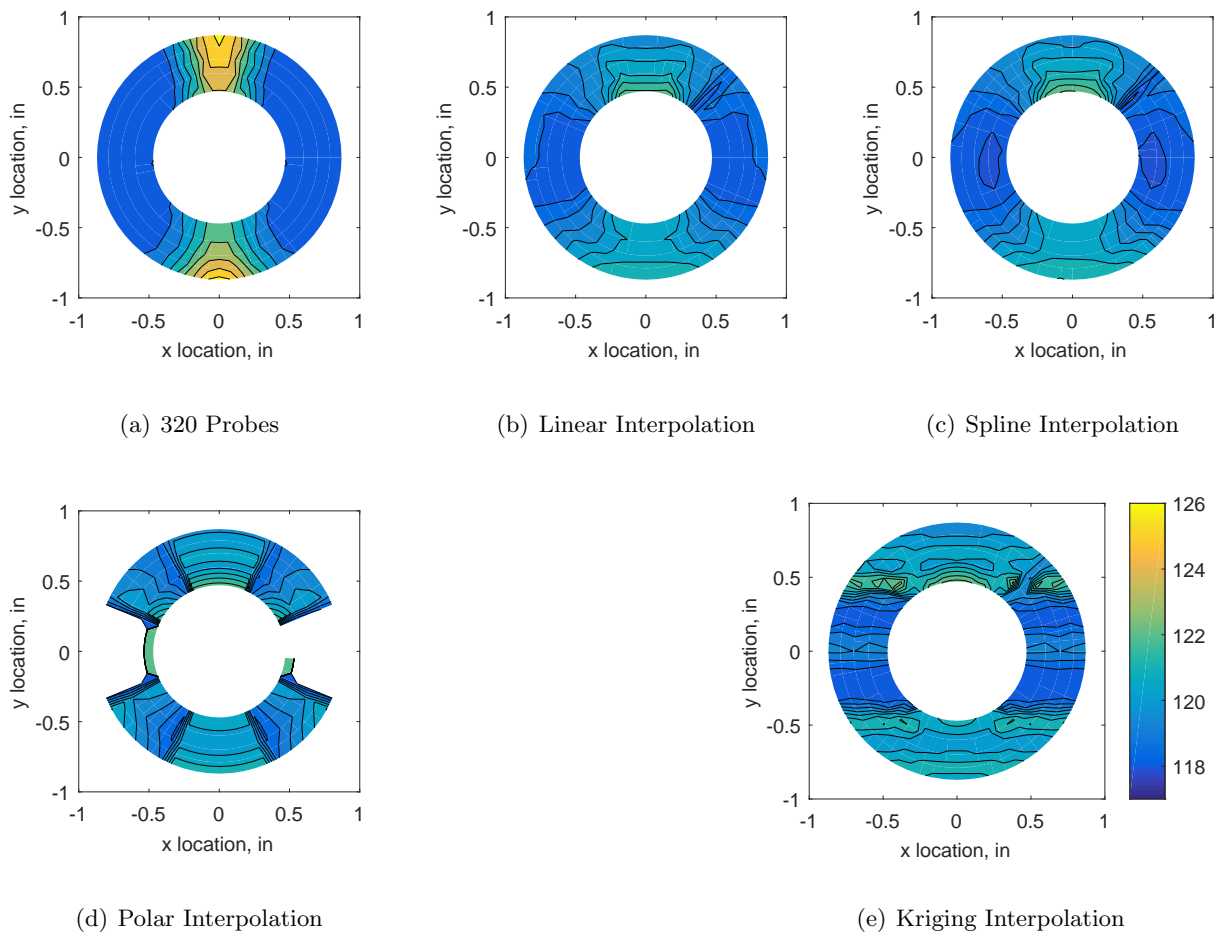
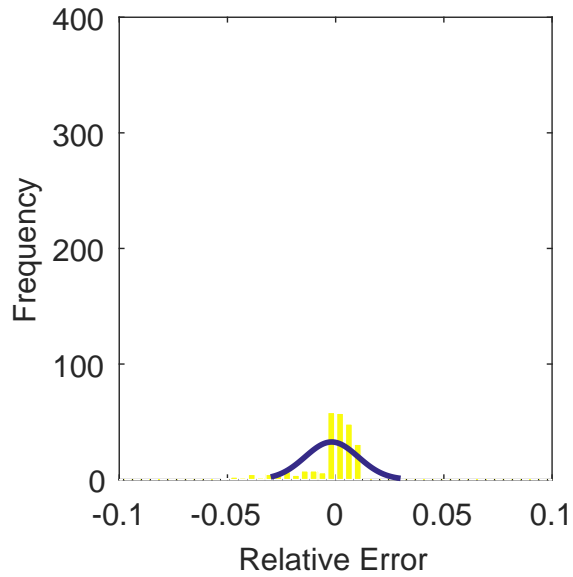
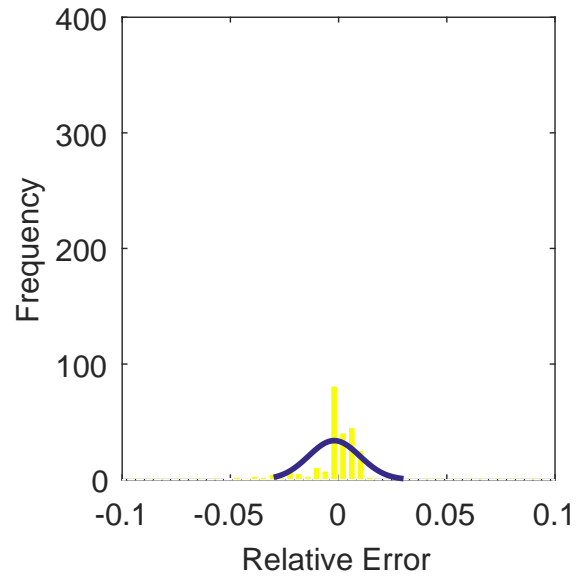


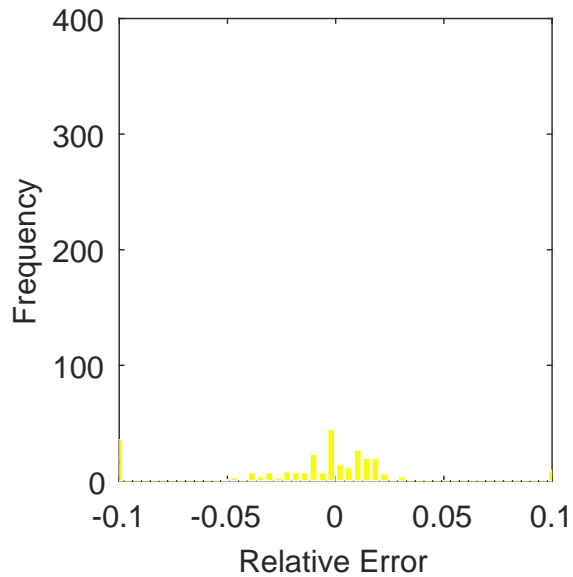
Figure C.138: Contour plots for the raw and interpolated values for the IMX inlet.



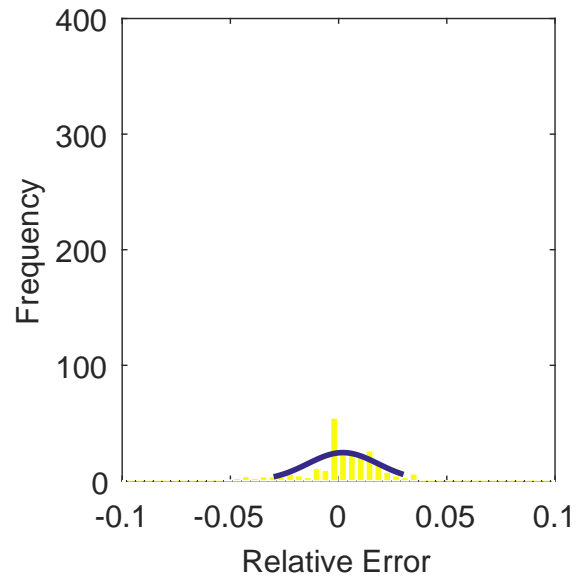
(a) Linear Interpolation Error



(b) Spline Interpolation Error

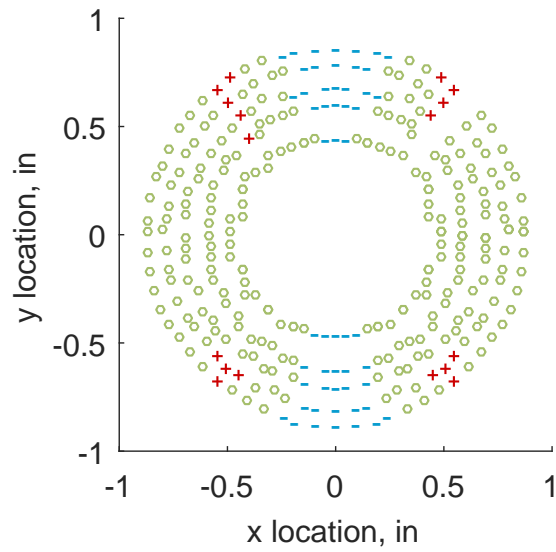


(c) Polar Interpolation Error

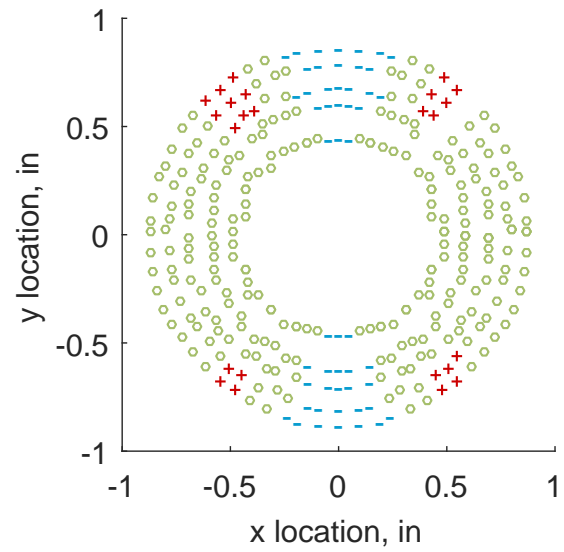


(d) Kriging Interpolation Error

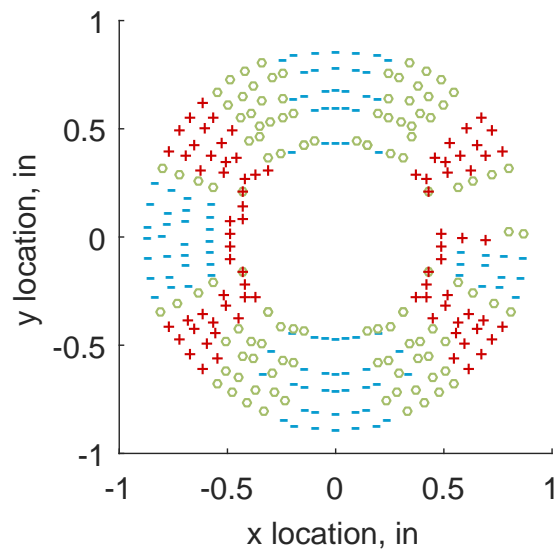
Figure C.139: Relative error for various interpolation schemes of run number R300, fourth clocking for the IMX inlet.



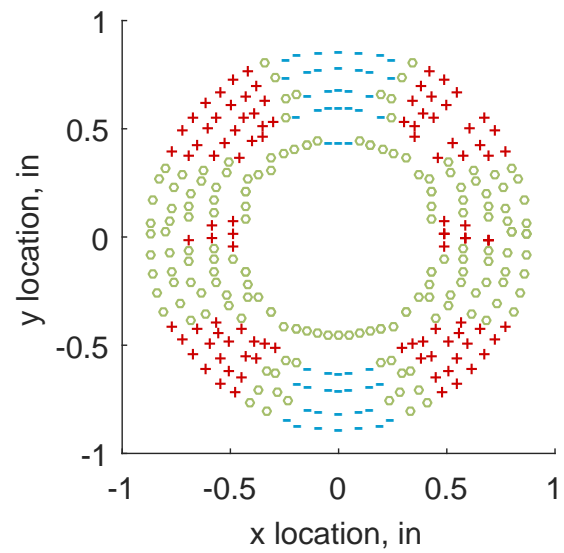
(a) Linear Interpolation



(b) Spline Interpolation



(c) Polar Interpolation



(d) Kriging Interpolation

Figure C.140: Interpolation error for the IMX inlet - symbols show locations that are within tolerance (o), over-predicted (+), and under-predicted (-).

Table C.60: Interpolation effects on the derived quantities for the IMX inlet run number R300, clocking C5.

	$K_\theta$	$K_r$	$K_a$	$IDC$	$IDT$
Linear	0.392	0.017	0.409	0.011	0.035
Spline	0.348	0.012	0.360	0.012	0.035
Polar	0.348	0.016	0.364	0.013	0.039
Kriging	NaN	NaN	NaN	NaN	NaN

### C.2.1.6 Fifth Clocking

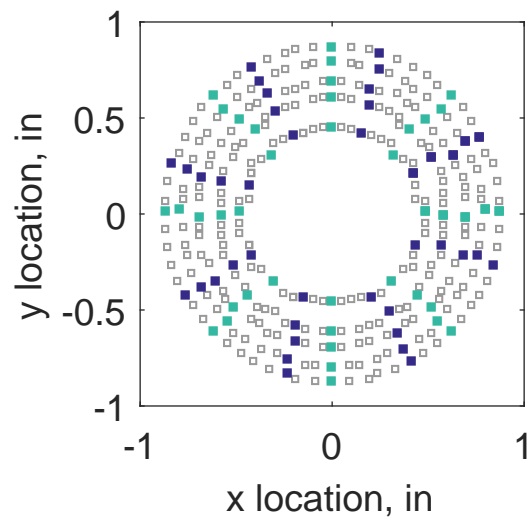


Figure C.141: Fifth clocking probe position

Table C.61: Interpolation results for the IMX inlet run number R300, clocking C6.

	Mean	Std. Dev.	Over-Prediction	In Tolerance	Under-Prediction
Linear	-0.0013	0.0026	26	202	52
Spline	-0.0016	0.0027	23	209	48
Polar	-0.0009	0.0034	62	157	61
Kriging	-0.0016	0.0012	0	278	2

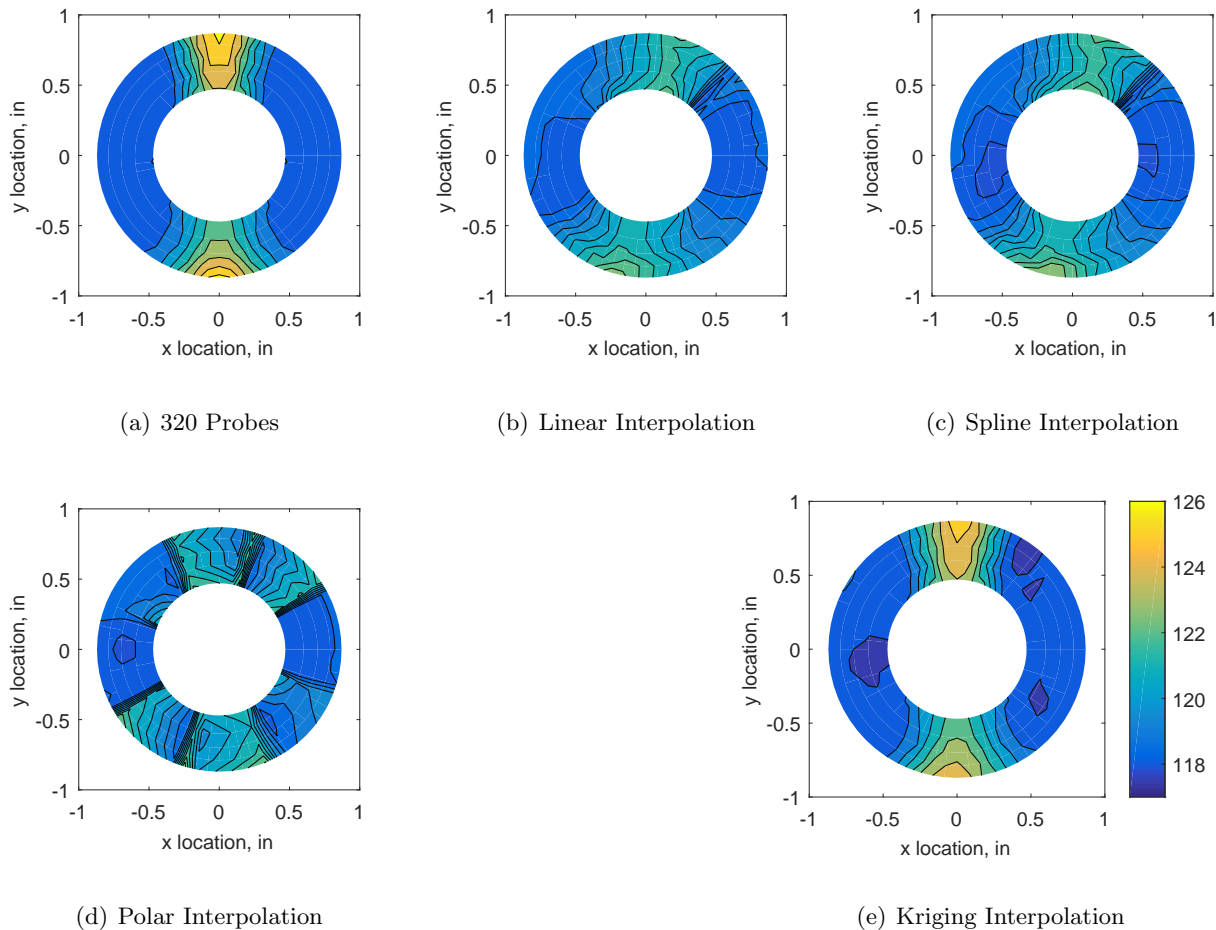
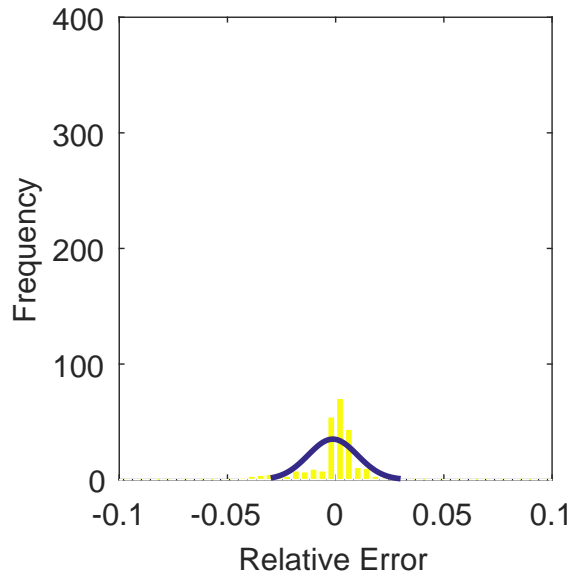
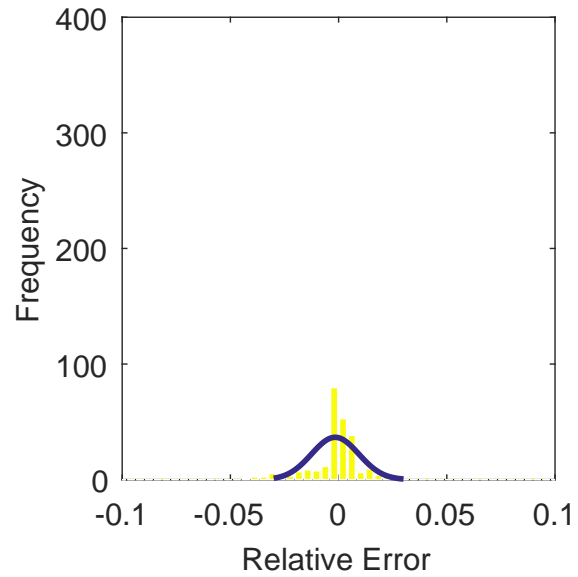


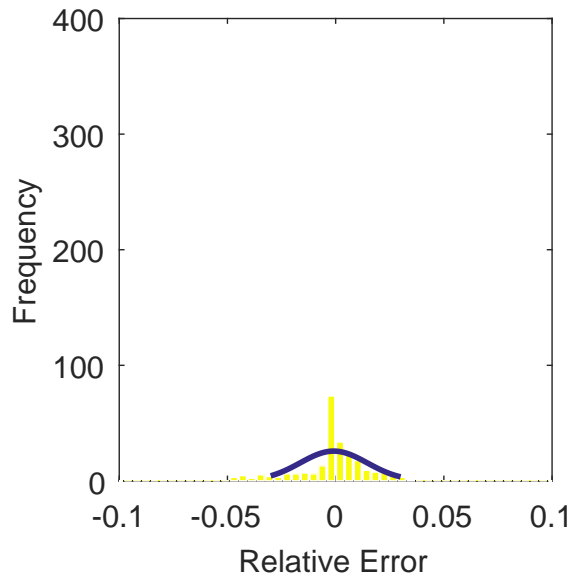
Figure C.142: Contour plots for the raw and interpolated values for the IMX inlet.



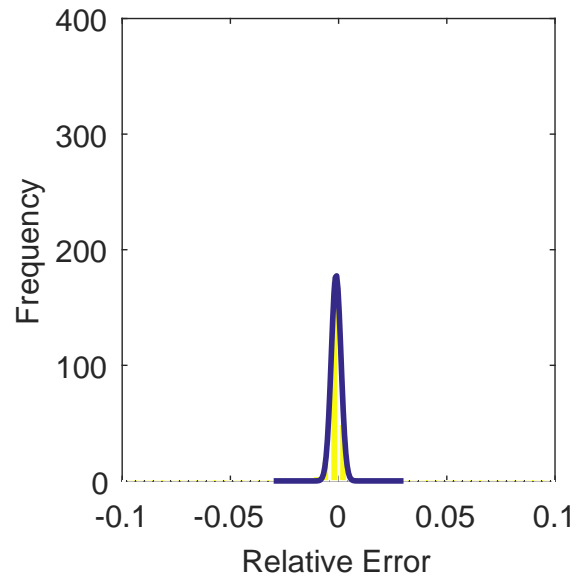
(a) Linear Interpolation Error



(b) Spline Interpolation Error

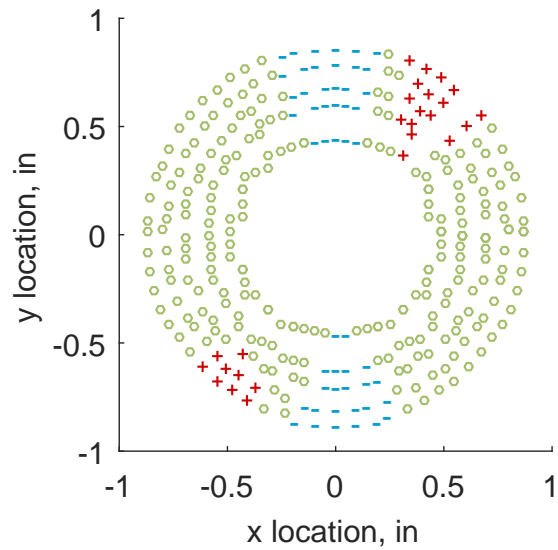


(c) Polar Interpolation Error

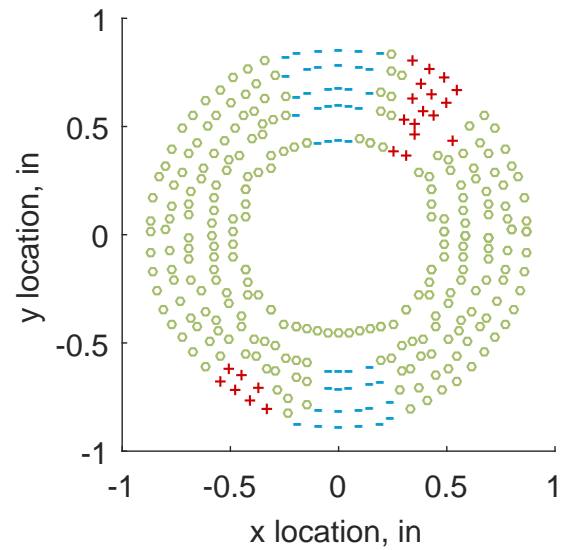


(d) Kriging Interpolation Error

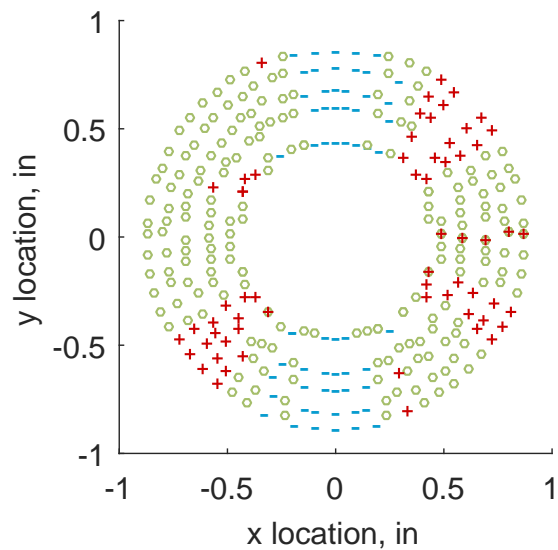
Figure C.143: Relative error for various interpolation schemes of run number R300, fifth clocking for the IMX inlet.



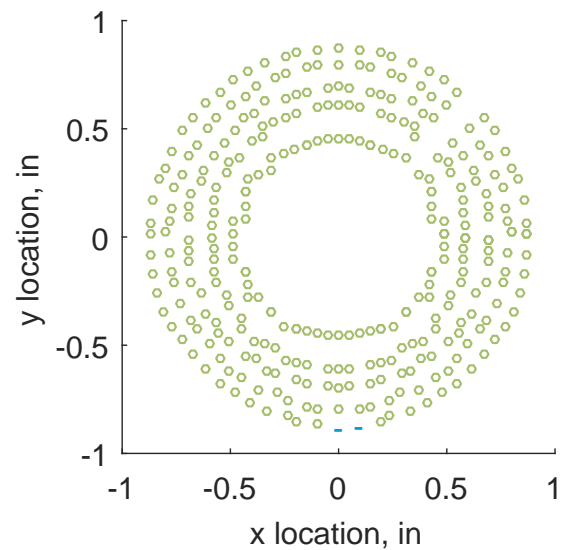
(a) Linear Interpolation



(b) Spline Interpolation



(c) Polar Interpolation



(d) Kriging Interpolation

Figure C.144: Interpolation error for the IMX inlet - symbols show locations that are within tolerance (o), over-predicted (+), and under-predicted (-).



Table C.62: Interpolation effects on the derived quantities for the IMX inlet run number R300, clocking C6.

	$K_\theta$	$K_r$	$K_a$	$IDC$	$IDT$
Linear	0.392	0.015	0.407	0.011	0.041
Spline	0.349	0.010	0.359	0.012	0.041
Polar	0.349	0.014	0.363	0.014	0.042
Kriging	0.349	0.019	0.367	0.013	0.041

### C.2.1.7 Sixth Clocking

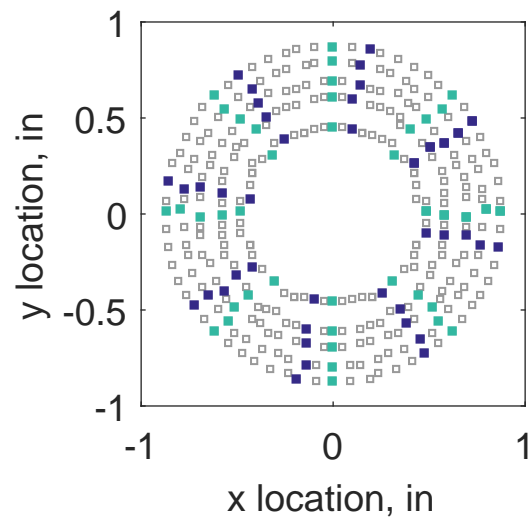


Figure C.145: Sixth clocking probe position

Table C.63: Interpolation results for the IMX inlet run number R300, clocking C7.

	Mean	Std. Dev.	Over-Prediction	In Tolerance	Under-Prediction
Linear	0.0005	0.0024	32	213	35
Spline	0.0002	0.0025	36	211	33
Polar	0.0008	0.0033	63	165	52
Kriging	0.0002	0.0009	0	280	0

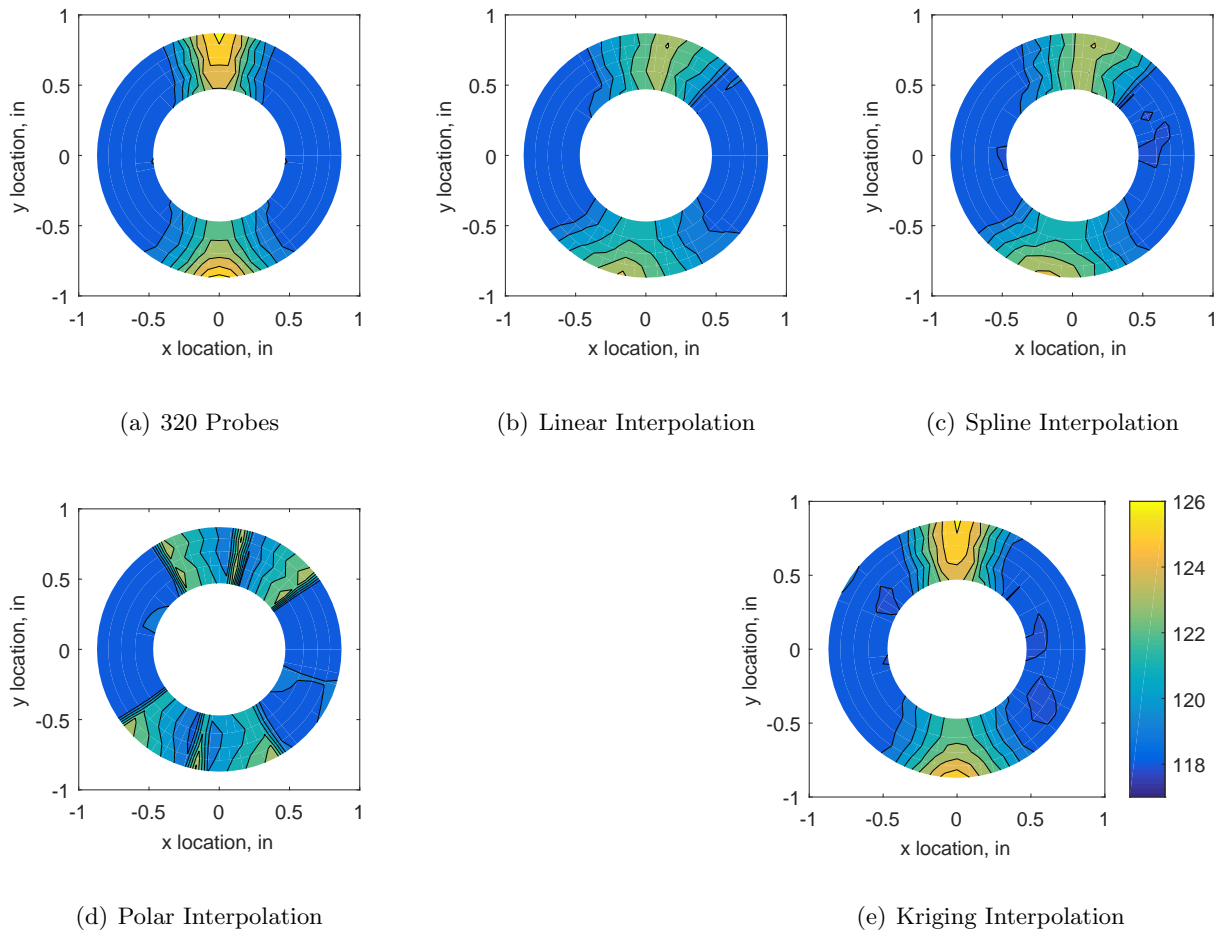
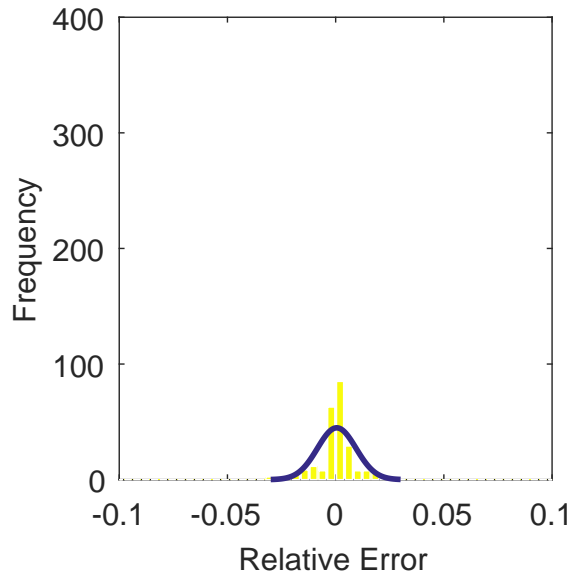
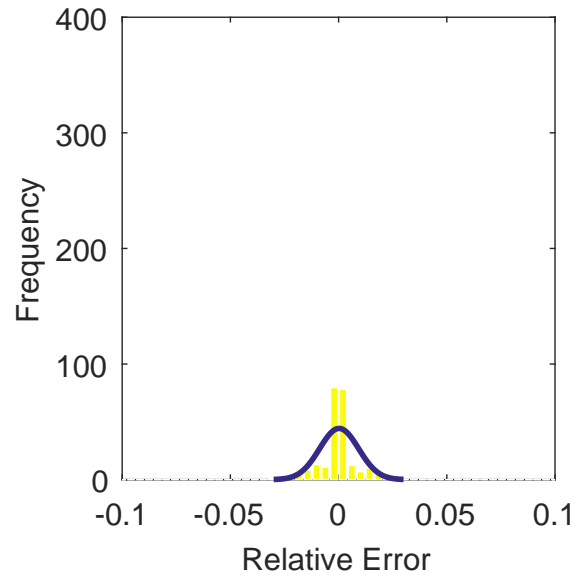


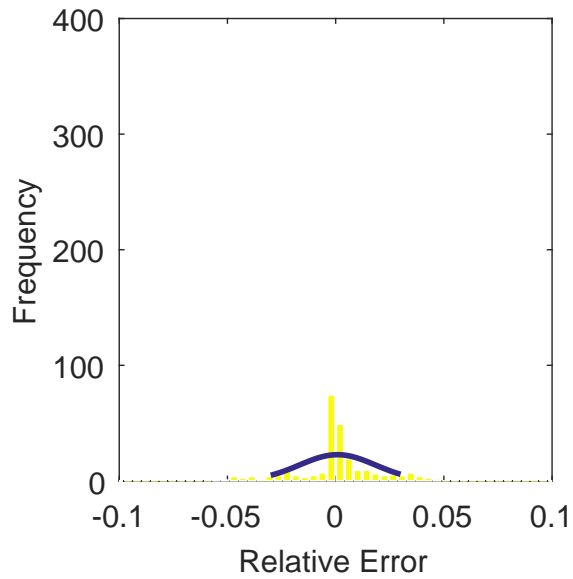
Figure C.146: Contour plots for the raw and interpolated values for the IMX inlet.



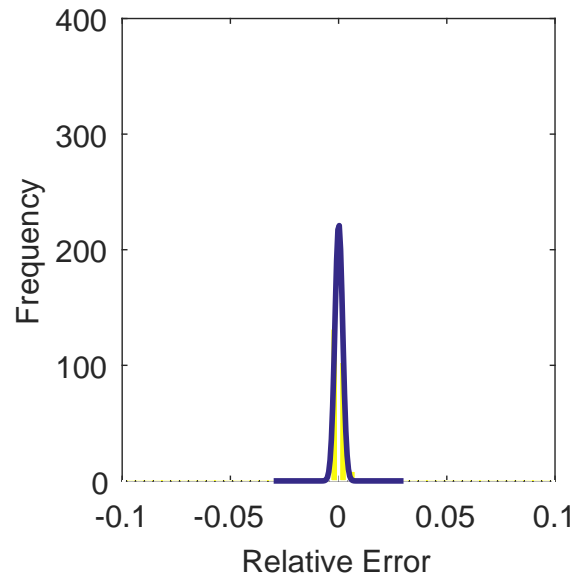
(a) Linear Interpolation Error



(b) Spline Interpolation Error

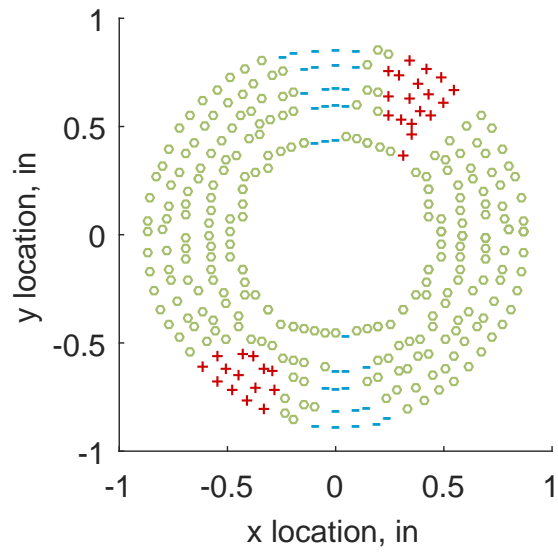


(c) Polar Interpolation Error

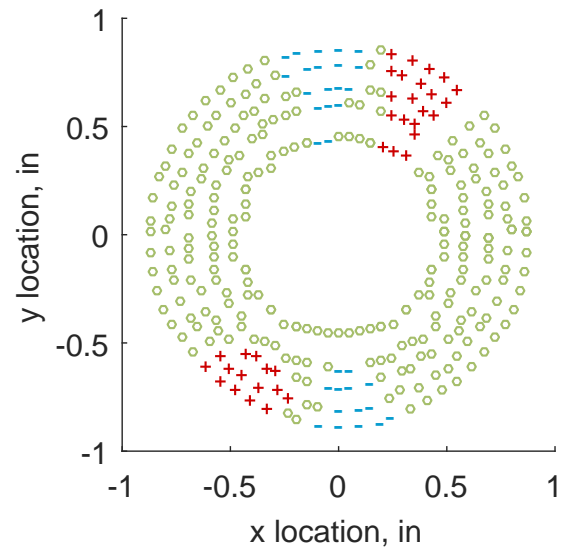


(d) Kriging Interpolation Error

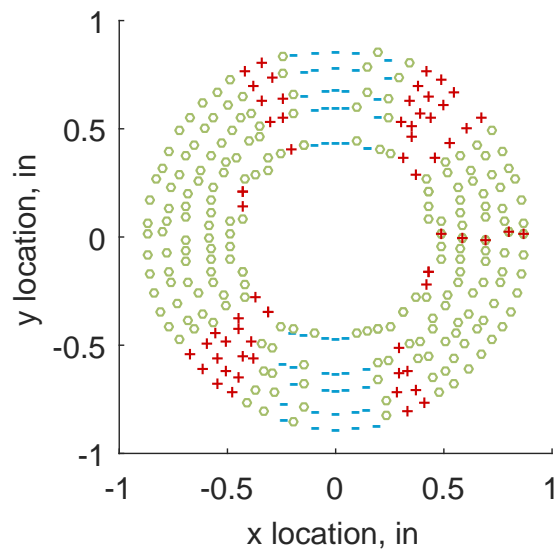
Figure C.147: Relative error for various interpolation schemes of run number R300, sixth clocking for the IMX inlet.



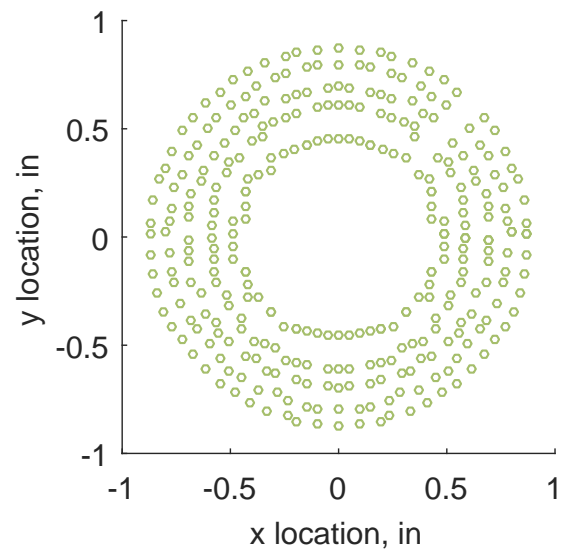
(a) Linear Interpolation



(b) Spline Interpolation



(c) Polar Interpolation



(d) Kriging Interpolation

Figure C.148: Interpolation error for the IMX inlet - symbols show locations that are within tolerance (o), over-predicted (+), and under-predicted (-).

Table C.64: Interpolation effects on the derived quantities for the IMX inlet run number R300, clocking C7.

	$K_\theta$	$K_r$	$K_a$	$IDC$	$IDT$
Linear	0.392	0.009	0.401	0.012	0.052
Spline	0.349	0.010	0.360	0.014	0.052
Polar	0.349	0.010	0.359	0.016	0.053
Kriging	0.349	0.010	0.360	0.014	0.052

### C.2.1.8 Seventh Clocking

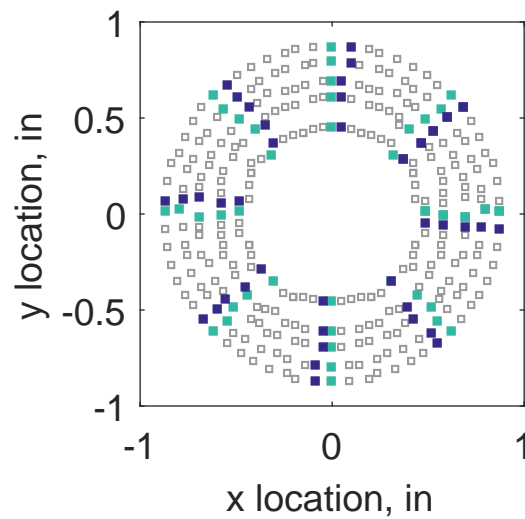


Figure C.149: Seventh clocking probe position

Table C.65: Interpolation results for the IMX inlet run number R300, clocking C8.

	Mean	Std. Dev.	Over-Prediction	In Tolerance	Under-Prediction
Linear	0.0023	0.0024	37	238	5
Spline	0.0017	0.0021	35	245	0
Polar	0.0026	0.0037	64	166	50
Kriging	0.0017	0.0012	8	272	0

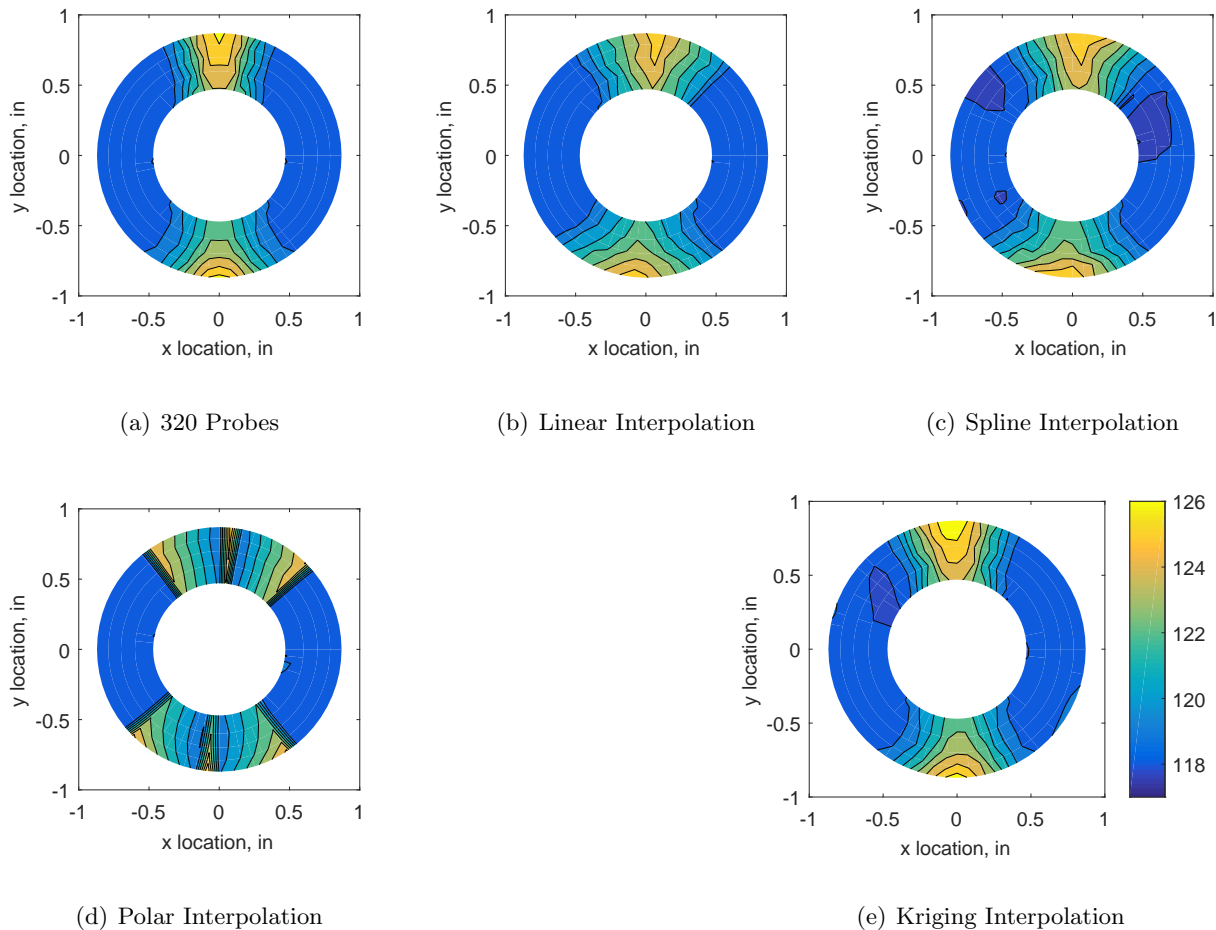
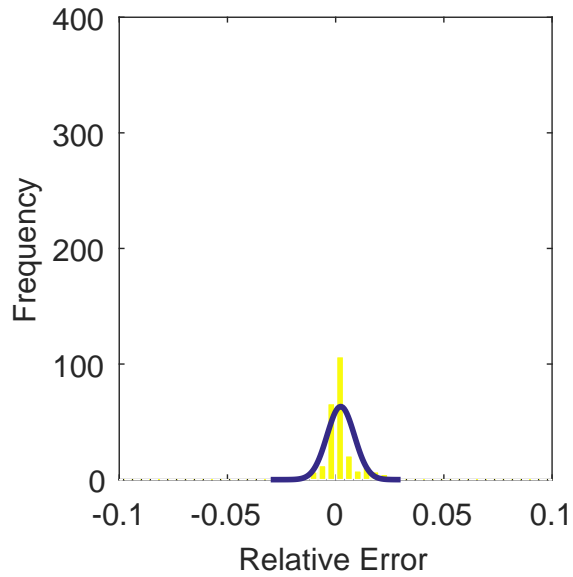
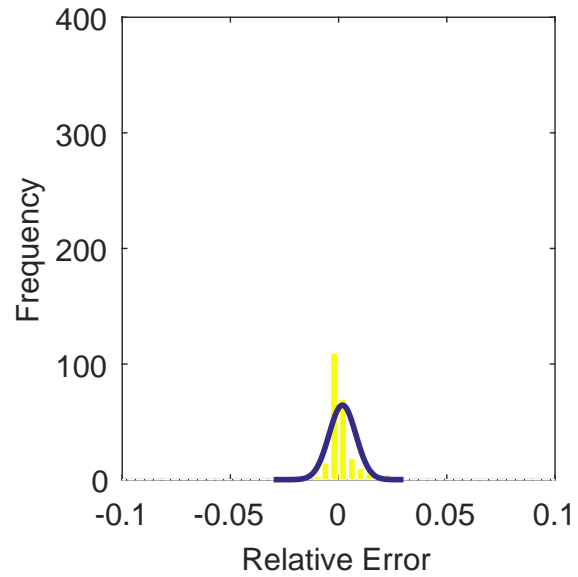


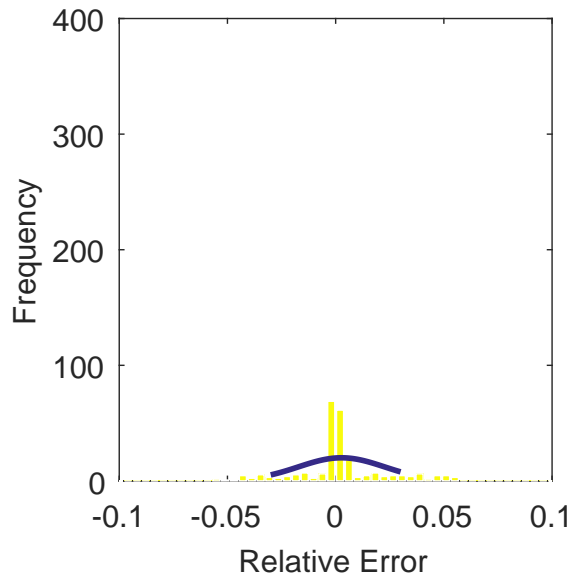
Figure C.150: Contour plots for the raw and interpolated values for the IMX inlet.



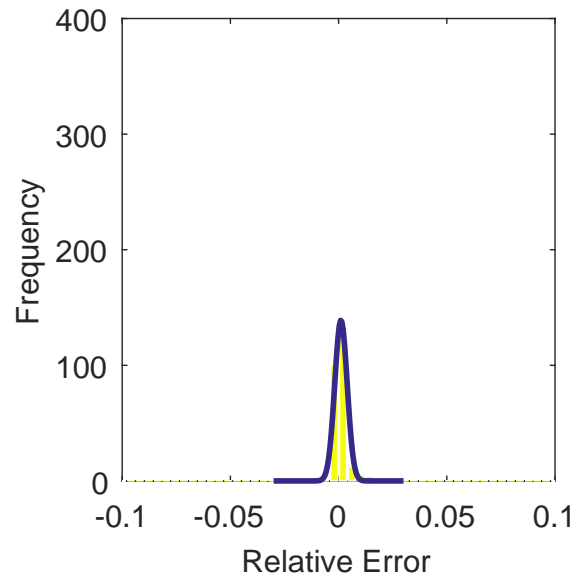
(a) Linear Interpolation Error



(b) Spline Interpolation Error

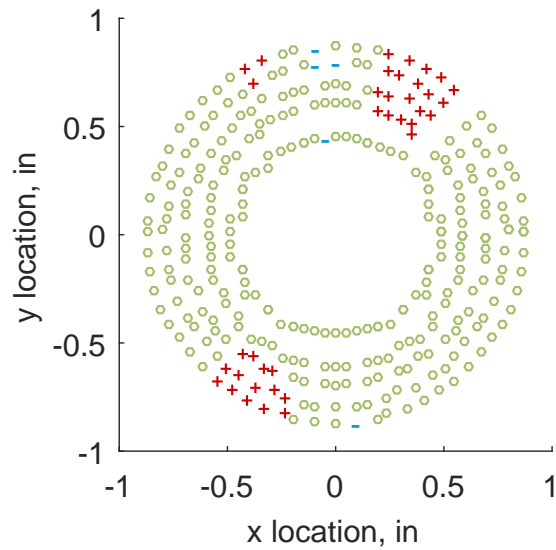


(c) Polar Interpolation Error

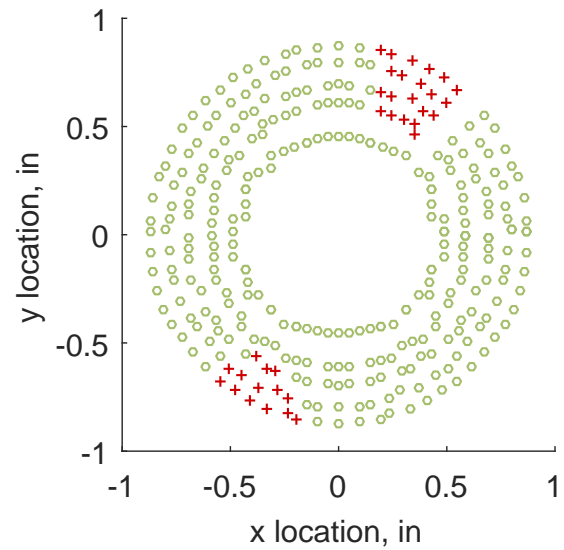


(d) Kriging Interpolation Error

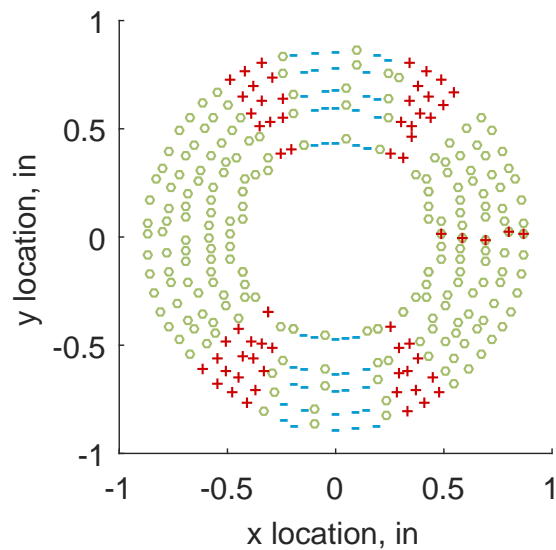
Figure C.151: Relative error for various interpolation schemes of run number R300, seventh clocking for the IMX inlet.



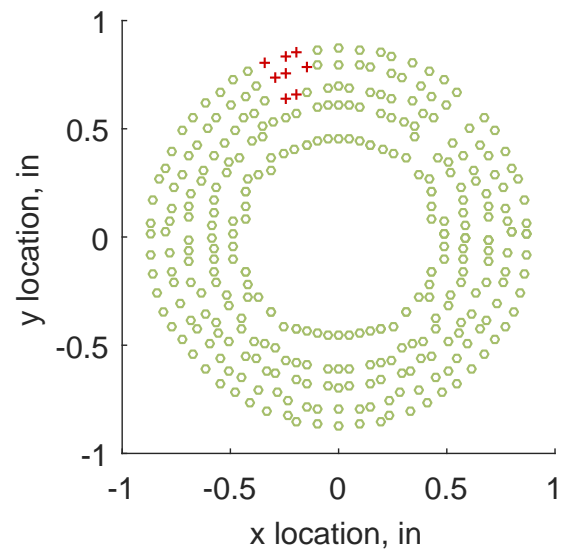
(a) Linear Interpolation



(b) Spline Interpolation



(c) Polar Interpolation



(d) Kriging Interpolation

Figure C.152: Interpolation error for the IMX inlet - symbols show locations that are within tolerance (o), over-predicted (+), and under-predicted (-).



Table C.66: Interpolation effects on the derived quantities for the IMX inlet run number R300, clocking C8.

	$K_\theta$	$K_r$	$K_a$	$IDC$	$IDT$
Linear	0.393	0.015	0.408	0.015	0.066
Spline	0.350	0.021	0.371	0.018	0.066
Polar	0.350	0.018	0.368	0.021	0.069
Kriging	0.350	0.015	0.365	0.017	0.066

## C.2.2 Run Number R310

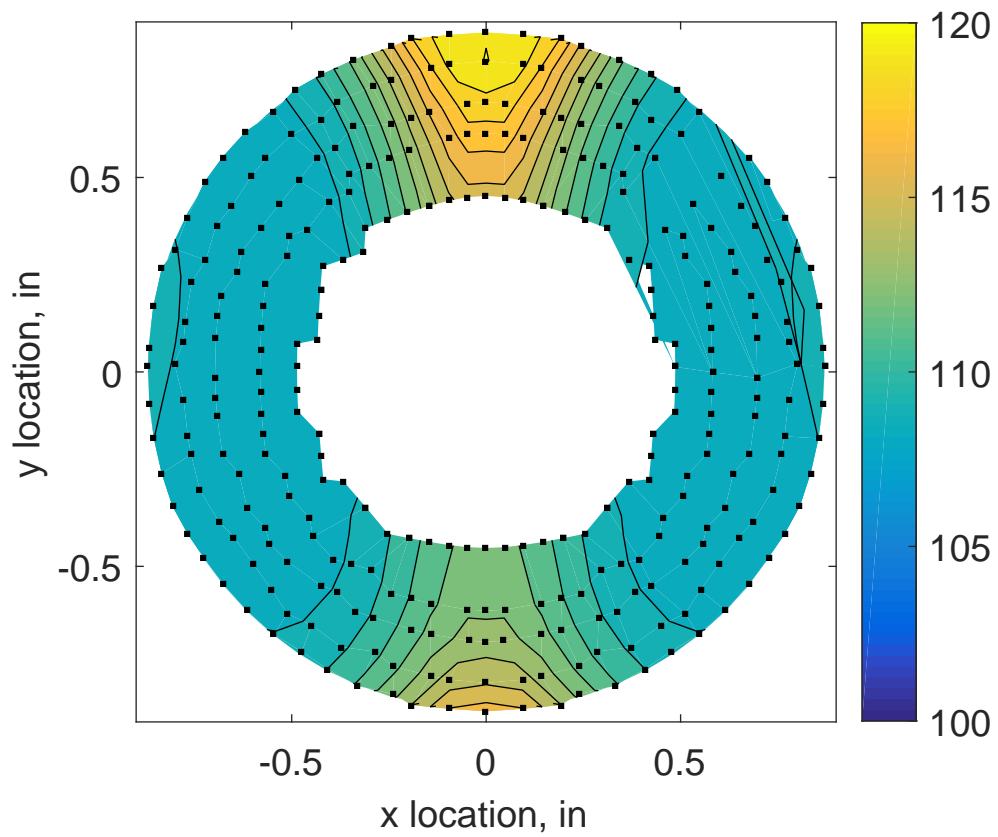


Figure C.153: IMX run number R310 raw pressure contour created with 320 probes.

### C.2.2.1 Zeroth Clocking

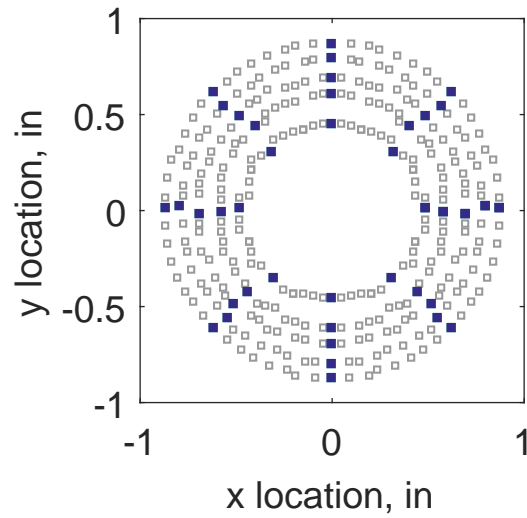
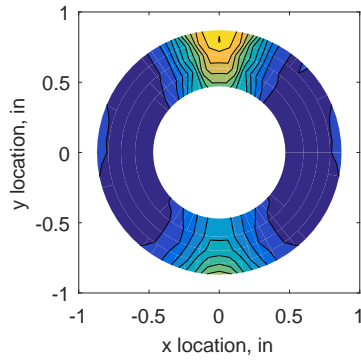


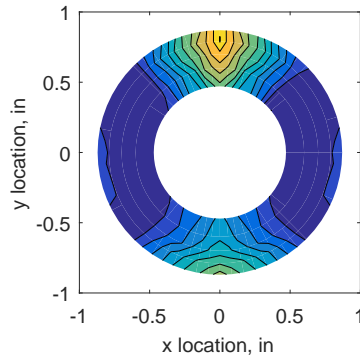
Figure C.154: Zeroth clocking probe position

Table C.67: Interpolation results for the IMX inlet run number R310, clocking C1.

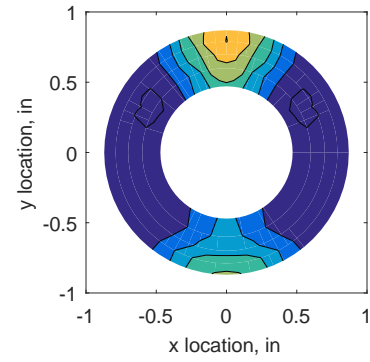
	Mean	Std. Dev.	Over-Prediction	In Tolerance	Under-Prediction
Linear	0.0027	0.0031	46	230	4
Spline	0.0024	0.0029	46	234	0
Polar	0.0037	0.0056	73	161	46
Kriging	0.0024	0.0021	30	250	0



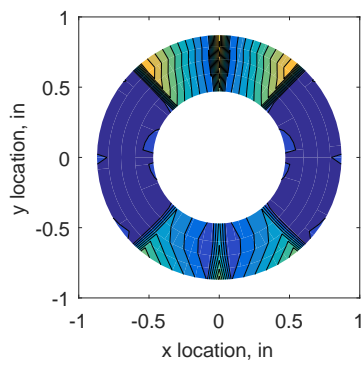
(a) 320 Probes



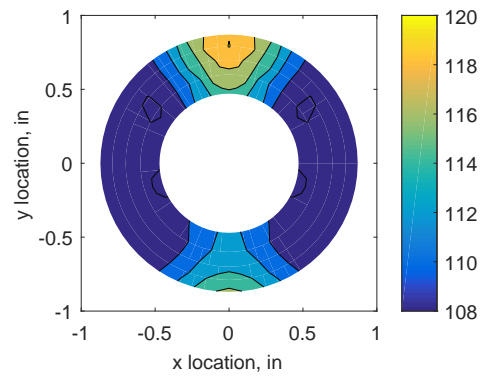
(b) Linear Interpolation



(c) Spline Interpolation

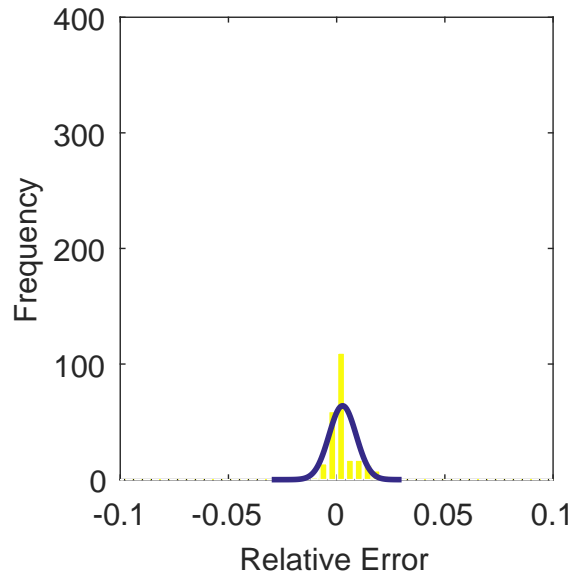


(d) Polar Interpolation

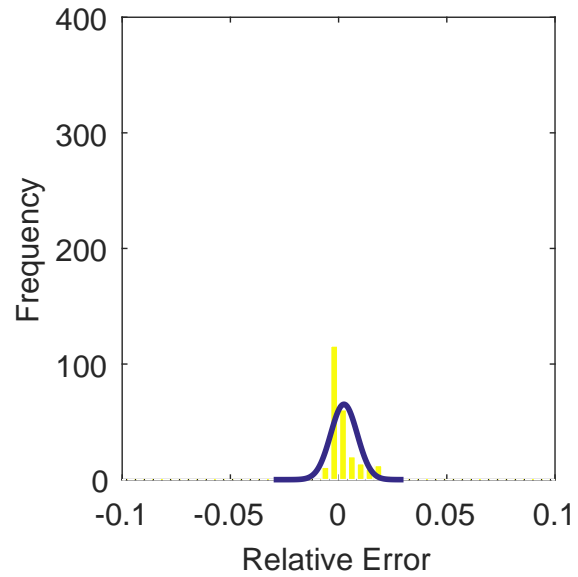


(e) Kriging Interpolation

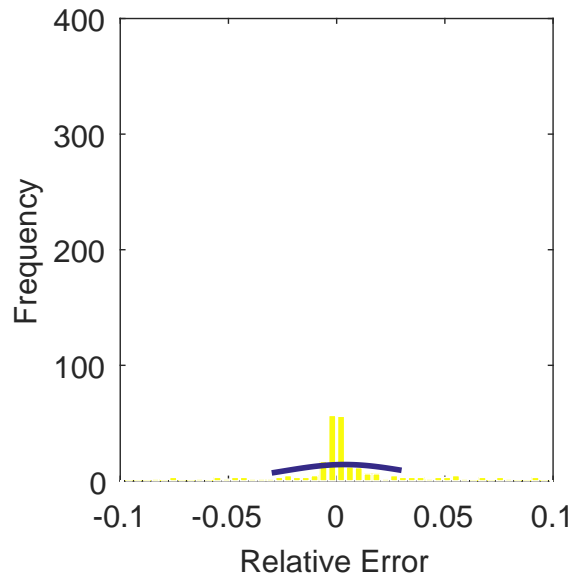
Figure C.155: Contour plots for the raw and interpolated values for the IMX inlet.



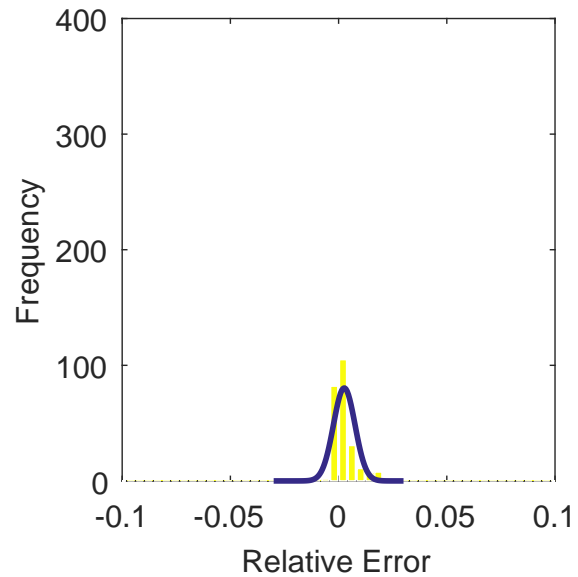
(a) Linear Interpolation Error



(b) Spline Interpolation Error

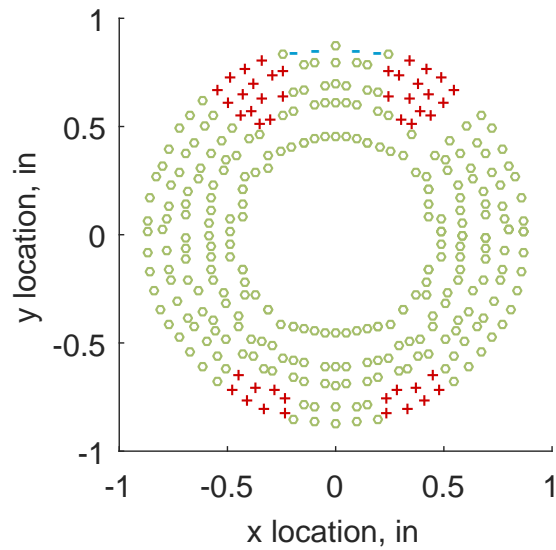


(c) Polar Interpolation Error

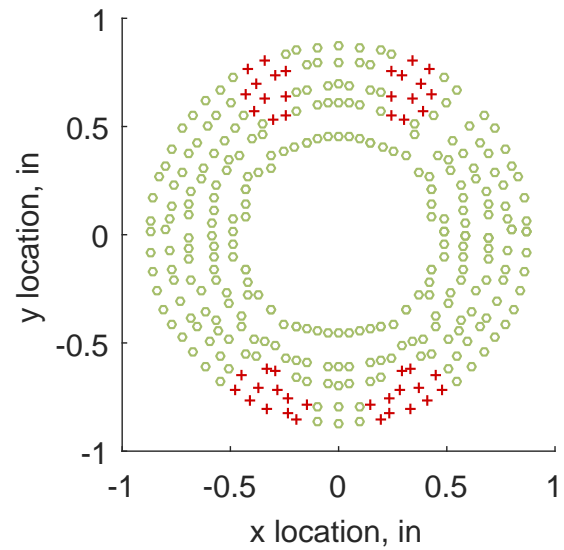


(d) Kriging Interpolation Error

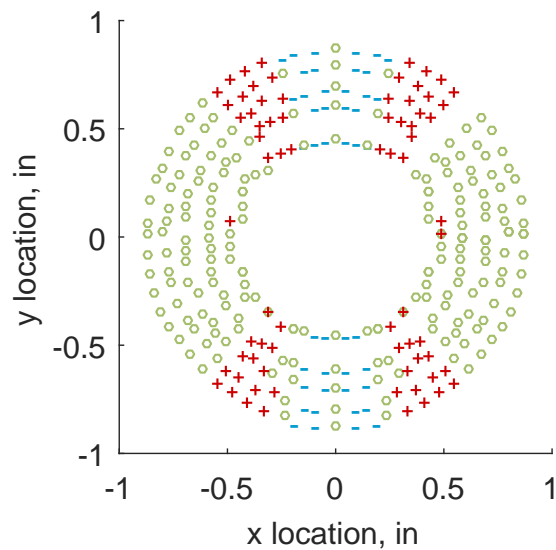
Figure C.156: Relative error for various interpolation schemes of run number R310, zeroth clocking for the IMX inlet.



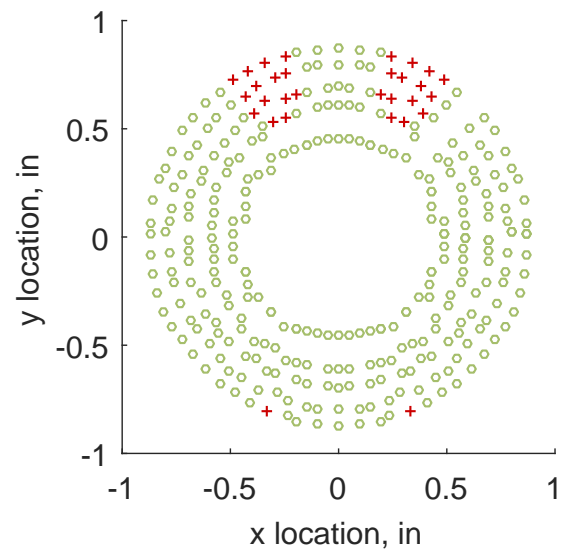
(a) Linear Interpolation



(b) Spline Interpolation



(c) Polar Interpolation



(d) Kriging Interpolation

Figure C.157: Interpolation error for the IMX inlet - symbols show locations that are within tolerance (o), over-predicted (+), and under-predicted (-).

Table C.68: Interpolation effects on the derived quantities for the IMX inlet run number R310, clocking C1.

	$K_\theta$	$K_r$	$K_a$	$IDC$	$IDT$
Linear	0.362	0.030	0.392	0.021	0.108
Spline	0.322	0.037	0.359	0.024	0.107
Polar	0.322	0.038	0.360	0.025	0.111
Kriging	0.322	0.028	0.351	0.024	0.107

### C.2.2.2 First Clocking

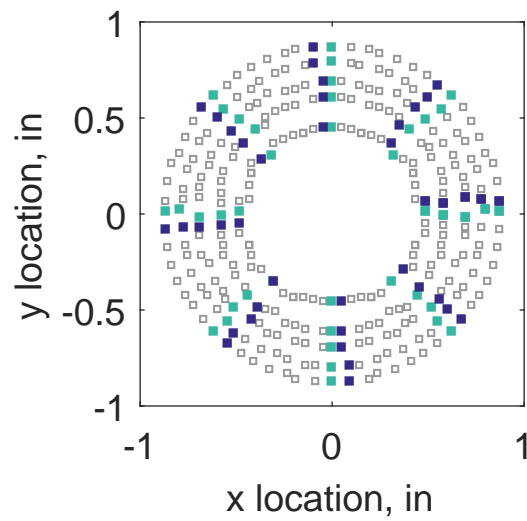


Figure C.158: First clocking probe position

Table C.69: Interpolation results for the IMX inlet run number R310, clocking C2.

	Mean	Std. Dev.	Over-Prediction	In Tolerance	Under-Prediction
Linear	0.0030	0.0030	42	225	13
Spline	0.0021	0.0025	38	235	7
Polar	0.0033	0.0056	66	162	52
Kriging	0.0021	0.0011	3	277	0

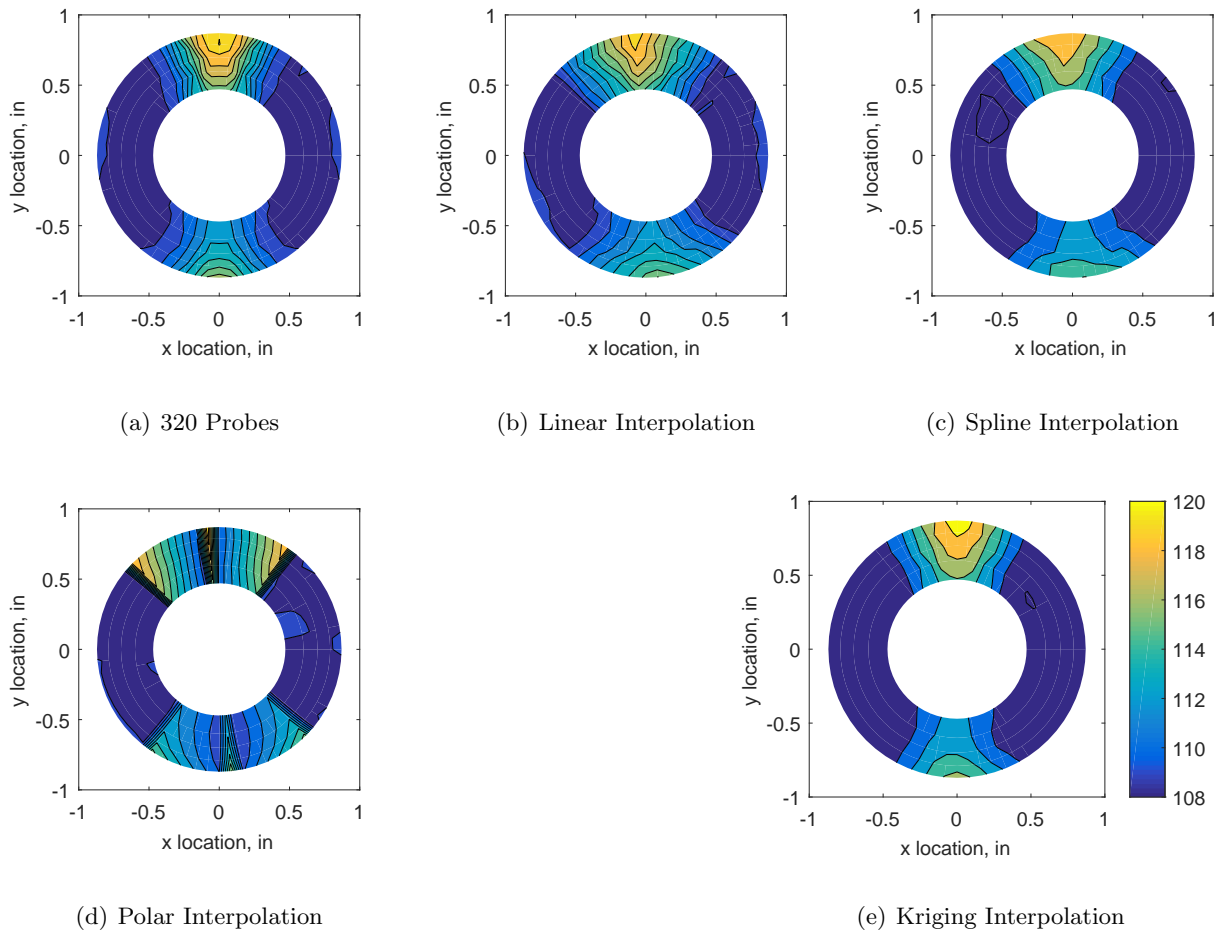
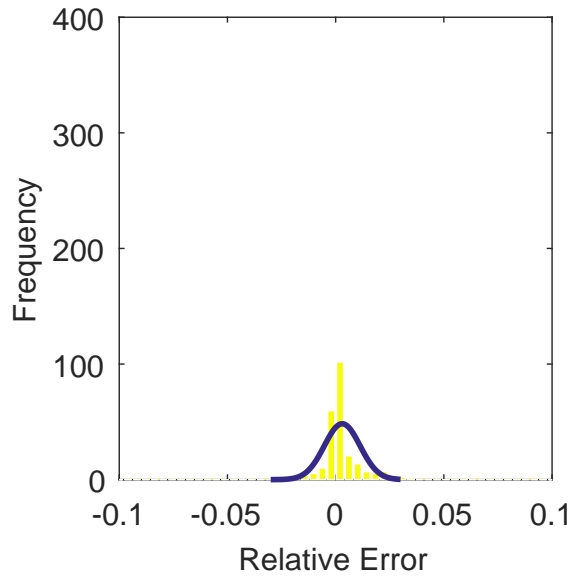
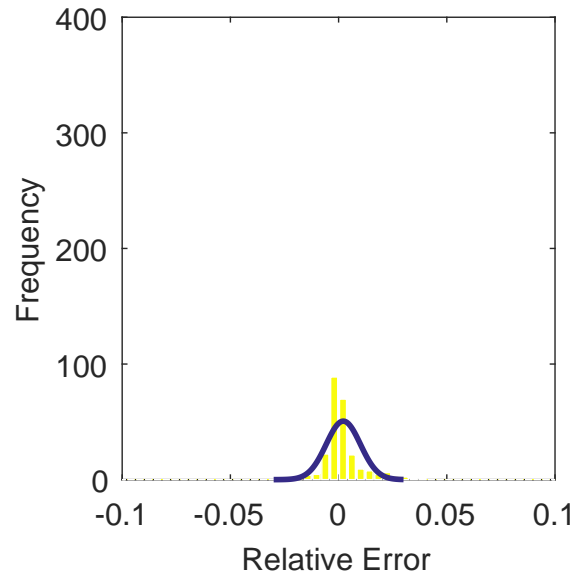


Figure C.159: Contour plots for the raw and interpolated values for the IMX inlet.

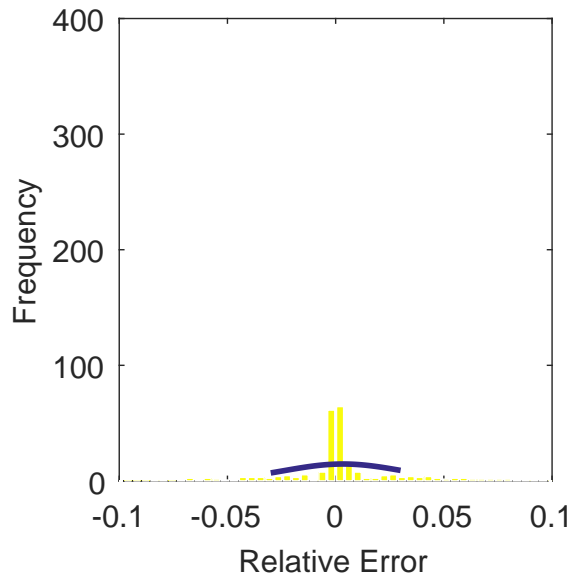




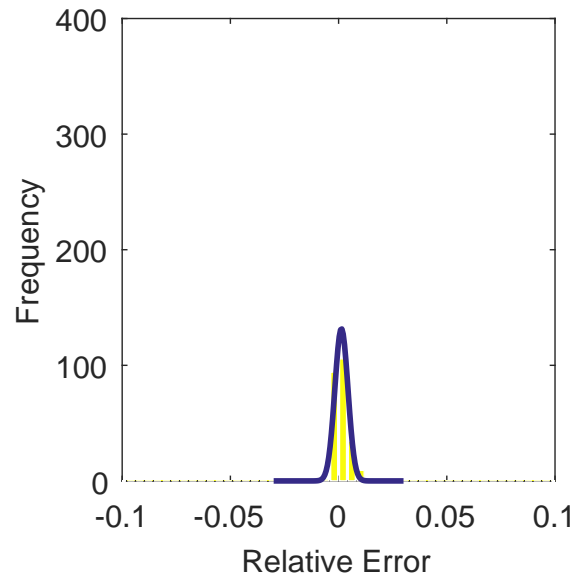
(a) Linear Interpolation Error



(b) Spline Interpolation Error

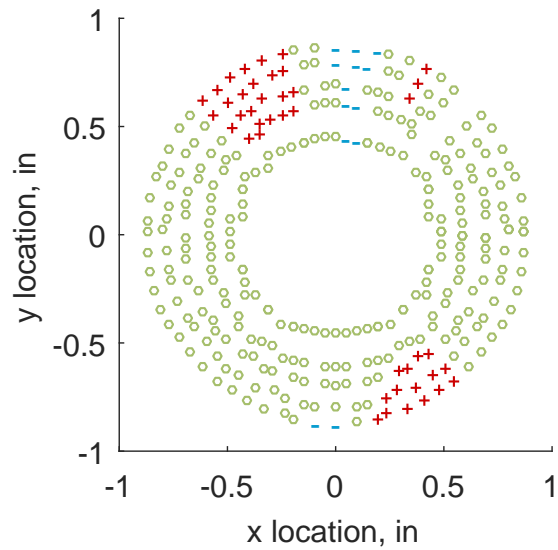


(c) Polar Interpolation Error

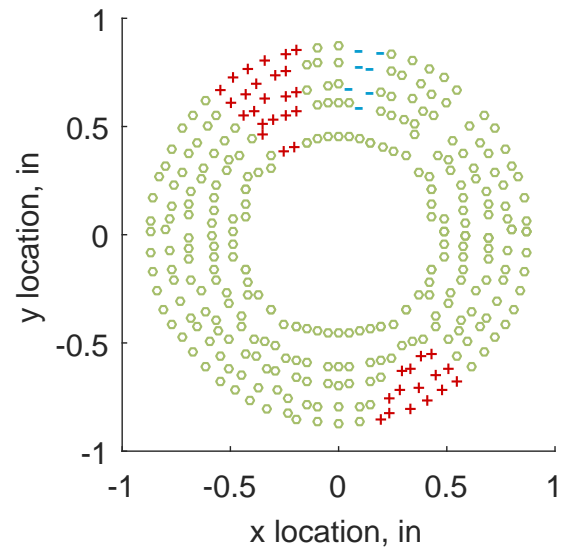


(d) Kriging Interpolation Error

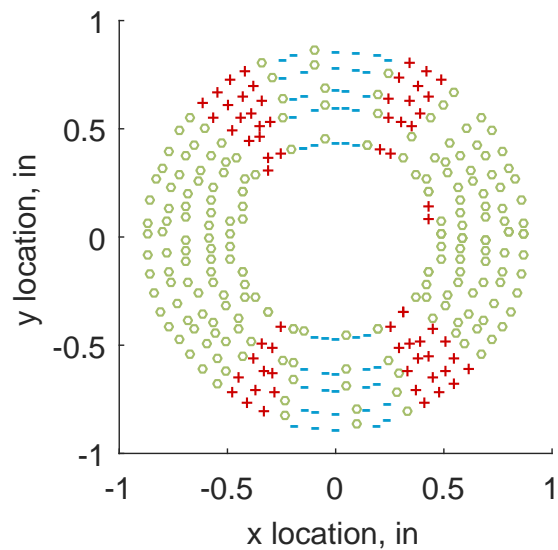
Figure C.160: Relative error for various interpolation schemes of run number R310, first clocking for the IMX inlet.



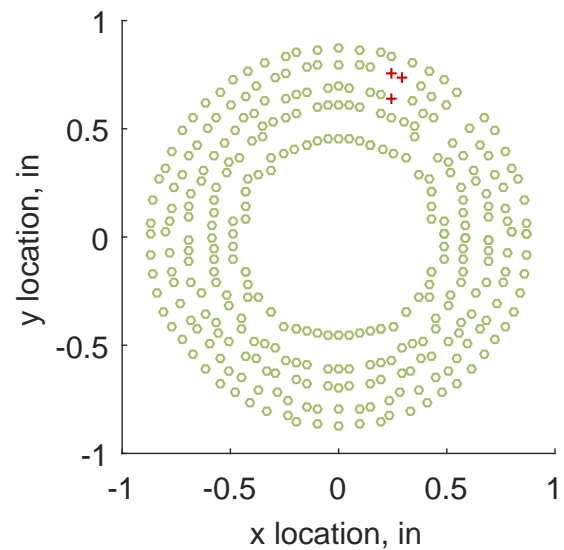
(a) Linear Interpolation



(b) Spline Interpolation



(c) Polar Interpolation



(d) Kriging Interpolation

Figure C.161: Interpolation error for the IMX inlet - symbols show locations that are within tolerance (o), over-predicted (+), and under-predicted (-).

Table C.70: Interpolation effects on the derived quantities for the IMX inlet run number R310, clocking C2.

	$K_\theta$	$K_r$	$K_a$	$IDC$	$IDT$
Linear	0.362	0.030	0.391	0.021	0.106
Spline	0.322	0.033	0.356	0.024	0.106
Polar	0.322	0.030	0.353	0.028	0.111
Kriging	0.322	0.028	0.351	0.023	0.106

### C.2.2.3 Second Clocking

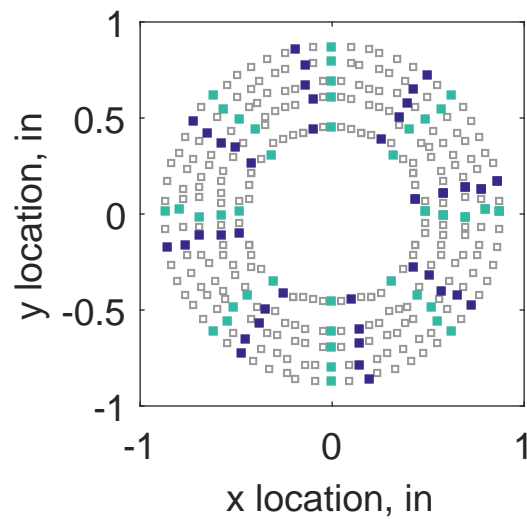


Figure C.162: Second clocking probe position

Table C.71: Interpolation results for the IMX inlet run number R310, clocking C3.

	Mean	Std. Dev.	Over-Prediction	In Tolerance	Under-Prediction
Linear	0.0011	0.0034	45	192	43
Spline	0.0006	0.0035	44	194	42
Polar	0.0013	0.0049	67	160	53
Kriging	0.0006	0.0018	3	275	2

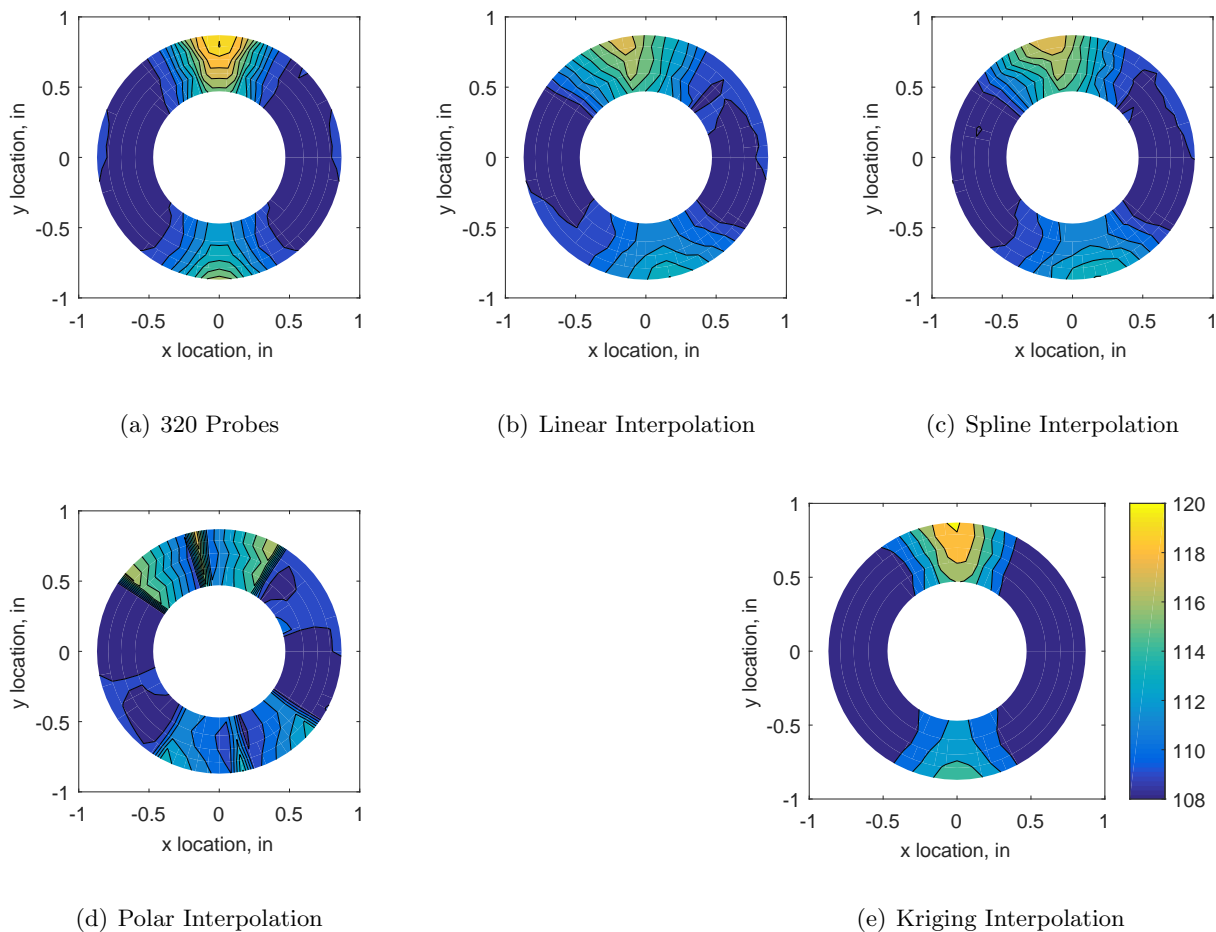
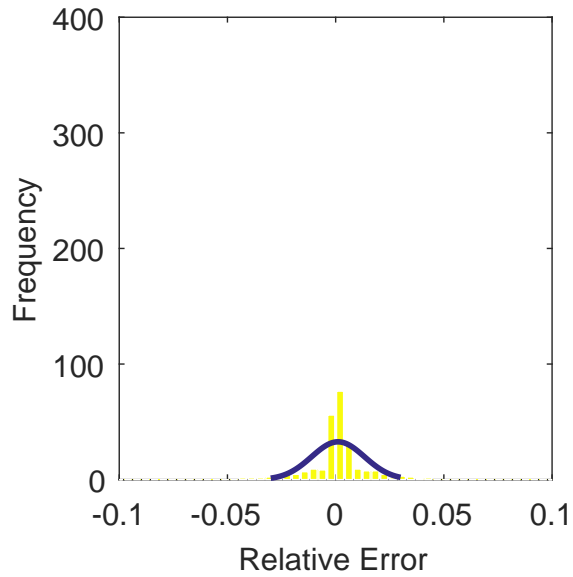
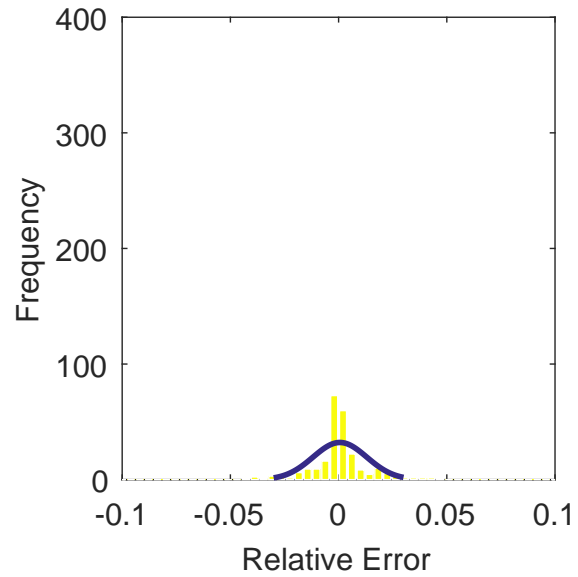


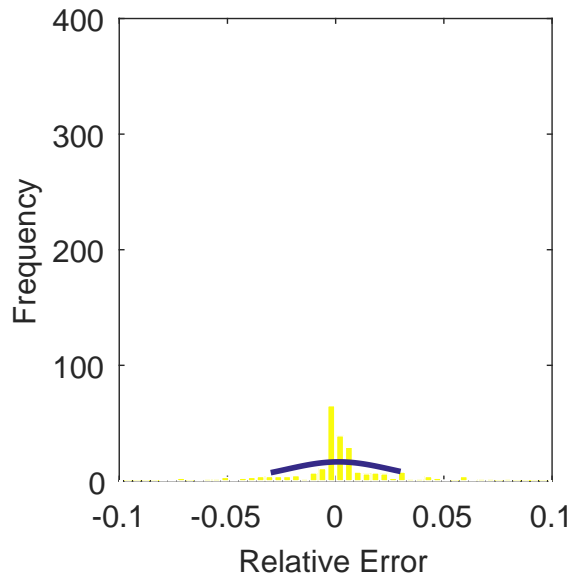
Figure C.163: Contour plots for the raw and interpolated values for the IMX inlet.



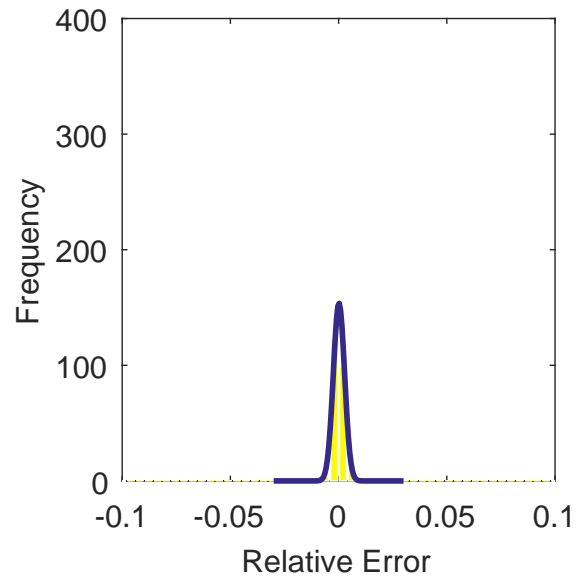
(a) Linear Interpolation Error



(b) Spline Interpolation Error

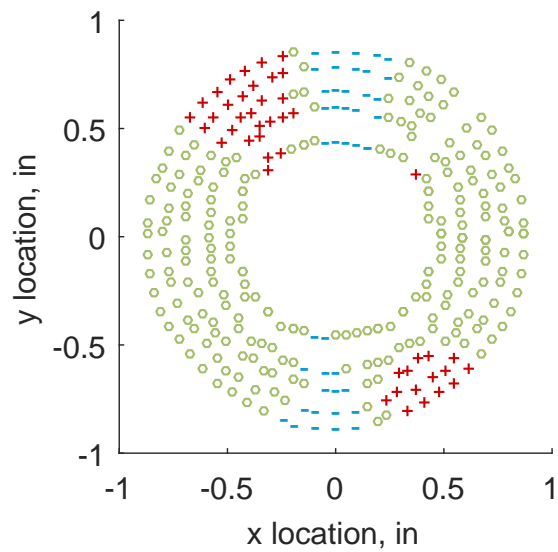


(c) Polar Interpolation Error

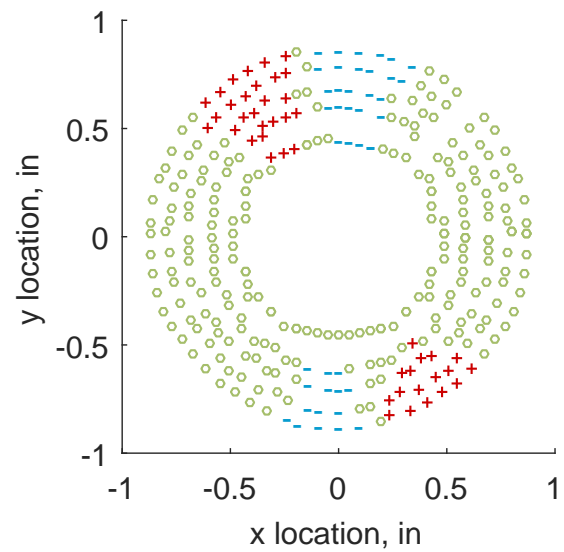


(d) Kriging Interpolation Error

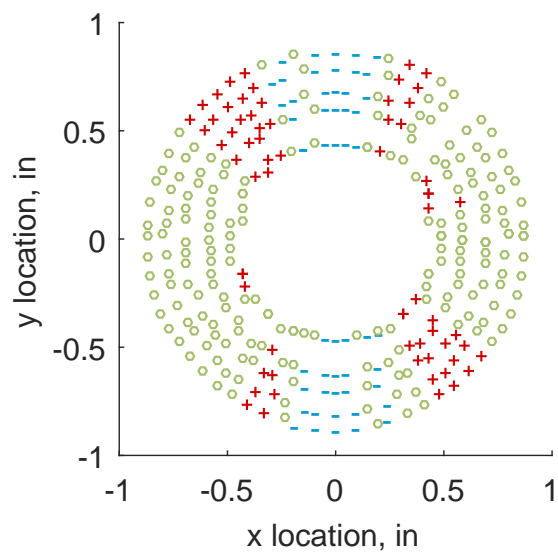
Figure C.164: Relative error for various interpolation schemes of run number R310, second clocking for the IMX inlet.



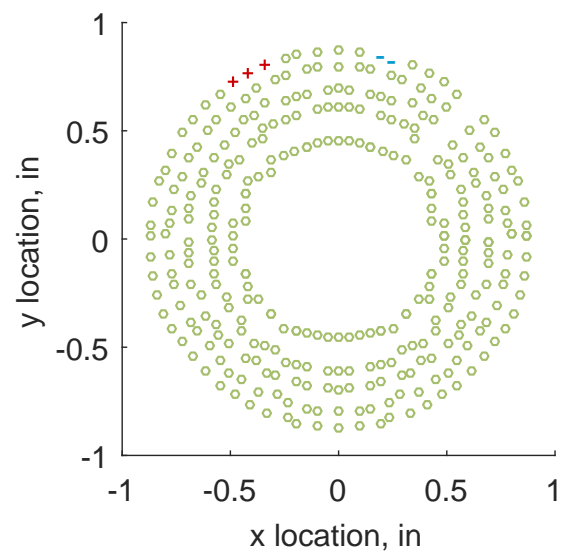
(a) Linear Interpolation



(b) Spline Interpolation



(c) Polar Interpolation



(d) Kriging Interpolation

Figure C.165: Interpolation error for the IMX inlet - symbols show locations that are within tolerance (o), over-predicted (+), and under-predicted (-).

Table C.72: Interpolation effects on the derived quantities for the IMX inlet run number R310, clocking C3.

	$K_\theta$	$K_r$	$K_a$	$IDC$	$IDT$
Linear	0.361	0.023	0.384	0.018	0.089
Spline	0.322	0.023	0.345	0.020	0.088
Polar	0.322	0.021	0.343	0.022	0.091
Kriging	0.322	0.021	0.343	0.020	0.088

#### C.2.2.4 Third Clocking

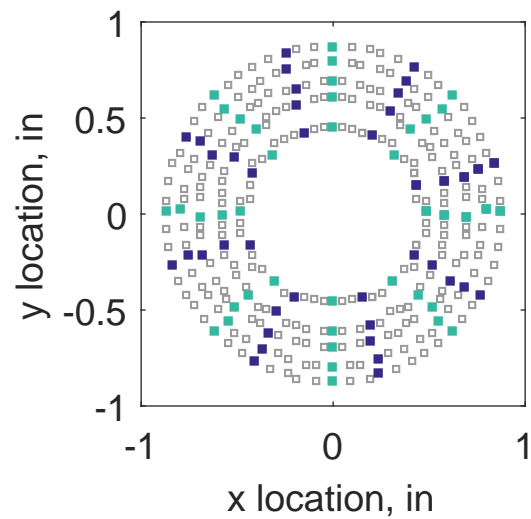


Figure C.166: Third clocking probe position

Table C.73: Interpolation results for the IMX inlet run number R310, clocking C4.

	Mean	Std. Dev.	Over-Prediction	In Tolerance	Under-Prediction
Linear	-0.0011	0.0038	45	176	59
Spline	-0.0015	0.0039	32	195	53
Polar	-0.0007	0.0046	79	137	64
Kriging	-0.0015	0.0016	0	274	6

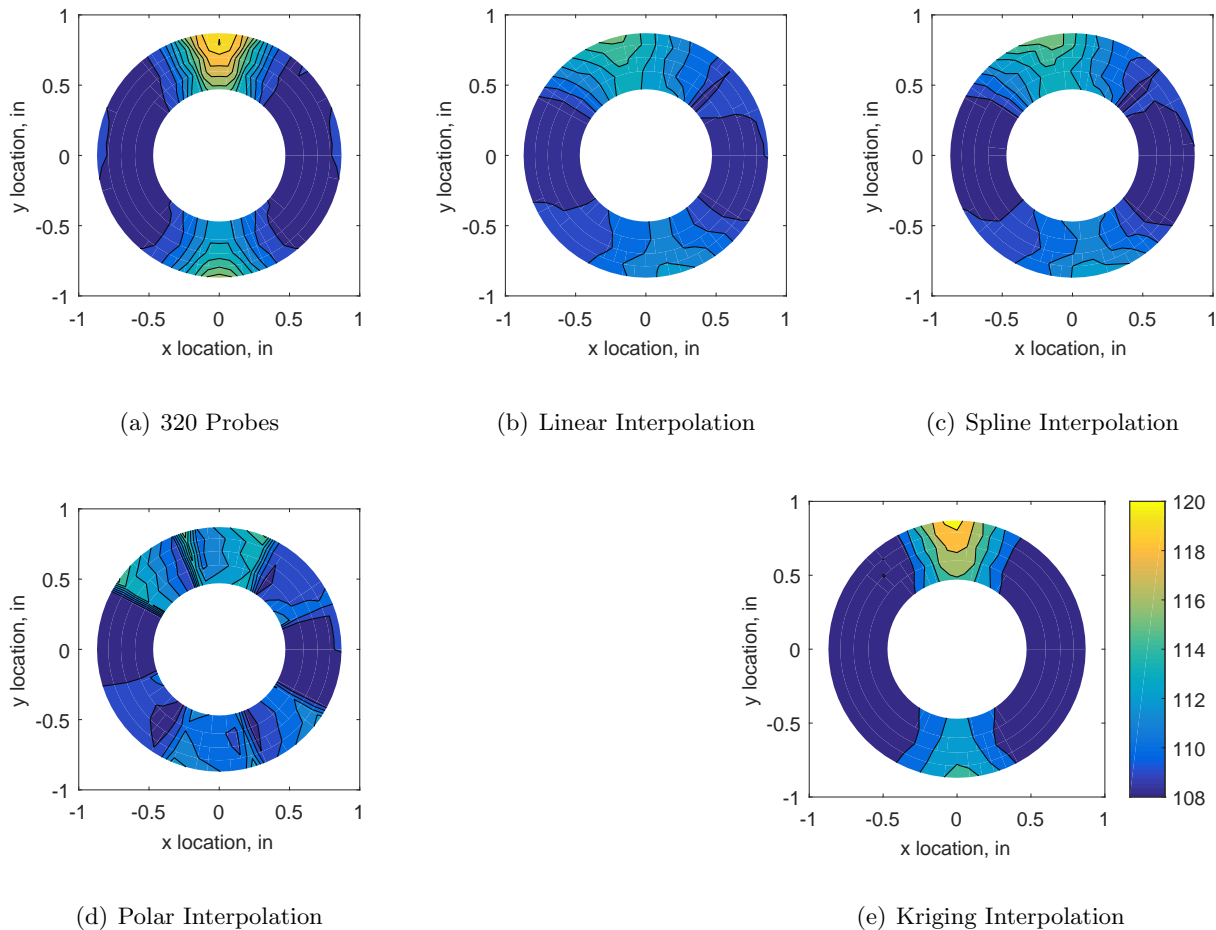
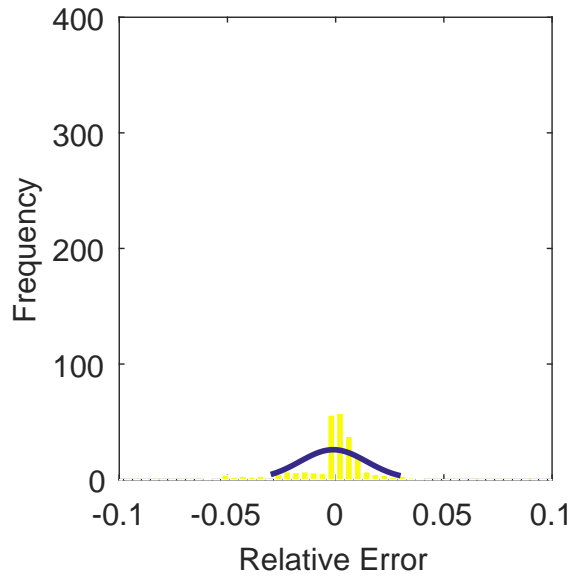
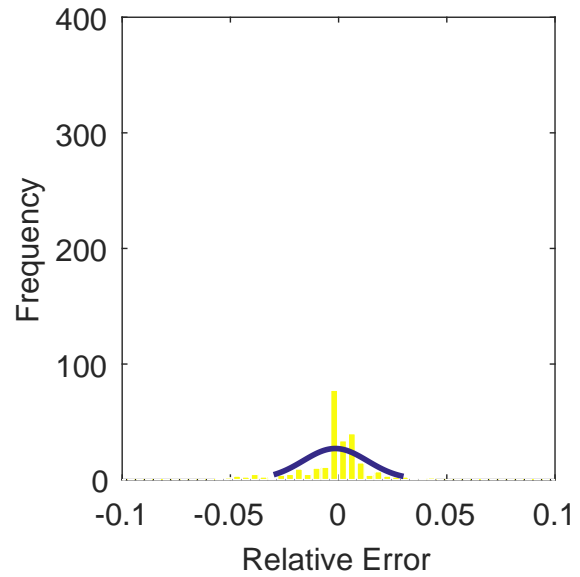


Figure C.167: Contour plots for the raw and interpolated values for the IMX inlet.

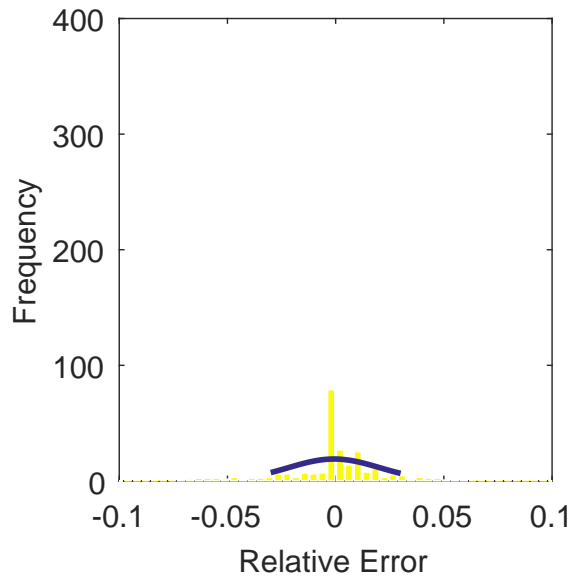




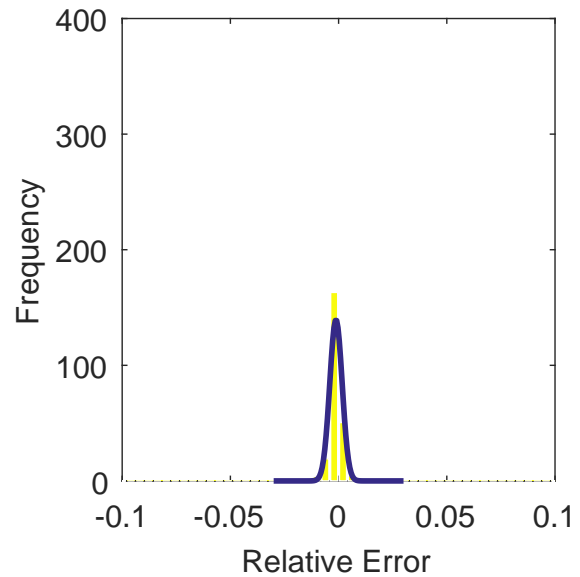
(a) Linear Interpolation Error



(b) Spline Interpolation Error

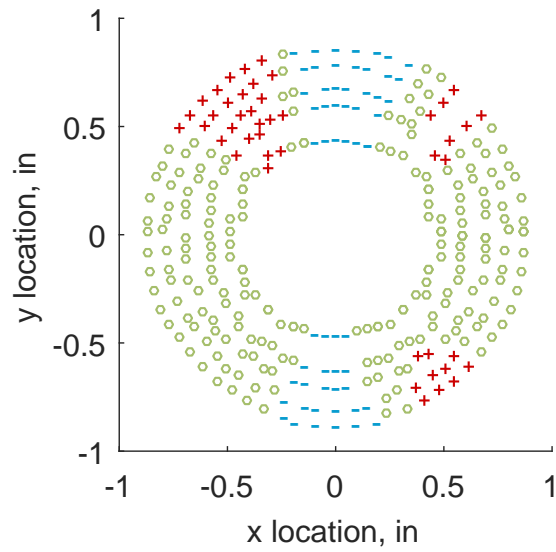


(c) Polar Interpolation Error

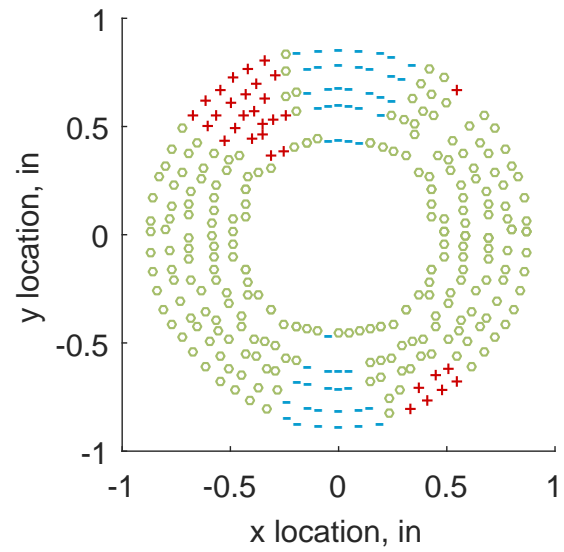


(d) Kriging Interpolation Error

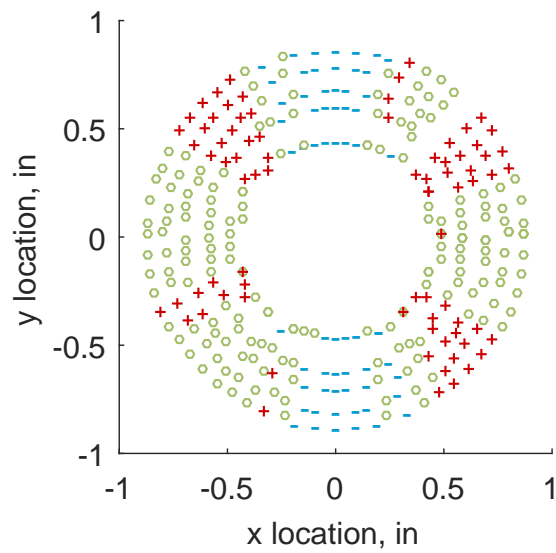
Figure C.168: Relative error for various interpolation schemes of run number R310, third clocking for the IMX inlet.



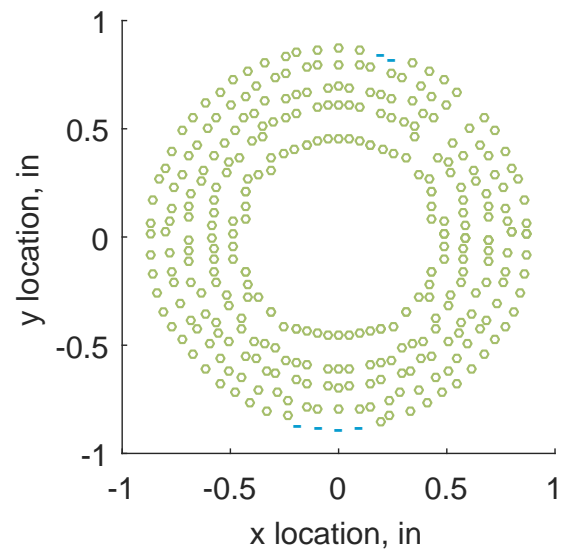
(a) Linear Interpolation



(b) Spline Interpolation



(c) Polar Interpolation



(d) Kriging Interpolation

Figure C.169: Interpolation error for the IMX inlet - symbols show locations that are within tolerance (o), over-predicted (+), and under-predicted (-).

Table C.74: Interpolation effects on the derived quantities for the IMX inlet run number R310, clocking C4.

	$K_\theta$	$K_r$	$K_a$	$IDC$	$IDT$
Linear	0.361	0.013	0.373	0.014	0.069
Spline	0.321	0.017	0.338	0.016	0.069
Polar	0.321	0.016	0.337	0.019	0.071
Kriging	0.321	0.013	0.334	0.018	0.070

#### C.2.2.5 Fourth Clocking

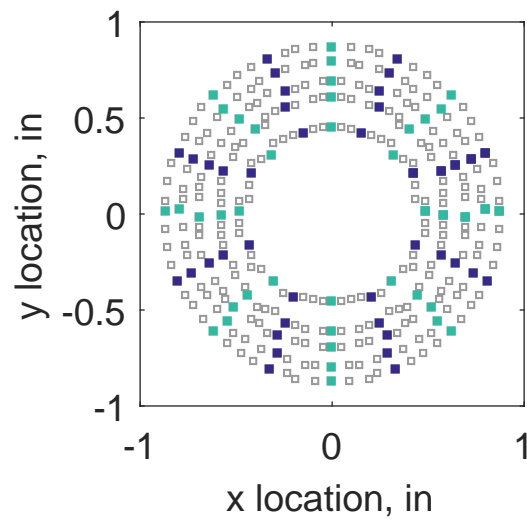


Figure C.170: Fourth clocking probe position

Table C.75: Interpolation results for the IMX inlet run number R310, clocking C5.

	Mean	Std. Dev.	Over-Prediction	In Tolerance	Under-Prediction
Linear	-0.0018	0.0048	52	170	58
Spline	-0.0022	0.0050	47	177	56
Polar	-0.0008	0.0049	82	130	68
Kriging	-0.0022	0.0064	107	115	58

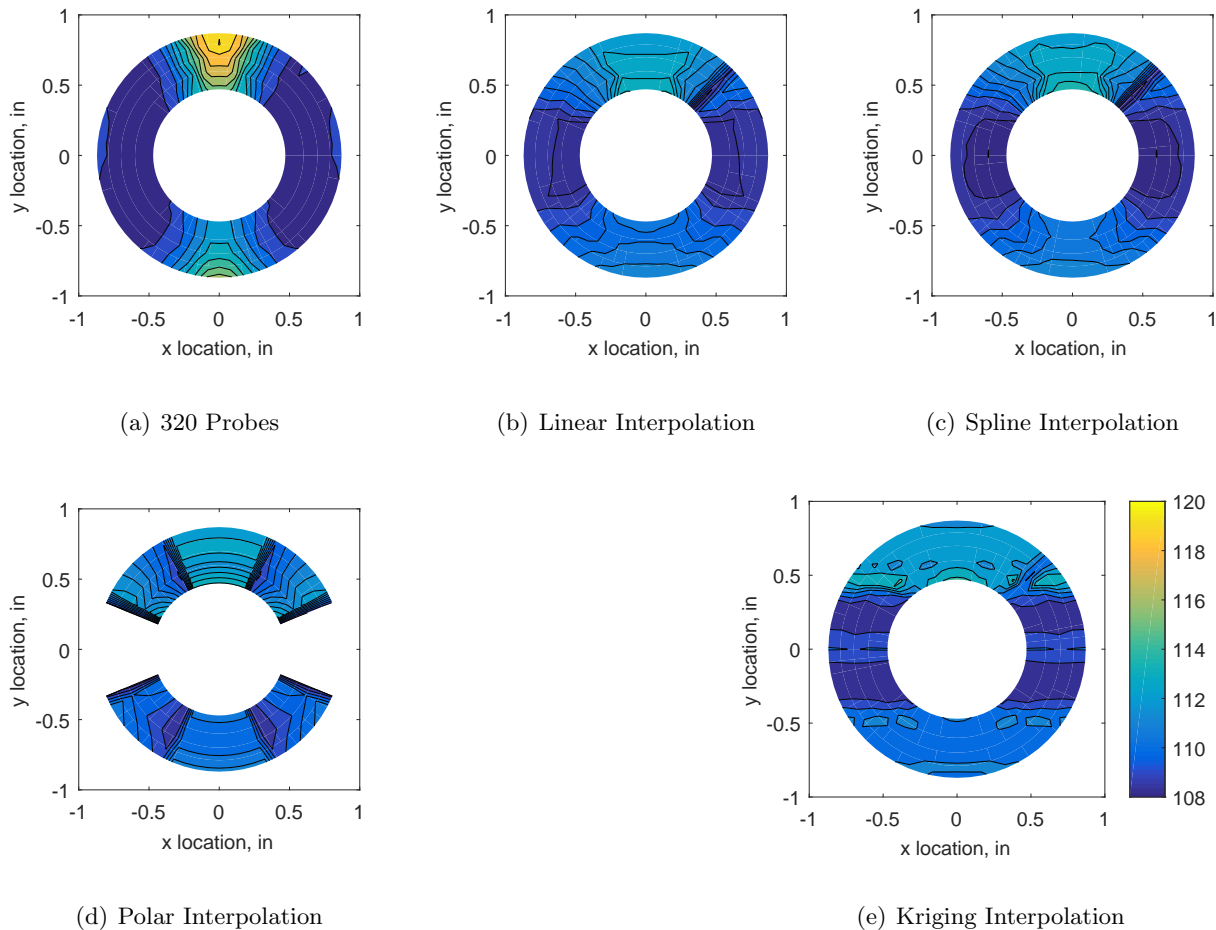
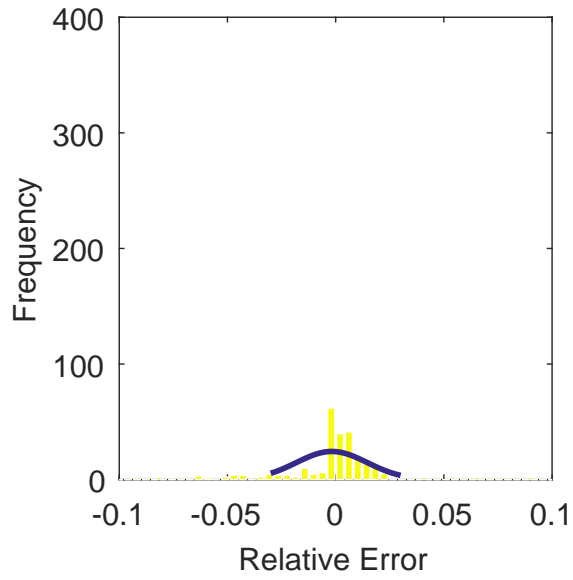
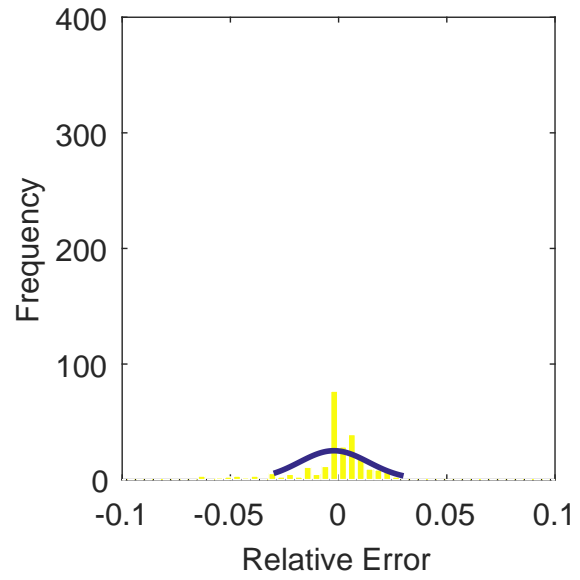


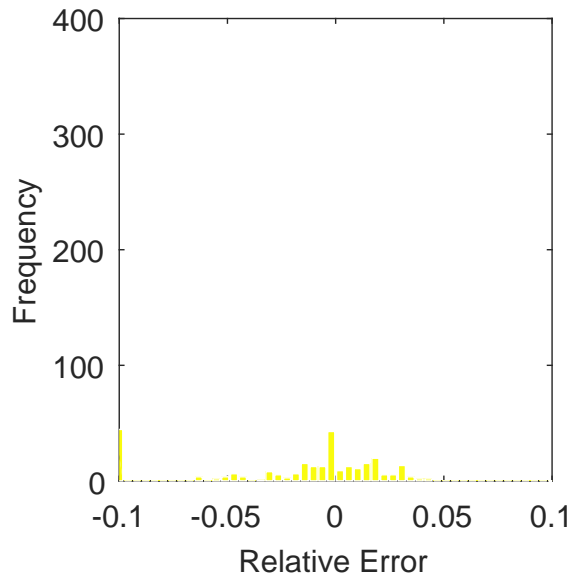
Figure C.171: Contour plots for the raw and interpolated values for the IMX inlet.



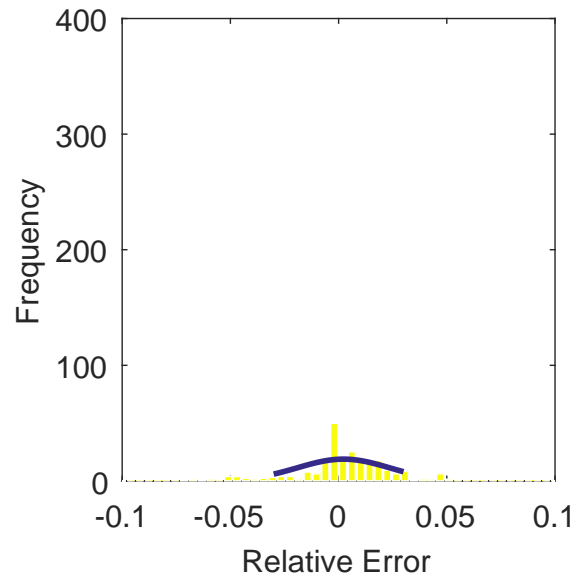
(a) Linear Interpolation Error



(b) Spline Interpolation Error

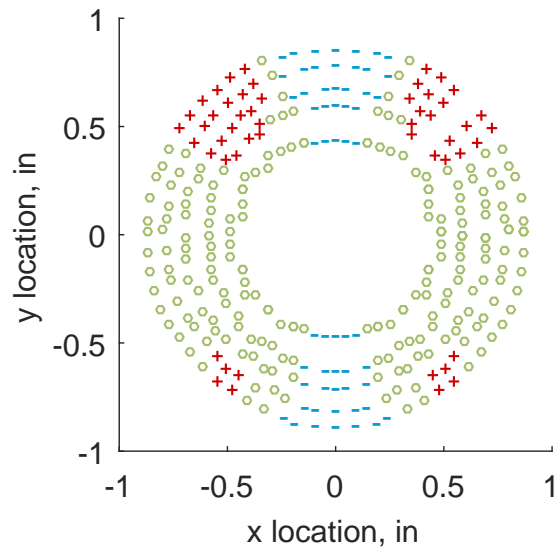


(c) Polar Interpolation Error

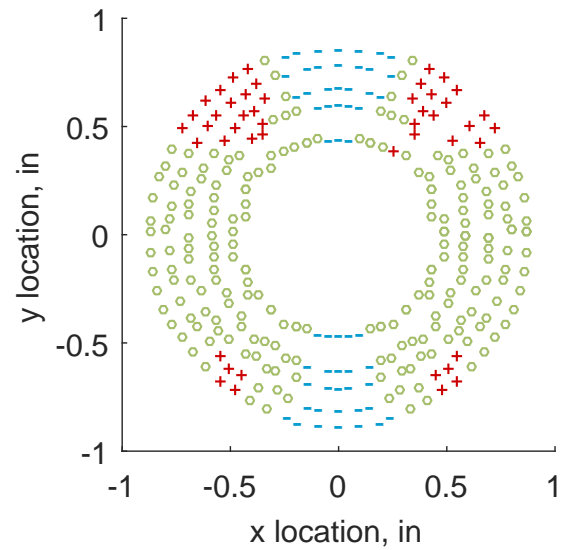


(d) Kriging Interpolation Error

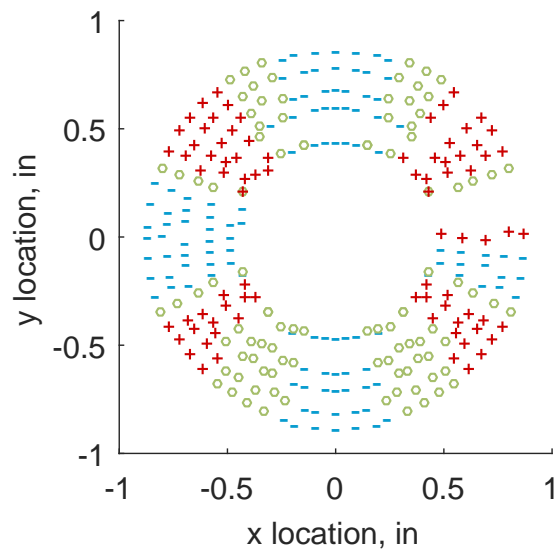
Figure C.172: Relative error for various interpolation schemes of run number R310, fourth clocking for the IMX inlet.



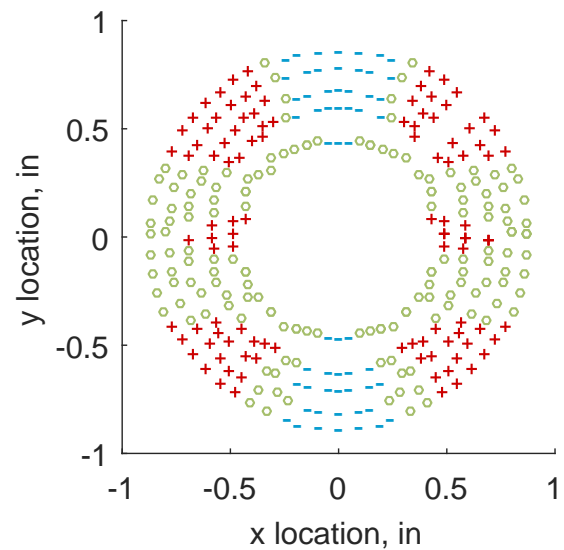
(a) Linear Interpolation



(b) Spline Interpolation



(c) Polar Interpolation



(d) Kriging Interpolation

Figure C.173: Interpolation error for the IMX inlet - symbols show locations that are within tolerance (o), over-predicted (+), and under-predicted (-).

Table C.76: Interpolation effects on the derived quantities for the IMX inlet run number R310, clocking C5.

	$K_\theta$	$K_r$	$K_a$	$IDC$	$IDT$
Linear	0.360	0.015	0.375	0.014	0.048
Spline	0.321	0.010	0.330	0.015	0.048
Polar	0.321	0.012	0.332	0.017	0.054
Kriging	NaN	NaN	NaN	NaN	NaN

### C.2.2.6 Fifth Clocking

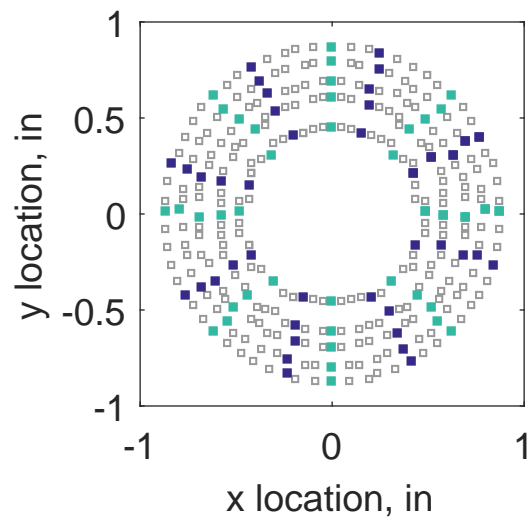


Figure C.174: Fifth clocking probe position

Table C.77: Interpolation results for the IMX inlet run number R310, clocking C6.

	Mean	Std. Dev.	Over-Prediction	In Tolerance	Under-Prediction
Linear	-0.0013	0.0038	44	177	59
Spline	-0.0018	0.0038	30	197	53
Polar	-0.0009	0.0045	80	136	64
Kriging	-0.0018	0.0018	0	272	8

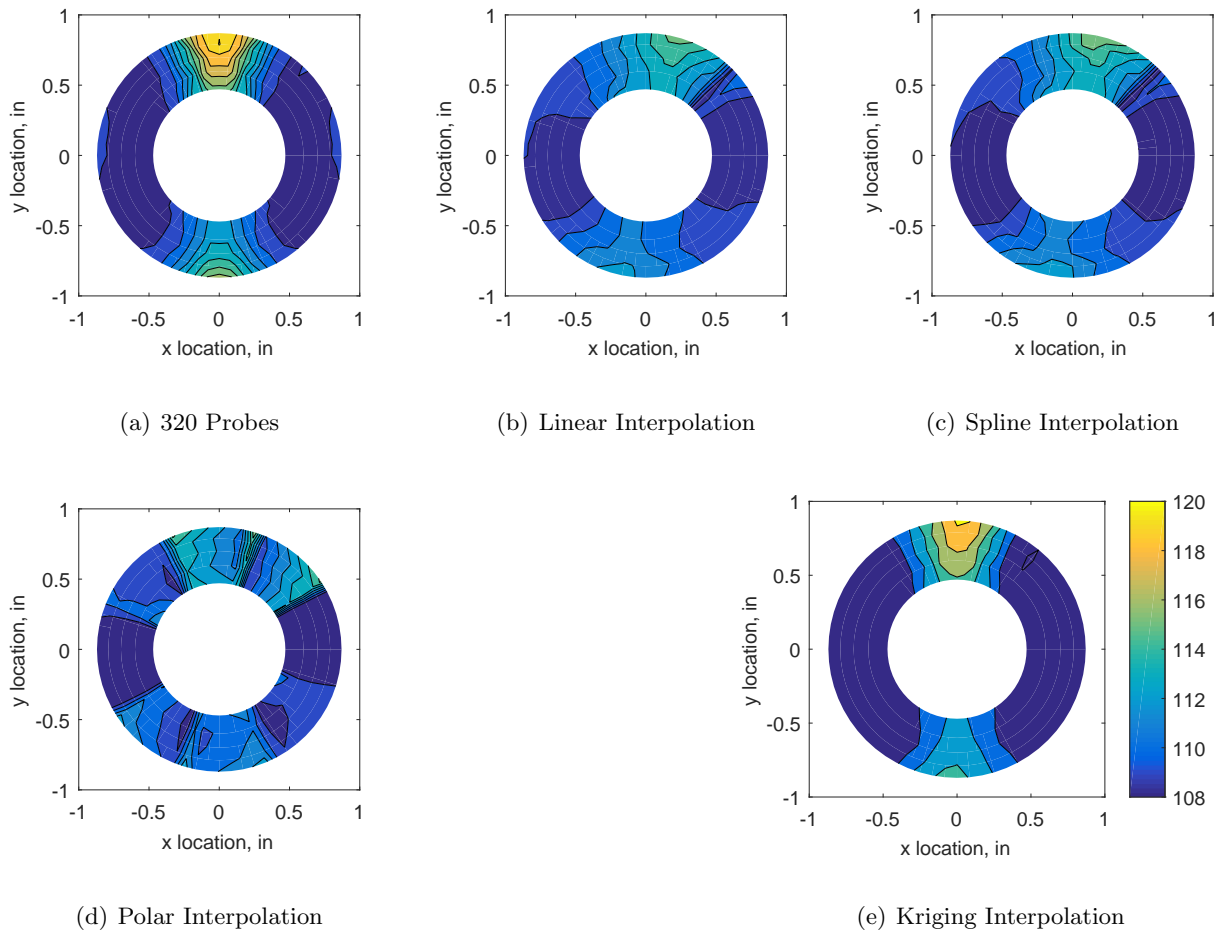
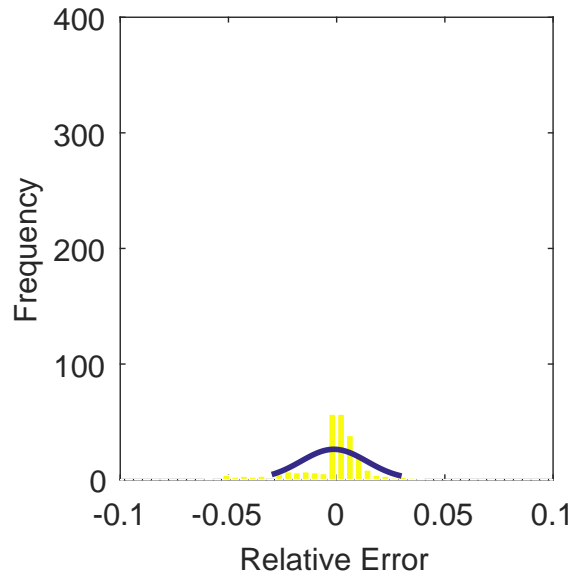
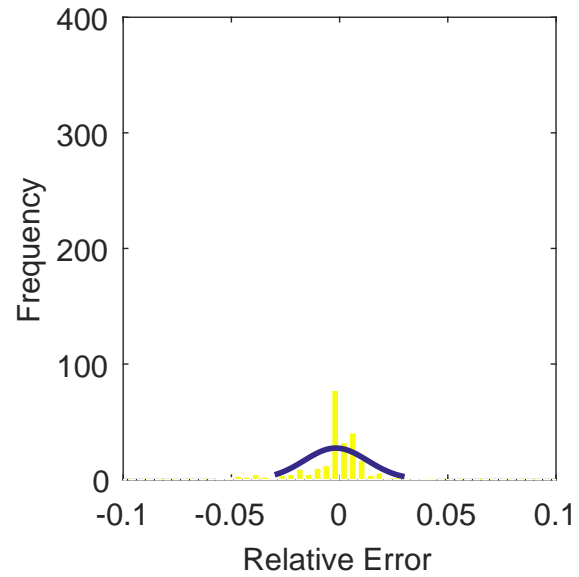


Figure C.175: Contour plots for the raw and interpolated values for the IMX inlet.

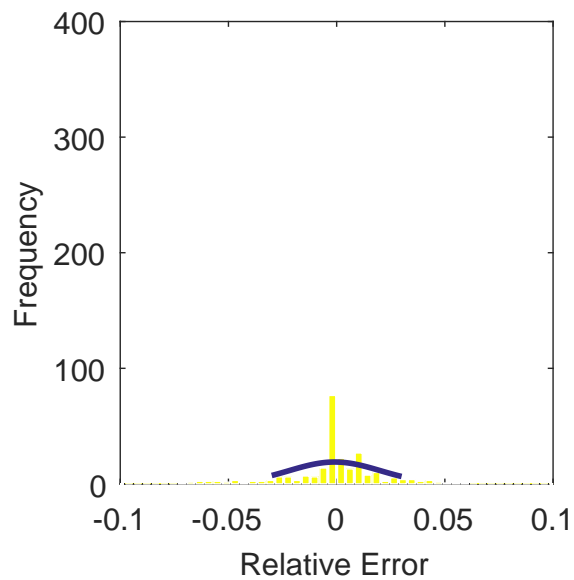




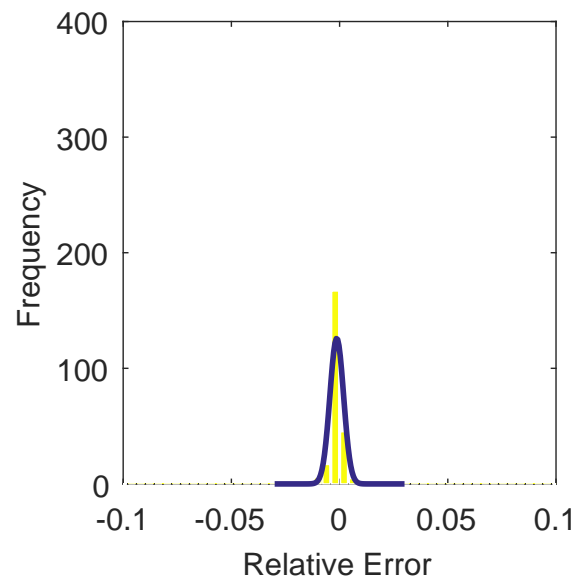
(a) Linear Interpolation Error



(b) Spline Interpolation Error

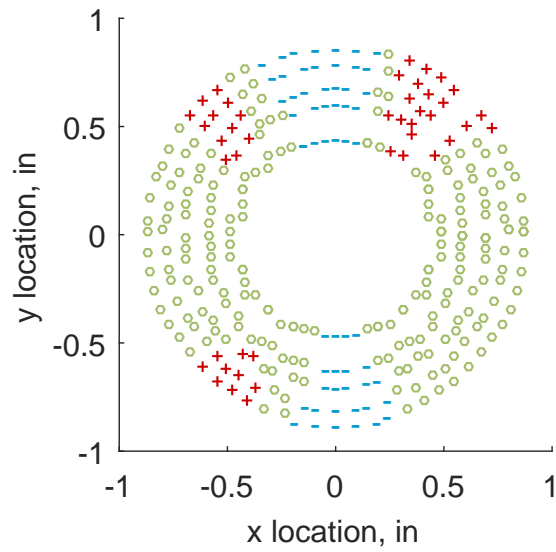


(c) Polar Interpolation Error

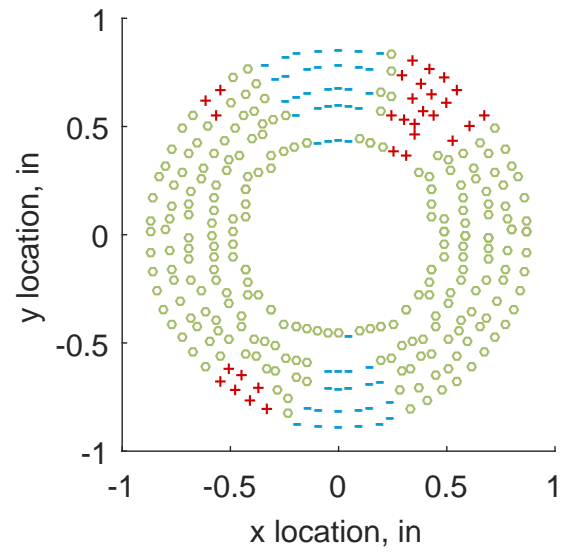


(d) Kriging Interpolation Error

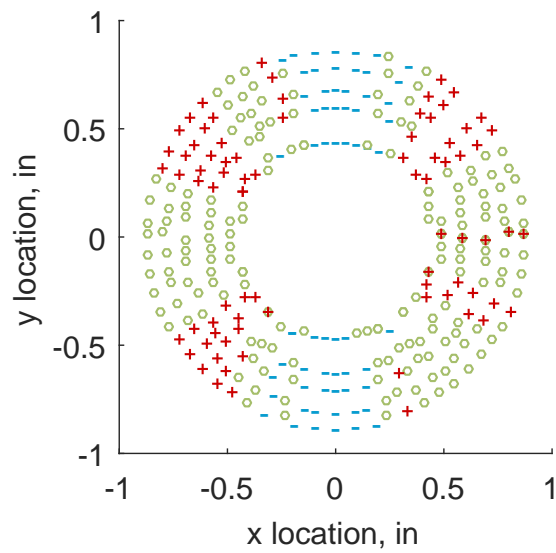
Figure C.176: Relative error for various interpolation schemes of run number R310, fifth clocking for the IMX inlet.



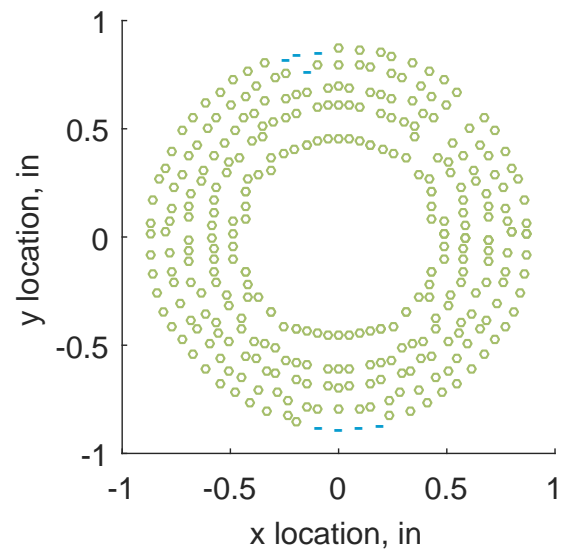
(a) Linear Interpolation



(b) Spline Interpolation



(c) Polar Interpolation



(d) Kriging Interpolation

Figure C.177: Interpolation error for the IMX inlet - symbols show locations that are within tolerance (o), over-predicted (+), and under-predicted (-).

Table C.78: Interpolation effects on the derived quantities for the IMX inlet run number R310, clocking C6.

	$K_\theta$	$K_r$	$K_a$	$IDC$	$IDT$
Linear	0.360	0.012	0.372	0.014	0.069
Spline	0.321	0.017	0.338	0.016	0.069
Polar	0.321	0.015	0.336	0.019	0.071
Kriging	0.321	0.014	0.335	0.018	0.070

### C.2.2.7 Sixth Clocking

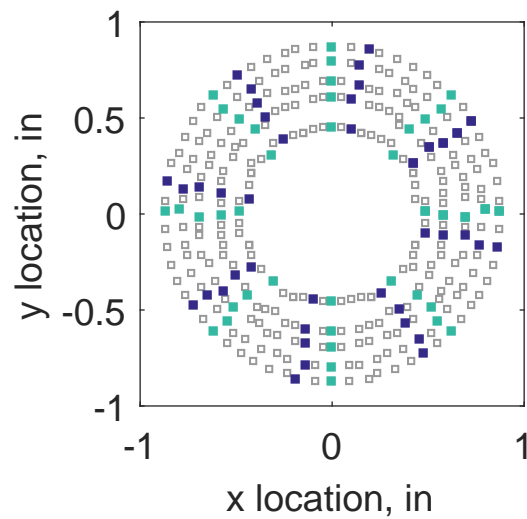


Figure C.178: Sixth clocking probe position

Table C.79: Interpolation results for the IMX inlet run number R310, clocking C7.

	Mean	Std. Dev.	Over-Prediction	In Tolerance	Under-Prediction
Linear	0.0008	0.0034	40	197	43
Spline	0.0004	0.0035	40	198	42
Polar	0.0012	0.0047	67	160	53
Kriging	0.0004	0.0019	0	278	2

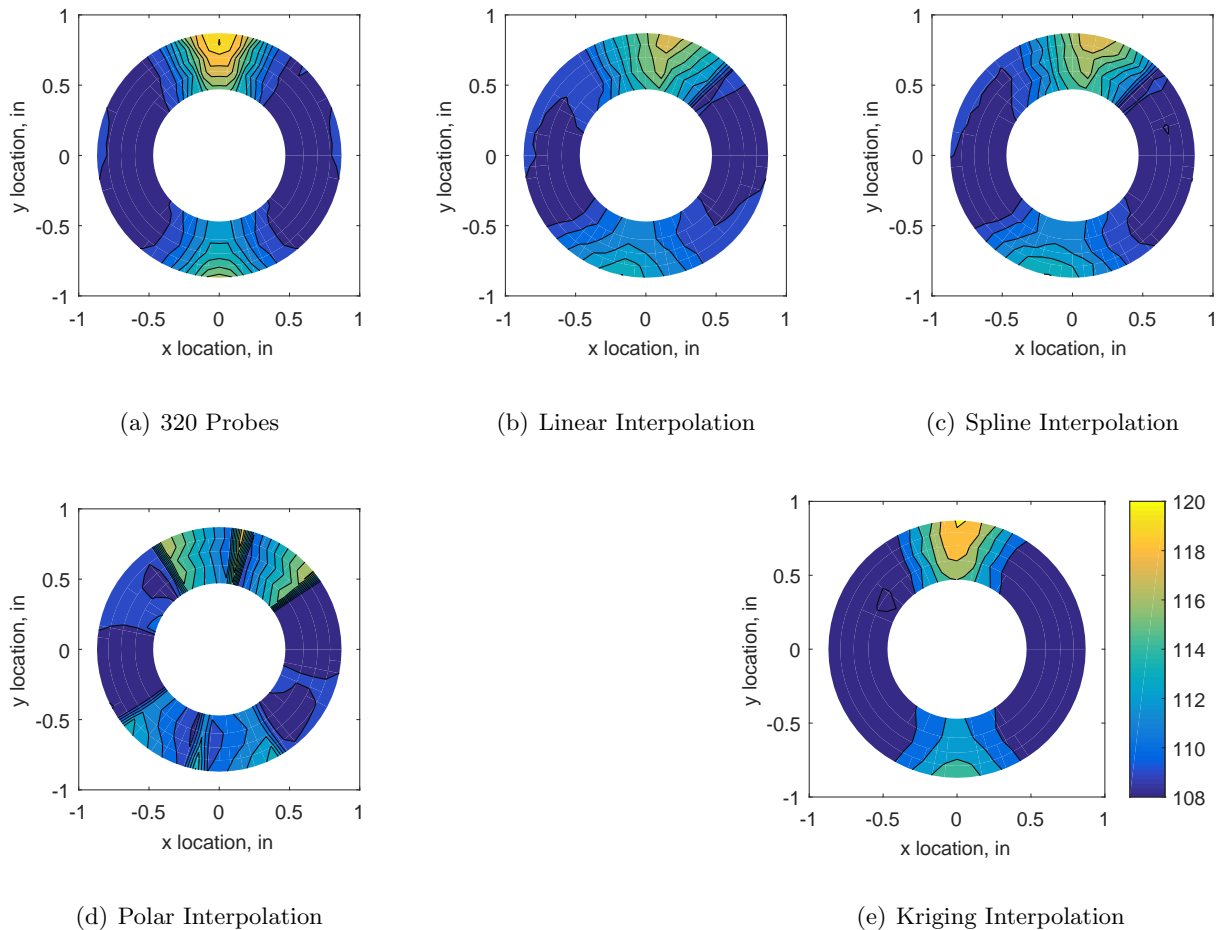
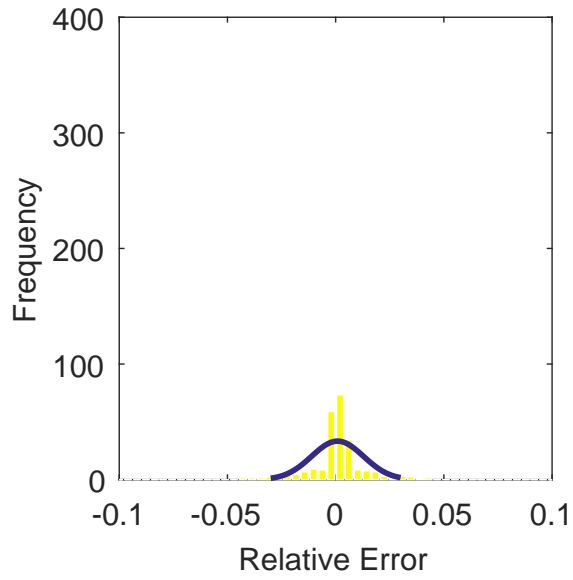
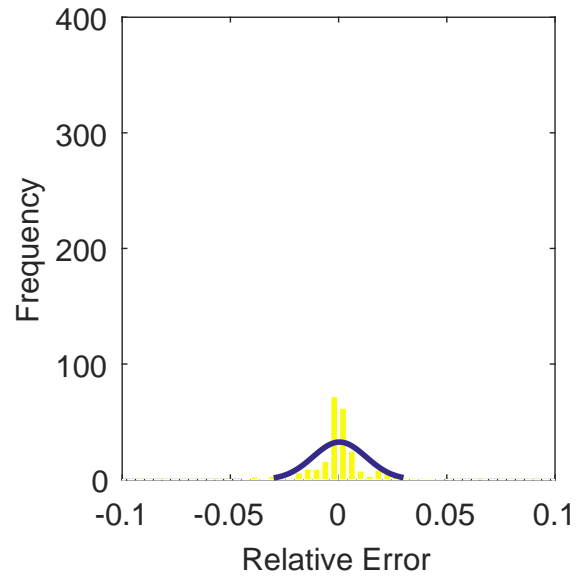


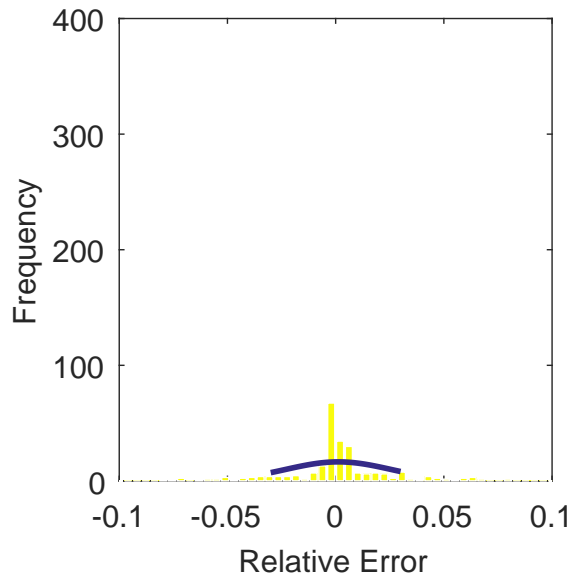
Figure C.179: Contour plots for the raw and interpolated values for the IMX inlet.



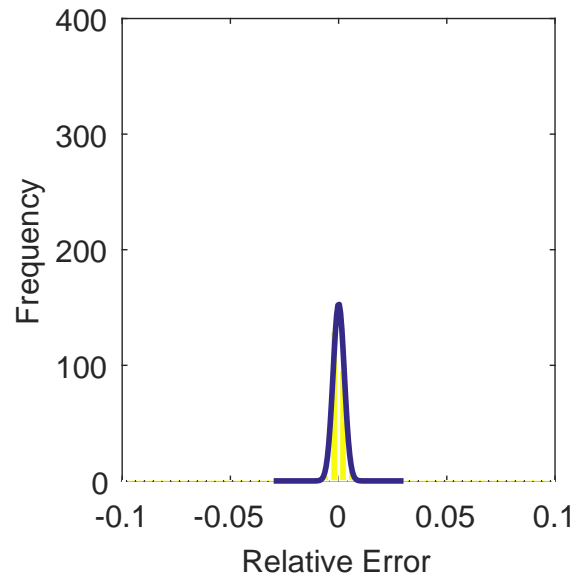
(a) Linear Interpolation Error



(b) Spline Interpolation Error

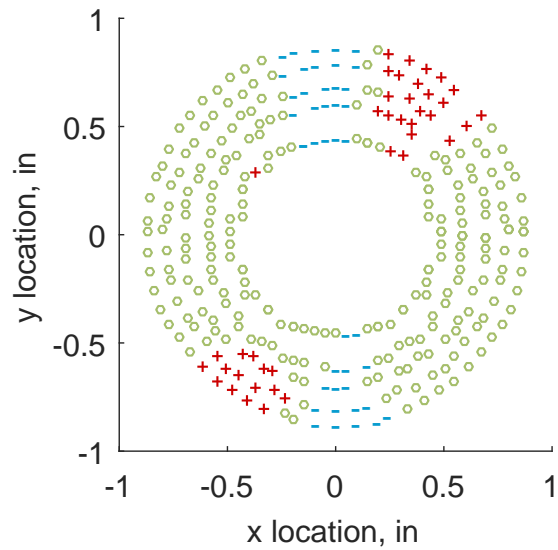


(c) Polar Interpolation Error

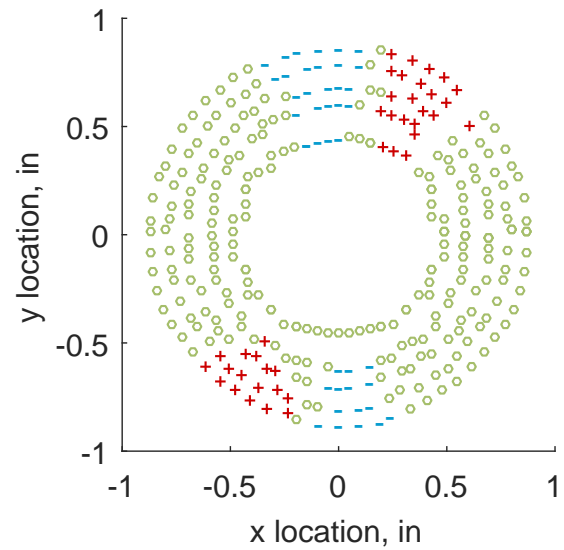


(d) Kriging Interpolation Error

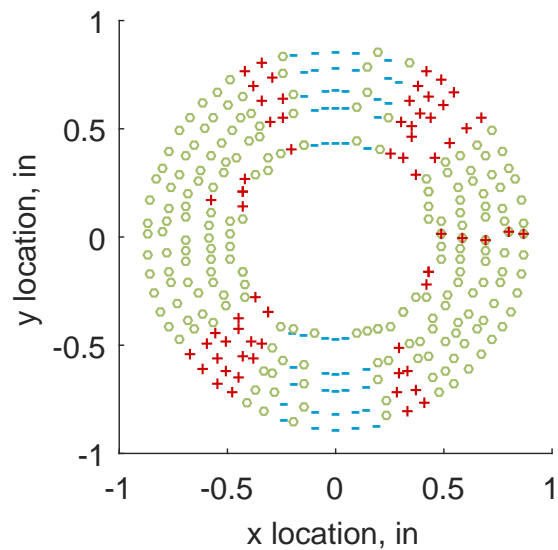
Figure C.180: Relative error for various interpolation schemes of run number R310, sixth clocking for the IMX inlet.



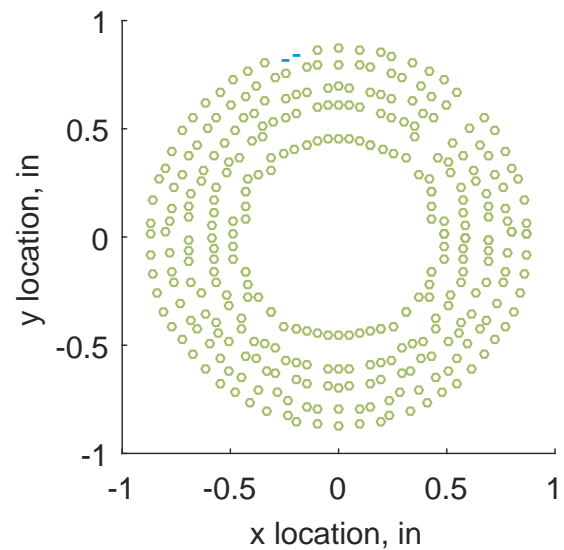
(a) Linear Interpolation



(b) Spline Interpolation



(c) Polar Interpolation



(d) Kriging Interpolation

Figure C.181: Interpolation error for the IMX inlet - symbols show locations that are within tolerance (o), over-predicted (+), and under-predicted (-).

Table C.80: Interpolation effects on the derived quantities for the IMX inlet run number R310, clocking C7.

	$K_\theta$	$K_r$	$K_a$	$IDC$	$IDT$
Linear	0.361	0.020	0.381	0.017	0.089
Spline	0.322	0.023	0.344	0.020	0.088
Polar	0.322	0.021	0.342	0.022	0.091
Kriging	0.322	0.020	0.342	0.020	0.088

### C.2.2.8 Seventh Clocking

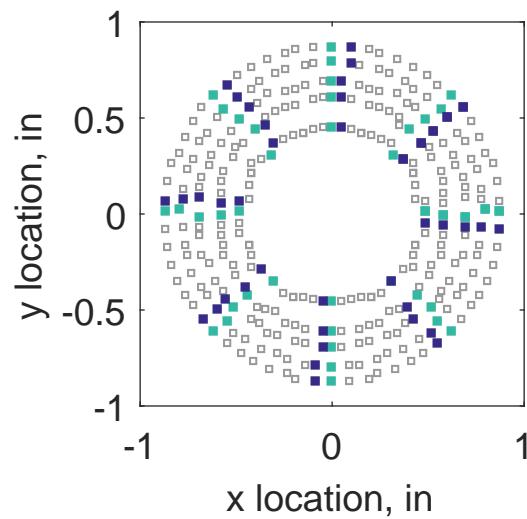


Figure C.182: Seventh clocking probe position

Table C.81: Interpolation results for the IMX inlet run number R310, clocking C8.

	Mean	Std. Dev.	Over-Prediction	In Tolerance	Under-Prediction
Linear	0.0028	0.0030	38	229	13
Spline	0.0020	0.0025	38	235	7
Polar	0.0033	0.0052	66	162	52
Kriging	0.0020	0.0011	3	277	0

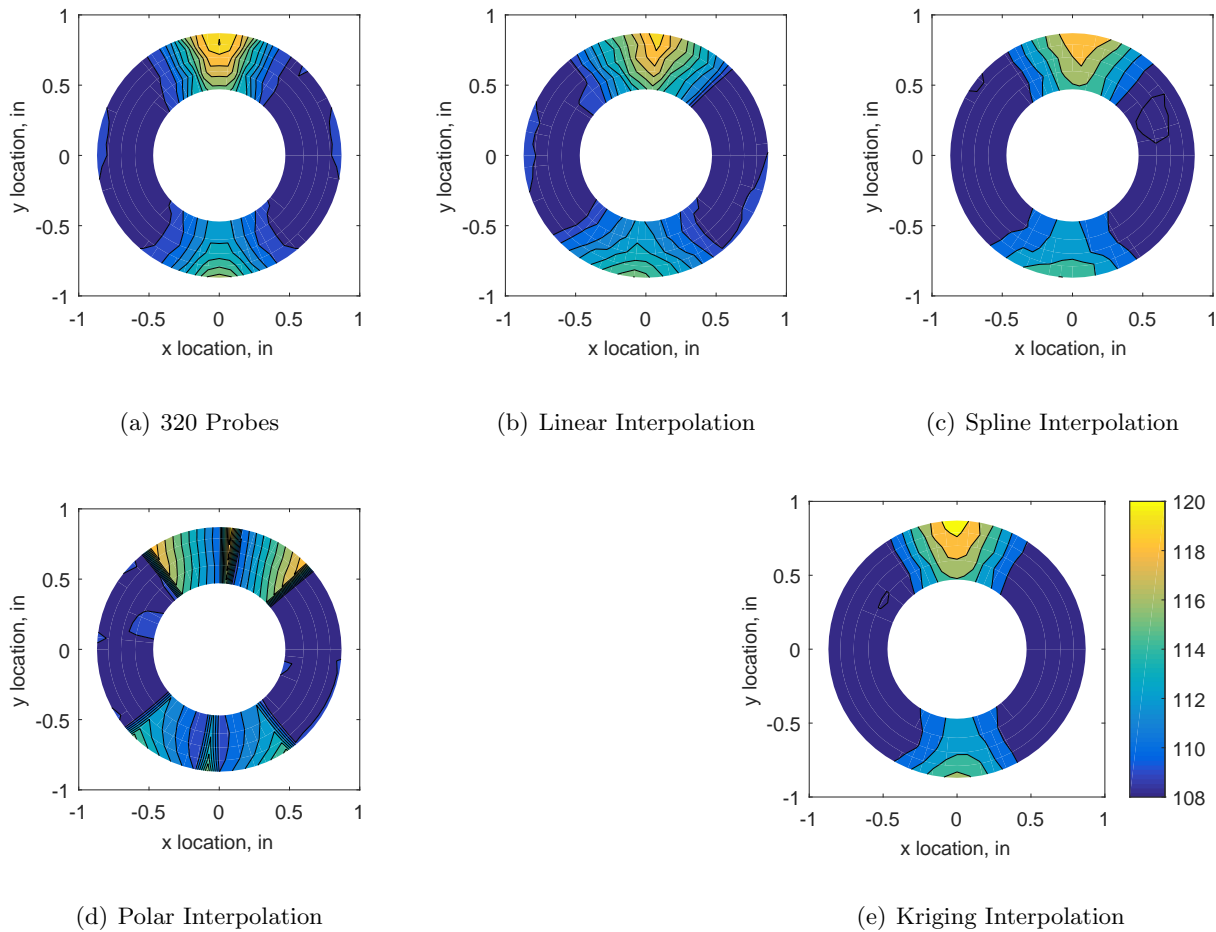
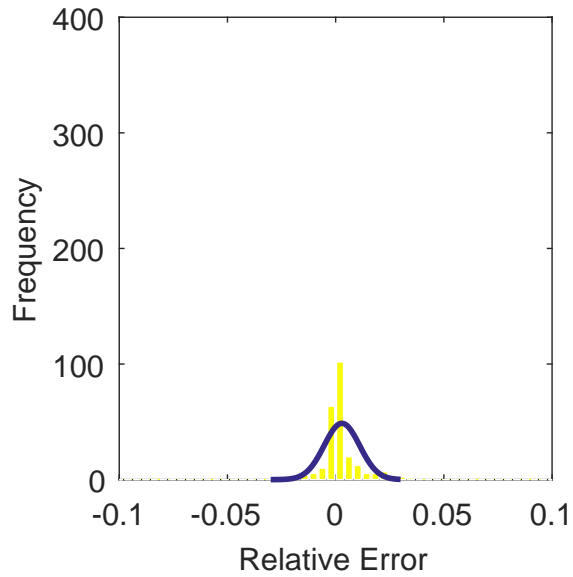
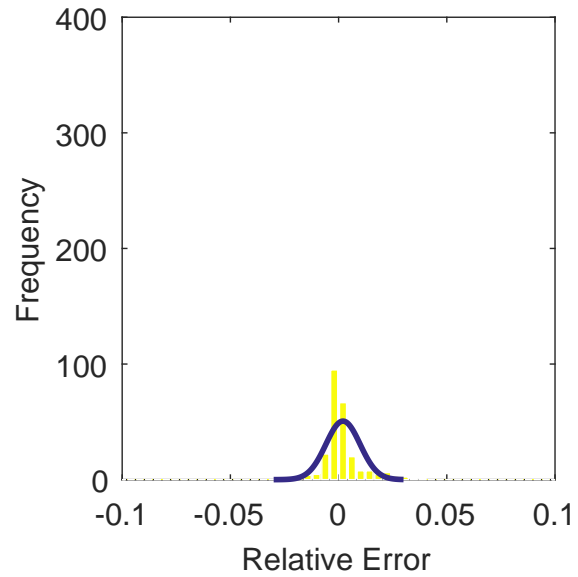


Figure C.183: Contour plots for the raw and interpolated values for the IMX inlet.

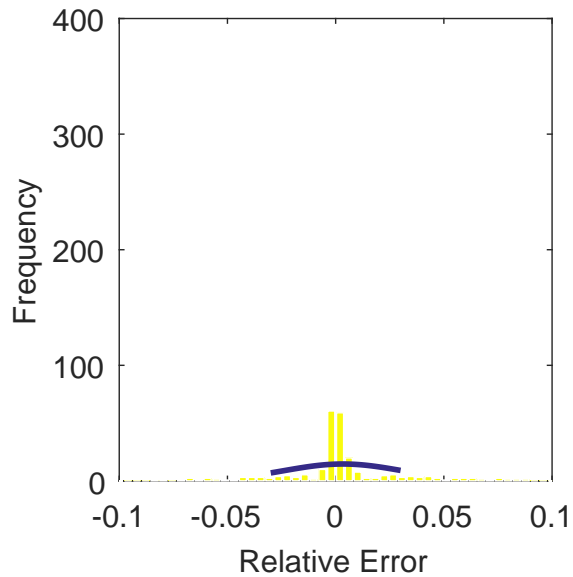




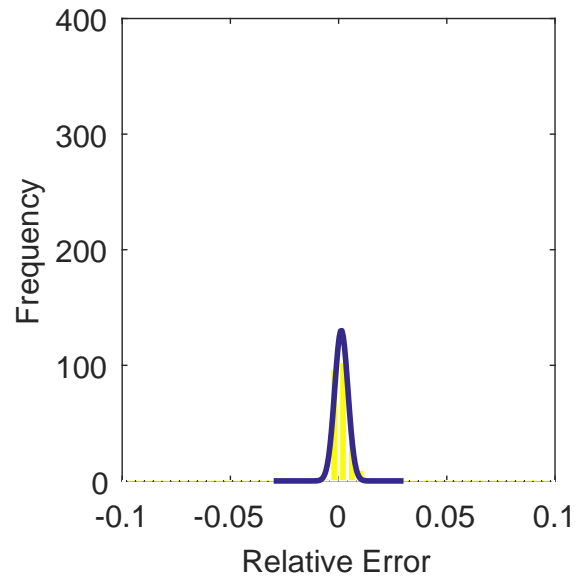
(a) Linear Interpolation Error



(b) Spline Interpolation Error

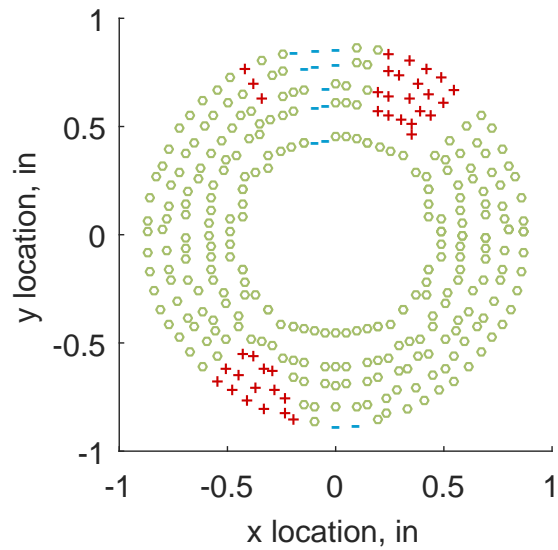


(c) Polar Interpolation Error

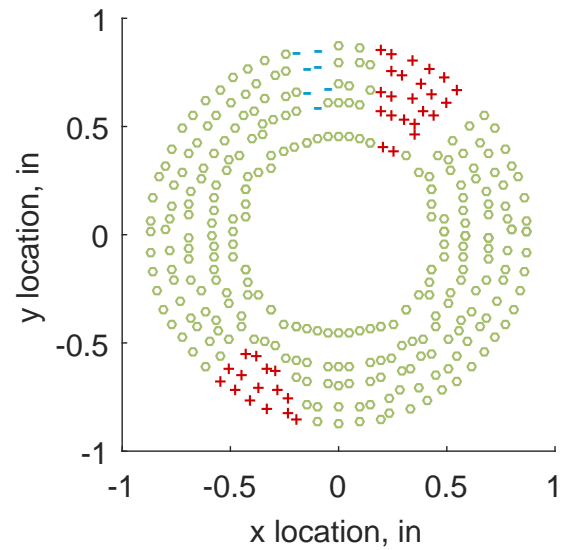


(d) Kriging Interpolation Error

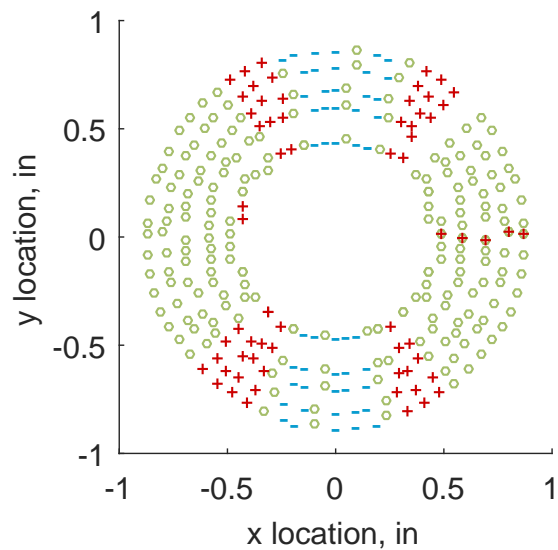
Figure C.184: Relative error for various interpolation schemes of run number R310, seventh clocking for the IMX inlet.



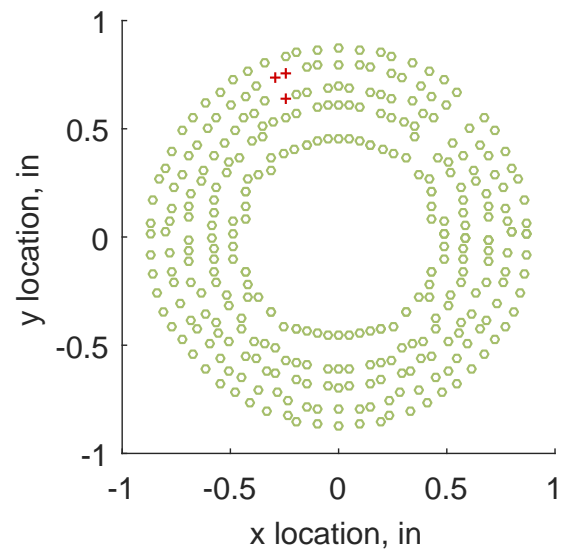
(a) Linear Interpolation



(b) Spline Interpolation



(c) Polar Interpolation



(d) Kriging Interpolation

Figure C.185: Interpolation error for the IMX inlet - symbols show locations that are within tolerance (o), over-predicted (+), and under-predicted (-).

Table C.82: Interpolation effects on the derived quantities for the IMX inlet run number R310, clocking C8.

	$K_\theta$	$K_r$	$K_a$	$IDC$	$IDT$
Linear	0.362	0.026	0.387	0.020	0.106
Spline	0.322	0.033	0.356	0.024	0.106
Polar	0.322	0.030	0.352	0.028	0.111
Kriging	0.322	0.027	0.349	0.023	0.106

## C.2.3 Run Number R320

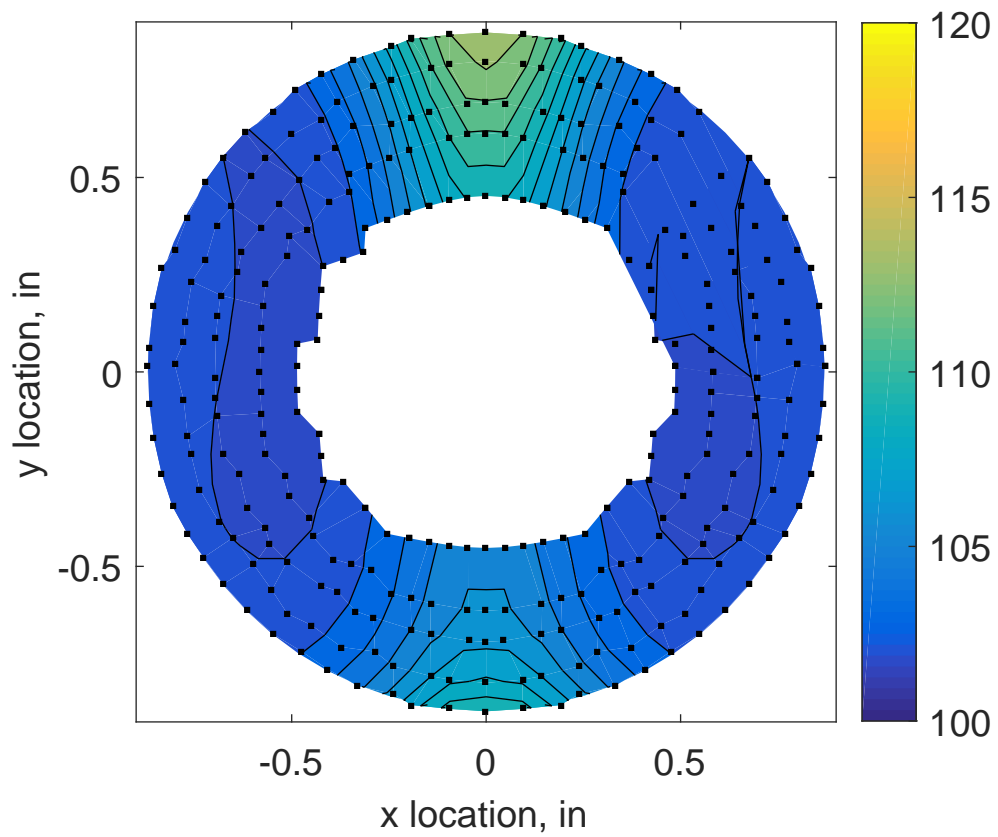


Figure C.186: IMX run number R320 raw pressure contour created with 320 probes.

### C.2.3.1 Zeroth Clocking

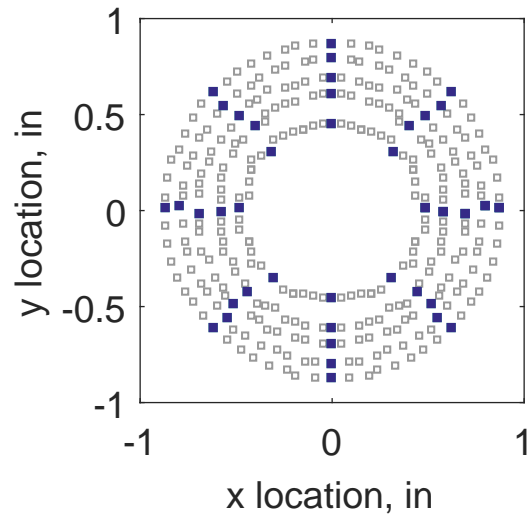
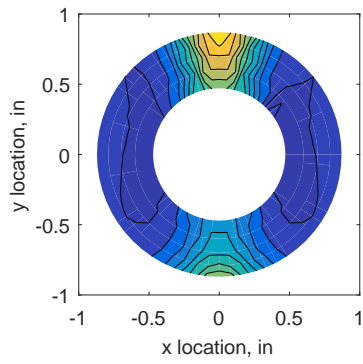


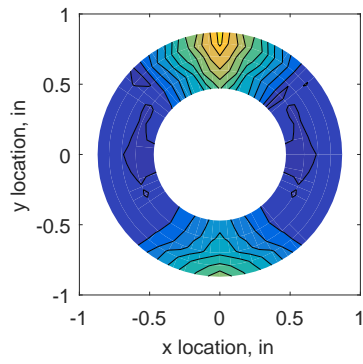
Figure C.187: Zeroth clocking probe position

Table C.83: Interpolation results for the IMX inlet run number R320, clocking C1.

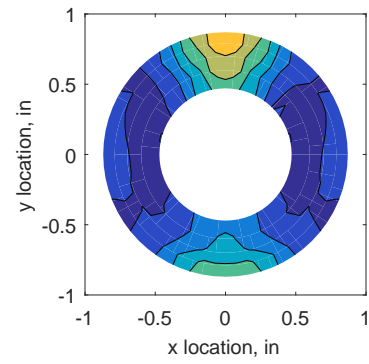
	Mean	Std. Dev.	Over-Prediction	In Tolerance	Under-Prediction
Linear	0.0029	0.0034	44	234	2
Spline	0.0027	0.0032	46	234	0
Polar	0.0040	0.0061	81	149	50
Kriging	0.0027	0.0024	22	258	0



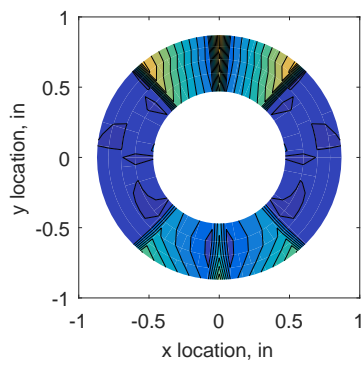
(a) 320 Probes



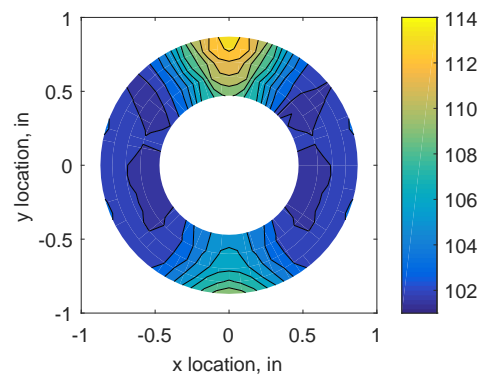
(b) Linear Interpolation



(c) Spline Interpolation

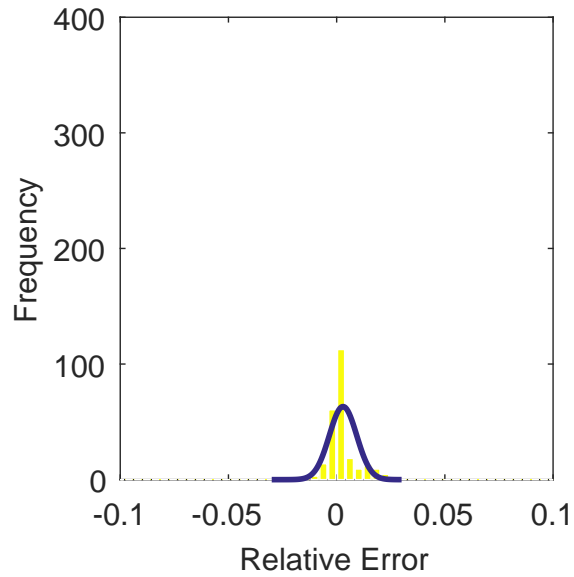


(d) Polar Interpolation

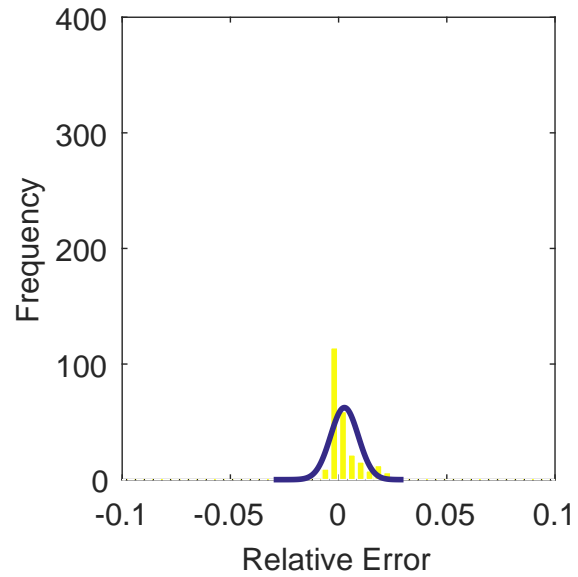


(e) Kriging Interpolation

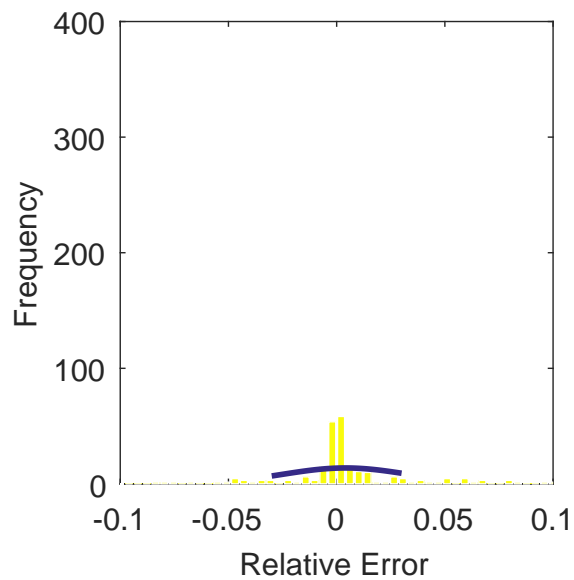
Figure C.188: Contour plots for the raw and interpolated values for the IMX inlet.



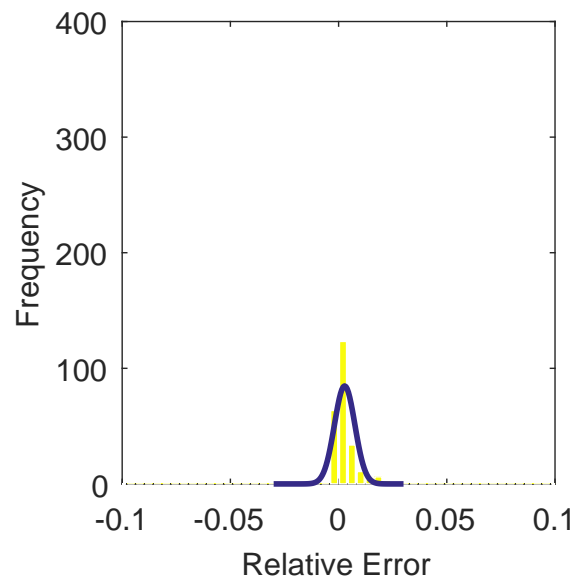
(a) Linear Interpolation Error



(b) Spline Interpolation Error

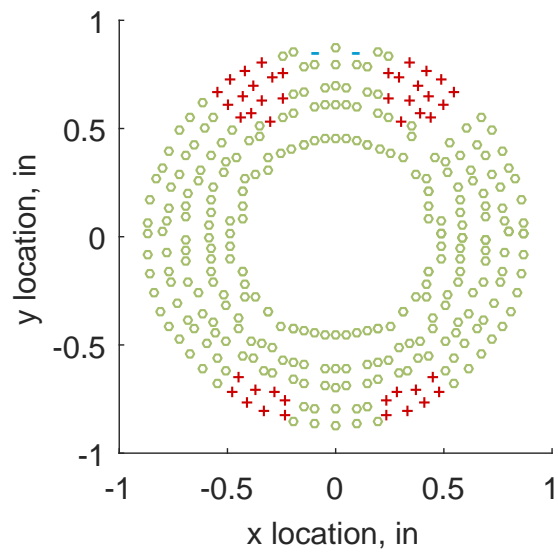


(c) Polar Interpolation Error

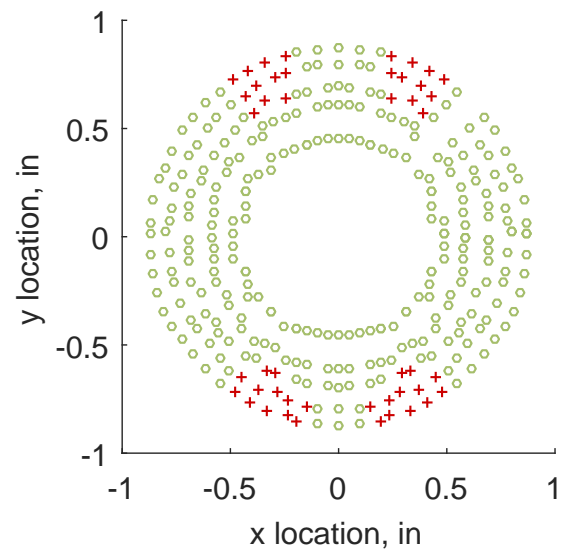


(d) Kriging Interpolation Error

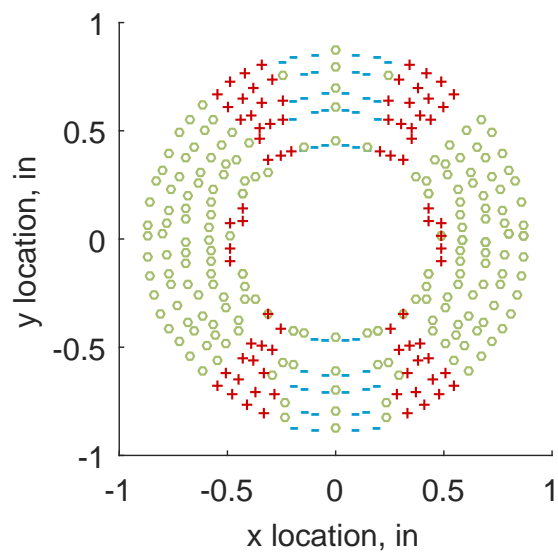
Figure C.189: Relative error for various interpolation schemes of run number R320, zeroth clocking for the IMX inlet.



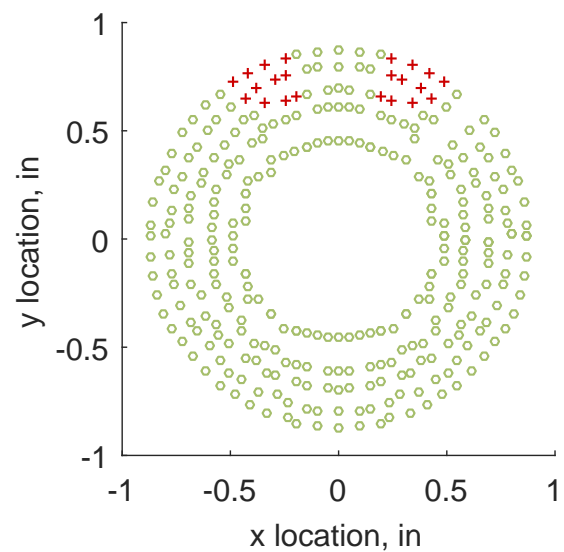
(a) Linear Interpolation



(b) Spline Interpolation



(c) Polar Interpolation



(d) Kriging Interpolation

Figure C.190: Interpolation error for the IMX inlet - symbols show locations that are within tolerance (o), over-predicted (+), and under-predicted (-).



Table C.84: Interpolation effects on the derived quantities for the IMX inlet run number R320, clocking C1.

	$K_\theta$	$K_r$	$K_a$	$IDC$	$IDT$
Linear	0.340	0.027	0.367	0.022	0.113
Spline	0.303	0.034	0.337	0.025	0.113
Polar	0.303	0.035	0.338	0.026	0.116
Kriging	0.303	0.025	0.328	0.025	0.113

### C.2.3.2 First Clocking

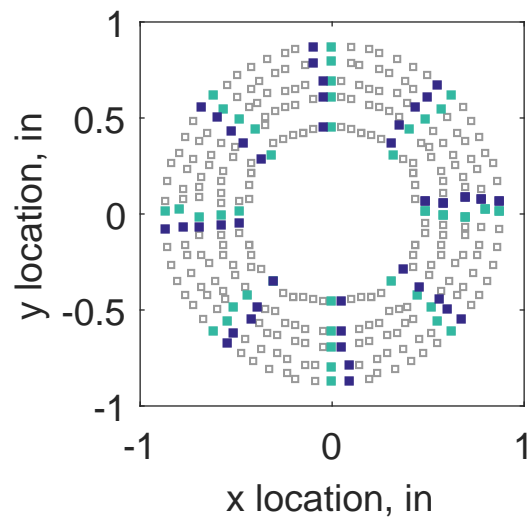


Figure C.191: First clocking probe position

Table C.85: Interpolation results for the IMX inlet run number R320, clocking C2.

	Mean	Std. Dev.	Over-Prediction	In Tolerance	Under-Prediction
Linear	0.0031	0.0033	43	222	15
Spline	0.0022	0.0028	38	236	6
Polar	0.0036	0.0059	70	159	51
Kriging	0.0022	0.0013	9	271	0

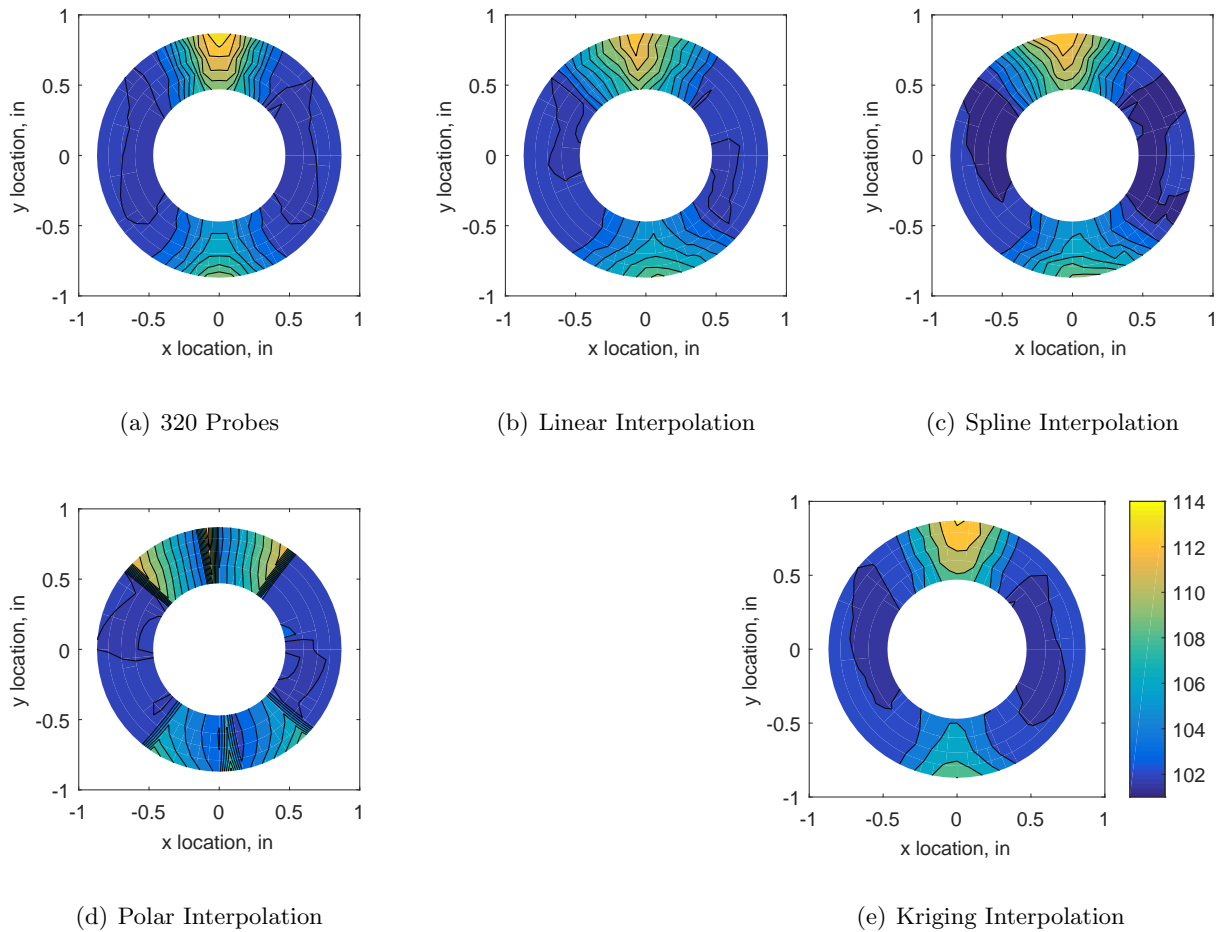
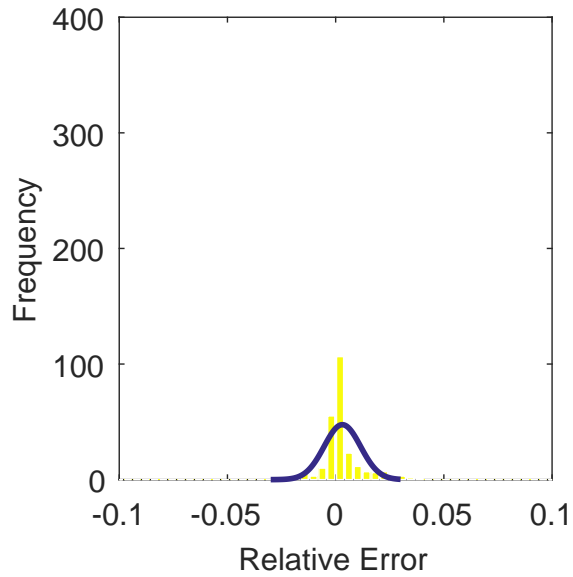
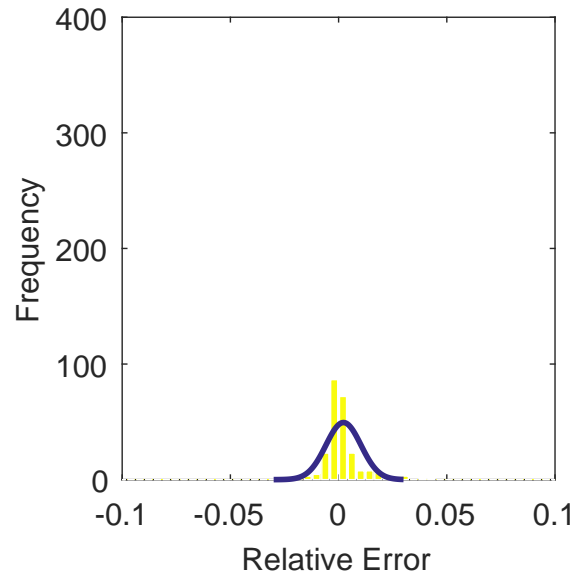


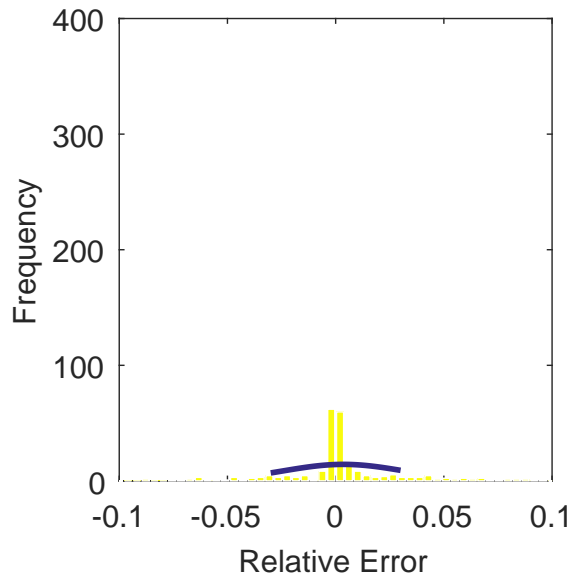
Figure C.192: Contour plots for the raw and interpolated values for the IMX inlet.



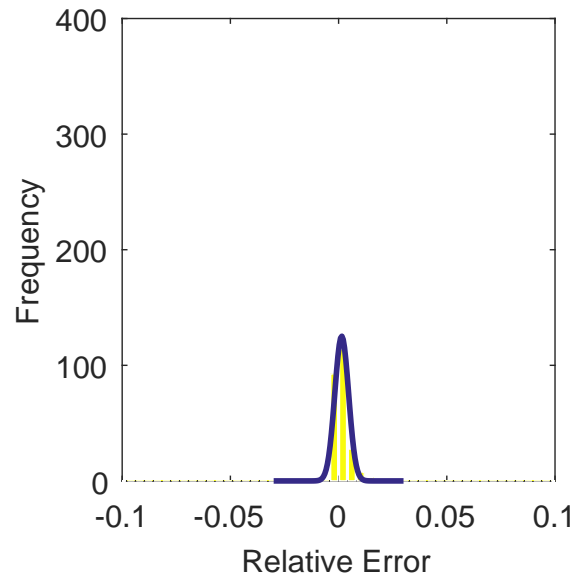
(a) Linear Interpolation Error



(b) Spline Interpolation Error

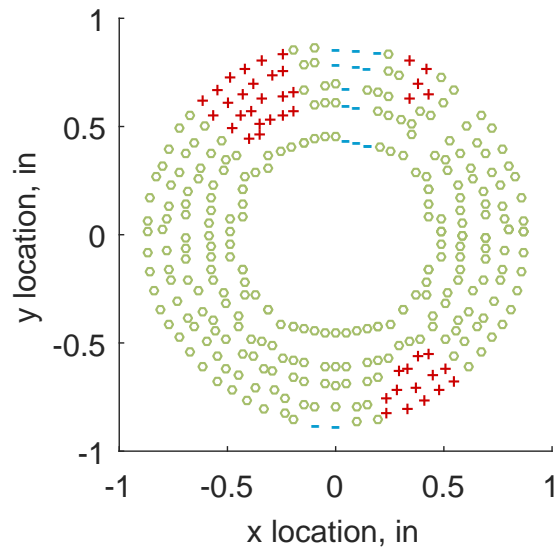


(c) Polar Interpolation Error

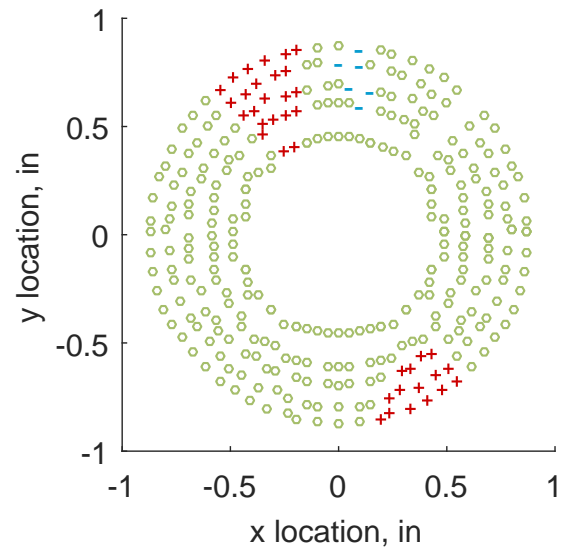


(d) Kriging Interpolation Error

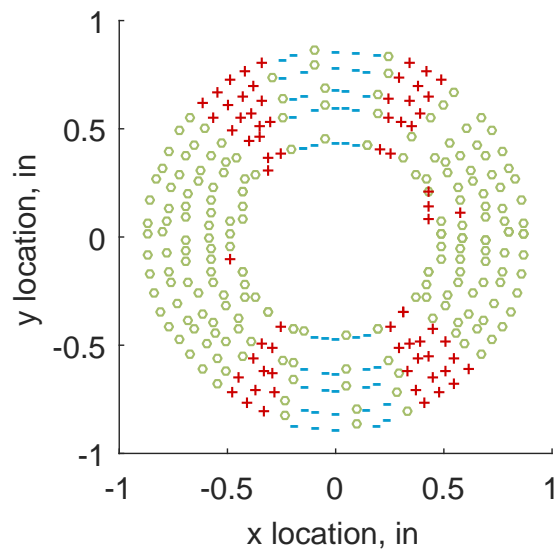
Figure C.193: Relative error for various interpolation schemes of run number R320, first clocking for the IMX inlet.



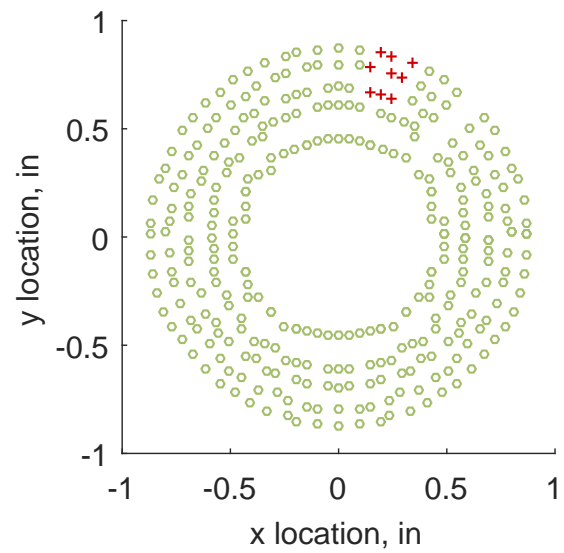
(a) Linear Interpolation



(b) Spline Interpolation



(c) Polar Interpolation



(d) Kriging Interpolation

Figure C.194: Interpolation error for the IMX inlet - symbols show locations that are within tolerance (o), over-predicted (+), and under-predicted (-).

Table C.86: Interpolation effects on the derived quantities for the IMX inlet run number R320, clocking C2.

	$K_\theta$	$K_r$	$K_a$	$IDC$	$IDT$
Linear	0.340	0.026	0.366	0.021	0.109
Spline	0.303	0.030	0.333	0.025	0.109
Polar	0.303	0.026	0.329	0.029	0.114
Kriging	0.303	0.024	0.327	0.024	0.109

### C.2.3.3 Second Clocking

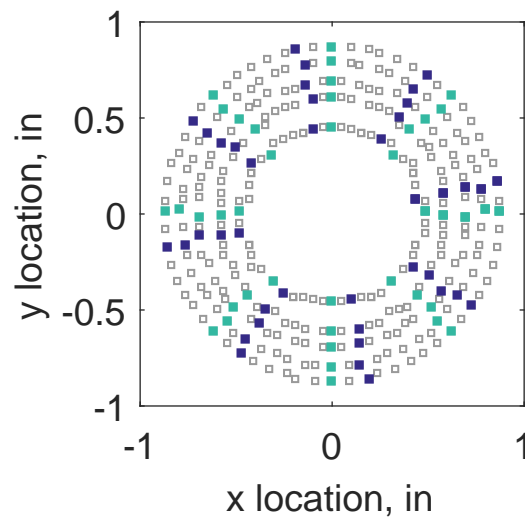
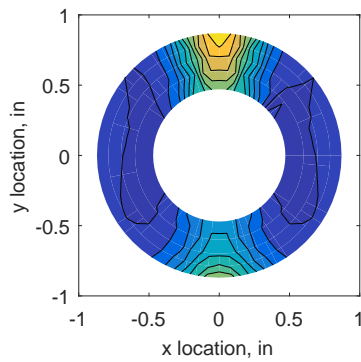


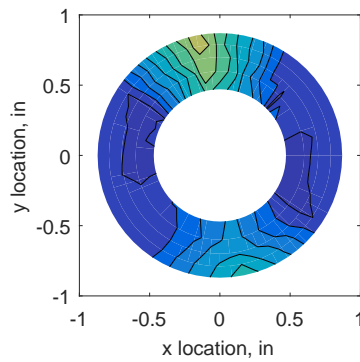
Figure C.195: Second clocking probe position

Table C.87: Interpolation results for the IMX inlet run number R320, clocking C3.

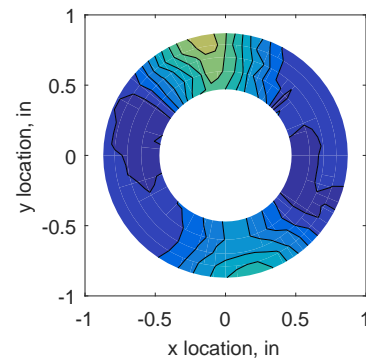
	Mean	Std. Dev.	Over-Prediction	In Tolerance	Under-Prediction
Linear	0.0009	0.0036	45	194	41
Spline	0.0005	0.0036	42	196	42
Polar	0.0013	0.0050	69	155	56
Kriging	0.0005	0.0011	0	280	0



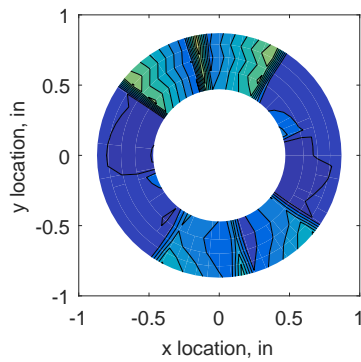
(a) 320 Probes



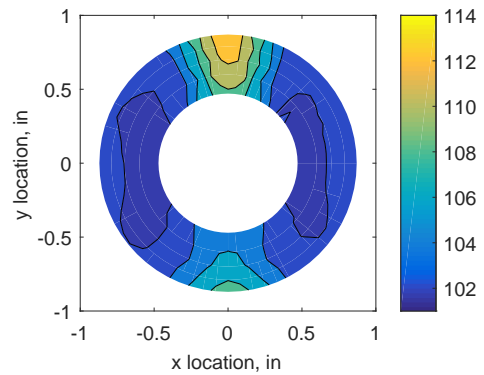
(b) Linear Interpolation



(c) Spline Interpolation

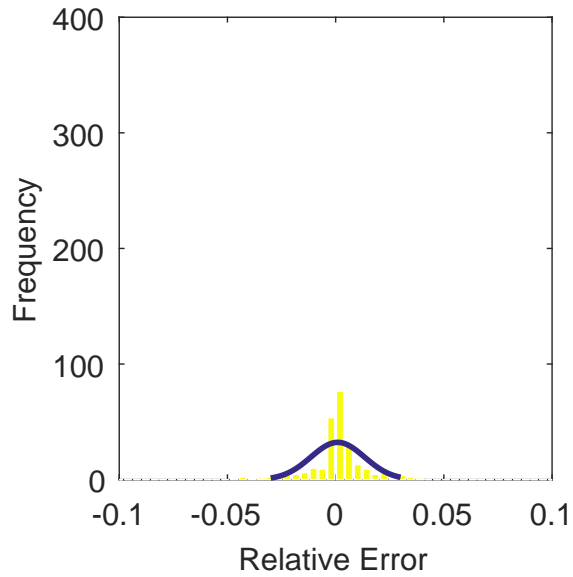


(d) Polar Interpolation

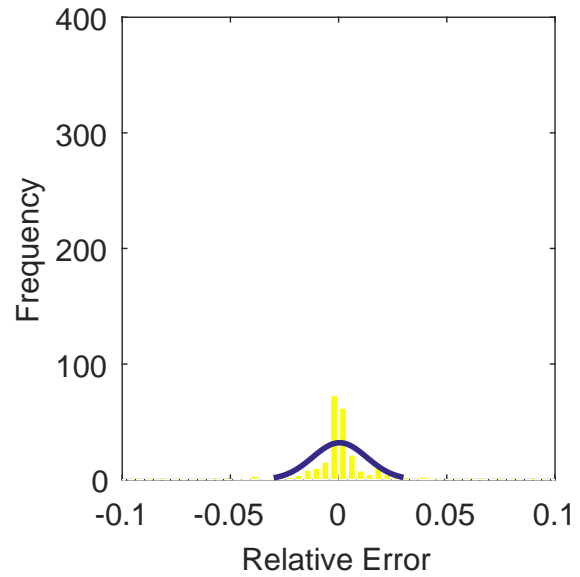


(e) Kriging Interpolation

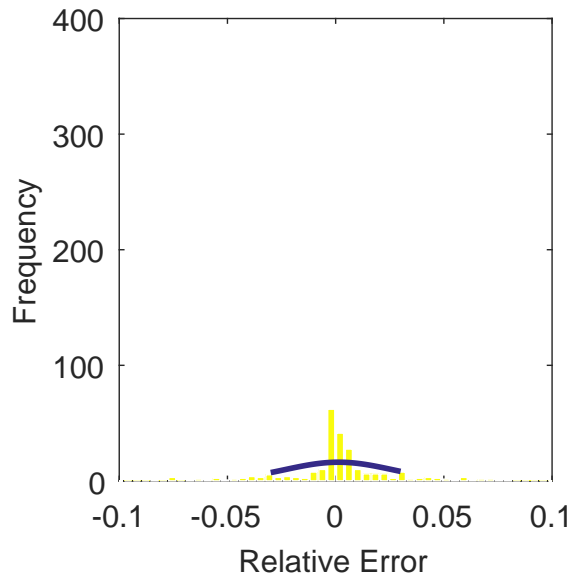
Figure C.196: Contour plots for the raw and interpolated values for the IMX inlet.



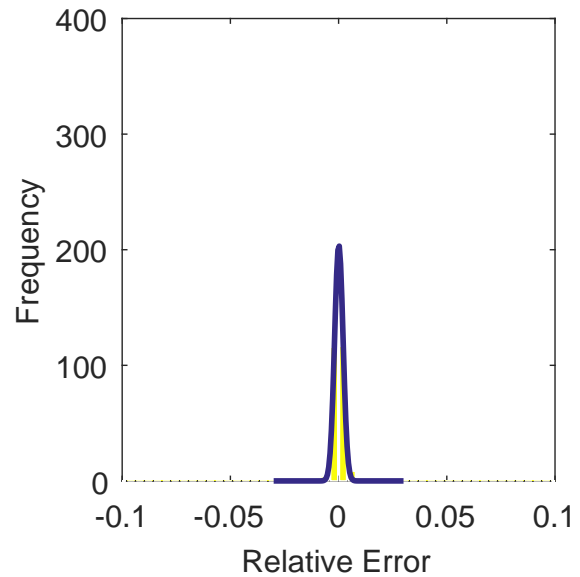
(a) Linear Interpolation Error



(b) Spline Interpolation Error

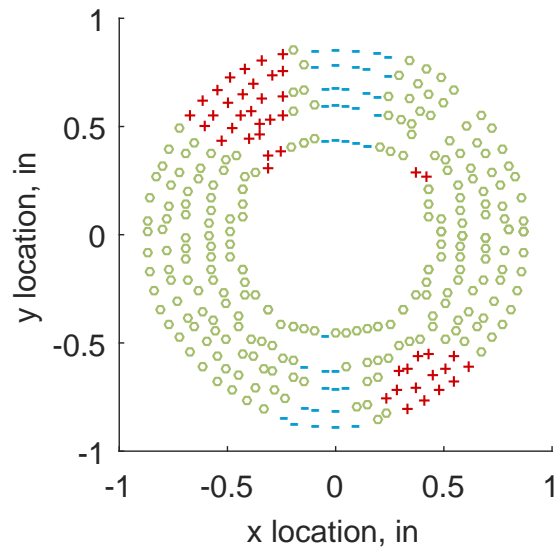


(c) Polar Interpolation Error

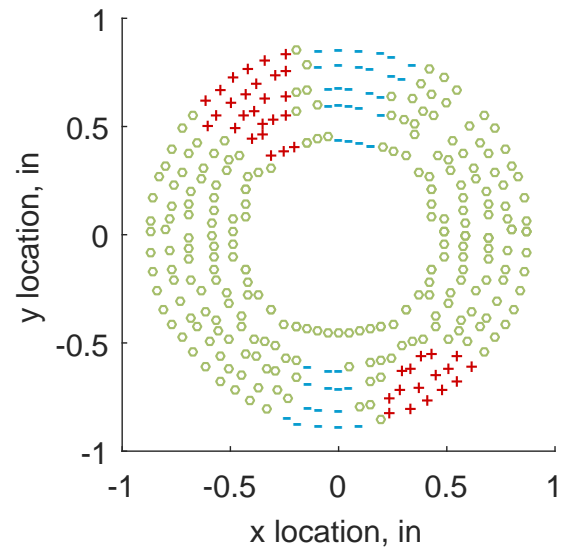


(d) Kriging Interpolation Error

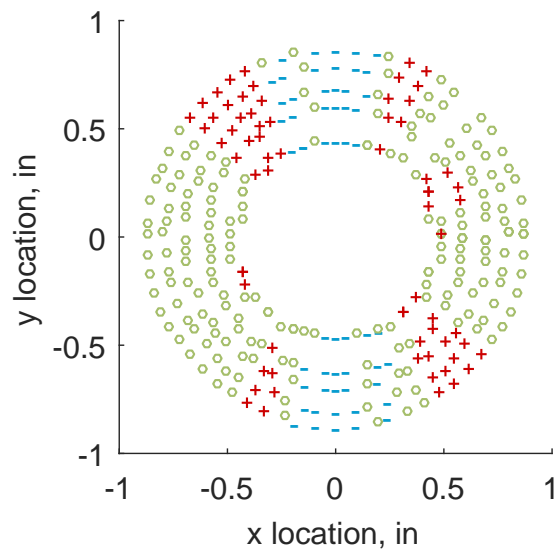
Figure C.197: Relative error for various interpolation schemes of run number R320, second clocking for the IMX inlet.



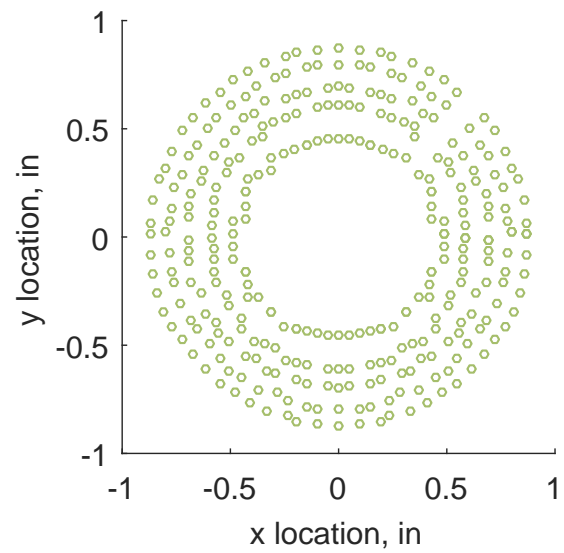
(a) Linear Interpolation



(b) Spline Interpolation



(c) Polar Interpolation



(d) Kriging Interpolation

Figure C.198: Interpolation error for the IMX inlet - symbols show locations that are within tolerance (o), over-predicted (+), and under-predicted (-).



Table C.88: Interpolation effects on the derived quantities for the IMX inlet run number R320, clocking C3.

	$K_\theta$	$K_r$	$K_a$	$IDC$	$IDT$
Linear	0.340	0.017	0.357	0.018	0.089
Spline	0.303	0.017	0.320	0.020	0.088
Polar	0.303	0.015	0.318	0.022	0.090
Kriging	0.303	0.015	0.318	0.020	0.088

#### C.2.3.4 Third Clocking

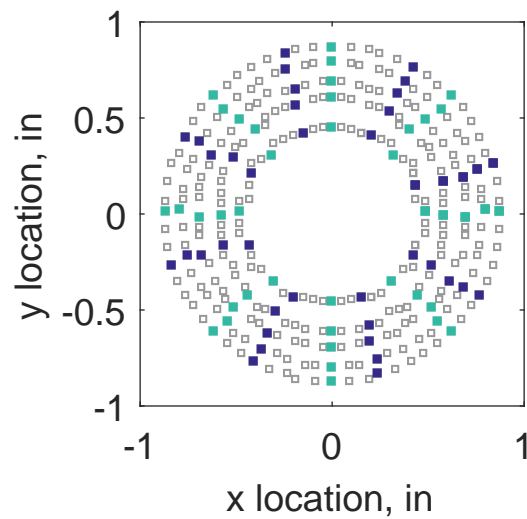


Figure C.199: Third clocking probe position

Table C.89: Interpolation results for the IMX inlet run number R320, clocking C4.

	Mean	Std. Dev.	Over-Prediction	In Tolerance	Under-Prediction
Linear	-0.0012	0.0040	44	178	58
Spline	-0.0016	0.0040	34	194	52
Polar	-0.0007	0.0048	83	133	64
Kriging	-0.0016	0.0017	1	270	9

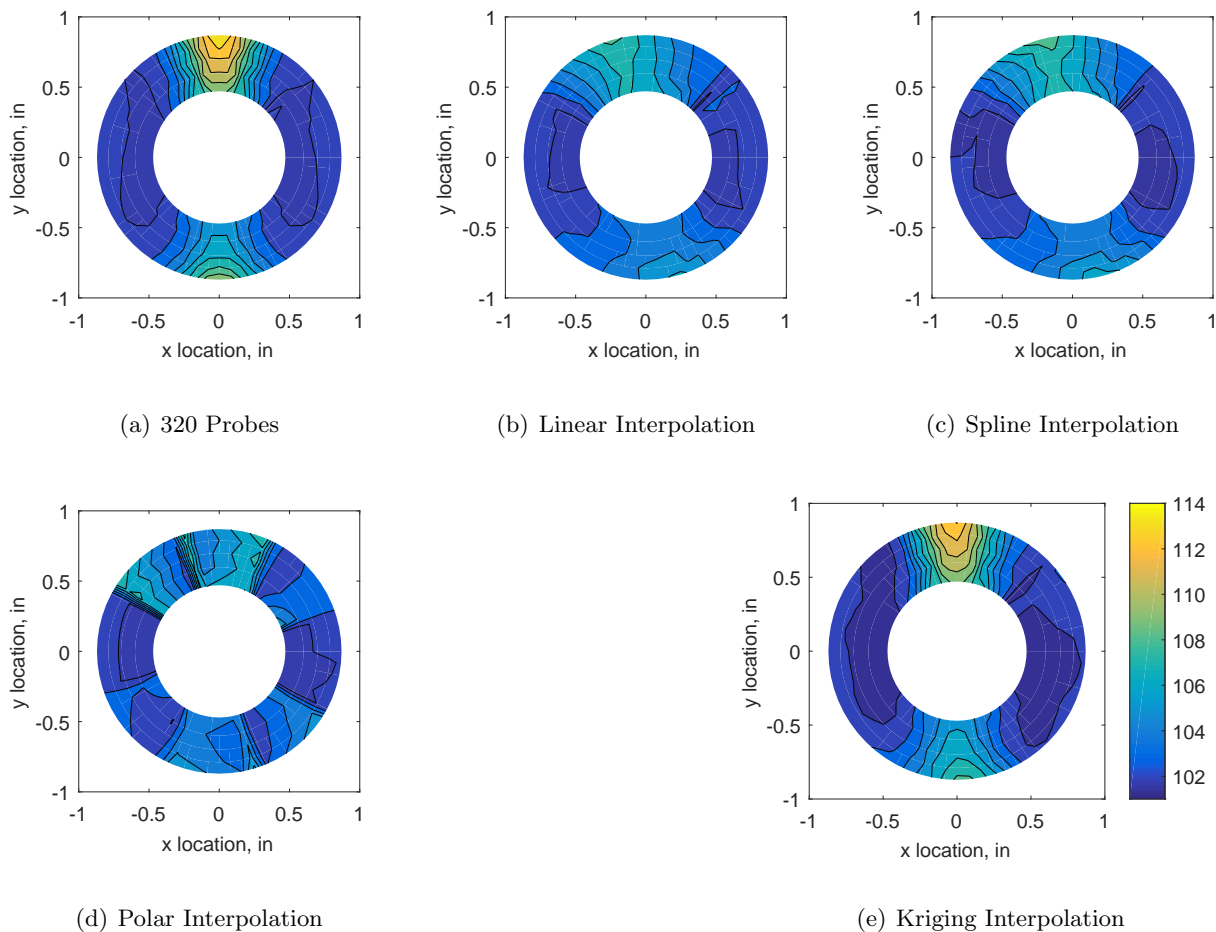
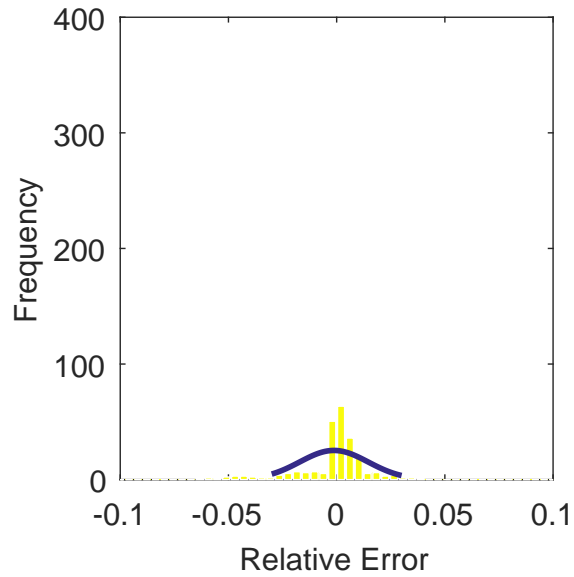
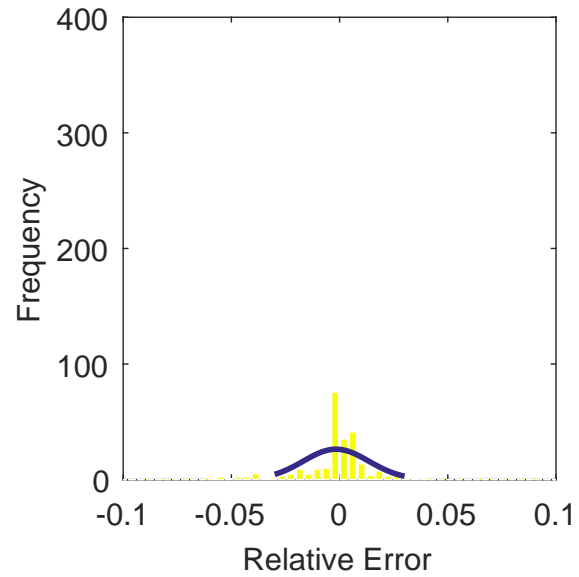


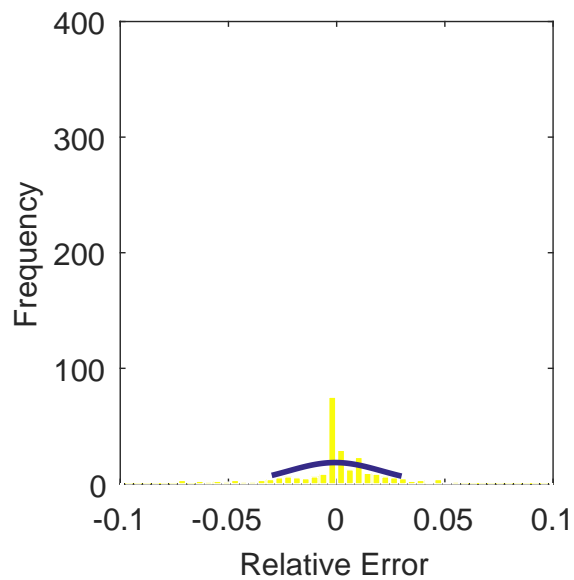
Figure C.200: Contour plots for the raw and interpolated values for the IMX inlet.



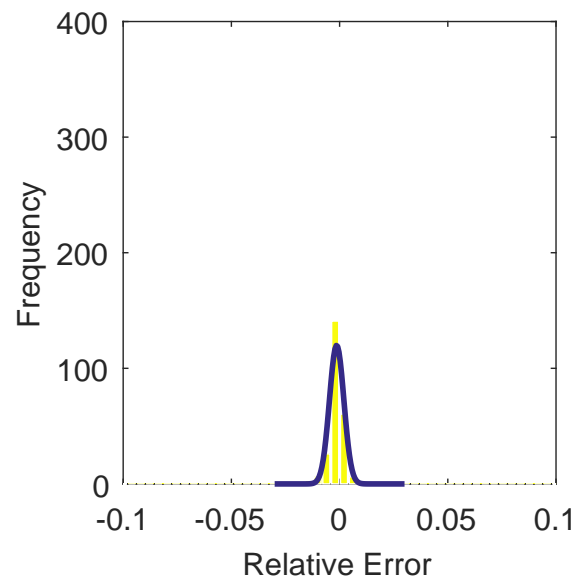
(a) Linear Interpolation Error



(b) Spline Interpolation Error

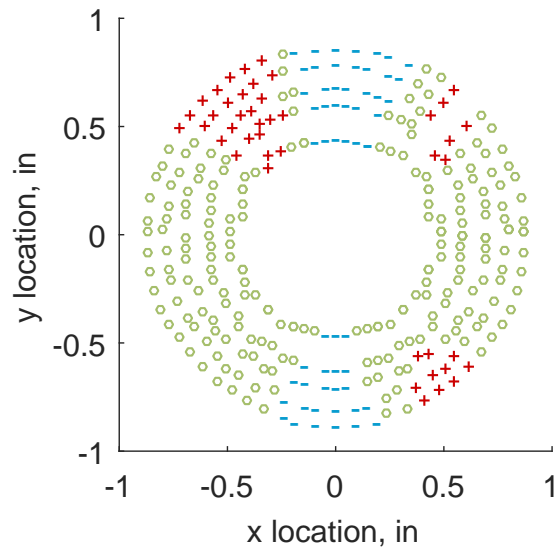


(c) Polar Interpolation Error

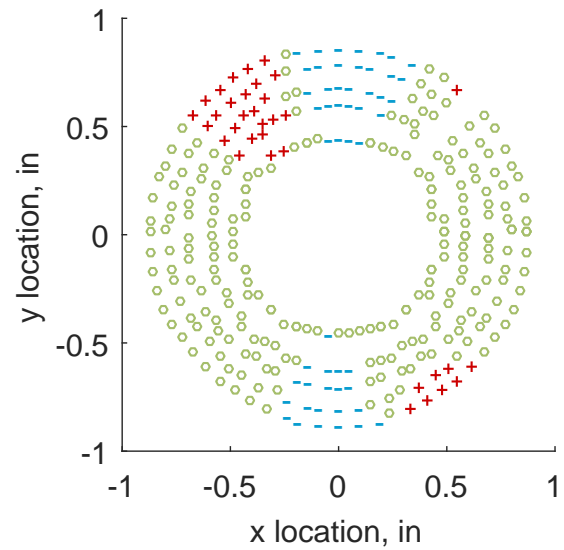


(d) Kriging Interpolation Error

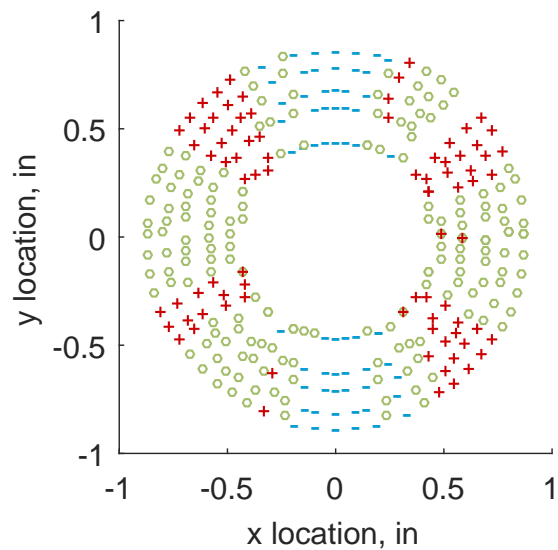
Figure C.201: Relative error for various interpolation schemes of run number R320, third clocking for the IMX inlet.



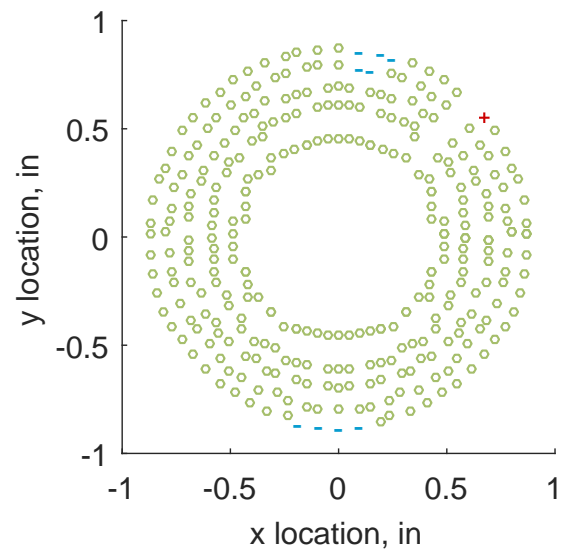
(a) Linear Interpolation



(b) Spline Interpolation



(c) Polar Interpolation



(d) Kriging Interpolation

Figure C.202: Interpolation error for the IMX inlet - symbols show locations that are within tolerance (o), over-predicted (+), and under-predicted (-).

Table C.90: Interpolation effects on the derived quantities for the IMX inlet run number R320, clocking C4.

	$K_\theta$	$K_r$	$K_a$	$IDC$	$IDT$
Linear	0.339	0.013	0.352	0.014	0.065
Spline	0.302	0.011	0.313	0.016	0.065
Polar	0.302	0.011	0.313	0.019	0.067
Kriging	0.302	0.015	0.317	0.018	0.065

### C.2.3.5 Fourth Clocking

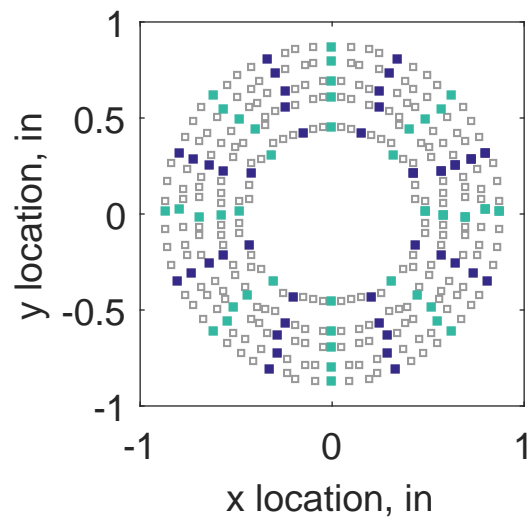
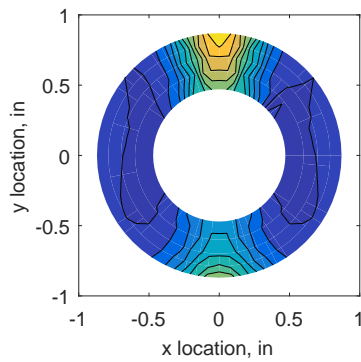


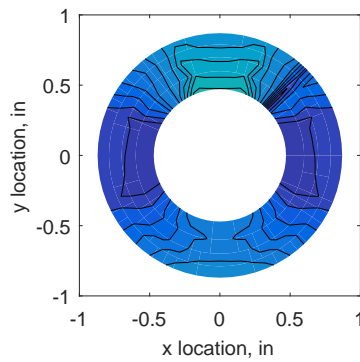
Figure C.203: Fourth clocking probe position

Table C.91: Interpolation results for the IMX inlet run number R320, clocking C5.

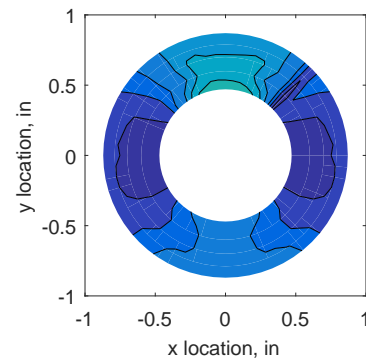
	Mean	Std. Dev.	Over-Prediction	In Tolerance	Under-Prediction
Linear	-0.0019	0.0050	52	170	58
Spline	-0.0023	0.0053	46	179	55
Polar	-0.0008	0.0052	82	124	74
Kriging	-0.0023	0.0067	127	98	55



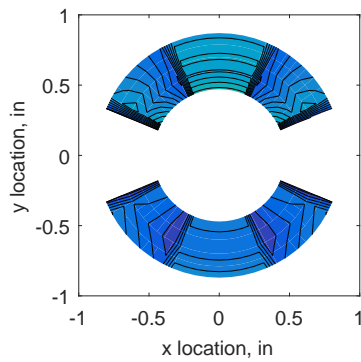
(a) 320 Probes



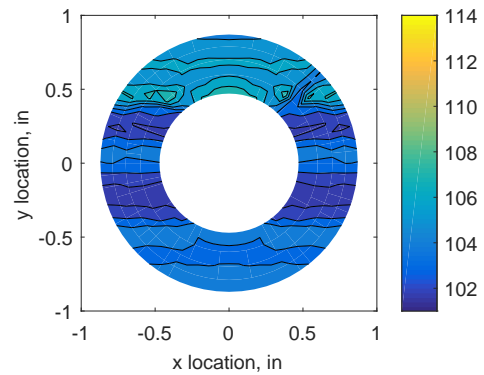
(b) Linear Interpolation



(c) Spline Interpolation

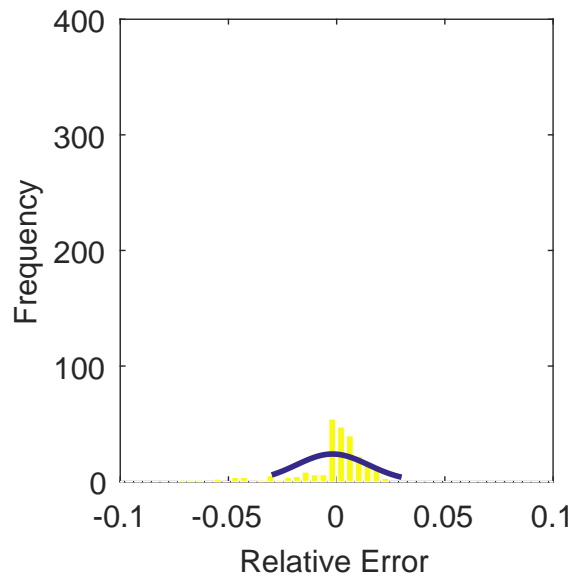


(d) Polar Interpolation

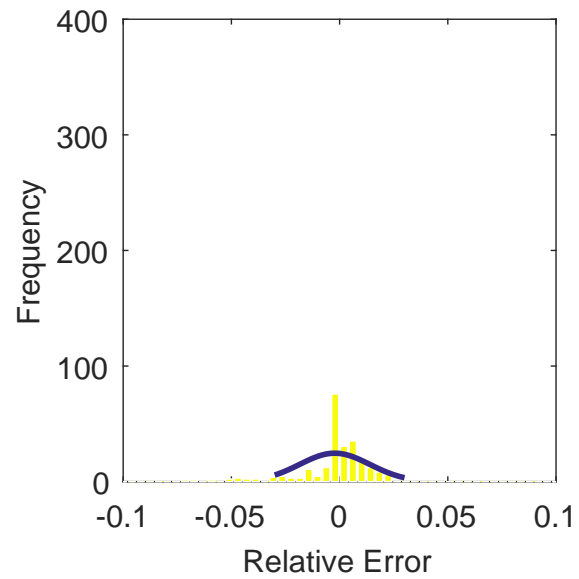


(e) Kriging Interpolation

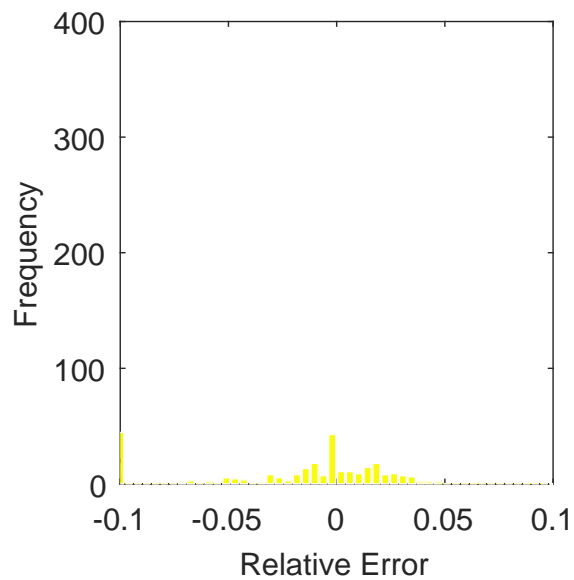
Figure C.204: Contour plots for the raw and interpolated values for the IMX inlet.



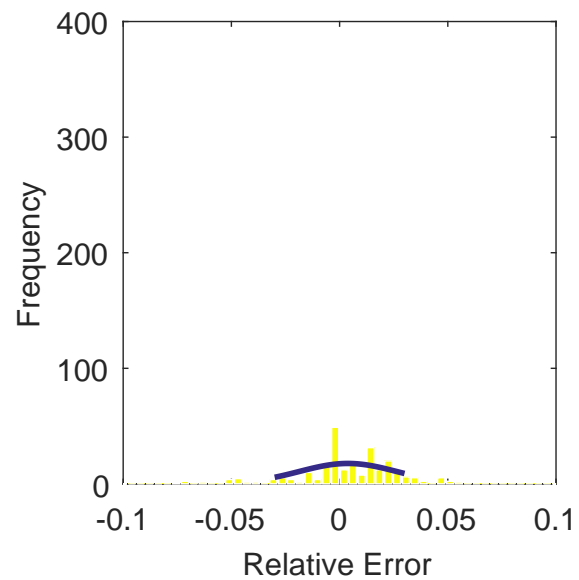
(a) Linear Interpolation Error



(b) Spline Interpolation Error

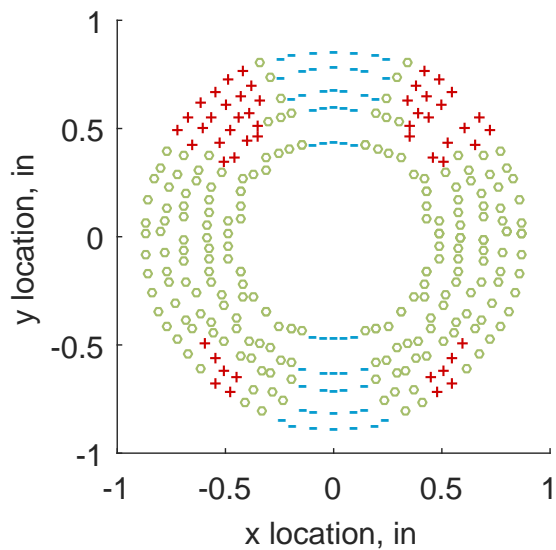


(c) Polar Interpolation Error

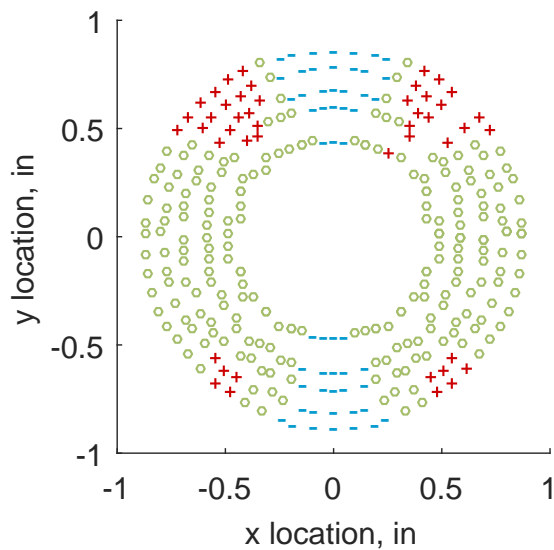


(d) Kriging Interpolation Error

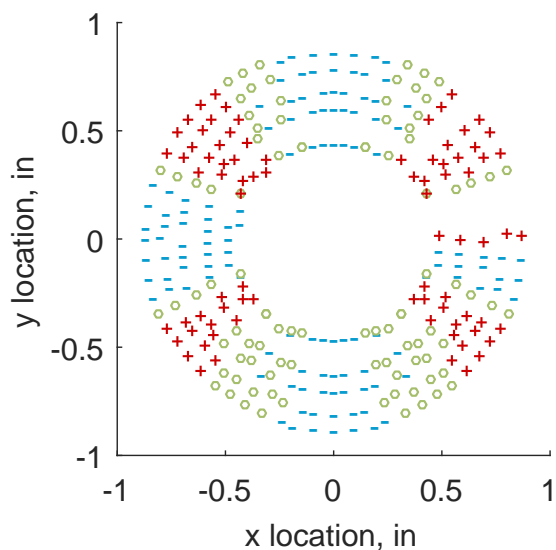
Figure C.205: Relative error for various interpolation schemes of run number R320, fourth clocking for the IMX inlet.



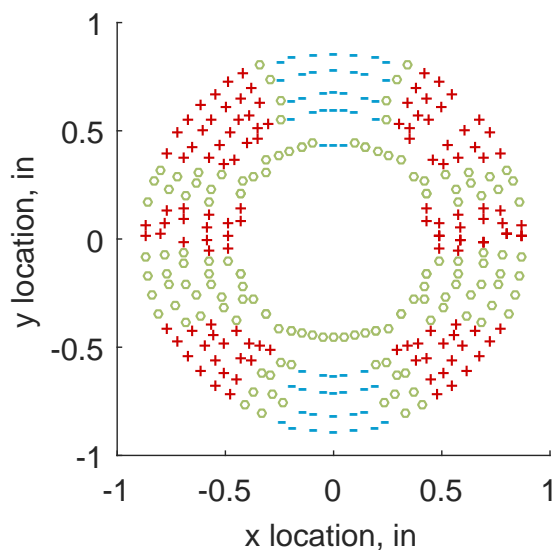
(a) Linear Interpolation



(b) Spline Interpolation



(c) Polar Interpolation



(d) Kriging Interpolation

Figure C.206: Interpolation error for the IMX inlet - symbols show locations that are within tolerance (o), over-predicted (+), and under-predicted (-).



Table C.92: Interpolation effects on the derived quantities for the IMX inlet run number R320, clocking C5.

	$K_\theta$	$K_r$	$K_a$	$IDC$	$IDT$
Linear	0.339	0.016	0.355	0.015	0.053
Spline	0.302	0.008	0.310	0.017	0.053
Polar	0.302	0.013	0.315	0.018	0.059
Kriging	NaN	NaN	NaN	NaN	NaN

### C.2.3.6 Fifth Clocking

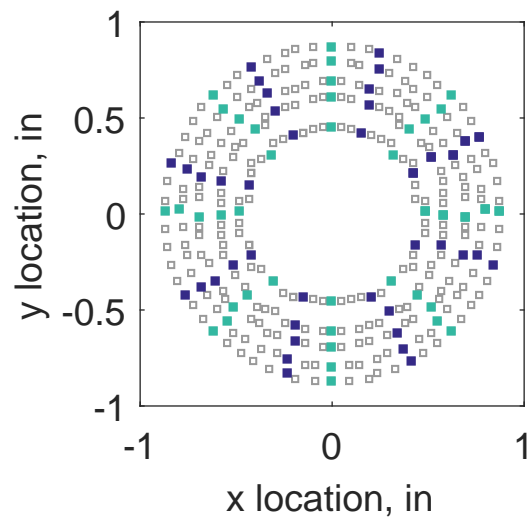
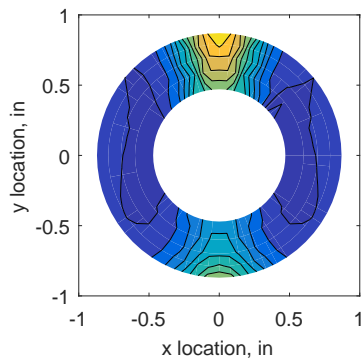


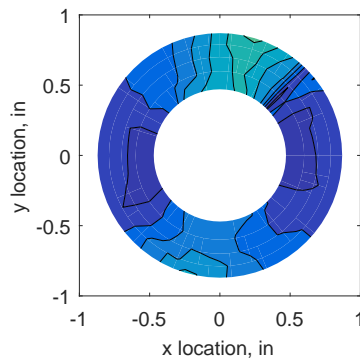
Figure C.207: Fifth clocking probe position

Table C.93: Interpolation results for the IMX inlet run number R320, clocking C6.

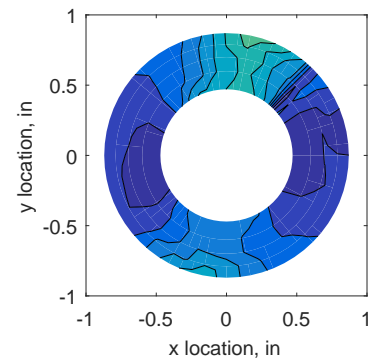
	Mean	Std. Dev.	Over-Prediction	In Tolerance	Under-Prediction
Linear	-0.0014	0.0040	43	179	58
Spline	-0.0018	0.0040	33	195	52
Polar	-0.0008	0.0047	82	134	64
Kriging	-0.0018	0.0019	0	270	10



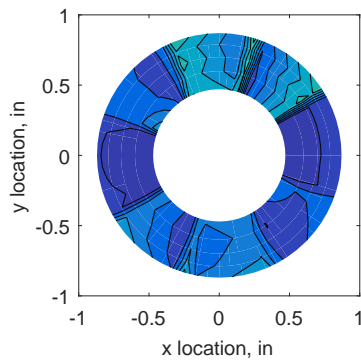
(a) 320 Probes



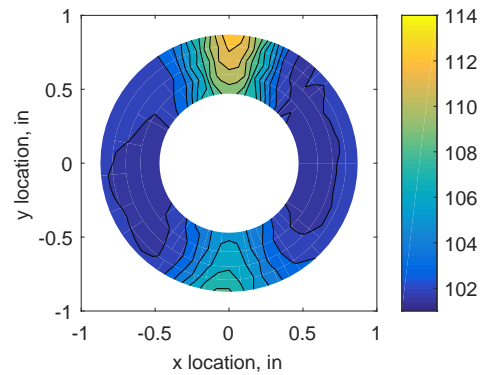
(b) Linear Interpolation



(c) Spline Interpolation

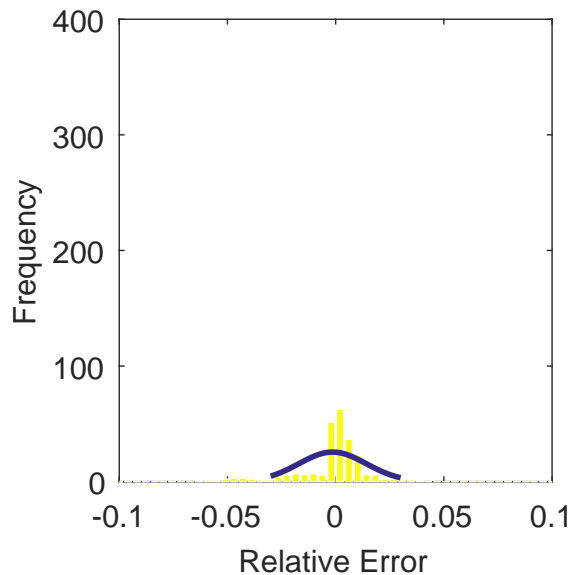


(d) Polar Interpolation

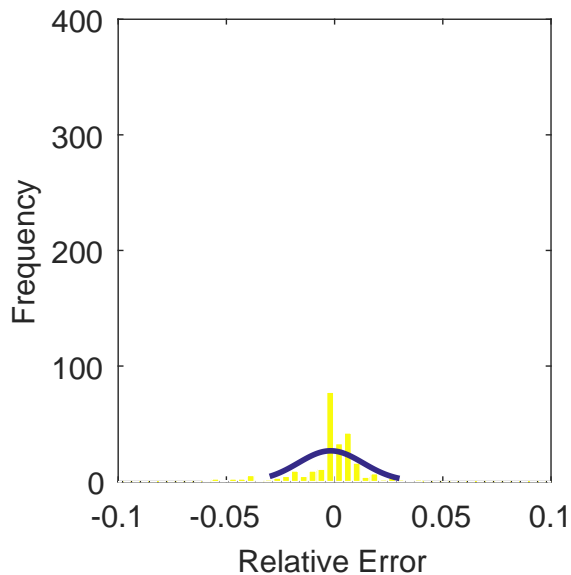


(e) Kriging Interpolation

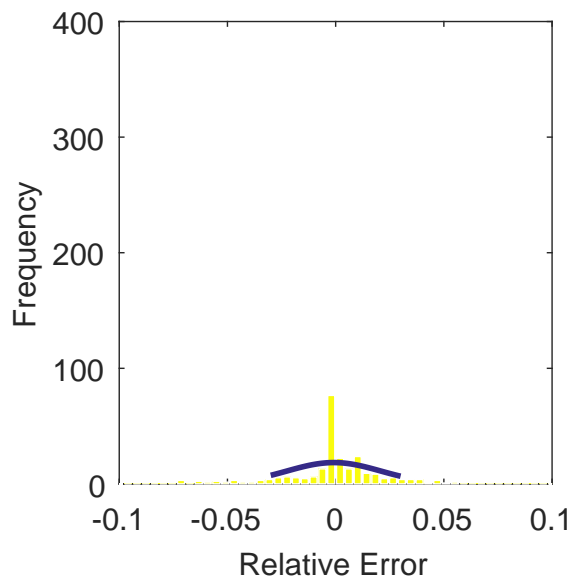
Figure C.208: Contour plots for the raw and interpolated values for the IMX inlet.



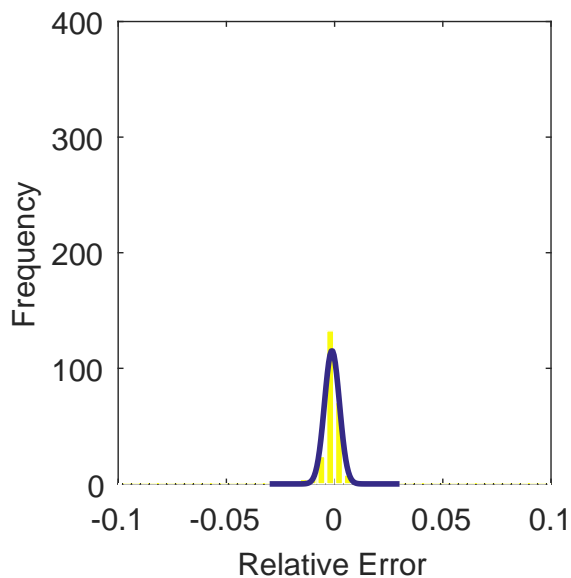
(a) Linear Interpolation Error



(b) Spline Interpolation Error

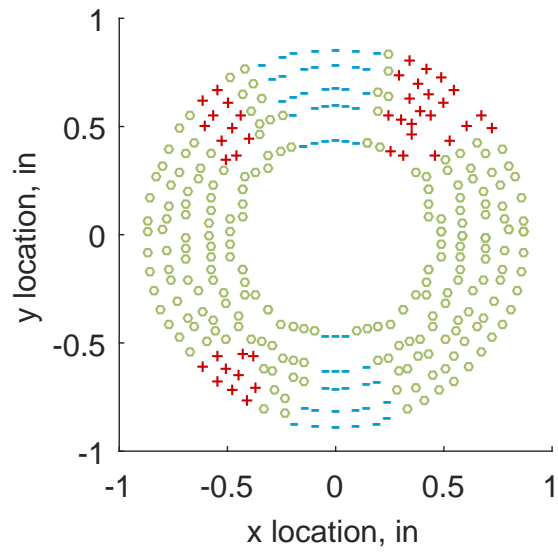


(c) Polar Interpolation Error

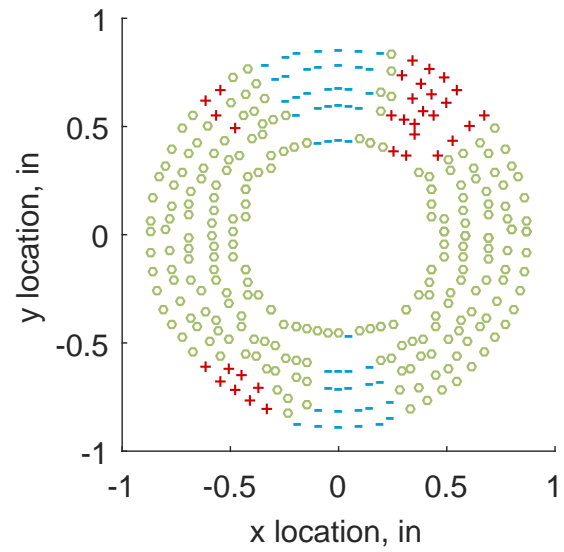


(d) Kriging Interpolation Error

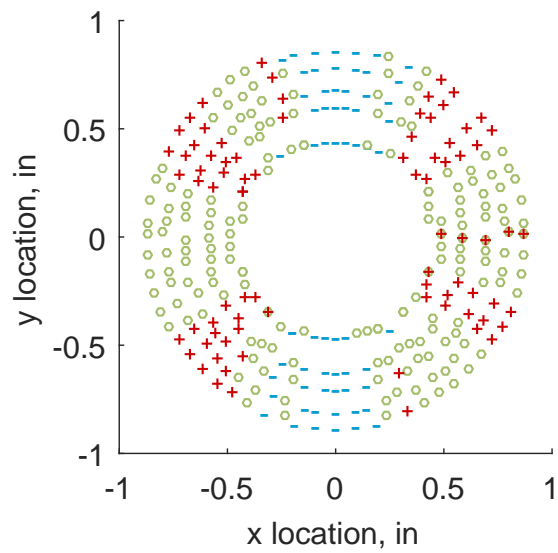
Figure C.209: Relative error for various interpolation schemes of run number R320, fifth clocking for the IMX inlet.



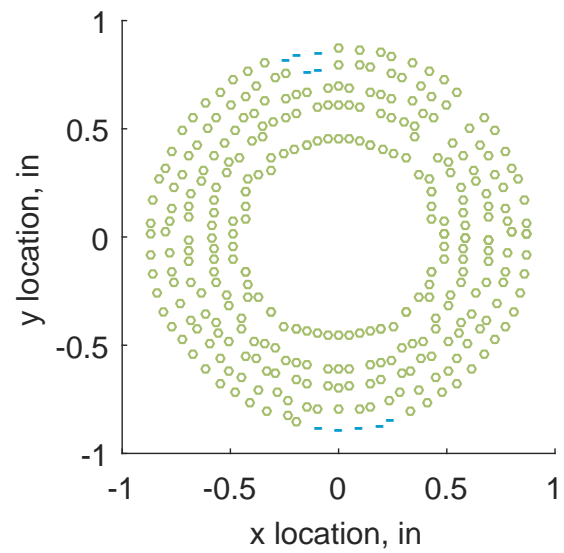
(a) Linear Interpolation



(b) Spline Interpolation



(c) Polar Interpolation



(d) Kriging Interpolation

Figure C.210: Interpolation error for the IMX inlet - symbols show locations that are within tolerance (o), over-predicted (+), and under-predicted (-).

Table C.94: Interpolation effects on the derived quantities for the IMX inlet run number R320, clocking C6.

	$K_\theta$	$K_r$	$K_a$	$IDC$	$IDT$
Linear	0.339	0.013	0.352	0.014	0.065
Spline	0.302	0.011	0.313	0.016	0.065
Polar	0.302	0.012	0.314	0.018	0.067
Kriging	0.302	0.016	0.318	0.017	0.065

### C.2.3.7 Sixth Clocking

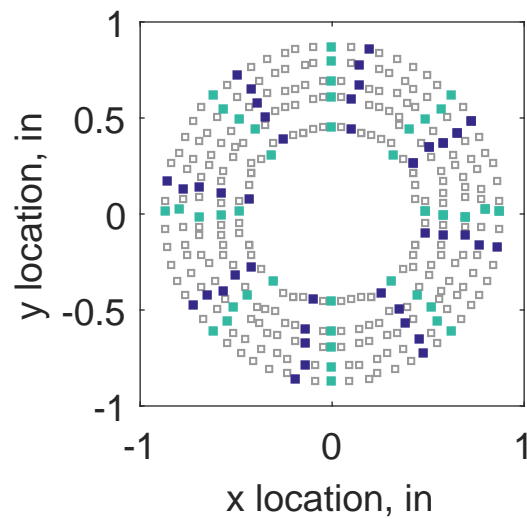


Figure C.211: Sixth clocking probe position

Table C.95: Interpolation results for the IMX inlet run number R320, clocking C7.

	Mean	Std. Dev.	Over-Prediction	In Tolerance	Under-Prediction
Linear	0.0007	0.0036	40	199	41
Spline	0.0003	0.0036	38	200	42
Polar	0.0012	0.0048	68	156	56
Kriging	0.0003	0.0012	0	280	0

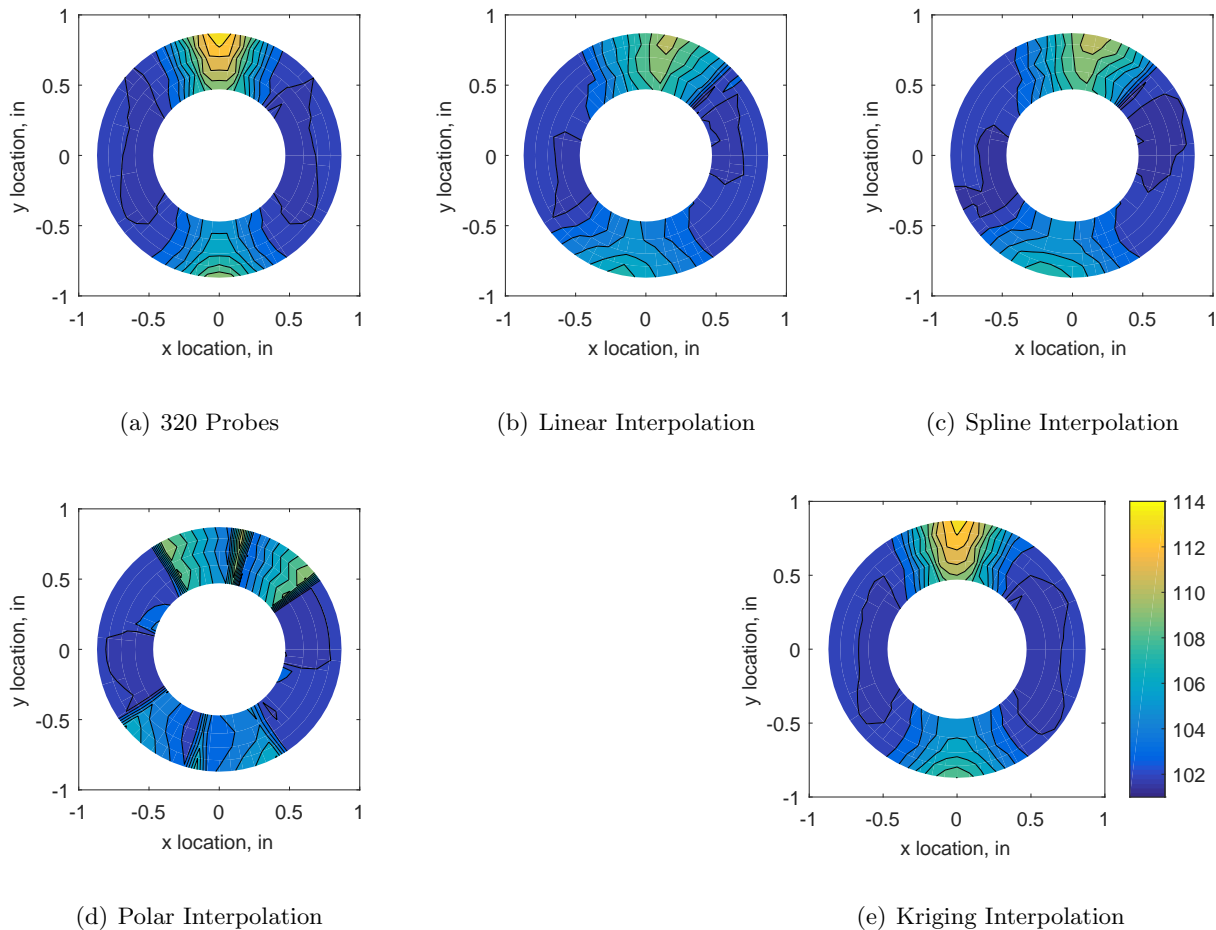
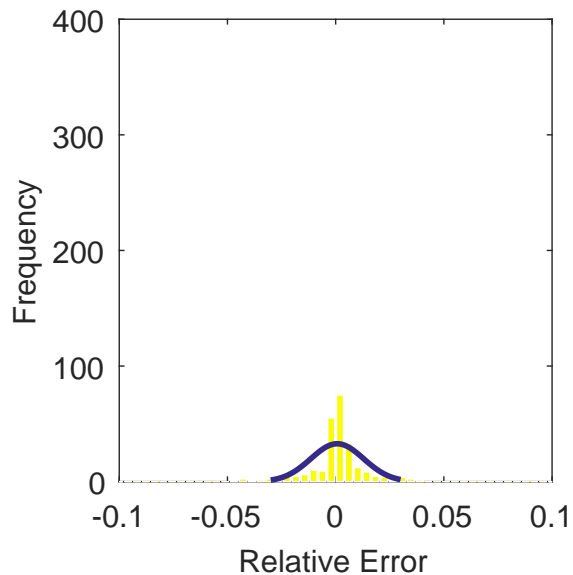
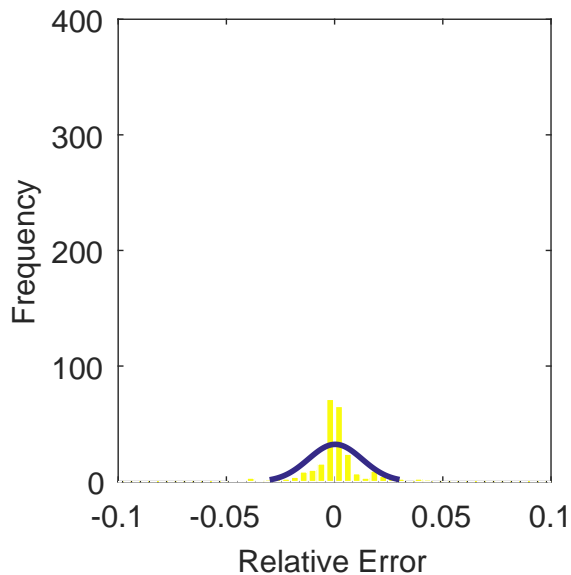


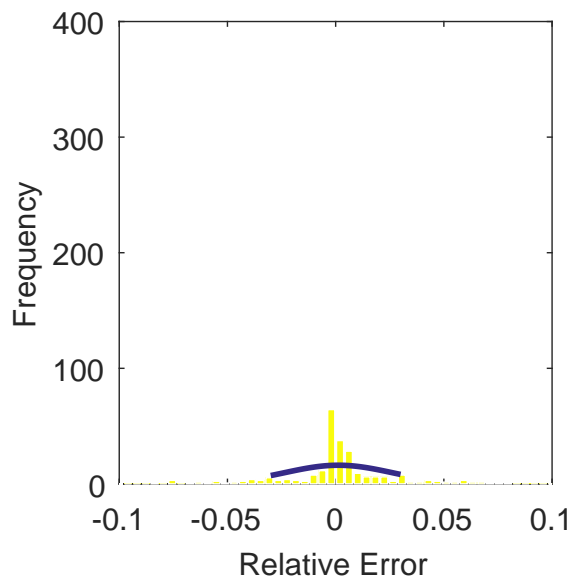
Figure C.212: Contour plots for the raw and interpolated values for the IMX inlet.



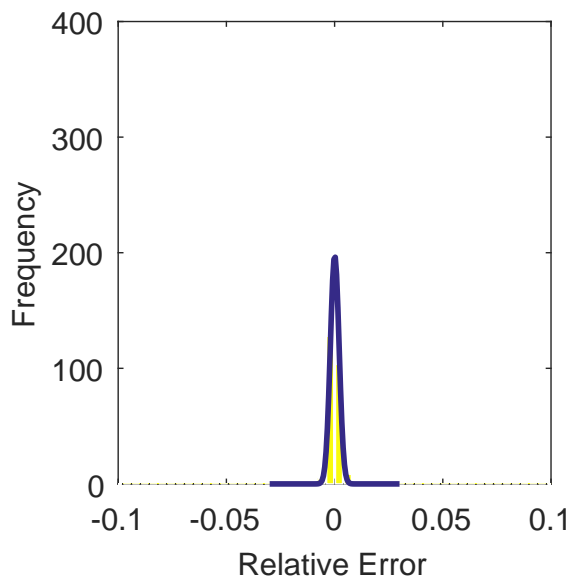
(a) Linear Interpolation Error



(b) Spline Interpolation Error

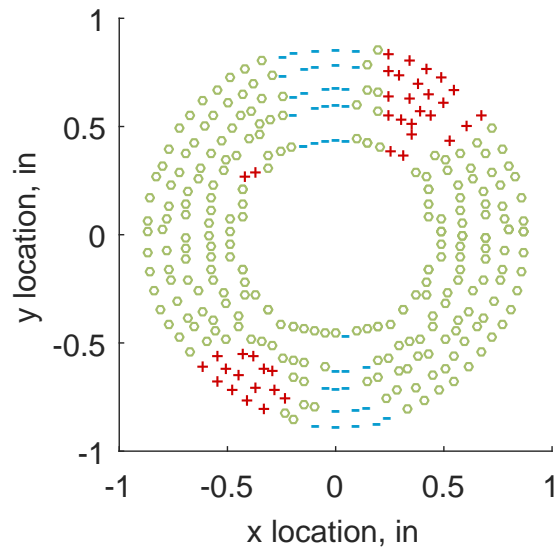


(c) Polar Interpolation Error

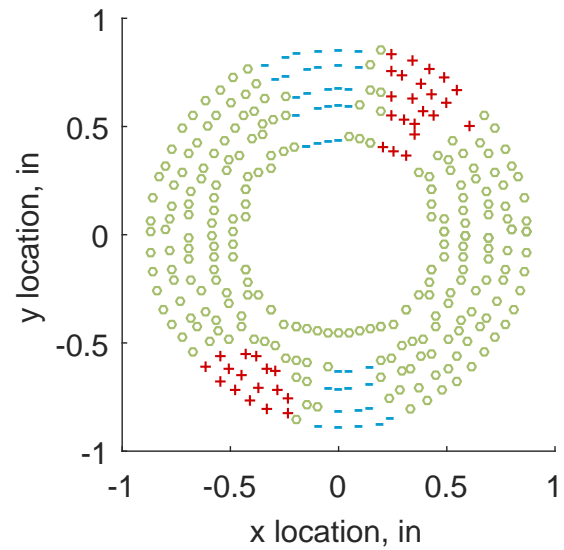


(d) Kriging Interpolation Error

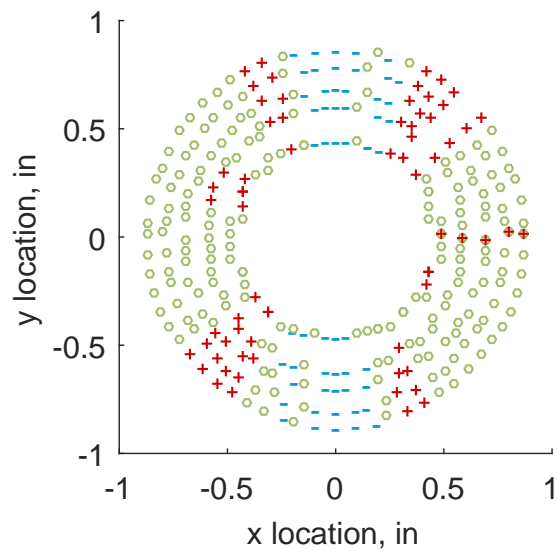
Figure C.213: Relative error for various interpolation schemes of run number R320, sixth clocking for the IMX inlet.



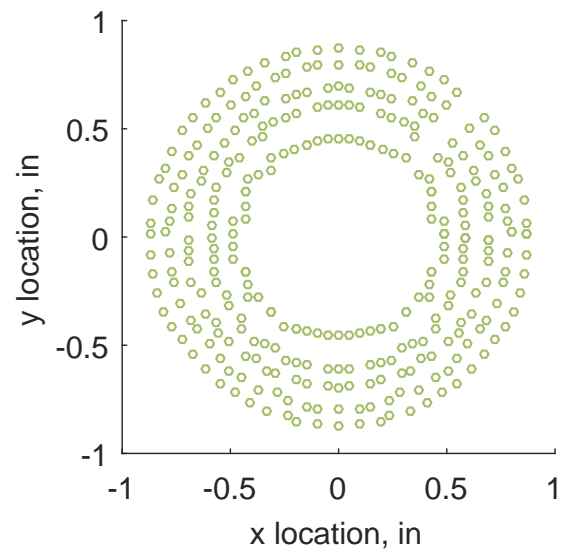
(a) Linear Interpolation



(b) Spline Interpolation



(c) Polar Interpolation



(d) Kriging Interpolation

Figure C.214: Interpolation error for the IMX inlet - symbols show locations that are within tolerance (o), over-predicted (+), and under-predicted (-).



Table C.96: Interpolation effects on the derived quantities for the IMX inlet run number R320, clocking C7.

	$K_\theta$	$K_r$	$K_a$	$IDC$	$IDT$
Linear	0.340	0.015	0.355	0.017	0.089
Spline	0.303	0.017	0.319	0.020	0.088
Polar	0.303	0.015	0.317	0.022	0.090
Kriging	0.303	0.014	0.317	0.020	0.088

### C.2.3.8 Seventh Clocking

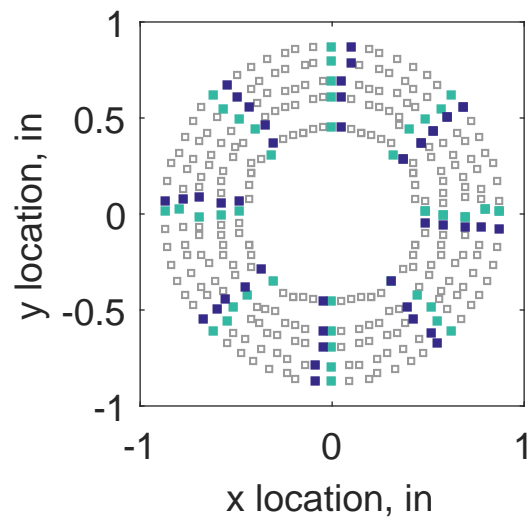


Figure C.215: Seventh clocking probe position

Table C.97: Interpolation results for the IMX inlet run number R320, clocking C8.

	Mean	Std. Dev.	Over-Prediction	In Tolerance	Under-Prediction
Linear	0.0029	0.0033	39	226	15
Spline	0.0021	0.0028	38	236	6
Polar	0.0035	0.0055	70	158	52
Kriging	0.0021	0.0013	8	272	0

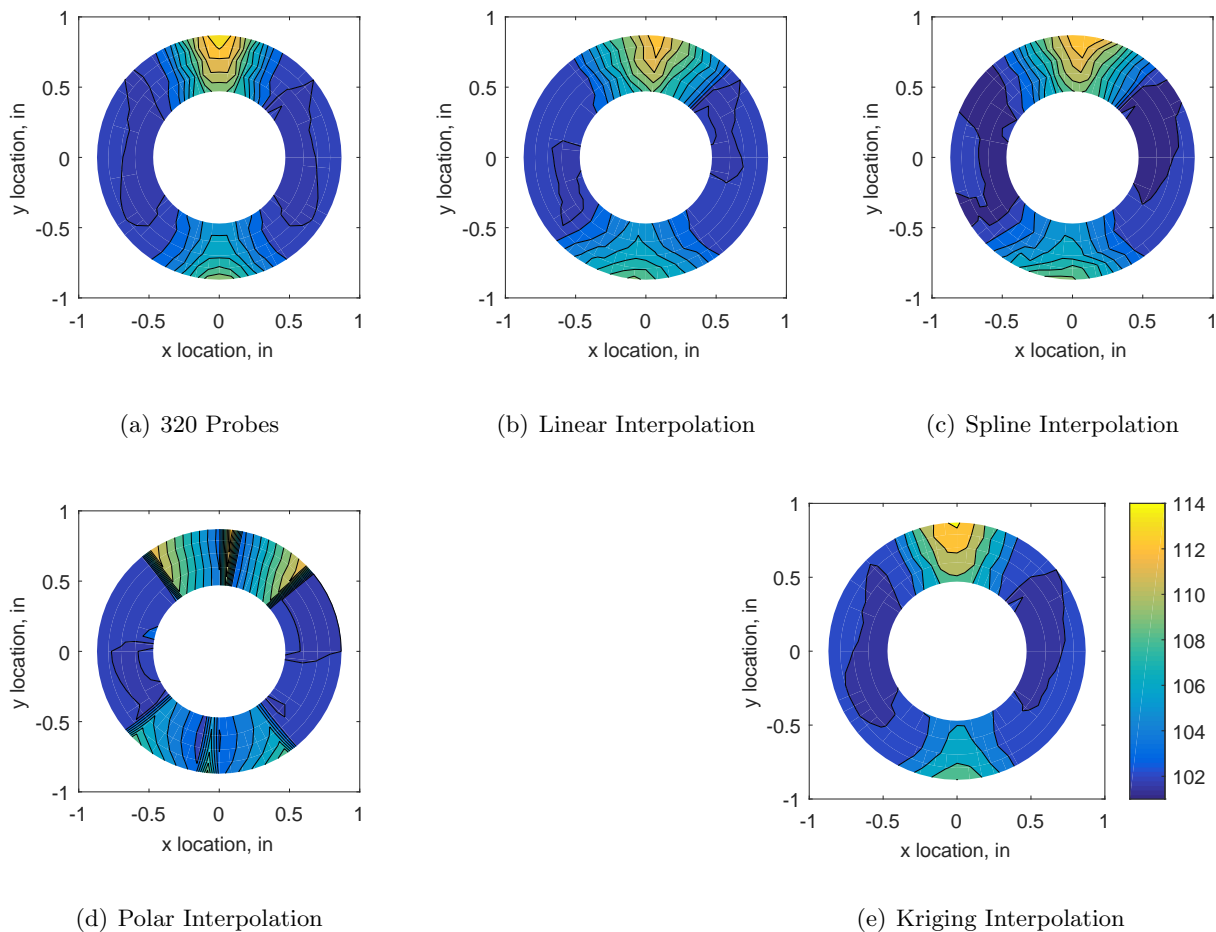
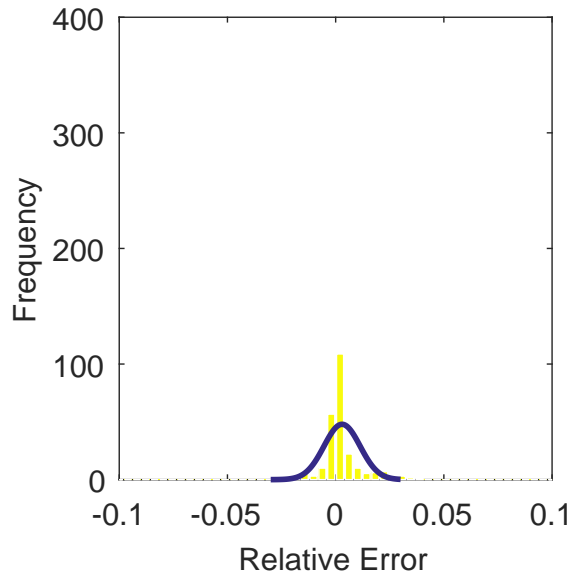
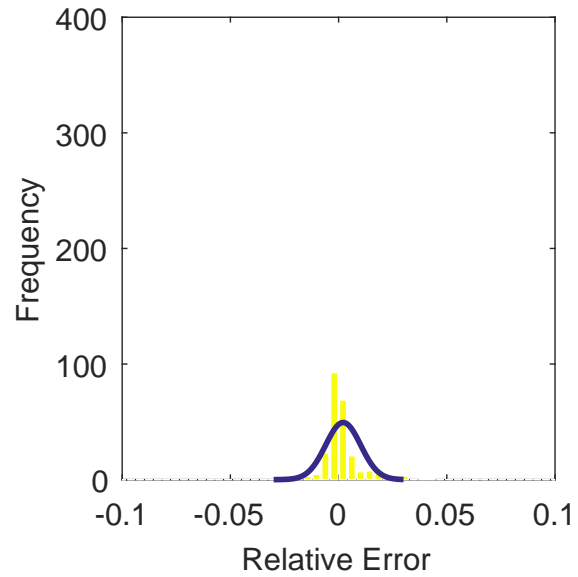


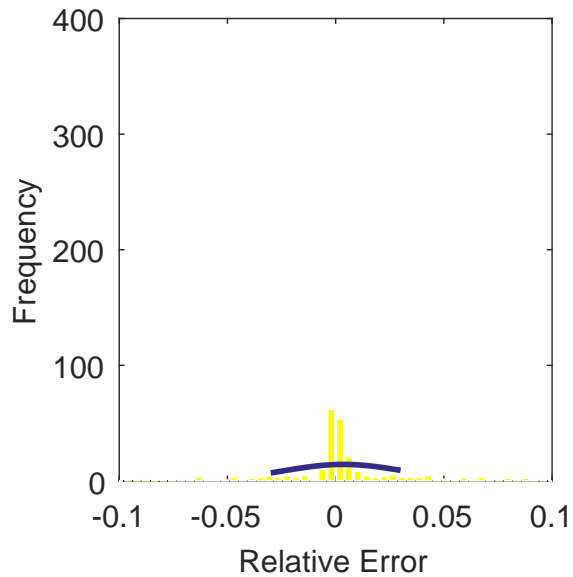
Figure C.216: Contour plots for the raw and interpolated values for the IMX inlet.



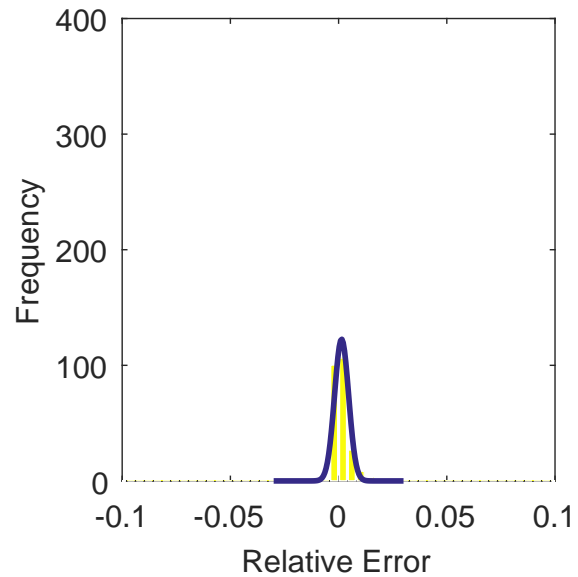
(a) Linear Interpolation Error



(b) Spline Interpolation Error

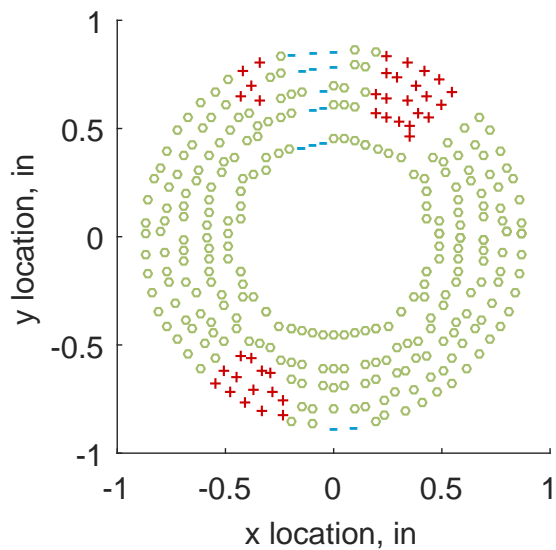


(c) Polar Interpolation Error

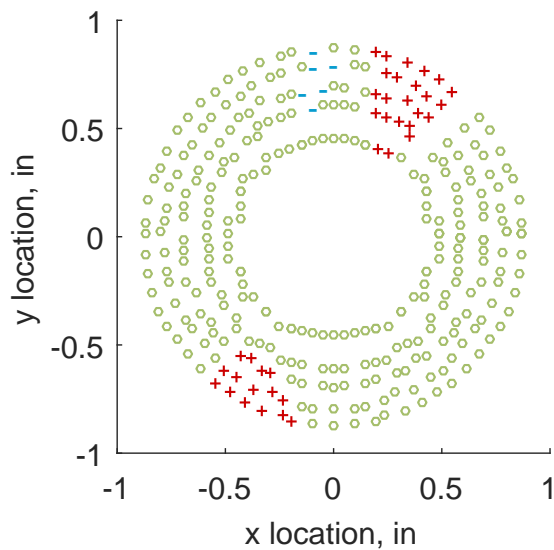


(d) Kriging Interpolation Error

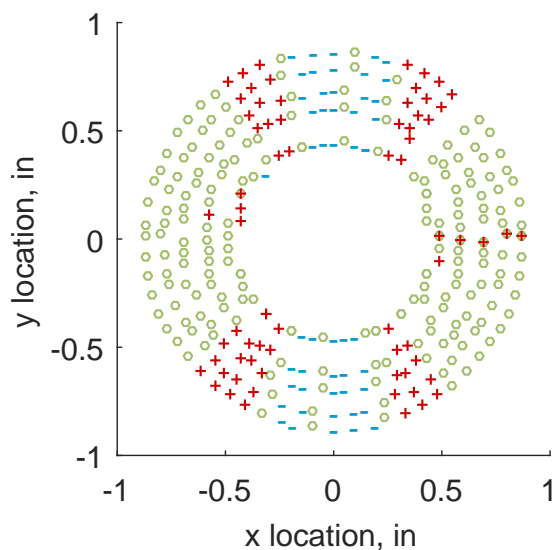
Figure C.217: Relative error for various interpolation schemes of run number R320, seventh clocking for the IMX inlet.



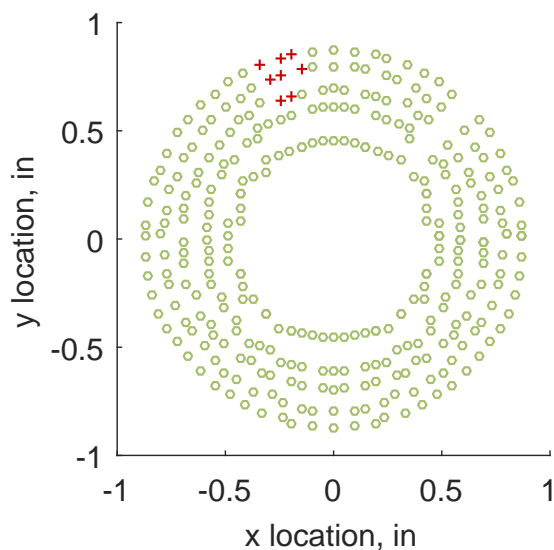
(a) Linear Interpolation



(b) Spline Interpolation



(c) Polar Interpolation



(d) Kriging Interpolation

Figure C.218: Interpolation error for the IMX inlet - symbols show locations that are within tolerance (o), over-predicted (+), and under-predicted (-).

Table C.98: Interpolation effects on the derived quantities for the IMX inlet run number R320, clocking C8.

	$K_\theta$	$K_r$	$K_a$	$IDC$	$IDT$
Linear	0.340	0.021	0.362	0.021	0.109
Spline	0.303	0.029	0.333	0.024	0.109
Polar	0.303	0.026	0.329	0.029	0.114
Kriging	0.303	0.022	0.326	0.024	0.109

### C.3 Tabulation of Results

#### C.3.1 Accuracy – Mean of the Error

Table C.99: Mean of the error results for the YF12 inlet

	Linear	Kriging	Spline	Polar
TC1C1	-0.166	-0.317	-0.212	-0.225
TC1C2	0.045	-0.121	-0.004	0.008
TC1C3	0.148	-0.032	0.098	0.105
TC1C4	0.171	0.010	0.137	0.174
TC1C5	0.171	0.083	0.128	0.152
TC1C6	0.150	-0.092	0.098	0.097
TC1C7	0.048	-0.141	0.013	0.028
TC2C1	-0.044	-0.132	-0.075	-0.082
TC2C2	0.070	-0.079	0.030	0.027
TC2C3	0.192	-0.002	0.139	0.125
TC2C4	0.135	-0.039	0.094	0.071
TC2C5	0.070	-0.087	0.027	-0.010
TC2C6	0.025	-0.112	-0.009	-0.042
TC2C7	-0.023	-0.108	-0.055	-0.081
TC3C1	-0.081	-0.159	-0.108	-0.093
TC3C2	0.051	-0.067	0.009	0.021
TC3C3	0.097	-0.008	0.052	0.067
TC3C4	0.070	-0.042	0.023	0.023
TC3C5	0.113	-0.016	0.062	0.045
TC3C6	0.119	0.009	0.073	0.045
TC3C7	0.085	-0.040	0.040	0.008

Table C.100: Mean of the error results for the IMX inlet

	Linear	Spline	Polar	Kriging
R300C1	0.0023	0.0022	0.0031	0.0015
R300C2	0.0024	0.0019	0.0027	0.0009
R300C3	0.0007	0.0004	0.0009	0.0001
R300C4	-0.0012	-0.0014	-0.0008	-0.0013
R300C5	-0.0018	-0.0020	0.0230	0.0021
R300C6	-0.0013	-0.0016	-0.0009	-0.0011
R300C7	0.0005	0.0002	0.0008	0.0001
R310C1	0.0027	0.0024	0.0037	0.0026
R310C2	0.0030	0.0021	0.0033	0.0013
R310C3	0.0011	0.0006	0.0013	0.0002
R310C4	-0.0011	-0.0015	-0.0007	-0.0012
R310C5	-0.0018	-0.0022	0.0769	0.0024
R310C6	-0.0013	-0.0018	-0.0009	-0.0013
R310C7	0.0008	0.0004	0.0012	0.0000
R320C1	0.0029	0.0027	0.0040	0.0028
R320C2	0.0031	0.0022	0.0036	0.0014
R320C3	0.0009	0.0005	0.0013	0.0001
R320C4	-0.0012	-0.0016	-0.0007	-0.0014
R320C5	-0.0019	-0.0023	0.0035	0.0041
R320C6	-0.0014	-0.0018	-0.0008	-0.0012
R320C7	0.0007	0.0003	0.0012	0.0000

### C.3.2 Precision – Standard Deviation of the Error

Table C.101: Standard deviation of the error results for the YF12 inlet

	Linear	Kriging	Spline	Polar
TC1C1	0.204	0.252	0.189	0.182
TC1C2	0.195	0.255	0.190	0.160
TC1C3	0.191	0.244	0.179	0.197
TC1C4	0.215	0.240	0.208	0.168
TC1C5	0.174	0.357	0.165	0.176
TC1C6	0.138	0.249	0.111	0.170
TC1C7	0.163	0.245	0.141	0.161
TC2C1	0.161	0.202	0.142	0.118
TC2C2	0.125	0.164	0.112	0.109
TC2C3	0.145	0.135	0.162	0.139
TC2C4	0.136	0.151	0.127	0.090
TC2C5	0.119	0.165	0.106	0.101
TC2C6	0.107	0.177	0.094	0.094
TC2C7	0.121	0.202	0.106	0.102
TC3C1	0.122	0.170	0.112	0.149
TC3C2	0.084	0.160	0.081	0.109
TC3C3	0.076	0.116	0.083	0.090
TC3C4	0.078	0.111	0.083	0.074
TC3C5	0.081	0.209	0.089	0.072
TC3C6	0.072	0.111	0.074	0.061
TC3C7	0.067	0.130	0.065	0.061



Table C.102: Standard deviation of the error results for the IMX inlet

	Linear	Spline	Polar	Kriging
R300C1	0.0026	0.0025	0.0040	0.0016
R300C2	0.0024	0.0021	0.0039	0.0010
R300C3	0.0024	0.0025	0.0034	0.0010
R300C4	0.0026	0.0027	0.0034	0.0012
R300C5	0.0034	0.0037	0.0037	0.0048
R300C6	0.0026	0.0027	0.0034	0.0012
R300C7	0.0024	0.0025	0.0033	0.0009
R310C1	0.0031	0.0029	0.0056	0.0021
R310C2	0.0030	0.0025	0.0056	0.0011
R310C3	0.0034	0.0035	0.0049	0.0018
R310C4	0.0038	0.0039	0.0046	0.0016
R310C5	0.0048	0.0050	0.0049	0.0064
R310C6	0.0038	0.0038	0.0045	0.0018
R310C7	0.0034	0.0035	0.0047	0.0019
R320C1	0.0034	0.0032	0.0061	0.0024
R320C2	0.0033	0.0028	0.0059	0.0013
R320C3	0.0036	0.0036	0.0050	0.0011
R320C4	0.0040	0.0040	0.0048	0.0017
R320C5	0.0050	0.0053	0.0052	0.0067
R320C6	0.0040	0.0040	0.0047	0.0019
R320C7	0.0036	0.0036	0.0048	0.0012

### C.3.3 Location Prediction – In Tolerance

Table C.103: Locations where the interpolation results are within 1% tolerance for the YF12 inlet - note, the original 40 locations are not included.

	Linear	Spline	Polar	Kriging
TC1C1	5	3	6	5
TC1C2	5	4	6	5
TC1C3	9	6	4	6
TC1C4	3	7	5	5
TC1C5	9	2	7	12
TC1C6	10	5	9	10
TC1C7	8	4	7	21
TC2C1	10	8	9	9
TC2C2	5	10	9	2
TC2C3	8	7	13	9
TC2C4	3	9	10	9
TC2C5	9	13	11	13
TC2C6	14	5	12	12
TC2C7	12	11	13	23
TC3C1	12	12	25	11
TC3C2	9	12	18	7
TC3C3	10	16	7	5
TC3C4	12	15	8	11
TC3C5	11	6	24	15
TC3C6	15	9	18	13
TC3C7	19	10	18	23

Table C.104: Locations where the interpolation results are within 1% tolerance for the IMX inlet - note, the original 40 locations are not included.

	Linear	Spline	Polar	Kriging
R300C1	246	244	170	268
R300C2	238	245	166	274
R300C3	209	208	165	280
R300C4	198	205	156	278
R300C5	209	204	75	126
R300C6	202	209	157	278
R300C7	213	211	165	280
R310C1	230	234	161	250
R310C2	225	235	162	277
R310C3	192	194	160	275
R310C4	176	195	137	274
R310C5	170	177	60	115
R310C6	177	197	136	272
R310C7	197	198	160	278
R320C1	234	234	149	258
R320C2	222	236	159	271
R320C3	194	196	155	280
R320C4	178	194	133	270
R320C5	170	179	54	98
R320C6	179	195	134	270
R320C7	199	200	156	280

### C.3.4 Location Prediction – Under-Shot

Table C.105: Locations where the interpolation results are under tolerance for the YF12 inlet

	Linear	Spline	Polar	Kriging
TC1C1	176	198	192	215
TC1C2	114	147	133	154
TC1C3	97	143	108	135
TC1C4	100	132	97	120
TC1C5	89	133	91	116
TC1C6	98	167	109	130
TC1C7	131	172	140	151
TC2C1	126	159	148	165
TC2C2	92	135	111	133
TC2C3	54	114	76	120
TC2C4	77	127	92	124
TC2C5	86	151	114	128
TC2C6	102	167	129	148
TC2C7	131	152	158	164
TC3C1	161	167	189	183
TC3C2	82	127	109	133
TC3C3	67	111	96	115
TC3C4	93	142	117	138
TC3C5	61	134	88	125
TC3C6	52	106	82	118
TC3C7	78	123	110	147

Table C.106: Locations where the interpolation results are under tolerance for the IMX inlet

	Linear	Spline	Polar	Kriging
R300C1	0	0	40	0
R300C2	5	0	50	0
R300C3	35	33	52	0
R300C4	52	48	61	2
R300C5	54	52	64	53
R300C6	52	48	61	2
R300C7	35	33	52	0
R310C1	4	0	46	0
R310C2	13	7	52	0
R310C3	43	42	53	2
R310C4	59	53	64	6
R310C5	58	56	68	58
R310C6	59	53	64	8
R310C7	43	42	53	2
R320C1	2	0	50	0
R320C2	15	6	51	0
R320C3	41	42	56	0
R320C4	58	52	64	9
R320C5	58	55	74	55
R320C6	58	52	64	10
R320C7	41	42	56	0

### C.3.5 Location Prediction – Over-Shot

Table C.107: Locations where the interpolation results are under tolerance for the YF12 inlet

	Linear	Spline	Polar	Kriging
TC1C1	99	79	82	100
TC1C2	161	129	141	161
TC1C3	174	131	168	179
TC1C4	177	141	178	195
TC1C5	182	145	182	192
TC1C6	172	108	162	180
TC1C7	141	104	133	148
TC2C1	144	113	123	146
TC2C2	183	135	160	185
TC2C3	218	159	191	191
TC2C4	200	144	178	187
TC2C5	185	116	155	179
TC2C6	164	108	139	160
TC2C7	137	117	109	133
TC3C1	107	101	66	126
TC3C2	189	141	153	180
TC3C3	203	153	177	200
TC3C4	175	123	155	171
TC3C5	208	140	168	180
TC3C6	213	165	180	189
TC3C7	183	147	152	150

Table C.108: Locations where the interpolation results are under tolerance for the IMX inlet

	Linear	Spline	Polar	Kriging
R300C1	34	36	70	12
R300C2	37	35	64	6
R300C3	36	39	63	0
R300C4	30	27	63	0
R300C5	17	24	71	101
R300C6	26	23	62	0
R300C7	32	36	63	0
R310C1	46	46	73	30
R310C2	42	38	66	3
R310C3	45	44	67	3
R310C4	45	32	79	0
R310C5	52	47	82	107
R310C6	44	30	80	0
R310C7	40	40	67	0
R320C1	44	46	81	22
R320C2	43	38	70	9
R320C3	45	42	69	0
R320C4	44	34	83	1
R320C5	52	46	82	127
R320C6	43	33	82	0
R320C7	40	38	68	0